



HAL
open science

Modeling and design of thermomechanical conversion systems for thermal energy harvesting applications

Arthur Arnaud

► **To cite this version:**

Arthur Arnaud. Modeling and design of thermomechanical conversion systems for thermal energy harvesting applications. Electric power. Université Grenoble Alpes, 2016. English. NNT: 2016GREAT024 . tel-01819399

HAL Id: tel-01819399

<https://theses.hal.science/tel-01819399>

Submitted on 20 Jun 2018

HAL is a multi-disciplinary open access archive for the deposit and dissemination of scientific research documents, whether they are published or not. The documents may come from teaching and research institutions in France or abroad, or from public or private research centers.

L'archive ouverte pluridisciplinaire **HAL**, est destinée au dépôt et à la diffusion de documents scientifiques de niveau recherche, publiés ou non, émanant des établissements d'enseignement et de recherche français ou étrangers, des laboratoires publics ou privés.

THÈSE

Pour obtenir le grade de

DOCTEUR DE LA COMMUNAUTÉ UNIVERSITÉ GRENOBLE ALPES

Spécialité : **Génie Electrique**

Arrêté ministériel : 7 août 2006

Présentée par

Arthur ARNAUD

Thèse dirigée par **Orphée CUGAT** et
codirigée par **Thomas SKOTNICKI**

préparée au sein de **STMicroelectronics** et du **G2ELAB**
dans l'**École Doctorale d'Electronique, Electrotechnique,
Automatique & Traitement du Signal (EEATS)**

Modélisation et fabrication de systèmes de conversion thermo-mécanique pour la récupération d'énergie thermique

Thèse soutenue publiquement le **24 Mars 2016**,
devant le jury composé de :

M. Skandar BASROUR

Professeur, Université Grenoble Alpes, Président du Jury

M. Elie LEFEUVRE

Professeur, Université Paris-Sud, Rapporteur

M. Emmanuel DEFAY

Ingénieur Docteur, Luxembourg Institute of Science and Technology, Rapporteur

M. Danick BRIAND

Enseignant-Chercheur, Ecole Polytechnique Fédérale de Lausanne, Examineur

M. Thomas SKOTNICKI

Directeur produits R&D, STMicroelectronics, Co-directeur

M. Orphée CUGAT

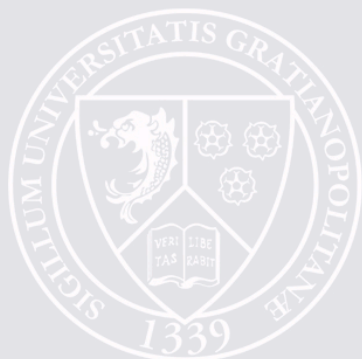
Directeur de Recherche, G2ELAB, CNRS, Directeur de thèse

M. Stéphane MONFRAY

Ingénieur Docteur, STMicroelectronics, Invité

M. Sébastien BOISSEAU

Ingénieur Docteur, CEA-LETI, Invité



Arthur Arnaud

MODELING AND DESIGN OF THERMOMECHANICAL CONVERSION SYSTEMS FOR THERMAL ENERGY HARVESTING APPLICATIONS

Modélisation et fabrication de systèmes de conversion
thermomécanique pour la récupération d'énergie thermique

Thèse de doctorat effectuée sous la direction de ORPHÉE CUGAT et THOMAS SKOTNICKI et encadrée par STÉPHANE MONFRAY
Au sein de l'entreprise STMicroelectronics et du laboratoire G2ELAB

MODELISATION ET FABRICATION DE SYSTEMES DE CONVERSION THERMO-MECANIQUE POUR LA RECUPERATION D'ENERGIE THERMIQUE

*Modeling and design of thermo-mechanical conversion systems
for thermal energy harvesting applications*

Arthur Arnaud

Thèse présentée le 24 Mars 2016
à l'Ecole doctorale Electronique, Electrotechnique,
Automatique, Télécommunication &
Signal (EEATS)
Université de Grenoble

Pour l'obtention du grade de Docteur de la Communauté Université
Grenoble Alpes
Spécialité : Génie Electrique



Thèse préparée à
STMicroelectronics
Laboratoire de Génie Electrique de Grenoble (G2ELAB)

dirigée par
Prof. Orphée Cugat – *Directeur de thèse*
Dr. Thomas Skotnicki – *Co-directeur de thèse*
Dr. Stéphane Monfray – *Encadrant de thèse*

*Si j'avais huit heures pour couper un arbre,
Je passerais six heures à affûter ma hâche.*

A. Lincoln

Remerciements

Bien qu'un manuscrit de these ne soit écrit que par une seule personne, la somme des résultats qu'il contient est généralement le fruit d'un travail d'équipe. Je tiens ainsi à remercier tout d'abord mes directeurs de these Orphée Cugat, Thomas Skotnicki et Jérôme Delamare, de même que mon encadrant Stéphane Monfray pour son expertise en récupération d'énergie, Jihane Boughaleb et Christophe Maître avec qui. Je souhaite aussi remercier les membres de l'équipe TSV de STMicroelectronics, Crolles, pour leur expertise technique qui a permis de concevoir des micro-bilames fonctionnels, plus particulièrement Yannick Pierre Sanchez, Frédéric Battegay, Mickaël Fourrel, Stéphanie Audran, ainsi que Marc Guillermet et Maurice Rivoire, ayant aussi participé à la fabrication des MEMS. Ce projet étant issu d'une collaboration avec les équipes du CEA-Leti, CEA-Liten, mes remerciements vont aussi à Sébastien Boisseau, Sébastien Quenard, Ulrich Soupremanien

Pour les avoir cotoyés et appréciés durant ces trois années de thèse, je souhaite exprimer toute ma sympathie aux membres de l'équipe Advanced Devices, en particulier Frédéric, Charles, Sonia, Nathalie, Sébastien, Aurélie ainsi qu'aux membres du laboratoire G2ELab en particulier Laetitia, Thibault, Paul, Boris, Elena, Benjamin, Dmitri, Guillaume. Mon amitié et mes remerciements vont aux thésards que j'ai cotoyé à STMicroelectronics, en particulier Gaspard, Loic, Alexia, Gabriel, Thomas M, Thomas F, Jocelyn, Maurin, Benjamin, Emilie, Antoine...

Mes derniers remerciements sont destinés aux personnes qui me sont les plus chères et les plus proches, ma sœur et mon frère, Guillaume et Amandine, pour leur soutien fraternel, ainsi que mes parents Thérèse et Thierry, qui nous ont offert à tous les trois l'éducation qui nous a permis de réussir nos études. Je tiens aussi à remercier chaleureusement la famille de Jihane, Fatima et Yahia, Sofia et Mounia. Enfin, mes derniers remerciements vont à celle qui m'aura soutenu durant toute cette thèse, Jihane. Cette thèse m'aura apporté bien plus qu'un épanouissement intellectuel, le bonheur d'être à tes côtés depuis trois ans.

Contents

Introduction. Context, applications and advances in energy harvesting	1
1. A short overview on Wireless Sensors Networks	3
2. An overview on energy harvesting technologies	4
2.1. <i>Vibration energy harvesting</i>	5
2.2. <i>Thermal energy harvesting</i>	6
2.3. <i>Photovoltaic energy harvesting</i>	7
2.4. <i>Other sources of energy harvesting</i>	8
3. Objectives of the thesis	8
3.1. <i>State of the project</i>	8
3.2. <i>Objectives and plan of the thesis</i>	11
4. Bibliography	12
Chapter 1. Materials and devices for thermal energy harvesting	17
1. Introduction	17
2. Maximal efficiency and maximal power of heat engines	17
2.1. <i>Carnot heat engine</i>	17
2.2. <i>Curzon-Ahlborn efficiency</i>	19
3. Thermoelectric generators	21
3.1. <i>Thermoelectric effect</i>	21
3.2. <i>Optimization of the performances of thermoelectric generators</i>	23
4. Pyroelectric generators	27
4.1. <i>Simple pyroelectric generators</i>	27

4.2. <i>Exploiting phase transitions of ferroelectric materials</i>	29
5. Fluid-based heat engines	30
5.1. <i>Downsizing of conventional heat engines</i>	30
5.2. <i>Heat engines using stationary fluids</i>	31
6. Solid-based heat engines	34
6.1. <i>Observations on phase transitions</i>	34
6.2. <i>Shape-memory-alloy-based heat engines</i>	35
6.2. <i>Energy harvesting from thermo-mechanical bistability</i>	37
7. Thermomagnetic heat engines	38
8. Synthesis	40
9. Conclusion	43
10. Bibliography	44
Chapter 2. Thermo-mechanical modeling of the bimetallic strip heat engine	49
1. Introduction	49
1.1. <i>Objectives of the chapter</i>	49
1.2. <i>Researches on thermally-induced instabilities of structures</i>	50
1.3. <i>Buckling of imperfect beams</i>	53
1.4. <i>Thermal snap-through</i>	55
1.5. <i>Plan of the chapter</i>	57
2. A first model of the instability of composite beams	58
2.1. <i>A short course on the theory of elasticity</i>	58
2.2. <i>Equilibrium of composite beams suffering from residual stress</i>	60
2.3. <i>Criterion of bistability</i>	64
2.4. <i>Simplification of the equations for a bimetallic beam</i>	68
2.5. <i>Equilibrium of composite beams with an initial curvature</i>	70
2.6. <i>Curvature and initial stress</i>	74
2.7. <i>Influence of the architecture</i>	74
3. Performances of the harvester using composite beams	77
3.1. <i>Evolution of the strain energy of the composite beams</i>	77
3.2. <i>Evolution of the entropy of the composite beams</i>	79
3.3. <i>Intrinsic mechanical performances of the harvester</i>	81
3.3. <i>Intrinsic mechanical performances of the harvester</i>	85

4. A second model of the instability of composite beams	85
4.1. Ritz approximation, Galerkin method, Cardan formula	85
4.2. Simplification of the model	88
4.3. Mechanical performances of the energy harvester	89
4.4. Experimental studies and validity of the reduced-order model	93
4.5. Figures of Merit	94
4.6. Study of the impact of the architecture on the performances	96
4.7. Synthesis on the second model	98
5. Thermal transfers and mechanical instability	99
5.1. Equations of the thermal transfers	99
5.2. Switched thermal capacitance model	99
5.3. Leakage paths and heat sink	105
5.4. Thermal transfers inside the bimetallic strip	108
6. Synthesis	113
7. Bibliography	115
Chapter 3. Conversion of the mechanical energy into electrical energy	119
1. Introduction	119
2. An overview on piezoelectricity	122
2.1. The history of piezoelectricity	122
2.1. Thermodynamics of piezoelectric materials	122
3. Equations of the pyroelectric bimetallic strip heat engine	127
3.1. Tertiary pyroelectric effect	127
3.2. Equilibrium equations of the piezoelectric bistable composite beam	129
4. Piezoelectric conversion using Stirling cycle	130
4.1. Stirling cycle	130
4.2. Implementation of the Stirling cycle	132
a. Stirling cycle I	132
b. Stirling cycle II	135
c. Stirling cycle III	136
d. Comparison of the three cycles and enhancement factors	138
e. Comparing piezoelectric materials	140
4.3. Influence of the architecture, extrinsic performances	

<i>of the energy harvester</i>	142
<i>a. Stirling cycles</i>	142
<i>b. Dynamic performances of the harvester for fixed external temperature and no architectural leakage</i>	145
<i>c. Dynamic performances of the harvester with Robin conditions and thermal conducting architecture</i>	149
5. Coupling with an oscillating piezoelectric transducer	151
5.1. <i>A short review of energy harvesting devices based on mechanical shock</i>	130
5.2. <i>Modeling the shock between two oscillators</i>	151
<i>a. Mason model of the piezoelectric oscillator</i>	151
<i>b. Modeling of the shock</i>	153
<i>c. Optimal mechanical energy</i>	154
5.3. <i>Electrical performances of the system</i>	159
<i>a. Open circuit voltage</i>	159
<i>b. Energy harvested with a SECE circuit</i>	163
<i>c. Overall performances of the energy harvester</i>	165
<i>d. Ways to improve the efficiency of the transduction</i>	166
6. Coupling with an electret transducer	168
6.1. <i>A short overview on electrets and electrostatic energy harvesting</i>	168
<i>a. A history of electrets</i>	168
<i>b. Types of electret and production</i>	169
<i>c. Energy harvesters exploiting electrets</i>	171
6.2. <i>Modeling the electret</i>	172
<i>a. Electric field and electrostatic pressure induced by an electret with a charge layer</i>	172
<i>b. Electric equations of the thermally bistable electrode</i>	173
6.3. <i>Mechanical equations of the bistable bimetallic electrode</i>	174
<i>a. Equilibrium of bistable beams under electrostatic pressure</i>	174
<i>b. Moderate electrostatic coupling</i>	175
6.4. <i>Harvesting heat with electret transduction</i>	177
<i>a. Possible thermodynamic cycles</i>	177
<i>b. Intrinsic performances of the bimetallic strip heat engine</i>	178
<i>c. Dynamic performances of the heat engine</i>	180
<i>d. Effect of the moderate electrostatic coupling</i>	

<i>on the performances of the heat engine</i>	182
7. Synthesis	185
<i>a. Design rules common to all harvesters</i>	185
<i>b. Design rules for pyroelectric bimetallic strip heat engines</i>	185
<i>c. Design rules for piezoelectric bimetallic strip heat engines</i>	186
<i>d. Design rules for plectrostaticbimetallic strip heat engines</i>	186
<i>e. Comparison of the various heat engines</i>	187
8. Conclusion	188
9. Bibliography	189
Chapter 4. Theoretical performances of the energy harvester at the microscale	195
1. Introduction	195
2. Thermo-mechanical instability at the microscale	195
<i>2.1. Equilibrium equation</i>	195
<i>2.2. Thermo-mechanical performances of bimetallic strips</i>	200
<i>2.3. Reduced-order model with the Galekerin method</i>	202
<i>a. Intrinsic performances</i>	202
<i>b. Extrinsic performances</i>	204
<i>c. Performances of the materials used in microelectronics</i>	205
<i>d. Impact of the variability of the residual stress on the performances of the bistable beams</i>	205
3. Pyroelectric coupling	206
<i>3.1. Equations of the piezoelectricity</i>	206
<i>3.2. Performances of the Stirling cycle</i>	207
<i>3.3. Dynamic behavior of the bimetallic strip at the microscale</i>	210
<i>a. Scaling law on the operation frequency</i>	210
<i>b. Simplified model of the harvester at the microscale</i>	212
<i>c. Performances of a bimetallic strip in a cavity</i>	213
4. Electrostatic coupling	214
<i>4.1. Performances in weak coupling</i>	214
<i>4.2. Performances in moderate coupling</i>	216
5. Synthesis	220
<i>a. Synthesis on the mechanical properties of the bimetallic strip</i>	

<i>heat engine</i>	220
<i>b. Synthesis on the dynamic behavior of the system</i>	221
<i>c. Synthesis on the pyroelectric bimetallic strip heat engines</i>	224
<i>d. Synthesis on the electrostatic bimetallic strip heat engines</i>	224
<i>e. Aging of the device</i>	224
6. Conclusion	225
7. Bibliography	226
Chapter 5. Silicon integration of thermo-mechanically bistable actuators	229
1. Introduction	229
2. A first fabrication process	229
2.1. A short overview on microlenses arrays	229
2.2. Fabrication process	230
<i>a. Microlenses process</i>	230
<i>b. Bimetallic layers deposition</i>	230
<i>c. Etching of bimetallic strips and photoresist's removal</i>	232
2.3. Characterization of microstructures	233
3. A second fabrication process	235
3.1. Short review on bistable thermal actuators	235
3.2. Design of new lithography masks	236
3.3. Design rules of bimetallic strips	238
3.4. Possible strategies for the development of the second process	239
3.5. Fabrication process developed at STMicroelectronics	243
3.6. First characterizations of thermal actuators	246
3.7. Alternative fabrication process	246
4. Conclusion	247
5. Bibliography	248
Conclusion	253

Glossary

α	Coefficient of thermal expansion
a	Beam's amplitude
a_o	Beam's initial amplitude
C_v, C_ε	Heat capacitances
d_o	Initial deflection
d_{bot}, d_{top}	Cavity's thickness
d_{top}	Beam's pseudo-force
\mathcal{D}	Electric displacement
d	Piezoelectric coefficient
δ	Damping coefficient
E	Young's modulus
ε	Dielectric permittivity
\mathcal{E}	Electric field
η_{TM}^{abs}	Absolute thermo-mechanical efficiency
η_{TM}^{rel}	Carnot relative thermo-mechanical efficiency
η_{TM}^{CA}	Curzon-Ahlborn relative thermo-mechanical efficiency
η_{MM}^{abs}	Absolute Mechano-mechanical efficiency
η_{ME}^{abs}	Absolute Mechano-electric efficiency
FOM_x	Figure of Merit associated to the quantity x
F_o	Mean residual stress force
f	Working frequency
\mathcal{F}, \mathcal{F}	Local and global Helmholtz free energy
ϕ_i	Mathematical functions
\mathcal{G}, \mathcal{G}	Local and global Gibbs free energy
i_e	Bending stiffness
k	Vector field
\mathcal{K}, \mathcal{K}	Local and global kinetic energy
L	Beam's length
$\mathcal{L}_S, \mathcal{L}_{SB}$	Latent heat of snap and snap-back
λ	Beam's length excess
M_o	Moment of residual stress
M_α	Beam's thermal expansion asymmetry coefficient
m_b	Mass of the bimetallic strip
m_{CC}	Mass of the clamped-clamped oscillator
m_{CF}	Mass of the clamped-free oscillator
m_p	Mass of the piezoelectric oscillator
m_{SS}	Mass of the supported-supported oscillator

Content

μ_b	Beam's thermal diffusivity
N	Axial force
N_α	Beam's mean thermal stress coefficient
N_e	Beam's axial stiffness
N_o	Beam's effective residual stress force
ν	Poisson's ratio
P_{top}, P_{bot}	Beam's effective residual stress force
Q	Heat
Q	Electric charge
ρ	Density
S	Strain tensor
σ	Local entropy
Σ	Global entropy
T	Relative temperature in Celsius degree
T_o	Temperature defined by the stress
T_{SB}	Snap-back temperature
T_S	Snap temperature
T_o	Initial residual stress
θ	Temperature in kelvin
θ_{ref}	Reference temperature in kelvin
\mathcal{T}	Stress tensor
u, \mathcal{U}	Local and global internal energy
u, w	Displacement fields
v	Width
W	Work
x, y, z	Position
z_o	Neutral axis
ZT	Figure of Merit of thermoelectric materials
P_M	Mechanical power
P_E	Electrical power
p	Pyroelectric coefficient
\mathcal{V}	Voltage

Content

Introduction

Context, applications and advances in energy harvesting

The terms “energy harvesting” or “energy scavenging” define the action of converting ambient energy under whichever form (heat, mechanical vibrations, light, electromagnetic energy...) into usable electric energy (by means of a power management circuit), either by using a single conversion step (direct conversion) or by a sequence of conversion steps (indirect conversion). Given the variety of energy sources that can be found in our surroundings, the field of energy harvesting has widely developed by adapting a large range of transducer technologies to the specificities of the energy requirements of electronic devices. Even if the idea of producing electric energy from local energy sources is not a new concept, the various devices designed or fabricated in the mid-20th century and reported in the literature were mainly intended to supply enough electric power to be classified as energy generators. Unlike outdoor photovoltaic plants or wind farms, energy harvesters only convert very small amounts of energy into electric energy, but quite sufficient to supply low-power electronics.

Indeed, the development of energy harvesting is strongly linked to the emergence of the Internet of Things (IoT). This notion of IoT was first introduced by Kevin Ashton [Shoenberger, 2002] to designate networks of devices such as sensors, actuators, RFID, industrial machines, computers, smart objects (connected cars, smart home...) connected with each other, mainly wirelessly. One of the aspects of the IoT is the development of Wireless Sensors Networks to respond to the growing needs for monitoring data in domains as diverse as industry, urban or natural environments, home, or even the human body (Fig.1.1.a) [Yick *et al.*, 2008; Zahid Kausar *et al.*, 2014]. Beyond the simple interest aroused by the potential new applications of IoT (Fig.1.1.b), the market of connected objects and smart sensors is growing and is expected to represent about 28 billion devices in 2020 against 9 billions in 2013 (Fig.1.1.c) with potential market revenues of more than 8900 billion USD by the end of 2020 [Bauer *et al.*; 2014; PwC, 2015]. The semiconductor industry would be a main actor and recipient of the development of this market.



Figure 1.1.1. a. Some applications of energy harvesting devices and Wireless Sensor Networks. b. Projected adoption of some connected devices [Bauer et al., 2014]. c. Evolution of the MEMS market until 2018 [McKinsey, 2014]. d. Simplified schematic explaining the architecture of a Wireless Sensing Node. e. Typical scenario for the power consumption of a Bluetooth Low Energy Sensor Node.

The sensors market is expected to grow annually by 40% [PwC, 2015] with potential revenues above 7 billion USD by 2019 [PwC, 2015], while MEMS market would grow up from 16 to 23 billion USD between 2015 and 2018 (Fig.1.1.d) mainly thanks to opportunities in consumer electronics and biomedical applications [McKinsey, 2014].

1 A short overview on Wireless Sensors Networks

The term Wireless Sensors Network (WSN) designates a group of Sensing Nodes spatially distributed and connected together by means of wireless connections, and whose main function is to collect data on their close surroundings and transmit them to an entity, either electronic or human, capable of interpreting them to take a decision. This definition enables to directly understand the generic architecture of a sensing node, which is necessary made of at least one sensor (pressure, temperature, humidity, light, movement, etc.), a radio transceiver, a microcontroller unit, all this powered by an energy source and its dedicated power management circuit (Fig.1.1.d). Typically, the most power-hungry components of the wireless node are the radio, the Analog-Digital Converter and the sensor. Taking the example of electronic components fabricated at ST-Microelectronics (Tab.1), we give a simple representation of the operation of a Bluetooth Low Energy node. At a data rate of 1 Mb/s, the maximal duration of wireless communication is around 1 ms. During this period, the radio consumes about 30 μJ to receive and transmit data. The output data rate of the accelerometer being 100 Hz (Tab.1.1), the approximate time to measure data on an accelerometer is about 10 ms [ST, AN3182, 2010], during which the node consumes about 40 μJ . The total consumption of the node in active mode is thus about 100 μJ , corresponding to 8.5 mW. As we will see most energy harvesters are not able to supply such levels of electric power. The solution to get around this problem is to use duty cycling [Anastasi *et al*, 2009] to reduce the equivalent power supply, and a storage device to feed the communicating node. As a consequence, by sending data every minute, the equivalent power needed by the node in active mode is 1.7 μW , whereas the power needed in standby mode is 4 μW . As a consequence, an energy harvester capable of delivering at least 5.7 μW of usable electric power would be able to feed a wireless sensor node. During the active mode of the wireless node, a micro-battery such as the EnFilm battery (Tab.1.1) is able to deliver up to 30 mW, enough to supply it [ST, AN3182, 2010].

As demonstrated with this example, the sustainability of WSNs is strongly linked to the possibility given to each sensing node of the Network to save energy by not communicating with the rest of the network over long periods of time. To allow this type of operation, new wireless communications standards were defined by industry consortiums like Zigbee Alliance and standardization organisms like IEEE: main communications standards used by Wireless Sensors Networks are IEEE 802.15.4 (used by Zigbee communication protocol), IEEE 802.15.1 (used by Bluetooth Low Energy devices) and IEEE 802.15.3 (defined for wireless sensors networks dedicated to wearable technologies (or Body Area Network)) [Yick *et al*, 2008]. As an example, to limit the power consumption of sensing nodes during data transmission, IEEE 802.15.4 limits the

transmission power to 0.5 mW [Adams, 2006]. As a consequence, the transmission range of wireless sensors is usually limited to around 10-50 meters.

2 An overview on energy harvesting technologies

The previous part showed that the development of energy harvesting devices generating at least more than the consumption of the node in standby mode (4 μ W in our study case) is sufficient to power wireless sensor nodes, complemented by an energy storage buffer between the generator and the sensing node. Literature on energy harvesting shows a large spectrum of generators and microgenerators demonstrating their capability to supply energy to these smart sensors. In this part, we present a short classification of generators according to the nature of the energy they scavenge as well as some examples of energy harvesters. Numerous synthesis works can be found in the literature providing more details on these technologies [Vullers *et al* 2009; Pryia and Inman, 2008; Briand *et al*, 2015].

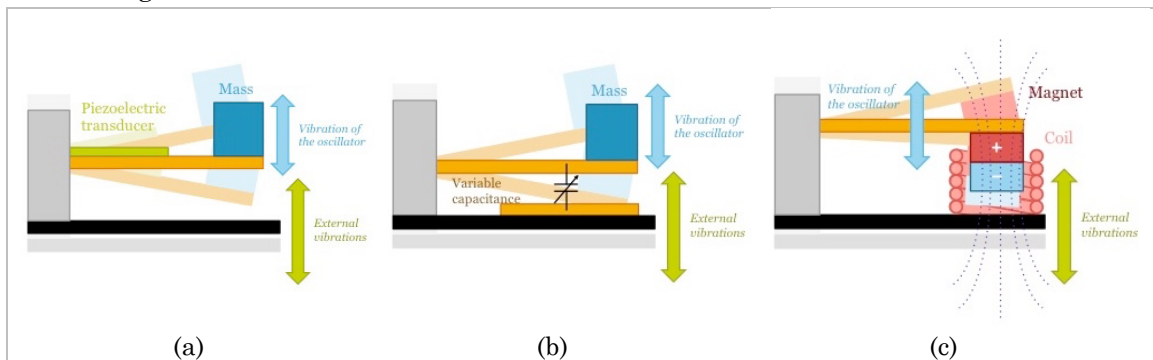
Table 1. Performances of some electronic components fabricated by ST-Microelectronics [ST, LM135, 2008; ST, BlueNRG, 2015; ST, STM32, 2015; ST, AN3182, 2010].

Mode	Components	Consumption/Supply
Standby	STM. BlueNRG®	1,3 – 2 μ A @ 2 V
	STM32L (Microcontroller)	0,3 μ A @ 2 V (without RTC) 0,9 μ A @ 2 V (with RTC)
Sleep	BlueNRG®	1,7 – 3,5 μ A @ 2 V
	STM32L (Microcontroller)	0,5 μ A @ 2 V (without RTC) 1,2 μ A @ 2 V (with RTC)
Active	BlueNRG®	1,3 – 2 μ A @ 2V @ 32 kHz
	STM32L (Microcontroller)	0,3 μ A @ 2 V
	AD Converter 12 bits	0,9 μ A @ 2 V
	DA Converter 12 bits	0,9 μ A @ 2 V
	H3LIS331DL (Accelerometer)	300 μ A @ 3V @ 100 Hz
	LM135 (Temperature sensor)	0,45 – 1 mA @ 3V
Reception (2.4GHz)	BlueNRG® Bluetooth LE radio	14,5 μ A @ 2V
Transmission (2.4GHz)	BlueNRG®	10,6 - 21 μ A @ 2V
	Bluetooth LE radio 0 dBm	15,4 μ A @ 2 V
	Bluetooth LE radio +5 dBm	21 μ A @ 2 V
	Bluetooth LE radio +5 dBm	10,6 μ A @ 2 V
Storage	Thin film Battery EnFilm EFL700A39	10 mA @ 3V 0,7 mAh

2.1 Vibration energy harvesting

Conversion of energy from mechanical vibrations into electrical energy is a technique perfectly suited to wireless sensors embedded on transport vehicles, industrial machines, clothing etc., even though the range of frequency and amplitude of mechanical energy is extremely variable between all these systems [Neri *et al.*, 2013]. As a result, vibration energy harvesting may be the field of energy harvesting that knew the broadest diversification in terms of transducing technologies. All vibration energy harvesters work on the principle of the resonant vibrations of an oscillator caused by the inertia of a seismic mass [Mitcheson *et al.*, 2008]. Three methods of conversion are commonly used to transform mechanical energy into electrical energy: either piezoelectric transduction to convert the mechanical stress of the oscillator into electric charges, electrostatic conversion based on capacitance variations induced by the displacement of the oscillator, or electro-magnetic conversion based on the creation of an electromotive force induced by the temporal variation of the magnetic field due to the displacement of a permanent magnet. Based on a generic spring-mass-damping lumped model, [Williams and Yates, 1996] established the equations giving the maximal energy that can be extracted from vibrations, and showed that the output power could be maximized by matching the resonant frequency of the linear oscillator to the frequency of the oscillations and by increasing the mechanical quality factor of the structure. This model owns the advantage of being common to every vibration energy harvester, enabling to define Figures of Merit based on the ratio between the generated electrical energy and the input mechanical energy calculated thanks to the acceleration of the oscillator. [Mitcheson *et al.*, 2008] therefore report a comparison between electromagnetic, piezoelectric and electrostatic energy harvesters, showing that the conversion efficiency of electromagnetic devices is about 1%, whereas it can reach about 20% for electrostatic energy harvesters and more than 30% for piezoelectric energy harvesters. In the case of a generator using a seismic mass of 1 g submitted to an acceleration of $10 \text{ m}\cdot\text{s}^{-2}$ at 100 Hz, an efficiency of 20% yields an output electrical power of around $16 \mu\text{W}$, which is enough to power a Wireless sensing node. In the case of piezoelectric energy harvesters, non-linear energy extraction techniques like SECE [Lefeuve *et al.*, 2007] or SSHI [Guyomar *et al.*, 2005] can help increasing the efficiency of the transduction.

Figure 2.1.1. Schematic vibration harvesters: a. piezoelectric, b. electrostatic, c. electromagnetic.



Yet the drawback of using high-Q linear oscillators is a narrowing of the frequency bandwidth of the generator which restricts access to the energy associated to frequencies other than the resonant frequency. This problem is even more relevant for miniaturized harvesters: their frequency grows with miniaturization and is inversely proportional to their length, while higher energy is generally associated to low frequencies [Neri *et al*, 2013]. Current research is oriented toward the design of non-linear oscillators (hardening or softening Duffing oscillators) to widen the oscillators' frequency bandwidth, bistable oscillators [Harne and Wang, 2013], coupled oscillators [Gu and Livermore, 2011], frequency tuning [Challa *et al*, 2008], or arrays of oscillators working at different resonant frequency [Zhu *et al*, 2009].

2.2 Thermal energy harvesting

Although the next chapter of this thesis manuscript is devoted to thermal energy harvesting technologies, we already present here a brief overview of thermal harvesters in order to have a global comparison between harvesting technologies. It is commonly admitted that the wide availability of low-grade heat flux makes heat a viable energy source to power WSN. Typically, heat flux around 5 mW.cm^{-2} can be generated from temperature difference of 5°C with natural convection, allowing energy harvesting from heat generated by the human body. However, thermodynamics limits the efficiency of thermal energy harvesters which cannot exceed the Carnot limit of around 1.7 % for a hot source at 30°C and a temperature difference of 5°C . As a consequence, no more than $83 \text{ }\mu\text{W.cm}^{-2}$ could be generated from such temperatures difference. Even though the efficiency of some conventional heat engines like Rankine generators can reach 60% of the Carnot limit, they generally work at very high temperatures which are less compatible with most WSN applications (around 565°C with a temperature difference of 530°C for the generators presented in [Lee and Frechette, 2006]). The main mature thermal generator technologies are based on thermoelectricity exploiting the Seebeck effect to directly convert heat into electrical energy. Theoretical efficiency of these devices generally reaches 14% of the Carnot limit at 30°C , corresponding to a power of $14 \text{ }\mu\text{W.cm}^{-2}$, enough to power wireless sensing nodes. However, the need for thermal matching between Seebeck generators and heat sink to maintain the thermal gradient across the energy harvester limits practical applications of thermal energy harvesting applied to body area networks. Therefore, although [Leonov *et al*, 2009; Leonov *et al*, 2007] developed Seebeck generators adapted to human body heat energy recovery, technologies of thermal generators are generally developed to harvest heat at higher temperatures (around 100°C), more adapted to industrial environments for instance. In such environment where the use of bulky heat sinks is less problematic, thermal energy harvesters can generate up to 10 mW.cm^{-2} , largely enough to power WSNs.

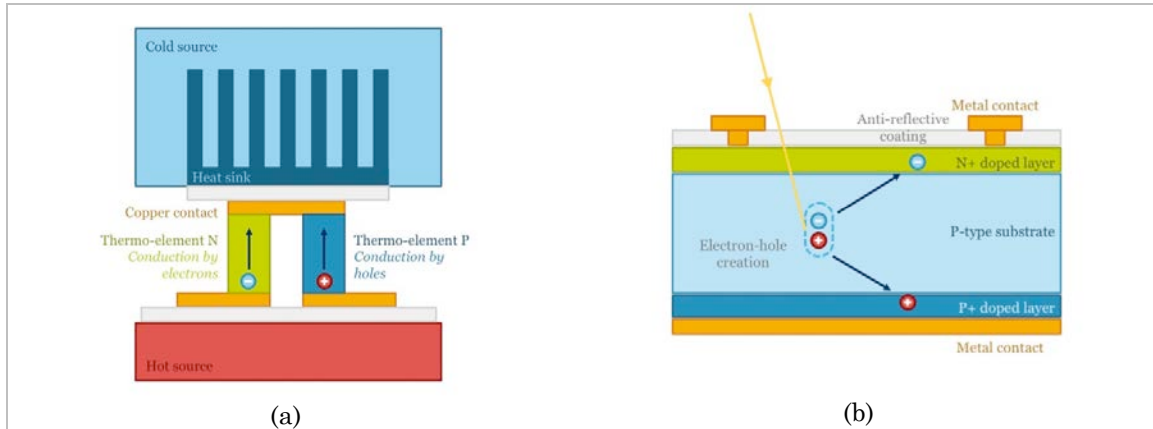


Figure 2.1.2. Simplified representation of: a. Thermoelectric PN junction with bulk heat sink for thermal energy harvesting. b. Solar cell for indoor/outdoor photovoltaic energy harvesting.

2.3 Photovoltaic energy harvesting

The advantage of harvesting energy from light to power WSNs is linked both to the ubiquity of these energy resources, and to the low-cost mature technologies, initially developed for solar energy production. Generally, we distinguish indoor from outdoor photovoltaic energy harvesting, given the difference of incident irradiance between these two cases (100 mW.cm^{-2} for outdoors direct sunlight, compared to 0.5 mW.cm^{-2} indoors) [Priya and Inman, 2008]. Moreover, the efficiency of solar cells depend not only on the cell technology but also on the irradiance of the light sources. Typically, monocrystalline silicon cells have an efficiency of about 14% for outdoor applications, but only 4% for indoor applications [Randall and Jacot, 2002]. Innovations like organic photovoltaic cells, even less efficient, are expected to lower the cost of energy harvesting devices but would also allow to power smart textiles [Wilson and Mather, 2015].

Table 2. Summary of some energy sources and potential energy density (for mechanical energy harvesters, we assume a mass of 10 g and a volume of 1cm^3)

Source	Characteristics of the source	Harvested energy
Light		
Indoor	$10\text{-}100 \text{ mW.cm}^{-2}$	$1.5\text{-}15 \text{ mW.cm}^{-3}$ @ $\eta=15\%$
Outdoor	0.5 mW.cm^{-2}	$30 \mu\text{W.cm}^{-3}$ @ $\eta=6\%$
Mechanical vibrations		
Human [Feenstra et al, 2014]	1.4m.s^{-2} @ 10 Hz	$32 \mu\text{W.cm}^{-3}$ @ $\eta=20\%$
Industrial [Beeby et al, 2014]	7m.s^{-2} @ 110 Hz	$71 \mu\text{W.cm}^{-3}$ @ $\eta=20\%$
Heat		
Human	5 mW.cm^{-2} @ $T_H=30^\circ\text{C}$ @	
Industrial losses	$T_C=25^\circ\text{C}$	$14 \mu\text{W.cm}^{-2}$ @ $ZT=1$
	375 mW.cm^{-2} @ $T_H=100^\circ\text{C}$ @	14 mW.cm^{-2} @ $ZT=1$
	$T_C=25^\circ\text{C}$	
RF radiations	100 mW @ 2.4 GHz (WiFi)	$0.1 \mu\text{W.cm}^{-2}$ @ 10 m

2.4 Others energy sources

Photovoltaic energy, mechanical vibrations and heat are the main technologies reviewed in this introduction because of the high levels of electric power that can be generated from these energy sources. However, other harvesting technologies exist, some of them exploiting the electro-magnetic radiations from the 900 MHz GSM band or the 2.4 GHz WiFi band, such as rectennas. Yet the amount of electric power generated by these devices is small: for a GSM signal of 2 W transmission power, the power received by a RFID tag at 10 m is around 2 μ W, and for a 100 mW WiFi signal, the received power is 0.1 μ W [Priya and Inman, 2008]. As a result, RF energy harvesting is more adapted to RFID recognition.

3 Objectives of this thesis

3.1 State of the project

Even if the working principle of the bimetallic strip heat engines is explained in deep detail in the next chapter, we give here a short description and we briefly recall the history of its development at STMicroelectronics. The idea of developing at STMicroelectronics a thermal energy harvester based on the thermal snap-through of bimetal thermostats (either shell-like thermostats or beam-like thermostats) was proposed by [Skotnicki et al, 2010]. The basic idea is to place the bimetallic strip between a hot source and a cold source so as to create a constant instability of the bimetallic strip, switching from a heat source to the one without discontinuity (Fig.3.1a). As a consequence, the bimetal thermostat realizes a thermo-mechanical transduction, generating kinetic energy from heat. A second conversion step is thus needed to transform the bimetallic strip's kinetic energy into electrical energy.

Up to now, two types of bimetallic strip heat engines were developed [Puscasu *et al*, 2014; Boisseau *et al*, 2013]. The first one is based on the mechanical energy transfer occurring during the shock between the bistable bimetallic strip and a piezoelectric oscillator and was jointly developed by STMicroelectronics, LGEF, CEA-Liten and Delta-concept. The current piezoelectric prototype and an exploded view revealing its architecture are represented in Fig.3.1c, whereas the bimetallic strip made of Invar-NC4 (Invar used as a thermo-mechanically passive material, and NC4 as an active material) is presented in Fig.3.1b. This device is currently able to generate up to 3 μ W of usable electric power with a bimetallic strip of hysteresis 67°C-70°C on a hot source at 100°C (equivalent surface density 0.26 μ W.cm⁻² if it is normalized by the harvester's surface or 0,46 μ W.cm⁻² if it is normalized by the bimetallic strip surface). The advantage of this generator is its capability to maintain a thermal gradient inside the passive architecture's cavity without needing any bulky heat sink. This is mainly linked to the slow working frequency of the bimetallic strip (around 0.25 Hz), which allows the piezoelectric transducer, whose function is also to cool down the bimetallic strips, to return to its equilibrium temperature once the bimetallic strip has snapped back. Thermal optimization of the passive architecture enabled to improve the thermal efficiency of the harvester by

reducing thermal leakage, and to increase the temperature difference in the cavity, thus widening the operating window of the generator [Boughaleb *et al.*, 2014]. Experimental measurements of the performances of these thermal generators are reported in [Puscasu *et al.*, 2012, Arnaud *et al.*, 2013, Puscasu *et al.*, 2014, Boughaleb *et al.*, 2014, Boughaleb *et al.*, 2015, Boughaleb *et al.*, 2016]. The latest experimental results (currently unpublished) demonstrated the capability of a single piezoelectric generator to power a WSN developed by STMicroelectronics and CEA-Leti in asynchronous mode with either Zigbee radio or Bluetooth Low-Energy, communicating acceleration or temperature data.

A second type of generator based on the use of bimetallic strip heat engines coupled with an electret-based capacitive transducer was jointly developed with CEA-Leti's R&D teams and Delta-Concept. In that case, the capability of generating electric energy from heat flux is not linked to the kinetic energy released by the switching bimetallic strips, but to the capacitance variations cause by the curvature reversal of the bistable membrane. The operation and performances of these electrostatic bimetallic strip heat engines are reported in [Boisseau *et al.*, 2013, Arnaud *et al.*, 2013]. Using Invar-B72M bimetallic strips (hysteresis temperatures of 47°C and 43°C) and FEP-based electrets (25 μm -thick layer) having a surface potential of 500 V, these devices are able to generate output power of around 5 μW at 2 Hz of working frequency. Experimental demonstration of their capability to power sensing nodes was demonstrate in [Arnaud *et al.*, 2013]. Until now, difficulties were encountered to operate electrostatic generators without bulky heat sink, linked to the absence of thermal optimization of this kind of device.

Based on scaling rules predicting a linear improvement of the surface density of generated power at the microscale [Puscasu *et al.*, 2012], two parallel thesis projects were impulsed in order to integrate micro bimetallic strip heat engines on silicon wafers using MEMS fabrication techniques. A first approach was to process thermo-mechanically bistable piezoelectric bimorphs in order to directly transform heat into electrical energy without decreasing the overall efficiency of the energy harvester, by multiplying the number of conversion steps. This work involved a collaboration between the Ceramics Laboratory LC of EPFL university at Lausanne and TIMA laboratory at Grenoble [Trioux *et al.*, 2014], demonstrating the generation of electrical charges due to the thermo-mechanical instability of Al-AlN bimorph beams.

The second approach, developed through a collaboration between STMicroelectronics, G2ELab and CEA-Leti consists in directly scaling down the electrostatic bimetallic strip heat engine to the sub-millimetric scale by developing a microelectronics process fully compatible with the facilities of the 300 mm clean room of STMicroelectronics in Crolles (near Grenoble).

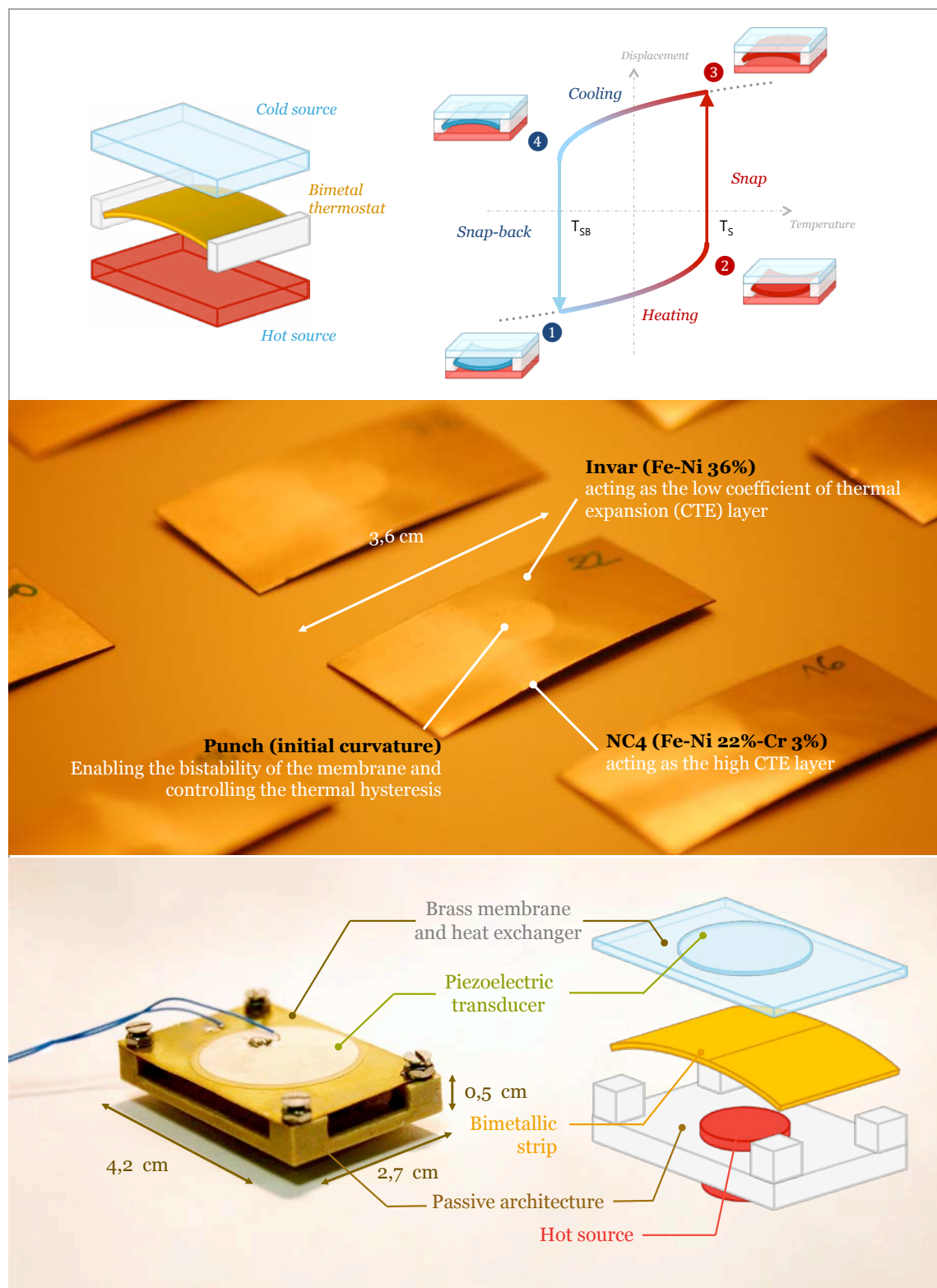


Figure 3.1. a. Principle of the bimetallic strip heat engine. b. Image of Invar-NC4 bimetallic strip fabricated by DeltaConcept and used in the piezoelectric generator. c. Architecture of the piezoelectric bimetallic strip heat engine.

3.2 Objectives and plan of the thesis

The aim of this PhD was initially to develop miniaturized bimetallic strip heat engines coupled with electret transducers using MEMS fabrication techniques, but also to contribute to the development of piezoelectric bimetallic strip heat engines at the macroscale. As few works were made on the accurate prediction the performances of the bimetallic strip heat engine and on the creation of design rules to guide the fabrication of microsystems, this PhD primarily focused on the modeling of the bimetallic strip heat engines.

This thesis manuscript thus is divided into five chapters starting from a state-of-the-art on thermal energy harvesting, to the design, fabrication and characterization of the bimetallic strip at the MEMS scale, including a comprehensive modeling of the various aspects of the energy harvester.

Chapter 1 presents an overview of the existing technologies dedicated to the conversion of thermal energy into electric energy by means of various effects such as the Seebeck effect, pyroelectricity, shape memory, thermomagnetism etc., enabling to compare these technologies with the bimetallic strip heat engines.

Chapter 2 sums up the modeling of the thermo-mechanical instability of composite beam, including bimetallic beams. The conditions of occurrence and the properties of the thermal snap-through are explicated. In this first chapter on the modeling of the device, we theoretically demonstrate the possibility to harvest heat by means of bistable composite beams thus justifying the name of “bimetallic strip heat engine”. A reduced-order model is then developed to obtain approximate equations of the various performances of the energy harvester, such as the energy produced during a complete cycle, the thermal efficiency, and the Carnot efficiency of the device. This will enable us to evaluate the performances of the primary conversion step of the bimetallic strip heat engine.

Chapter 3 is devoted to the modeling of the conversion of the mechanical energy into electrical energy by means of piezoelectric materials, piezoelectric transducers or electrets-based transducers. For each of these converters, we developed models to explain the influence of the parameters of the system on the performances of the system. We finally compare each device in order to find which architecture is the most efficient one. This will enable us to find in which directions the future developments must be carried out in order to improve the performances of the current energy harvesters, but also to find the theoretical limits of our devices and to compare it with other technologies of thermal energy harvesters.

Chapter 4 extends the use of the models developed in Chapters 2 and 3 to the simulations of the performances of the bimetallic strip heat engine at the micrometric scale. We finally extract scaling rules from these models, enabling to make a comparison between the performances of the bimetallic strip heat engine at the microscale and at the macroscale.

Chapter 5 finally describes the fabrication of the thermally bistable beams at the microscale as well as the characterization of these structures at the microscale.

4 Bibliography

- Adams, J. (2006). An Introduction to IEEE STD 802.15.4. *2006 IEEE Aerospace Conference*.
- Anastasi, G., Conti, M., Di Francesco, M. and Passarella, A. (2009). Energy conservation in wireless sensor networks: A survey. *Ad Hoc Networks*, 7(3), pp.537-568.
- Arnaud, A., Boisseau, S., Monfray, S., Puscasu, O., Despesse, G., Boughaleb, J., Sanchez, Y., Battégay, F., Fourel, M., Audran, S., Boeuf, F., Delamare, J., Delepierre, G., Pitone, G. and Skotnicki, T. (2013). Piezoelectric and electrostatic bimetal-based thermal energy harvesters. *J. Phys.: Conf. Ser.*, 476, p.012062.
- Bauer, H., Patel, M. and Veira, J. (2014). *The Internet of Things: Sizing up the opportunity*. [online] Mckinsey.com. Available at: http://www.mckinsey.com/insights-high_tech_telecomsinternet/the_internet_of_things_sizing_up_the_opportunity
- Beeby, S., Torah, R., Tudor, M., Glynne-Jones, P., O'Donnell, T., Saha, C. and Roy, S. (2007). A micro electromagnetic generator for vibration energy harvesting. *J. Micromech. Microeng.*, 17(7), pp.1257-1265.
- Boisseau, S., Despesse, G., Monfray, S., Puscasu, O. and Skotnicki, T. (2013). Semi-flexible bimetal-based thermal energy harvesters. *Smart Mater. Struct.*, 22(2), p.025021.
- Boughaleb, J., Arnaud, A., Cottinet, P., Monfray, S., Gellenne, P., Kermel, P., Quenard, S., Boeuf, F., Guyomar, D. and Skotnicki, T. (2015). Thermal modeling and optimization of a thermally matched energy harvester. *Smart Mater. Struct.*, 24(8), p.085025.
- Boughaleb, J., Arnaud, A., Cottinet, P., Monfray, S., Quenard, S., Boeuf, F., Guyomar, D. and Skotnicki, T. (2015). Analysis of the thermal impact of a bimetal on the dynamic behavior of a thermal energy harvester. *Sensors and Actuators A: Physical*, 236, pp.104-115.
- Boughaleb, J., Arnaud, A., Monfray, S., Cottinet, P., Quenard, S., Boeuf, F., Guyomar, D. and Skotnicki, T. (2016). Design and performance benchmark of various architectures of a piezoelectric bimetallic strip heat engine. *Optical materials*.
- Briand, D., Yeatman, E. and Roundy, S. (2015). *Micro energy harvesting*.
- Calhoun, B., Daly, D., Verma, N., Finchelstein, D., Wentzloff, D., Wang, A., Seong-Hwan Cho, and Chandrakasan, A. (2005). Design Considerations for Ultra-Low Energy Wireless Microsensor Nodes. *IEEE Transactions on Computers*, 54(6), pp.727-740.

- Challa, V., Prasad, M., Shi, Y. and Fisher, F. (2008). A vibration energy harvesting device with bidirectional resonance frequency tunability. *Smart Mater. Struct.*, 17(1), p.015035.
- Feenstra, J., Granstrom, J. and Sodano, H. (2008). Energy harvesting through a backpack employing a mechanically amplified piezoelectric stack. *Mechanical Systems and Signal Processing*, 22(3), pp.721-734.
- Gartner.com, (2014). *Gartner's 2014 Hype Cycle for Emerging Technologies Maps the Journey to Digital Business*. [online] Available at: <http://www.gartner.com/newsroom/id/2819918>
- Gu, L. and Livermore, C. (2011). Impact-driven, frequency up-converting coupled vibration energy harvesting device for low frequency operation. *Smart Mater. Struct.*, 20(4), p.045004.
- Guyomar, D., Badel, A., Lefeuvre, E. and Richard, C. (2005). Toward energy harvesting using active materials and conversion improvement by nonlinear processing. *IEEE Transactions on Ultrasonics, Ferroelectrics and Frequency Control*, 52(4), pp.584-595.
- Harne, R. and Wang, K. (2013). A review of the recent research on vibration energy harvesting via bistable systems. *Smart Mater. Struct.*, 22(2), p.023001.
- Kwong, J. and Chandrakasan, A. (2008). Advances in Ultra-Low-Voltage Design. *IEEE Solid-State Circuits Newsl.*, 13(4), pp.20-27.
- Lefeuvre, E., Audigier, D., Richard, C. and Guyomar, D. (2007). Buck-Boost Converter for Sensorless Power Optimization of Piezoelectric Energy Harvester. *IEEE Transactions on Power Electronics*, 22(5), pp.2018-2025.
- Leonov, V., Torfs, T., Fiorini, P. and Van Hoof, C. (2007). Thermoelectric Converters of Human Warmth for Self-Powered Wireless Sensor Nodes. *IEEE Sensors J.*, 7(5), pp.650-657.
- McKinsey, (2014). How big data and connected consumer products could boost the market for MEMS technology. [online] Available at: http://www.mckinsey.com/client-service/semiconductors/latest_thinking
- Mitcheson, P., Yeatman, E., Rao, G., Holmes, A. and Green, T. (2008). Energy Harvesting From Human and Machine Motion for Wireless Electronic Devices. *Proceedings of the IEEE*, 96(9), pp.1457-1486.
- Neri, I., Travasso, F., Mincigrucci, R., Vocca, H., Orfei, F. and Gammaitoni, L. (2012). A real vibration database for kinetic energy harvesting application. *Journal of Intelligent Material Systems and Structures*, 23(18), pp.2095-2101.
- Press, G. (2014). Internet of Things by the numbers: Market estimates and forecasts. [online] *Forbes.com*. Available at: <http://www.forbes.com/sites/gilpress/2014/08/22/internet-of-things-by-the-numbers-market-estimates-and-forecasts/>
- Priya, S. and Inman, D. (2008). *Energy harvesting technologies*. New York: Springer.

- Puscasu, O., Monfray, S., Savelli, G., Maitre, C., Pemeant, J., Coronel, P., Domanski, K., Grabiec, P., Ancey, P., Cottinet, P., Guyomar, D., Bottarel, V., Ricotti, G., Bimbaud, I., Boeuf, F., Gaillard, F. and Skotnicki, T. (2012). An innovative heat harvesting technology (HEATec) for above-Seebeck performance. *2012 International Electron Devices Meeting*.
- Puscasu, O., Monfray, S., Boughaleb, J., Cottinet, P., Rapisarda, D., Rouvière, E., Delepierre, G., G.Pitone, Maitre, C., Boeuf, F., Guyomar, D. and Skotnicki, T. (2014). Flexible bimetal and piezoelectric based thermal to electrical energy converters. *Sensors and Actuators A: Physical*, 214, pp.7-14.
- PwC, (2015). *The Internet of Things: The next growth engine for the semiconductor industry*. [online] Available at: <http://www.pwc.com/gx/en/industries/technology/publications/internet-of-things.html>
- Raghunathan, V., Schurgers, C., Sung Park, and Srivastava, M. (2002). Energy-aware wireless microsensor networks. *IEEE Signal Process. Mag.*, 19(2), pp.40-50.
- Randall, J. and Jacot, J. (2003). Is AM1.5 applicable in practice? Modelling eight photovoltaic materials with respect to light intensity and two spectra. *Renewable Energy*, 28(12), pp.1851-1864.
- Schoenberger, C. R. (2002). The internet of things. [online] *Forbes.com*. Available at: <http://www.forbes.com/global/2002/0318/092.html>
- STMicroelectronics (2010), Application Note AN3182, Tilt measurement using a low-g 3-axis accelerometer.
- STMicroelectronics (2015), STM32L152x6/8/B datatsheet
- STMicroelectronics (2015), BlueNRG datasheet, Bluetooth® low energy wireless network processor
- STMicroelectronics (2008), LM135-LM235-LM335 datatsheet
- Trioux, E., Monfray, S., Skotnicki, T., Basrou, S. and Mural, P. (2014). Characterization of piezoelectric material for micro thermal harvesters. *J. Phys.: Conf. Ser.*, 557, p.012087.
- Vullers, R., van Schaijk, R., Doms, I., Van Hoof, C. and Mertens, R. (2009). Micropower energy harvesting. *Solid-State Electronics*, 53(7), pp.684-693.
- Wilson, J. and Mather, R. (2015). Photovoltaic energy harvesting for intelligent textiles. *Electronic Textiles*, pp.155-171.
- Yick, J., Mukherjee, B. and Ghosal, D. (2008). Wireless sensor network survey. *Computer Networks*, 52(12), pp.2292-2330.
- Zahid Kausar, A., Reza, A., Saleh, M. and Ramiah, H. (2014). Energizing wireless sensor networks by energy harvesting systems: Scopes, challenges and approaches. *Renewable and Sustainable Energy Reviews*, 38, pp.973-989.

Zhu, D., Tudor, M. and Beeby, S. (2009). Strategies for increasing the operating frequency range of vibration energy harvesters: a review. *Measurement Science and Technology*, 21(2), p.022001.

Chapter 1

Materials and devices for thermal energy harvesting

1 Introduction

In the introduction of this thesis, we briefly exposed some aspect of thermal energy harvesting, without giving a clear overview of the various technologies developed to transform heat into electrical energy. This first chapter thus is a state-of-the-art on thermal energy harvester. In a first time, we present some theoretical background on heat engines which enables to give to establish Figure-of-Merits that can be used to compare thermal generators with each other. Then we present main technologies of heat engines: thermo-electric generators, pyroelectric generators, fluid-based heat engines, solid-based heat engines, and thermomagnetic generators.

2 Maximal efficiency and maximal power of heat engines

2.1 Carnot heat engine

Thermodynamically speaking, heat is a form of energy that is differs from other form of energy qualified as “noble” like mechanical, electric, magnetic, chemical, nuclear, kinetic, radiative energies, in the sense that heat cannot be transform with an efficiency of 1 into another form of energy, whereas mechanical energy, electrical energy etc. can be fully converted in an other form of the energy, or degraded with an efficiency of 1 into heat. The other difference between thermal generators and other generators is also is that heat engines needs two heat sources at different temperatures to generate a quantity of work.

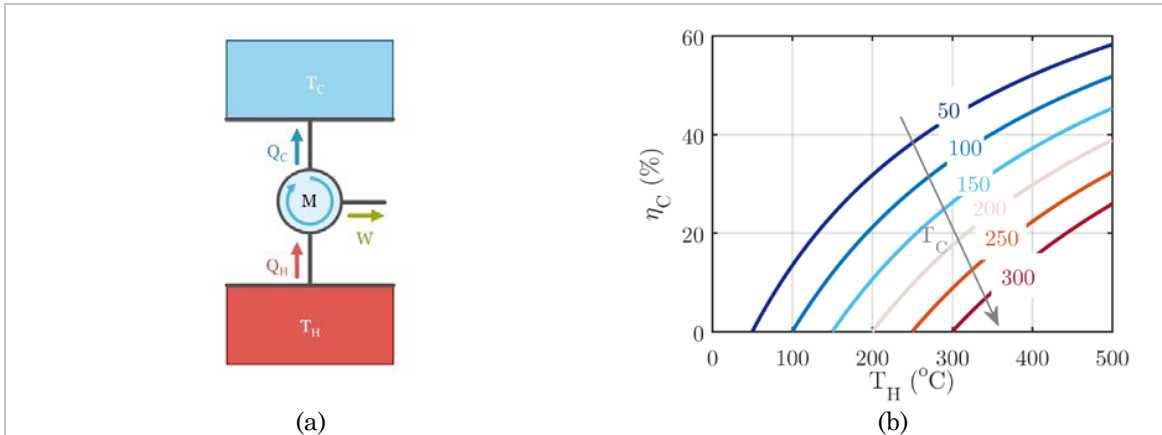


Figure 2.1.1. *a. Representation of the Carnot heat engine. b. Efficiency of the Carnot heat engine as a function of the hot source's temperature.*

This last observation historically is the first statement of thermodynamics' second principle by Sadi Carnot claiming that “la production de la puissance motrice est due dans les machines à vapeur, non à une consommation réel du calorique, mais à son transport d'un corps chaud à un corps froid” [Carnot, 1824]. This can be translated into equations by applying the first principle (1.1.1a) and second principle to the heat engine presented in Fig.2.1.1a.

$$Q_H = W + Q_C \quad (2.1.1a)$$

$$d\Sigma = \frac{Q_H}{T_H} - \frac{Q_C}{T_C} > 0 \quad (2.1.1b)$$

As a consequence we find that the heat engine's efficiency cannot exceed a value that is only function of the external temperatures, explaining why Carnot stated that “La puissance motrice de la chaleur est indépendante des agents mis en oeuvre pour la réaliser: sa quantité est fixée uniquement par les températures des corps entre lesquels se fait, en dernier résultat, le transport du calorique”. Hence the Carnot efficiency can only be reached for a reversible transformation.

$$\eta = \frac{W}{Q_H} < \eta_C = 1 - \frac{T_C}{T_H} \quad (2.1.2a)$$

The strength of Carnot's model is to give a simple expression of the maximal theoretical efficiency for all heat engines without making assumption on the type of working medium. Efficiency of Carnot heat engines is plotted in Fig.2.1.1a as function of the hot source's temperature and for various values of the cold source's temperature. Typically for a hot source at 100°C and a cold source at 50°C, the maximal theoretical efficiency of a heat engine is of 13,5% and reaches 58,2% at 500°C. Yet the drawback of the Carnot's model is to assume a fully reversible transformation whereas thermal transfers are known to be an irreversible process. As a consequence, Carnot engine is a generating for which no thermal transfers occur, infinitely slowly cycled, and producing zero power.

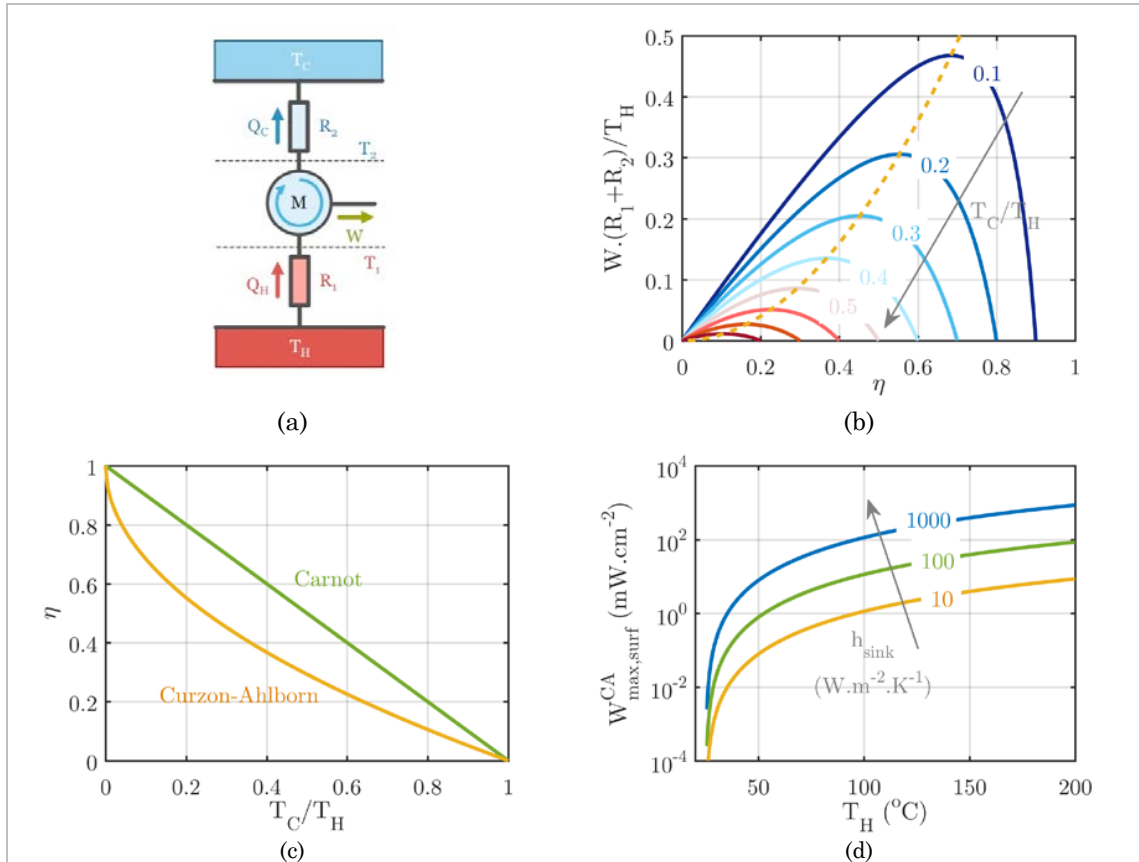


Figure 2.1.2. a. Representation of the Curzon-Ahlborn heat engine. b. Evolution of the normalized power against the intrinsic Carnot efficiency for various values of the ratio T_C/T_H . c. Comparison of the Curzon-Ahlborn efficiency and Carnot efficiency for various values of T_C/T_H . d. Surface density of output power generated by a heat engine working with a bulky heat sink or with a planar heat sink.

Carnot heat engine thus is not the ideal model to describe real thermal heat engines even if it furnishes a Figure of Merit to compare the performances of heat engines with each other.

2.2 Curzon-Ahlborn efficiency

Curzon-Ahlborn heat engine describes a generic model of reversible Carnot thermal generator taking into account thermal diffusive transfers between the hot source and the cold source. As a consequence this heat engine is qualified by the term “endoreversible” [Chen *et al.*, 2001]. With this model, Curzon and Ahlborn found an expression giving the efficiency at maximum power of the generator represented in Fig.2.1.2a [Curzon and Ahlborn, 1975]. For the detail, the demonstration of this formula is generally attributed to Curzon and Ahlborn, but is also named Chambadal-Novikov-Curzon-Ahlborn efficiency because of earlier independent demonstrations by Chambadal and by Novikov, both in

1957. However Vaudrey *et al* [Vaudrey *et al*, 2014] found prior demonstration of the formula of the efficiency at maximal power by Yvon in 1955 and Reitlinger in 1929.

Curzon-Ahlborn model is a starting point for various models of heat engines [Chen *et al*, 2001], including the model of the Stefan-Boltzmann engine [Bauer, 2015]. This engine is used to calculate the theoretical maximal efficiency of photovoltaic cells by replacing Fourier-type thermal transfers by Stefan-Boltzmann radiative transfers. It is based on the fact that incident flux of photons are either converted in electron-holes pairs or transformed into heat, elevating the temperature of the solar cell. The main difficulty in developing this model is linked to the non-linearity of radiative transfers. Similarly, the Muser engine assumes that radiative energy transfers only occur between the hot source and the solar cell [Muser, 1957].

To demonstrate the expression of the Curzon Ahlborn efficiency, we simply need to write the expressions of the input and output heat flux as a function of the temperatures of the system (2.1.3a and 2.1.3b) and the reversibility of the heat engine (2.1.3c) and the conservation of the energy (2.1.3d). The Carnot efficiency of the mover gives a link between the temperature T_1 and T_2 (2.1.3e).

$$\dot{Q}_H = \frac{1}{R_1} \cdot (T_H - T_1) \quad (2.1.3a)$$

$$\dot{Q}_C = \frac{1}{R_2} \cdot (T_2 - T_C) \quad (2.1.3b)$$

$$\frac{\dot{Q}_H}{T_1} - \frac{\dot{Q}_C}{T_2} = 0 \quad (2.1.3c)$$

$$\dot{Q}_H = \dot{W} + \dot{Q}_C \quad (2.1.3d)$$

$$\eta = 1 - T_2/T_1 \quad (2.1.3e)$$

Hence the expression of the temperatures T_1 and T_2 are simply given by (2.1.4a) and (2.1.4b), while the power is given by (2.1.4c).

$$T_1 = \frac{R_2}{R_1 + R_2} \cdot T_H + \frac{R_1}{R_1 + R_2} \cdot \frac{1}{1 - \eta} \cdot T_C \quad (2.1.4a)$$

$$T_2 = \frac{R_2}{R_1 + R_2} \cdot (1 - \eta) \cdot T_H + \frac{R_1}{R_1 + R_2} \cdot T_C \quad (2.1.4b)$$

$$\dot{W} = \frac{1}{R_1 + R_2} \cdot \frac{\eta}{1 - \eta} \cdot ((1 - \eta) \cdot T_H - T_C) \quad (2.1.4c)$$

Fig.2.1.2b represents the evolution of the power as a function of the intrinsic efficiency of the reversible heat engine for various values of the ratio T_C/T_H showing that there exists

an optimal value of the efficiency that maximizes the output power. Logically we observe that reducing the temperature difference between the two heat sources decreases the generator's output power. A simple derivation of this last equation enables to find that the power is maximized when the efficiency is a simple function of the external temperatures (2.1.5a). This value of the efficiency is the Curzon-Ahlborn bound [Curzon and Ahlborn, 1975]. The maximal power generated by the heat engine is then given by (2.1.5b). Thermal energy harvesters being generally in contact with the hot source and evacuating heat by means of a heat sink, we can rewrite this last equation to express the surface density of power generated by the Curzon-Ahlborn generator. Logically we see with this equation that the best way to produce energy is to use a bulky heat sink in order to evacuate more heat from the device.

$$\eta_{opt}^{CA} = 1 - \sqrt{\frac{T_C}{T_H}} \quad (2.1.5a)$$

$$\dot{W}_{max}^{CA} = \frac{\eta_{opt}^{CA 2} \cdot T_H}{R_1 + R_2} \quad (2.1.5b)$$

$$\dot{W}_{max,surf}^{CA} = \eta_{opt}^{CA 2} \cdot T_H \cdot h_{sink} \quad (2.1.5c)$$

The evolution of the Curzon-Ahlborn efficiency is plotted against the ratio in Fig.2.1.2c, showing that it is lower than the Carnot efficiency of around 30% for a ratio T_C/T_H equal to 0,4. In the same time, Fig.2.1.2d represents the evolution of the maximal power generated by the Curzon Ahlborn efficiency, showing that the maximal power is of around 100mW.cm⁻² for a heat engine working at 100°C with a bulky heat sink. Equation (2.1.5) provides a useful metrics for the evaluation of the performances of various heat engines. Equation (2.1.6) defines the Curzon-Ahlborn relative efficiency of a thermal generator. Carnot relative efficiency and Curzon-Ahlborn relative efficiency furnish two solutions to compare heat engines.

$$\eta_{CA} = \frac{\eta_{abs}}{\eta_{opt}^{CA}} \quad (2.1.6)$$

3 Thermoelectric generators

Thermoelectric generators being the most widely used technology to convert heat into electrical energy, we first present an overview on the theory and the development of thermoelectric materials and thermoelectric generators.

3.1 Thermoelectric effect

Discovery of the thermoelectric effect is the results of three successive discoveries: the Seebeck effect, describing the creation of voltage drop across a junction of two materials, was first observed by Seebeck in 1821 [Seebeck, 1821], measuring the displacement of a

needle placed on a thermocouple he heated. The second discovery is due to Peltier in 1834 [Peltier, 1834] observing a temperature change of the two materials of Seebeck's thermocouple when the is is crossed by electric current. Finally, Thomson (also named Lord Kelvin) demonstrated in 1851 that heat rejection or heat absorption can also occurs in a single material, and that Peltier effect (characterized by the coefficient π), Seebeck effect (characterized by the parameter α) and Thomson effect (τ) are linked by two equations reproduced in (3.1.1a) and (3.1.1b) [Thomson, 1851].

$$\pi_{AB} = \alpha_{AB} \cdot T \quad (3.1.1a)$$

$$\frac{d\alpha_{AB}}{dT} = \frac{\tau_A - \tau_B}{T} \quad (3.1.1b)$$

Yet Thomson demonstrated the relation between the heat generated by a thermoelectric element and the current flowing through it, the rigorous demonstration of the link between thermal transfers and thermoelectricity is associated to the work of Onsager and to its development of the theory of irreversible thermodynamics in 1931[Onsager, 1931]. Applied to thermoelectricity, this theory shows that Seebeck coefficient simply expresses the coupling effect between the thermal flux J_Q and the electric current J_N , and that the thermal gradient is the driving force of heat flux and is equivalent to the by its nature to electric field [Callen, 1960].

$$J_N = \sigma \cdot \mathcal{E} + \alpha \cdot \sigma \cdot T^2 \cdot \nabla \left(\frac{1}{T} \right) \quad (3.1.2a)$$

$$J_Q = \alpha \cdot \sigma \cdot T \cdot \mathcal{E} + (\alpha^2 \cdot \sigma \cdot T + \kappa) \cdot T^2 \cdot \nabla \left(\frac{1}{T} \right) \quad (3.1.2b)$$

Rewriting this last equation in short-circuit enables to define the adimensional Figure of Merit ZT of the thermoelectric materials, as defined by Altenkirch in 1911 [Rowe, 1995].

$$J_Q = -\kappa \cdot \left(\frac{\alpha^2 \cdot \sigma}{\kappa} \cdot T + 1 \right) \cdot \nabla T \quad (3.1.3a)$$

$$Z \cdot T = \frac{\alpha^2 \cdot \sigma}{\kappa} \cdot T \quad (3.1.3b)$$

As seen this factor increases as the electrical conductivity in the material, the square of the Seebeck coefficient and is inversely proportional to the thermal conductivity of the materials. A large part of the research on thermoelectricity is devoted to materials engineering in order to enhance this factor of Merit in order to boost the performances of thermoelectric generators. First techniques developed consisted in increasing the electrical conductivity of semiconductors by doping materials. Yet this technique is limited by the fact that Seebeck effect degrades with very strong doping. Current researchs mainly deals with fabrication of nanostructured materials or superlattices to increase phonons scattering given that phonons are known to be mainly responsible for the

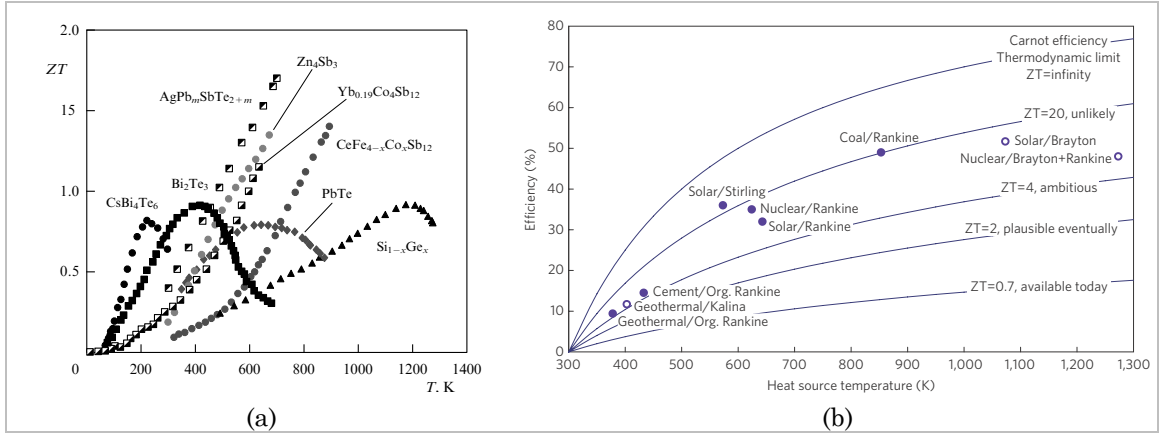


Figure 3.1.1. *a. Typical ZT of some thermoelectric materials [Dmitriev and Zvyagin, 2010]. b. Comparison between the performances of various sources of energy and thermoelectric ZT factor [Vining, 2009].*

thermal conductivities of semi-conductor materials. Extensive reviews of these techniques can be found in [Dmitriev and Zvyagin, 2010] or [Alam and Ramakrishna, 2012]. Fig.3.1.1a presents the evolution of ZT against the temperature for some thermoelectric materials. For applications at ambient temperatures or less than 100°C, this figure shows that best materials are bismuth telluride (Bi₂Te₃ or similar compounds). Typically, a ZT factor equal to 4 is considered as the minimum value so that thermoelectric effect be used to produce energy and be competitive with solar energy as a exemple [Vining, 2009]. Maximal values experimentally measured are between 2 -2,5 [Ohta, 2007].

3.2 Optimization of the performances of thermoelectric generators

The first attempt to model the operation and efficiency of thermoelectric generators is due to Rayleigh in 1885 [Rowe, 1995] but was really achieved by Ioffe in 1957 [Ioffe, 1957]. Considering the basic thermocouple made of two semiconductor legs (length l , and cross sections S_N and S_P , resistivities ρ_N and ρ_P , thermal diffusivity κ_P and κ_N , Seebeck coefficients α_N and α_P), he showed that the optimal design that maximized the intrinsic efficiency of the generator is obtained by matching the cross section according to (3.2.1a), and the load resistance according to (3.2.1b) where T_m is the average temperature of the heat engine and R the equivalent electrical resistance of the thermoelectric element. The optimization of the semiconductor rods' sections leads to the expression of the equivalent Z factor given by (3.2.1c). Hence the output voltage of a single thermocouple is then simply given by (3.2.1d), whereas the efficiency of the heat engine is given by (3.2.1e). To raise the output voltage up to some volts, generators are made of hundreds of series thermocouples.

$$S_N = S_P \cdot \sqrt{\frac{\rho_N \cdot \kappa_P}{\rho_P \cdot \kappa_N}} \quad (3.2.1a)$$

$$R_L = R \cdot \sqrt{1 + Z \cdot T_m} \quad (3.2.1b)$$

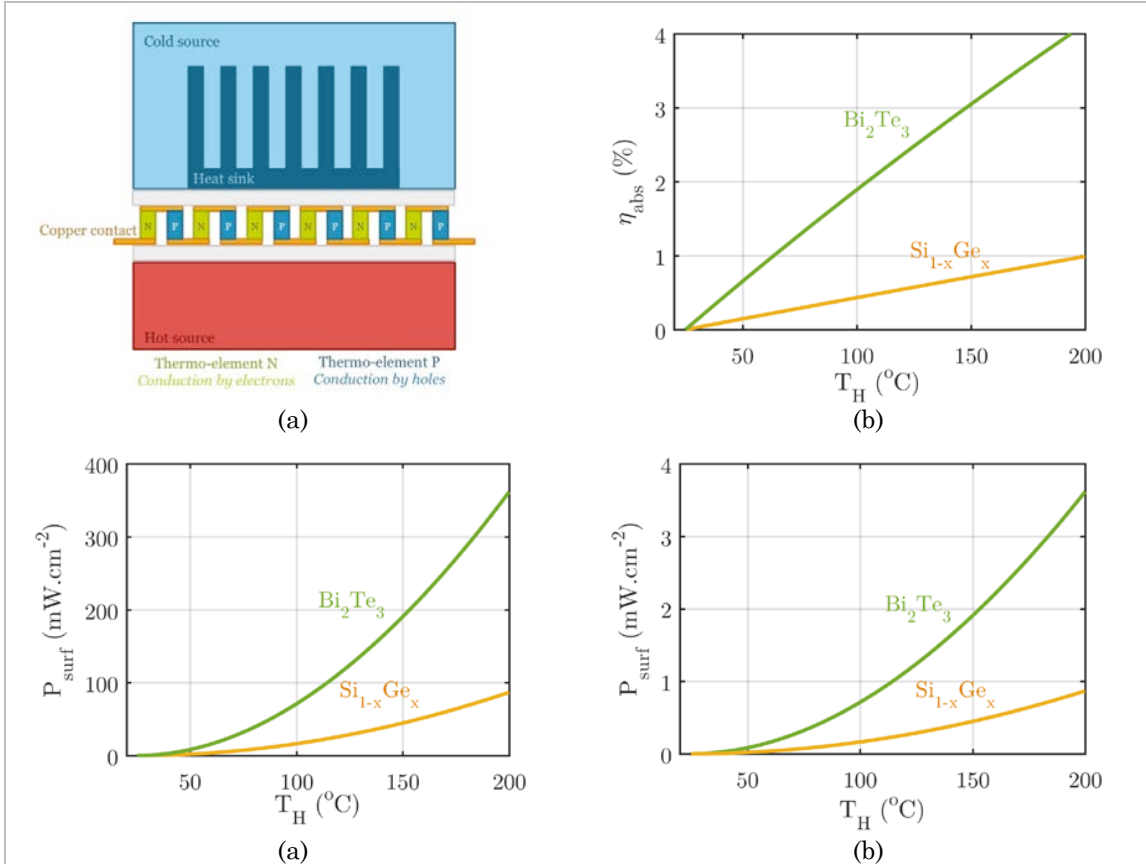


Figure 3.1.2. a. Representation of the thermoelectric generator. b. Evolution of the thermal efficiency of two thermoelectric generators using either SiGe-based thermocouples or Bi_2Te_3 -based thermocouples (cold source at room temperature). c. Evolution of the output power with a bulky heat sink ($h=1000\text{W}\cdot\text{K}^{-1}\cdot\text{m}^{-2}$). d. Evolution of the output power delivered by both generators with a planar heat sink ($h=10\text{W}\cdot\text{K}^{-1}\cdot\text{m}^{-2}$).

$$Z = \left(\frac{\alpha_P - \alpha_N}{\sqrt{\rho_N \cdot \kappa_N} + \sqrt{\rho_{NP} \cdot \kappa_P}} \right)^2 \quad (3.2.1c)$$

$$V_{max} = \frac{\sqrt{1 + Z \cdot T_m}}{1 + \sqrt{1 + Z \cdot T_m}} \cdot (\alpha_P - \alpha_N) \cdot (T_1 - T_2) \quad (3.2.1d)$$

$$\eta_{abs} = \frac{T_1 - T_2}{T_1} \cdot \frac{\sqrt{1 + Z \cdot T_m} - 1}{\sqrt{1 + Z \cdot T_m} + T_2/T_1} \quad (3.2.1e)$$

These expressions do not require any hypothesis on the way heat is evacuated from, or supplied to the thermal generator. Understanding that the Seebeck generator is equivalent to a simple thermal resistance, the maximal value of heat flux crossing the harvester is obtained by matching the thermal resistance of the heat exchangers to the generator's equivalent thermal resistance. Hence the temperature difference across the

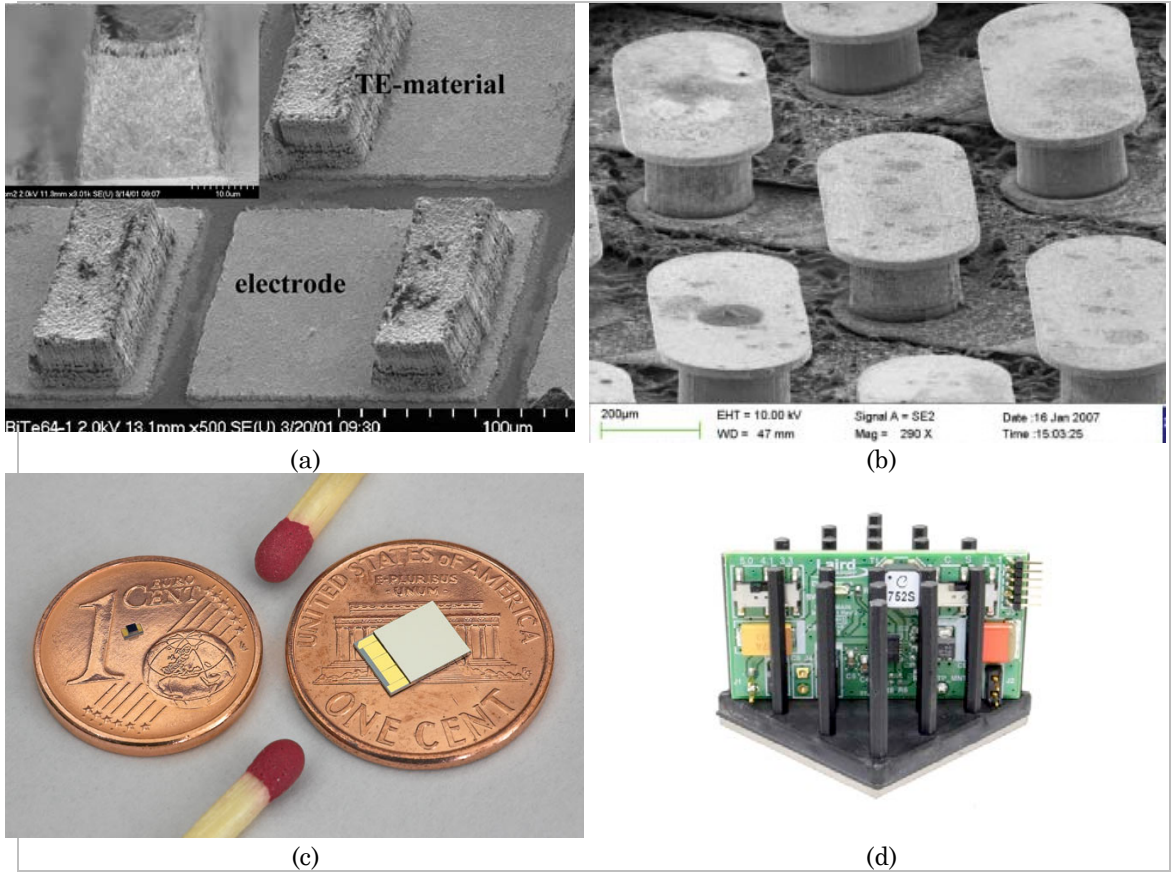


Figure 3.1.3. a. Architecture of thermoelectric generator presented in [Bottner et al, 2004]. b. Thermocouples made of Cu and Ni legs [Briand et al, 2015]. d. Technologies developed by Micropelt [Micropelt]. d. Wireless sensing node developed by Laird [Laird].

generator is half the external temperature and the thermal flux flowing through the generator is simply given by (3.1.4a). The maximal power is then given by (3.1.4b) if a heat sink (either planar or bulky) is used.

$$\dot{Q} = \frac{T_H - T_C}{2 \cdot R_{sink}} \quad (3.1.4a)$$

$$P_{max} = \eta_{abs} \cdot \dot{Q} = \frac{(T_H - T_C)^2}{4 \cdot T_H} \cdot \frac{\sqrt{1 + Z \cdot T_m} - 1}{\sqrt{1 + Z \cdot T_m} + T_2/T_1} \cdot h_{sink} \cdot S_{sink} \quad (3.1.4b)$$

As an example, we plot in Fig.3.1.2 the evolution of the performances of two generators either made of Si-Ge thermocouples ($Z=5 \cdot 10^{-4} \text{ K}^{-1}$) or Bi_2Te_3 thermocouples ($Z=3 \cdot 10^{-3} \text{ K}^{-1}$). For a device working without heat sink (planar heat sink indeed), SiGe-based generator produces $160 \mu\text{W} \cdot \text{cm}^{-2}$ whereas Bi_2Te_3 -based generator produces $700 \mu\text{W} \cdot \text{cm}^{-2}$ for a heat source at 100°C and the threshold value of $10 \mu\text{W} \cdot \text{cm}^{-2}$ necessary to power Wireless Sensing node is reached for a temperature of 33°C for Bi_2Te_3 -based generator and for 45°C for SiGe-based generator. With a massive heat sink, the power can be multiplied by 1000

reaching $700 \mu\text{W}\cdot\text{cm}^{-2}$ with Bi_2Te_3 . For an effective temperature difference of 5°C across the generator (hot source at 35°C), the Bi_2Te_3 -based generator is expected to deliver $2,1 \text{ mW}\cdot\text{cm}^{-2}$, closed to the $1,8 \text{ mW}\cdot\text{cm}^{-2}$ produced in the same conditions by Micropelt's generators [Briand *et al*, 2015].

Once the thermoelectric materials are chosen, Ioffe's optimal design leaves only the legs' length as a variable parameter. [Mayer and Ram, 2006] proposed an optimization of the thickness of the energy harvester in order to match the thermal impedance of a given heat sink using the previous techniques. This approach is followed by Leonov in [Leonov, 2011] to design compact wearable thermo-electric generators: with doped poly-silicon-based thermocouples, its generator achieved generating up to $9 \mu\text{W}\cdot\text{cm}^{-2}$ from the heat evacuated by a human body and the ambient air at 20°C (in agreement with previous curves). Since industrialization of thermal generator is only possible for low-cost products, Rowe and Min [Rowe and Min, 1996] proposed a cost-driven optimization of the performances of thermoelectric generators consisting in scaling down the size of the thermocouple so that the volume of matter used is minimal and then to design a thermally matched heat sink so that the generated power be maximal. This strategy can be justified by the fact that heat sink are cheaper than thermoelectric materials. Rowe and Min found a minimal value of thermocouple's length around $500 \mu\text{m}$ explained by the relative increase of parasitic thermal resistance at the microscale that degrades the performances of the thermal generator. Yet the evolution of the microelectronics since the publication of Rowe and Min enabled reducing this minimum size. As an example, thermocouples produced by Micropelt based on bismuth telluride measure $36 \mu\text{m}$ and around 500 series thermocouples can generate voltages of around $0,5\text{V}$ with a fixed temperature difference of 5°C . Taking into account the price of thermoelectric materials, heat sink, manufacturing costs, Leblanc *et al* [Leblanc *et al*, 2014] used Rowe and Min's optimization scheme to evaluate the price of thermoelectric energy, showing that the mean cost of $\text{Bi}_2\text{-Te}_3$ modules was of around $80\$/\text{W}$ for low-grade heat applications (heat source below 100°C). Precise comparison of performances of thermoelectric generators can be found in [Briand *et al*, 2015].

Table 3. Performances of some thermoelectric generators

Generator	$\Delta T ; T_H$ ($^\circ\text{C}$)	V_{out} (V)	V_{out} (1 TC) (mV)	S (cm^2)	P_{surf} ($\text{mW}\cdot\text{cm}^{-2}$)	Comment
Micropelt	5 ; -	0,55	0,95	0,14	1,77	$(\text{Bi,Sb})_2(\text{Te,Se})_3$ Bulk heat sink
Nextreme/Laird	10 ; -	0,26	-	0,1	15	Bi_2Te_3 Bulk heat sink
Perpetua	5 ; -	3,66	-	6,4	0,078	Bi_2Te_3 Bulk heat sink
Bottner et al, 2004	5 ; -	0,043	3,6	0,01	0,056	$(\text{Bi,Sb})_2\text{Te}_3$
Leonov <i>et al</i> , 2011	14; 37	0,9	0,52	12	0.009	SiGe Planar heat sink

4 Pyroelectric generators

4.1 Simple pyroelectric generators

Pyroelectricity refers to the property of some piezoelectric materials to polarize under a raise or a decrease of their temperature. Basically, pyroelectric materials can be described by means of the two constitutive equations exposed in (4.2.1), showing that pyroelectric effect represents the proportionality factor between the temperature and the polarization but also the proportionality factor between the electric field and the entropy.

$$d\mathcal{D} = p \cdot dT + \varepsilon \cdot d\mathcal{E} \quad (4.2.1a)$$

$$d\Sigma = \frac{\rho \cdot c}{T} \cdot dT + p \cdot d\mathcal{E} \quad (4.2.1b)$$

In short circuit, these two equations can be rewritten under the form (4.2.2) showing that the current is directly proportionnal to temporal temperature's fluctuations. Moreover it allows introducing the electrothermal coupling factor, equivalent to the piezoelectric coupling factor, representing the capability of the pyroelectric material to convert heat into electric energy.

$$\dot{\mathcal{D}} = p \cdot \dot{T} \quad (4.2.2a)$$

$$\dot{Q} = \rho \cdot c \cdot \left(1 - \frac{p^2 T}{\varepsilon \cdot \rho \cdot c}\right) \cdot \dot{T} + \frac{p}{\varepsilon} \cdot \dot{\mathcal{D}} \quad (4.2.2b)$$

$$k_{th} = \frac{p^2 T}{\varepsilon \cdot \rho \cdot c} \quad (4.2.2c)$$

As a consequence, many works presented the generation of electricity from heat by means of pyroelectric materials. [Mane *et al*, 2011] presented the cycling light heating and convective cooling of PMN-PT and PZT samples using a rotating wheel, enabling to generate power densities of about $8.6 \mu\text{W}\cdot\text{cm}^{-3}$ (equivalent to a surface power density of $0.23 \mu\text{W}\cdot\text{cm}^{-2}$) at a frequency of 0,1 Hz and a with a temperature change rate of $8 \text{ K}\cdot\text{s}^{-1}$. Quite similar experiences with similar measured values of power densities are reported in [Zhang *et al*, 2011; Cuadras *et al*, 2010].

In [Sebald *et al*, 2009], Sebald and co-workers presented the evaluation of the mean power generated by a $\text{Pb}(\text{MgNb})_{0.3}\text{PbTiO}_3$ compound over a whole day, showing that the mean generated power along a day is of $1 \mu\text{W}\cdot\text{cm}^{-3}$. Similarities between pyroelectric generators and piezoelectric energy harvesters allowed Sebald coworkers to propose in [Sebald *et al*, 2008] various models of the performances of pyroelectric generators performing either resistive or SECE-like, SSHI-like or Carnot cycles, pointed out the matter of the electrothermal coupling factor as a determinant of pyroelectric generators' performances. For a SECE-like cycle (Fig.4.1.1), the Carnot relative efficiency is given by (4.2.3a) and the power by (4.2.3b).

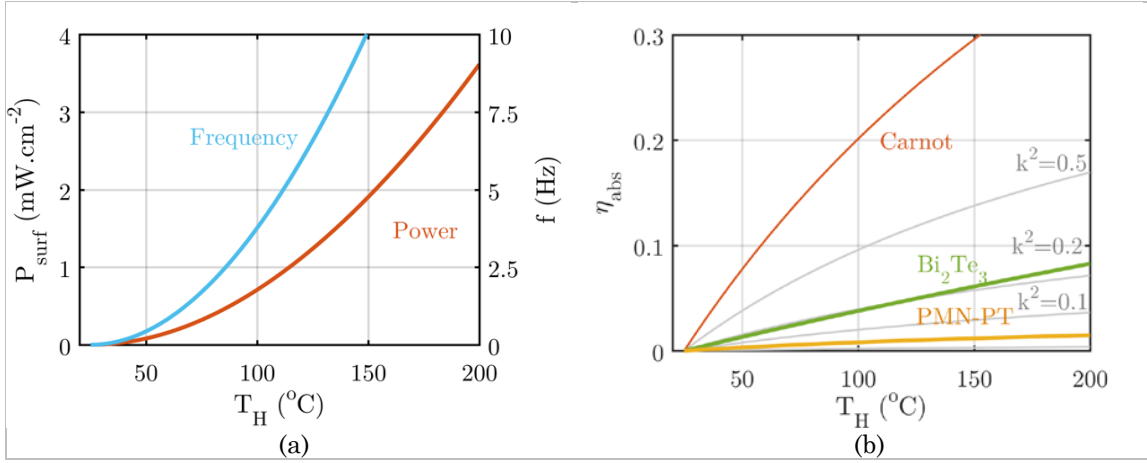


Figure 4.1.1. *a.* Performances of a thermoelectric generator as a function of the temperature and cycling frequency of a pyroelectric generator. *b.* Comparison between the efficiencies of a 200- μm thick PMN-PT layer and a thermoelectric generator working with a planar heat sink.

$$\eta_{\text{rel}} = \frac{k_{\text{th}}^2}{1 + 0.5 \cdot k_{\text{th}}^2 \cdot \frac{T_H - T_C}{T_H}} \quad (4.1.1d)$$

$$\dot{W} = \frac{p^2}{\varepsilon} \cdot (T_H - T_C)^2 \cdot f \quad (4.1.1d)$$

From the observation that with values of electrothermal coupling factor of 10% and using SSHI power-management circuit, the theoretical efficiency of pyroelectric generators could reach 50% of the intrinsic Carnot efficiency, Sebald *et al* concluded by saying that pyroelectric generators could be more performant than thermoelectric generators. In fact, the conclusion must be lightly qualified: In Fig.4.1.1a we plot the power generated by a thermoelectric material working without heat sink and the frequency at which a pyroelectric generator made of a 200- μm thick PMN-PT layer and cycled in a temperature difference of 5°C must operate so that it can generate the same power than the thermoelectric generator. As an example, to generate 700 $\mu\text{W}.\text{cm}^{-2}$ (like a thermoelectric generator at 100°C), the pyroelectric generator must be cycled at 3.7 Hz with a temperature change rate of 18.5°C.s⁻¹. The characteristic time of propagation of heat into a 200- μm thick PMN-PT layer is of around 1.2s (0.8Hz). As a consequence, there is a chance that the pyroelectric layer thermalizes when the frequency of the temperature variations raises. In the same time, Fig.4.1.1b shows that equivalent efficiencies between thermoelectric and pyroelectric generators can be obtained if pyroelectric materials having an electro-thermal coupling factor of 20% can be found. In the case of PMN-PT, the value of this coefficient is only 0.4%.

4.2 Exploiting phase transitions of ferroelectric materials

Previous models assumed that the physical parameters of the pyroelectric materials were assumed to be constant whatever the temperature, they indeed depends on the temperature and are known to strongly vary around the Curie temperature for ferroelectric materials [Callen, 1960]. As a consequence, various thermodynamic cycles were developed to exploit the variation of these performances, notably the decrease of the dielectric permittivity near the Curie temperature [Clingman and Moore, 1961; Hoh, 1963]. In [Olsen *et al*, 1981] Olsen *et al* demonstrated the operation of Ericsson cycle producing $0,25 \text{ J.cm}^{-3}$ with a Carnot efficiency of 3,4%. Several demonstrations of pyroelectric heat engines exploiting phase transitions are reported in the litterature [Khodayari et al, 2009; Guyomar et al, 2008; Navid *et al*, 2010], showing the possibility to reach efficiency of 55,4% [Navid *et al*, 2010]. From these publications, only [Navid *et al*, 2010] and [Nguyen et al, 2010] report operation of real heat engines. The other demonstrations are made by placing ferroelectric sample in hot bath and cold bath to observe a thermal cycling. The comparison of data given in [Guyomar et al, 2008] and describing experimental performances of PMN-PT-based generators in the frame of the Sebald's model, and data reported in [Khodayari et al 2009] which describes the performances of relaxor crystals realizing a ferroelectric-to-ferroelectric phase transition, enable to see that exploiting phase transitions would enable to gain at least one order of magnitude on the performances of pyroelectric generators.

Table 4. Performances of some pyroelectric generators reported in the literature. FE-FE designates a Ferromagnetic phase to Ferromagnetic phase transition whereas FE-PA designate a Ferroelectric-paraelectric phase transition.

N°	Work	$\Delta T ; T_H$ (°C)	W_{vol} (mJ.cm ⁻³)	f (Hz)	P_{surf} (mW.cm ⁻²)	η_{rel} (%)	ZT_{eq} T_m (°C)	Comment
1	Sebald <i>et al</i> , 2009	16 ; 28	-	0,03	1.10^{-5}	2,4	0,1 20	Resistive No trans. (Exp.)
2	Guyomar <i>et al</i> , 2008	35 ; 140	56	-	-	-	-	Stirling FE-FE (Exp.)
3	Khodayari <i>et al</i> , 2009	10 ; 110	30	0,1	0,3	5,5	0,24 105	Ericsson FE-FE (Exp.)
4	Khodayari <i>et al</i> , 2009	60 ; 160	250	0,1	2,5	1	0,04 130	Ericsson FE-FE (Exp.)
5	Guyomar <i>et al</i> , 2008	7 ; -	-	0,2	0,016	0,05	-	SSHI No trans. (Exp.)
6	Olsen <i>et al</i> , 1981	33 ; 178	250	0,128	15	3,4	0,14 161,5	Ericsson FE-PA (Exp.)
7	Nguyen <i>et al</i> , 2010	15 ; 85	0,058	0,12	0,043	1,26	0,05 73	Ericsson FE-PA (Exp.)
8	Navid <i>et al</i> , 2010	40 ; 185	38	0,5	-	55,4	10,4 165	Ericsson FE-PA (Theory)

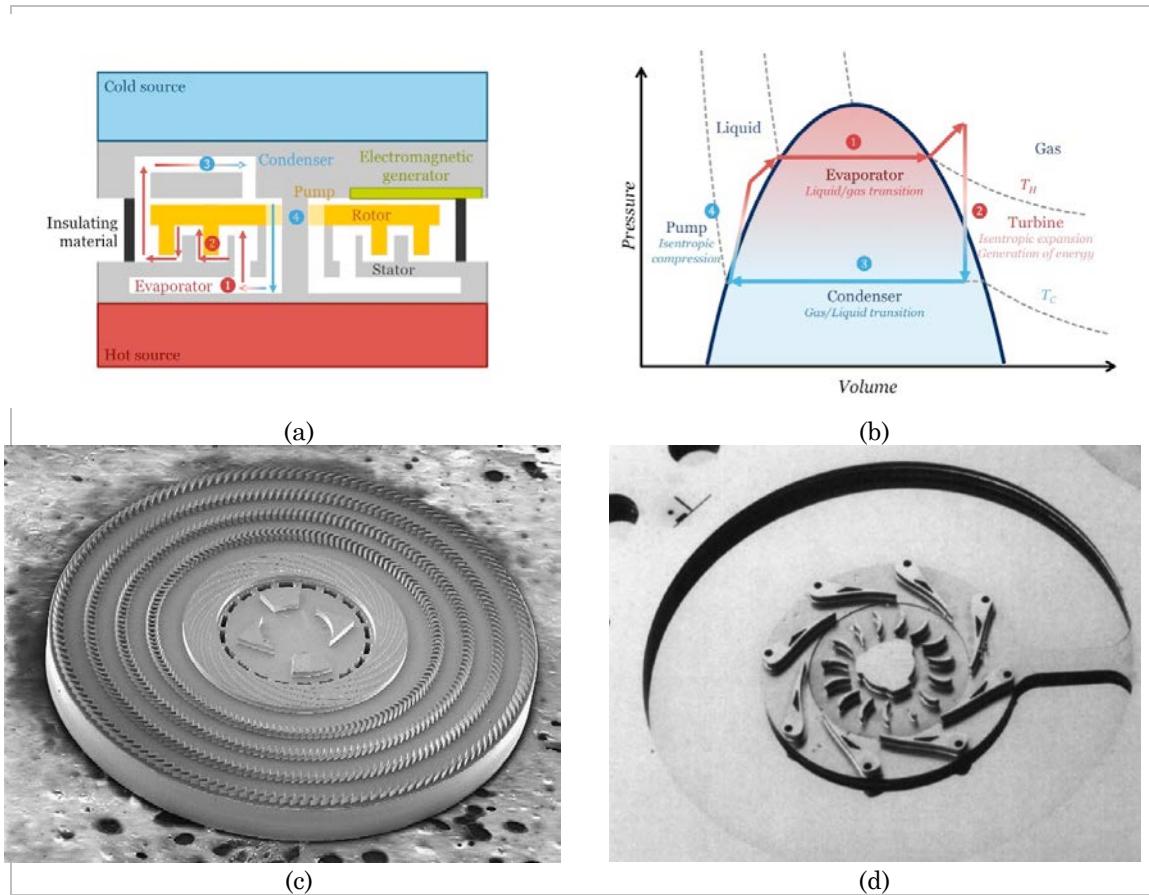


Figure 5.1.1. *a. Representation of the Rankine cycle. b. Simplified architecture of a miniaturized Rankine generator. c. Rotor of a Rankine generator presented in [Lee et al, 2011]. d. Rotor of a Brayton generator presented in [Epstein, 2004].*

5 Fluid-based heat engines

5.1 Downsizing of conventional heat engines

The comparison between fluid-based heat engines and thermoelectric and pyroelectric generators reveals that the performances of these last devices can be considered as weak. As an example, Fig.3.1.1 shows that the equivalent ZTs of Stirling and Rankine engines are of around 20 [Vining, 2009]. Because of these high theoretical efficiencies, many works reports the silicon integration of Rankine cycle [Lee and Frechette, 2011; Frechette et al, 2009]. Modeling of the operation of this heat engine and of its performances at the microscale are presented in [Frechette et al, 2009] and [Cui amd Brisson, 2008]. Fig.5.1.1a represents a simplified schematic of the Rankine engine developed by Lee and coworkers [Lee et al, 2011] whereas Fig.5.1.1c and Fig.5.1.1d show some images of MEMS turbines. In order to understand the operation of the micro-Rankine engine, we represented in Fig.5.1.1b the Rankine cycle. Basically, the fluid is vaporized in contact with the hot source. The expansion of the steam produced during the phase transition is then used to

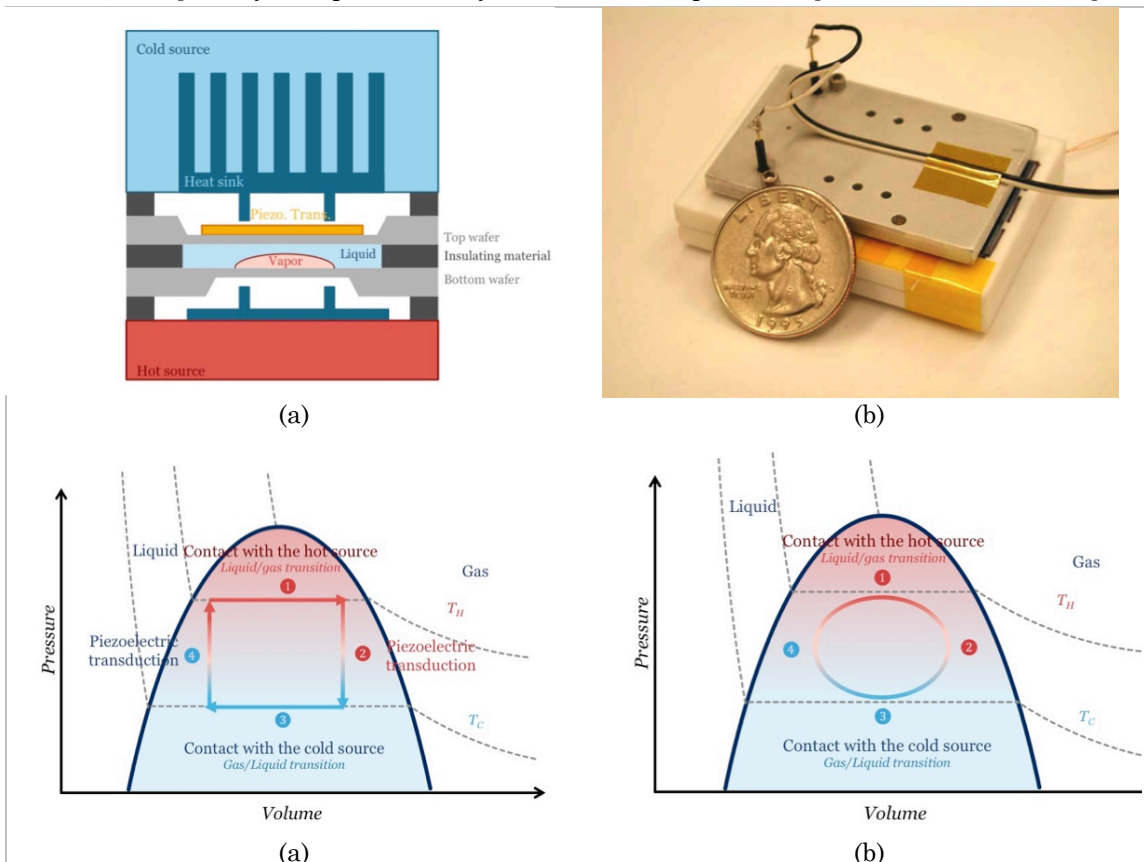
make the turbine turn (where comes the name of “steam engine”), producing a mechanical energy that can be converted into electrical energy by means of an electromagnetic converter. The vapor is then condensed in contact with the cold source in the condenser and then a pump drives the fluid back to the evaporator (Fig.5.1.1b). Given that a phase transition occurs at a fixed temperature, and a fixed pressure, and that compression and expansion can be adiabatic (isentropic), the theoretical efficiency of Rankine engine is closed to Carnot efficiency. In [Frechette *et al*, 2008], Frechette and his coworkers estimated the efficiency of Rankine engines working either between 800°C and -50°C or between 400°C and 250°C, corresponding to conditions found in microcombustion as an example [Fernandez-Pello, 2002]. In the case of an engine working between 800°C and -50°C, they demonstrated the possibility to harvest up to 12,5W.cm⁻² of electrical energy by means of an electromagnetic converter having an efficiency of 50%. These levels of power correspond to a Carnot efficiency of 14,7%, inferior to the theoretical efficiency of a Rankine engine (55,5% of Carnot efficiency in the same conditions). Similar results are found by Cui and Brisson (6,8W.cm⁻² and Carnot efficiency of 18,8% for temperatures between 500°C and 25°C), even if they do not consider the transformation of shaft mechanical power into electrical power. The explanation of this performances degradation are explained in [Frechette *et al*, 2008; Deam *et al*, 2008; Fernandez-Pello, 2002]: As heat engines are scaled down to the microscale, surface effects like viscosity become important and are a source of irreversibility. As a consequence, a large part of the energy is lost by frictions in the turbine and in the bearing of the turbine’s rotor. The other consequence of the size reduction, common to all types of thermal energy harvesters, is the increase of heat leakage due to the passive architectures, the change of the nature of thermal transfers occurring in working fluids, from a convective regim to a conductive regim, as explained in [Deam *et al*, 2008; Fernandez-Pello, 2002]. Other heat engines based on the circulation of a working fluid like Stirling engines [Nakajima *et al*, 1989], Brayton engines [Epstein, 2004] or Wrangle [Lee *et al*, 2004] which have also proposed to generate electrical energy from heat are expected to face the same problems.

5.2 Heat engines using stationary fluids

Given the drawbacks of using circulating fluids in classical Rankine generators, another type of heat engine have been designed, whose design was directly thought to be functional at the microscale and which does not require that the fluid circulates from the hot source to the cold source to produce work. As a consequence, no viscous effect can degrades the performances of these heat engines. These generators are reffered to as “P³ heat engines” in [Whalen *et al*, 2003] or “Saturation Phase-change Internal Carnot Engine” in [Lurie and Kribus, 2010]. The simplified schematic of this energy harvester is presented in Fig.5.2.1a whereas Fig.5.2.1b shows a picture of the device fabricated by [Whalen *et al*, 2003]. It basically consists in a cavity created by the sealing of two silicon wafers that contains a saturated fluid. In the design proposed by Whalen *et al*, the thin membranes delimiting the cavity are made of a piezoelectric layer whose function is to transform the mechanical pressure into electrical energy. The heat engine operates as following: in a first time, heat is provided to the saturated fluid through the bottom

membrane. Being saturated, the fluid follows a phase transition (which is isothermal and isobaric like other phase transitions), which leads to the increase of steam volume in the cavity which applies pressure on the piezoelectric membrane. With the deformation of the piezoelectric membrane, the cavity comes into contact with the cold source, which reduces the part of the steam in the cavity which returns to its initial state. In order to guarantee the asymmetry of the displacement, the bottom membrane is smaller and thus more rigid. Therefore, the cycle described by P^3 heat engine is similar to the Rankine cycle but with a stationary fluid. Given that the vapor or the liquid phases are never saturated, Lurie and Kribus assumed that the thermal efficiency of the cycle is equal to the Carnot efficiency. Starting from this assumption, they developed a lumped thermal capacitance model they coupled with the equation of the piezoelectric transducer to evaluate the performances of the generators. With their model they estimated the possibility to produce up to $34\text{W}\cdot\text{cm}^{-2}$ at a frequency of 1kHz with a cavity of $100\mu\text{m}$ of thickness and with a Carnot efficiency of $26,6\%$, and showing a linear increase of the performances when the dimensions are scaled down.

Figure 5.2.1. a. Simplified schematic of a P^3 heat engine. b. Image of the thermal generator fabricated by [Whalen et al, 2003]. c. Carnot cycle assumed in [Lurie and Kribus, 2010]. d. Cycle experimentally observed and reported in [Bardaweel et al, 2012].



Yet three arguments can qualify to these results. First, the assumption of Lurie that there is no performances degradations due to any heat losses linked to the passive architecture. The second is on the fact that external temperatures are fixed whatever the scaling of the device. The last arguments comes from the comparison of this model with the experimental measurements made by Bardaweel *et al*, and reported in [Bardaweel *et al*, 2012] showing that the real thermodynamic cycle cannot be described by a Carnot engine since it looks like a loop (Fig.5.2.1c). We can try to explain that by seeing that contrary to conventional Rankine engines, the various phases of the thermodynamic cycle are coupled: as a consequence, the compression and expansion steps are not adiabatic and cannot be represented by isentropic curves, since heat is supplied or rejected from the system at the time as mechanical energy is harvested by the piezoelectric transducer. Similarly, phase transition steps are not isobaric because of the deformation of the piezoelectric membrane. As a consequence, the heat engine operation cannot be described by a Carnot cycle.

Measurements of the equivalent thermal resistance of the generator were performed by Cho and coworkers, showing that this resistance was very weak (around 1K.W^{-1}) and without any strategy to actively evacuate heat from the generator, this last one rapidly thermalizes and stops working. Therefore they proposed to use liquid-metal micro-droplet array either to supply heat to the device or to evacuate heat from it. In the first case of figure, the performances of the generators rapidly degrades if the thermal switch's frequency is increase because of the thermalization of the heat engine and the degradation of the efficiency due to the raise of the thermal switch's power consumption. In the second case of figure, the improvement of heat evacuation linked to the raise of the thermal switch's operating frequency largely balances the raise of the switch's consumption. For a device working between 40°C and 60°C , mean power densities of around $1,4\text{ mW.cm}^{-2}$ are measured with an active heat supply at 5Hz (corresponding to a Carnot efficiency of $0,23\%$) and 10 mW.cm^{-2} with an active heat evacuation at 100 Hz (corresponding to a relative efficiency of $1,7\%$). The conclusions of that experiments first shows that Lurie and Kribus overestimated the efficiency of their devices and the thermal behavior of P³-heat engines (theoretical working frequency at 1kHz without active heat evacuation). This enables to conclude that despite a simple concept that can be directly scaled down to the microscale, stationary fluid-based heat engine are less efficient than thermoelectric generators and miniaturized Rankine generators. Typical performances of some fluid-based heat engines are then recalled in Table.5.

Table 5. Performances of some fluid-based heat engines.

N ^o	Work	$\Delta T ; T_H$ (°C)	W_{vol} (mJ.cm ⁻³)	f (Hz)	P_{surf} (mW.cm ⁻²)	η_{rel} (%)	ZT_{eq} T_m (°C)	Engine
9	Frechette <i>et al.</i> , 2009	375 ; 400	93.6	64000	1600 T→M	9,4	0,32 213	Rankine (theory)
10	Frechette <i>et al.</i> , 2009	850 ; 800	1308	64000	25000 T→M	28	1,16 375	Rankine (theory)
11	Cui and Brisson, 2008	470 ; 500	-	-	6800 T→M	18,8	0,75 265	Rankine (theory)
12	Cho <i>et al.</i> , 2007	40 ; 60	28	5	1,4 T→M	0,23	0,008 7 40	P-3 active (Exper.)
13	Cho <i>et al.</i> , 2007	40 ; 60	10	100	10 T→M	1,7	0,066 40	P-3 active (Exper.)
14	Lurie and Kribus, 2010	110 ; 140	3,3	1090	34000 T→E	26,6	1,65 85	P-3 passive (theory)

6 Solid-based heat engines

6.1 Observations on phase transitions

The two previous types of heat engines presented, pyroelectric generators and fluid-based heat engines, have shown the interest of exploiting phase transitions, that are non-linear thermodynamic phenomena, to transform heat into mechanical energy. In fluid-based heat engines, the phase transition that is exploited is the liquid-gas first-order phase transition whose order parameter is the density of the phase which strongly varies at the boiling temperature, enabling to produce large mechanical stress. In the case of pyroelectric heat engines, it is either the first-order phase transition of ferroelectric materials, from a ferroelectric state to a paraelectric state or from a ferroelectric state to another ferroelectric state, or the second-order phase transition from a ferroelectric state to a paraelectric state. In the first case, the order parameter that strongly evolves is the permanent polarization of ferroelectric materials at the Curie temperature (the polarization is a first partial derivative of the energy). In the second case, it is the strong variation of the pyroelectric coefficient (secondary partial derivative of the energy), and of the related electrocaloric effect near the Curie temperature that are exploited. The fact that most of the phase transitions occur at fixed temperatures and that transitions are characterized by a hysteretic behavior according to Landau's theory and Devonshire's theory [Uzunov, makes them perfectly suitable to the creation of heat engines.

Starting from this observation, a lot of phase transitions can be potentially exploited to transform heat into another energy. In the category of solid-based heat engines, we can class heat engines based on phase transitions associated to a mechanical order parameter

(strain, stress displacement) even if some of them use pyroelectric effect to convert heat into electricity. In the category of thermo-magnetic heat engines, we will class thermal generators based on a phase transition associated to a magnetic order parameter (magnetization) even if a piezoelectric materials is used to finally convert heat into mechanical energy.

6.2 Shape-memory-alloy-based heat engines

Shape-memory-alloys are materials that are known to exhibit an hysteretic thermomechanical behavior associated to a first-order transition from a highly compliant phase (Martensitic phase) to a less compliant phase (Austenitic phase) resulting from the change of the crystal structure of the metallic alloy [Mohd Jani et al, 2014]. As a consequence, when a pre-stressed martensite material is heated until becoming an austenite, it recovers a part of its initial strain by becoming stiffer. If it is cooled down to a temperature lower than the one of the martensite to austenite temperature, it comes back to its initial state. The hysteretic behavior of Shape-Memory-Alloys is represented in Fig. 6.2.1a. The term of Shape-Memory-Effect comes from the fact that between the transition temperatures, the shape of the alloy kept the memory of its last phase transition. Nitinol is one of the most used shape-memory alloy because of its important strain recovery which can reach 10% (corresponding to a mechanical energy density of $4\text{J}\cdot\text{cm}^{-3}$) Yet, fatigue issues are often encountered with SMA. [Kahn et al, 1998] reports a decrease of 60% of the recovery strain after 10000 cycles (meaning that at a frequency of 0,01Hz, the performances degradation is observed after 11 days), and permanent elastic deformation of 2,5% after 800 cycles for TiNi wires submitted to a stress of 600 MPa. Contrary to other phase transitions that occur at a fixed temperature, Martensite phase transition is characterized by a progressive evolution from a phase to the other one. As a consequence, four temperatures are necessary to describe this thermodynamic cycle. From a thermodynamic point of view, this feature of martensite phase transition cannot be modeled with Landau's or Devonshire's theories but with Landau-Ginzburg theory [Falk, 1982].

As an hysteretic loop followed anti-clockwise is associated to the production of energy in thermodynamics, some works have addressed the issue of designing thermal heat engines exploiting Shape-Memory alloys [Nersessian, 2005; Namli, 2011; Zakharov et al, 2012; Saltzbrenner, 1984; Chang and Huang, 2010], or the issue of evaluating the theoretical efficiency of these heat engines [Mohamed 1979; Golestaneh, 1978; Liu 2004]. Given the complexity of the description of the shape-memory alloys, evaluations of the performances strongly vary from a paper to another. In his paper, Liu evaluated the density of mechanical energy generated by Nitinol to $22\text{ J}\cdot\text{cm}^{-3}$ with intrinsic efficiency of the conversion of 5,64%, quite in agreement with the data reported in [Mohamed 1979] ($27\text{ J}\cdot\text{cm}^{-3}$ per cycle, thermal efficiency of 9,4%). In both case, the Carnot relative efficiency is between 40 and 50% assuming that the SMA is cycled between its austenitic temperature A_f and its martensitic temperature M_f . Yet none experimental measurements obtained such levels of efficiency. In [Saltzbrenner, 1984], Saltzbrenner reported the performances

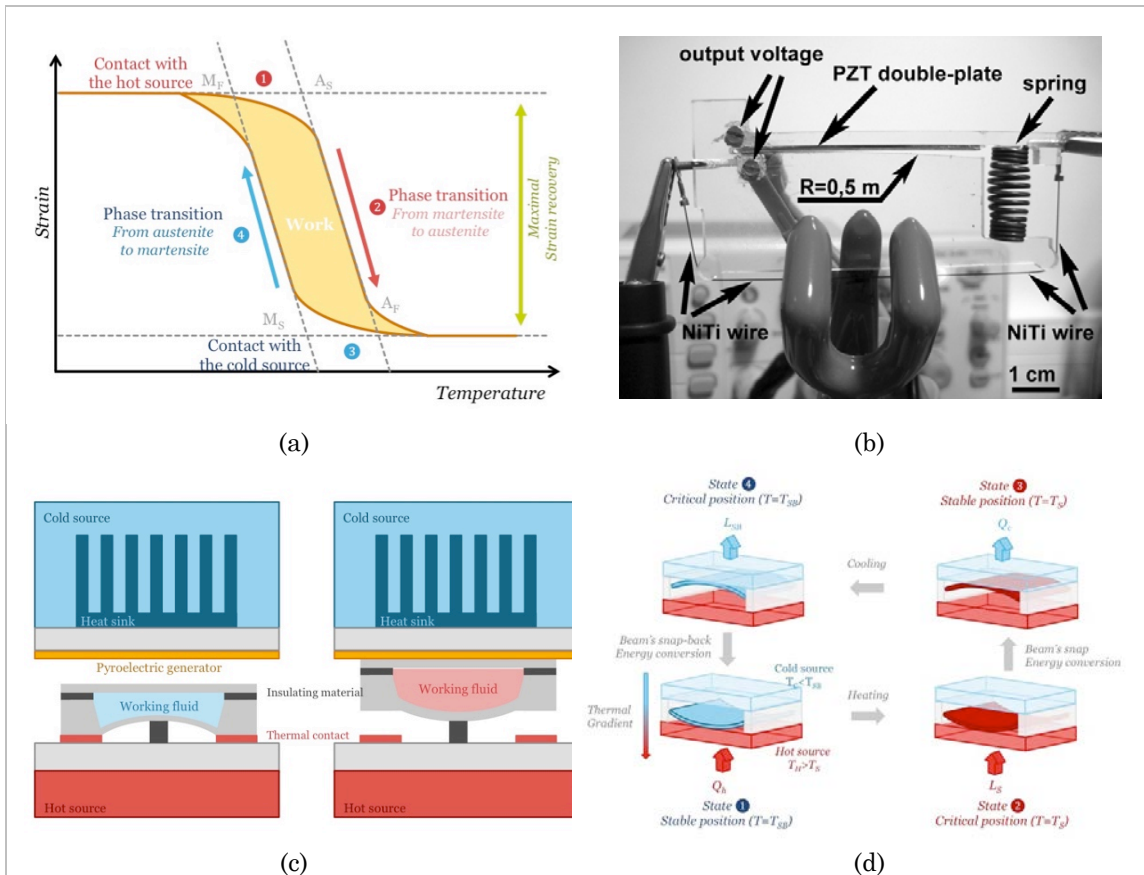


Figure 5.1.1. a. Natural cycle of Shape-Memory-Alloy heat engine b. Architecture of the SMA-based generator proposed in [Zakharov et al, 2012]. c. Bistable thermal switch presented in [Ravindran et al, 2012]. d. Thermodynamic cycle of the bimetallic strip heat engine.

of Nitinol realizing either a Stirling cycle or an Ericsson cycle. In the case of the Ericsson cycle, he obtained an energy density of $3,6 \text{ J.cm}^{-3}$ and a Carnot efficiency of 3% by cycling a Nitinol sample between 25°C and 190°C . In order to finally produce electrical energy, Chang and Huang proposed to couple SMA materials with pyroelectric generators. In this way, by using sudden strain recovery of SMA, it would be possible to cycle a pyroelectric between two heat sources. In [Chang and Huang, 2010] they thus simulated the behavior of a pyroelectric generator cycled between 27 and 37°C and obtained energy density of around $1,2 \text{ mJ.cm}^{-3}$ per cycle with a Carnot relative efficiency of 0,08%. Another proof of concept of SMA-based heat engine is reported in [Zakharov et al, 2012] reporting energy densities of 3mJ.cm^{-3} by using the stress generated by a NiTiCu ribbon on a piezoelectric cantilever beam, and densities of $0,75\text{mJ.cm}^{-3}$ by laminating SMA with MFC pyroelectric material.

6.3 Energy harvesting from thermo-mechanical bistability

Other types of mechanical instabilities have been explored to realize thermal energy harvesters. In [Huesgen et al, 2010] and in [Ravindran et al, 2011], researchers from Imtek reported the fabrication and the operation of a heat engine based on the mechanical snap-through of an initially-curved membrane. A schematic of the heat engine is presented in Fig.6.1.b. When the device is in contact with the hot source, thermal transfers occur between the heat source and the bistable actuator, causing the expansion of the fluid contained in the cavity delimited by the bistable membrane. As the fluid applies a pressure on the curved-membrane, this one can buckle if the pressure exceeds its critical load. Once it has snapped, the cavity comes in contact with the cold source, discharging the heat of the fluid until the snap-back load is reached, causing the return of the cavity to its initial position. A similar device was already presented by Song and coworkers in [Song et al, 2007] at the difference that the fluid in the cavity was biphasic. As we can see, the architecture and the operation of this thermal generator are quite similar to those of the P³ heat engine, but the difference is that there is no phase transition of the fluid contained in the cavity. In [Ravindran et al, 2011], Ravindran et al demonstrated the use of the bistable beam as a thermal switch, conveying heat for the hot source to a pyroelectric transducer located on the cold source. In that case of figure, the displacement of the bistable membrane enables to create temporal temperature variations inside the pyroelectric materials. Their device was able to generate up to $1.33\mu\text{W}\cdot\text{cm}^{-2}$ from a thermal gradient of 80°C . In these experimental conditions the thermal efficiency is $1.8\cdot 10^{-4}\%$ and the working frequency of $7,04\text{Hz}$, thanks to the use of liquid metal droplets to improve thermal transfer between the heat sources and the engine chamber.

Finally the other type of heat engine we can put in this category is the bimetallic strip heat engine. As we will demonstrate it in the next part, bimetallic strip heat engines are based on the first-order phase transition of a thermo-mechanically bistable membrane. The four different phases composing the thermodynamic cycle of the heat engine are recalled in Fig.6.1d. With the experiments developed at STMicroelectronics and CEA-LETI only one paper [Ravindran *et al*, 2014] reports experimental measurements of the performances of the bimetallic strip heat engine. In this paper, they proposed a numerical model of the bistability of the bimetallic membrane, enabling to evaluate the efficiency of the thermomechanical transduction between $0,01\%$ and $0,04\%$. In order to compare bimetallic strips with other thermal energy harvesters, we normalize the energy by their volume.

Table 5. Performances of some solid-based heat engines

N ^o	Work	$\Delta T ; T_H$ (°C)	W_{vol} (mJ.cm ⁻³)	f (Hz)	P_{vol} (μ W.cm ⁻²)	η_{rel} (%)	ZT_{eq} T_m (°C)	Engine
15	Liu, 2004	40 ; 70	22,4.10 ³	-	-	48,3	6,6 40	SMA (theory) T→M
16	Mohamed, 1979	28 ; 33	27.10 ³	-	-	45	5,56 19	SMA (theory) T→M
17	Saltzbrenner, 2008	165 ; 190	3,6.10 ³	0,001	1310 T→M	3,1	0,11 108	SMA (Exper.) Ericsson
18	Chang and Huang, 2010	10 ; 37	1,2	0,01	1,2 if t=100 μ m	0,08	3,2.1 0 ⁻³ 32	SMA + Pyro (Theory)
19	Chang and Huang, 2010	10 ; 37	4,2	0,07	3 if t=100 μ m	0,02	8.10 ⁻⁴ 32	SMA + Pyro (Exper.)
20	Huesgen <i>et al</i> , 2012	37 ; 97	4.10 ⁻³	0,72	0,58 T→M	0,18	6,9.1 0 ⁻³ 78,5	Bistable membrane
21	Ravindran <i>et al</i> , 2012	80 ; 140	0,95.10 ⁻³	7,04	1,34 T→E	0,093	3,4.1 0 ⁻³ 110	Bist. Memb. + Pyro
22	Boisseau <i>et al</i> , 2012	24 ; 60	7,3.10 ⁻³	3	3,3 T→E	0,5	0,02 48	BSHE + electret
23	Bimetallic strip alone	75 ; 100	0,2	0,22	2,2 T→M	0,2	7,2.1 0 ⁻³ 67,5	BSHE

7 Thermomagnetic heat engines

Thermomagnetic coupling is the last physical effect we have not studied yet. The operation of thermo-magnetic generators using phase transitions of ferromagnetic materials is quite similar to the operation of pyroelectric generators using phase transitions of ferroelectric materials. The basic idea is to thermally cycle a ferroelectric materials near its phase transitions to observe abrupt variations of its magnetization. Most of the phase transitions exploited are first-order phase transitions, either from a ferromagnetic phase to a paramagnetic phase, or from a ferromagnetic phase to an antiferromagnetic phase [Hsu et al, 2011]. Yet Ujihara reported the exploitation of a second-order phase transition [Ujihara, 2007]. The possibility to generate electrical energy from heat by means of thermomagnetic coupling is generally first attributed to Edison and Tesla in the late 19th century [Edison, 1887; Tesla, 1890] whereas the first evaluation of the efficiency of thermomagnetic generators is due to Brillouin and Iskenderias [Brillouin and Iskenderias, 1948] finding values around 55% of Carnot. The basic principle of the thermomagnetic heat engine is presented in Fig.7.1.1a. It consists in placing a ferromagnetic material in the air gap of magnet so that, when the temperature of the ferromagnetic evolves around the Curie temperature of the ferromagnetic material, the variation of the ferromagnetic material's magnetization induces the creation of a current

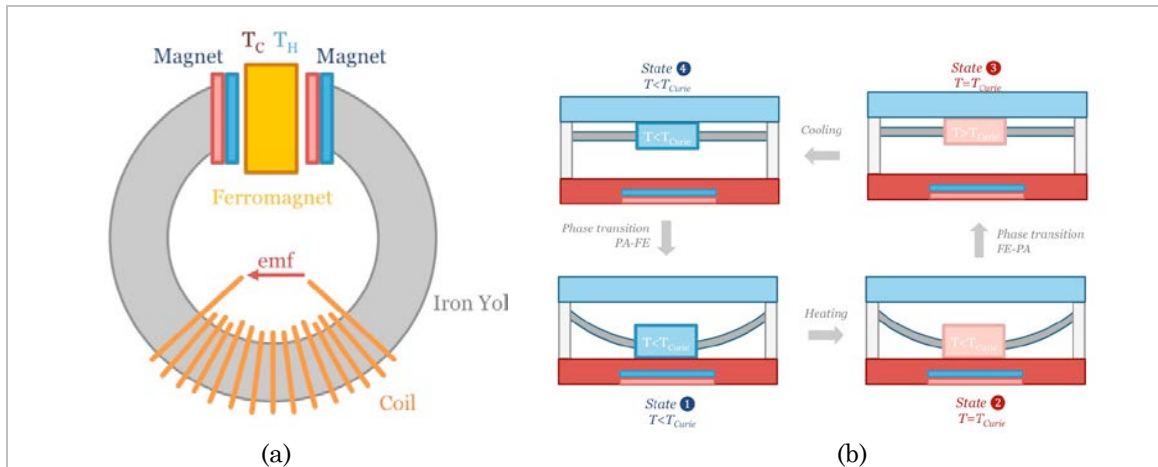


Figure 7.1.1. *a. Representation of a basic thermomagnetic heat engine (temperature fluctuations). b. Principle of the thermomagnetic heat engine presented in [Ujihara et al, 2007].*

in the solenoid surrounding the magnet. Since the work of Brilouin and Iskenderias, many authors evaluated the performance of thermomagnetic generators performing various thermodynamic cycles, including Rankine cycle [Song et al, 2013] and Ericsson cycle [Song et al, 2013, Solomon 1988, Kirol and Mills, 1984]. The main part of these generators uses Gadolinium as a ferromagnet given its low Curie temperature (15°C). In [Elliott, 1959], Elliot demonstrated the possibility to produce up to $3,2 \text{ J}\cdot\text{cm}^{-3}$ per cycle with a Carnot efficiency of 7,4% from a temperature variations (23°C of temperature difference varying at 0,17 Hz). Simulating the performances of Gadolinium used with Ericsson cycle, Kirol and Mills reported lower electrical energy density ($71\text{mJ}\cdot\text{cm}^{-3}$) but higher Carnot efficiencies (47%) [Kirol and Mills, 1984].

Other works report the generation of electric energy from heat flowing in thermal gradients. As an example, Solomon reports the simulated performances of a rotary thermomagnetic heat engine, made of a rotor and a stator, the heat being supplied from outside of the engine, and evacuated from inside the engine. In a thermal gradient of 65°C , he reported thermo-mechanical efficiencies of around 60% of Carnot and mechanical energy densities of $2,2\text{mJ}\cdot\text{cm}^{-3}$. The last possibility to harvest heat and to convert it into electrical energy is to use the generator whose architecture is presented in Fig. 7.1.1b. In this configuration, the ferromagnetic element is initially in a paramagnetic state and in contact with the cold source. As a consequence it is cooled down to a temperature lower than its Curie temperature for which it becomes ferromagnetic. As a consequence, it is attracted by the permanent magnet generating a force that is higher than the restoring force of the springs. As it comes in contact with the hot source, its temperature increases, and exceeds the Curie temperature and cancelling the magnetic force. The ferromagnetic materials then comes back to its initial state. Modeling of this type of device was performed by [Hsu et al, 2013] and [Post et al, 2013] whereas the first proof of concept is reported in [Ujihara et al, 2007] using piezoelectric membrane to realize the springs and piezoelectric transducers to convert the mechanical energy into electrical energy. In this

paper, the authors claim the possibility to produce $1,57 \text{ mW.cm}^{-2}$ by using piezoelectric membrane and up to $2,6 \text{ mW.cm}^{-2}$ by using piezoelectric stacks. They did not give any values for the thermo-mechanic transduction. In order to find complete modeling of these devices, we can report to the works of Hsu *et al*, or Post *et al* [Hsu *et al*, 2011; Post *et al*, 2013]. In the first of these papers, the authors indicate the possibility to reach Carnot efficiencies of 11,5% for a thermal gradient of 20°C if energy is directly converted into magnetic energy. In [Post *et al*, 2013] is reported the dynamic modeling of the same device than in [Hsu *et al*, 2011], showing that a thermomagnetic generator made of Gadolinium can work at 0,3Hz and can produce up to $0,15 \text{ mW.cm}^{-2}$ with an efficiency of 0,65% of Carnot. By using a new category of materials called Heusler alloys whose excellent magneto-caloric properties were demonstrated in [Srivastava *et al*, 2010] and [Song *et al*, 2013].

Table 7. Performances of some thermomagnetic heat engines

Nº	Work	$\Delta T ; T_H$ ($^\circ\text{C}$)	W_{vol} (mJ.cm^{-3})	f (Hz)	P_{vol} (mW.cm^{-3})	η_{rel} (%)	ZT_{eq} T_m ($^\circ\text{C}$)	Comments
24	Elliott, 1959	23 ; 27	$3,2 \cdot 10^3$	0,17	550	7,43	0,33 16	Temp.fluct. (theory)
25	Hsu <i>et al</i> , 2011	50 ; 50	106	-	-	0,63	0,024 25	Therm. Grad (theory)
26	Hsu <i>et al</i> , 2011	5 ; 15	-	-	-	11,5	0,58 12,5	Therm. Grad (theory)
27	Post <i>et al</i> , 2013	20 ; 16	0,5	0,3	0,15 T→E	0,65	0,025 6	Therm. Grad FE-PA (Theory)
28	Post <i>et al</i> , 2013	2; 151	1,5	0,8	1,2 T→E	0.65	0,026 150	Therm. Grad FE-AF (Theory)
29	Solomon, 1989	65 ; 90	2,2	0,5	4,4 T→M	60	12,9 57,5	Therm. Grad FE-PA (Theory)
30	Kirol and Mills, 1984	24 ; 60	24,8	0,25	6,2 T→E	7,5	0,34 42	Temp.fluct. (theory)
31	Kirol and Mills, 1984	24 ; 60	71	0,1	7,1 T→E	47	6,34 42	Temp.fluct. (theory)

8 Synthesis

In this last part, we want to try to establish a comparison between every type of thermal energy harvester. In order to do so, for each harvester, we only retain the data concerning the density of energy, the thermal gradient used to produce this energy, the equivalent ZT of the thermal generator and the mean temperature at which the simulations or the experimental measurements are done. We do not take into account surface density of power since they depend on the working frequency of the device. Given that all technologies have not been developed, some theoretical works either choose an arbitrary value or present simulations of thermal transfers, whereas some experimental works

boost the frequency by imposing a fixed thermal gradient, or slowly cycle by alternating cold baths and hot baths. Some others, like the piezoelectric bimetallic strip heat engines directly work without any heat sink. In our comparison, we compare directly the data of energy, even if some of them are of mechanical nature, whereas others are of electrical nature. A good solution would be to choose a typical value of piezoelectric conversion efficiency when there could be a deformation of a membrane (example of P³ heat engine) to convert mechanical energy into electrical energy, or the efficiency of an electrostatic conversion when there is a rotatory motion, as for Rankine engines. As there is no direct notion of energy density for thermoelectric generator, we will take as a reference the electrical energy generated by a Micropelt generator during 1s when it works with a temperature difference of 5°C. Given that the surface of the generator is 2,4mm x 3,3 mm x 1,1 mm (however we can argue that the volume to be taken into account is the volume of thermoelectric material since the other works used this volume to evaluate the volume density of generated energy), we find an energy density of around 30mJ.cm⁻³ at 5°C. This enable us to evaluate how the working frequency of cyclic heat engines must evolve in order that it produces as much power as a Seebeck generator. Fig.8.1.1a. compares the performances of the heat engines with respect to their efficiencies(equivalent ZT) and their working temperatures. As we can notice, most of the thermal generators have a ZT lower than 1, except for SMA-based heat engines (15 and 16), two thermomagnetic generators (29 and 31) and two fluid-based heat engines (14 and 10). Yet we can see that the corresponding works are simulation works. As we explained, 14 made a mistake on the thermodynamic cycle of P³ heat engines and (31 and 29) correspond to first historical evaluations of thermomagnetic heat engines.

Except for these cases, we can observe that most of the heat engines have a ZT between 0.01 and 1. As the thermal gradient is the driving force associated to heat, we represent in Fig.8.1.1b the density of mechanical energy as a function of the thermal hysteresis needed to produce this energy. In this figure we also plot the curve corresponding to the energy produced by a thermoelectric generator during a second, 10 seconds, 100 seconds... With these curves we can directly see at which frequency a thermal generator must be cycled in order to produce the same volume density of power than a thermoelectric generator. As an example, for the same volume of energy harvester and for the same temperature difference, a pyroelectric material needs only to be cycled at 0,1Hz to reach the same level of energy density than a thermoelectric generator. However as we observed before, it can be difficult to find practical situations where temperature can vary of 30 degrees in 5 seconds. The working frequencies of Rankine engines being greater than 1kHz, these generators can reach output power densities 1000 times higher than thermoelectric generators.

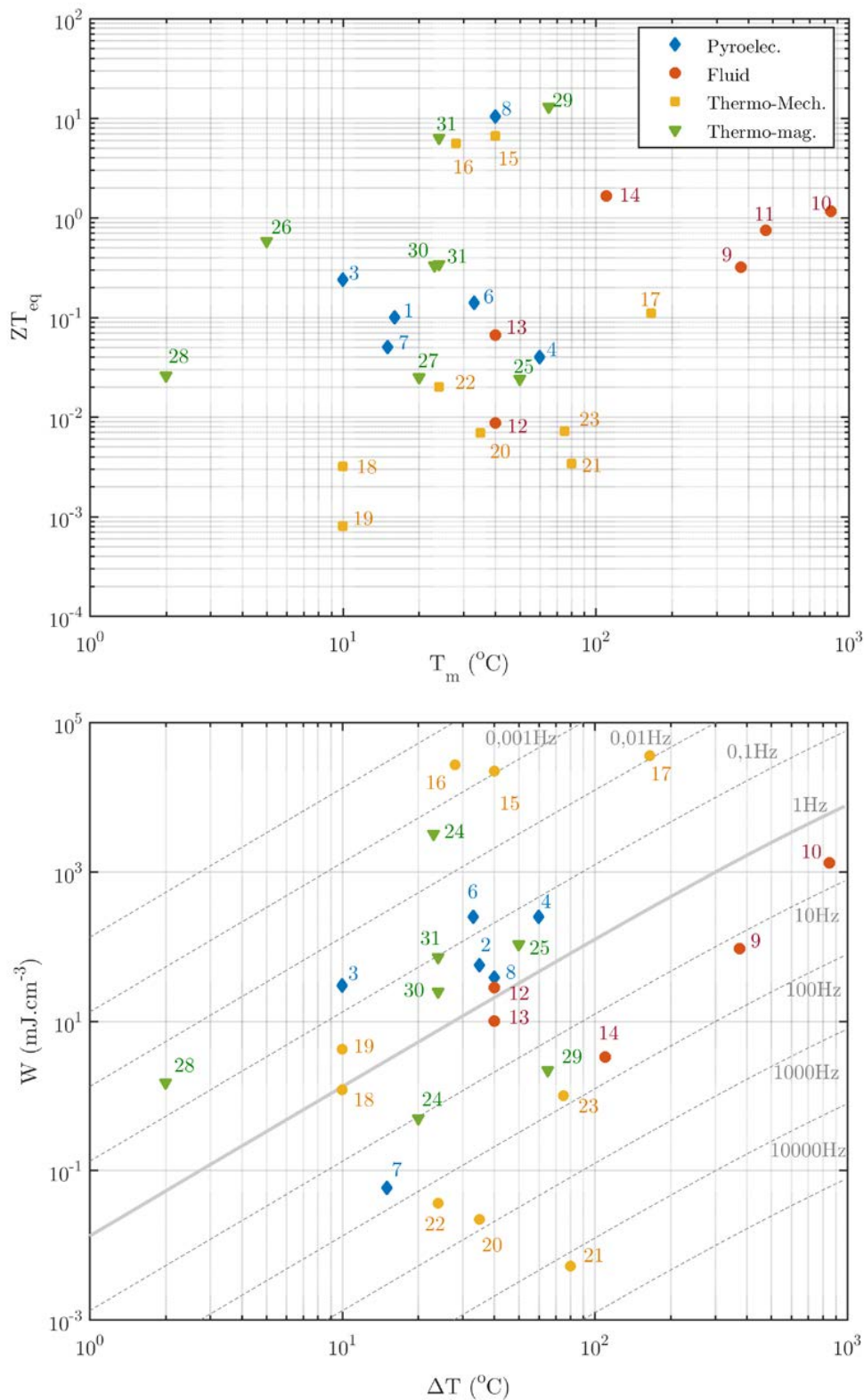


Figure 8.1.1. a. Comparison of the ZT of various heat engines with respect to the mean operation temperature. b. Density of energy versus temperature difference needed to produce it

Except for these cases, we can observe that most of the heat engines have a ZT between 0.01 and 1. As the thermal gradient is the driving force associated to heat, we represent in Fig.8.1.1b the density of mechanical energy as a function of the thermal hysteresis needed to produce this energy. In this figure we also plot the curve corresponding to the energy produced by a thermoelectric generator during a second, 10 seconds, 100 seconds... With these curves we can directly see at which frequency a thermal generator must be cycled in order to produce the same volume density of power than a thermoelectric generator. As an example, for the same volume of energy harvester and for the same temperature difference, a pyroelectric material needs only to be cycled at 0,1Hz to reach the same level of energy density than a thermoelectric generator. However as we observed before, it can be difficult to find practical situations where temperature can vary of 30 degrees in 5 seconds. The working frequencies of Rankine engines being greater than 1kHz, these generators can reach output power densities 1000 times higher than thermoelectric generators.

From these two graphs we can observe some tendencies common to each categories of heat engines. First, Rankine engines and other similar heat engines using circulating working fluids are perfectly suited for high temperatures applications like microcombustion given their high power densities. Secondly, pyroelectric heat engines and thermomagnetic heat engines can be as efficient as thermoelectric generators. Finally, given the weak thermo-mechanical coupling, solid based heat engines (except Shape-Memory alloys) and stationary fluids heat engines are the less efficient heat engines especially if we take into account the needs to couple these heat engines with electro-mechanical transducers.

9 Conclusion

In this first chapter, we present an overview of various thermal coupling phenomenas that can be exploited to harvest heat and the various technologies exploiting these phenomena. We detailed the theoretical operation of thermoelectric generators, pyroelectric generators, thermomagnetic generators and heat engines using either working fluids or working solids. The comparison of these technologies showed that thermoelectric generators are the most efficient technology to harvest heat, followed by pyroelectric generators and thermomagnetic generators. Fluid-based heat engines can be particularly efficient to convert heat into mechanical energy at high temperatures, whereas stationary fluid-based heat engines and solid-based heat engines are the least efficient technologies, about one hundred times less efficient than conventional thermoelectric generators, for the conversion of heat into mechanical energy. The final efficiency of these generators would also be decreased because of the necessity of using a second conversion step to transform this mechanical energy into electrical energy. This first study on the state of the art of heat engines raises a first question on the interest of developing bimetallic strip heat engines to commercially compete with thermoelectric generators. Yet, looking for modeling this kind of devices and developing thermo-mechanically bistable structure

stays interesting from a scientific point of view, especially if other types of applications than thermal energy harvesting can be found for miniaturized bimetallic strips.

10 Bibliography

- Alam, H. and Ramakrishna, S. (2013). A review on the enhancement of figure of merit from bulk to nano-thermoelectric materials. *Nano Energy*, 2(2), pp.190-212.
- Bardaweel, H., Richards, R., Richards, C. and Anderson, M. (2012). Characterization of the thermodynamic cycle of a MEMS-based external combustion resonant engine. *Microsystem Technologies*, 18(6), pp.693-701.
- Bauer, G. (2015). Photovoltaic Solar Energy Conversion. *Lecture Notes in Physics*.
- Bottner, H., Nurnus, J., Gavrikov, A., Kuhner, G., Jagle, M., Kunzel, C., Eberhard, D., Plescher, G., Schubert, A. and Schlereth, K. (2004). New thermoelectric components using microsystem technologies. *Journal of Microelectromechanical Systems*, 13(3), pp.414-420.
- Briand, D., Yeatman, E. and Roundy, S. (2015). *Micro energy harvesting*.
- Carnot, S. (1824). *Réflexions sur la puissance motrice du feu*. Paris: Bachelier.
- Callen, H. (1960). *Thermodynamics*. New York: Wiley.
- Chang, H. and Huang, Z. (2010). Laminate composites with enhanced pyroelectric effects for energy harvesting. *Smart Mater. Struct.*, 19(6), p.065018.
- Chen, J., Yan, Z., Lin, G. and Andresen, B. (2001). On the Curzon–Ahlborn efficiency and its connection with the efficiencies of real heat engines. *Energy Conversion and Management*, 42(2), pp.173-181.
- Cho, J., Weiss, L., Richards, C., Bahr, D. and Richards, R. (2007). Power production by a dynamic micro heat engine with an integrated thermal switch. *J. Micromech. Microeng.*, 17(9), pp.S217-S223.
- Christiaanse, T. and Brück, E. (2014). Proof-of-Concept Static Thermomagnetic Generator Experimental Device. *Metallurgical and Materials Transactions E*, 1(1), pp.36-40.
- Clingman, W. and Moore, R. (1961). Application of Ferroelectricity to Energy Conversion Processes. *J. Appl. Phys.*, 32(4), p.675.
- Cuadras, A., Gasulla, M. and Ferrari, V. (2010). Thermal energy harvesting through pyroelectricity. *Sensors and Actuators A: Physical*, 158(1), pp.132-139.
- Cui, L. and Brisson, J. (2005). Modeling of MEMS-Type Rankine Cycle Machines. *J. Eng. Gas Turbines Power*, 127(3), p.683.
- Curzon, F. and Ahlborn, C. (1975). Efficiency of a Carnot engine at maximum power output. *Am. J. Phys.*, 43(1), p.22.

- Deam, R., Lemma, E., Mace, B. and Collins, R. (2008). On Scaling Down Turbines to Millimeter Size. *J. Eng. Gas Turbines Power*, 130(5), p.052301.
- Dmitriev, A. and Zvyagin, I. (2010). Current trends in the physics of thermoelectric materials. *Physics-USpekhi*, 53(8), pp.789-803.
- Elliott, J. (1959). Thermomagnetic Generator. *J. Appl. Phys.*, 30(11), p.1774.
- Epstein, A. (2004). Millimeter-Scale, Micro-Electro-Mechanical Systems Gas Turbine Engines. *J. Eng. Gas Turbines Power*, 126(2), p.205.
- Falk, F. (1982). Landau theory and martensitic phase transitions. *J. Phys. Colloques*, 43(C4), pp.C4-3-C4-15.
- Fernandez-Pello, A. (2002). Micropower generation using combustion: Issues and approaches. *Proceedings of the Combustion Institute*, 29(1), pp.883-899.
- Fr chet te, L., Lee, C., Arslan, S. and Liu, Y. (2003). Design of a Microfabricated Rankine Cycle Steam Turbine for Power Generation. *Microelectromechanical Systems*.
- Golestaneh, A. (1978). Efficiency of the solid-state engine made with Nitinol memory material. *J. Appl. Phys.*, 49(3), p.1241.
- Guyomar, D., Pruvost, S. and Sebald, G. (2008). Energy harvesting based on FE-FE transition in ferroelectric single crystals. *IEEE Transactions on Ultrasonics, Ferroelectrics and Frequency Control*, 55(2), pp.279-285.
- Guyomar, D., Sebald, G., Lefeuvre, E. and Khodayari, A. (2008). Toward Heat Energy Harvesting using Pyroelectric Material. *Journal of Intelligent Material Systems and Structures*, 20(3), pp.265-271.
- LeBlanc, S., Yee, S., Scullin, M., Dames, C. and Goodson, K. (2014). Material and manufacturing cost considerations for thermoelectrics. *Renewable and Sustainable Energy Reviews*, 32, pp.313-327.
- Hoh, S. (1963). Conversion of thermal to electrical energy with ferroelectric materials. *Proceedings of the IEEE*, 51(5), pp.838-845.
- Hsu, C., Sandoval, S., Wetzlar, K. and Carman, G. (2011). Thermomagnetic conversion efficiencies for ferromagnetic materials. *J. Appl. Phys.*, 110(12), p.123923.
- Kahn, H., Huff, M. and Heuer, A. (1998). The TiNi shape-memory alloy and its applications for MEMS. *J. Micromech. Microeng.*, 8(3), pp.213-221.
- Khodayari, A., Pruvost, S., Sebald, G., Guyomar, D. and Mohammadi, S. (2009). Nonlinear pyroelectric energy harvesting from relaxor single crystals. *IEEE Transactions on Ultrasonics, Ferroelectrics and Frequency Control*, 56(4), pp.693-699.
- Kirol, L. and Mills, J. (1984). Numerical analysis of thermomagnetic generators. *J. Appl. Phys.*, 56(3), p.824.
- Lee, C. (2004). Design and fabrication of a micro Wankel engine using MEMS technology. *Microelectronic Engineering*, 73-74, pp.529-534.
- Leonov, V. (2011). Simulation of maximum power in the wearable thermoelectric generator with a small thermopile. *Microsystem Technologies*, 17(4), pp.495-504.

- Liu, Y. (2004). The work production of shape memory alloy. *Smart Mater. Struct.*, 13(3), pp.552-561.
- Lurie, E. and Kribus, A. (2010). Analysis of a microscale 'Saturation Phase-change Internal Carnot Engine'. *Energy Conversion and Management*, 51(6), pp.1202-1209.
- Mane, P., Jingsi Xie, Leang, K. and Mossi, K. (2011). Cyclic energy harvesting from pyroelectric materials. *IEEE Transactions on Ultrasonics, Ferroelectrics and Frequency Control*, 58(1), pp.10-17.
- Mayer, P. and Ram, R. (2006). Optimization of Heat Sink-Limited Thermoelectric Generators. *Nanoscale and Microscale Thermophysical Engineering*, 10(2), pp.143-155.
- Mohamed, H. (1979). Thermal conversion efficiency of an ideal thermoelastic marmem cycle. *J Mater Sci*, 14(6), pp.1339-1343.
- Mohd Jani, J., Leary, M., Subic, A. and Gibson, M. (2014). A review of shape memory alloy research, applications and opportunities. *Materials & Design*, 56, pp.1078-1113.
- Müser, H. (1957). Thermodynamische Behandlung von Elektronenprozessen in Halbleiter-Randschichten. *Zeitschrift für Physik*, 148(3), pp.380-390.
- Nakajima, N., Ogawa, K. and Fujimasa, I. (n.d.). Study on micro engines-miniaturizing Stirling engines for actuators and heatpumps. *IEEE Micro Electro Mechanical Systems*, , *Proceedings*, 'An Investigation of Micro Structures, Sensors, Actuators, Machines and Robots'.
- Navid, A., Vanderpool, D., Bah, A. and Pilon, L. (2010). Towards optimization of a pyroelectric energy converter for harvesting waste heat. *International Journal of Heat and Mass Transfer*, 53(19-20), pp.4060-4070.
- Nguyen, H., Navid, A. and Pilon, L. (2010). Pyroelectric energy converter using co-polymer P(VDF-TrFE) and Olsen cycle for waste heat energy harvesting. *Applied Thermal Engineering*, 30(14-15), pp.2127-2137.
- Ohta, H. (2007). Thermoelectrics based on strontium titanate. *Materials Today*, 10(10), pp.44-49.
- Olsen, R., Briscoe, J., Bruno, D. and Butler, W. (1981). A pyroelectric energy converter which employs regeneration. *Ferroelectrics*, 38(1), pp.975-978.
- Onsager, L. (1931). Reciprocal Relations in Irreversible Processes. I. *Phys. Rev.*, 37(4), pp.405-426.
- Peltier, J. (1834). Nouvelles expériences sur la caloricit  des courants  lectriques, *Annales de chimie*, vol. 56, 371.
- Post, A., Knight, C. and Kisi, E. (2013). Thermomagnetic energy harvesting with first order phase change materials. *J. Appl. Phys.*, 114(3), p.033915.
- Ravindran, S., Roulet, M., Huesgen, T., Kroener, M. and Woias, P. (2012). Performance improvement of a micro thermomechanical generator by incorporating Galinstan® micro droplet arrays. *J. Micromech. Microeng.*, 22(9), p.094002.

- Rayleigh, L. (1885). On the thermodynamic efficiency of the thermopile, *Philosophical Magazine Series 5*, vol. 20, 361.
- Rowe, D. and Min, G. (1996). Design theory of thermoelectric modules for electrical power generation. *IEE Proceedings - Science, Measurement and Technology*, 143(6), pp.351-356.
- Srivastava, V., Song, Y., Bhatti, K. and James, R. (2010). The Direct Conversion of Heat to Electricity Using Multiferroic Alloys. *Advanced Energy Materials*, 1(1), pp.97-104.
- Salzbrenner, R. (1984). Shape memory heat engines. *J Mater Sci*, 19(6), pp.1827-1835.
- Sebald, G., Guyomar, D. and Agbossou, A. (2009). On thermoelectric and pyroelectric energy harvesting. *Smart Mater. Struct.*, 18(12), p.125006.
- Sebald, G., Lefeuvre, E. and Guyomar, D. (2008). Pyroelectric energy conversion: Optimization principles. *IEEE Transactions on Ultrasonics, Ferroelectrics and Frequency Control*, 55(3), pp.538-551.
- Seebeck, T. (1821). Ueber den magnetismus der galvenische kette. abh. k, *Akad. Wiss., Berlin*, vol. 289.
- Solomon, D. (1989). Thermomagnetic mechanical heat engines. *J. Appl. Phys.*, 65(9), p.3687.
- Song, G., Kim, K. and Lee, Y. (2007). Simulation and experiments for a phase-change actuator with bistable membrane. *Sensors and Actuators A: Physical*, 136(2), pp.665-672.
- Song, Y., Bhatti, K., Srivastava, V., Leighton, C. and James, R. (2013). Thermodynamics of energy conversion via first order phase transformation in low hysteresis magnetic materials. *Energy & Environmental Science*, 6(4), p.1315.
- Thomson, W. (1851). On a mechanical theory of thermo-electric currents, *Proceedings of the Royal Society of Edinburgh*.
- Ujihara, M., Carman, G. and Lee, D. (2007). Thermal energy harvesting device using ferromagnetic materials. *Appl. Phys. Lett.*, 91(9), p.093508.
- Vaudrey, A., Lanzetta, F. and Feidt, M. (2014). H. B. Reitlinger and the origins of the efficiency at maximum power formula for heat engines. *Journal of Non-Equilibrium Thermodynamics*, 39(4).
- Vining, C. (2009). An inconvenient truth about thermoelectrics. *Nature Materials*, 8(2), pp.83-85.
- Whalen, S., Thompson, M., Bahr, D., Richards, C. and Richards, R. (2003). Design, fabrication and testing of the P3 micro heat engine. *Sensors and Actuators A: Physical*, 104(3), pp.290-298.
- Zakharov, D., Lebedev, G., Cugat, O., Delamare, J., Viala, B., Lafont, T., Gimeno, L. and Shelyakov, A. (2012). Thermal energy conversion by coupled shape memory and piezoelectric effects. *J. Micromech. Microeng.*, 22(9), p.094005.

Zhang, Q., Agbossou, A., Feng, Z. and Cosnier, M. (2011). Solar micro-energy harvesting with pyroelectric effect and wind flow. *Sensors and Actuators A: Physical*, 168(2), pp.335-342.

Chapter 2

Thermo-mechanical modeling of the bimetallic strip heat engine

1 Introduction

1.1 Objectives of the chapter

As bimetallic strip heat engines' operation relies on the unstable behavior of bimetallic strips, the heart of the modeling of our devices is linked to the comprehension of thermal snap-through and of the energetical properties of beams and structures exhibiting thermally hysteretic behavior. As a consequence, this second chapter aims at providing a simple model thermo-mechanical instability of some geometries of composite membranes, among which the bimetallic beams. Given that the description of thermo-mechanical instabilities is not an isolated case in mechanics, we will first present an overview of some examples of mechanical instabilities of structures, either caused by thermal stress of external actions, and we will consider the effects of imperfection on the behavior of these structures. After that, we will establish and solve the accurate equilibrium equations and the reduced-order equations of laminated beams suffering both from thermal stress and from residual stress, enabling us to find the conditions under which thermal snap-through could occur. Our model will enable us to extend the demonstration to the case of initially curved laminated beams and to simplify the various results to the simplest laminated beams, which are the bimetallic beams. We will then focus on the evolution of the energy and the entropy of bistable beams to demonstrate the possibility to convert heat into mechanical energy and to evaluate the efficiency of this transduction. As the dynamic behavior of the energy harvester can only be deduced from the study of thermal transfers inside the harvester, we finally will then present a simple model of switched thermal capacitance enabling to express the power generated by the heat engine and to find the optimal device's design enabling to maximize the performances of the generator.

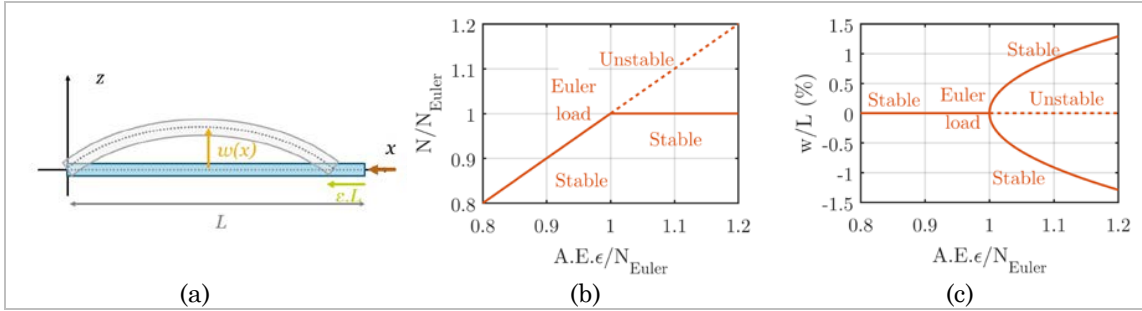


Figure 1.1.1. a. Illustration of the buckling of a straight beam. b. Evolution of the compressive load p as a function of the strain ϵ . c. Evolution of the beam's deflection and pitchfork bifurcation of the straight beam.

1.2 Researches on thermally-induced instabilities of structures

The research on these thermo-mechanical instabilities is at the crossroads between two domains of mechanics, treating in the first place the consequence of thermal stress on the mechanical response of solid materials, but also tackling the issue of mechanical instabilities, broadly described by non-linear mechanics [Thompson and Hunt, 1973]. Thermal stress is often associated with reliability issues, and the effect of temperature variations on the mechanical behavior of engineered structures has often been studied to find solutions to avoid their thermally-induced failures. As explained by Thornton in [Thornton, 1993] this field of research has benefited from the emergence of aeronautics [Schuman and Back, 1930] and the development of supersonic flights: The rise of the flight speeds of aeroplanes emphasized the need to address the issues of aerodynamic heating and their consequences such as thermo-mechanical flexure or buckling of structures. It also led to the development of new materials such as Functionally Graded Materials (FGM) to prevent such phenomena [Ravichandran, 1995, Niino and Maeda, 1990].

Before giving an overview on the research about thermo-mechanical stability issues, we need to explain what buckling is. Early modeled in 1744 by Euler in the case of perfectly straight beams (Fig.1.1.1a) [Euler, 1744, Timoshenko and Gere, 1961], buckling describes the loss of stability of a structure submitted to a compressive in-plane load N , causing the bifurcation of the beam from an unstable equilibrium position to a stable one, which is accompanied by out-of-plane displacements. Euler demonstrated that the action of the axial load produces a strain in the straight beam (thickness t , length L) given by (1.1.1a), and that the equilibrium equation of the beam is described by equation (1.1.1b). In these equations, E is the Young modulus of the beam, A its cross-section, I its inertial moment and w its shape.

$$N = E.A.\epsilon \quad (1.1.1a)$$

$$E.I.w_{,xx} + N.w = 0 \quad (1.1.1b)$$

With this equation, Euler showed that the simply-supported beam remains straight until the load N reaches the value, known as the first Euler load (1.1.2a), corresponding to the eigenvalue of (1.1.1). When the load p equals the Euler load, the beam can be curved, taking the shape of a half-sine wave (1.1.2b).

$$w(x) = 0 \text{ if } N \leq E.I. \frac{\pi^2}{L^2} = N_{Euler} \quad (1.1.2a)$$

$$w(x) = w_1 \cdot \sin\left(\frac{\pi}{L} \cdot x\right) \quad (1.1.2b)$$

Other eigenvalues can be found, each time the compressive load equals a multiple of the first Euler buckling load, the odd multiples describing symmetrical beam shapes and the even multiples corresponding to asymmetrical beam shapes (1.1.3b).

$$w(x) = w_n \cdot \sin\left(\frac{n \cdot \pi}{L} \cdot x\right) \quad (1.1.3a)$$

$$N_n = E.I. \frac{n^2 \cdot \pi^2}{L^2} \quad (1.1.3b)$$

The difficulty arises when it is necessary to describe precisely the shape of the beam after it buckles. Equation (1.1.1) does not allow finding the amplitude of the beam's deflection. It is then necessary to resort to non-linear mechanics to find the post-buckling behavior of the beam. As demonstrated in (Marguerre, 1967) when the beam buckles, the compressive axial load modifies the deflection of the beam, according to (1.1.4). The non-linear integral term then corresponds to the difference between the curved beam's length and its chord.

$$N = E.A \left(\varepsilon - \frac{1}{2.L} \cdot \int_0^L w_x^2 \cdot dx \right) \quad (1.1.4)$$

The amplitude of the deflection after buckling is then a solution of the polynomial equation (1.1.5). Fig.1.1.1b and Fig.1.1.1c plot the evolution of the axial load p and the displacement of the beam's middle as a function of the normalized strain of the beam. It shows that a perfectly straight beam can buckle in the two opposite directions with the same probability, and that the straight position is unstable after the bifurcation point. The shape of the equilibrium diagram of the perfectly straight beam recalls the shape of a pitchfork, hence the name of pitchfork bifurcation.

$$w_1^2 = \frac{4.L^2}{\pi^2} \cdot \left(\varepsilon - \frac{N_{Euler}}{E.A} \right) \quad (1.1.5)$$

The previous equations can be modified to predict the thermal buckling of a simply supported and axially-constrained beam. When temperature rises, it normally entails the thermal expansion of the beam, linked to its coefficient of thermal expansion α . Given that the beam is axially restrained, a thrust is created (1.1.6a). The thermal stress can then lead to the buckling of the beam if it reaches the Euler load. The temperature associated to the buckling of the beam is then (1.1.6b).

$$N^T = E.A.\alpha.T \quad (1.1.6a)$$

$$\Delta T_{crit} = \frac{t^2}{12.\alpha} \cdot \frac{\pi^2}{L^2} \quad (1.1.6b)$$

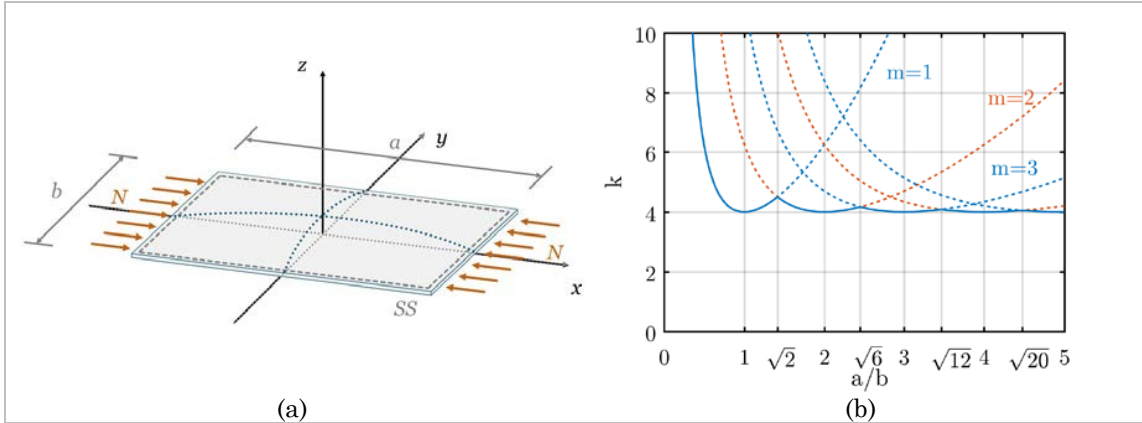


Figure 1.1.2. *a. Representation of the first buckling load of a simply-supported beam axially loaded. b. Evolution of the buckling coefficient as a function of the shape ratio a/b for $n=1$.*

As beams represent a restrained class of mechanical structure, several researches dealt with the behavior of plates and shells. Bryan [Bryan, 1890] first established the equation of buckling of an uniaxially compressed rectangular plate having its four edges simply supported, showing that it obeys equation (1.1.7a). The solution of the buckling equation is then given by (1.1.7b), and the critical charge is a function of the length a and the width b (1.1.7c) (Reddy, 2006). In these equations, D is the flexural stiffness of the beam and t its thickness.

$$D \cdot \nabla^4 w = N \cdot w_{,xx} \quad (1.1.7a)$$

$$w(x, y) = w_1 \cdot \sin\left(\frac{m \cdot \pi \cdot x}{a}\right) \cdot \sin\left(\frac{n \cdot \pi \cdot y}{b}\right) \quad (1.1.7b)$$

$$N_{Euler} = \frac{\pi^2 \cdot a^2 \cdot D}{m^2} \cdot \left(\frac{m^2}{a^2} + \frac{n^2}{b^2}\right)^2 = \frac{\pi^2 \cdot D}{b^2} \cdot k \quad (1.1.7c)$$

$$k = \left(\frac{b \cdot m}{a} + n^2 \frac{a}{b \cdot m}\right)^2 \quad (1.1.7d)$$

The lowest values of the critical load being obtained for $n=1$, it is common practice to plot the evolution of the buckling coefficient k as a function of the ratio a/b (Fig.1.1.2b). This figure shows that the longer and narrower the beam is, the more k tends towards a constant value ($k \rightarrow 4$) but the higher the buckling mode is. For ratios a/b lower than unity, the increase of the plate's stiffness makes the buckling harder, explaining why the buckling coefficient increases.

$$\Delta T_{crit} = \frac{\pi^2 \cdot t^2}{12 \cdot \alpha} \cdot \left(\frac{m^2}{a^2} + \frac{n^2}{b^2}\right) \quad (1.1.9a)$$

$$\frac{m^2}{a^2} \cdot N_x + \frac{n^2}{b^2} \cdot N_y = \pi^2 \cdot D \cdot \left(\frac{m^2}{a^2} + \frac{n^2}{b^2}\right)^2 \quad (1.1.9b)$$

As with Euler's equation in the case of beams, (1.1.8) does not describe the postbuckling behavior of plates. By using the Von Karman stress tensor, the Airy stress function F obeys the equations (1.1.10a-b).

$$\nabla^4 F = E \cdot t \cdot (w_{xy}^2 - w_{xx} \cdot w_{yy}) \quad (1.1.10a)$$

$$D \cdot \nabla^4 w = F_{yy} \cdot w_{xx} - 2 \cdot F_{xy} \cdot w_{xy} + F_{xx} \cdot w_{yy} \quad (1.1.10b)$$

[Tauchert, 1991; Thornton, 1993] give extensive bibliographies on the research works on the resolution of these equations for various types of plates and boundary conditions, using either numerical approaches or analytical simplifications like Ritz or Galerkin methods. Other methods based on the writing of the energy of the plate have been used to study the equilibrium of plates, such as Berger's method [Berger, 1954] or Banerjee's method [Bannerjee and Data, 1981].

1.3 Buckling of imperfect beams

In the previous part, we presented the behavior of perfectly straight beams and plates made of a single material. We explained that these structures follow a pitchfork bifurcation and that their buckling loads are associated to a single value of the temperature given by (1.1.6b) and (1.1.9a). However, the behaviors of composite or initially curved structures, or structures with heat conduction across their thickness, are different. The mechanical response of these structures to an external stress can be greatly affected by these properties, and their behavior tend to diverge from the behavior of perfectly straight and homogeneous structures. This explains why these properties are called imperfections. To take a simple example, in the case of an initially curved beam, Euler's equation (1.1.1b) is modified into (1.2.1a). If the geometrical imperfection is an initial parabolic shape (1.2.1b), the beam's shape is given by (1.2.1c), and the equilibrium equation becomes (1.2.1d).

$$E \cdot I \cdot w_{xx} + p \cdot w = E \cdot I \cdot w_{o,xx} \quad (1.2.1a)$$

$$w_o(x) = a_o \cdot \left(1 - \left(\frac{2 \cdot x}{L} \right)^2 \right) \quad (1.2.1b)$$

$$w(x, y) = \frac{8a_o}{L^2 \cdot k^2 \cdot \cos\left(\frac{k \cdot L}{2}\right)} \cdot \left(\cos(k \cdot x) - \cos\left(k \cdot \frac{L}{2}\right) \right) \quad (1.2.1c)$$

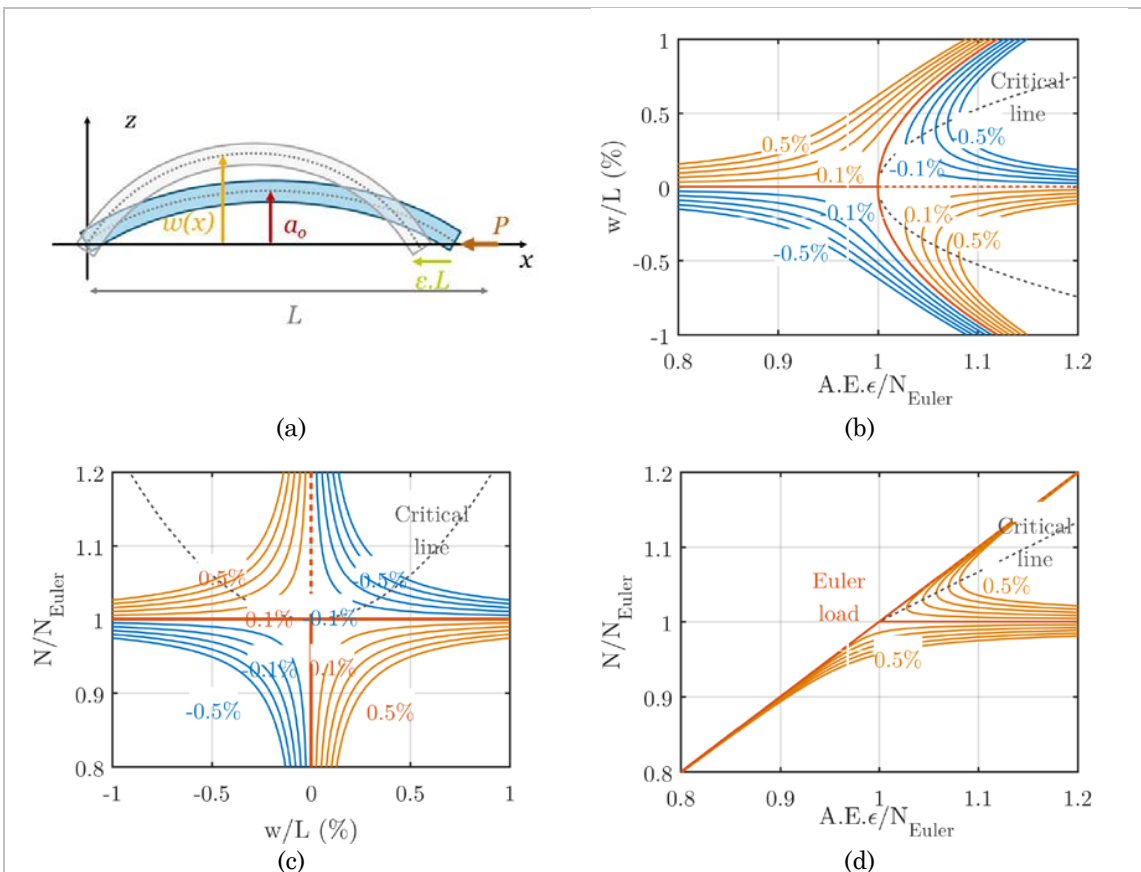
$$N = E \cdot I \cdot k^2 = E \cdot A \cdot \left(\varepsilon - \frac{1}{2 \cdot L} \cdot \int_0^L w_x^2 - w_{o,x}^2 \cdot dx \right) \quad (1.2.1d)$$

Fig.1.2.1b-d. plot the beam deflection amplitude against the beam's shortening and axial load, for various values of the imperfection a_o/t . Fig.1.2.1b shows that the beam thus curves in the direction fixed by its initial imperfection before reaching the Euler load. It is particularly interesting to note the existence of an assymetric secondary equilibrium branch for high values of p . This branch shows that the beam can pass from one side to the other by a saddle-node bifurcation when it reaches the values represented by the gray dashed-line. The equilibrium positions located between the two gray dashed lines are unstable. These same curves can be obtained when studying the thermal buckling of

imperfect axially-constrained isotropic beams, by noticing that the end-shortening can be replaced by thermal expansion $\alpha.T$.

The description of the behavior of inhomogeneous structures under the effect of spatially homogeneous temperature variations, or isotropic structures with variations of the temperature through their thickness is quite similar. Given that the thermal expansion is not the same across the structure's thickness, in addition to a load NT , a thermal moment M^T appears which behaves like an imperfection. For an axially constrained and simply supported beam, Euler's equation becomes (1.2.2a), whereas in the frame of the Van-Karman theory, the equilibrium equations of a plate become (1.2.2b-c) (Boley, 2012). We can directly observe in (1.2.2a) that the thermal stress moment plays directly the same part as the geometrical imperfection in (1.2.1a). This explains why the equilibrium paths described by (1.2.2) are similar to those plotted in Fig.1.2.1b-d.

Figure 1.2.1. *a. Imperfect simply-supported beam. b. Relative beam deflection amplitude vs. normalized beam shortening for various values of imperfection a_0/t with a ratio $t/L=5\%$. c. Normalized axial load vs. beam amplitude. d. Normalized axial load vs. normalized beam shortening.*



$$E \cdot I \cdot w_{,xx} + \left(N^T - \frac{E \cdot A}{2 \cdot L} \cdot \int_0^L w_{,x}^2 \cdot dx \right) \cdot w = \nabla^2 M^T \quad (1.2.2a)$$

$$\nabla^4 F = E \cdot t \cdot (w_{,xy}^2 - w_{,xx} \cdot w_{,yy}) - (1 - \nu) \cdot \nabla^2 N^T \quad (1.2.2b)$$

$$D \cdot \nabla^4 w = F_{,yy} \cdot w_{,xx} - 2 \cdot F_{,xy} \cdot w_{,xy} + F_{,xx} \cdot w_{,yy} - \nabla^2 M^T \quad (1.2.2c)$$

Without seeking to be exhaustive, we can find various studies on the thermal buckling of composite beams. [Vosoughi *et al*, 2012], and [Vaz *et al*, 2010] explained the effect of the dependence of the mechanical properties on the buckling temperature of composite beams. [Samsam Shariat and Eslami, 2006], [Kiani and Eslami, 2010] and [Shukla and Nath 2002] also studied the evolution of the buckling temperature of FGM plates for various thermal profiles. Here again, (Tauchert, 1991) gives a large overview on the research on the subject.

1.4 Thermal snap-through

Snap-through (or oil-canning) is a form of buckling that is characterized by a sudden jump of a structure from an equilibrium position to another. Snap-through can be observed when a load is applied on a curved structure or when two imperfections have antagonistic effects on the behavior of a structure. A classical problem to introduce the snap-through phenomenon is the behavior of the Mises truss [Mises, 1923], an arch made of two linear springs k , and initially curved (angle θ_0), submitted to the effect of a load Q . As demonstrated in [Thompson and Hunt, 1973], the potential energy of such a system can be approximated by a fourth-order polynomial (1.3.1a). In the same time, the potential energy of the load can be approximated by (1.3.1b) and the arch's deflection a by (1.3.1c). Given that the equilibrium positions are the extrema of the total energy, the equilibrium equation is given by (1.3.1d).

$$\mathcal{W}_M = \frac{1}{16} \cdot k \cdot L^2 \cdot (\theta^4 - 2 \cdot \theta_0^2 \cdot \theta^2 + \theta_0^4) \quad (1.3.1a)$$

$$\mathcal{W}(Q) = Q \cdot \frac{L}{2} \cdot (\theta - \theta_0) \quad (1.3.1b)$$

$$a = \frac{L}{2} \cdot (\theta - \theta_0) \quad (1.3.1c)$$

$$Q = -k \cdot \frac{L}{2} \cdot \theta \cdot (\theta^2 - \theta_0^2) \quad (1.3.1d)$$

Fig.1.3.1b plots the evolution of Q as a function of θ . Given that the equilibrium position is a third-order polynomial, three positions can coexist if the initial curvature is positive ($\theta_0 > 0$). This condition corresponds to the criterion of bistability of the arch. To know which positions are allowed, it is necessary to derivate the equilibrium equation to study the stability of the equilibrium (1.3.2a). This equation shows that two equilibrium positions are critical (1.3.2b); the positions are called limit points. For these values of Q , the beam snaps from one position to the other.

$$\frac{dQ}{d\theta} = k \cdot \frac{L}{2} \cdot (3 \cdot \theta^2 - \theta_0^2) \quad (1.3.2a)$$

$$\theta = \pm \frac{\theta_o}{\sqrt{3}} \tag{1.3.2b}$$

Snap-through can also be a consequence of the thermal stress acting on curved beam. The first explanation of this type of thermal snap-through is due to Timoshenko who modeled the instability of bimetallic thermostats in [Timoshenko, 1925]. In this article, he demonstrated that the curvature caused by the difference of thermal expansion of the two layers of a bimetallic beam produces a curvature ρ verifying (1.3.3a). Under this assumption, the axial thrust p due to the reduction of the curvature of a bimetallic beam having an initial deflection w_o is given by (1.3.3d).

$$\frac{t}{\rho} = \frac{3}{2} \cdot (\alpha_2 - \alpha_1) \cdot T \tag{1.3.3a}$$

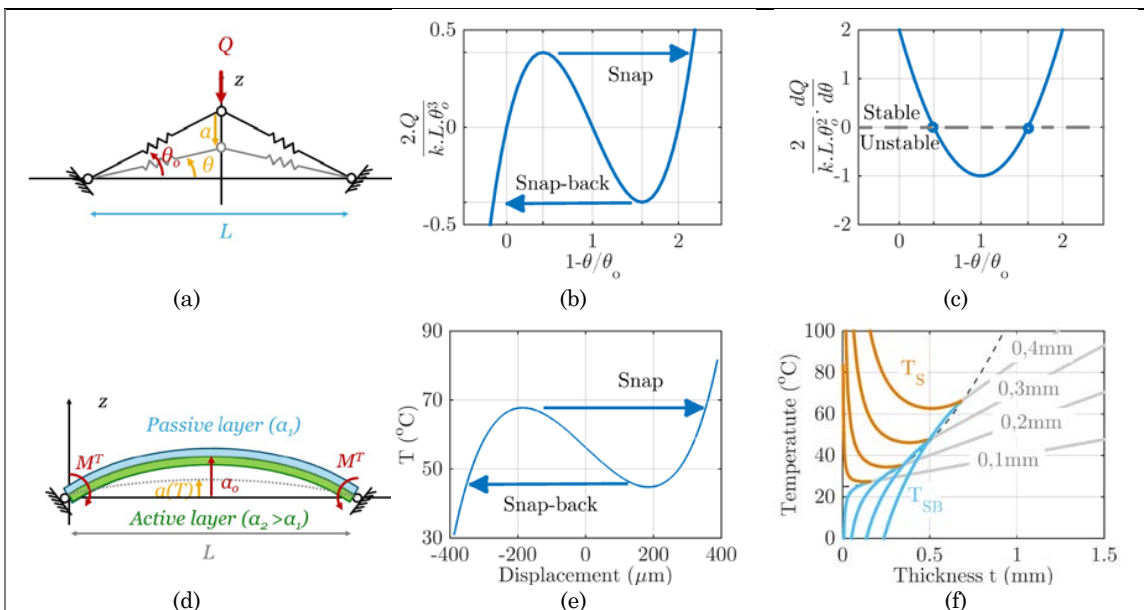
$$w_o(x) = a_o \cdot \sin\left(\frac{\pi \cdot x}{L}\right) \tag{1.3.3b}$$

$$w(x) = \frac{a_o - a(T)}{1 - N/N_{Euler}} \cdot \sin\left(\frac{\pi \cdot x}{L}\right) \tag{1.3.3c}$$

$$\left(1 - \frac{N}{N_{Euler}}\right)^2 \cdot \left(1 - \frac{4 \cdot I}{a_o^2 \cdot A} \cdot \frac{N}{N_{Euler}}\right) = \left(1 - \frac{a(T)}{a_o}\right) \tag{1.3.3d}$$

Hence he found that the bimetallic beam can be bistable if its initial deflection is superior to its thickness according to (1.3.4a). In that case, the temperatures at which the beam snaps and snaps back are given by (1.3.4b-c) and plotted in Fig.1.3.1d.

Figure 1.3.1. a. Arch submitted to the effect of a static load. b. Equilibrium path of the arch. c. Stability of the equilibrium positions. d. Bimetallic beam studied by Timoshenko. e. Equilibrium of bimetallic beam according to Timoshenko for an Al-Invar beam ($L=40\text{mm}$, $t=0.1\text{mm}$). Snap and Snap-Back temperatures of the beam as a function of its thickness.



$$1 - \frac{4.I}{a_0^2.A} > 0 \Leftrightarrow a_0 > \frac{t}{\sqrt{3}} \quad (1.3.4a)$$

$$T_S = \frac{16}{3} \cdot \frac{a_0 \cdot t}{L^2 \cdot (\alpha_2 - \alpha_1)} \left(1 + \frac{2 \cdot \sqrt{3} a_0^2}{t^2} \cdot \sqrt{\left(1 - \frac{t^2}{3 \cdot a_0^2}\right)^3} \right) \quad (1.3.4b)$$

$$T_{SB} = \frac{16}{3} \cdot \frac{a_0 \cdot t}{L^2 \cdot (\alpha_2 - \alpha_1)} \left(1 - \frac{2 \cdot \sqrt{3} a_0^2}{t^2} \cdot \sqrt{\left(1 - \frac{t^2}{3 \cdot a_0^2}\right)^3} \right) \quad (1.3.4c)$$

The strength of Timoshenko's model is to give the conditions of occurrence of the bistability and the temperatures associated to the instability of the beam. However, a closer examination of these equations shows that the mean thermal expansion of the beam is not taken into account, which can be a problem when the difference of thermal expansion between the two materials constituting the bimetallic beam is weak. In that case, the effect of the mean thermal expansion of the beam cannot be neglected and Timoshenko's model loses its validity. [Burgreen and Regal, 1971] solved this problem and showed that in certain conditions, the approximation of a first order buckling mode was false and that the beam can snap with a third-order buckling mode, but at very high temperature. [Rutgerson and Bottega, 2002], [Karlson and Bottega, 2000] also studied extreme behaviors of bimetallic beams. [Orthwein, 1984] also studied the thermal snap-through of bimetallic beams from a manufacturing point of view and showed the difficulty to obtain weak variability around the limit of stability. [Michael and Kwok, 2006] and [Cabal and Ross, 2002] studied the thermal instability of bimorph beams at the microscale. In a similar approach, [Moghadassie and Stanciulescu, 2013] studied the snap-through of shallow arches under the combined effects of a static load and thermal stress.

The phenomenon of thermal snap-through has also been studied for other structures than beams. Wittrick studied the instability of free bimetallic shells and found the conditions on the initial curvature to observe thermal snap-through [Wittrick, 1951]. This work was extended by Aggarwala and Saibel to the case of simply-supported spherical shells [Aggarwala and Saibel 1970] and by Kosel and Battista in the case of free open spherical shells, conical shells and cubic shells [Kosel and Battista, 2007]. The thermal snap-through of plates has also been studied: [Irschik, 1986] used Berger's approximation of the strain energy of a simply-supported plate to demonstrate the snap-through of initially curved plates, and [Heuer and Ziegler, 2004] used it to model the thermal snap-buckling (snap-through associated to a second order buckling mode) of composite plates

1.5 Plan of the chapter

The continuation of this chapter is divided into six parts. The first part presents the first model we developed to explain the instability of composite beams. Starting from a basic recall on mechanics, it presents the demonstration of the non-linear Euler equation given in (1.1.4), and solves it in the case of a simply supported beam. This enables to find the criterion of bistability of composite beams, and to compare it with the criterion given by [Timoshenko, 1925]. The second part is devoted to the study of the energetic properties of bistable beams, to the demonstration of the phase transition associated to thermal snap-through, and to the evaluation of the performances of bimetallic strips as a prime mover of our heat engine. The third part presents a simplified model of thermo-mechanical

bistability with the final objective of providing analytical expressions of the performances of the heat engine. Because it is necessary to understand the role of thermal transfers in the occurrence of bistability, and their impact on the performances of the harvester, the fourth part of this chapter treats the modeling of these thermal transfers, but also the way they modify the dynamic behavior of bimetallic strips.

2 A first model of the instability of composite beams

2.1 A short course on the theory of elasticity

The goal of mechanics of the elastic body is to predict how a system deforms and moves under the action of external forces. In order to link causes (external forces f_{ext} , heat fluxes q_{ext}) to final effects (displacement fields u , v and w), four different kinds of equations are needed: thermodynamic, constitutive, kinematic, and kinetic equations. Thermodynamics explains how a system exchanges energy with its surroundings, and is useful to determine equilibrium positions of a system by using the principle of virtual displacement. The first principle (2.1.1a) states that the variations of the internal energy du and the kinetic energy $d\mathcal{k}$ of a system are equal to the work of external forces dW_{ext} and the external flux dQ_{ext} . The second principle (2.1.1b) describes the evolution of systems and will be useful to model thermal transfers inside the harvesters.

$$du + d\mathcal{k} = \delta Q_{ext} + \delta W_{ext} \quad (2.1.1a)$$

$$d\sigma = \frac{\delta Q_{ext}}{\theta_{ext}} \geq 0 \quad (2.1.1b)$$

The expression of the internal energy as a function of the extensive parameters of the systems, or the expression of one of its Legendre transformations enables to find the constitutive equations of a material, which link the body's extensive parameters to its intensive parameters by means of physical properties of the body. Particularly, by means of the Gibbs energy of the body \mathcal{g} (2.1.2a), the strain tensor and the entropy can be approximated as functions of the body's temperature and the stress tensor.

$$d\mathcal{g} = d(u - \theta \cdot \sigma - \mathcal{T} \cdot \mathcal{S}) = -\sigma \cdot d\theta - \mathcal{S} \cdot d\mathcal{T} \quad (2.1.2a)$$

$$d\sigma = \left. \frac{\partial \sigma}{\partial \theta} \right|_{\mathcal{T}} \cdot d\theta + \left. \frac{\partial \sigma}{\partial \mathcal{T}} \right|_{\theta} \cdot d\mathcal{T} \quad (2.1.2b)$$

$$d\mathcal{S} = \left. \frac{\partial \mathcal{S}}{\partial \theta} \right|_{\mathcal{T}} \cdot d\theta + \left. \frac{\partial \mathcal{S}}{\partial \mathcal{T}} \right|_{\theta} \cdot d\mathcal{T} \quad (2.1.2c)$$

These last two equations are the constitutive equations of the body. In the case of a low-stressed material, at constant temperature, the relation between the stress and the strain tensor is linear (Hooke's law). In that case, the variation symbol can be suppressed in (2.1.2c). Similarly, at constant stress, the thermal expansion can be linearized. Thus equation (2.1.2c) can be transformed into (2.1.3) where T is the relative temperature difference.

$$\mathcal{S} = \left. \frac{\partial \mathcal{S}}{\partial \theta} \right|_{\mathcal{T}} \cdot \mathcal{T} + \left. \frac{\partial \mathcal{S}}{\partial \theta} \right|_{\mathcal{T}} \cdot T \quad (2.1.3)$$

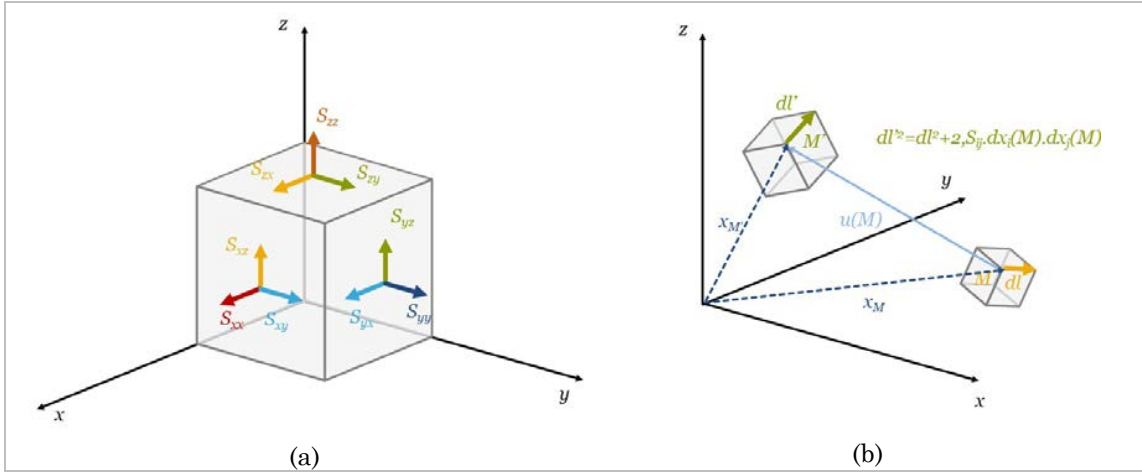


Figure 2.1.1. *a. Representation of the strain tensor components. b. Representation of the link between the displacement fields and the strain tensor.*

For orthotropic materials, each coefficient of the strain tensor (see Fig.2.1.1a) can be written as functions of the body's physical parameters E (Young's modulus), ν (Poisson's ratio) and α (coefficient of thermal expansion).

$$\mathcal{S}_{xx} = \frac{1}{E} \cdot (\mathcal{T}_{xx} - \nu \cdot (\mathcal{T}_{yy} + \mathcal{T}_{zz})) + \alpha \cdot T \quad (2.1.4a)$$

$$\mathcal{S}_{yy} = \frac{1}{E} \cdot (\mathcal{T}_{yy} - \nu \cdot (\mathcal{T}_{xx} + \mathcal{T}_{zz})) + \alpha \cdot T \quad (2.1.4b)$$

$$\mathcal{S}_{zz} = \frac{1}{E} \cdot (\mathcal{T}_{zz} - \nu \cdot (\mathcal{T}_{xx} + \mathcal{T}_{yy})) + \alpha \cdot T \quad (2.1.4c)$$

$$\mathcal{S}_{xy} = \mathcal{S}_{yx} = \frac{1 + \nu}{E} \cdot \mathcal{T}_{xy} \quad (2.1.4d)$$

$$\mathcal{S}_{yz} = \mathcal{S}_{zy} = \frac{1 + \nu}{E} \cdot \mathcal{T}_{yz} \quad (2.1.4e)$$

$$\mathcal{S}_{xz} = \mathcal{S}_{zx} = \frac{1 + \nu}{E} \cdot \mathcal{T}_{xz} \quad (2.1.4f)$$

As a matter of convenience, the Voigt-Kelvin notation is often used (2.1.5) [Reddy, 2006].

$$\mathcal{S}_{xx} = \mathcal{S}_1 ; \mathcal{S}_{yy} = \mathcal{S}_2 ; \mathcal{S}_{zz} = \mathcal{S}_3 ; \mathcal{S}_{yz} = \mathcal{S}_4 ; \mathcal{S}_{xz} = \mathcal{S}_5 ; \mathcal{S}_{xy} = \mathcal{S}_6 \quad (2.1.5)$$

With the thermodynamic principles and constitutive equations, two final equations are needed to describe the behavior of the elastic body. The kinetic equation directly links the stress tensor's components to the body force N and to its inertia (2.1.6a.).

$$\nabla \mathcal{S} + \rho \cdot N = \rho \cdot \frac{\partial^2 u}{\partial t^2} \quad (2.1.6a)$$

$$\mathcal{S}_{xx,x} + \mathcal{S}_{xy,y} + \mathcal{S}_{xz,z} + \rho \cdot N_x = \rho \cdot \frac{\partial^2 u}{\partial t^2} \quad (2.1.6b)$$

$$\mathcal{S}_{xy,x} + \mathcal{S}_{yy,y} + \mathcal{S}_{yz,z} + \rho \cdot f_y = \rho \cdot \frac{\partial^2 v}{\partial t^2} \quad (2.1.6c)$$

$$\mathcal{S}_{xz,x} + \mathcal{S}_{yz,y} + \mathcal{S}_{zz,z} + \rho \cdot f_z = \rho \cdot \frac{\partial^2 w}{\partial t^2} \quad (2.1.6d)$$

The last relation to be considered is on the kinematics of the elastic body. Once the components of the strain tensor have been determined by means of the kinetic equations and constitutive laws, it is necessary to find how the strain is related to the displacement of the elastic body. Based upon geometrical considerations (see Fig.2.1.1b), it can be demonstrated [Reddy, 2006] that the strain tensor's components obey the Green-Lagrange equation (2.1.7a). When deformations are small, the quadratic terms of the Green-Lagrange strain tensor are neglected (2.1.7b). However, to study the behavior of unstable membranes, this term will play a crucial role.

$$\mathcal{S}_{ij} = \frac{1}{2} \cdot (u_{i,j} + u_{j,i} + u_{k,i} \cdot u_{k,j}) \quad (2.1.7a)$$

$$\mathcal{S}_{ij} \approx \frac{1}{2} \cdot (u_{i,j} + u_{j,i}) \quad (2.1.7b)$$

Once the various equations of mechanics have been given, it is necessary to see which assumptions can be made to simplify them in order to explain the behavior of thermo-mechanically bistable beams.

2.2 Equilibrium equations of composite beams suffering from residual stress

In this second part, we seek to study the static behavior of the composite beams submitted to the effect of the residual stress and to homogeneous variations of the temperature. Fig.2.2.1a represents the composite beam of dimensions (L, v, t) studied in this work. In this figure, the composite structure of the beam is modeled by assuming a z -dependence of the physical properties of the beam (2.2.1).

$$E = E(z) ; \alpha = \alpha(z) ; \rho = \rho(z) ; C_\varepsilon = C_\varepsilon(z) \dots \quad (2.2.1)$$

In order to describe the physical properties of composite beams, a set of parameters $(N_e, I_e, N_\alpha, M_\alpha, m_b, C_v)$ represents respectively the beam's axial stiffness n_e , bending stiffness i_e , mean thermal expansion N_α , thermal expansion asymmetry m_α , mass m_b and heat capacity C_v . These six values are defined by equations (2.2.2a) to (2.2.2f) with the help of (2.2.2g) defining the neutral axis of the beam.

$$N_e = v \cdot \int_0^t E(z) \cdot \delta z \quad (2.2.2a)$$

$$I_e = v \cdot \int_0^t E(z) \cdot (z - z_0)^2 \cdot \delta z \quad (2.2.2b)$$

$$N_\alpha = v \cdot \int_0^t E(z) \cdot \alpha(z) \cdot \delta z \quad (2.2.2c)$$

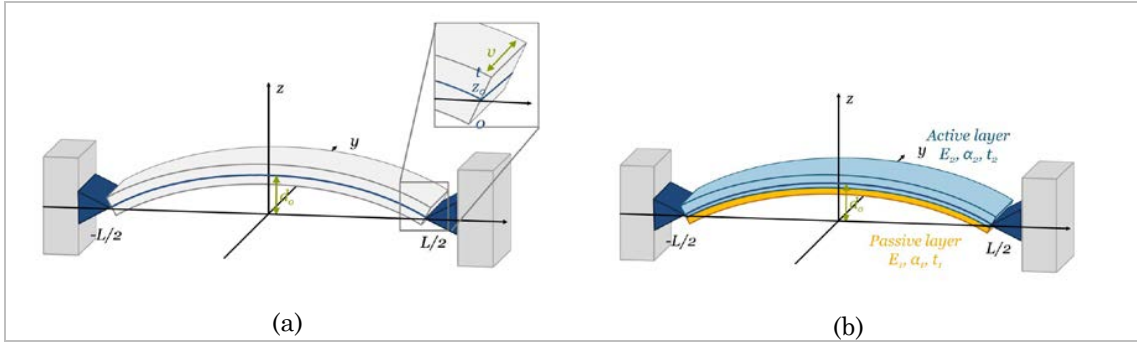


Figure 2.2.1. *a. Representation of the composite beam studied in this chapter b. Simplification in the case of a bimetallic beam made of an active layer and a passive layer ($\alpha_2 > \alpha_1$).*

$$M_\alpha = v. \int_0^t E(z). \alpha(z). (z - z_o). \delta z \quad (2.2.2d)$$

$$m_b = v. L. \int_0^t \rho(z). \delta z \quad (2.2.2e)$$

$$C_v = v. L \int_0^t \rho(z). C_\epsilon(z). \delta z \quad (2.2.2f)$$

$$z_o \text{ such that } \int_0^t E(z). (z - z_o). \delta z = 0 \quad (2.2.2g)$$

Each material layer of the beam being stressed by a residual stress σ_o measured at the reference temperature θ_o (expressed in kelvin degrees), two other parameters are defined to take into account the effect of the residual stress on the behavior of the beam. F_o is defined by (2.2.3a) and represents the resultant force created by the residual stress of each layer. Similarly to m_a , M_o is mathematically defined as the barycenter of the residual stress, and physically as the moment associated to the force F_o (2.2.3b).

$$F_o = v. \int_0^t \mathcal{T}_o(z). \delta z \quad (2.2.3a)$$

$$M_o = v. \int_0^t \mathcal{T}_o(z). (z - z_o). \delta z \quad (2.2.3b)$$

In the case of a beam, the equations presented in the previous part can be simplified since the strain and stress tensors' components depending on the y-axis are zero (2.2.3a). Most beam deformations can be studied in the frame of the Euler-Bernoulli beam theory [Reddy, 2006]: this theory assumes that the cross sections stay straight (Hyp.1), inextensible (Hyp.2), and perpendicular to the bending line (Hyp. 3). The first two assumptions imply that the transverse stress is also null (2.2.3b) whereas the third one leads to neglecting the transverse shear stress (2.2.3c).

$$\mathcal{S}_{yy} = \mathcal{S}_{xy} = \mathcal{S}_{yz} = 0 \quad (2.2.3a)$$

$$\mathcal{S}_{zz} = w_{,z} = 0 \Rightarrow w(x, z) = w(x) \quad (2.2.3b)$$

$$\mathcal{S}_{xz} = u_{,z} + w_{,x} = 0 \Rightarrow u(x, z) = u(x, z_0) - z \cdot w_{,x}(x) \quad (2.2.3c)$$

The axial displacement of each point of the beam can then be known if the displacement of the neutral axis is known for instance. Hence, the axial strain can be expressed by means of the Green-Lagrange tensor (2.1.6a), leading to the expression of the Van Karman strain (2.2.4c). The stress tensor is given by (2.2.4b).

$$\mathcal{S}_{xx} = u_{,x}(x, z_0) + \frac{1}{2} \cdot w_{,x}^2(x, z_0) - (z - z_0) \cdot w_{,xx}(x, z_0) \quad (2.2.4a)$$

$$\mathcal{T}_{xx} = E \cdot (\mathcal{S}_{xx} - \alpha \cdot T) + \mathcal{T}_0 \quad (2.2.4b)$$

To determine the equilibrium equations of the composite beam, the strain energy's expression is integrated over the whole beam volume Ω in order to apply the principle of virtual displacement. In that case, the variation of the beam's strain energy and kinetic energy is equal to the work of the external forces (2.2.5a). Equation (2.2.5a) can then be developed in (2.2.5b), neglecting the kinetic energy variation linked to the axial displacement u .

$$d\mathcal{W}_M + d\mathcal{K} = d\mathcal{W}_{ext} \quad (2.2.5a)$$

$$\int_{\Omega} \left(\mathcal{T}_{xx} \cdot d\mathcal{S}_{xx} + \frac{1}{2} \cdot \rho \cdot w_{,tt}^2 \right) \cdot \delta\Omega = d\mathcal{W}_{ext} \quad (2.2.5b)$$

In the case of an axially constrained beam, no external force works since axial displacement is forbidden (2.2.6a). Hence, $d\mathcal{W}_{ext}$ vanishes in (3.2.5b). The fields u and w being independent variables, the principle of virtual displacement can be projected on each displacement field. Hence (2.2.5b) is equivalent to (2.2.6b) and (2.2.6c).

$$u\left(\frac{L}{2}\right) = u\left(-\frac{L}{2}\right) = 0 \quad (2.2.6a)$$

$$\int_{\Omega} \mathcal{T}_{xx} \cdot du_{,x} \cdot \delta\Omega = 0 \quad (2.2.6b)$$

$$\int_{\Omega} \left(\frac{1}{2} \cdot \rho \cdot w_{,tt}^2 + \mathcal{T}_{xx} \cdot (w_{,x} \cdot dw_{,x} - (z - z_0) \cdot dw_{,xx}) \right) \cdot \delta\Omega = 0 \quad (2.2.6c)$$

We first treat the equation projected on the axial displacement u . The integration by parts of (2.2.6b) gives a boundary equation and a general equation for u (2.2.7a). Given the boundary conditions (2.2.6a), the first term vanishes, leading to (2.2.7b).

$$\int_{\Omega} \mathcal{T}_{xx} \cdot du_{,x} \cdot \delta\Omega = [\mathcal{T}_{xx} \cdot du]_{\Omega} - \int_{\Omega} \mathcal{T}_{xx,x} \cdot du \cdot \delta\Omega = 0 \quad (2.2.7a)$$

$$\int_{\Omega} \mathcal{T}_{xx,x} \cdot du \cdot \delta\Omega = 0 \quad (2.2.7b)$$

Equation (2.2.7b) is the weak formulation of the equilibrium. A strong formulation is given by (2.2.8a). This expression can be developed with the beam parameters given in (2.2.2).

$$\int_0^t \mathcal{T}_{xx,x} dz = 0 \Rightarrow \int_{\Omega} \mathcal{T}_{xx,x} du \cdot \delta\Omega = 0 \quad (2.2.8a)$$

$$\int_0^t \mathcal{T}_{xx,x} dz = n_e \cdot \left(u_{,x} + \frac{1}{2} \cdot w_{,x}^2 \right)_{,x} = 0 \quad (2.2.8b)$$

By making a double integration of this last expression, we can find that the axial displacement is constant and is given by (2.2.9a), where λ represents the difference between the length of the curved beam and the length L of the straight beam, already presented in the introduction of this chapter. The beam stretching is directly equal to the ratio of λ over the length of the clamp (2.2.9b). Hence, the axial strain can be rewritten in (2.2.9c).

$$u_{,x} + \frac{1}{2} \cdot w_{,x}^2 = \frac{\lambda}{L} \quad (2.2.9a)$$

$$\lambda = \frac{1}{2} \cdot \int_{-L/2}^{L/2} w_{,x}^2 \cdot dx \quad (2.2.9b)$$

$$\mathcal{S}_{xx} = \frac{\lambda}{L} - (z - z_o) \cdot w_{,xx}(x, z_o) \quad (2.2.9c)$$

Similarly, we treat the formulation of the equilibrium given by (2.2.6c). Taking the case of a simply supported beam, the beam's edges cannot move (2.2.10a), but can rotate in order to cancel the moment created by the variation of the temperature and the residual stress (2.2.10b). It is interesting to note in (2.2.10b) the antagonistic effects caused by the residual stress asymmetry and the asymmetry of the thermal expansion $M_a T$. If both effects are positive, M_o gives a convex shape to the beam whereas $M_a T$ tends to give a concave shape to the beam. The fact that both effects have the same sign is a necessary condition to observe any bistable phenomenon.

$$w\left(-\frac{L}{2}\right) = w\left(\frac{L}{2}\right) = 0 \quad (2.2.10a)$$

$$i_e \cdot w_{,xx}\left(\frac{L}{2}\right) = i_e \cdot w_{,xx}\left(-\frac{L}{2}\right) = M_o - M_a T \quad (2.2.10b)$$

Hence the boundary equation resulting from a double integration by parts of (2.2.6c) vanishes (2.2.11a). The equilibrium is then described by (2.2.11b).

$$\left[(\mathcal{T}_{xx} \cdot w_{,x} + z \cdot \sigma_x) \cdot dw - z \cdot \mathcal{T}_{xx} \cdot dw_{,x} \right]_{\Omega} = 0 \quad (2.2.11a)$$

$$\begin{aligned} \int_{\Omega} \left(\rho \cdot w_{,tt}^2 \cdot dw + \mathcal{T}_{xx} \cdot (w_{,x} \cdot dw_{,x} - z \cdot dw_{,xx}) \right) \cdot \delta\Omega \\ = - \int_{\Omega} \left(\rho \cdot w_{,tt}^2 + (\mathcal{T}_{xx} \cdot w_{,x})_{,x} + z \cdot \mathcal{T}_{xx,xx} \right) \cdot dw \cdot \delta\Omega = 0 \end{aligned} \quad (2.2.11b)$$

The strong formulation of the equilibrium is then (2.2.12).

$$\int_0^t \left(\rho \cdot w_{,tt}^2 + (\mathcal{T}_{xx} \cdot w_{,x})_{,x} + z \cdot \mathcal{T}_{xx,xx} \right) \cdot dz = 0 \quad (2.2.12)$$

By developping this equation, we finally establish the non-linear Euler equation, which describes the equilibrium of the beam (2.2.13a). The terms between brackets correspond to the axial thrust applied by the clamp on the beam (2.2.13b): as the beam cannot move, a thrust $i_e.k^2$ tends to appear to balance the effect of the residual stress force F_o , the beam's mean thermal expansion and the beam's stretching force $N_e.\lambda/L$. That way, the static equilibrium (omitting inertia) is described by (2.2.13c).

$$\frac{m_b}{L} \cdot w_{,tt}^2 + \left(N_\alpha \cdot T - N_e \cdot \frac{\lambda}{L} - F_o \right) \cdot w_{,xx} + I_e \cdot w_{,xxxx} = 0 \quad (2.2.13a)$$

$$I_e \cdot k^2 = N_\alpha \cdot T - N_e \cdot \frac{\lambda}{L} - F_o \quad (2.2.13b)$$

$$k^2 \cdot w_{,xx} + w_{,xxxx} = 0 \quad (2.2.13c)$$

The equilibrium equation (2.2.13d) can be rewritten by defining two forces N and N_o by (2.2.14a) and (2.2.14b): N describes the effect of the beam's internal forces and N_o is an invariant of the transformation, representing the effective residual force acting on the beam.

$$N = N_e \cdot \frac{\lambda}{L} - N_\alpha \cdot \left(T - \frac{M_o}{M_\alpha} \right) - I_e \cdot k^2 \quad (2.2.14a)$$

$$N_o = N_\alpha \cdot \frac{M_o}{M_\alpha} - F_o \quad (2.2.14b)$$

Hence the beam's equilibrium is simply described by the equality (2.2.15).

$$N = N_o \quad (2.2.15)$$

2.3 Criterion of bistability

In order to study the non-linear Euler equation (2.2.13a), we first find the general solution of (2.2.13d) and we then determine the amplitude of the beam deflexion using (2.2.15). The general forms of the solution to (2.2.13d) are the functions sine and cosine and the linear functions of the position x (2.3.1a-b). These functions can be regrouped according to their parity (2.3.1c).

$$w_1(x) = a \cdot \cos(k \cdot x) + b \quad (2.3.1a)$$

$$w_2(x) = c \cdot \sin(k \cdot x) + d \cdot x \quad (2.3.1b)$$

$$w(x) = w_1(x) + w_2(x) \quad (2.3.1c)$$

The two boundary conditions on the displacement field w given in (2.2.10a) and (2.2.10b) help reducing the number of unknown parameters.

$$a \cdot \cos\left(\frac{k \cdot L}{2}\right) + b + c \cdot \sin\left(\frac{k \cdot L}{2}\right) + d \cdot \frac{L}{2} = 0 \quad (2.3.2a)$$

$$a \cdot \cos\left(\frac{k \cdot L}{2}\right) + b - c \cdot \sin\left(\frac{k \cdot L}{2}\right) - d \cdot \frac{L}{2} = 0 \quad (2.3.2b)$$

$$a.k^2.\cos\left(\frac{k.L}{2}\right) + c.k^2.\sin\left(\frac{k.L}{2}\right) = \frac{M_\alpha.T - M_o}{I_e} \quad (2.3.2c)$$

$$a.k^2.\cos\left(\frac{k.L}{2}\right) - c.k^2.\sin\left(\frac{k.L}{2}\right) = \frac{M_\alpha.T - M_o}{I_e} \quad (2.3.2d)$$

These equations show that the beam shape associated to symmetrical buckling mode w_1 can be non-zero even when k is not an odd multiple of π/L , because of the effect of the asymmetries m_a and M_o . However, asymmetrical modes only occur when k is a multiple of π/L (2.3.3d).

$$w_1(x) = a.\left(\cos(k.x) - \cos\left(\frac{k.L}{2}\right)\right) \quad (2.3.3a)$$

$$a = \frac{M_\alpha.T - M_o}{I_e.k^2.\cos\left(\frac{k.L}{2}\right)} \text{ with } k \neq (2.n + 1).\frac{\pi}{L} \text{ with } n \in \mathbb{N} \quad (2.3.3b)$$

$$w_2(x) = c.\left(\sin(k.x) - \frac{2}{L}.\sin\left(\frac{k.L}{2}\right)\right) \quad (2.3.3c)$$

$$c \neq 0 \text{ if } k = 2.n.\frac{\pi}{L} \text{ with } n \in \mathbb{N} \quad (2.3.3d)$$

A particular solution is obtained for the equivalent relative temperature $T_o = M_o/M_\alpha$. At this point either the wave vector k is equal to the first buckling load, or the amplitude is zero and the beam is straight (2.3.4).

$$T = \frac{M_o}{M_\alpha} \Rightarrow k = \frac{\pi}{L} \text{ or } a = 0 \quad (2.3.4)$$

Equation (3.3.3b) enables to calculate the length λ (2.3.5).

$$\lambda = \frac{1}{4}.(k^2.L - k.\sin(k.L)).a^2 \quad (2.3.5)$$

Hence the equilibrium of the beam is described by a second order polynomial of a (2.3.6a). As a matter of convenience, we define two functions of k , ϕ_1 and ϕ_2 . We also define d_o representing the deflexion of the middle of the beam's centre line (2.3.6d).

$$\frac{N_e}{4.L}.\phi_1(k).a^2 - \frac{N_\alpha.I_e}{M_\alpha}.\phi_2(k).a + I_e.k^2 - N_o = 0 \quad (2.3.6a)$$

$$\phi_1(k) = k^2.L - k.\sin(k.L) \quad (2.3.6b)$$

$$\phi_2(k) = k^2.\cos\left(\frac{k.L}{2}\right) \quad (2.3.6c)$$

$$d_o = w(0) = a.\left(1 - \cos\left(\frac{k.L}{2}\right)\right) \quad (2.3.6d)$$

In Fig.2.3.1, the equilibrium paths predicted by (2.3.6a) are plotted for various values of the normalized force N_o/N_{Euler} for an Al-Invar beam ($L = 40$ mm, $t = 150 + 150$ μ m) and for $T_o = 100^\circ\text{C}$. Fig.2.3.1a is the typical figure associated to bistability: it represents the relative displacement of the beam's middle d_o/L as a function of the temperature T/T_o . Fig.2.3.1b and Fig.2.3.1c respectively represent the evolution of the normalized axial

thrust k^2 and the length λ/L as a function of temperature. These figures show that for monostable beams, only one equilibrium position is authorized whatever the beam's temperature. As N_o progressively increases, the sensitivity of the beam to temperature decreases and the beam amplitude varies less rapidly. When N_o exceeds a critical value, the beam becomes bistable and up to three possible equilibrium positions exist simultaneously. The central position is unstable and the beam trajectory exhibits a hysteretic behavior characterized by two temperature T_s and T_{SB} at which the beams snaps from an unstable position (which is a limit point) to a stable position. In Fig.2.3.1b and 2.3.1c, the occurrence of the bistability is characterized by a loop when the axial thrust exceeds the Euler load. Fig.2.3.1d represents the deformation of a bistable beam for the four values of amplitude that characterize the hysteresis cycle.

Table 2.3.1. Properties of the bimorph in Al-Invar and value chosen of M_o so that $T_o=100^\circ\text{C}$.

Dimensions (mm^2)	N_e (N)	I_e ($N.m^2$)	M_α ($N.K^{-1}$)	M_α ($N.m.K^{-1}$)	C_v ($J.K^{-1}$)	N_{Euler} (N)	M_o ($N.m$)
40 x 4	9.26x10 ⁵	6.94x10 ⁻⁴	1.15	7.63 x10 ⁻⁵	0.15	4.27	7.63x10 ⁻³

Equation (2.3.6a) enables to identify the criterion of bistability, distinguishing monostable beams from bistable beams. We know from (2.3.4) that at the temperature $T_o=M_o/M_\alpha$, the beam can be perfectly straight ($\alpha=0$). For this value of temperature, Equation (2.3.6a) becomes (2.3.7).

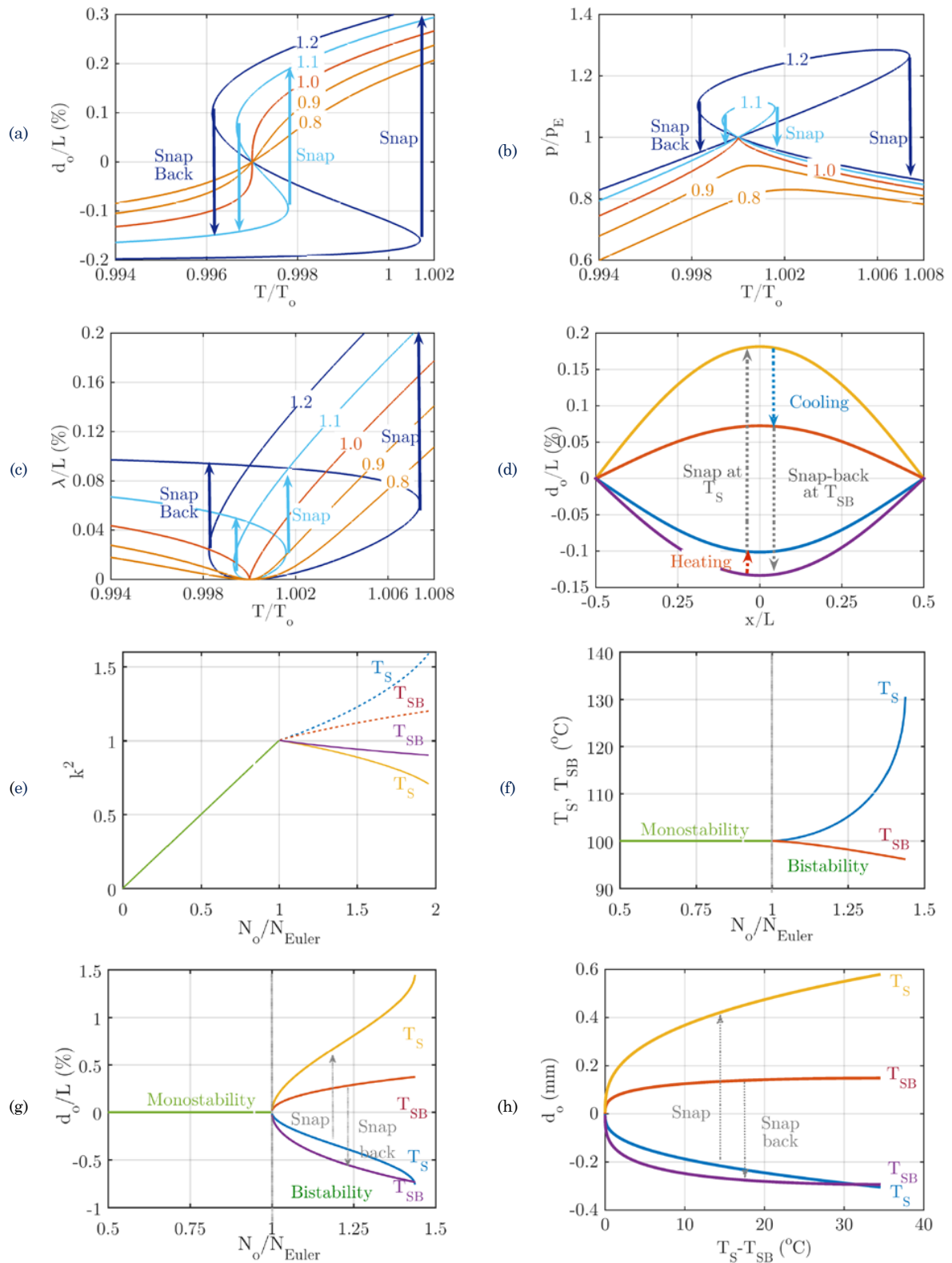
$$\frac{N_e \cdot \pi^2}{4 \cdot L^2} \cdot a^2 + i_e \cdot \frac{\pi^2}{L^2} - N_o = 0 \quad (2.3.7)$$

Necessary, if the force N_o exceeds the first Euler buckling mode, (2.3.7) has two other solutions at this temperature and the beam is de facto bistable. The criterion of bistability is then (2.3.8a). The criterion of stability can also be rewritten under the form (2.3.8b). This equation means that the temperature defined by the two imperfections must be higher than the buckling temperature of the straight beam in order to observe a bistable behavior.

$$N_o = N_\alpha \cdot \frac{M_o}{M_\alpha} - F_o \geq I_e \cdot \frac{\pi^2}{L^2} = N_{Euler} \quad (2.3.8a)$$

$$\frac{M_o}{M_\alpha} \geq \frac{I_e}{N_\alpha} \cdot \frac{\pi^2}{L^2} + \frac{F_o}{N_\alpha} \quad (2.3.8b)$$

Figure 2.3.1. a. Equilibrium paths in the (d_o, T) plane for various values of N_o/N_{Euler} . b. Equilibrium paths in the plane (pt, T) . c. Equilibrium paths in the plane (λ, T) . d. Beam's shape for $N_o/N_{Euler} = 1.1$. e-f-g-h. Properties of an Al-Invar beam.



Equation (2.3.7a) is derivated to study the stability of the equilibrium position (2.3.9).

$$dN = \left(\frac{N_e \cdot M_\alpha}{2 \cdot I_e \cdot L} \cdot \frac{\phi_1(k)}{\phi_2(k)} \cdot a - N_\alpha \right) \cdot dT + \left(\frac{N_e \cdot a^2}{4 \cdot L} \cdot \left(\phi_1'(k) - 2 \cdot \frac{\phi_1(k) \cdot \phi_2'(k)}{\phi_2(k)} \right) + 2 \cdot I_e \cdot k \right) \cdot dk \quad (2.3.9)$$

The stability of the equilibrium is associated to the sign of the second partial derivative of the strain energy and to the convexity/concavity of the strain energy. The beam can snap only when the stability disappears. Hence we find that there is equivalence between the nullity of the strain energy's second derivative and the nullity of the first derivative of the force N (2.3.10).

$$d^2 \mathcal{W}_{mec} = 0 \Leftrightarrow \left. \frac{\partial N}{\partial \lambda} \right|_T = 0 \Leftrightarrow \left. \frac{\partial N}{\partial a} \right|_T = 0 \Leftrightarrow \left. \frac{\partial N}{\partial k} \right|_T = 0 \quad (2.3.10)$$

Hence, the limit points are characterized by (2.3.11).

$$\left. \frac{\partial N}{\partial k} \right|_T = 0 \Leftrightarrow \frac{n_e}{4 \cdot L} \cdot a^2 \cdot \left(\phi_1'(k) - 2 \cdot \frac{\phi_1(k) \cdot \phi_2'(k)}{\phi_2(k)} \right) + 2 \cdot i_e \cdot k = 0 \quad (2.3.11)$$

Computing (2.3.6a) and (2.3.11) enables to find the values of the beam's amplitude associated to the limit points and then to deduct the critical temperatures. Fig.2.3.1e shows the evolution of the critical load as a function of the normalized force Po/P_E for an Al-Invar beam ($L = 40$ mm, $t = 400 + 400$ μm). The evolution of the snap and snap-back temperatures for the same beam is represented in Fig.2.3.1f, and the displacement of the beam in Fig.2.3.1g. Fig.2.3.1h plots the dependence of the beam amplitude on the thermal hysteresis. Logically, the rise of N_o widens the thermal hysteresis. As a consequence, the displacement of the beam during the snap and the snap-back is increased. The difference between these displacements is linked to the effect of the mean thermal expansion, which increases the thrust of the clamp on the beam when the beam is heated and snaps, and then decreases this thrust when the beam snaps back.

2.4 Simplification of the equations for a bimetallic beam

The bimetallic beam represents the simplest case among beams presenting an asymmetry of the coefficients of thermal expansion. Considering the stack presented in Fig.2.2.1a, we can simplify the expression of the beam's parameters (2.3.2b-h) by introducing the ratio of the layers' thicknesses (2.4.1a).

$$t_{12} = t_1 + t_2 ; r_{12} = \frac{t_1}{t_2} \quad (2.4.1a)$$

$$z_o = \frac{(E_1 - E_2) \cdot r_{12}^2 + E_2}{2 \cdot ((E_1 - E_2) \cdot r_{12} + E_2)} \quad (2.4.1b)$$

$$N_e = v \cdot t_{12} \cdot (E_1 \cdot r_{12} + E_2 \cdot (1 - r_{12})) \quad (2.4.1c)$$

$$I_e = v \cdot \frac{t_{12}^3}{3} \cdot (E_1 \cdot \alpha_1 \cdot r_{12} + E_2 \cdot \alpha_2 \cdot (1 - r_{12})) \quad (2.4.1d)$$

$$N_\alpha = v \cdot t_{12} \cdot (E_1 \cdot \alpha_1 \cdot r_{12} + E_2 \cdot \alpha_2 \cdot (1 - r_{12})) \quad (2.4.1e)$$

$$M_\alpha = v \cdot \frac{t^2}{2} \cdot (2 \cdot z_o \cdot r_{12} - r_{12}^2) \cdot E_1 \cdot (\alpha_2 - \alpha_1) \quad (2.4.1f)$$

$$F_o = v \cdot t \cdot (\sigma_1 \cdot x + \sigma_2 \cdot (1 - x)) \quad (2.4.1g)$$

$$M_o = v \cdot \frac{t^2}{2} \cdot (2 \cdot z_o \cdot x - x^2) \cdot \left(\frac{E_1}{E_2} \cdot \mathcal{J}_2 - \mathcal{J}_1 \right) \quad (2.4.1h)$$

In that case, the temperature T_o and the force N_o can be simplified into (2.4.2a) and (2.4.2b).

$$T_o = \left(\frac{\mathcal{J}_2}{E_2} - \frac{\mathcal{J}_1}{E_1} \right) / (\alpha_2 - \alpha_1) + \theta_o \quad (2.4.2a)$$

$$N_o = N_e \cdot \left(\frac{\mathcal{J}_2}{E_2} \cdot \alpha_1 - \frac{\mathcal{J}_1}{E_1} \cdot \alpha_2 \right) / (\alpha_2 - \alpha_1) \quad (2.4.2b)$$

The criterion of bistability cannot be simplified further. To illustrate the role of each parameter, we take the case of a bimetallic beam where the neutral axis is placed at the interface between the two materials ($z_o=x$). To obtain this case, x must verify (2.4.3a). The criterion of stability thus becomes (2.4.3b).

$$r_{12} = \frac{\sqrt{E_2}}{\sqrt{E_2} + \sqrt{E_1}}; \quad \frac{t_1}{t_2} = \sqrt{\frac{E_2}{E_1}} \quad (2.4.3a)$$

$$\frac{(\sqrt{E_2} + \sqrt{E_1})^2}{\sqrt{E_1} \cdot E_2 \cdot (\alpha_2 - \alpha_1)} \cdot \left(\frac{\sigma_2}{E_2} \cdot \alpha_1 - \frac{\sigma_1}{E_1} \cdot \alpha_2 \right) \geq \frac{\pi^2}{3} \cdot \frac{t_{12}^2}{L^2} \quad (2.4.3b)$$

Equation (2.4.3b) then shows that bimetallic beams with a low thermal asymmetry and a small equivalent Young modulus are more sensitive to the effect of the residual stress; in these conditions the Euler load is reached for smaller values of the residual stress. Similarly, beams with a high aspect ratio (thin and long beams) have a smaller Euler load and easily become unstable. The bistability equation also shows that if material 2 is used as an active layer and material 1 as a passive layer ($\square_2 > \square_1$), the best solution to produce a bistable beam is to create a compressive stress in the passive layer ($\sigma_1 < 0$) (Fig.2.4.1b) and a tensile stress in the active layer ($\sigma_2 > 0$) (Fig.2.4.1a). In this case, both thermal asymmetry and residual asymmetry are positive, so the beam initially has a convex shape.

Experimentally, it can be difficult to process simply-supported bimetallic beams with a different values of residual stress in either material. The simplest solution is to apply an initial thrust N_i to the beam in order to buckle it. By using (2.3.9), we can express this force (2.4.4a) and deduce the criterion of bistability (2.4.4b). The temperature T_o associated to this force is then the temperature at which the thrust is applied ($T_o=0$).

$$N_i = N_e \cdot \frac{\lambda}{L} \quad (2.4.4a)$$

$$N_i \geq \frac{\pi^2}{3} \cdot \frac{v \cdot t_{12}^3}{L^2} \cdot \frac{E_1 \cdot E_2}{(\sqrt{E_2} + \sqrt{E_1})^2} \quad (2.4.4b)$$

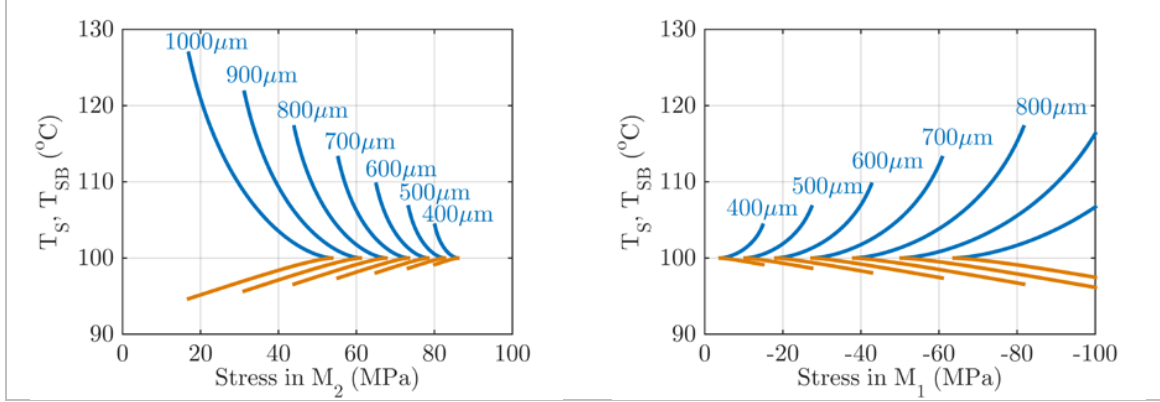


Figure 2.4.1. Dependence of the hysteresis temperature of an Al-Invar beam: a. on the tensile stress in the Al layer. b. on the compressive stress in the Invar layer.

2.6 Equilibrium of composite beams with an initial curvature

The previous part presented the modeling of the instability of initially-stressed beams, contrary to the models of [Timoshenko, 1925], [Burgreen and Regal, 1971], and [Cabal and Ross, 2002] where the beams are initially curved. In this part, we show that initially-curved beams can be modeled with the previous equations, assuming that the beams have an initial polynomial shape. In the case of beams with an initial curvature w_o , the axial strain is given by (3.6.1).

$$\mathcal{S}_{xx} = u_{,x} + \frac{1}{2} \cdot (w_x^2 - w_{o,x}^2) - (z - z_o) \cdot (w_{,xx} - w_{o,xx}) \quad (2.6.1)$$

Without detailing the demonstration of the principle of virtual displacement, we can find that the equilibrium is described by the non-linear Euler equation (2.6.2a) with the boundary equations (2.6.2c).

$$\frac{m_b}{L} \cdot \frac{d^2 w}{dt^2} + \left(N_\alpha \cdot T - \frac{N_e}{2 \cdot L} \cdot \int_{-\frac{L}{2}}^{\frac{L}{2}} (w_x^2 - w_{o,x}^2) \cdot dx \right) \cdot w_{,xx} + I_e \cdot (w_{,xxxx} - w_{o,xxxx}) = 0 \quad (2.6.2a)$$

$$iI_e \cdot k^2 = N_\alpha \cdot T - \frac{nN_e}{2 \cdot L} \cdot \int_{-\frac{L}{2}}^{\frac{L}{2}} (w_x^2 - w_{o,x}^2) \cdot dx \quad (2.6.2b)$$

$$I_e \cdot \left(w_{,xx} \left(\pm \frac{L}{2} \right) - w_{o,xx} \left(\pm \frac{L}{2} \right) \right) = -M_\alpha \cdot T ; w \left(\pm \frac{L}{2} \right) = 0 ; u \left(\pm \frac{L}{2} \right) = 0 \quad (2.6.2c)$$

In [Timoshenko, 1925], [Burgreen and Regal, 1971] and [Cabal and Ross, 2002], the beam's initial shape is assumed to be a half-sine function (2.6.3a) because this solution is ideal when Galerkin's method is used to approximate the beam shape, since it is the general solution of the Euler equation. In that case, the equilibrium equation is (2.6.3d).

$$w_o(x) = a_o \cdot \cos\left(\frac{\pi \cdot x}{L}\right) \quad (2.6.3a)$$

$$w(x) = a \cdot \left(\cos(k \cdot x) - \cos\left(\frac{k \cdot L}{2}\right) \right) + \frac{a_o}{1 - \left(\frac{k \cdot L}{\pi}\right)^2} \cdot \cos\left(\frac{\pi \cdot x}{L}\right) \quad (2.6.3b)$$

$$a = \frac{M_\alpha \cdot T}{i_e \cdot \phi_2(k)} \quad (2.6.3c)$$

$$\begin{aligned} \frac{N_e}{4 \cdot L} \cdot \phi_1(k) \cdot a^2 - a \cdot \phi_2(k) \cdot \left(\frac{2 \cdot L \cdot a_o \cdot a}{\pi \cdot \left(1 - \left(\frac{k \cdot L}{\pi}\right)^2\right)^2} - \frac{N_\alpha \cdot I_e}{M_\alpha} \right) + I \cdot k^2 \\ + \frac{\pi^2 \cdot a_o^2}{4 \cdot L} \cdot \left(\frac{1}{\left(1 - \left(\frac{k \cdot L}{\pi}\right)^2\right)} - 1 \right) = 0 \end{aligned} \quad (2.6.3d)$$

This equation has been numerically solved in [Cabal and Ross, 2002]. However the complexity of this equation did not allow to find a criterion of stability for the composite beams. Instead of using (2.6.3a) as the beam's initial shape, we use the polynomial function given in (2.6.4a). Hence the equilibrium is described by (2.6.4b).

$$w_o(x) = a_o \cdot \left(1 - \left(\frac{2 \cdot x}{L} \right)^2 \right) \quad (2.6.4a)$$

$$\frac{N_e}{4 \cdot L} \cdot \phi_1(k) \cdot a^2 - \frac{N_\alpha \cdot I_e}{m_\alpha} \cdot \phi_2(k) \cdot a + I_e \cdot k^2 - \frac{8 \cdot N_e}{3 \cdot L^2} \cdot a_o^2 - \frac{8 \cdot N_\alpha \cdot I_e}{M_\alpha \cdot L^2} \cdot a_o = 0 \quad (2.6.4b)$$

The equation for initially curved beams is then the same as for initially-stressed beams if F_o and M_o are defined by (2.6.5a) and (2.6.5b). Whatever the sign of the initial curvature, initially-curved beams behave as if a compressive stress was applied to them. Fig.2.6.1a shows the equivalent residual stress in the layers of a bimetallic beam as a function of the initial curvature. The thicker the beam, the more compressive the stress in the bimetallic beam. Fig.2.6.1b-d represent the equilibrium path of curved beams for various values of the normalized deflection a_o/t .

$$F_o = -\frac{8 \cdot N_e}{3 \cdot L^2} \cdot a_o^2 \quad (2.6.5a)$$

$$M_o = \frac{8 \cdot I_e}{L^2} \cdot a_o \quad (2.6.5b)$$

Thus the bistability criterion of an initially-curved beam is (2.6.6).

$$\frac{8 \cdot N_e}{3 \cdot L^2} \cdot a_o^2 - \frac{8 \cdot N_\alpha \cdot I_e}{M_\alpha \cdot L^2} \cdot a_o \geq I_e \cdot \frac{\pi^2}{L^2} \quad (2.6.6)$$

If we develop this criterion for bimetallic beams with the neutral axis at the interface between both layers, the equation becomes (2.6.7).

$$\frac{8.(\sqrt{E_2} + \sqrt{E_1})^2}{t^2 \cdot \sqrt{E_1 \cdot E_2}} \cdot a_o^2 + \frac{2.(\sqrt{E_2} \cdot \alpha_2 + \sqrt{E_1} \cdot \alpha_1)}{t \cdot \sqrt{E_1} \cdot (\alpha_2 - \alpha_1)} \cdot a_o \geq \pi^2 \quad (2.6.7)$$

In Fig.2.6.1f, we compare the occurrence of the bistability and the snap and snap-back temperatures predicted by the previous model, by the previous model with the assumption that $n_a=0$, and by Timoshenko's model. This shows that Timoshenko's model cannot be used to predict the temperature of an axially-restrained beam whose mean thermal expansion is not negligible. However, if it is possible to create a clamp that can move to balance the mean thermal dilatation, as assumed by Timoshenko, its model gives good accuracy with the current model. In order to find its criterion of bistability, [Timoshenko, 1925] neglected the influence of the mean thermal expansion on the instability of composite beams, and assumed the same Young modulus for both materials. In that case, the criterion of bistability only depends on the ratio of the beam's thickness over its deflexion (2.6.8a). With the first assumption, (2.6.7) becomes (2.6.8b) and by assuming that the bimetallic beam is made of materials with very different coefficients of thermal expansion. In that case the solution of the polynomial (2.6.7) tends towards the value (2.8c).

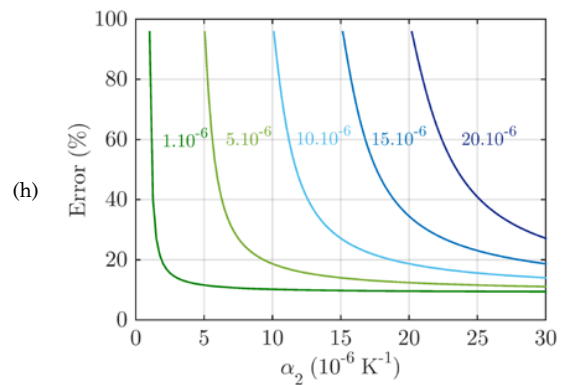
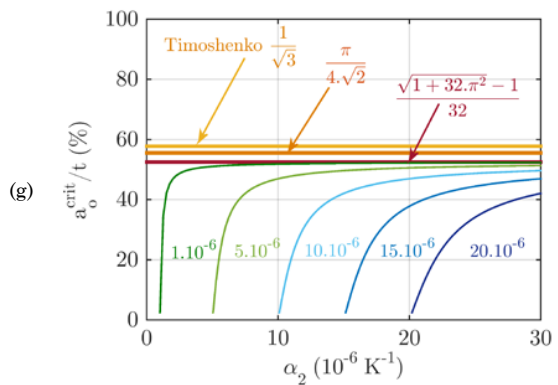
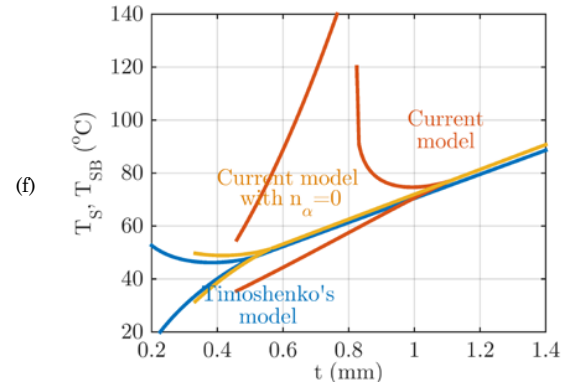
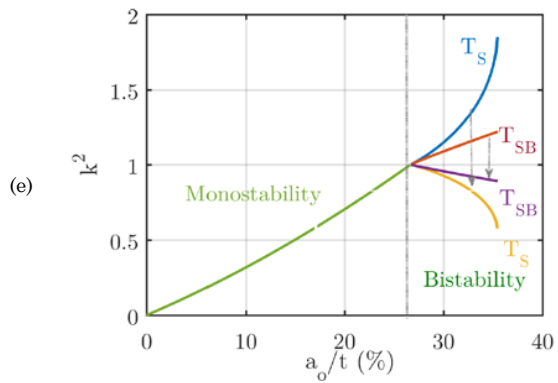
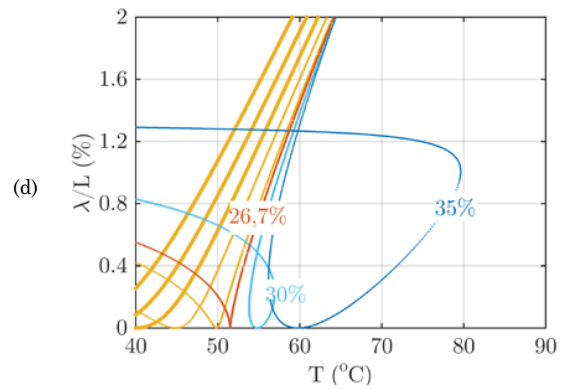
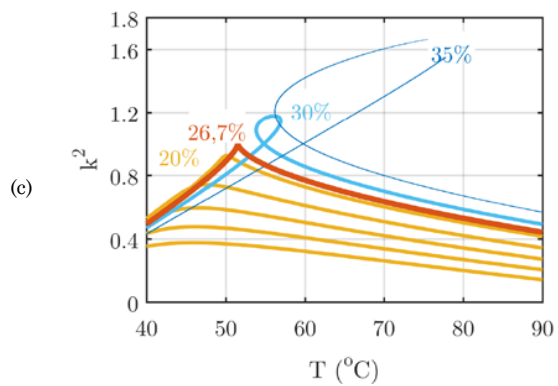
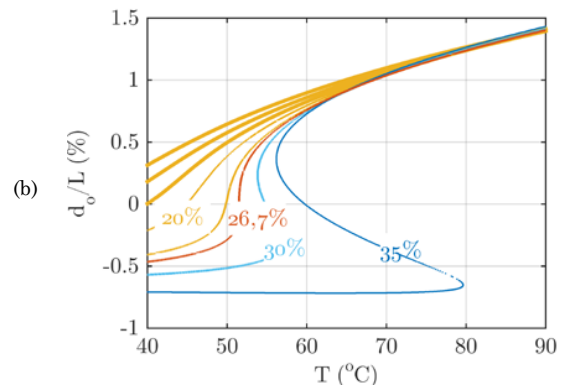
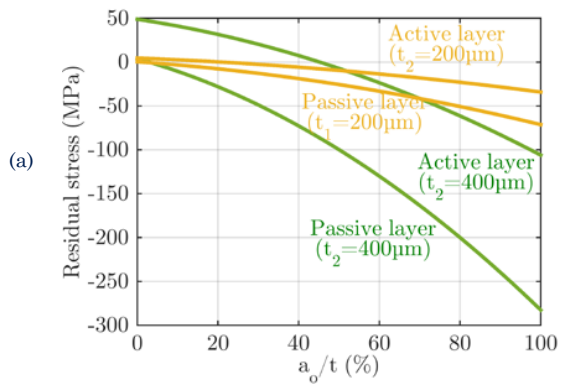
$$\frac{a_o}{t} \geq \frac{1}{\sqrt{3}} \approx 0.577 \dots \quad (2.6.8a)$$

$$\frac{32 \cdot a_o^2}{t^2} + \frac{2 \cdot (\alpha_2 + \alpha_1)}{t \cdot (\alpha_2 - \alpha_1)} \cdot a_o \geq \pi^2 \quad (2.6.8b)$$

$$\frac{a_o}{t} \geq \frac{\sqrt{1 + 32 \cdot \pi} - 1}{32} \approx 0.525 \dots \quad (2.6.8c)$$

Finally, Fig.2.6.1g gives the critical value of initial deflection associated with the occurrence of the bistability as a function of the coefficient of thermal expansion (CTE) of the active layer, and for various CTE of the passive layer. This figure logically shows that for bimetallic beams with a small CTE mismatch, the bistability is observed for small values of the initial deflection. It also shows that for such beams Timoshenko's model cannot be applied, since the error made is important (Fig.2.6.1h). As shown by Orthwein, small variations of the initial curvatures can result in large variations of the beam's thermal hysteresis.

Figure 2.6.1. *a. Equivalence between initial curvature and residual stress. b-c. Equilibrium path for various values of initial deflection. d. Evolution of the critical charges of the beam as a function of its initial curvature. e. Critical thrust of the beam against initial curvature. f. Snap and snap-back temperatures according to Timoshenko's model and the current model, for an initial curvature of 300 μm . g. Comparison of the criteria of bistability of both models. h. Relative error of Timoshenko's model.*



2.7 Curvature and initial stress

Given the previous equations, the criterion of bistability of beams having an initial curvature and an initial residual stress depends on the sum of the forces N_o associated to both imperfections (2.7.1). The equation of equilibrium thus stays unchanged (3.21).

$$N_o = \frac{N_\alpha}{N_\alpha} \cdot \left(\frac{8 \cdot I_e \cdot a_o}{L^2} + M_o \right) + \left(\frac{8 \cdot N_e}{3 \cdot L} \cdot a_o^2 - F_o \right) \geq I_e \cdot \frac{\pi^2}{L^2} \quad (2.7.1)$$

2.8 Influence of the architecture

In the previous equations, we did not take into account the fact that the beam must be in contact with the hot source until it snaps, and in contact with the cold source until it snaps back. In order to model the influence of the architecture and to see how it can impact the properties of the bistable beams, we study the behavior of the system represented in Fig.2.8.1. The height of the cavity measured from the beam's clamp to the bottom of the cold source is d_{top} , and d_{bot} from the clamp to the top of the hot source. Given that the beam has a thickness t , the dimensions to be considered are the beam's center deflection d_o and the $d_{top-t+z_o}$ and d_{bot-z_o} . The minimal conditions on these dimensions to observe the working of the device are given by (2.8.1a) and (2.8.1b) (Fig.2.8.1a).

$$d_o(T_{SB}) \geq d_{top} + t - z_o = d_{top}^{max} \quad (2.8.1a)$$

$$d_o(T_S) \leq d_{bot} - z_o = d_{bot}^{max} \quad (2.8.1b)$$

We can assume that the contacts between the beam and the two heat sources are punctual. In that case, by constraining the beam, the heat sources create a force F_{top} (or F_{bot}) on the beam's middle: the equilibrium equation of the beam in contact with the top surface thus becomes (2.8.2).

$$\frac{m_b}{L} \cdot w_{,tt}^2 + \left(N_\alpha \cdot T - N_e \cdot \frac{\lambda}{L} - F_o \right) \cdot w_{,xx} + I_e \cdot w_{,xxxx} + F_{top} \cdot \delta(x) = 0 \quad (2.8.2)$$

And the boundary conditions are given by (2.8.3).

$$I_e \cdot w_{,xx} \left(\frac{L}{2} \right) = M_o + \frac{F_{top} \cdot L}{2} - M_\alpha \cdot T \quad (2.8.3a)$$

$$I_e \cdot w_{,xx} \left(-\frac{L}{2} \right) = M_o + \frac{F_{top} \cdot L}{2} - M_\alpha \cdot T \quad (2.8.3b)$$

Following the same approach as in Section 2.3, the equilibrium equation (2.8.2) can be rewritten into (2.8.4).

$$F_{top} = \frac{2 \cdot M_\alpha}{N_\alpha \cdot L} \cdot \left(\frac{N_e}{4 \cdot L} \cdot \phi_1(k) \cdot a^2 - N_\alpha \cdot (T - T_o) + I_e \cdot k^2 - N_o \right) \quad (2.8.4)$$

During the heating and cooling phases, the evolution of F_{top} can be plotted as a function of the temperature by using the fact that the beam's maximal deflection is constant. During heating, a must be replaced by (2.8.5a), and by (2.8.5b) during cooling.

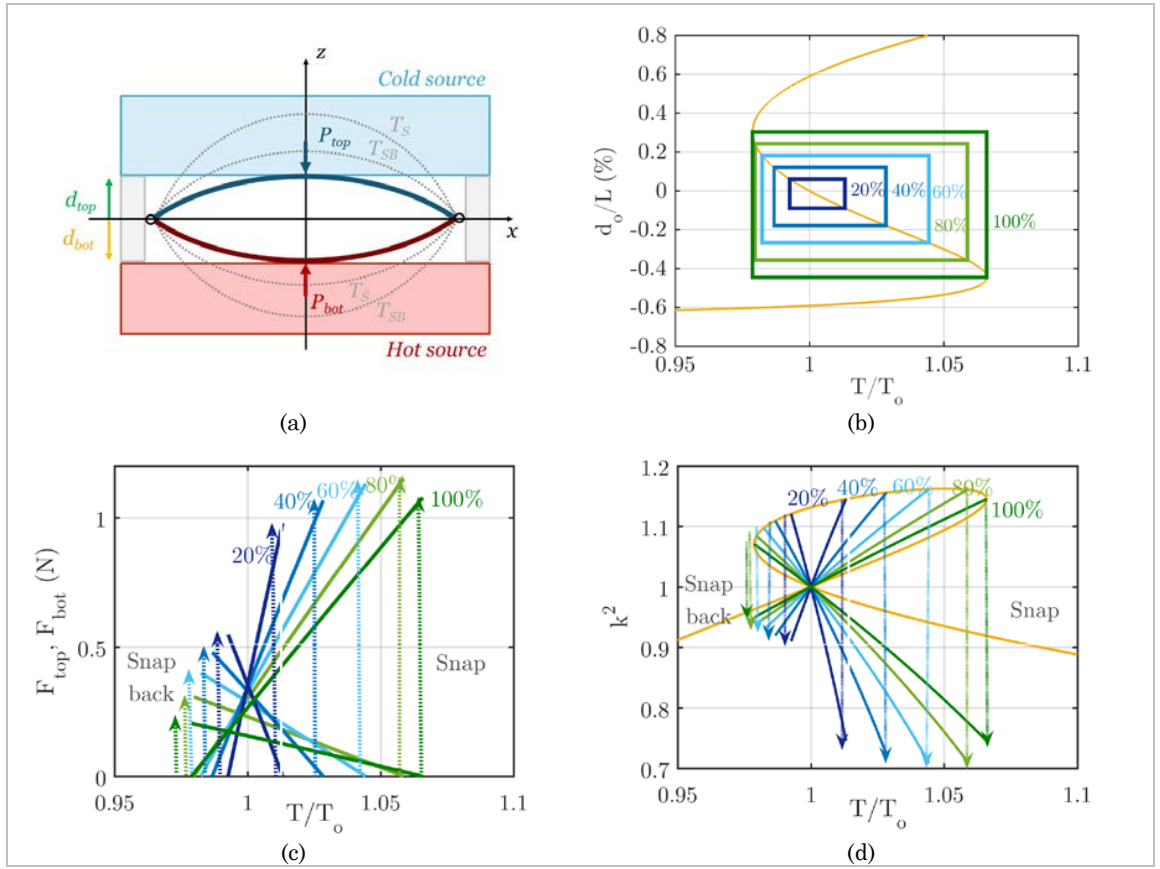


Figure 2.8.1. *a. Schematics of the beam in the cavity. b. Comparison between the thermal hysteresis of a free beam and the thermal hysteresis of a beam in a cavity, for various ratios of the cavity's thickness-to-deflexion. c. Evolution of the forces developed by the cavity on the beam. d. Evolution of the clamp thrust developed by the beam.*

$$a_{bot} = \frac{d_{bot} - z_o}{1 - \cos\left(\frac{k \cdot L}{2}\right)} \quad (2.8.5a)$$

$$a_{top} = \frac{d_{top} + t - z_o}{1 - \cos\left(\frac{k \cdot L}{2}\right)} \quad (2.8.5b)$$

The beam thus snaps and snaps back when the load F_{top} vanishes (2.8.6a). The snap back temperature is then given by (2.8.6b) and the snap temperature by (2.8.6c).

$$\frac{N_e}{4 \cdot L} \cdot \phi_1(k_{top}) \cdot a_{top}^2 - N_\alpha \cdot T + I_e \cdot k_{top}^2 - N_o = 0 \quad (2.8.6a)$$

$$T_{SB} = T_o + \frac{1}{M_\alpha} \cdot \frac{I_e \cdot k_{top}^2 \cdot \cos\left(\frac{k_{top} \cdot L}{2}\right) \cdot (d_{top} - t + z_o)}{1 - \cos\left(\frac{k_{top} \cdot L}{2}\right)} \quad (2.8.6b)$$

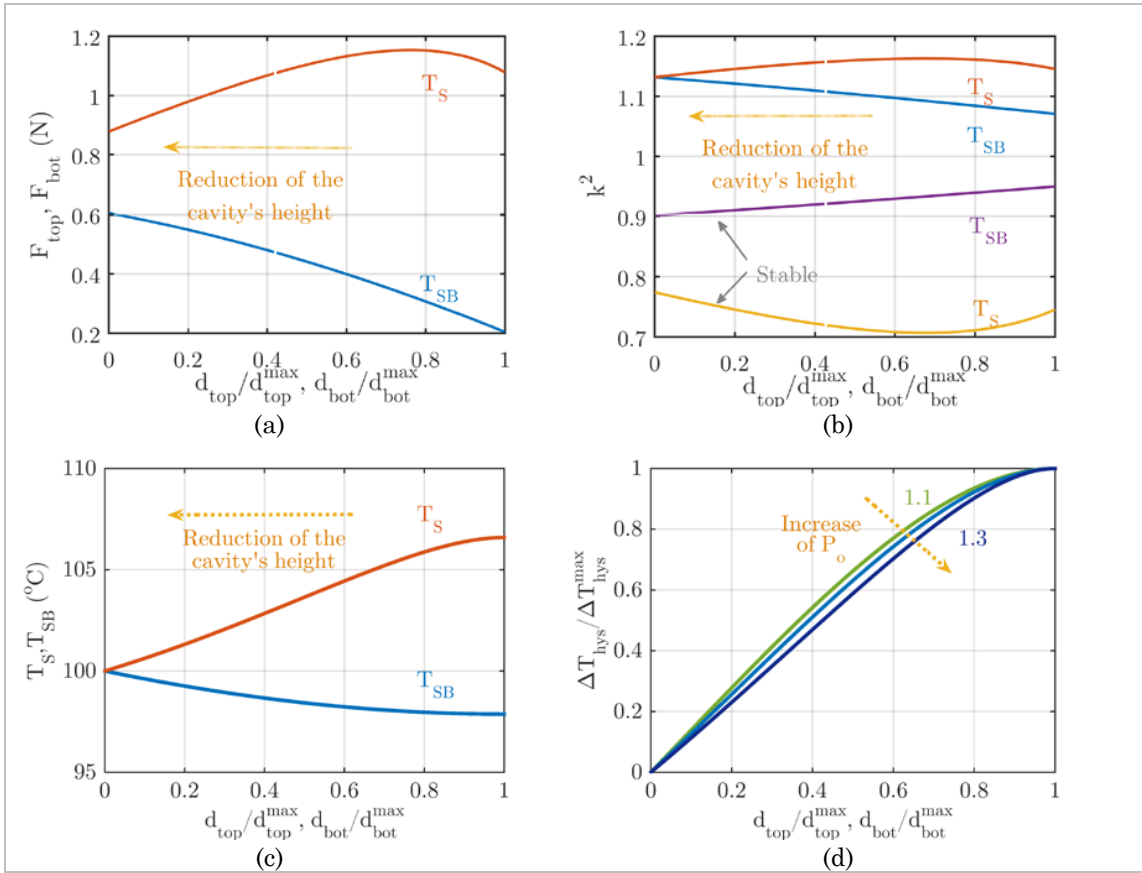


Figure 2.8.2. a. Scheme of the beam in the cavity. b. Comparison between the thermal hysteresis of a free beam and the thermal hysteresis of a beam in a cavity, for various ratios of the cavity's thickness-to-deflexion. C. Evolution of the forces developed by the cavity on the beam. d. Evolution of the clamp thrust as as function of temperature.

$$T_S = T_o + \frac{1}{M_\alpha} \cdot \frac{I_e \cdot k_{bot}^2 \cdot \cos\left(\frac{k_{bot} \cdot L}{2}\right) \cdot (d_{bot} - z_o)}{1 - \cos\left(\frac{k_{bot} \cdot L}{2}\right)} \quad (2.8.6c)$$

Fig.2.8.1b. represents the equilibrium paths of an Al-Invar beam ($L = 40$ mm, $t = 400 + 400$ μ m) for various values of the cavity's thickness and for $N_o/N_{Euler}=1.28$. Here 100% represents the ratio between the cavity's height and the maximal allowed cavity's height given by (2.8.1). This figure clearly shows that, by reducing the cavity's thickness, the thermal hysteresis is modified and decreases. This phenomenon was numerically shown in [Ravindran et al, 2014] but without physical explanations. Fig. 2.8.1c represents the evolution of the force developed by the architecture on the beam to reduce its curvature. Typical values of the force are around 1 N during the snap and 0.3 N at snap-back, in agreement with the experimental data measured on the harvester prototypes. The force is greater during the snap than at snap-back because of the asymmetry of the thermal hysteresis due to the effect of the beam's mean thermal expansion. This figure can be compared with Fig.2.8.1d representing the evolution of the axial thrust.

For the aforementioned beam, the Euler load is 112 N. This shows that it can be more interesting to attempt to harvest the strain energy associated to the clamp's thrust instead of harvesting the strain energy associated to the forces F_{bot} and F_{top} . To quantify the influence of the cavity's height reduction on the properties of the bistable beam, the forces developed by the cavity on the beam, the clamp's thrust and the thermal hysteresis are represented as functions of the cavity's relative height in Fig.2.8.2. This figure shows that the reduction of the cavity's thickness is accompanied by a reduction of all the parameters of the composite beam, due to the impact of the architecture on the bistability of the beam. Fig.2.8.2d shows a quasi-linear proportionality relation between the decrease of the relative hysteresis and the reduction of the cavity's height.

3 Performances of the harvester using composite beams

3.1 Evolution of the strain energy of the composite beams

Studying the evolution of the beam's strain energy along an equilibrium trajectory is a good solution to deeply understand the origins and the signification of the bistability. The expression of the beam's potential energy can be found according to two methods. Since the equilibrium positions are the extrema of the strain energy and the equilibrium equation its first derivative, the integration of this last equation enables to find the strain energy function. Yet the best solution is to integrate the local expression of the strain energy on the whole beam's volume.

$$w_M = \frac{1}{2} \cdot E \cdot S_{xx}^2 + (\mathcal{J}_o - E \cdot \alpha \cdot T) \cdot S_{xx} \quad (3.1.1)$$

When this last expression is developed with the help of the axial strain expression and integrated, the strain energy can be written as the sum of the stretching energy, the bending energy, and the energies due to the residual stress and the thermal stress, as defined by (3.1.2a) to (3.1.2d).

$$\mathcal{W}_M = \mathcal{W} + \mathcal{W}_o - \mathcal{W}_{th} \quad (3.1.2a)$$

$$\mathcal{W} = \frac{N_e}{2 \cdot L} \cdot \lambda^2 + \frac{I_e}{2} \cdot \left(\int_{-\frac{L}{2}}^{\frac{L}{2}} w_{,xx}^2 \cdot dx \right) \quad (3.1.2b)$$

$$\mathcal{W}_o = F_o \cdot \lambda - M_o \cdot \left(\int_{-\frac{L}{2}}^{\frac{L}{2}} w_{,xx} \cdot dx \right) \quad (3.1.2c)$$

$$\mathcal{W}_{th} = N_\alpha \cdot T \cdot \lambda - M_\alpha \cdot T \cdot \left(\int_{-\frac{L}{2}}^{\frac{L}{2}} w_{,xx} \cdot dx \right) \quad (3.1.2d)$$

Knowing that the solutions of the non-linear equations are the harmonic functions, it is interesting to study how the energy evolves for the cosine functions that verify the boundary equations (2.3.3c). In that case, the energy can be written under the form (3.1.3).

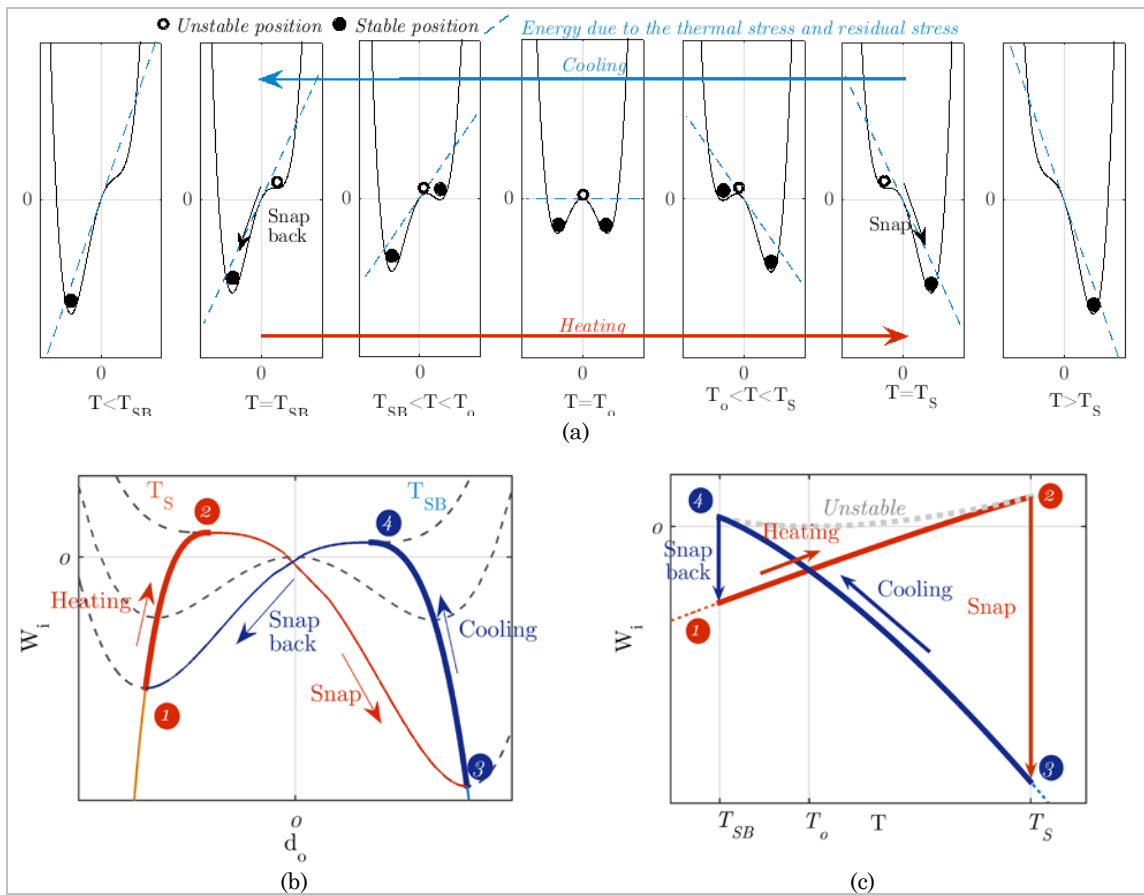


Figure 3.1.1. a. Evolution of the strain energy of a bistable beam (in black) and part of the energy due to the thermal stress in blue. b. Thermodynamic cycle of the heat engine in the (d_o, W_M) diagram. c. Thermodynamic cycle of the heat engine in the (T, W_M) diagram.

$$W_M = \frac{N_e}{2.L} \cdot \lambda^2 + I_e \left(k^2 - 2 \cdot \frac{k^3 \cdot \sin(k.L)}{\varphi_1(k)} \right) \cdot \lambda + (F_o - N_\alpha \cdot T) \cdot \lambda \quad (3.1.3)$$

The shape of the curve of the beam's free work is difficult to guess with this equation. However it must be noted that λ is a quadratic function of the beam's amplitude. Therefore the beam's free work is a fourth-order polynomial of the strain energy. According to the sign of the function of k between the brackets, the strain energy will evolve from a double potential well to a single potential well. The residual stress force and mean thermal stress act as external fields that desymmetrize the shape of the free work. Fig.3.1.1a shows the action of these fields for a bistable beam. It shows that when the external field vanishes at T_o , three equilibrium positions coexist, the central one being unstable and playing the role of a potential barrier. When the external field is non-null, one of the stable positions becomes a global stable position (or minimum minimorum) and the other one a local stable position. However, the beam cannot switch from one position to the other because of the potential barrier. When either the snap temperature or snap-back temperature is reached, the local stable position and the unstable position merge to form a limit point (or inflexion point). The beam thus slides along the potential well to reach the unique stable position and releases its strain energy. Fig.3.1.1b then represents the evolution of the beam's strain energy as a function of its deflection, and Fig.3.1.1c

represents the strain energy as a function of temperature. The asymmetry of the butterfly shape is due to the effect of the mean thermal expansion which increases the kinetic energy release during the beam snap and reduces it during snap-back.

3.2 Evolution of the entropy of the composite beams

The local expression of the entropy being given by (3.2.1a), we can deduce the expression of the beam's entropy by integrating (3.2.1a) on the whole beam's volume. The result is given in (3.2.1b).

$$\sigma = \frac{c_v}{T + \theta_{ref}} + E \cdot \alpha \cdot S_{xx} \quad (3.2.1a)$$

$$\Sigma = \left(4 \cdot I_e \cdot \frac{k^3 \cdot \sin(k \cdot L)}{k^2 \cdot L - k \cdot \sin(k \cdot L)} + N_\alpha \cdot (T - T_o) \right) \cdot \frac{\lambda}{(T - T_o)} + C_v \cdot \ln \left(\frac{T + \theta_{ref}}{T_o} \right) \quad (3.2.1b)$$

The other way to find the expression of the beam's entropy is to write the differential of the beam's Helmholtz free energy. Given (3.1.8), the Helmholtz free energy is a function of the privileged variables λ and T .

$$d\mathcal{F} = -\Sigma \cdot dT + (N - N_o) \cdot d\lambda \quad (3.2.2)$$

This last equation shows the beam entropy and force N as the first partial derivatives of the Helmholtz free energy. They can be written in function of T and λ .

$$dN = N_{,T}^\lambda \cdot dT + N_{,\lambda}^T \cdot d\lambda \quad (3.2.3a)$$

$$d\Sigma = \Sigma_{,T}^\lambda \cdot dT + \Sigma_{,\lambda}^T \cdot d\lambda \quad (3.2.3b)$$

Applying the Schwartz theorem on the partial derivatives of the beam's free energy and strain energy is a first step needed to find the entropy's expression. Equation (3.2.3a) can hence be interpreted as a Maxwell relation linking $\Sigma_{,\lambda}^T$ the partial derivative of the entropy with respect to λ , to $N_{,T}^\lambda$ the partial derivative of the force N with respect to the temperature.

$$\Sigma_{,\lambda}^T = -N_{,T}^\lambda \quad (3.2.5a)$$

$$\Sigma_{,k}^T = \lambda_{,T}^k \cdot N_{,k}^T - \lambda_{,k}^T \cdot N_{,T}^k \quad (3.2.5b)$$

Knowing the expression of the coefficients ($\lambda_{,k}^T$, $\lambda_{,T}^k$, $N_{,k}^T$, $N_{,T}^k$, $\Sigma_{,T}^k$) allows deducing the expression of each coefficient. The first four coefficients can be easily found, by differentiating the expressions of the force N and beam length excess at the equilibrium.

$$N_{,T}^k = \frac{n_e}{L} \cdot \lambda_{,T}^k - N_\alpha \quad (3.2.6a)$$

$$N_{,k}^T = \frac{n_e}{L} \cdot \lambda_{,k}^T + 2 \cdot I_e \cdot k \quad (3.2.6b)$$

$$\lambda_{,T}^k = 2 \cdot \frac{\lambda}{T} \quad (3.2.6c)$$

$$\lambda_{,k}^T = \frac{1}{4} \cdot \left(\varphi_1' - 2 \cdot \varphi_1 \cdot \frac{\varphi_2'}{\varphi_2} \right) \cdot a^2 \quad (3.2.6d)$$

In particular, the dependance of the entropy with respect to k is found using (3.2.5b). By integrating (3.2.7), we find the expression of the beam's entropy given in

$$\Sigma_{,k}^T = 2 \cdot I_e \cdot k \cdot \lambda_{,T}^k + N_\alpha \cdot \lambda_{,k}^T \quad (3.2.7)$$

The advantage of this last method is that it enables to describe the beam as a classical thermodynamic body, whose constitutive equations are given by (3.2.8a) and (3.2.8b). In these matrices, the diagonal terms represent direct effects whereas antidiagonal terms represent coupling terms.

$$d \begin{pmatrix} \Sigma \\ N \end{pmatrix} = \begin{pmatrix} \frac{C_\lambda}{T + \theta_{ref}} & -N_{,T}^\lambda \\ N_{,T}^\lambda & N_{,\lambda}^T \end{pmatrix} \cdot d \begin{pmatrix} T \\ \lambda \end{pmatrix} \quad (3.2.8a)$$

$$d \begin{pmatrix} \Sigma \\ N \end{pmatrix} = \begin{pmatrix} \frac{C_k}{T + \theta_{ref}} & \lambda_{,T}^k \cdot N_{,k}^T - \lambda_{,k}^T \cdot N_{,T}^k \\ N_{,T}^k & N_{,k}^T \end{pmatrix} \cdot d \begin{pmatrix} T \\ k \end{pmatrix} \quad (3.2.8b)$$

We can especially express the heat capacitance of the beam as

$$C_k = C_v + \left(4 \cdot I_e \cdot \frac{k^3 \cdot \sin(k \cdot L)}{k^2 \cdot L - k \cdot \sin(k \cdot L)} + 2 \cdot N_\alpha \cdot (T - T_o) \right) \cdot \frac{\lambda \cdot (T + \theta_{ref})}{(T - T_o)^2} \quad (3.2.9a)$$

$$C_\lambda = C_v + \left(4 \cdot I_e \cdot \frac{k^3 \cdot \sin(k \cdot L)}{k^2 \cdot L - k \cdot \sin(k \cdot L)} - 8 \cdot I_e \cdot k \cdot \frac{\lambda}{\lambda_{,k}^T} \right) \cdot \frac{\lambda \cdot (T + \theta_{ref})}{(T - T_o)^2} \quad (3.2.9b)$$

What is interesting for us it to plot the evolution of the beam's entropy and the derivative of the entropy as a function of the temperature (Fig.3.2.1a). These two figures show that the beam's entropy presents two discontinuities at T_S and T_{SB} . The discontinuities are also visible on the plot of the beam's heat capacitance that becomes infinite for these temperatures. In fact these discontinuities correspond to the thermal hysteresis observed on the evolution of N . N and Σ being the first derivatives of the Helmholtz free energy, these discontinuities reveal that the thermal snap-through corresponds to a first-order phase change, which stable phase is the unsnapped state of the beam, and the paraphase is the snapped beam [Uzunov, 1993], [Callen, 1960]. The existence of this hysteresis on the (T, Σ) diagram is particularly interesting since the area enclosed by the loop corresponds to a work. It shows that if the unsnapped beam is heated until it snaps, then cools down until it snaps back, the loop is followed counter-clockwise. The area is then negative, meaning that the beam behaves like a heat engine and produces work from two heat sources. The different steps of the thermodynamic cycle of the bimetallic strip heat engine are presented in Fig.3.2.1c. The work supplied by our heat engine can then be compared to the work produced by a Carnot engine in the same conditions (Fig.3.2.1.b). By comparing the two areas, it can be observed that the efficiency of the heat engine is reduced, which can be attributed to the weak thermo-mechanical coupling effect inside solid materials.

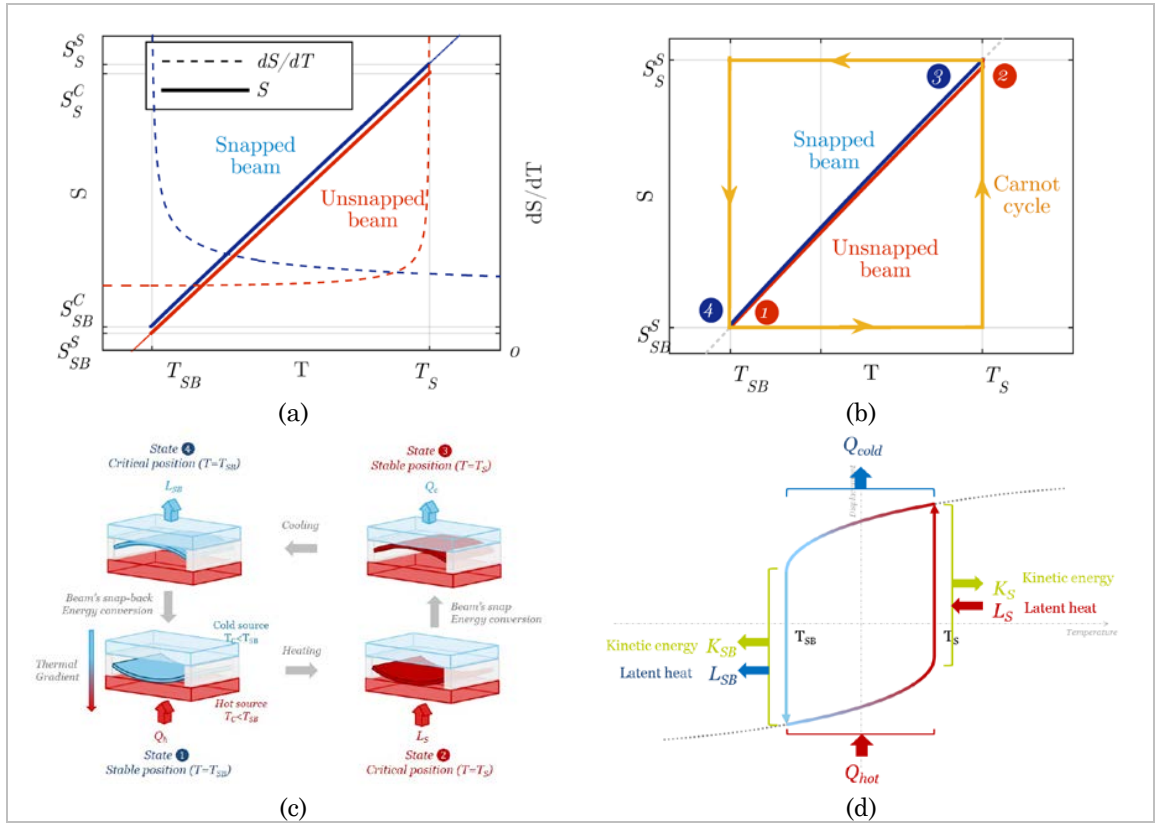


Figure 3.2.1. *a.* Evolution of the beam's entropy as a function of temperature. *b.* Thermodynamic cycle of the heat engine and comparison with the Carnot cycle. *c.* Illustration of the four phases of the heat engine's cycle. *d.* Details of the energetic transfers inside the harvester.

Two last features associated to the first order transition must be cleared. As with other first-order transitions, the thermal snap-through is characterized by a Curie temperature at which the bistability disappears. This temperature is none other than the temperature given by the bistability criterion.

$$T_C = \frac{I_e}{N_\alpha} \cdot \frac{\pi^2}{L^2} + \frac{F_0}{N_\alpha} \quad (3.2.11)$$

As the beam must increase its entropy to snap and to decrease it to snap back, an extra amount of energy must be supplied to the beam at T_S and rejected at T_{SB} . These two latent heats are proportional to the entropy's discontinuities and are given by (3.2.12).

$$L_S = T_S \cdot \Delta S(T_S) \quad (3.2.12)$$

3.3 Intrinsic mechanical performances of the harvester

Now that we have established all the equations necessary to describe the bimetallic strip heat engine, we are able to evaluate its performances. Taking the example of the Al-Invar

beam, we first evaluate the latent heat associated to the beam's snap and snap-back (Fig.3.3.1a) and the kinetic energy released in the same time (Fig.3.3.1b). In the configuration where the kinetic energy is transferred to a piezoelectric transducer, the sum of these two quantities represents the maximal thermo-mechanical efficiency of the harvester. For a 3K-hysteresis beam, the available mechanical energy is of 115 μJ whereas for a 20 K-hysteresis beam it is 1.52 mJ.

$$\mathcal{W}_M = \mathcal{K}(T_S) + \mathcal{K}(T_{SB}) \quad (3.3.1)$$

Another important parameter of the heat engine is its thermo-mechanical efficiency. This efficiency is obtained by dividing the total amount of energy by sum of Q_{hot} the heat provided by the hot source to heat the bimetal plus the latent heat associated to the beam's snap (3.3.1). This efficiency can be compared to the Carnot efficiency representing the maximal theoretical efficiency of a heat engine. The formula of this relative efficiency is given by (3.3.2b).

$$\eta_{TM}^{abs} = \frac{\mathcal{K}(T_S) + \mathcal{K}(T_{SB})}{Q_{hot} + \mathcal{L}_h(T_S)} \quad (3.3.2a)$$

$$\eta_{TM}^C = \frac{T_S + \theta_{ref}}{T_S - T_{SB}} \cdot \eta_{TM}^{abs} \quad (3.3.2b)$$

Fig.3.3.1c shows the evolution of the thermal efficiency of the harvester as a function of the thermal hysteresis of the bistable beams. This figure must be compared with Fig.3.3.1d showing the dependence of the Carnot efficiency on the thermal hysteresis. The thermal efficiency is better for highly unstable beams than for beams with weak hystereses, but the Carnot efficiency rapidly falls under one percent when the thermal hysteresis widens. This means that large thermal hysteresis enables to harvest more energy but the transformation followed by the beam in these conditions is less reversible. As an example, the thermal efficiency of a 3K-hysteresis beam is of 0.01% and its relative efficiency is 1.2%. In the same time, the efficiency of a 20K-hysteresis beam is 0.02% for a Carnot efficiency of 0.38%.

We can now study the performances of nine different bimetals in order to evaluate the impact of the physical properties of materials. These bimetals are made of a passive metallic layer with a low coefficient of thermal expansion (Invar, tungsten, titanium) and an active metallic layer highly sensitive to temperature variations. (copper, brass, aluminum). The bimetals are designed to have thermal hystereses of 1 K, 2 K and 3 K. The choice of these low values of thermal hysteresis makes sense when the aim of these heat engines is to harvest low-grade heat energy: as explained in the first chapter, small hystereses allow to harvest heat in a wider range of temperatures and potentially to reach higher switching frequencies, in order to increase the power generated by the bimetals. The nine bimetals all have the same dimensions (20x2x0.5 mm³). The thickness ratio of both materials is chosen so that the neutral axis is located at the limit between the metallic layers, and the residual stress asymmetry is adjusted so that the hystereses be centered around 75°C (348 K). Tab.3.3.1 reports the bimetals' main properties: the bending stiffness i_e serves to calculate the buckling load (6), whereas the ratio of the thermal stress coefficients describes the bimetal's thermal behavior: a bimetal with a high value of m_α/n_α is more sensitive to the temperature and will bend easily. The evolution of m_α is slightly different and is higher for tungsten-based bimetals than for Invar-based bimetals because of the stiffness of tungsten: the active layer can thus be thicker than the passive tungsten layer, then causing an increase of the thermal asymmetry.

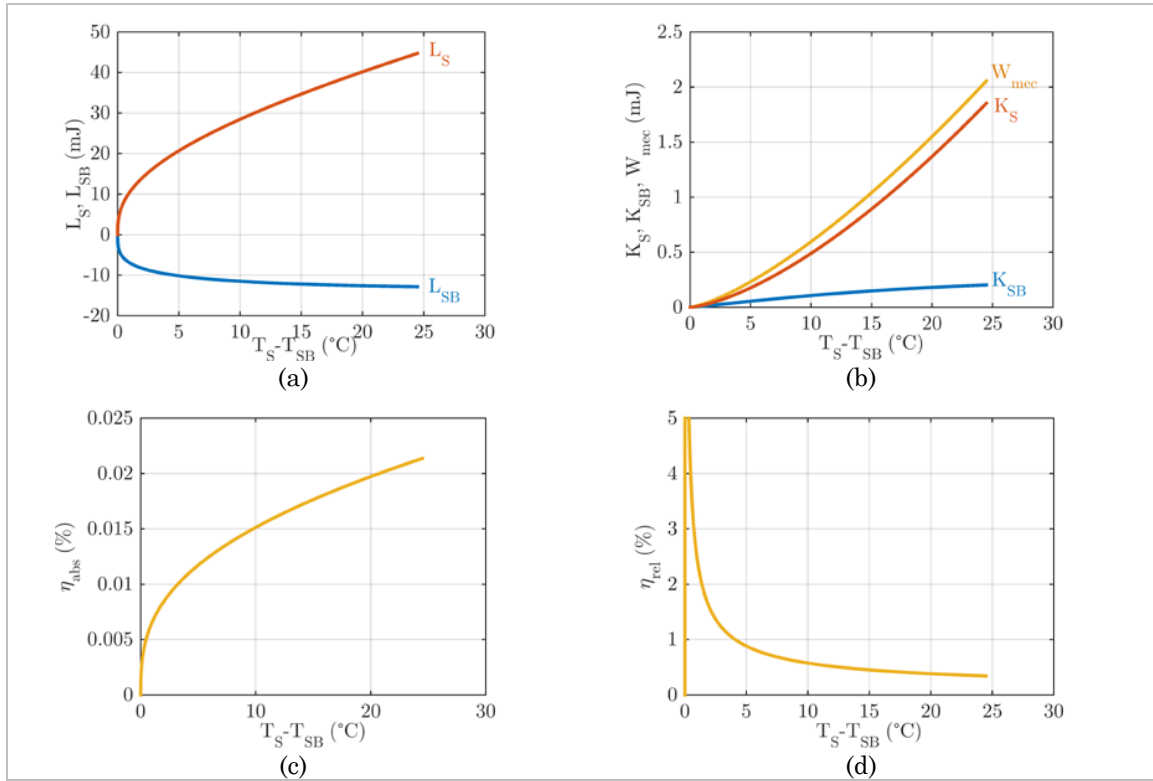


Figure 3.3.1. *a. Evolution of the beam's entropy as a function of temperature. b, c. Details of the transition at T_S and T_{SB} . d. Evolution of the heat capacitance of the beam as a function of temperature.*

Fig.3.3.2b reports the residual stress measured for the 2 K-hysteresis beams and calculated by using P_0 and the snap temperature. Given the high sensitivity of the bimetals to residual stress, the stress levels for 1 K and 3 K are almost equal. This figure shows that the residual stress is more important for Al-W bimetals since they have the greatest value of M_α . To obtain hysteresis around 75°C, the asymmetry of the residual stress must be more important for these bimetals.

Fig.3.3.2c shows that the energy density is directly correlated to the thermal stress asymmetry m_α : this density is highest for W/Al bimetals. By normalizing the surface density by the total deflection, we obtain a volume energy density independent of the size of the beam if the beam is proportionally scaled down. We can compare the values of surface densities with those calculated with the data reported in [Ravindran et al, 2014] and [Puscasu et al, 2014]. [Ravindran et al, 2014] gave a simulated density of around 83 $\mu\text{J}\cdot\text{cm}^{-2}$ (200 μJ ; 40x6x0.28 mm³; 5 K hysteresis) while [Puscasu et al, 2014] reports experimental mechanical energy densities of around 60 $\mu\text{J}\cdot\text{cm}^{-2}$ (Invar/NC4; 36x18x0.3 mm³; 3 K hysteresis). This first comparison validates the coherence of our mode (in Section 4.4 we go further in comparing our model with experiments). Table 3.3.1 presents the Carnot efficiency of the nine bimetals

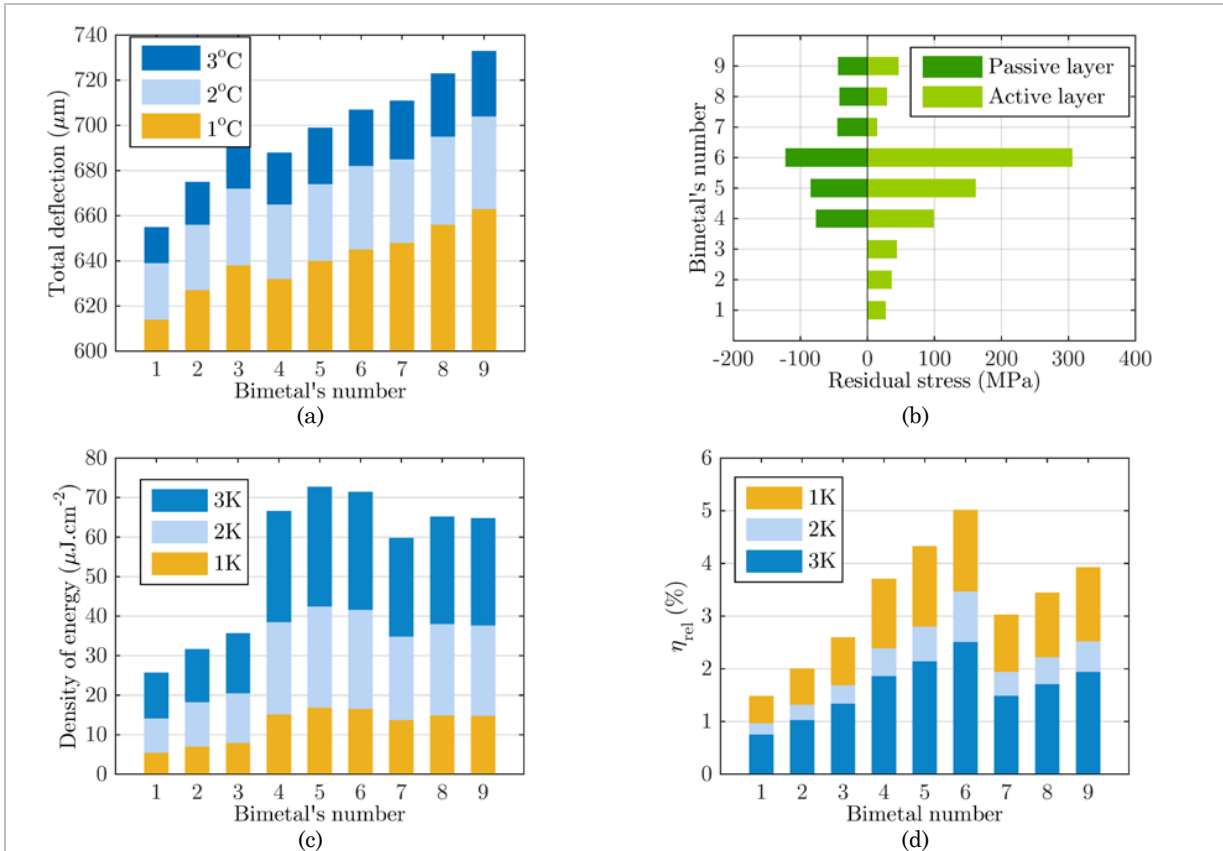


Figure 3.3.2. *a. Total deflexion during the snap of the beam. b. Residual stress in the layers of the bimetallic beams. c. Density of mechanical energy provided by the bimetals. d. Theoretical Carnot efficiency of the heat engines.*

Bimetal	Ti/Cu	Ti/CuZn	Ti/Al	W/Cu	W/CuZn	W/Al	FeNi/Cu	FeNi/CuZn	FeNi/Al
Number	1	2	3	4	5	6	7	8	9
x (%)	51/ 49	47.8/ 52.2	43.5/ 56.5	36/ 64	33.1/ 66.9	29.4/ 70.6	48.7/ 51.3	45.6/ 54.4	41.3/ 58.7
I_e ($10^{-3} \text{ N}\cdot\text{m}^2$)	2.6	2.3	1.9	4.4	3.8	3.0	2.8	2.5	2.6
N_a ($\text{N}\cdot\text{K}^{-1}$)	1.63	1.56	1.39	2.08	1.95	1.7	1.2	1.15	1.02
M_a ($10^{-5} \text{ N}\cdot\text{m}\cdot\text{K}^{-1}$)	6.32	7.55	8.00	16.6	17.3	16.4	13.7	14.1	13.5
M_a/N_a (10^{-5} m)	3.88	4.84	5.76	7.98	8.87	9.65	11.42	12.26	13.26

Table 3.3.1. *Properties of the bimetals. The bimetals at the left of the table slowly bend when temperature changes because their m_a is low. At the opposite, the bimetals at the right of the table bend faster but have a low value of n_a .*

3.4 Synthesis on the first model

In this part, we developed a first model to describe the properties of bistable composite beams that are simply supported and submitted to the effect of residual stress. By extension, we studied the case of initially-curved beams and extended the criterion of bistability demonstrated by Timoshenko who neglected the effect of the mean thermal expansion. This first model enabled us to demonstrate the first-order phase transition associated to the thermal snap-through of composite beams and to evaluate the performances of the bimetallic strip heat engines for the first time. However, we have seen that this model does not allow to simply predict the influence of each physical parameters of the beams. For this reason we propose in the next part to approximate the solution of the problem by using the Galerkin method. This second model hereunder will enable to find analytical expressions describing the performances of the heat engine and to create Figures of Merit to compare various composite beams.

4 A second model of the instability of composite beams

4.1 Ritz approximation, Galerkin method, Cardan formula

There are two way to proceed in order to obtain the simplified equilibrium equations of the simply supported beams: the first consists in looking for solutions of the non-linear Euler equation under the form of a function series verifying the linear equations, and the second to write the strain energy function associated to the solutions of the linear Euler Equation and to derivate it in order to obtain the equilibrium equation. Both methods give the same results, and we expose here the first method which is widely used for the study of the instability of mechanical structures. The static equilibrium equation of composite beams is recalled below. In order to simplify the equations, the beam is now assumed to be located between $x = 0$ and $x = L$. This assumption does not modify the problem.

$$k^2 \cdot w_{,xx} + w_{,xxxx} = 0 \quad (4.1.1a)$$

$$I_e \cdot k^2 = N_\alpha \cdot T - \frac{N_e}{2 \cdot L} \cdot \int_{-\frac{L}{2}}^{\frac{L}{2}} w_{,x}^2 \cdot dx - F_o \quad (4.1.1b)$$

$$I_e \cdot w_{,xx}(0) = I_e \cdot w_{,xx}(L) = M_o - M_\alpha \cdot T ; w(0) = w(L) = 0 \quad (4.1.1c)$$

The general solution of the Euler equation (4.1.1a) verifying the boundary conditions (4.1.1c) is a sum of the harmonic functions given by (4.1.2a). The temperature is also developed into Fourier series (4.1.2b).

$$w(x) = \sum_{n=1}^{+\infty} w_n \cdot \sin\left(n \cdot \pi \cdot \frac{x}{L}\right) \quad (4.1.2a)$$

$$T(x) = \frac{4}{\pi} \cdot \sum_{n=0}^{+\infty} \frac{T}{2 \cdot n + 1} \cdot \sin\left((2 \cdot n + 1) \cdot \pi \cdot \frac{x}{L}\right) \quad (4.1.2b)$$

Galerkin's method leads to equation (4.1.3a). When writing Euler's equation, we see that the assymetrical modes are independent of temperature and can only appear when the axial thrust equals the even multiple of the first Euler buckling load.

$$\frac{N_e \cdot \pi^2}{4 \cdot L^2} \cdot \sum_{n=1}^{+\infty} n^2 \cdot w_n^2 - N_\alpha \cdot T + I_e \cdot k^2 + F_o = 0 \quad (4.1.3a)$$

$$\left(k^2 - (2 \cdot i + 1)^2 \cdot \frac{\pi^2}{L^2} \right) \cdot w_{2 \cdot i + 1} = \frac{4}{(2 \cdot i + 1) \cdot \pi} \cdot \frac{M_\alpha \cdot T - M_o}{I_e} \quad (4.1.3b)$$

$$\left(k^2 - (2 \cdot i)^2 \cdot \frac{\pi^2}{L^2} \right) \cdot w_{2 \cdot i} = 0 \quad (4.1.3c)$$

If the study is limited to the first two buckling modes, the equations become

$$\frac{N_e \cdot \pi^2}{4 \cdot L^2} \cdot (w_1^2 + 4 \cdot w_2^2) - N_\alpha \cdot T + I_e \cdot k^2 + F_o = 0 \quad (4.1.4a)$$

$$\left(k^2 - \frac{\pi^2}{L^2} \right) \cdot w_1 = \frac{4}{\pi} \cdot \frac{M_\alpha \cdot T - M_o}{I_e} \quad (4.1.4b)$$

$$\left(k^2 - 4 \cdot \frac{\pi^2}{L^2} \right) \cdot w_2 = 0 \quad (4.1.4c)$$

In that case, as long as the second buckling mode does not appear, the equilibrium equation is given by a third-polynomial of the beam's amplitude.

$$\frac{N_e \cdot \pi^2}{4 \cdot L^2} \cdot w_1^3 + \left(I_e \cdot \frac{\pi^2}{L^2} - N_\alpha \cdot T + F_o \right) \cdot w_1 + \frac{4}{\pi} \cdot (M_o - M_\alpha \cdot T) = 0 \quad (4.1.6)$$

Following the same reasoning than before, the criterion of bistability can be deduced by noticing that for $T = T_o$, three real solutions exist if the force P_o exceeds the first Euler buckling load. In order to find the temperatures associated to the limit points, two methods can be used. First, the equilibrium equation can be derivated in order to obtain a second equation, which gives the critical value of the beam's deflection amplitude at this point, once combined with the critical equation.

$$\frac{3 \cdot N_e \cdot \pi^2}{4 \cdot L^2} \cdot w_1^2 + \left(I_e \cdot \frac{\pi^2}{L^2} - N_\alpha \cdot T + F_o \right) = 0 \quad (4.1.7)$$

The second method consists in using Cardan's formula for the resolution of third-order polynomials. This way, we directly find that the limit points are characterized by a critical amplitude verifying (4.1.8a). When the beam switches, its deflexion is finally equal to twice this critical value. The snap and snap-back temperatures are then given by the nullity of the discriminant (4.1.8c). This last equation enables to directly plot the (N_o, T) diagram of equilibrium of the composite beam showing the occurrence of the bistability, the area where the beam is unstable, and the areas where the snapped position (paraphase) is stable and where the unsnapped state is stable.

$$w_S^C = \frac{6}{\pi} \cdot \frac{M_\alpha \cdot T_S - M_o}{I_e \cdot \frac{\pi^2}{L^2} - N_\alpha \cdot T_S + F_o} ; w_{SB}^C = \frac{6}{\pi} \cdot \frac{M_\alpha \cdot T_{SB} - M_o}{I_e \cdot \frac{\pi^2}{L^2} - N_\alpha \cdot T_{SB} + F_o} \quad (4.1.8a)$$

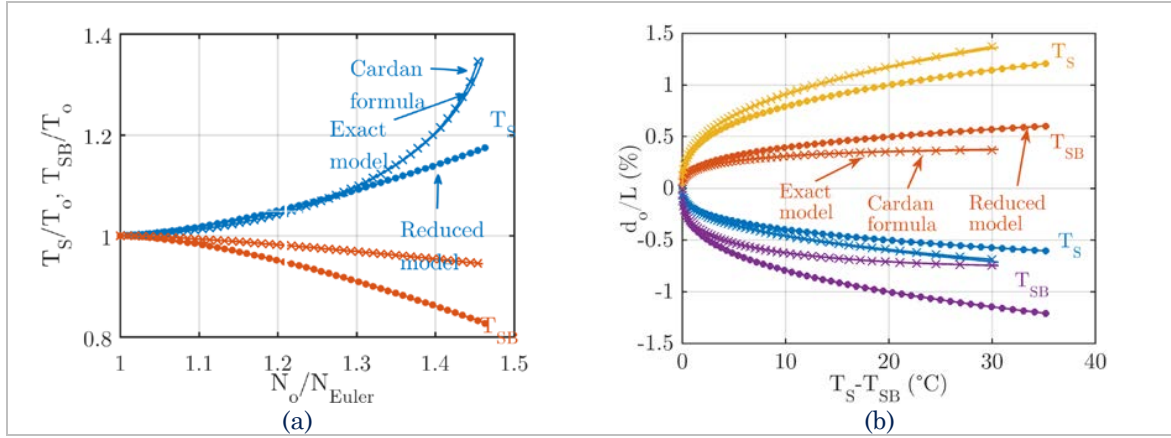


Figure 4.1.1. *a. Comparisons between the exact model, the model with Cardan's formula and the reduced model. b. Evolution of the Al-Invar beam's deflection as a function of the thermal hysteresis predicted by the three models.*

$$w_S^S = -2 \cdot w_S^C ; w_{SB}^S = -2 \cdot w_{SB}^C \quad (4.1.8b)$$

$$\Delta = 27 \cdot N_e \cdot m_\alpha^2 \cdot \left(T - \frac{M_o}{M_\alpha}\right)^2 + \left(I_e \cdot \frac{\pi^2}{L^2} - N_\alpha \cdot T + F_o\right)^3 = 0 \quad (4.1.8c)$$

This discriminant must be studied to explain when bistability occurs and to find the expression of the snap and snap-back temperatures as a function of the force P_o . By defining the parameters p and q by (4.1.9a) and (4.1.9b) and X by (4.1.9c), we find that the study of Δ is equivalent to the study of (4.1.9d).

$$p = -\frac{9 \cdot N_e \cdot M_\alpha^2}{N_\alpha^2 \cdot L^2} \quad (4.1.9a)$$

$$q = -\frac{\sqrt{27 \cdot N_e} \cdot M_\alpha}{N_\alpha \cdot L} \cdot \left(N_o - I_e \cdot \frac{\pi^2}{L^2} + \frac{2 \cdot N_e \cdot M_\alpha^2}{N_\alpha^2 \cdot L^2}\right) \quad (4.1.9b)$$

$$X^2 = N_\alpha \cdot T - F_o - I_e \cdot \frac{\pi^2}{L^2} \quad (4.1.9c)$$

$$\frac{1}{\sqrt{27 \cdot N_e}} \cdot X^3 - \frac{M_\alpha}{N_\alpha \cdot L} \cdot X^2 + \frac{M_\alpha}{N_\alpha \cdot L} \cdot \left(I_e \cdot \frac{\pi^2}{L^2} - N_o\right) = 0 \quad (4.1.9d)$$

The discriminant of this polynomial is then given by (4.1.10a). It shows that if X is located between the values given by (4.1.10a), the beam is bistable. The values of X associated to the snap and snap-back temperatures are given by (4.1.10b-d). The temperatures are then found by using the definition of X given by (4.1.9c). These approximated formulae enable to depict the evolution of the hysteresis temperature with very good accuracy (see Fig.4.1.1).

$$\Delta = \left(N_o - I_e \cdot \frac{\pi^2}{L^2}\right) \cdot \left(N_o - I_e \cdot \frac{\pi^2}{L^2} - \frac{4 \cdot N_e \cdot M_\alpha^2}{N_\alpha^2 \cdot L^2}\right) \quad (4.1.9a)$$

$$X_S = \frac{\sqrt{3 \cdot N_e \cdot M_\alpha}}{N_\alpha \cdot L} \cdot \left(1 + 2 \cdot \cos\left(\frac{\phi - \pi}{3}\right)\right) \quad (4.1.9b)$$

$$X_{SB} = \frac{\sqrt{3 \cdot N_e \cdot M_\alpha}}{N_\alpha \cdot L} \cdot \left(1 + 2 \cdot \cos\left(\frac{\phi + \pi}{3}\right)\right) \quad (4.1.9c)$$

$$\cos(\phi) = \frac{N_\alpha^2 \cdot L^2}{2 \cdot M_\alpha^2 \cdot n_e} \cdot \left(N_o - I_e \cdot \frac{\pi^2}{L^2} + \frac{2 \cdot N_e \cdot M_\alpha^2}{N_\alpha^2 \cdot L^2}\right) \quad (4.1.9d)$$

4.2 Simplification of the model

Solving the previous equations in order to find analytical expressions of the performances of the heat engine is not easy. The difficulty arises mainly from the cross term of the beam's deflexion amplitude and the temperature due to the mean thermal expansion represented by n_α . Great simplifications can be derived from the assumption that thermal expansion has a weak effect on the beam's mechanical behaviour if the temperature is between the snap and the snap-back temperatures. The equilibrium equation given in (4.1.1) can thus be simplified into (4.2.1)

$$\frac{N_e \cdot \pi^2}{4 \cdot L^2} \cdot w_1^3 + \left(I_e \cdot \frac{\pi^2}{L^2} - N_o\right) \cdot w_1 + \frac{4}{\pi} \cdot (M_o - M_\alpha \cdot T) = 0 \quad (4.2.1)$$

Hence by derivating this equation we directly conclude that the limit points are located in

$$w_{SB}^C = -w_S^C = \frac{2 \cdot L}{\pi} \sqrt{\frac{1}{3 \cdot N_e} \cdot \left(N_o - I_e \cdot \frac{\pi^2}{L^2}\right)} \quad (4.2.2)$$

By injecting this equation in (4.2.1), we show that the thermal hysteresis is centered around the value T_o and verifies (4.2.3a). The snap and snap-back temperatures are then given by (4.2.3b) and (4.2.3c), and the beam's deflexion at the limit points can directly be expressed as a function of the thermal hysteresis. Logically with these equations we observe the stress force N_o is, the more unstable the beam becomes and its thermal hysteresis widens and the displacement of the beam increases.

$$\Delta T = \frac{2 \cdot L}{M_\alpha} \cdot \sqrt{\frac{1}{27 \cdot N_e} \cdot \left(N_o - I_e \cdot \frac{\pi^2}{L^2}\right)^3} \quad (4.2.3a)$$

$$T_S = \frac{M_o}{M_\alpha} + \frac{\Delta T}{2} \quad (4.2.3b)$$

$$T_{SB} = \frac{M_o}{M_\alpha} - \frac{\Delta T}{2} \quad (4.2.3c)$$

$$w_S^C = -\frac{1}{\pi} \cdot \sqrt[3]{4 \cdot \frac{M_\alpha \cdot L^2}{N_e} \cdot \Delta T} \quad (4.2.3d)$$

4.3 Mechanical performances of the energy harvester

Now that we have validated the approximation on the effect of the mean thermal expansion, we establish the expression of the performance of the harvester. The main physical parameters are represented in Fig.4.3.1a. At the limit points the shape of the strain energy well can be developed by taking into account the expression of the snap and snap-back temperatures. Equation (4.3.1) shows that the system oscillates around a position between w_s^c and $-3.w_s^c$, representing the positions having the same potential energy.

$$\mathcal{W}_M = \frac{N_e \cdot \pi^4}{32 \cdot L^3} \cdot (w_1 - w_s^c)^3 \cdot (w_1 + 3 \cdot w_s^c) + \frac{3 \cdot N_e \cdot \pi^4}{32 \cdot L^3} \cdot w_s^c{}^4 \quad (4.3.1)$$

When the beam snaps, it releases an amount of kinetic energy verifying (4.3.2).

$$\Delta\mathcal{K}(w^S) = \mathcal{W}_M(w^C) - \mathcal{W}_M(w^S) = \frac{27 \cdot N_e \cdot \pi^4}{32 \cdot L^3} \cdot w_s^c{}^4 \quad (4.3.2)$$

The kinetic energy release also has (4.3.2) for expression when the beam snaps back, since the strain energy well is spatially symmetrical because the thermal expansion is neglected. The available mechanical energy produced by the composite beam is then twice this value. By using the expression (4.2.3d), it can be expressed as a function of the thermal hysteresis, showing a 4/3-power dependence. Its evolution is plotted against the beam's thermal hysteresis in Fig.4.3.1e, showing the relatively good agreement between the reduced model and the exact model exposed in Section 2. The underestimation of the mechanical energy is due to the effect of the mean thermal expansion that increases the snap energy more than it decreases the snap-back energy. Globally, the sum of these two quantities is higher than the energy quantity predicted by the reduced model

$$\Delta\mathcal{W}_M = 2 \cdot \Delta\mathcal{K}(w^S) = 27 \cdot \sqrt[3]{\frac{(M_\alpha \cdot \Delta T)^4}{16 \cdot N_e \cdot L}} \quad (4.3.3)$$

The maximal force produced by the switching beam is obtained at the position $-w_s^c$. This force is a linear function of the thermal hysteresis, as shown in Fig.4.3.1b. Values between 1 and 2 N can be measured when the thermal hysteresis ranges between 10 and 20°C.

$$F_{max} = \frac{N_e \cdot \pi^4}{2 \cdot L^3} \cdot w_s^c{}^3 = \frac{2 \cdot M_\alpha \cdot \pi}{L} \cdot \Delta T \quad (4.3.4)$$

In the frame of the Ritz approximation, the kinetic energy is given by (4.3.5).

$$\mathcal{K} = \frac{1}{2} \cdot \frac{m_b}{L} \cdot \int_0^L \dot{w}^2 \cdot dx = \frac{1}{4} \cdot m_b \cdot \dot{w}_1^2 \quad (4.3.5)$$

This expression enables to extract some dynamic parameters associated to the snap-through. Assuming that the beam has a null speed a null acceleration at the limit point, we can express the formula of the speed, the power, and the natural frequency of the switching beam. However, the switching duration cannot be found since the integral (4.3.6) is indefinite. We will further study the beam's dynamic behaviour later.

$$\Delta t = \int_{w_S^C}^{w_S^S} \frac{1}{\dot{w}_1} \cdot dw_1 = \left[\sqrt{\frac{2 \cdot m_b \cdot L}{N_e} \cdot \frac{L}{w_S^C} \cdot \sqrt{\frac{w_1 + 3 \cdot w_S^C}{w_S^C - w_1}}} \right]_{w_S^C}^{w_S^S} \quad (4.3.6)$$

By approximating the potential well as a second-order polynomial in the vicinity of the stable position, the natural frequency of vibration of the composite beam can be expressed by (4.3.7). Its evolution is plotted against the thermal hysteresis in Fig.4.3.2a. The fact that the frequency ranges between 500 and 1500 Hz for a hysteresis between 1 and 30°C explains why the jumping poppers can produce audible sound when it snaps, and is in agreement with the results of (Pandey *et al*, 2014).

$$f_o = \frac{3 \cdot \pi}{4} \cdot \frac{w_S^C}{L} \cdot \sqrt{\frac{N_e}{m_b \cdot L}} \quad (4.3.7)$$

The switching speed is given by (4.3.8). We find that the maximal speed is reached when the strain energy is minimal. The maximal speed is about 1.3 m.s⁻¹ for a 10 K-hysteresis beam (Fig.4.3.1c).

$$v_{max} = \pi^2 \cdot \sqrt{\frac{27 \cdot N_e}{8 \cdot m_b \cdot L^3} \cdot w_S^C^2} \quad (4.3.8)$$

The power generated by the beam is the product of the speed by the force of the bimetal. By derivating (4.3.1), we find that the power is maximal for two values of the beam's deflexion amplitude. For these values, the power is given by (4.3.9d) and (4.3.9e) and is plotted in Fig.4.3.1d.

$$P_M = \frac{N_e \cdot \pi^6}{8\sqrt{8} \cdot L^4} \cdot \sqrt{\frac{N_e}{m_b \cdot L}} \cdot (w_S^C - w_1)^3 \cdot (w_1 + 2 \cdot w_S^C) \cdot \sqrt{(w_S^C - w_1) \cdot (w_1 + 3 \cdot w_S^C)} \quad (4.3.9a)$$

$$w_{p1} = -\left(2 + \frac{\sqrt{15}}{5}\right) \cdot w_S^C \approx -2,78 \cdot w_S^C \quad (4.3.9b)$$

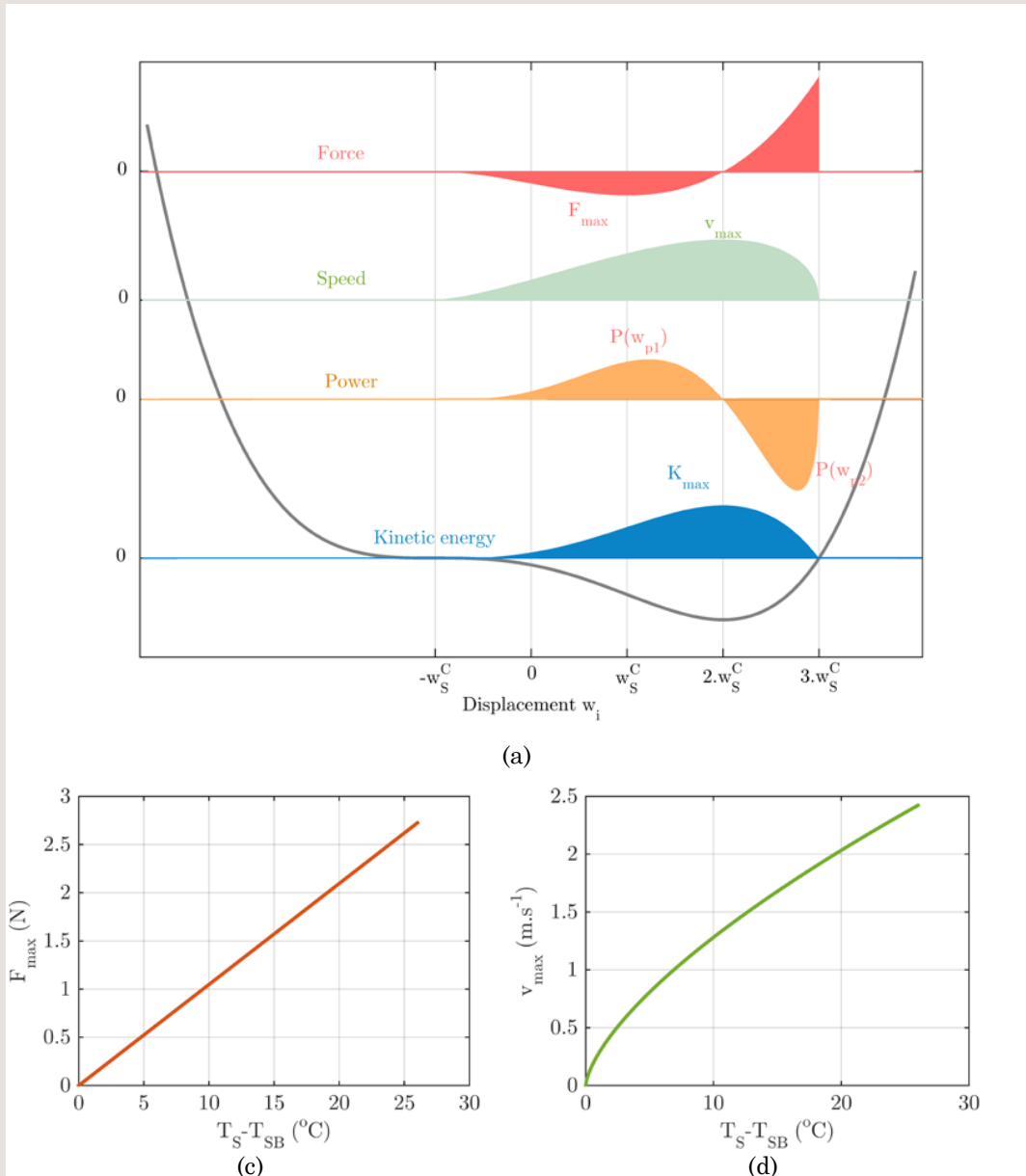
$$w_{p2} = -\left(2 - \frac{\sqrt{15}}{5}\right) \cdot w_S^C \approx -1,23 \cdot w_S^C \quad (4.3.9c)$$

$$P(w_{p1}) \approx -1,70 \cdot \pi^6 \cdot N_e \frac{w_S^C^5}{L^4} \cdot \sqrt{\frac{N_e}{m_b \cdot L}} \quad (4.3.9d)$$

$$P(w_{p2}) \approx 0,75 \cdot \pi^6 \cdot N_e \frac{w_S^C^5}{L^4} \cdot \sqrt{\frac{N_e}{m_b \cdot L}} \quad (4.3.9e)$$

To finish, we study the thermal properties of the bistable beams and the efficiency of the transduction. The entropy discontinuity is given by (4.3.10a). This equation leads to the analytical solutions of the latent heats of snap and snap-back.

Figure 4.3.1. a. Total deflexion during the snap of the beam. b. Residual stress in the layers of the bimetallic beams. c. Density of mechanical energy provided by the bimetals. d. Carnot efficiency of the heat engines



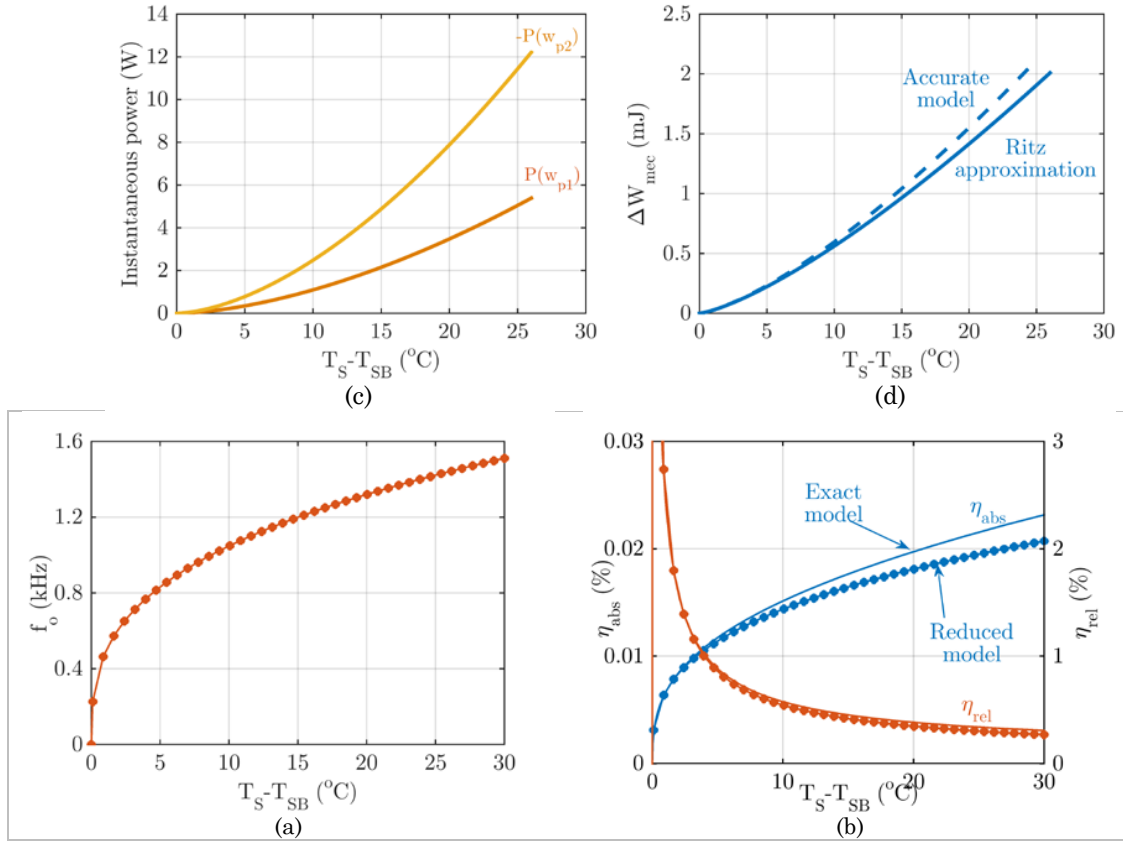


Figure 4.3.2. *a. Evolution of the fundamental frequency of the switching beam. b. Comparison of the Carnot efficiencies and thermal efficiencies of the harvester predicted by the reduced model and the exact model of Section 2.*

$$\Delta S = \pm 6 \cdot \sqrt[3]{4} \cdot \sqrt[3]{\frac{m_\alpha^4}{L \cdot n_e}} \cdot \Delta T \quad (4.3.10a)$$

$$L_S = 6 \cdot \sqrt[3]{4} \cdot \left(\theta_{ref} + \frac{M_o}{m_\alpha} + \frac{\Delta T}{2} \right) \cdot \sqrt[3]{\frac{m_\alpha^4}{L \cdot n_e}} \cdot \Delta T \quad (4.3.10b)$$

$$L_{SB} = -6 \cdot \sqrt[3]{4} \cdot \left(\theta_{ref} + \frac{M_o}{m_\alpha} - \frac{\Delta T}{2} \right) \cdot \sqrt[3]{\frac{m_\alpha^4}{L \cdot n_e}} \cdot \Delta T \quad (4.3.10c)$$

In order to evaluate the efficiency of the transduction, we first evaluate the heat provided to the beam by the hot source during the heating phase. The total heat supplied by the hot source is the sum of the heat provided to the beam to increase its temperature from T_{SB} to T_S , and the latent heat needed for the beam to snap.

$$Q_{tot} = C_v \cdot \Delta T + 8 \cdot \sqrt[3]{4 \cdot \frac{m_\alpha^4}{L \cdot n_e}} \cdot \Delta T \cdot \left(\theta_{ref} + \frac{M_o}{m_\alpha} \right) \quad (4.3.11)$$

In this case, the efficiency of our heat engine, which is the ratio between the mechanical energy generated and the heat supplied by the hot source, shows a cube-root dependence on the thermal hysteresis for large values of this thermal hysteresis. The Carnot efficiency is obtained by normalizing the efficiency of the heat engine by the Carnot efficiency in the same conditions.

$$\eta_{TM}^{abs} = \frac{\Delta \mathcal{W}_M}{Q_h} = 27 \cdot \sqrt[3]{\frac{M_\alpha^4}{16 \cdot N_e \cdot L \cdot C_v^3}} \cdot \sqrt[3]{\Delta T} \quad (4.3.12a)$$

$$\eta_{TM}^{rel} = \frac{T_S + \theta^o}{\Delta T} \cdot \eta_{TM}^{abs} = 27 \cdot \sqrt[3]{\frac{M_\alpha^4}{16 \cdot N_e \cdot L \cdot C_v^3}} \cdot \frac{T_S + \theta^o}{\sqrt[3]{\Delta T^2}} \quad (4.3.12b)$$

In the case of a beam with small thermal hysteresis, and as long as the latent heat can be neglected, the thermal hysteresis can also be neglected with respect to the mean temperature M_o/m_α . The relative efficiency then shows a $-2/3$ exponential dependence on the thermal hysteresis (4.3.13), linked to the fact that the Carnot efficiency increases linearly with the difference in temperature between the hot source and the cold source.

$$\eta_{TM}^{rel} \approx 27 \cdot \sqrt[3]{\frac{M_\alpha^4}{16 \cdot N_e \cdot L \cdot C_v^3}} \cdot \frac{T_o + \theta_{ref}}{\sqrt[3]{\Delta T^2}} \quad (4.3.12)$$

4.4 Experimental studies and validity of the reduced-order model

In order to attempt to explain the properties of the bimetals used in the current harvester, we realized a series of measurement on bimetallic shells (Fig.4.4.1a). The main problem with these membranes is that they do not behave like simply-supported curved beams, but like free curved shells. The model we developed in this chapter would not normally fit the experimental data concerning the performances of the harvesters. However, by assuming that the buckled shape of these membranes is cut into a square membrane (Fig.4.4.1b), the deflection of the beam can be described by (4.4.1) according to (Bryan, 1890).

$$w(x, y) = w_1(t) \cdot \sin\left(\frac{\pi \cdot x}{L}\right) \cdot \sin\left(\frac{\pi \cdot y}{L}\right) \quad (4.4.1)$$

With this equation, it is possible to calculate the expression of the kinetic energy of the membrane as a function of the speed of the shell's center (4.4.2b). This last equation give us a corrective factor that will be used to first adjust the kinetic energy of snap calculated with the experimental measurement of the speed of the bistable shell's center.

$$\mathcal{K} = \frac{1}{2} \cdot \int_{\frac{L}{4}}^{\frac{3L}{4}} \int_0^L \int_0^t \rho(z) \cdot w_{,t}^2(x, y) \cdot dx \cdot dy \cdot dz \quad (4.4.2a)$$

$$\mathcal{K} = m_b \cdot \frac{\pi + 2}{16 \cdot \pi} \cdot w_{,t}^2\left(\frac{L}{2}, \frac{L}{2}\right) \quad (4.4.2b)$$

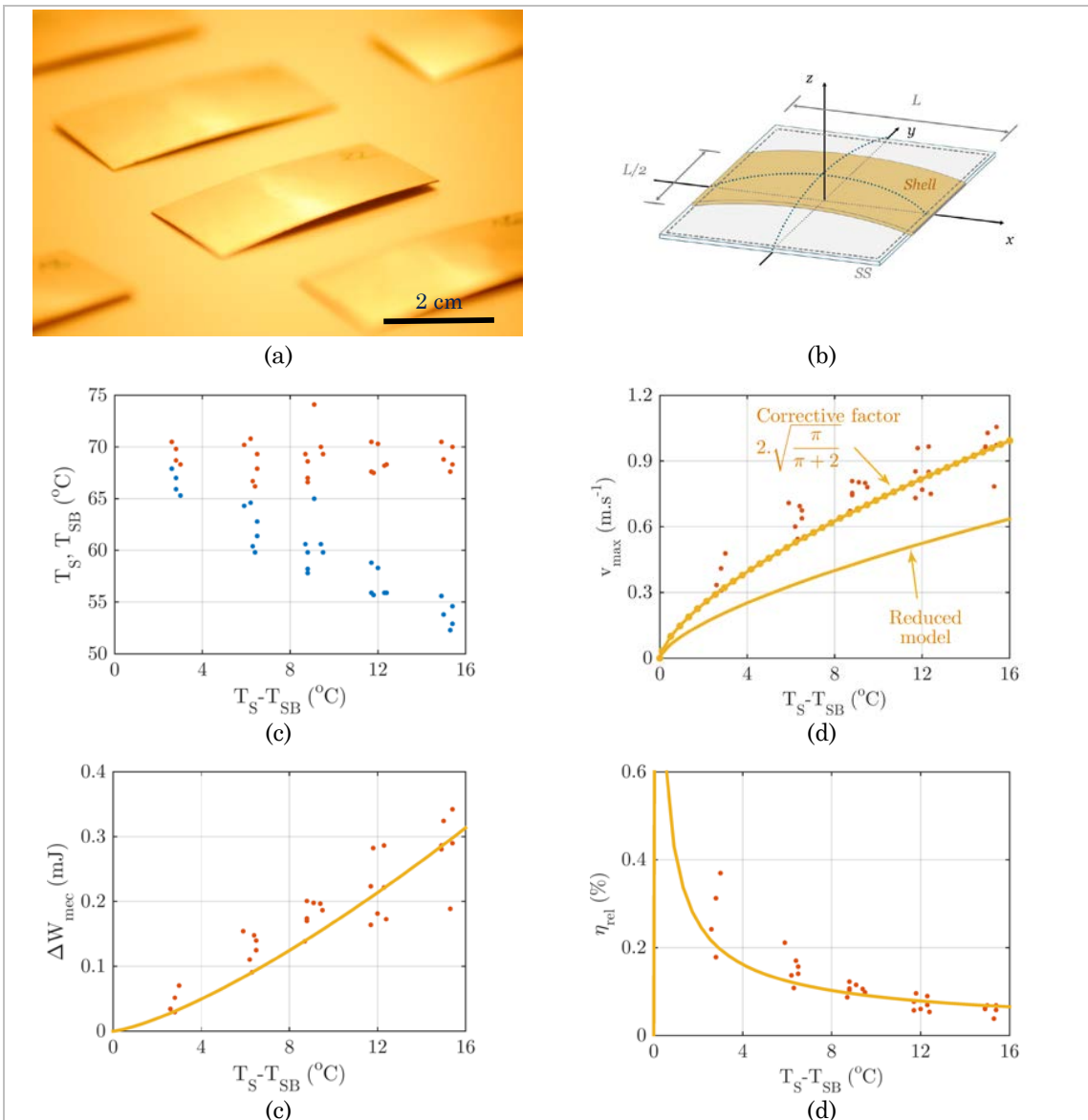


Figure 4.4.1. *a. Image of the bimetallic shells characterized in this part. b. Schematized hypothesis for the calculation of the kinetic energy. c-e. Comparison between experimental data and the reduced model.*

The bimetallic shells studied in this part are made of NC4 alloy as active layer and Invar as passive layer. The bistability of these shells comes from the dent stamped on their center which gives them an initial curvature. The dimensions of the shells are $3.6 \times 1.8 \times 0.03$ cm³. Shells of various hystereses have been chosen with typical values centered around 3, 6, 9, 12 and 15°C (Fig.4.4.1c). For all these bimetal thermostats, we measured the switching speed using a velocimeter (Polytec OFV-505). Once the switching speed is measured, it is possible to find the value of the mechanical energy produced by the harvester by using (4.4.2d), the thermal efficiency of the transduction by knowing the heat capacitance of the bimetallic shell, and the Carnot efficiency of the transduction (Fig.4.4.1e) if the hot source is assumed to be equal to the snap temperature of the bimetal

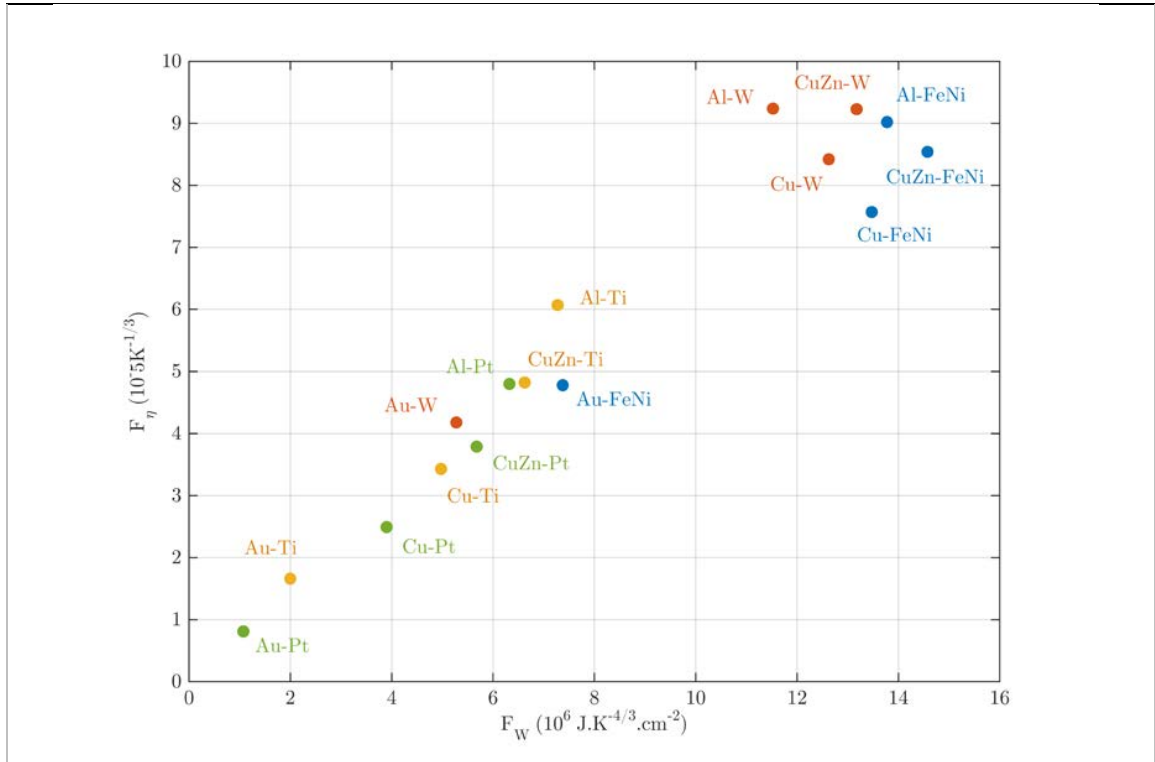
thermostat. In Figures 4.4.1 (next page), we superimpose the various values predicted by the reduced model in the same conditions. The comparison between these curves and the experimental data shows that it is possible to explain the tendencies observed on the harvester in operation. Fig.4.4.1d shows that by adjusting the speed given by the model by the factor calculated with the expression of the kinetic energy (4.4.2b), it is possible to fit with a relatively good precision the speed measured on the harvester prototypes. With these results we can conclude that by adding fitting parameters to the reduced model, it would be possible to create a compact model able to explain the performances of the future devices.

4.5 Figures of Merit

It is also important to compare various bimetallic couples used as prime mover in the bimetallic strip heat engine in order to see the impact of the materials properties on the performances of the heat engine. To do so, we observe that the harvested energy and the efficiencies are functions of the beam's parameters and geometry. We thus define two Figures of Merit, FOM_w describing the potential energy generated by the bimetallic beams (4.5.1), and FOM_η the efficiency of the thermo-mechanical transduction (31).

$$FOM_w = 27 \cdot \sqrt[3]{\frac{M_\alpha^4}{16 \cdot N_e \cdot L}} \quad (4.5.1a)$$

Figure 4.5.1. Figures of Merit for sixteen different bimetals.



$$FOM_{\eta} = \frac{27}{C_v} \cdot \sqrt[3]{\frac{M_{\alpha}^4}{16 \cdot N_e \cdot L}} = \frac{FOM_{\mathcal{W}}}{C_v} \quad (4.5.1b)$$

Using (4.5.1) and (4.5.2), we compare sixteen different bimetal couples, made of an active layer (aluminum, brass (CuZn), copper (Cu) or gold (Au)) and a passive layer (Invar (FeNi), tungsten (W), titanium (Ti), platinum (Pt)). Even if the choice of these materials is not always realistic since some materials like Gold would not be used, it enables to describe a wide range of values of physical properties. To compare these bimetals, we choose the same beam geometrie (20 x 2 x 0.5 mm) with the same thickness for each material layer. Fig.4.5.1 represents both Figures of Merit for these bimetals. As we can see, there is a strong correlation between both parameters. For these bimetals, their heat capacity is very similar, the difference between each bimetal is mainly linked to their axial stiffness and above all to their thermal asymmetry m_{α} . Logically, we observe that bimetallic beams with high thermal asymmetry can generate more energy because they are more easily bistable.

Similarly, they convert a larger part of heat into strain energy and are thus more efficient in fine. Among these seventeen bimetals, we find that the best bimetals are the couples CuZn-FeNi for harvested energy and CuZn-W for efficiency. Because bimetallic beams made of FeNi or W give the best efficiencies, it could be concluded that the choice of the passive layer has a great influence on the performance of the bimetallic strip heat engine

4.6 Study of the impact of the architecture on the performances

The use of the Ritz approximation of the beam deflexion shape and of the Galerkin method is very useful to study the impact of the harvester's architecture on the composite beam's bistability. We define the two deflections w_{bot} and w_{top} by (4.6.1a-b), which must verify (4.7.1c) so that the system works.

$$w_{bot} = d_{bot} - z_o \quad (4.6.1a)$$

$$w_{top} = d_{top} + t - z_o \quad (4.6.1b)$$

$$|w_{bot}| \leq |w_S^c|; |w_{top}| \leq |w_S^c| \quad (4.6.1b)$$

The existence of the force Q applied by the architecture on the beam modifies the equilibrium equation which becomes (4.6.2a) when the beam is snapped, and (4.6.2b) when the beam is unsnapped

$$F_{top} = \frac{N_e \cdot \pi^4}{8 \cdot L^3} \cdot w_{top}^3 + \frac{\pi^2}{2 \cdot L} \cdot \left(I_e \cdot \frac{\pi^2}{L^2} - N_o \right) \cdot w_{top} + \frac{2\pi}{L} \cdot (M_o - M_{\alpha} \cdot T) \quad (4.6.2a)$$

$$-F_{bot} = \frac{N_e \cdot \pi^4}{8 \cdot L^3} \cdot w_{bot}^3 + \frac{\pi^2}{2 \cdot L} \cdot \left(I_e \cdot \frac{\pi^2}{L^2} - N_o \right) \cdot w_{bot} + \frac{2\pi}{L} \cdot (M_o - M_{\alpha} \cdot T) \quad (4.6.2b)$$

The snap and snap-back temperatures are then given by the nullity of these two equations, and the thermal hysteresis by (4.6.3)

$$\Delta T_{cav} = \frac{L}{2 \cdot \pi \cdot M_{\alpha}} \cdot \left(\frac{N_e \cdot \pi^4}{8 \cdot L^3} \cdot (w_{bot}^3 - w_{top}^3) + \frac{\pi^2}{2 \cdot L} \cdot \left(I_e \cdot \frac{\pi^2}{L^2} - N_o \right) \cdot (w_{bot} - w_{top}) \right) \quad (4.6.3c)$$

Once the beam snaps or snaps back, the architecture applies a maximal force on the beam, which can be found by combining (4.6.2a) and (4.6.2b).

$$F_{top}^{max} = -F_{bot}^{max} = \frac{2\pi}{L} \cdot M_\alpha \cdot \Delta T_{cav} \quad (4.6.4)$$

When the beam is in contact with the hot source or the cold source, its strain energy is a simple linear function of the temperature. The kinetic energy released during the snap is then given by (4.6.5). The kinetic energy of snap-back is obtained by replacing w_{bot} by w_{top} and reversely.

$$\Delta \mathcal{K}(T_s) = \frac{N_e \cdot \pi^4}{32 \cdot L^3} \cdot (w_{bot}^4 + 3 \cdot w_{top}^4 - 4 \cdot w_{top}^3 \cdot w_{bot}) + \frac{\pi^2}{4 \cdot L} \cdot \left(I_e \cdot \frac{\pi^2}{L^2} - N_o \right) \cdot (w_{bot} - w_{top})^2 \quad (4.6.5)$$

The total mechanical energy produced by the harvester is then given by (4.6.6a). When the deflections of the beam in contact with the heat sources are equal to a percentage of the critical deflection w_s^c (4.6.6b), the expression of the energy can be simplified into (4.6.6c).

$$\Delta \mathcal{W}_M^{cav} = \left(\frac{N_e \cdot \pi^4}{8 \cdot L^3} \cdot (w_{top} + w_{bot})^2 + \frac{\pi^2}{2 \cdot L} \cdot \left(I_e \cdot \frac{\pi^2}{L^2} - N_o \right) \right) \cdot (w_{bot} - w_{top})^2 \quad (4.6.6a)$$

$$|w_{bot}| = |w_{top}| = r_w \cdot |w_s^c| \quad (4.6.6b)$$

$$\Delta \mathcal{W}_M^{cav} = \left(\frac{3 \cdot N_e \cdot \pi^4}{2 \cdot L^3} \cdot r_w^2 \cdot w_s^{c2} + \frac{2 \cdot \pi^2}{L} \cdot \left(I_e \cdot \frac{\pi^2}{L^2} - N_o \right) \right) \cdot r_w^2 \cdot w_s^{c2} \quad (4.6.6c)$$

With this last hypothesis, the thermal hysteresis becomes (4.6.7a) (Fig.4.6.1a). We directly see that the kinetic energy release can be simply expressed as a function of the thermal hysteresis (4.6.7b).

$$\Delta T_{cav} = \frac{3}{2} \cdot \left(r_w - \frac{r_w^3}{3} \right) \cdot \Delta T \quad (4.6.7a)$$

$$\Delta \mathcal{W}_M^{cav} = 2 \cdot F_{top}^{max} \cdot r_w \cdot |w_s^c| = \frac{8}{9} \cdot \left(r_w^2 - \frac{r_w^4}{3} \right) \cdot \Delta \mathcal{W}_M \quad (4.6.7b)$$

The thermal efficiency can be approximated by (4.7.9) by neglecting the latent heat of snap, and by replacing the critical deflexion by its expression (4.2.3d). Using the expression of the thermal efficiency of the harvester outside de cavity (4.3.11a), we can find a linear relation between the two efficiencies. It shows that the best efficiency can be reached when the cavity thickness equals the deflection of the beam before it snaps and snaps back ($r_w=1$). In that case, the efficiency of the harvester represents 59.3% of the efficiency of the efficiency of a beam that is not constrained by any architecture.

$$\eta_{TM}^{abs,cav} = 4 \cdot r_w \cdot \sqrt[3]{\frac{4 \cdot M_\alpha^4}{N_e \cdot L \cdot C_v^3} \cdot \Delta T} = \frac{16}{27} \cdot r_w \cdot \eta_{TM}^{abs} \quad (4.6.8)$$

The Carnot efficiency is obtained by normalizing the thermal efficiency by the efficiency of the Carnot engine working between the snap and snap-back temperatures. By using the expression of the thermal hysteresis (4.6.7a), the Carnot efficiency of the transduction of the beam inside the cavity can be expressed as a function of the Carnot efficiency of the

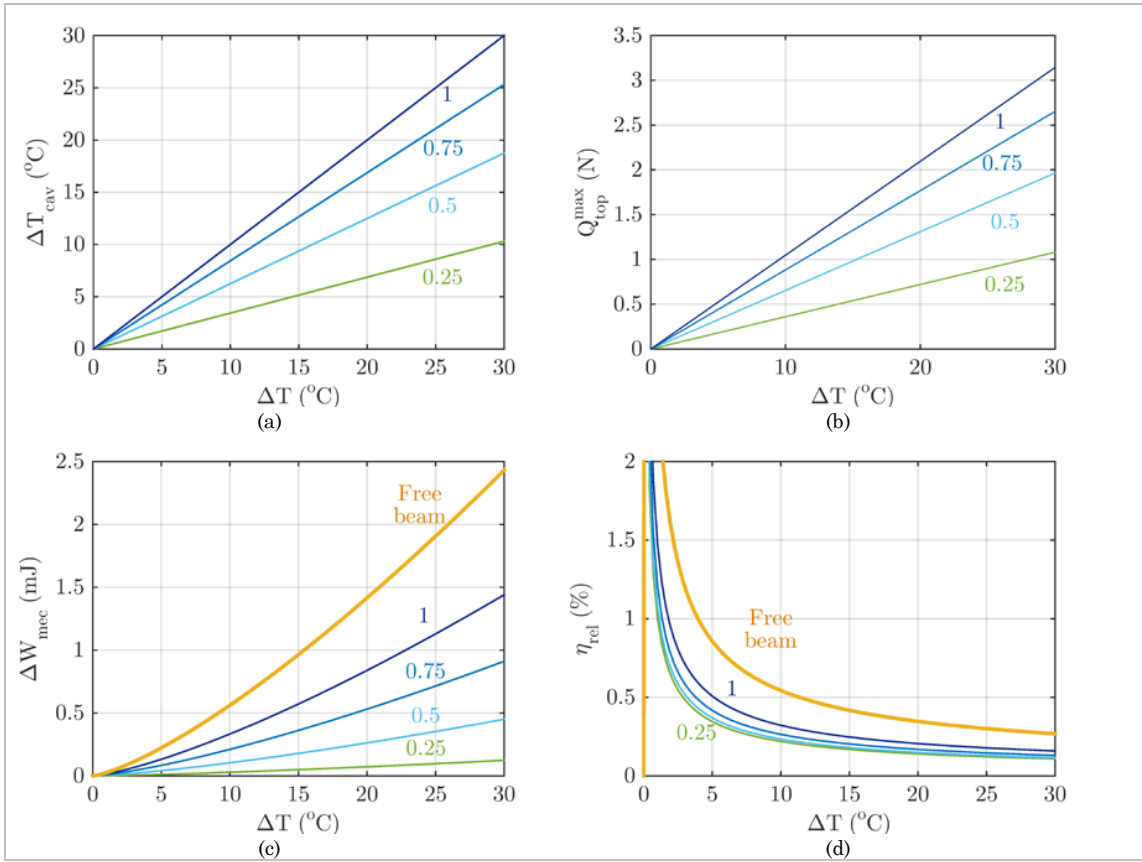


Figure 4.6.1. *a. Thermal hysteresis of the beam in the cavity as a function of its true hysteresis and for various values of the ratio r_w . b. Evolution of the force generated by the architecture of the harvester as a function of the hysteresis of the beam. c. Comparison of the available energies produced by the harvester for various value of the cavity's thickness-to-deflexion ratio. d. Evolution of the Carnot efficiency of the harvester.*

beam without the cavity (4.6.9b). This last equation shows that the Carnot efficiency of the harvester with $r_w=1$ is of 59.3% of the efficiency of the not constrained beam and if r_w tends to 0, it becomes equal to 39.5% of this maximal efficiency (by assuming that the latent heat is still negligible) (Fig.4.6.1d).

$$\eta_{TM}^{rel,cav} = \frac{\eta_{abs,cav}}{\Delta T_{cav}} \cdot \left(T_o + \frac{\Delta T_{cav}}{2} \right) \quad (4.6.9a)$$

$$\eta_{TM}^{rel,cav} = \frac{32}{27(3 - r_w^2)} \cdot \eta_{TM}^{rel} \quad (4.6.9b)$$

4.8 Synthesis on the second model

In this second model, we used a strong method to simplify the equations describing the state of the simply-supported composite beams. Using the Ritz approximation of the beam's shape, we proposed laws on the available mechanical energy and the efficiency of

the harvester, and we created Figures of Merit to compare materials. However, we can observe that this model first assumed that the temperature was homogeneous through the whole beam. This leads to forget the role played by thermal transfers on the bistability, and to neglect the influence of the thermal conductivity of materials on the duration of the heating and cooling phases. In order to correct this mistake, the next part is devoted to the modeling of the thermal transfers inside the composite beams, and to the study of the dynamic behavior of the harvester.

5 Thermal transfers and dynamic behavior of the energy harvester

5.1 Equations of the thermal transfers

In the previous parts, the analysis of the equilibrium of the system was based on the principle of virtual displacement which was derived from the first thermodynamic principle. In order to study the thermal transfers and how they affect the bistability of the composite beams, we need to use the second thermodynamic principle which states that the system evolves so that the entropy of the systems is the sum of the entropies carried into the system by heat transfers (5.1.1a). The phenomenological law of Fourier [Boley, 2012] gives a direct link between the heat flux and the thermal gradient for conductive heat transfers (5.1.1b), where κ represents the thermal conductivity of the material.

$$\sigma_{,t} = \frac{q_{,t}}{T + \theta_{ref}} \quad (5.1.1a)$$

$$q_{,t} = \nabla j_q = -\kappa \cdot \nabla^2 T \quad (5.1.1b)$$

By locally writing the entropy as a function of temperature and the parameters of the beam, the equation of the second principle becomes (5.1.2). Because of the weak thermo-mechanical coupling inside solid materials, the variation of the entropy associated to the strain can be neglected, and the classical law of heat transfer manque la fin. In this way, the study of the thermal transfers in the harvesters can be decoupled from their consequences on the instability of the beam. Consideration of the influence of the strain on the thermal transfer has been treated in numerous publications among which (Novacki, 1970) and (Fox, 1969).

$$c_S \cdot T_{,t} + \alpha \cdot (T + \theta_{ref}) \cdot \mathcal{S}_{xx,t} = -\kappa \cdot \nabla^2 T \quad (5.1.2a)$$

$$c_S \cdot T_{,t} = -\kappa \cdot \nabla^2 T \quad (5.1.2b)$$

In this part, conduction will be considered as the main form of heat transfer occurring in the heat engine. In order to obtain a model that is simple yet accurate, we represent the harvester as as beam punctually heated in its center and thermally insulated at its edges (Fig.5.1.a). The boundary conditions of the problem are then given by the Robin condition at the interface between the heat sources and the beam (5.1.3a), and the Neuman condition (5.1.3b) at the beam's edges. In this equation h is the coefficient of thermal exchange of the medium.

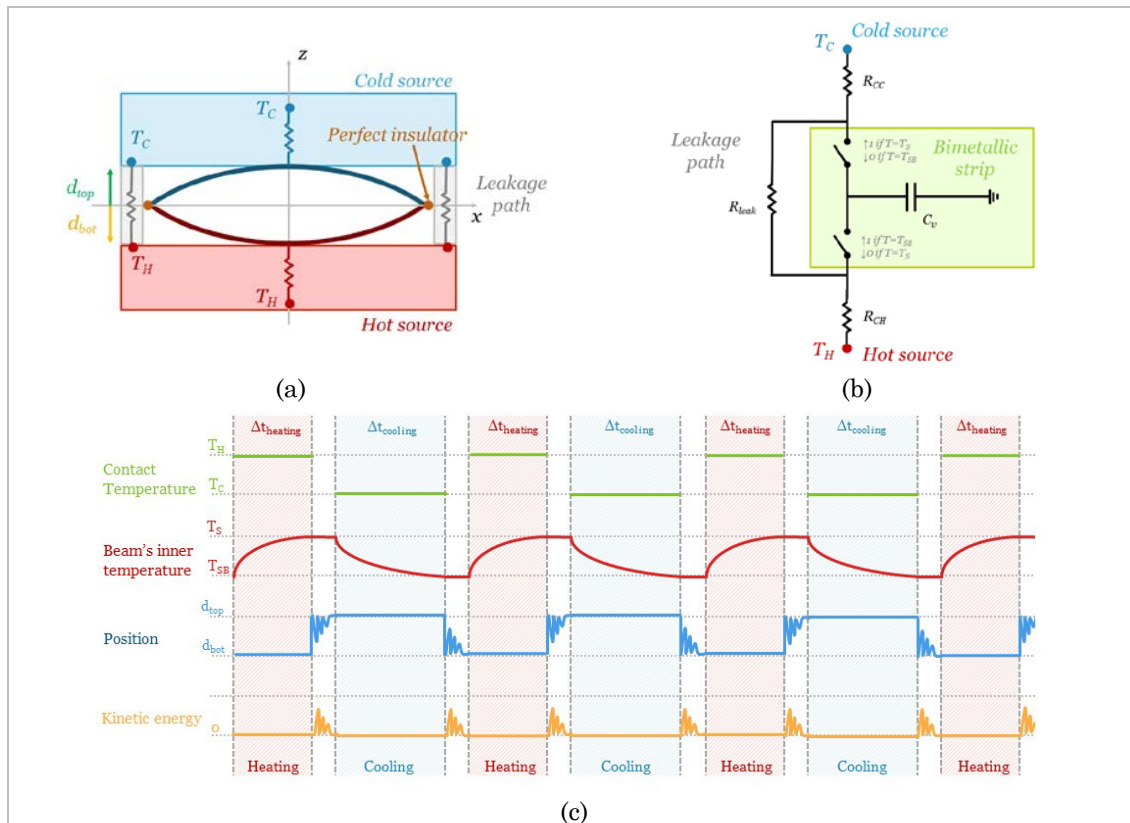
$$\nabla T(0) = \frac{h}{k} \cdot (T_{ext} - T(0)) \quad (5.1.3a)$$

$$\nabla T \left(\frac{L}{2} \right) = \nabla T \left(-\frac{L}{2} \right) = 0 \tag{5.1.3b}$$

5.2 Switched thermal capacitance model

In this first model, we assume that the thermal transfers are limited by the contact resistances between the heat sources and the bistable beam, so that the thermal gradient in the beam is negligible and the temperature is homogeneous across the beam. This hypothesis can be justified if the Biot number obtained with (5.1.2a) is weak. Given that the heat can spread in two directions, both through the beam’s thickness and along the beam’s length, we define two Biot numbers for the thermal transfer. The first Biot number compares the propagation of the heat through the thickness of the beam with the conduction at the interface of the heat source and the beam. Given the thickness of the beam, it can easily be assumed that the temperature is homogenous through the beam’s thickness ($Bi_1 < 0.2$). In these conditions, the error is inferior to 5% [Rohsenow and Hartnett, 1973]. The second Biot number compares the propagation of the heat through the half length of the beam with the external heat supply.

Figure 5.2.1. a. Scheme of the harvester and thermal transfers. b. Equivalent lumped capacitance model of the harvester. c. Simplified representation of the evolution of some parameters of the harvester in the frame of the lumped capacitance model.



In this part, the difference of propagation in the beam due to the variation of the thermal conductivity of the layers composing the beam is neglected, and the thermal resistivity ($1/\kappa_b$) of the beam is taken as the average value of the resistivities of the materials. If we can assume that the second Biot number is also small, the system can simply be modeled with the equivalent lumped capacitance model of Fig.5.2.1b where R_{CC} and R_{CH} represent the contact resistances between the cold source and the beam at the upper position and between the hot source and the beam at the lower position. The composite beam then behaves like a simple switched thermal capacitance that can switch at T_S and snaps back at T_{SB} .

$$Bi_1 = \frac{h \cdot t}{\lambda_b} \quad (5.2.1a)$$

$$Bi_2 = \frac{h \cdot L \cdot l_{contact}}{\kappa_b \cdot t} \quad (5.2.1b)$$

$$\frac{1}{\kappa_b} = \frac{1}{t} \cdot \int_0^t \frac{1}{\kappa(z)} \cdot \delta z \quad (5.2.1c)$$

In that case, the mechanical equation of the reduced model is still valid (5.2.2a), and the equation of the thermal transfers is given by (5.2.2b).

$$\frac{m_b}{2} \cdot w_{,tt} + \frac{N_e \cdot \pi^4}{8 \cdot L^3} \cdot w^3 + \frac{\pi^2}{2 \cdot L} \cdot \left(N_o - I_e \cdot \frac{\pi^2}{L^2} \right) \cdot w + \frac{2 \cdot \pi}{L} \cdot (M_o - M_\alpha \cdot T) = 0 \quad (5.2.2a)$$

$$q_{,t} = \frac{T_H - T}{R_{CH}} \quad (5.2.2b)$$

Given that the beam is initially at T_{SB} and switches at T_S , the temporal evolution of the temperature is given by (5.2.3a) when the beam is unsnapped. Similarly, the evolution of the temperature when the beam cools down is given by (5.2.3b).

$$T(t) = (T_{SB} - T_H) \cdot e^{-t/R_{CH} \cdot C_v} + T_H \quad (5.2.3a)$$

$$T(t) = (T_C - T_S) \cdot e^{-t/R_{CC} \cdot C_v} + T_C \quad (5.2.3b)$$

These formulae give the duration of the heating phase (5.2.4a) and cooling phase (5.2.4b) of a beam constrained in a cavity. Logically, we can observe that the harvester cannot work if the hot source is colder than the snap temperature, nor if the cold source is hotter than the snap-back temperature.

$$\Delta t_{heating} = R_{CH} \cdot C_v \cdot \ln \left(\frac{T_H - T_{SB,cav}}{T_H - T_{S,cav}} \right) \quad (5.2.4a)$$

$$\Delta t_{cooling} = R_{CC} \cdot C_v \cdot \ln \left(\frac{T_{S,cav} - T_C}{T_{SB,cav} - T_C} \right) \quad (5.2.4b)$$

Hence the cycling frequency of the system is

$$f = \frac{1}{C_v \cdot \left(R_{CC} \cdot \ln \left(\frac{T_{S,cav} - T_C}{T_{SB,cav} - T_C} \right) + R_{CH} \cdot \ln \left(\frac{T_H - T_{SB,cav}}{T_H - T_{S,cav}} \right) \right)} \quad (5.2.5)$$

If the thermal hysteresis of the beam is weak compared to the external gradient $T_H - T_C$, it can be approximated at the first order by (5.2.6).

$$f \approx \frac{1}{C_v \cdot \Delta T_{cav}} \cdot \frac{(T_o - T_C) \cdot (T_H - T_o)}{R_{CC} \cdot (T_H - T_o) + R_{CH} \cdot (T_o - T_C)} \quad (5.2.6)$$

This expression clearly shows that for a given set of temperatures (T_C , T_H , T_o), the switching frequency is higher for weakly unstable beams than for beams with large thermal hystereses. Moreover, it directly expresses the frequency as a function of the equivalent resistance of the switched capacitance R_{Cv} (5.2.7a) and the heat flux q_{eff} (5.2.7b). Assuming that the mean thermal hysteresis temperature T_o is equal to the average of the heat sources' temperatures, and that the contact resistances are equal, the thermal flux is given by (5.2.7c) and is a decreasing function of the thermal hysteresis.

$$R_{Cv} = \frac{1}{C_v \cdot f} \quad (5.2.7a)$$

$$\dot{q}_{eff} = \frac{\Delta T_{cav}}{R_{CC} \cdot \ln\left(\frac{T_{S,cav} - T_C}{T_{SB,cav} - T_C}\right) + R_{CH} \cdot \ln\left(\frac{T_H - T_{SB,cav}}{T_H - T_{S,cav}}\right)} \quad (5.2.7b)$$

$$\dot{q}_{eff} = \frac{1}{2 \cdot R_{CC}} \cdot \frac{\Delta T_{cav}}{\ln\left(1 + \frac{\Delta T_{cav}}{T_H - T_C}\right) - \ln\left(1 - \frac{\Delta T_{cav}}{T_H - T_C}\right)} \quad (5.2.7c)$$

With this expression, we can deduce the expression of the mean mechanical power generated by a harvester, that is the product of the strain energy by the frequency of the cycle (5.2.8a). By using (5.2.7c), the available power (5.2.8b) and thermal efficiency (5.2.8c) can be expressed as a function of the beam's thermal hysteresis in the cavity. A Carnot-relative efficiency can also be defined as a function of the device's working conditions.

$$P_M = f \cdot \Delta E_{mec} \quad (5.2.8a)$$

$$P_M = r \cdot \frac{\sqrt[3]{72 \cdot \left(r_w - \frac{r_w^3}{3}\right)^2 \cdot M_\alpha^4}}{N_e \cdot L \cdot C_v^3 \cdot R_{CC}^3} \cdot \frac{\sqrt[3]{\Delta T_{cav}^4}}{\ln\left(1 + \frac{\Delta T_{cav}}{T_H - T_C}\right) - \ln\left(1 - \frac{\Delta T_{cav}}{T_H - T_C}\right)} \quad (5.2.8b)$$

$$\eta_{TM}^{abs,int} = 2 \cdot r \cdot \sqrt{\frac{72 \cdot \left(r_w - \frac{r_w^3}{3}\right)^2 \cdot M_\alpha^4 \cdot \Delta T_{cav}}{N_e \cdot L \cdot C_v^3}} \quad (5.2.8c)$$

$$\eta_{TM}^{rel,int} = 2 \cdot r \cdot \sqrt{\frac{72 \cdot \left(r_w - \frac{r_w^3}{3}\right)^2 \cdot M_\alpha^4 \cdot \Delta T_{cav}}{N_e \cdot L \cdot C_v^3}} \cdot \frac{T_H + 273.15}{T_H - T_C} \quad (5.2.8d)$$

It is interesting to plot the evolution of the output power of the generator (Fig.5.2.2c) to see that it is not a monotonic function of the thermal hysteresis, but that it presents an optimal value for a given ratio of the beam's thermal hystereses. Clearly, for small thermal hystereses (either associated to naturally weakly unstable beams or to the cavity's thinning), the small amount of kinetic energy produced by the beam is counterbalanced by the increase of the beam's operating frequency (Fig.5.2.2a) and the

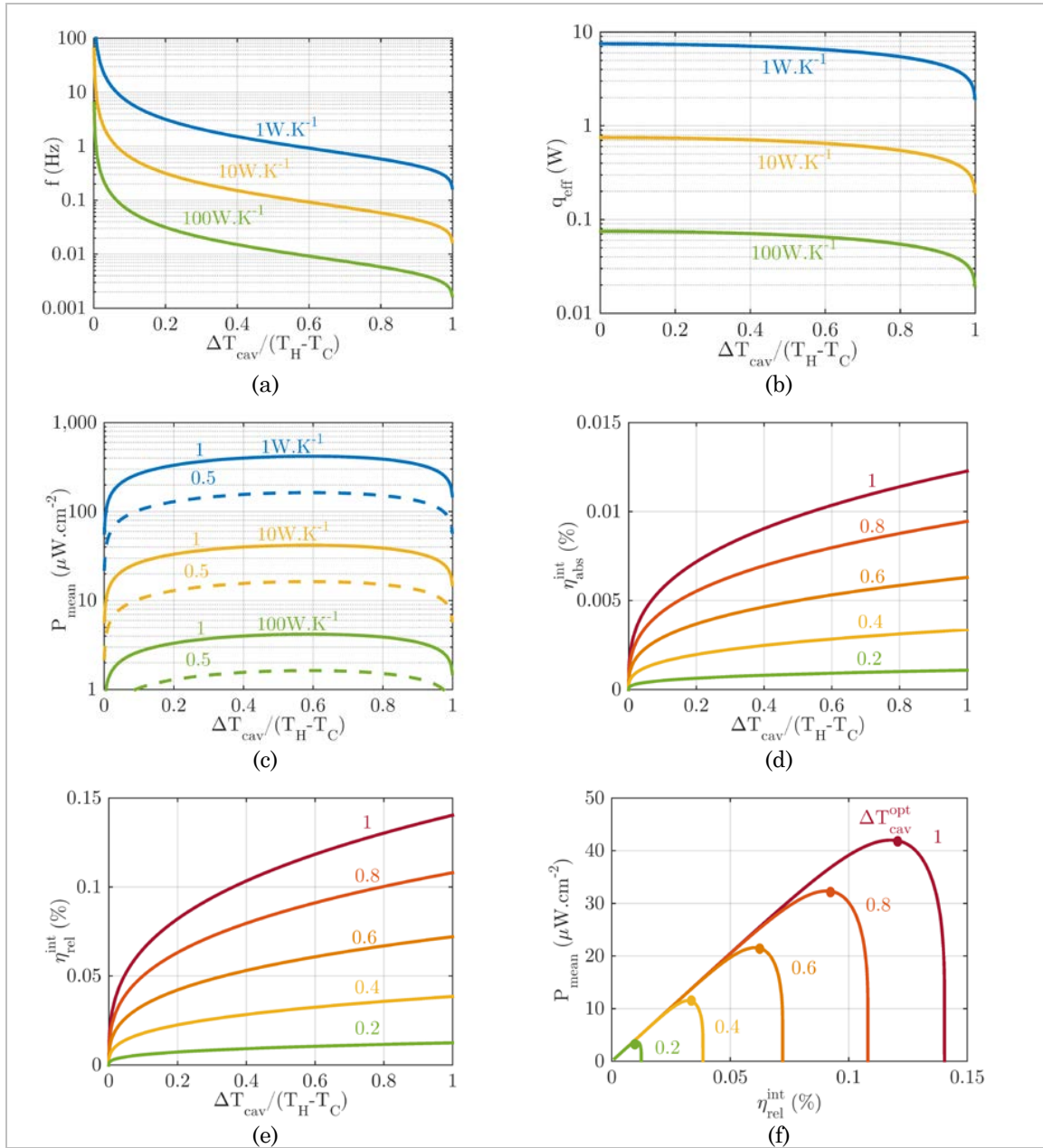


Figure 5.2.2. *a. Evolution of the frequency of an Al-Invar beam as a function of the ratio of the thermal gradients and for various values of the contact resistance R_{cc} . b. Evolution of the thermal flux as a function of the ratio of the thermal gradients and for various resistance's values and for $T_H - T_C = 30 \text{ K}$. c. Evolution of the output power for various values of R_{cc} and of the cavity's size factor r_w . d. Evolution of the thermal efficiency for $R_{cc} = 10 \text{ W.K}^{-1}$ and various values of the cavity's size factor. e. Carnot efficiency of the harvester in the same conditions. f. Surface power density against Carnot efficiency in the same conditions.*

thermal flux (Fig.5.2.2b). However, the thermal efficiency (Fig.5.2.2d) and the Carnot efficiency remain small (Fig.5.2.2e). For a contact resistance of 10 W.K^{-1} , the simulation of the operating frequency agrees with the experimental measurements (around 0.5 Hz).

Closer simulated values can be obtained with a contact resistance of 35 K.W^{-1} . In these conditions, the average surface power density is around $20\text{-}30 \mu\text{W.cm}^{-2}$ for an efficiency around $0.005\text{-}0.01\%$. Here again, the simulated values are in agreement with experimental data. Logically, by decreasing this contact resistance, the device's performances are boosted by the increase of the switching frequency of the prime mover. For large thermal hystereses, the output power is degraded by the reduction of the operating frequency, whereas the efficiency of the transduction is maximized. When the beam's hysteresis equals the temperature difference between the two heat sources, the Carnot efficiency is maximal and is given by (4.7.10a). As with the Carnot heat engine, this efficiency means that the harvester does not supply output power, since the transformation must be infinitely slow to be reversible, and the operating frequency is then null. In order to optimize the harvester, one should not first focus on the transduction efficiency but on the output power. The analysis of equation (5.2.8b) shows that the output power is maximal when the beam's thermal hysteresis approximately verifies (5.2.9a). This optimum is clearly visible in Fig.5.2.2f. Equation (5.2.9a) can be inverted in order to obtain the optimal beam's thermal hysteresis (5.2.9b) (see Fig.5.2.3a). For this optimal point, the maximal output power is given by (5.2.9c) and the thermal efficiency by (5.2.9d).

$$\Delta T_{cav}^{opt} \approx 0.589. (T_H - T_C) \quad (5.2.9a)$$

$$\Delta T^{opt} \approx 1.178. \frac{T_H - T_C}{3. r_w - r_w^3} \quad (5.2.9b)$$

$$P_M^{opt} \approx 1.52. r. \sqrt[3]{\frac{\left(r_w - \frac{r_w^3}{3}\right)^2 \cdot M_\alpha^4 \cdot (T_H - T_C)^4}{N_e \cdot L \cdot C_v^3 \cdot R_{CC}^3}} \quad (5.2.9c)$$

$$\eta_{TM}^{abs,int,opt} \approx 2.45. r. \sqrt[3]{\frac{\left(r_w - \frac{r_w^3}{3}\right)^2 \cdot M_\alpha^4 \cdot (T_H - T_C)}{N_e \cdot L \cdot C_v^3}} \quad (5.2.9d)$$

Instead of using the Carnot efficiency to compare the efficiency of the transduction with other harvesters, we define the Curzon-Ahlborn relative efficiency by (5.2.10a). Hence the maximal efficiency of the transduction is given by (5.2.10b).

$$\eta_{TM}^{CA,int} = 2. r. \sqrt[3]{\frac{72. \left(r_w - \frac{r_w^3}{3}\right)^2 \cdot M_\alpha^4 \cdot \Delta T_{cav}}{N_e \cdot L \cdot C_v^3}} \cdot \frac{\sqrt{T_H + 273.15}}{\sqrt{T_H} - \sqrt{T_C}} \quad (5.2.10a)$$

$$\eta_{TM}^{CA,int,opt} = 2.45. r. \sqrt[3]{\frac{\left(r_w - \frac{r_w^3}{3}\right)^2 \cdot M_\alpha^4 \cdot (T_H - T_C)}{N_e \cdot L \cdot C_v^3}} \cdot \frac{\sqrt{T_H + 273.15}}{\sqrt{T_H} - \sqrt{T_C}} \quad (5.2.9b)$$

The evolution of the device's performances is plotted in Fig.5.2.3 as a function of the external thermal gradient. This figures show that by increasing the temperature differences between the two heat sources, the output power and the thermal efficiency increase but the Curzon-Ahlborn efficiency decreases. For a hot and cold sources at 50°C and 25°C respectively, the energy harvester's efficiency and the output power represent

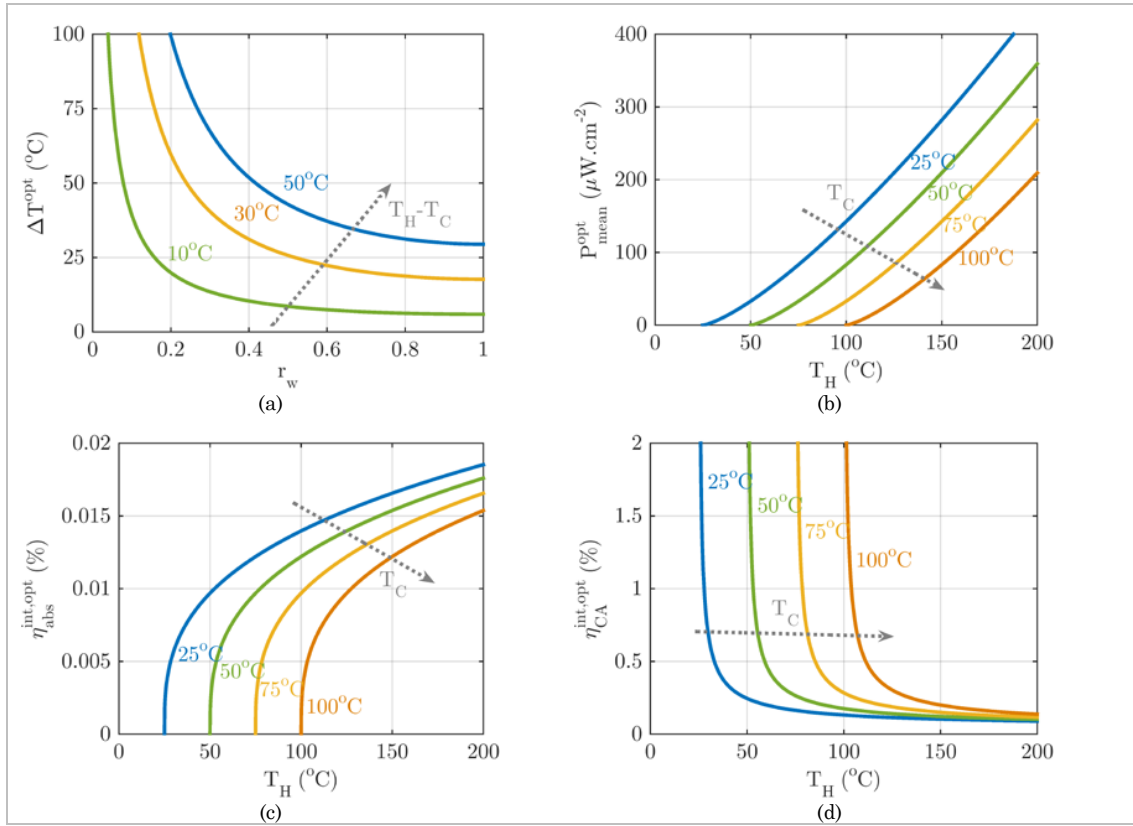


Figure 5.2.3. a. Evolution of the optimal bimetal's thermal hysteresis as a function of the cavity thinning and the thermal gradient. b. Evolution of the maximal output power as a function of the heat sources' temperatures. c. Evolution of the optimized thermal efficiency as a function of the heat sources' temperatures. d. Evolution of the Curzon-Ahlborn efficiency of the device.

around 0.25% of the maximal efficiency and maximal power that can be generated by a perfect endoreversible heat engine.

5.3 Leakage paths and heat sink

At this stage it becomes necessary to take into account the real conditions of the harvester and to include thermal leakages, as well as imperfect thermal transfers with the ambient surrounding, if the boundary conditions are Robin conditions instead of Dirichlet conditions (Temperature prescribed at the interface), as in the case of a heat sink. In the electrical model presented in Fig.5.2.1b, we have not taken into account the effect of the leakage path modeled by the resistance R_{leak} . As explained in Chapter 1, this resistance impacts the efficiency of the harvester since a part of the heat flowing from the hot source to the cold source travels through the leakage path and is not used to produce energy. A simple application of Kirchhoff's law gives the real efficiency of the device (5.3.1a). Most of the time, the leakage flux is dominant and the efficiency becomes (5.3.1b). The optimum thermal hysteresis is conserved but its efficiency decreases (5.3.1c).

$$\eta_{TM}^{abs,ext} = \frac{P_M}{\dot{q}_{leak} + \dot{q}_{eff}} \quad (5.3.1a)$$

$$\eta_{TM}^{abs,ext} = \frac{\dot{q}_{eff}}{\dot{q}_{leak}} \cdot \eta_{abs,1} \quad (5.3.1b)$$

$$\eta_{TM}^{abs,ext,opt} \approx 1.52 \cdot r \cdot \sqrt[3]{\frac{\left(r_w - \frac{r_w^3}{3}\right)^2 \cdot M_\alpha^4 \cdot R_{leak}^3 \cdot (T_H - T_C)}{N_e \cdot L \cdot C_v^3 \cdot R_{CC}^3}} \quad (5.3.1c)$$

The effect of the heat sink on thermal transfers can be modeled as a thermal resistance in series with the harvester: Boughaleb, 2015] proved that this assumption leads to a description of the harvester with a relatively good accuracy. The thermal gradient inside the harvester is simply given by the voltage divider equation (5.3.2).

$$T_H - T_C = \frac{R_{leak}}{R_{leak} + R_{sink}} \cdot (T_H - T_{amb}) \quad (5.3.2a)$$

$$P_M^{opt} \approx 1.52 \cdot r \cdot \sqrt[3]{\frac{\left(r_w - \frac{r_w^3}{3}\right)^2}{L}} \cdot \sqrt[3]{\frac{M_\alpha^4}{N_e \cdot C_v^3}} \cdot \sqrt[3]{\frac{R_{leak}^4}{R_{CC}^3 \cdot (R_{leak} + R_{sink})^4}} \cdot \sqrt[3]{(T_H - T_{amb})^4} \quad (5.3.2b)$$

$$\eta_{TM}^{abs,ext,opt} \approx 1.52 \cdot r \cdot \sqrt[3]{\frac{\left(r_w - \frac{r_w^3}{3}\right)^2}{L}} \cdot \sqrt[3]{\frac{M_\alpha^4}{N_e \cdot C_v^3}} \cdot \sqrt[3]{\frac{R_{leak}^4}{R_{CC}^3 \cdot (R_{leak} + R_{sink})^4}} \cdot \sqrt[3]{(T_H - T_{amb})} \quad (5.3.2c)$$

In these conditions, the Curzon-Ahlborn relative efficiency of the energy harvester is given by (5.3.3c).

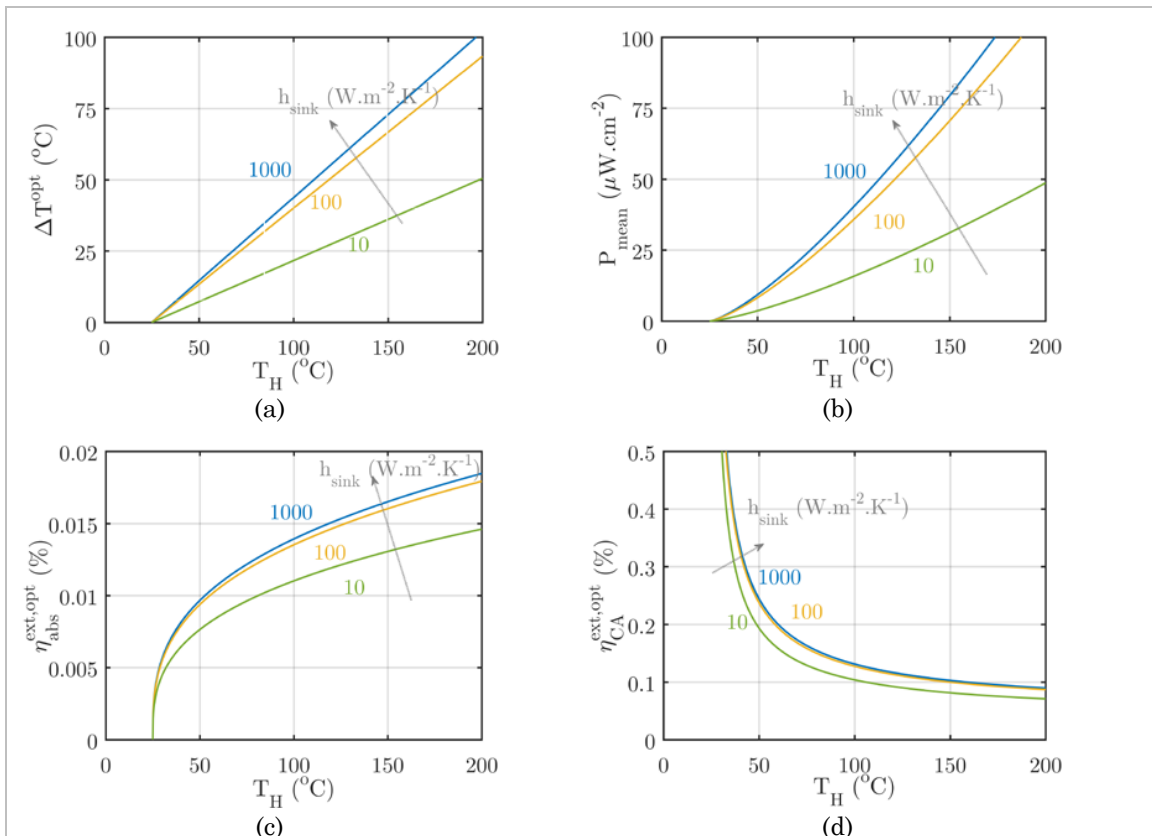
$$\eta_{TM}^{CA,ext,opt} \approx 1.52 \cdot r \cdot \sqrt[3]{\frac{\left(r_w - \frac{r_w^3}{3}\right)^2}{L}} \cdot \sqrt[3]{\frac{M_\alpha^4}{N_e \cdot C_v^3}} \cdot \sqrt[3]{\frac{R_{leak}^4}{R_{CC}^3 \cdot (R_{leak} + R_{sink})^4}} \cdot \sqrt[3]{(T_H - T_{amb})} \cdot \frac{\sqrt{T_H + 273.15}}{\sqrt{T_H} - \sqrt{T_{amb}}} \quad (5.3.3c)$$

To clarify these equations, Fig.5.3.1 presents the evolution of the parameters and performances of the energy harvester as a function of the hot source's temperature and for various values of the heat transfert coefficient of the heat sink used as a cold source of the system, assuming an ambient temperature of 25°C. The plane heat sink has a heat transfer coefficient of 10 W.m⁻².K⁻¹, representing a thermal resistance of 625 K.W⁻¹ if the heat sink has the same surface as the bistable beams. The leakage resistance of the harvester is taken equal to this value in order to be closer to the experimental conditions presented in [Boughaleb et al, 2015 1]. Fig.5.3.1a demonstrates that the presence of a heat sink with a great heat transfer coefficient allows the use of a prime mover with larger thermal hysteresis, and thus enables to generate more power with greater efficiency. For instance, at 100°C, a plane heat sink (10 W.m⁻².K⁻¹) limits the output power density to 16 μW.cm⁻² whereas this power can be more than doubled (35 μW.cm⁻²) by using a heat sink with cooling fins and with a heat transfer coefficient of 100 W.m⁻².K⁻¹. Whatever the type of heat sink, the operating frequency of the device is constant and independent of the working temperature (0.027 Hz). This observation was made on the current harvester without being explained: although the harvester was thermally optimized, no enhancement of the working frequency was observed. For the three types of heat sink, the

Curzon-Ahlborn efficiency is around 0.13% and is a decreasing function of the hot source temperature. From these results, it can be concluded that it is better to use a heat sink with cooling fins to increase the thermal gradient in the cavity and to improve the performances of the energy harvester, even if this heat sink would decrease the compactness of the device.

Finally we compare the performances of bimetallic beams with a fixed thermal hysteresis value of 3°C, with or without heat sink. The first curves in Fig.5.3.2a give the values of the snap and snap-back temperatures of the beams as a function of the hot source temperature. As an example, for a hot source at 100°C, without any heat sink (plane heat sink in fact), the best bimetal with a hysteresis of 3°C must snap at 83°C and snap back at 80°C. Experimentally, 80°C-77°C bimetals are used in the current harvester. When a heat sink is used, these values are lower because of the increased thermal gradient inside the cavity (65°C-68°C). At this temperature, the first harvester works at 0.22 Hz (in agreement with experimental data), whereas the heat sink boosts the frequency up to 0.41 Hz (Fig.5.3.2b). Fig.5.3.2c shows the evolution of the output power generated by the 3°C-hysteresis beam with and without heat sink. The presence of a heat sink almost doubles the surface density of power generated by the harvester whatever the hot source temperature (from 9.3 to 17.3 $\mu\text{W}\cdot\text{cm}^{-2}$).

Figure 5.3.1. *a. Optimal value of the thermal hysteresis as a function of the hot source temperature. b. Surface density of output power of the generator against hot source temperature. c. Thermal efficiency of the system. d. Curzon-Ahlborn efficiency of the device.*



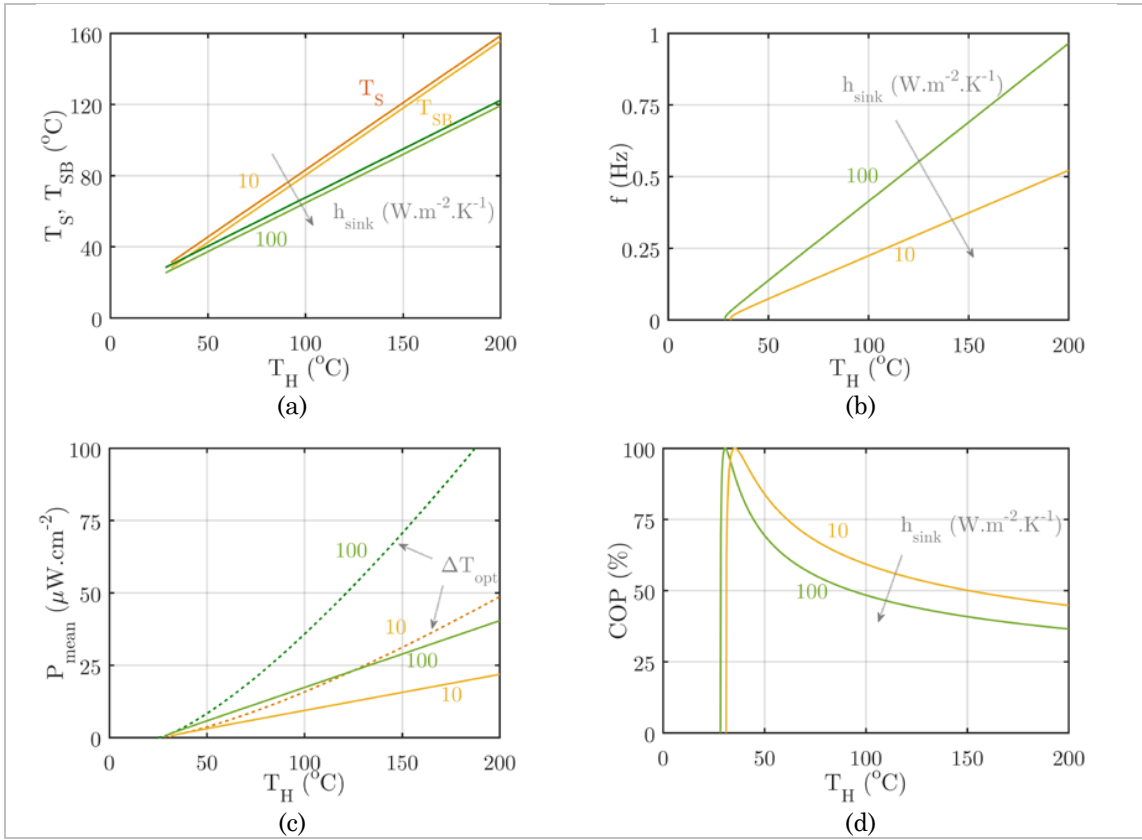


Figure 5.3.2. a. Optimal snap and snap-back temperatures of an Al-Invar beam assuming a fixed thermal hysteresis of 3°C. b. Operating frequency of the Al-Invar beam as a function of the hot source temperature. c. Surface densities of output power of the generator against hot source temperature for a 3°C thermal hysteresis and for the optimal thermal hysteresis. d. Coefficient of Performance of the system as a function of the hot source temperature and for the device working with and without a heat sink.

Fig.5.3.2c compares the output power of the 3°C hysteresis beam with the maximal output power generated by the beam with optimal thermal hysteresis. These values are still in agreement with experimental data. Fig.5.2.2d represents the ratio between these two efficiencies and defines a Coefficient of Performance (COP), given by (5.3.4). This figure shows that this COP is a decreasing function of the thermal hysteresis, after that the value of 3°C is not yet an optimal value, because the optimal thermal hysteresis widens with the hot source temperature. At 100°C, the 3°C-hysteresis beam reaches 59.4% of the maximal output power without heat sink and 48.3% with a heat sink.

$$COP(\Delta T) = \frac{P_M^{opt}}{P_M(\Delta T)} \quad (5.3.4)$$

5.4 Thermal transfers inside the bimetallic strip

To see the influence of the thermal transfers inside the prime mover on the cycling frequency of the system, we will treat the opposite case and assume that the beam experiences a thermal shock each time it comes in contact with the hot source or the cold source. First we need to establish the equation of the mechanical equilibrium with a spatially inhomogeneous temperature. Assuming that the temperature can be written as a function of separable variables (5.4.1a), the thermal properties of the beam can be modified into (5.4.1b) and (5.4.1c).

$$T(x, z) = T_x(x) \cdot T_z(z) \quad (5.4.1a)$$

$$N_\alpha = v \cdot \int_0^t E(z) \cdot \alpha(z) \cdot T_z(z) \cdot \delta z \quad (5.4.1b)$$

$$M_\alpha = v \cdot \int_0^t E(z) \cdot \alpha(z) \cdot T_z(z) \cdot (z - z_o) \cdot \delta z \quad (5.4.1c)$$

In this case, by applying the principle of virtual displacement, the expression of the axial strain is modified into (5.4.2a), with the definition of the mean temperature (5.4.2b). The non-linear Euler equation becomes (5.3.2c).

$$\mathcal{S}_{xx} = \frac{\lambda}{L} + \frac{N_\alpha}{N_e} \cdot (T_x(x) - \bar{T}) - (z - z_o) \cdot w_{,xx}(x, z_o) \quad (5.4.2a)$$

$$\bar{T} = \frac{1}{L} \cdot \int_0^L T(x) \cdot dx \quad (5.4.2b)$$

$$\frac{m_b}{L} \cdot w_{,tt}^2 + \left(N_\alpha \cdot \bar{T} - n_e \cdot \frac{\lambda}{L} - F_o \right) \cdot w_{,xx} + I_e \cdot w_{,xxxx} = M_\alpha \cdot T_{x,xx} \quad (5.4.2c)$$

Once the mechanical equations are established, we need to treat the propagation of heat along the half-length of the beam, assuming perfect contact with the hot source in $x = L/2$ and perfect isolation in $x = 0$. By using the separation of variables and the expression (5.4.3a) for the temperature distribution [Boley, 2012], the heat conduction problem can be easily treated and the Fourier heat transfer law becomes (5.3.3b). The boundary conditions of the problem are then given by (5.4.3c) and (5.4.3d). In these equations, κ represents the thermal diffusivity of the materials. To model the behavior of the composite beam, we take a mean value μ_b defined by (5.4.3e).

$$T(x, t) = \chi(x) \cdot \tau(t) + T_H \quad (5.4.3a)$$

$$\chi \cdot \tau_{,t} = \mu \cdot \tau \cdot \chi_{,xx} \quad (5.4.3b)$$

$$\chi(L/2) = 0 \quad (5.4.3c)$$

$$\chi_{,x}(0) = \chi_{,x}(L) = 0 \quad (5.4.3d)$$

$$\frac{1}{\mu_b} = \frac{1}{t} \cdot \int_0^t \frac{\rho \cdot C_v}{\kappa} \cdot \delta z \quad (5.4.3e)$$

The two differential equations to solve are then (5.4.4a) and (5.4.4b), introducing the constant λ .

$$\chi(x) = a \cdot \cos(\lambda \cdot x) + b \cdot \sin(\lambda \cdot x) \quad (5.4.4a)$$

$$\tau(t) = c \cdot \exp(-\lambda^2 \cdot \mu_b \cdot t) \quad (5.4.4b)$$

With the boundary conditions, it can be shown that χ is quantified and inversely proportional to the beam length (5.4.5b). The function χ is then a Fourier serie as well as the temperature distribution. During the heating of the beam (initial homogeneous temperature T_i), the temperature profile thus obeys (5.4.5d).

$$\chi_{,x}(0) = 0 \Rightarrow b = 0 \quad (5.4.5a)$$

$$\chi\left(\frac{L}{2}\right) = 0 \Rightarrow \lambda \cdot L = (2 \cdot n + 1) \cdot \pi \quad \text{for } n > 0 \quad (5.4.5b)$$

$$\chi(x) = \sum_{n=0}^{+\infty} a_{2 \cdot n + 1} \cdot \cos\left((2 \cdot n + 1) \cdot \pi \cdot \frac{x}{L}\right) \quad \text{pour } x \in \left[0, \frac{L}{2}\right] \quad (5.4.5c)$$

$$T(x, t) = T_H + \sum_{n=0}^{+\infty} 2 \cdot \frac{(T_i - T_H) \cdot (-1)^n}{(2 \cdot n + 1) \cdot \pi} \cdot e^{-(2 \cdot n + 1)^2 \cdot \frac{\pi^2}{L^2} \cdot \mu_b \cdot t} \cdot \cos\left((2 \cdot n + 1) \cdot \pi \cdot \frac{x}{L}\right) \quad (5.4.5d)$$

Once the initial heating of the beam is known, we can treat the periodic heating and cooling of the beam with the same procedure. The temperature profile on the beam's half-length during heating is given by (5.4.6a), and by (5.4.6b) during cooling. The working period of the system is given by (5.4.6c).

$$T_i^H(x, t) = T_H + \sum_{n=0}^{+\infty} a_{2 \cdot n + 1} \cdot e^{-(2 \cdot n + 1)^2 \cdot \frac{\pi^2}{L^2} \cdot \mu_b \cdot (t - \phi_i - \Delta t_C)} \cdot \cos\left((2 \cdot n + 1) \cdot \pi \cdot \frac{x}{L}\right) \quad (5.4.6a)$$

$$T_i^C(x, t) = T_C + \sum_{n=0}^{+\infty} b_{2 \cdot n + 1} \cdot e^{-(2 \cdot n + 1)^2 \cdot \frac{\pi^2}{L^2} \cdot \mu_b \cdot (t - \phi_i)} \cdot \cos\left((2 \cdot n + 1) \cdot \pi \cdot \frac{x}{L}\right) \quad (5.4.6b)$$

$$\phi_i = \Delta t_i + (i - 1) \cdot (\Delta t_H + \Delta t_C) \quad (5.4.6c)$$

By assuming the continuity of the thermal profile between the heating and cooling phases, we can deduce the expression of the Fourier serie's coefficients by solving the equatio system (5.4.7a-b) along the interval $[0, L/2]$.

$$a_{2 \cdot n + 1} \cdot \left(e^{-(2 \cdot n + 1)^2 \cdot \frac{\pi^2}{L^2} \cdot \mu_b \cdot \Delta t_H} - 1 \right) = b_{2 \cdot n + 1} \cdot \left(1 - e^{-(2 \cdot n + 1)^2 \cdot \frac{\pi^2}{L^2} \cdot \mu_b \cdot \Delta t_C} \right) \quad (5.4.7a)$$

$$T_H - T_C = \sum_{n=0}^{+\infty} a_{2 \cdot n + 1} \cdot \left(\frac{e^{-(2 \cdot n + 1)^2 \cdot \frac{\pi^2}{L^2} \cdot \mu_b \cdot (\Delta t_C + \Delta t_H)} - 1}{1 - e^{-(2 \cdot n + 1)^2 \cdot \frac{\pi^2}{L^2} \cdot \mu_b \cdot \Delta t_C}} \right) \cdot \cos\left((2 \cdot n + 1) \cdot \pi \cdot \frac{x}{L}\right) \quad (5.4.7b)$$

In order to apply the Galerkin method to the mechanical equilibrium equation, the thermal profile must be developed in Fourier series along the whole beam's length during heating (5.4.8a) and cooling. The coefficients c_n during heating can be calculated as functions of the a_n coefficients in (5.4.8b).

$$f(x) = \sum_{n=0}^{+\infty} c_n \cdot e^{-\frac{\pi^2}{L^2} \cdot \mu_b \cdot (t - \phi_i - \Delta t_C)} \cdot \sin\left(n \cdot \pi \cdot \frac{x}{L}\right) \quad (5.4.8a)$$

$$\begin{aligned} & c_{2,n+1} \\ &= \frac{2}{\pi} \cdot \sum_{i=0}^{+\infty} \frac{a_{2,i+1}}{2 \cdot i + 1} \cdot e^{-\frac{\pi^2}{L^2} \cdot \mu_b \cdot (t - \phi_i - \Delta t_C)} \\ &+ \frac{1}{\pi} \cdot \sum_{\substack{i=0 \\ i \neq n}}^{+\infty} a_{2,i+1} \cdot \frac{2 \cdot n - 2 \cdot i \cdot (-1)^{n+i} + 1 - (-1)^{n+i}}{(n-i) \cdot (i+n+1)} \cdot e^{-\frac{\pi^2}{L^2} \cdot \mu_b \cdot (t - \phi_i - \Delta t_C)} \end{aligned} \quad (5.4.8b)$$

Given that we only study the first-order buckling mode, only the first Fourier coefficient c_1 matters. In its expression, we can neglect other terms after the first terms a_1 . This could be partly justified by the n -decay of the a_n parameters. With this assumption, the first term a_1 is given by (5.4.9a) and the equilibrium equation during the beam's heating becomes (5.4.9b).

$$a_1 = 2 \cdot (T_H - T_C) \cdot \frac{1 - e^{-\frac{\pi^2}{L^2} \cdot \mu_b \cdot \Delta t_C}}{e^{-\frac{\pi^2}{L^2} \cdot \mu_b \cdot (\Delta t_C + \Delta t_H)} - 1} \quad (5.4.9a)$$

$$\frac{N_e \cdot \pi^2}{4 \cdot L^2} \cdot w_1^3 + \left(I_e \cdot \frac{\pi^2}{L^2} - N_o \right) \cdot w_1 + \frac{4 \cdot (M_o - M_\alpha \cdot T_H)}{\pi} - \frac{2 \cdot M_\alpha}{\pi} \cdot a_1 \cdot e^{-\frac{\pi^2}{L^2} \cdot \mu_b \cdot (t - \phi_i - \Delta t_C)} = 0 \quad (5.4.9b)$$

In this case, the beam switches when its temperature profile verifies (5.3.10a) during heating and (5.4.10b) during cooling.

$$(T_H - T_C) \cdot \frac{1 - e^{-\frac{\pi^2}{L^2} \cdot \mu_b \cdot \Delta t_C}}{e^{-\frac{\pi^2}{L^2} \cdot \mu_b \cdot (\Delta t_C + \Delta t_H)} - 1} \cdot e^{-\frac{\pi^2}{L^2} \cdot \mu_b \cdot \Delta t_H} = T_S - T_H \quad (5.4.10a)$$

$$(T_C - T_H) \cdot \frac{1 - e^{-\frac{\pi^2}{L^2} \cdot \mu_b \cdot \Delta t_H}}{e^{-\frac{\pi^2}{L^2} \cdot \mu_b \cdot (\Delta t_C + \Delta t_H)} - 1} \cdot e^{-\frac{\pi^2}{L^2} \cdot \mu_b \cdot \Delta t_C} = T_{SB} - T_C \quad (5.4.10b)$$

By solving this equation system, we finally find solutions close to (5.2.4b) and (5.2.4c) obtained with the lumped capacitance model (5.4.11). The evaluation of the operating frequency of the system shows that this value is too high to explain the frequencies measured experimentally. This shows that the thermal transfers are limited by the contact resistance between the heat sources and the bistable beam.

$$\Delta t_H = \frac{L^2}{\pi^2 \cdot \mu_b} \cdot \ln\left(\frac{T_H - T_{SB}}{T_H - T_S}\right) \quad (5.4.11a)$$

$$\Delta t_C = \frac{L^2}{\pi^2 \cdot \mu_b} \cdot \ln\left(\frac{T_S - T_C}{T_{SB} - T_C}\right) \quad (5.4.11b)$$

$$f = \frac{\pi^2 \cdot \mu_b}{2 \cdot L^2} \cdot \frac{1}{\ln\left(\frac{T_S - T_C}{T_{SB} - T_C}\right) + \ln\left(\frac{T_H - T_{SB}}{T_H - T_S}\right)} \quad (5.4.11c)$$

A simple calculation of the heat supplied to the beam during the heating phase shows that the quantity of heat is preserved. A more accurate model would have taken into account

the fact that the Biot number is not infinite, leading to a result similar to the one presented in (Boley, 2012), by taking into account the difference of propagation in both layers and the influence of the contact size on the heat transfers [Incropera and DeWitt, 2002], or by taking into account higher-mode Fourier coefficients. However, these models would lose in comprehension what they would attempt to gain in precision.

$$Q_H = C_v \cdot (T_S - T_{SB}) \quad (5.4.12)$$

The previous calculations are still valid, and the optimal power and the thermal efficiency of the optimal point are given by (5.4.13). These formulae are written in a way to separate geometric parameters from physical parameters of the composite beams, and to define new Figures of Merit taking into account the thermal diffusive properties of materials: FOM_f is directly equal to the thermal diffusivity of the beam and is the Figure of Merit of the device's operating frequency (5.4.13c), FOM_P the Figure of Merit of the maximal output power (5.4.13d), and FOM_η the Figure of Merit of the efficiency associated to the optimal thermal gradient (5.4.13e).

$$P_M^{opt} \approx 1.52 \cdot \pi^2 \cdot r \cdot \sqrt[3]{\frac{\left(r_w - \frac{r_w^3}{3}\right)^2}{L^7}} \cdot \sqrt[3]{\frac{M_\alpha^4 \cdot \mu_b^3}{N_e}} \cdot \sqrt[3]{(T_H - T_C)^4} \quad (5.4.13a)$$

$$\eta_{TM}^{abs,int} \approx 2.45 \cdot r \cdot \sqrt[3]{\frac{\left(r_w - \frac{r_w^3}{3}\right)^2}{L}} \cdot \sqrt[3]{\frac{m_\alpha^4}{N_e \cdot C_v^3}} \cdot \sqrt[3]{T_H - T_C} \quad (5.4.13b)$$

$$FOM_f = \mu_b \quad (5.4.13c)$$

$$FOM_P = \sqrt[3]{\frac{M_\alpha^4 \cdot \mu_b^3}{N_e}} \quad (5.4.13d)$$

$$F_\eta = \sqrt[3]{\frac{M_\alpha^4}{N_e C_v^3}} \quad (5.4.13e)$$

The comparison of these three Figures of Merit is presented in Fig.5.4.1 for twenty-five bimetallic couples. This figures shows that the best materials are not only the materials with the largest difference of thermal expansion coefficients but also with the largest thermal diffusivity. As explained in Section 4.5, bimetallic couples made of Aluminum are best suited for the conversion of heat into mechanical energy

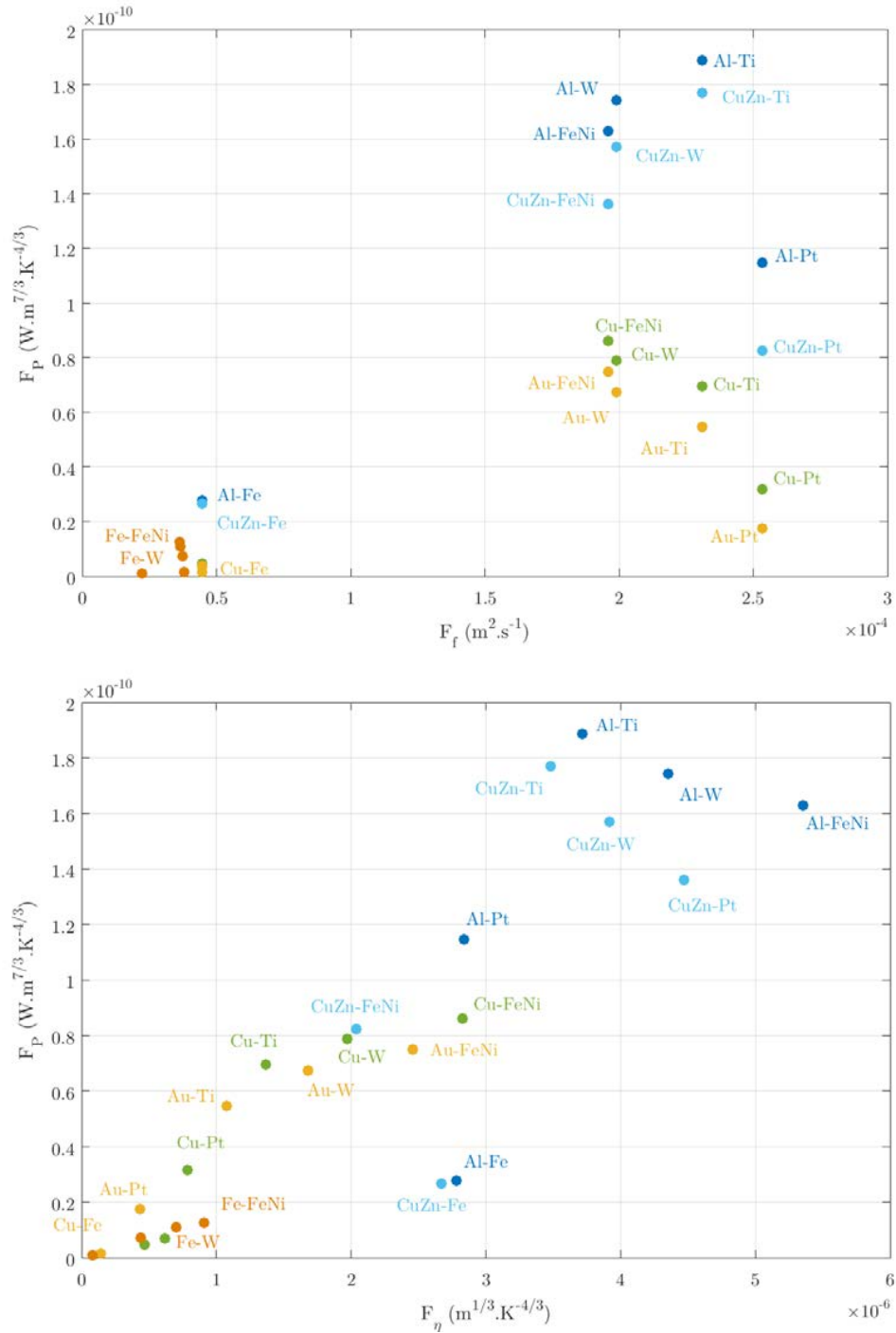


Figure 5.4.1. a. Figure of merit of the output power versus thermal diffusivity. b. Figure of merit of the output power vs thermal efficiency.

6 Conclusion

In this first chapter about the working principle of our device, we presented the modeling of the thermo-mechanical instability of composite beams using the principle of virtual displacement. This model helped us explain the origins of the thermal snap-through of simply-supported beams either initially stressed or initially curved. For both cases, we found the criterion of bistability and described the evolution of the critical load, of the characteristic temperatures of hysteresis, and of the beam displacement associated to the first and second order buckling modes. For initially-curved bimetallic beams, we proved that our model was more accurate than Timoshenko's model since it takes into account the mean thermal expansion of beams.

Contrary to a simple study of the thermal snap-through of composite beams, we also clarified the thermodynamic properties of bistable beams, and studied the evolution of the strain energy and the entropy of such structures. This enabled us to show the equivalence between thermal snap-through of thermo-mechanically bistable beams and first-order phase transition. With these results, we explained the thermodynamic cycle of the bimetallic strip heat engine and we theoretically demonstrated the possibility to harvest heat with bistable beams. By using these results, we first evaluated the performances of our heat engine for various types of bimetallic couples. We found that in the best cases, the efficiency of the thermo-mechanical transduction does not exceed few percents of Carnot when the thermal hysteresis is below 1°C, and is generally of around 0,1% of the Carnot efficiency. In agreement with the data reported in the first chapter and with experimental data, these various results also support the idea that bimetallic strip heat engines are less efficient than thermoelectric generator to harvest heat fluxes, and thus contradict the estimations reported in Puscasu's thesis (Puscasu, 2014).

Because of the complexity of this first model based on non-linear mechanics, we developed in a second time a reduced order model based on a Ritz approximation of the beam's deflection and the application of the Galerkin method. This second model enabled us to analytically extract the properties of bistable beams, and to describe the performances of the heat engine (available energy, maximal power, switching force, switching speed, latent heat of snap, thermal efficiency, Carnot efficiency) as functions of the physical parameters of the mechanical structures. The most important formula found with this model are reported in Table 6. We finally established Figures of Merit to compare the materials, showing that performances are improved by the use of materials with large difference of thermal expansion coefficients, justifying the use of Invar as a material for the passive layer.

By modeling the double role played by the architecture which must ensure thermal transfers between the heat sources and the bimetallic strip by applying mechanical action on this strip, we show how it modifies the performances of the energy harvester but also how the switching frequency of the bimetallic strip evolves as function of the physical properties of the bimetallic strip's materials. We showed that thermal transfers are mainly driven by the contact resistance between the heat sources and the prime mover and not by the thermal transfers inside the prime mover, explaining why the switching frequency of the device has never exceeded few tenths of hertz so far, and the generated power few microwatts. As a consequence, future investigations to increase the performances of the generator must be carried on the improvement of thermal transfers

In the last part of this chapter, we studied and modeled the thermal transfers inside the harvester in order to understand their role in the dynamic behavior of the system. This led us to find expressions of the device's operating frequency, maximal power and efficiency as functions of the external working conditions. A first lumped-capacitance model helped us to find leakage paths inside the energy harvester and to quantify their impact on the device's efficiency. A second model was established to characterize the propagation of heat in the bistable beam and to see its impact on the working frequency of the device.

7 Bibliography

- Aggarwala, B. and Saibel, E. (1970). Thermal stability of bimetallic shallow spherical shells. *International Journal of Non-Linear Mechanics*, 5(1), pp.49-62.
- Banerjee, B. and Datta, S. (1981). A new approach to an analysis of large deflections of thin elastic plates. *International Journal of Non-Linear Mechanics*, 16(1), pp.47-52.
- Batista, M. and Kosel, F. (2007). Thermoelastic stability of bimetallic shallow shells of revolution. *International Journal of Solids and Structures*, 44(2), pp.447-464.
- Bauer, H. (1968). Nonlinear Response of Elastic Plates to Pulse Excitations. *Journal of Applied Mechanics*, 35(1), p.47.
- Berger, Howard M. (1954) *A new approach to the analysis of large deflections of plates*. Dissertation (Ph.D.), California Institute of Technology.
- Boley, B. (2012). *Theory of Thermal Stresses*. Dover Publications.
- Boughaleb, J., Arnaud, A., Cottinet, P., Monfray, S., Gelenne, P., Kermel, P., Quenard, S., Boeuf, F., Guyomar, D. and Skotnicki, T. (2015). Thermal modeling and optimization of a thermally matched energy harvester. *Smart Mater. Struct.*, 24(8), p.085025.
- Bryan, G. (1890). On the Stability of a Plane Plate under Thrusts in its own Plane, with Applications to the "Buckling" of the Sides of a Ship. *Proceedings of the London Mathematical Society*, s1-22(1), pp.54-67.
- Burgreen, D. and Regal, D. (1971), Higher mode buckling of bimetallic beam. *Journal of the Engineering Mechanics Division*, 97(4), pp.1045-1056
- Cabal, A. and Ross, D. S. (2002), Snap-Through Bilayer Microbeam, *Nanotech* 1 230–3
- Callen, H. (1960). *Thermodynamics*. New York: Wiley.
- Domokos, G., Holmes, P. and Royce, B. (1997). Constrained Euler buckling. *Journal of Nonlinear Science*, 7(3), pp.281-314.
- Euler, L. (1744). *Methodus inveniendi lineas curvas maximi minimive proprietate gaudentes*. Lausannæ: apud Marcum-Michaelem Bousquet & socios.
- Fox, N. (1969). Generalised thermoelasticity. *International Journal of Engineering Science*, 7(4), pp.437-445.
- Heuer, R. and Ziegler, F. (2004). Thermoelastic stability of layered shallow shells. *International Journal of Solids and Structures*, 41(8), pp.2111-2120.

- Incropera, F. and DeWitt, D. (2002). *Fundamentals of heat and mass transfer*. New York: J. Wiley.
- Irschik, H. (1986). Large thermoelastic deflections and stability of simply supported polygonal panels. *Acta Mechanica*, 59(1-2), pp.31-46.
- Karlsson, A. and Bottega, W. (2000). On thermal buckling of patched beam-plates. *International Journal of Solids and Structures*, 37(34), pp.4655-4690.
- Kiani, Y. and Eslami, M. (2010). Thermal buckling analysis of functionally graded material beams. *International Journal of Mechanics and Materials in Design*, 6(3), pp.229-238.
- Marguerre, K. (1947). *On the application of the energy method to stability problems*. Washington, D.C.: National Advisory Committee for Aeronautics.
- Michael, A. and Kwok, C. (2006). Design criteria for bi-stable behavior in a buckled multi-layered MEMS bridge. *Journal of Micromechanics and Microengineering*, 16(10), pp.2034-2043.
- Mises, R. (1923). Über die Stabilitätsprobleme der Elastizitätstheorie. *ZAMM - Zeitschrift für Angewandte Mathematik und Mechanik*, 3(6), pp.406-422.
- Moghaddasie, B. and Stanciulescu, I. (2013). Equilibria and stability boundaries of shallow arches under static loading in a thermal environment. *International Journal of Non-Linear Mechanics*, 51, pp.132-144.
- Murphy, K. and Ferreira, D. (2001). Thermal buckling of rectangular plates. *International Journal of Solids and Structures*, 38(22-23), pp.3979-3994.
- Niino, M. and Maeda, S. (1990). Recent development status of functionally gradient materials. *ISIJ International*, 30(9), pp.699-703.
- Nowacki, W. (1970). Problems of thermoelasticity. *Progress in Aerospace Sciences*, 10, pp.1-63.
- Orthwein, W. (1984). Thermal Buckling of a Bimetallic Strip. *Journal of Vibration Acoustics Stress and Reliability in Design*, 106(4), p.538.
- Pandey, A., Moulton, D., Vella, D. and Holmes, D. (2014). Dynamics of snapping beams and jumping poppers. *Europhysics Letters*, 105(2), p.24001.
- Puscasu, O., Dispositifs innovants pour la récupération de l'énergie thermique. Thermique [physics.class-ph]. INSA de Lyon, 2014. Français.
- Ravichandran, K. (1995). Thermal residual stresses in a functionally graded material system. *Materials Science and Engineering: A*, 201(1-2), pp.269-276.
- Reddy, J. and Reddy, J. (2006). *Theory and analysis of elastic plates and shells*. Boca Raton, Fla.: CRC.
- Rohsenow, W. and Hartnett, J. (1973). *Handbook of heat transfer*. New York: McGraw-Hill.
- Rutgerson, S. and Bottega, W. (2002). Thermo-elastic buckling of layered shell segments. *International Journal of Solids and Structures*, 39(19), pp.4867-4887.
- Samsam Shariat, B. and Eslami, M. (2006). Thermal buckling of imperfect functionally graded plates. *International Journal of Solids and Structures*, 43(14-15), pp.4082-4096.

- Schuman, L. and Back, G. (1930). *Strength of rectangular flat plates under edge compression*. Washington, D.C.: G.P.O.
- Shukla, K. and Nath, Y. (2002). Buckling of Laminated Composite Rectangular Plates Under Transient Thermal Loading. *Journal of Applied Mechanics*, 69(5), p.684.
- Tauchert, T. (1991). Thermally Induced Flexure, Buckling, and Vibration of Plates. *Applied Mechanics Reviews*, 44(8), p.347.
- Timoshenko, S. (1925), Analysis of bi-metal thermostat, *Journal of the Optical Society of America*, 11(3), p.233.
- Timoshenko, S. and Gere, J. (1961). *Theory of elastic stability*. New York: McGraw-Hill.
- Thompson, J. and Hunt, G. (1973). *A general theory of elastic stability*. London: J. Wiley.
- Thornton, E. (1993). Thermal Buckling of Plates and Shells. *Applied Mechanics Reviews*, 46(10), p.485.
- Uzunov, D. (1993). *Introduction to the theory of critical phenomena*. Singapore: World Scientific.
- Vahidi, B. and Huang, N. (1969). Thermal Buckling of Shallow Bimetallic Two-Hinged Arches. *Journal of Applied Mechanics*, 36(4), p.768.

Chapter 3

Conversion of the mechanical energy into electrical energy

1 Introduction

The previous chapter addressed the issue of modeling the thermo-mechanical behavior of composite beams, and demonstrated the capability of a bistable beam to behave like a heat engine and to convert thermal energy into mechanical energy when it is placed between two heat sources. The aim of a thermal energy harvester being to create electrical charges from heat, it is necessary to study the various ways to convert mechanical energy into electric energy. The literature on the harvesting of mechanical energy shows that two solutions are mainly conceivable due to their ease of implementation and their efficiency: piezoelectric conversion (and pyroelectric conversion) and electret-based capacitive transduction.

Four different types of harvesters will be studied in this chapter. Fig.1a represents the architecture of a thermo-mechanically bistable piezoelectric composite membrane: when the composite membrane deforms due to thermal stress, part of the mechanical energy is directly converted into electric charges stored in the piezoelectric capacitance. This first architecture presents numerous advantages: first, even if the variation of the strain energy of the switching membrane is quite large during a complete cycle, this variation does not reflect the strain energy variations seen by each layer of the composite beam which can experience a large amount of stress, either tensile or compressive. However this stress, especially when it is tensile, can speed up aging of piezoelectric materials and ceramics [Chaplya *et al*, 2006, Tsujiura *et al*, 2014]. Another advantage of this architecture is the possibility to exploit the pyroelectric effect of some materials to significantly improve the performances of the harvester. Contrary to the third architecture, the thermal optimization of the harvester is decorrelated from the optimization of the electro-mechanical conversion. Yet the advantages of thermally cycling a piezoelectric material deposited on the bistable membrane can be counterbalanced by

the increase of the leakage current at high temperatures [Lipscomb *et al*, 2009] and by the operating limit imposed by the Curie point and the loss of polarization in the case of ferroelectric materials [Olsen and Evans, 1983]. Finally, another advantage of the bistable piezoelectric composite membrane is the possibility to fabricate either at the macroscale by depositing piezoelectric layer on a bistable membrane [Capsal *et al*, 2012, Savelli *et al*, 2014], or to process them at the microscale by using conventional MEMS fabrication techniques [Michael and Kwok, 2006, Arnaud *et al*, 2013, Trioux *et al*, 2014] and the availability of methods to deposit piezoelectric materials (ZnO, AlN, PZT, BaTiO₃ etc.). In that case, the piezoelectric layer can also play the role of the thermally passive layer of the bistable membrane. However, the size reduction of the piezoelectric harvester is accompanied by an increase of the impedance of the system and the reduction of the output voltages of the piezoelectric generators, which represents a challenge for the development of adapted power management circuits.

Fig.1b represents the coupling between a bistable composite beam and two piezoelectric stacks. In this case, the piezoelectric stacks harvest the work of the thrust exerted by the bistable beam on its clamps. Contrary to the first architecture, the temperature variations inside the piezoelectric stacks would be negligible and the pyroelectric effect would not have any impact on the performances of the harvester. This architecture has been conceived to exploit the high piezoelectric coupling factor of the 3-3 mode. However, the high compressive stiffness of piezoelectric stacks can reduce the efficiency of the transduction, if the bistable beam is not able to deform the stacks sufficiently. Here again, contrary to the third architecture, the fact that the thermal optimization of the harvester is decoupled from its electromechanical optimization can represent a benefit for the improvement in performances of the harvester.

Fig.1c represents the coupling between a bistable composite beam and oscillating piezoelectric transducer. This solution represents the first architecture that has experimentally been developed at ST-Microelectronics [Puscasu *et al*, 2012, Arnaud *et al*, 2013, Boughaleb *et al*, 2015]. In this configuration, the switching membrane hits a clamped-clamped bimorph beam that converts the energy due to the impact of the bistable beam into electric energy by using conventional power management circuits dedicated to piezoelectric mechanical energy harvesters. The initial idea which lead to this architecture was the possibility to use the piezoelectric oscillating beam both as an electromechanical transducer and a heat exchanger. This way, the thermal energy harvester would be able to work without any heat sink, thus increasing the compactness of the device. However this strategy presents the drawback to intimately link the optimization of the mechanical energy transfer between the bistable membrane and the piezoelectric transducer, and the optimization of the thermal gradient inside the cavity of the harvester [Boughaleb *et al*, 2015]. Moreover, this type of system requires an additional conversion step (mechanical shock between the transducer and the bistable membrane) which efficiency impacts the global efficiency of the harvester. It has also been observed that the type of material used for the fabrication of the passive part of the system has an impact on the mechanical damping of the piezoelectric oscillator and reduces the efficiency of the electromechanical transduction. Yet these mechanical losses can be reduced by the design of adapted piezoelectric oscillators [Arnaud *et al*, 2013].

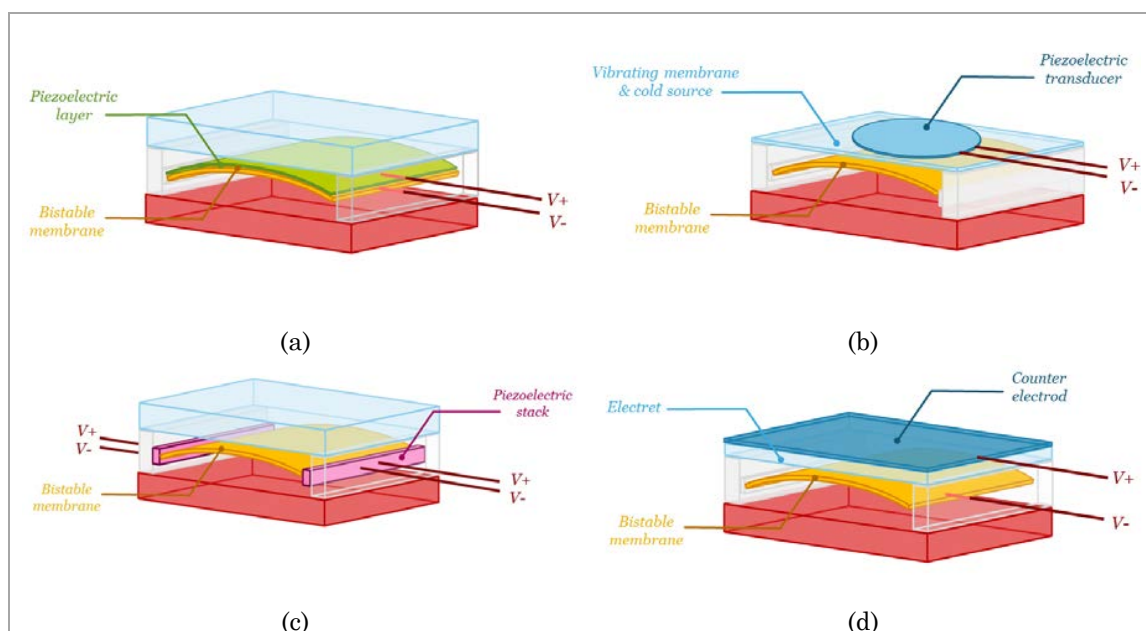


Figure 1.1. *a. Piezoelectric bimetallic strip heat engine. b. Coupling between a piezoelectric transducer and a bimetallic strip heat engine. c. Coupling between a bimetallic strip and a 3-3 piezoelectric stack. d. Coupling between a bimetallic strip and an electret transducer.*

Finally Fig.1d represents the coupling between a bistable composite beam and an electret. This type of device was jointly developed with the CEA-Leti [Boisseau *et al*, 2013, Arnaud *et al*, 2013]. In this configuration, the switching bistable beam displaces electrical charges in the electrical field induced by an electret, causing at the same time a variation of the capacitance formed by the bistable membrane and a counter-electrode placed on the opposite side of the electret. Contrary to other electrostatic converters, electret-based transducers are passive devices that do not require any external voltage source to harvest energy. When electrets are fabricated using a Corona discharge, their surface potential can easily be controlled and adjusted [Sessler, 1987], which allows to control and optimize the coupling between the bistable membrane and the electret. The high output voltages of the electret-based transducer ease the implementation of dedicated power management circuits [Boisseau, 2011] even if their performances can be impacted by the small variations of capacitance of the bistable beam and the presence of parasitic capacitances. Largely used for the fabrication of microphones [Kestelman *et al*, 2000] the integration of electrets in MEMS devices is perfectly controlled, making it possible to consider the size reduction of the electrostatic bimetallic strip heat engine. Moreover reliability tests reported in the literature [Suzuki, 2011] or performed at the CEA on our devices have shown the high stability of Corona electrets. From an industrial point of view, electret-based transducers thus represent low-cost energy harvesting solutions that are effective at the macroscale as well as at the microscale.

This chapter is divided as follows: in Section 2 we explain the origins of piezoelectricity. Sections 3 and 4 are devoted to the modeling of the pyroelectric bimetallic strip heat engine, Section 5 to the coupling between an oscillating piezoelectric transducer and a bistable beam, and Section 6 to the electret-based capacitive transduction. For these two

architectures, theoretical results will be compared with experimental data. Finally, Section 7 presents a synthesis of the device performances and a comparison of the various architectures.

2 An overview on piezoelectricity

2.1 The history of piezoelectricity

Piezoelectricity refers to the property of some dielectric materials to produce electrical charges in response to a mechanical stress or, reversely, to deform when they are placed in an electric field. Although the direct effect and the reverse effect were scientifically explained at the end of the 19th century (the direct effect was studied by Jacques and Pierre Curie in 1880 [Curie and Curie, 1880] and the reverse effect suggested by Gabriel Lippmann in 1881 [Lippmann, 1881] and demonstrated by the Curie brothers [Curie and Curie, 1881], first applications of the piezoelectricity appeared at the beginning of the 20th century [Brissaud and Baland, 2007] mainly in the field of acoustics (Langevin's ultrasonic transducer in 1919 (Sonar)) and in the field of electro-mechanical resonators and filters (Quartz oscillators by Cady in 1921). Piezoelectricity is currently used in sensors, mechanical actuators, ultrasonic transducers, microphones, SAW filters, delay lines, clocks, gas lighters... [Tichy *et al*, 2010]. Applications in energy harvesting only appear in the middle of the 1980s and really emerge in the 1990: [Häsler *et al*, 1984] probably reported the first use of piezoelectric materials (PVDF) for the generation of electrical energy.

Pyroelectricity is the property of some classes of piezoelectric materials that polarize under a variation of their temperature. The study of the pyroelectric effect by William Thomson (Lord Kelvin) is prior to the study of piezoelectricity [Thomson, 1878] and the explanation of the links between pyroelectricity and piezoelectricity is due to Woldemar Voigt's work, who thermodynamically described both effects in 1890. Pyroelectricity is currently exploited in infrared photodetectors and thermal imaging [Lang, 2005]. First investigations on the use of the pyroelectric effect to harvest heat are linked to [Clingman and Moore, 1961].

The following paragraphs address basic knowledge about piezoelectricity and pyroelectricity. First we come back to the electrostatic behavior of dielectric materials and then we explain the constitutive equations of piezoelectric and pyroelectric materials by means of the expression of the internal energy, which allows to introduce a classification of piezoelectric and pyroelectric materials. We finally introduce piezoelectric and pyroelectric coupling factors and we simplify the constitutive equations of piezoelectric materials for the study of piezoelectric beams and for 3-1 and 3-3 coupling.

2.2 Thermodynamics of piezoelectric materials

In order to understand the origins of the piezoelectric, pyroelectric and electrocaloric effects, we go back to the local expression of the internal energy u of a dielectric material placed in a stress field and an electrostatic field. The internal energy being a function of extensive parameters it is a privileged function of the entropy σ , the strain tensor S_i and the electrical displacement matrix D_i (2.2.1).

$$du = \theta \cdot d\sigma + \mathcal{T}_i \cdot d\mathcal{S}_i + \mathcal{E}_i \cdot d\mathcal{D}_i \quad (2.2.1)$$

The absolute temperature θ , the stress tensor T_i and the electrical field matrix E_i are then defined as the first partial derivatives of the internal energy (2.2.2).

$$\theta = \left. \frac{\partial u}{\partial \sigma} \right|_{\mathcal{S}_i, \mathcal{D}_i} = u_{,\sigma}^{\mathcal{S}, \mathcal{D}} \quad (2.2.2a)$$

$$\mathcal{T}_i = \left. \frac{\partial u}{\partial \mathcal{S}_i} \right|_{\sigma, \mathcal{D}_i} = u_{,\mathcal{S}_i}^{\sigma, \mathcal{D}} \quad (2.2.2b)$$

$$\mathcal{E}_i = \left. \frac{\partial u}{\partial \mathcal{D}_i} \right|_{\sigma, \mathcal{S}_{ij}} = u_{,\mathcal{D}_i}^{\sigma, \mathcal{S}} \quad (2.2.2c)$$

Since it is difficult to guarantee a constant entropy than a constant temperature during a transformation, it is more adapted to define new thermodynamic potentials that are functions of intensive parameters instead of extensive parameters. These potentials are usually defined with the help of the Legendre transformation [Callen, 1960]. For example, the Helmholtz free energy \mathcal{f} is the potential that uses the temperature θ as a variable instead of the entropy σ . The entropy is then the partial derivative of \mathcal{f} when \mathcal{S}_i and \mathcal{D}_i are kept constant. The Helmholtz free energy is defined by (2.2.3).

$$\mathcal{f} \equiv u[\theta] = u - \theta \cdot \sigma \quad (2.2.3a)$$

$$d\mathcal{f} = -\sigma \cdot d\theta + \mathcal{T}_i \cdot d\mathcal{S}_i + \mathcal{E}_i \cdot d\mathcal{D}_i \quad (2.2.3b)$$

Other Legendre transformations can be defined such as enthalpy $h(\sigma, T_i, E_i)$, elastic enthalpy $h_e(\sigma, T_i, D_i)$, electric enthalpy $h_e(\sigma, S_i, E_i)$, elastic Gibbs function $g_s(\theta, T_i, D_i)$ etc. [Tichy *et al.*, 2010]. The best suitable transformation for the description of piezoelectric materials is the Gibbs function g which is a privileged function of the three intensive parameters θ , T_i and E_i . Hence the extensive parameters become the first partial derivatives of the Gibbs function (2.2.4).

$$\mathcal{g} \equiv u[\theta, \mathcal{T}_i, \mathcal{E}_i] = u - \theta \cdot \sigma - \mathcal{T}_i \cdot \mathcal{S}_i - \mathcal{E}_i \cdot \mathcal{D}_i \quad (2.2.4a)$$

$$d\mathcal{g} = -\sigma \cdot d\theta - \mathcal{S}_i \cdot d\mathcal{T}_i - \mathcal{D}_i \cdot d\mathcal{E}_i \quad (2.2.4b)$$

$$\sigma = \left. \frac{\partial \mathcal{g}}{\partial \theta} \right|_{\mathcal{T}_i, \mathcal{E}_i} = \mathcal{g}_{,\theta}^{\mathcal{T}\mathcal{E}} \quad (2.2.4c)$$

$$\mathcal{S}_{ij} = \left. \frac{\partial \mathcal{g}}{\partial \mathcal{T}_i} \right|_{\theta, \mathcal{E}_i} = \mathcal{g}_{,\mathcal{T}_i}^{\theta\mathcal{E}} \quad (2.2.4d)$$

$$\mathcal{D}_i = \left. \frac{\partial \mathcal{g}}{\partial \mathcal{E}_i} \right|_{\theta, \mathcal{T}_i} = \mathcal{g}_{,\mathcal{E}_i}^{\theta\mathcal{T}} \quad (2.2.4e)$$

Following the same approach used in Chapter 3, we can linearize the expression of the extensive parameters as a function of the intensive parameters (2.2.5).

$$d\sigma = \sigma_{,\theta}^{\mathcal{T}\mathcal{E}} \cdot d\theta + \sigma_{,\mathcal{T}_i}^{\theta\mathcal{E}} \cdot d\mathcal{T}_{ij} + \sigma_{,\mathcal{E}_i}^{\theta\mathcal{T}} \cdot d\mathcal{E}_i \quad (2.2.5a)$$

$$d\mathcal{S}_{ij} = \mathcal{S}_{,\theta}^{\mathcal{T}\mathcal{E}} \cdot d\theta + \mathcal{S}_{,\mathcal{T}_i}^{\theta\mathcal{E}} \cdot d\mathcal{T}_{ij} + \mathcal{S}_{,\mathcal{E}_i}^{\theta\mathcal{T}} \cdot d\mathcal{E}_i \quad (2.2.5b)$$

$$d\mathcal{D}_i = \mathcal{D}_{,\theta}^{\mathcal{J}\varepsilon} \cdot d\theta + \mathcal{D}_{,\mathcal{J}}^{\theta\varepsilon} \cdot d\mathcal{T}_{ij} + \mathcal{D}_{,\varepsilon}^{\theta\mathcal{J}} \cdot d\varepsilon_i \quad (2.2.5c)$$

These three equations can be written as a tensor of matrices (2.2.6a) in which the diagonal terms describe the main physical effects (thermal heating represented by the heat capacity (2.2.6b), Hooke's law associated to the compliance matrix (2.2.6c), and the electrostatic law associated to relative permittivity matrix (2.2.6d)) and the non-diagonal terms correspond to coupling phenomena.

$$d \begin{pmatrix} \sigma \\ \mathcal{S} \\ \mathcal{D} \end{pmatrix} = \begin{pmatrix} \sigma_{,\theta}^{\mathcal{J}\varepsilon} & \sigma_{,\mathcal{J}}^{\theta\varepsilon} & \sigma_{,\varepsilon}^{\theta\mathcal{J}} \\ \mathcal{S}_{,\theta}^{\mathcal{J}\varepsilon} & \mathcal{S}_{,\mathcal{J}}^{\theta\varepsilon} & \mathcal{S}_{,\varepsilon}^{\theta\mathcal{J}} \\ \mathcal{D}_{,\theta}^{\mathcal{J}\varepsilon} & \mathcal{D}_{,\mathcal{J}}^{\theta\varepsilon} & \mathcal{D}_{,\varepsilon}^{\theta\mathcal{J}} \end{pmatrix} \cdot d \begin{pmatrix} \theta \\ \mathcal{T} \\ \varepsilon \end{pmatrix} \quad (2.2.6a)$$

$$\theta \cdot (\sigma_{,\theta}^{\mathcal{J}\varepsilon}) = \rho \cdot c_{th}^{\mathcal{J}} \quad (2.2.6b)$$

$$\mathcal{S}_{,\mathcal{J}}^{\theta\varepsilon} = s_{ij} \quad (2.2.6c)$$

$$\mathcal{D}_{,\varepsilon}^{\theta\mathcal{J}} = \varepsilon_{ij}^{\mathcal{J}} \quad (2.2.6d)$$

In (2.2.6), $\mathcal{S}_{,\theta}^{\mathcal{J}\varepsilon}$ and $\sigma_{,\mathcal{J}}^{\theta\varepsilon}$ correspond to the thermo-mechanical coupling (thermal expansion), $\sigma_{,\varepsilon}^{\theta\mathcal{J}}$ and $\mathcal{D}_{,\theta}^{\mathcal{J}\varepsilon}$, if they are non-zero, represent the thermo-electrical coupling for a pyroelectric material (respectively the electrocaloric effect and pyroelectric effect), and $\mathcal{D}_{,\mathcal{J}}^{\theta\varepsilon}$ and $\mathcal{S}_{,\varepsilon}^{\theta\mathcal{J}}$ the electro-mechanical coupling for a piezoelectric material (respectively the direct piezoelectric effect and the reverse piezoelectric effect). As these matrices are the first partial derivatives of the extensive parameters, they are also the second partial derivatives of the Gibbs function. It is then possible to apply the Shwarz theorem (2.2.7).

$$\left. \frac{\partial^2 \mathcal{G}}{\partial X_i \partial X_j} \right|_{X_j, X_k} = \left(\left. \frac{\partial^2 \mathcal{G}}{\partial X_j \partial X_i} \right|_{X_i, X_k} \right)^t \quad (2.2.7)$$

This theorem enables to express the Maxwell relations for a dielectric body which show that the direct piezoelectric effect and the reverse piezoelectric effect are described by the same matrix d_{ij} (2.2.8a): the proportionality relation between D_i and T_{ij} is the same as between S_{ij} and E_i . Similarly, the electrocaloric and pyroelectric effects are described by the same matrix p (4.8b), and the thermal expansion by a single matrix α (2.2.8c).

$$(\mathcal{S}_{,\varepsilon}^{\theta\mathcal{J}})^t = \mathcal{D}_{,\mathcal{J}}^{\theta\varepsilon} = d_{ij} \quad (2.2.8a)$$

$$(\sigma_{,\varepsilon}^{\theta\mathcal{J}})^t = \mathcal{D}_{,\theta}^{\mathcal{J}\varepsilon} = p_i^{\mathcal{J}} \quad (2.2.8b)$$

$$(\sigma_{,\mathcal{J}}^{\theta\varepsilon})^t = \mathcal{S}_{,\theta}^{\mathcal{J}\varepsilon} = \alpha_{ij} \quad (2.2.8c)$$

Thus the constitutive equations of the dielectric body (2.2.5) can be rewritten with the newly defined parameters (2.2.9).

$$d\sigma = \frac{\rho \cdot c_{th}^{\mathcal{J}}}{\theta} \cdot d\theta + (\alpha_{ij})^t \cdot d\mathcal{T}_{ij} + (p_i^{\mathcal{J}})^t \cdot d\varepsilon_i \quad (2.2.9a)$$

$$d\mathcal{S}_i = \alpha_{ij} \cdot d\theta + s_{ij} \cdot d\mathcal{T}_j + (d_{ij})^t \cdot d\varepsilon_j \quad (2.2.9b)$$

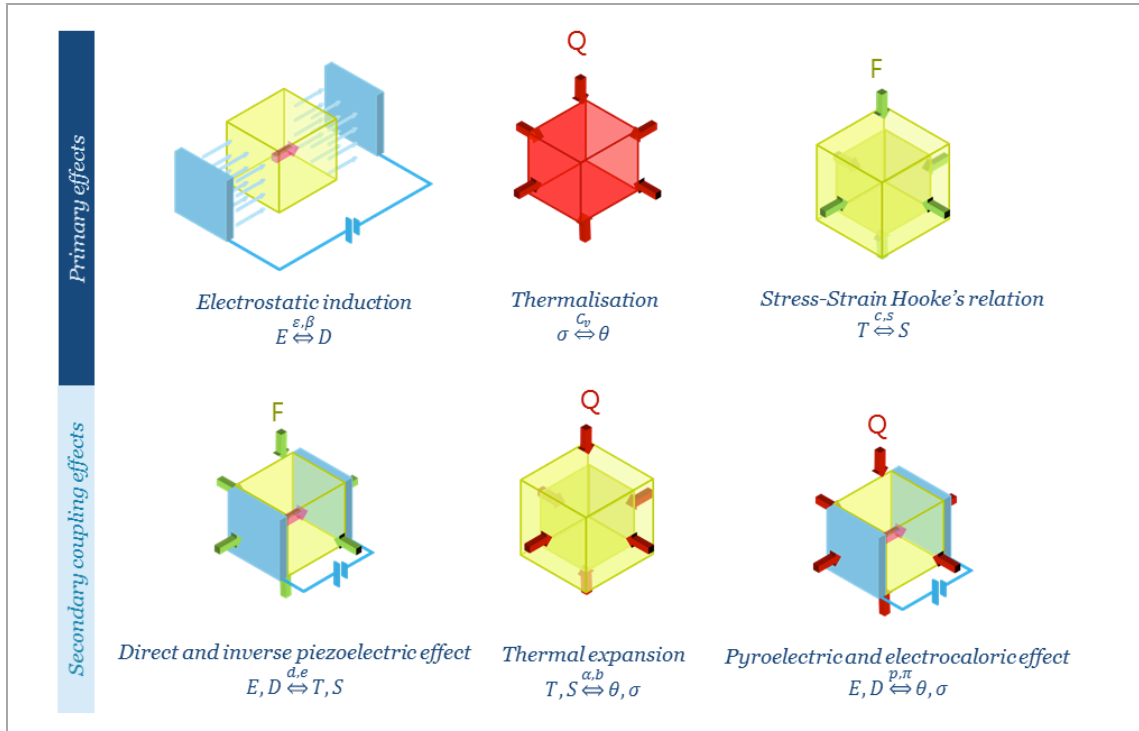


Figure 2.2.1. Main physical effects in a pyroelectric material.

$$dD_i = p_i \cdot d\theta + d_{ij} \cdot dT_j + \varepsilon_{ij}^T \cdot dE_j \quad (2.2.9c)$$

We now introduce a matrix notation similarly to the one presented in [IEEE, 1988]. Instead of limited this matrix to the piezoelectric effect only, we add the thermal effects. We know from the mechanics that the link between the compliance matrix is a 6x6 matrix. Since there are three coordinates to describe the polarization and the electric field, the permittivity matrix is a 3x3 matrix. The piezoelectric effect is then described by a 6x6 matrix. To obtain a square matrix by adding the thermal effects, we define a 6x3 matrix for the thermal expansion, a 3x3 matrix for the heat capacity (2.2.10). Given that this matrix is associated to the properties of crystallographic structures, 32 different matrices with various symmetry properties can be written [Brissaud and Baland, 2007]. The most complex matrix corresponds to the triclinic class of crystals and is represented in Fig.2.2.2. In this figure, each point represents an independent value of parameters.

$$d \begin{pmatrix} \sigma \\ S \\ \mathcal{D} \end{pmatrix} = \begin{pmatrix} \rho \cdot c_{th}^T & \alpha^t & p^t \\ \theta & s & d^t \\ \alpha & s & d^t \\ p & d & \varepsilon \end{pmatrix} \cdot d \begin{pmatrix} \theta \\ \mathcal{T} \\ \mathcal{E} \end{pmatrix} \quad (2.2.10)$$

Thanks to symmetries, it can be shown that only 20 of these matrices describe pyroelectric materials, and 10 of these matrices possess non-zero pyroelectric term. To illustrate these properties of symmetry, we present in Fig.2.2.2 the matrices corresponding to the crystallographic class 4mm to which belong perovskite crystals (BaTiO_3 , PbTiO_3 , PZN-PT, PMN-PT) [Tichy *et al*, 2010] and 6mm to which belong wurtzite crystals (AlN , ZnO , GaN).

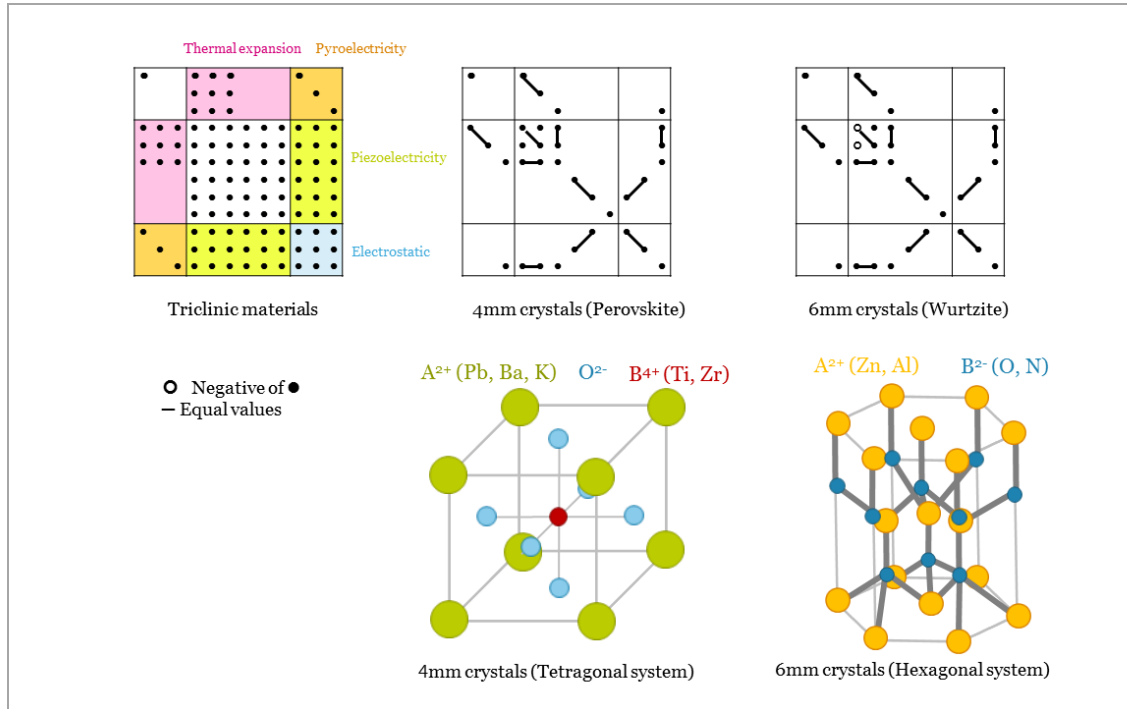


Figure 2.2.2. Matrix representation of the thermal, mechanical and electrical properties of solid materials, and matrix and lattices associated to Perovskites and Wurtzites.

For these materials, the number of physical parameters is reduced and only three parameters are needed to describe the piezoelectric effect. To reduce the number of constitutive equations to get the simplest description of the piezoelectric beam, it is necessary to take into account the configuration of the electrodes of the capacitor. Being deposited on the surface of the beam, the only component of the electrical field to be considered is the term E_3 associated to the relative permittivity ϵ_3 . In the frame of the Euler-Bernoulli assumptions, the only term of the stress tensor is the axial strain σ_1 . This implies that the piezoelectric coupling inside the piezoelectric layer will be described by the coefficient d_{31} only. Finally, there are only three constitutive equations for the description of the piezoelectric capacitor. The previous matrix can be rewritten in (2.2.11).

$$d \begin{pmatrix} \sigma \\ \mathcal{S} \\ \mathcal{D} \end{pmatrix} = \begin{pmatrix} \frac{\rho \cdot c_{ih}^T}{\theta} & \alpha & p_3 \\ \alpha & s_1 & d_{31} \\ p_3 & d_{31} & \epsilon_3 \end{pmatrix} \cdot d \begin{pmatrix} \theta \\ \mathcal{T} \\ \mathcal{E} \end{pmatrix} \quad (2.2.11)$$

Along this chapter, we will compare the performances of various piezoelectric materials whose properties are recalled in Tab.2.2.1.

Material	GaN	AlN	ZnO	PVDF	PZT-4	PZT-5H	PMN-PT
ρ	6,15	3,26	5,61	1,76	7,6	7,4	8,2
E (GPa)	301	350	127	2,74	81,3	60,9	14,9
α (10^{-6}K^{-1})	3,2	5,2	4,3	120	3	3	9,5
c_{th} ($\text{J}\cdot\text{kg}^{-1}\cdot\text{K}^{-1}$)	490	740	497	1120	440	460	312
d_{31} ($10^{-12}\text{C}\cdot\text{N}^{-1}$)	-1,9	-2,0	-5,0	21	-123	-274	-1330
p_3 ($10^{-6}\text{C}\cdot\text{m}^{-2}\cdot\text{K}^{-1}$)	4,8	6-8	9,4	33	260	260-450	1790
ϵ_3 (-)	11,2	10	8,83	11,00	635	1470	916
k_p^2 (%)	2,9E-03	8,6E-03	0,02	0,21	0,13	0,06-0,17	5,76
$\text{FOM}_{w^{pyro}}$ ($\text{J}\cdot\text{m}^{-3}\cdot\text{K}^{-2}$)	0,23	0,55	1,13	11,19	12,03	5,20-15,57	395,25
$\text{FOM}_{w^{pyro}'}$ ($\text{m}^3\cdot\text{J}^{-1}$)	0,03	0,10	0,15	2,88	1,08	0,45-1,34	60,39

Table 2.2.1. Physical properties of some pyroelectric materials (based on [Bowen et al, 2014]) and figures of merit of pyroelectric generators

3 Equations of the pyroelectric bimetallic strip heat engine

3.1 Tertiary pyroelectric effect

The modeling of the thermo-mechanical instability of composite beams in the previous chapter enabled to establish the expression of the strain tensor in the case of a buckled beam. In this chapter, we will only focus on the thermo-mechanical instability described by a first-order buckling mode. The corresponding model has been presented in the previous chapter. In this case, (4.14a) is the expression of the strain tensor.

$$\mathcal{S}_1 = \frac{\lambda}{L} + (z - z_o) \cdot \frac{\pi^2}{L^2} \cdot w_1 \cdot \cos\left(\frac{\pi \cdot x}{L}\right) \quad (3.1.1a)$$

$$\lambda = \frac{\pi^2}{4 \cdot L} \cdot w_1^2 \quad (3.1.1b)$$

Since the expression of the axial strain is known, it is better to use constitutive equations where the axial strain is used as a parameter. By using the electric Gibbs function, the axial stress T_1 , the entropy σ and the electrical displacement D_3 are simply expressed as functions of the electrical field, the temperature and the axial strain (3.1.2).

$$d\sigma = \frac{\rho \cdot c_{th}^s}{\theta} \cdot d\theta + E \cdot \alpha \cdot d\mathcal{S}_1 + p_3^s \cdot d\mathcal{E}_3 \quad (3.1.2a)$$

$$dT_1 = -E \cdot \alpha \cdot d\theta + E \cdot d\mathcal{S}_1 - e_{31} \cdot d\mathcal{E}_1 \quad (3.1.2b)$$

$$d\mathcal{D}_3 = p_3^S \cdot d\theta + e_{31} \cdot d\mathcal{S}_1 + \varepsilon_{33}^S \cdot d\mathcal{E}_3 \quad (3.1.2c)$$

These equations introduce new parameters such as the pyroelectric coefficient p_3^S , the relative dielectric permittivity ε_{33}^S , and the piezoelectric modulus e_{31} . By combining the equations of (3.1.2), these parameters can be expressed as functions of those given in (2.2.9).

$$\rho \cdot c_{th}^S = \rho \cdot c_{th}^T - E \cdot \alpha^2 \cdot \theta = \rho \cdot c_{th}^T (1 - \gamma_G \cdot \alpha \cdot \theta) \quad (3.1.3a)$$

$$e_{31} = E \cdot d_{31} \quad (3.1.3b)$$

$$p_3^S = p_3^T - E \cdot \alpha \cdot d_{31} \quad (3.1.3c)$$

$$\varepsilon_{33}^S = \varepsilon_{33}^T - E \cdot d_{31}^2 \quad (3.1.3d)$$

Equation (3.1.3c) shows that the pyroelectric effect can be decomposed into two terms, the first term being the pyroelectric coefficient at constant strain is known as the primary effect [Bhalla and Newnham, 1980], since it directly links the variation of the polarization to the variation of the temperature. The secondary effect represents the contribution of the thermal expansion and the piezoelectric effect. As explained in [Korotosov *et al*, 1994, Xu-Sheng, 1993], a tertiary effect also exists due to the spatial variation of the temperature entailing a thermal shear stress inside the material.

The beam modeled in this part is represented in Fig.3.1.1. In this model, the piezoelectric layer has a thickness noted t_p and its middle line is located in z_p and is polarized with two parallel electrodes only. In the model, the impact of the electrodes on the properties of the composite beams is neglected because of their weak thickness. To model the pyroelectric/piezoelectric composite beam, the equations (4.15) are integrated on the whole beam volume. In weak coupling, the impact of the polarization of the piezoelectric material on the value of z_o can be neglected. In that case, we can simplify the expression of some integrals:

$$\int_0^t p_3^S \cdot dz = p_3^S \cdot t_p \quad (3.1.4a)$$

$$\int_0^t e_{31} \cdot (z - z_o) \cdot dz = e_{31} \cdot t_p \cdot (z_p - z_o) \quad (3.1.4b)$$

Hence the electrical displacement can be integrated on the whole volume, leading to the expression of the variation of the electrical charge Q_e stored on the piezoelectric capacitance (3.1.5).

$$dQ_e = v \cdot L \cdot \varepsilon_{33}^S \cdot d\mathcal{E}_1 + L \cdot v \cdot p_3^S \cdot d\theta + e_{31} \cdot v \cdot \left(d\lambda + \frac{2 \cdot \pi \cdot (z_p - z_o)}{L} \cdot dw_1 \right) \quad (3.1.5)$$

By introducing C_p the static capacitance of the piezoelectric layer (3.1.6a), and V_p the voltage difference across the piezoelectric capacitance, we give the law describing the evolution of the charge as a function of the temperature variation, piezoelectric voltage and displacement of the beam (3.1.6b).

$$C_p = \varepsilon_{33}^S \cdot \frac{v \cdot L}{t_p} \quad (3.1.6a)$$

$$dQ_e = C_p \left(-dV_p + \frac{t_p \cdot p_3^S}{\epsilon_{33}^S} \cdot d\theta + \frac{\pi \cdot t_p \cdot e_{31}}{2 \cdot L^2 \cdot \epsilon_{33}^S} \cdot (\pi \cdot w_1 + 4 \cdot (z_p - z_o)) \cdot dw_1 \right) \quad (3.1.6b)$$

This last equation demonstrates that the charge carried by the piezoelectric capacitor is directly a function of its voltage, and that the variation of the beam's temperature during the heating and cooling phases creates electrical charges due to the pyroelectric effect. The last terms show the real contribution of the thermo-mechanical bistability to the increase of the charge generated. As the beam's displacement is a function of temperature, it is possible to describe this contribution as a kind of tertiary pyroelectric effect. By derivating the displacement with respect to the temperature at equilibrium yields (3.1.7).

$$\left. \frac{dQ_e}{dT} \right|_{u_p} = \frac{t_p \cdot p_3^S}{\epsilon_{33}^S} + \frac{t_p \cdot e_{31}}{\epsilon_{33}^S} \cdot \frac{8 \cdot M_\alpha \cdot (\pi \cdot w_1 + 4 \cdot (z_p - z_o))}{3 \cdot N_e \cdot w_1^2 + 4 \cdot L^2 \cdot \left(I_e \cdot \frac{\pi^2}{L^2} - N_o \right)} \quad (3.1.7)$$

This tertiary effect thus is given by (3.1.8). It shows that the sign of this effect depends of the sign of the beam's curvature, the position of the piezoelectric layer with respect to the neutral fiber and the value of the thermal asymmetry. Logically it can be observed that the increase of the thermal asymmetry, representing the thermal sensitivity of the bistable beam, and the use of highly piezoelectric materials enhance the beam's pyroelectric effect. We will see in the next sections that this effect boosts the performances of the heat engine when the beam thermal hysteresis is small.

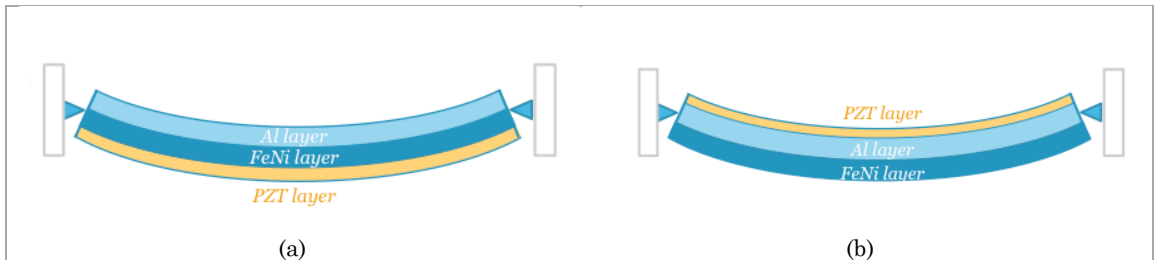
$$p_3^{III} = e_{31} \cdot \frac{8 \cdot M_\alpha \cdot (\pi \cdot w_1 + 4 \cdot (z_p - z_o))}{3 \cdot n_e \cdot w_1^2 + 4 \cdot L^2 \cdot \left(I_e \cdot \frac{\pi^2}{L^2} - N_o \right)} \quad (3.1.8)$$

3.2 Equilibrium equations of the piezoelectric bistable composite beam

We now treat the constitutive equation describing the mechanical behavior of the composite beam. The fact that the piezoelectric material is polarized by an electric field E modifies the stress in the beam. The impact of this stress can be modeled using two parameters F_E and M_E , representing the piezoelectric force (3.2.1a) and the piezoelectric moment (3.2.1b).

$$F_\varepsilon = -v \cdot \int_0^t e_{31}(z) \cdot dz \cdot \varepsilon = -v \cdot t_p \cdot e_{31} \cdot \varepsilon = C_p \cdot \frac{t_p \cdot e_{31}}{L \cdot \epsilon_{33}^S} \cdot V_p \quad (3.2.1a)$$

Figure 3.1.1. Schematic of the beam with the piezoelectric layer deposited a. on the active layer. b. on the passive layer.



$$M_{\mathcal{E}} = -v \cdot \int_0^t e_{31}(z) \cdot (z - z_o) \cdot dz \cdot \mathcal{E} = (z_p - z_o) \cdot F_{\mathcal{E}} \quad (3.2.1b)$$

This way, the thermo-mechanical equilibrium of the beam is described by equation (3.2.2).

$$\frac{N_e \cdot \pi^2}{8 \cdot L^3} \cdot w_1^3 + \frac{\pi^2}{2 \cdot L} \cdot \left(I_e \cdot \frac{\pi^2}{L^2} + F_{\mathcal{E}} + F_o - N_{\alpha} \cdot T \right) \cdot w_1 + \frac{2 \cdot \pi}{L} \cdot (M_o + M_{\mathcal{E}} - M_{\alpha} \cdot T) = 0 \quad (3.2.2)$$

Three cases can be treated: in the general case (3.2.2) is solved with the help of (3.1.6b) to see the influence of the piezoelectric capacitor's voltage on the instability of the beam. In the second case, a mean value of the output voltage is taken into account. The results of the reduced-order model are then modified, mainly by replacing the residual stress force N_o by N_o^{elec} (3.2.3a). One of the main consequences is the modification of the criterion of instability (3.2.3b). The last solution is the weak electro-mechanical coupling; in this case we recall that the equilibrium equation is simply (3.2.3c). This last approach will mainly be followed in the rest of the chapter.

$$N_o^{elec} = N_o + \left(\frac{N_{\alpha}}{M_{\alpha}} \cdot (z_p - z_o) - 1 \right) \cdot F_{\mathcal{E}} \quad (3.2.3a)$$

$$N_o^{elec} \geq I_e \cdot \frac{\pi^2}{L^2} \quad (3.2.3b)$$

$$\frac{N_e \cdot \pi^2}{8 \cdot L^3} \cdot w_1^3 + \frac{\pi^2}{2 \cdot L} \cdot \left(I_e \cdot \frac{\pi^2}{L^2} - N_o \right) \cdot w_1 + \frac{2 \cdot \pi}{L} \cdot (M_o - M_{\alpha} \cdot T) = 0 \quad (3.2.3c)$$

The last equation to be treated is the variation of entropy of the beam. As demonstrated in the previous chapter, knowing the expression of the beam entropy and using the Fourier law enable to study the thermal exchanges between the beam and its surroundings and to find the temporal evolution of the temperature.

$$d\mathcal{S} = \frac{C_{th}^S}{\theta} \cdot d\theta + N_{\alpha} \cdot d\lambda + 2 \cdot \frac{\pi}{L} \cdot M_{\alpha} \cdot da + C_p \cdot \frac{t_p \cdot p_3^S}{\varepsilon_{33}^S} \cdot dU_p \quad (3.2.4)$$

4 Pyroelectric conversion using a Stirling cycle

4.1 Stirling cycle

Even if the simplest solution to harvest the pyroelectric charges is to connect a resistance to the piezoelectric capacitor, this type of cycle is not the most efficient. Moreover, the optimization of the load resistance depends on the frequency of the heating and cooling phases, which depends on the external thermal gradient. In these conditions, looking for other thermodynamic cycles can lead to a solution to increase the efficiency of the harvester. In this part we study the implementation of the Stirling cycle to harvest heat. As explained in the Chapter 2, this cycle is originally divided in four phases: isochoric heating, isothermal expansion, isochoric cooling and isothermal compression. The volume being an extensive parameter, the equivalent parameter in the case of the electric Stirling cycle is the electric displacement. The isochoric transformations are then replaced by heating at constant electric displacement or at constant electrical charge. The Stirling cycle is represented in Fig.4.1.1a. During the heating phase, the elevation of the voltage

difference across the pyroelectric generator increases the potential energy of the electrical charges. These charges are then harvested by closing the circuit once the maximal potential is reached. By opening the circuit during the cooling phase, the generator voltage decreases while the charge is kept constant. The circuit is finally closed to recharge the capacitor. The analysis of the theoretical performances of the Stirling cycle was presented in [Sebald *et al*, 2008]. This work defined two figures of Merit for the performances of pyroelectric generators. The first FOM recalled in (4.1.1a) is related to the output energy of the generator (4.1.1b). The second one is also called electro-thermal coupling factor and is given by (4.1.1c). The Carnot efficiency of the Stirling cycle (temperatures θ_h and θ_c) is then given by (4.1.1d), which can be simplified into (4.1.1e) in the case of low electro-thermal coupling.

$$FOM_W^{pyro} = \frac{p^2}{\epsilon_{33}^\theta} \quad (4.1.1a)$$

$$\mathcal{W}_E = \frac{p^2}{\epsilon_{33}^\theta} \cdot (\theta_h - \theta_c)^2 \quad (4.1.1b)$$

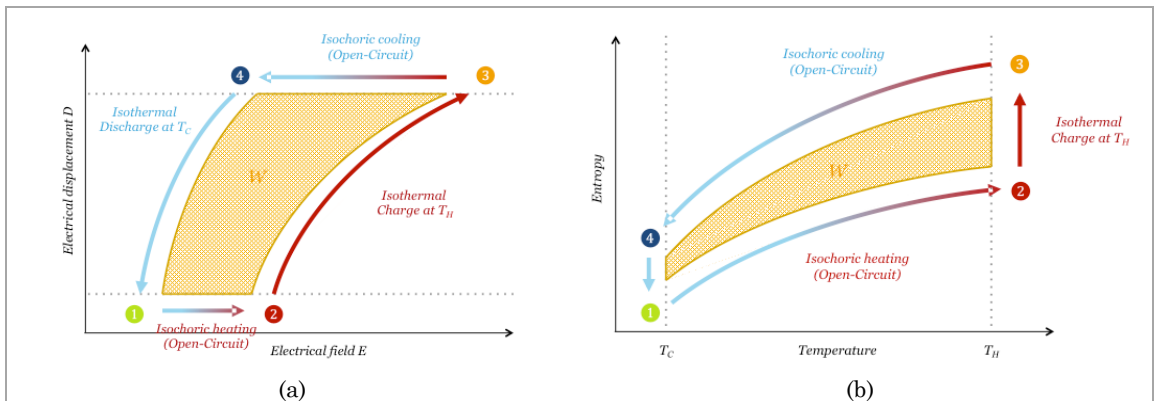
$$k^2 = \frac{p^2}{\epsilon_{33}^\theta \cdot \rho \cdot c_{th}^T} \cdot \theta_h \quad (4.1.1c)$$

$$\eta_{rel} = \frac{k^2}{1 + 0.5 \cdot k^2 \cdot \frac{\theta_h - \theta_c}{\theta_h}} \quad (4.1.1d)$$

$$\eta_{rel} \approx k^2 \quad (4.1.1e)$$

Another Figure of Merit for the energy has also been defined in [Bowen *et al*, 2015]. This FOM just comes from the expression of the heat stored in the heat capacitance during the whole cycling of the pyroelectric generator (4.1.2a) and is quite similar to the expression of the electro-thermal coupling factor, apart from the fact that it is independent from the working temperature (4.1.2b). The typical values of these FOM are reported in Tab.2.2.1, showing that PMN-PT is the best material to harvest heat, followed by PZT ceramics.

Figure 4.1.1. *a. Representation of the Stirling cycle in the plan (E,D). b. Representation of the Stirling cycle in the plan (S,T)*



$$Q_{hot} = \rho \cdot c_{th}^T \cdot (\theta_h - \theta_c) \quad (4.1.2a)$$

$$FOM_{\mathcal{W}}^{pyro'} = \frac{p^2}{\varepsilon_{33}^\theta \cdot (\rho \cdot c_{th}^T)^2} \quad (4.1.2b)$$

$$\mathcal{W}_E = FOM_{\mathcal{W}}^{pyro'} \cdot Q_{hot}^2 \quad (4.1.2c)$$

Even if the Stirling cycle is less efficient than the Olsen-Ericsson cycle [Olsen *et al*, 1984, & 1985], it has the advantage of not requiring any external polarization voltage to work and it is similar to the SECE cycle currently used to harvest piezoelectric energy from mechanical vibrations. As a consequence, the circuits devoted to mechanical energy harvesting can be used with the Stirling generator, such as SECE [Sebald *et al*, 2008] or PSCE circuits [Hehn *et al*, 2012]. As explained in [Sebald *et al*, 2008], a way to boost up the efficiency of the pyroelectric generator would be to use SSHI architectures instead of SECE circuits.

4.2 Implementation of the Stirling cycle

In the case of the bimetallic strip heat engine, several types of Stirling cycles can be implemented given the possibility to deposit the piezoelectric layer on the active layer of the bimetallic beam or on its passive layer, and given the possibility to polarize the piezoelectric capacitor at different steps of the hysteretic cycle of the bistable bimetallic beam. In this study, we will consider three different scenarios of operation.

a. Stirling cycle I

In this first scenario, the piezoelectric capacitor is charged and discharged each time the beam is about to switch from a critical equilibrium point to a stable equilibrium point (Fig.4.2.1a). To describe every step of the Stirling cycle, we write the evolution of the electrical charges carried by the piezoelectric capacitor and its voltage for each phase of the cycle. The first step is the initial heating of the system from the reference temperature to the beam's snap temperature. During this first step, the voltage increases from 0 to V_o (4.2.1a). The circuit is then closed, leading to the creation of a charge Q_o (4.2.1b).

$$\mathcal{V}_o = \frac{t_p \cdot p_3^S}{\varepsilon_{33}^S} \cdot (T_S - T_{ref}) + \frac{\pi \cdot t_p \cdot e_{31}}{2 \cdot L^2 \cdot \varepsilon_{33}^S} \cdot \left(\frac{\pi}{2} \cdot (w_S^{C^2} - w_{ref}^2) + 4 \cdot (z_p - z_o) \cdot (w_S^C - w_{ref}) \right) \quad (4.2.1a)$$

$$Q_S^C = C_p \cdot \mathcal{V}_o \quad (4.2.1b)$$

Table 4.2.1. Properties of the bistable beam made of Al-Invar and PZT-5H.

Position of the piezoelectric layer	N_e (N)	I_e (N.m ²)	N_a (N.K ⁻¹)	M_a (N.m.K ⁻¹)	z_p (mm)
On the passive layer	$4,90 \cdot 10^5$	$7,76 \cdot 10^{-3}$	3,72	$4,77 \cdot 10^{-4}$	0,05
On the active layer	$4,90 \cdot 10^5$	$9,58 \cdot 10^{-3}$	3,72	$3,37 \cdot 10^{-4}$	0,45

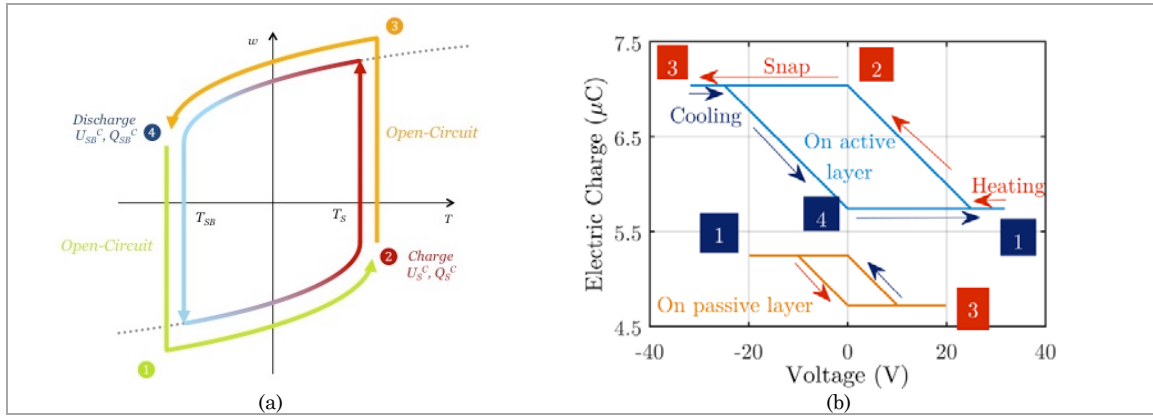


Figure 4.2.1. *a. Principle of the first Stirling cycle. b. Stirling cycles of the heat engine for a thermal hysteresis of 3°C in the (Q,V) plane, when the piezoelectric layer is deposited on the active layer or on the passive layer.*

Then the bimetallic beam snaps and is cooled in open circuit. During this phase, the voltage of the piezoelectric capacitor reaches a maximal value when the beam snaps (4.2.2a). The final voltage of the piezoelectric layer is given by (4.2.2b). By closing the circuit, the variation of the charge carried by the capacitor is given by (4.2.2c).

$$\mathcal{V}_{SB}^S = \frac{\pi \cdot t_p \cdot e_{31}}{2 \cdot L^2 \cdot \epsilon_{33}^S} \cdot \left(\frac{3 \cdot \pi}{2} \cdot w_S^C - 8 \cdot (z_p - z_o) \cdot w_S^C \right) \quad (4.2.2a)$$

$$\mathcal{V}_{SB}^C = -\frac{t_p \cdot p_3^S}{\epsilon_{33}^S} \cdot \Delta T - 4 \cdot \frac{\pi \cdot t_p \cdot e_{31}}{L^2 \cdot \epsilon_{33}^S} \cdot (z_p - z_o) \cdot w_S^C \quad (4.2.2b)$$

$$Q_{SB}^C - Q_S^C = C_p \cdot \mathcal{V}_{SB}^C \quad (4.2.2c)$$

Similarly, when the bimetal snaps back and is heated by the hot source, the generated voltage is given by (4.2.3a), and the charge generated by this voltage change is given by (4.2.3b).

$$\mathcal{V}_S^C = \frac{t_p \cdot p_3^S}{\epsilon_{33}^S} \cdot \Delta T + 4 \cdot \frac{\pi \cdot t_p \cdot e_{31}}{L^2 \cdot \epsilon_{33}^S} \cdot (z_p - z_o) \cdot w_S^C \quad (4.2.3a)$$

$$Q_S^C - Q_{SB}^C = C_p \cdot \mathcal{V}_S^C \quad (4.2.3b)$$

The two voltages being of opposite sign, we can define a maximal output voltage by taking the absolute values of these voltages.

$$\mathcal{V}_I = |\mathcal{V}_S^C| = |\mathcal{V}_{SB}^C| = \left| \frac{t_p \cdot p_3^S}{\epsilon_{33}^S} \cdot \Delta T + 4 \cdot \frac{\pi \cdot t_p \cdot e_{31}}{L^2 \cdot \epsilon_{33}^S} \cdot (z_p - z_o) \cdot w_S^C \right| \quad (4.2.4)$$

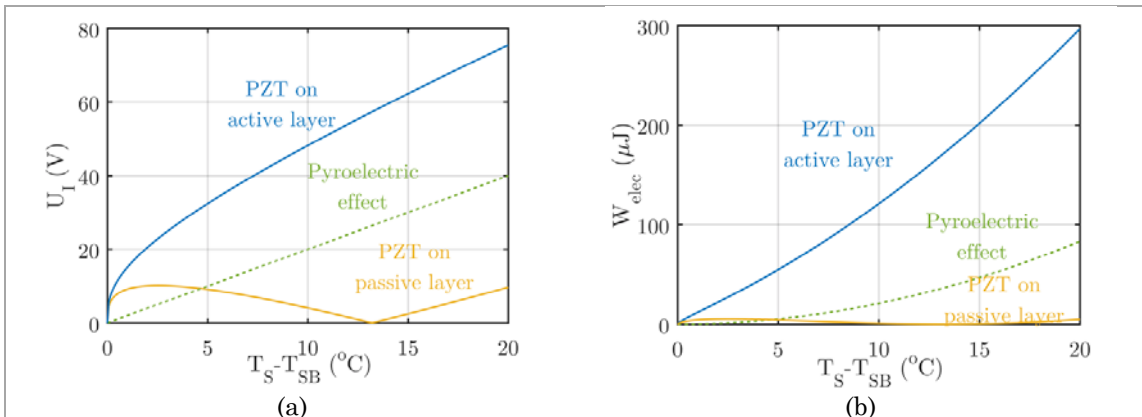
With these equations, it is possible to plot the thermodynamic cycle of the Stirling heat engine in the plan (Q,V), (Fig.4.2.1b), when the piezoelectric layer is deposited on the active layer or on the passive layer. Two differences can be observed between these two configurations. First, the areas enclosed by the two loops are different, meaning that the two types of beams do not produce the same energy. The fact that the thermo-mechanical properties of the piezoelectric layer modify the value of the thermal asymmetry, plays an important role in the modification of the generated energy. Generally, as the thermal

expansion coefficient of the piezoelectric material is lower than the active layer's one, the thermal sensitivity of the beam is better if the piezoelectric layer is deposited on the passive layer, partly explaining the increase of the generated energy by the increase of the critical curvature w_s^c . The second effect is linked to the position of the piezoelectric layer with respect to the neutral axis. When the piezoelectric layer is deposited on the active layer, the term $(z_p - z_o)$ is negative, and given that the critical curvature w_s^c and the piezoelectric modulus e_{31} are also negative, the charges created by the pyroelectric effect are added to the charges created by the curvature of the piezoelectric layer. In the other case, when the piezoelectric layer is deposited on the passive layer, the pyroelectric charges are subtracted to the charges linked to the piezoelectric effect. The position of the neutral axis also modifies the way the capacitor is charged or discharged when the piezoelectric layer is deposited on the passive layer. If the pyroelectric effect is predominant, the capacitor charges when the beam is at T_S , and discharges at T_{SB} , like when the piezoelectric layer is on the active layer. In the other case, the capacitor charges at T_{SB} and discharges at T_S . From the previous equations, it is possible to calculate the energy generated by the Stirling cycle (4.2.5).

$$\mathcal{W}_E = C_p \cdot \mathcal{V}_l^2 = C_p \cdot \left(\frac{t_p \cdot p_3^s}{\varepsilon_{33}^s} \cdot \Delta T + 4 \cdot \frac{\pi \cdot t_p \cdot e_{31}}{L^2 \cdot \varepsilon_{33}^s} \cdot (z_p - z_o) \cdot w_s^c \right)^2 \quad (4.2.5)$$

Fig.4.2.2a and Fig.4.2.2b respectively represent the evolutions of the maximal output voltage and the electrical energy generated by the device as functions of the beam's thermal hysteresis for a beam made of Aluminum, Invar and PZT-5H (properties given in Tab.4.2.1). These figures first show that for weak thermal hystereses, the tertiary pyroelectric effect is predominant over the primary pyroelectric effect, explaining why the bimetallic strip heat engine helps harvesting more energy than a simple PZT layer used as pyroelectric generator. As an example, for a hysteresis of 5°C, the pyroelectric bimetallic strip heat engine produces 54 μJ instead of 5 μJ for the pyroelectric generator. However, when the piezoelectric layer is on the passive layer of the bimetallic strip, the piezoelectric charges and the pyroelectric charges neutralize each other for a thermal hysteresis of 13°C. For wider hystereses, the charges are mainly generated by the pyroelectric effect.

Figure 4.2.2. a. Evolution of the output voltage generated by the bimetallic strip heat engine. b. Evolution of the available electrical energy per cycle.



b. Stirling cycle II

In that second case, the ‘‘isochoric’’ phases begin once the beam snaps (or snaps back) and finish after the beam snaps back (or snaps). The charge and discharge of the piezoelectric capacitor happen when the beam’s equilibrium is stable (in 2 and 4). The principle of this second thermodynamic cycle is presented in Fig.4.2.3a. Following the same approach as for the first type of Stirling cycle, we can express the main variations of the piezoelectric capacitor’s voltage and charge. During the beam’s heating and the beam’s snap, the voltage evolves according to (4.2.6).

$$\mathcal{V}_S^S = \frac{t_p \cdot p_3^S}{\varepsilon_{33}^S} \cdot \Delta T - 8 \cdot \frac{\pi \cdot t_p \cdot e_{31}}{L^2 \cdot \varepsilon_{33}^S} \cdot (z_p - z_o) \cdot w_S^C \quad (4.2.6a)$$

$$\mathcal{Q}_S^S - \mathcal{Q}_{SB}^S = C_p \cdot \mathcal{V}_S^S \quad (4.2.6b)$$

Similarly, during the beam’s cooling and the beam’s snap-back, the voltage evolves according to (4.2.7). We can thus define a maximal voltage by (4.2.7c). This last expression directly shows that the output voltage generated by this type of Stirling cycle is greater because of the wider variations of the beam’s curvature during the two ‘‘isochoric’’ phases of the cycle (twice more curvature). The expression of the output energy is unchanged and is given by (4.2.7d). With these expressions, we can plot the evolution of the electrical charges and the capacitor’s voltage along the whole cycle (Fig4.2.3b).

$$\mathcal{V}_{SB}^S = -\frac{t_p \cdot p_3^S}{\varepsilon_{33}^S} \cdot \Delta T + 8 \cdot \frac{\pi \cdot t_p \cdot e_{31}}{L^2 \cdot \varepsilon_{33}^S} \cdot (z_p - z_o) \cdot w_S^C \quad (4.2.7a)$$

$$\mathcal{Q}_{SB}^S - \mathcal{Q}_S^S = C_p \cdot \mathcal{V}_{SB}^S \quad (4.2.7b)$$

$$\mathcal{V}_{II} = |\mathcal{V}_S^S| = \left| \frac{t_p \cdot p_3^S}{\varepsilon_{33}^S} \cdot \Delta T - 8 \cdot \frac{\pi \cdot t_p \cdot e_{31}}{L^2 \cdot \varepsilon_{33}^S} \cdot (z_p - z_o) \cdot w_S^C \right| \quad (4.2.7c)$$

$$\mathcal{W}_E = C_p \cdot \mathcal{V}_{II}^2 = C_p \cdot \left(\frac{t_p \cdot p_3^S}{\varepsilon_{33}^S} \cdot \Delta T - 8 \cdot \frac{\pi \cdot t_p \cdot e_{31}}{L^2 \cdot \varepsilon_{33}^S} \cdot (z_p - z_o) \cdot w_S^C \right)^2 \quad (4.2.7d)$$

Fig.4.2.3c and Fig.4.2.3d compare the evolution of the output voltage and available energy when the piezoelectric layer is deposited on the active or passive layer of the bimetallic beams, whereas Fig.4.2.3b represents the thermodynamic cycle of the heat engine for a beam having a hysteresis of 3°C. Contrary to the previous cycle, the change of the sign of the piezoelectric effect in the expression of the output voltage has for consequence that the pyroelectric and piezoelectric effects are summed when the piezoelectric layer is deposited on the passive layer and subtracted when it is on the active layer. As a result, the first case generates much more energy. For a hysteresis of 5°C, the heat engine generates 120 µJ instead of 63 µJ when the piezoelectric layer is on the active layer and 5 µJ for the simple pyroelectric generator. Once again, it can be observed that for hysteresis around 16°C, the pyroelectric generator produces more energy than the bimetallic strip heat engine with PZT on the active layer, because of the antagonism between the pyroelectric and piezoelectric effects.

c. Stirling cycle III

The last Stirling cycle enables to separate the charges created during the heating and cooling phases of the thermodynamic cycle of the bimetallic strip, from the charges created during the beam's two switching events. This cycle is then made of two charges, two discharges and four iso-charges (Fig.4.2.4a). The bimetal is first heated up to the snap temperature and is charged before it snaps. The quantities associated to these two steps are given by (4.2.8).

$$\mathcal{V}_o = \frac{t_p \cdot p_3^S}{\varepsilon_{33}^S} \cdot (T_S - T_{ref}) + \frac{\pi \cdot t_p \cdot e_{31}}{2 \cdot L^2 \cdot \varepsilon_{33}^S} \cdot \left(\frac{\pi}{2} \cdot (w_S^C - w_{ref}^2) + 4 \cdot (z_p - z_o) \cdot (w_S^C - w_{ref}) \right) \quad (4.2.8a)$$

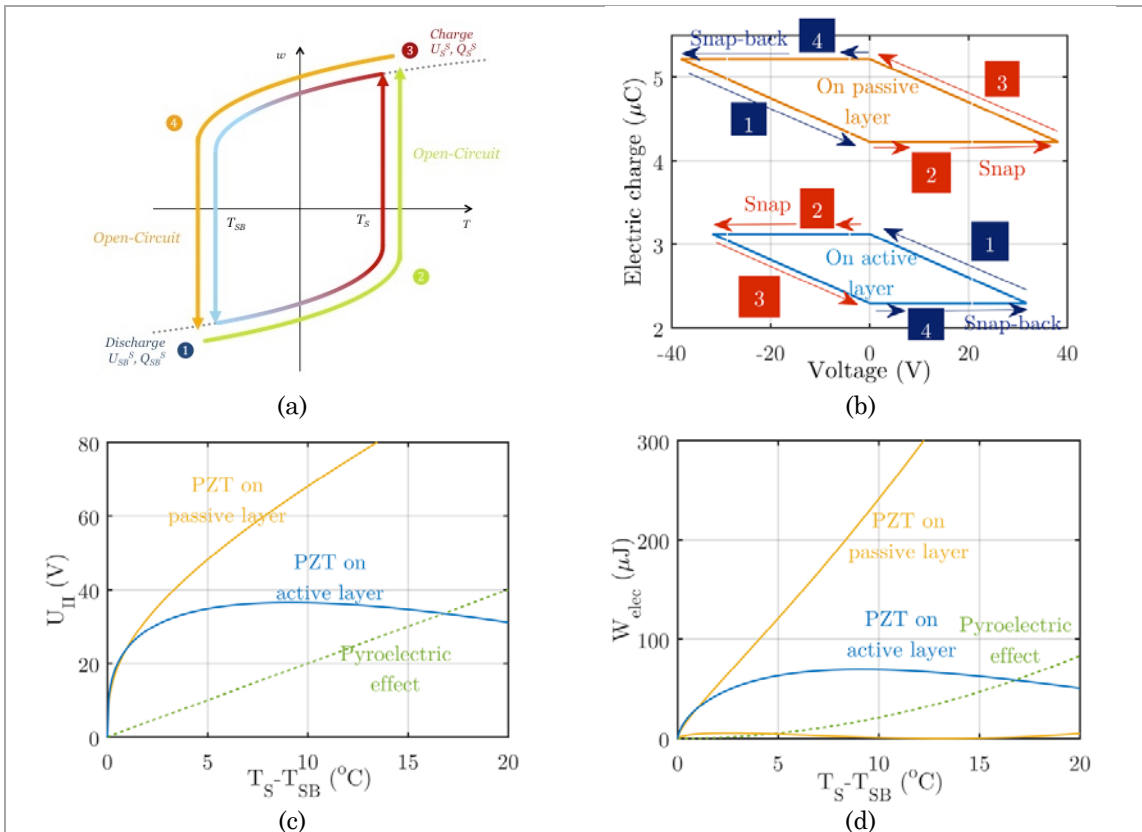
$$\mathcal{Q}_S^C = C_p \cdot \mathcal{V}_o \quad (4.2.8b)$$

The bimetal then snaps in open-circuit and is discharged once it has snapped.

$$\mathcal{V}_S^S = \frac{\pi \cdot t_p \cdot e_{31}}{L^2 \cdot \varepsilon_{33}^S} \cdot \left(\frac{3 \cdot \pi}{4} \cdot w_S^C - 6 \cdot (z_p - z_o) \cdot w_S^C \right) \quad (4.2.9a)$$

$$\mathcal{Q}_S^S - \mathcal{Q}_S^C = C_p \cdot \mathcal{V}_S^S \quad (4.2.9b)$$

Figure 4.2.3. a. Principle of the second Stirling cycle. b. Stirling cycles of the heat engine for a thermal hysteresis of 3°C in the (Q,V) plane when the piezoelectric layer is deposited on the active layer or on the passive layer. c. Output voltage as a function of thermal hysteresis. d. Available energy vs. thermal hysteresis.



The same operations happen when the bimetal is cooled down to its snap-back temperature and snaps back to return to its initial configuration

$$\mathcal{V}_{SB}^C = -\frac{t_p \cdot p_3^S}{\epsilon_{33}^S} \cdot \Delta T - \frac{\pi \cdot t_p \cdot e_{31}}{L^2 \cdot \epsilon_{33}^S} \cdot \left(\frac{3 \cdot \pi}{4} \cdot w_S^{C2} - 2 \cdot (z_p - z_o) \cdot w_S^C \right) \quad (4.2.10a)$$

$$\mathcal{Q}_{SB}^C - \mathcal{Q}_S^S = C_p \cdot \mathcal{V}_{SB}^C \quad (4.2.10b)$$

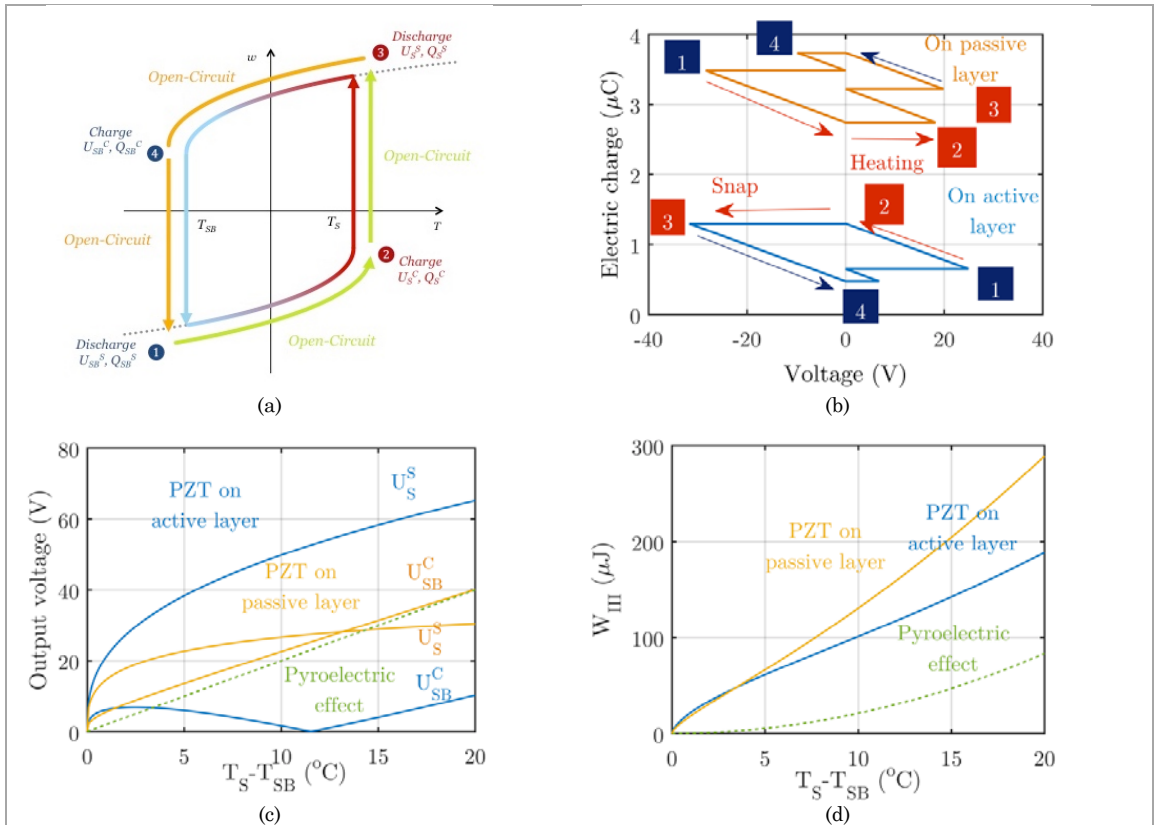
$$\mathcal{V}_{SB}^S = \frac{\pi \cdot t_p \cdot e_{31}}{L^2 \cdot \epsilon_{33}^S} \cdot \left(\frac{3 \cdot \pi}{4} \cdot w_S^{C2} + 6 \cdot (z_p - z_o) \cdot w_S^C \right) \quad (4.2.10c)$$

$$\mathcal{Q}_{SB}^S - \mathcal{Q}_{SB}^C = C_p \cdot \mathcal{V}_{SB}^S \quad (4.2.10d)$$

Thus we can demonstrate that the energy generated by the thermodynamic cycle is expressed by (4.2.11).

$$\mathcal{W}_E = \frac{1}{2} \cdot C_p \cdot (\mathcal{V}_{SB}^C{}^2 + \mathcal{V}_S^C{}^2 + \mathcal{V}_{SB}^S{}^2 + \mathcal{V}_S^S{}^2) \quad (4.2.11a)$$

Figure 4.2.4. a. Principle of the third Stirling cycle. b. Stirling cycles of the heat engine for a thermal hysteresis of 3°C in the (Q,V) plane when the piezoelectric layer is deposited on the active layer or on the passive layer. c. Output voltage as a function of the thermal hysteresis. d. Available energy vs thermal hysteresis



$$\begin{aligned} \mathcal{W}_E = c_p \cdot & \left(\left(\frac{t_p \cdot p_3^s}{\epsilon_{33}^s} \cdot \Delta T + \frac{\pi \cdot t_p \cdot e_{31}}{L^2 \cdot \epsilon_{33}^s} \cdot (z_p - z_o) \cdot w_S^c \right)^2 + 2 \cdot \left(\frac{3 \cdot \pi^2 \cdot t_p \cdot e_{31}}{4 \cdot L^2 \cdot \epsilon_{33}^s} \cdot w_S^{c2} \right)^2 \right. \\ & \left. + 9 \cdot \left(\frac{\pi \cdot t_p \cdot e_{31}}{L^2 \cdot \epsilon_{33}^s} \cdot (z_p - z_o) \cdot w_S^c \right)^2 \right) \end{aligned} \quad (4.2.11b)$$

Following the same reasoning as for the other two cycles, we consider the two possible cases for the position of the piezoelectric layer on the bimetallic beam, and we plot the evolution of the electrical charge and capacitor's voltage along the thermodynamic cycle in Fig.4.2.4b. The area enclosed by the cycle's loop is smaller when the piezoelectric layer is deposited on the beam's active layer, which can be understood thanks to 4.2.11a giving the device's output voltage when the beam is heated or cooled. Equation 4.2.11d enables to plot the evolution of the available energy as a function of the thermal instability of the beam, showing that, even if the PZT on the passive layer produces more energy than the PZT on the active layer, the fact of decoupling the beam's switching from the beam's heating and cooling reduces the difference of performance between the two configurations.

d. Comparison of the three cycles and enhancement factors

To ease the comparison between these three different cycles, Fig.4.2.6a presents the evolutions of the output energy for the heat engine for the best configuration (PZT on the active layer for the first cycle, PZT on the passive layer for the other two), emphasizing the fact that the second type of Stirling cycle produces more energy than the other two cycles. To complete the study, we also plot in Fig.4.2.5b the evolution of the Carnot efficiency of these engines obtained by dividing the electrical energy by the heat provided by the hot source (and assuming that the latent heat of snap is still negligible). It is important to note that for small thermal hysteresis, the bimetallic strip heat engine yields higher conversion efficiencies than a simple pyroelectric generator. Yet, whatever the cycle, this thermal efficiency rapidly falls below the efficiency of the pyroelectric generator, mainly because of the higher heat capacitance of the bimetallic beams which need more heat per cycle. Whatever the value of the thermal hysteresis, the efficiency of the heat engine stays low, generally below one percent of Carnot.

Using the expression of the critical beam's amplitude (4.2.12a), it is possible to re-express the output energy and the thermal efficiency of the device. This way, the maximal output voltage generated by the second Stirling cycle is given by (4.2.12b), the electrical energy per cycle by (4.2.12c) and the Carnot efficiency by (4.2.12d).

$$w_S^c = -\frac{1}{\pi} \cdot \sqrt[3]{4 \cdot \frac{M_\alpha \cdot L^2}{N_e} \cdot \Delta T} \quad (4.2.12a)$$

$$V_{II} = \left| \frac{t_p \cdot p_3^s}{\epsilon_{33}^s} \cdot \Delta T + 8 \cdot \sqrt[3]{4 \cdot \frac{t_p \cdot e_{31}}{\epsilon_{33}^s} \cdot (z_p - z_o) \cdot \sqrt[3]{\frac{M_\alpha}{N_e \cdot L^4} \cdot \Delta T}} \right| \quad (4.2.12b)$$

$$\mathcal{W}_E = L \cdot v \cdot t_p \cdot \frac{p_3^{s2}}{\epsilon_{33}^s} \cdot \Delta T^2 \cdot \left(1 + 8 \sqrt[3]{4 \cdot \frac{z_p - z_o}{L} \cdot \frac{e_{31}}{p_3^s} \cdot \sqrt[3]{\frac{M_\alpha}{N_e \cdot L} \cdot \frac{1}{\Delta T^2}}} \right)^2 \quad (4.2.12c)$$

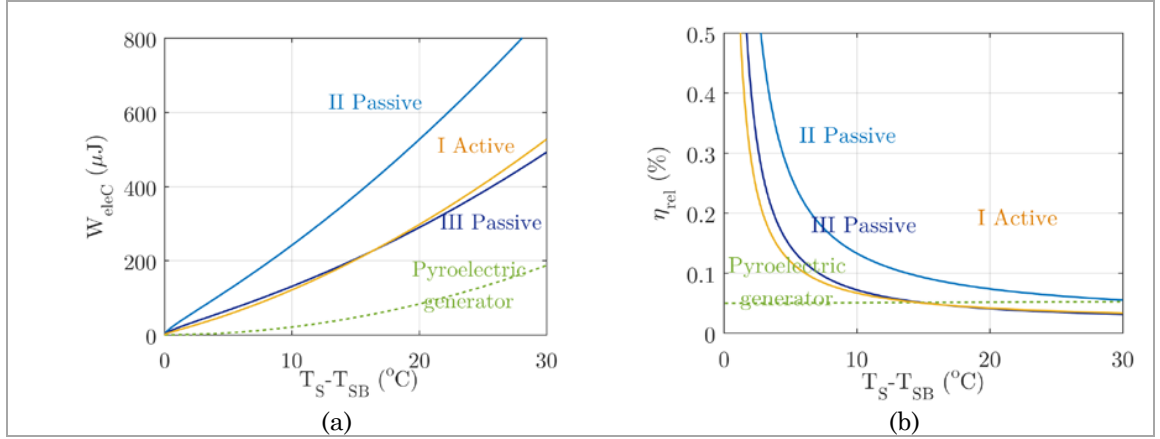


Figure 4.2.5. a. Comparison of the electrical energy produced by each cycle. b. Comparison Carnot efficiency of each cycle.

$$\eta_{TE}^{rel} = \frac{p_3^{s^2} \cdot (T_S + \theta_{ref})}{\varepsilon_{33}^s \cdot \rho_{pyro} \cdot c_{pyro}} \cdot \frac{L \cdot v \cdot t_p \cdot \rho_{pyro} \cdot c_{pyro}}{C_v} \left(1 + 8^{\frac{3}{4}} \cdot \frac{z_p - z_o}{L} \cdot \frac{e_{31}}{p_3^s} \cdot \sqrt[3]{\frac{M_\alpha}{N_e \cdot L}} \cdot \frac{1}{\sqrt[3]{\Delta T^2}} \right)^2 \quad (4.2.12d)$$

These formulae enable to redefine the Figures of Merit of the novel pyroelectric generator in order to take into account the effect of the tertiary pyroelectric effect. The FOM of the energy is then given by (4.2.13a) and the modified electro-thermal coupling factor by (4.2.13b).

$$FOM_W^{PBSHE} = FOM_W^{pyro} \cdot \left(1 + 8^{\frac{3}{4}} \cdot \frac{z_p - z_o}{L} \cdot \frac{e_{31}}{p_3^s} \cdot \sqrt[3]{\frac{M_\alpha}{N_e \cdot L}} \cdot \frac{1}{\sqrt[3]{\Delta T^2}} \right)^2 \quad (4.2.13a)$$

$$k_{PBSHE}^2 = k_{pyro}^2 \cdot \frac{L \cdot v \cdot t_p \cdot \rho_{pyro} \cdot c_{pyro}}{C_v} \cdot \left(1 + 8^{\frac{3}{4}} \cdot \frac{z_p - z_o}{L} \cdot \frac{e_{31}}{p_3^s} \cdot \sqrt[3]{\frac{M_\alpha}{N_e \cdot L}} \cdot \frac{1}{\sqrt[3]{\Delta T^2}} \right)^2 \quad (4.2.13b)$$

Hence the performances of the systems are given by (4.2.14).

$$\mathcal{W}_E^{PBSHE} = F_W^{BSHE} \cdot L \cdot v \cdot t_p \cdot \Delta T^2 \quad (4.2.14a)$$

$$\eta_{TE}^{abs,PBSHE} = k_{BSHE}^2 \cdot \eta_{TE}^{abs,pyro} \quad (4.2.14b)$$

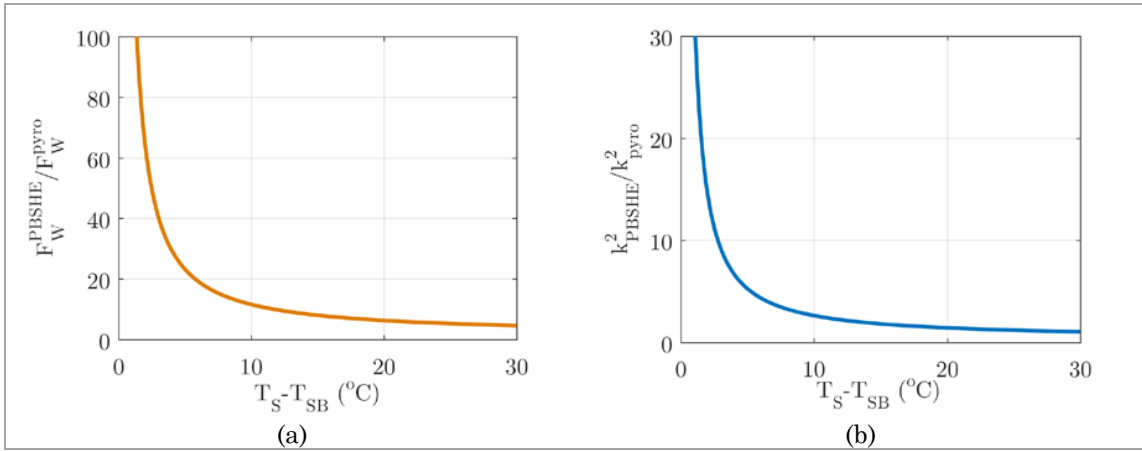


Figure 4.2.6. a. Evolution of the improvement factor of the Figure of Merit of the available energy for the second Stirling cycle. b. Improvement factor of the electro-thermal coupling factor.

The analysis of the new FOM and the new electro-thermal coupling factor reveals two important facts explaining the observations made on Fig.4.2.5. First the tertiary pyroelectric effect is efficient for low thermal hystereses and its impact on the energy becomes less important as the thermal hysteresis widens, because of its 2/3 power dependence on the thermal hysteresis. The relative increase of the FOM is plotted in Fig.4.2.6a showing a FOM enhanced by a factor x23 for a hysteresis of 5°C using thermo-mechanical bistability. The second observation is the degradation of the electro-thermal coupling factor for wide hystereses. Because of the ratio of heat capacitances, the advantage of using the bistability is lost for very large hystereses: for a hysteresis of 3°C, the electro-thermal coupling factor is improved by a factor 5, while it falls below 1 above 30°C of hysteresis.

e. Comparing piezoelectric materials

Now that we found the best type of Stirling cycle, we compare the performances of the heat engine when the PZT layer is replaced by another pyroelectric material. Using the data from Tab.2.2.1, we calculate the FOM and the electro-thermal coupling factor (also corresponding to the intrinsic Carnot efficiency of the beam) obtained with a beam having a hysteresis of 3°C. The data obtained are represented in Fig.4.2.7a where the FOM of the pyroelectric bimetallic strip heat engine is plotted against the FOM of the pyroelectric generator, and in Fig.4.2.7b which compares the Carnot efficiency of the two heat engines. Because of the weak stiffness of PVDF, the performance of the heat engine based on PVDF is weakly increased by the use of the bimetallic strip. In contrary for all other materials, the improvement of the FOM is significant and PMN-PT stays the best material to harvest heat, even if the greatest improvement is observed for PZT soft ceramics. Fig.4.2.7b shows that for PMN-PT and PVDF, with a beam having a hysteresis of 3°C, the use of the bimetallic strip heat engine does not increase the Carnot efficiency of the transduction nor the electro-thermal coupling factor of the pyroelectric material. However, for the other materials, the improvement of the efficiency is important, passing from 0.17% to 0.58% for PZT-5H. PMN-PT is the best material with an efficiency of 3.6%.

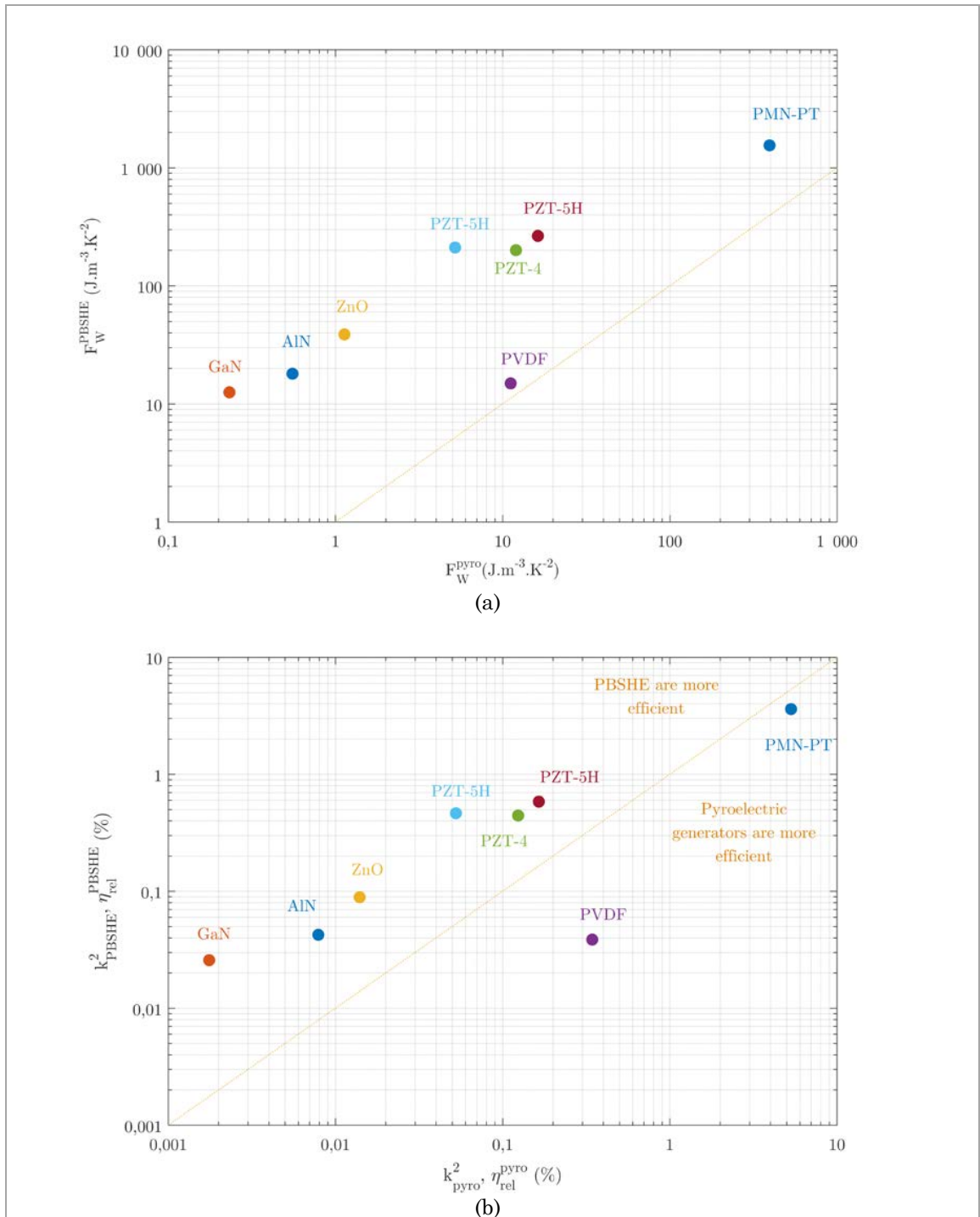


Figure 4.2.7. a. Comparison of the Figures of Merit of the pyroelectric bimetallic strip heat engine and the pyroelectric generators using various pyroelectric materials. b. Comparison of the electro-thermal coupling factor of the pyroelectric materials using the two types of heat engine.

4.3 Influence of the architecture, extrinsic performances of the energy harvester

In the previous part, we considered the intrinsic performances of the pyroelectric bimetallic strip heat engine when it is polarized according to the Stirling cycle. The modeled performances thus correspond to the case of a bimetallic strip not constrained into an architecture, and they could be reached if the heat engine is used to harvest slow variations of the temperature. To obtain the generated power, it would be necessary to multiply the previous formula of the available energy by the frequency of the temperature variations. In the previous chapter we treated both the modeling of the thermal transfers inside the energy harvester (bimetallic strip and architecture), and the modeling of the architecture's impact on the mechanical bistability of the bimetallic beam. We especially demonstrated that the architecture modifies the bimetal thermostat's thermal hysteresis, thereby increasing the operation frequency of the device, but also that it degrades the energetical performances of the devices. The consequence of these two results is the occurrence of an optimal design that maximizes the output energy of the system. In this part, we will describe the main effects of the architecture on the dynamic performances of the energy harvester when a pyroelectric material is used to convert the beam's mechanical strain into electrical energy.

a. Stirling cycles

We follow the same reasoning than in the previous chapter and we consider a beam constrained in an architecture characterized by w_{top} and w_{bot} , which verify (4.3.1a) and (4.3.1b), and by a total thickness given by (4.3.1c). Fig.4.4.1a recalls the scheme of the harvester's architecture whereas Fig.4.4.1b gives the evolution of the thickness of the device's cavity as a function of the beam's intrinsic thermal hysteresis when a PZT-5H-Al-Invar beam is used as a prime mover of the heat engine. We recall that the thermal hysteresis of the beam in the cavity is a function of the ratio r_w and the intrinsic thermal hysteresis and is given by (4.3.1d).

$$|w_{bot}| = |w_{top}| = r_w \cdot |w_S^c| \quad (4.3.1a)$$

$$r_w \leq 1 \quad (4.3.1b)$$

$$t_{cav} = |w_{bot}| + |w_{top}| + t \quad (4.3.1c)$$

$$\Delta T_{cav} = \frac{3}{2} \cdot \left(r_w - \frac{r_w^3}{3} \right) \cdot \Delta T \quad (4.3.1d)$$

As for the description of the Stirling cycles for a non-constrained beam, we can write the evolution of the electrical charge carried by the pyroelectric capacitor as a function of its output voltage. In brief, we can demonstrate that the maximal output voltage for the first Stirling cycle is given by (4.3.2a). This expression leads to find (4.3.2b) as an expression of the electrical energy produced by the energy harvester during a complete cycle. It can be seen that the Stirling cycle of the constrained beam produces as much energy as the non-constrained beam when the thickness ratio is equal to 1.

$$\mathcal{V}_I^{cav} = |\mathcal{V}_S^c| = |\mathcal{V}_{SB}^c| = \left| \frac{t_p \cdot p_3^s}{\varepsilon_{33}^s} \cdot \Delta T_{cav} - 4 \cdot \frac{\pi \cdot t_p \cdot e_{31}}{L^2 \cdot \varepsilon_{33}^s} \cdot (z_p - z_o) \cdot w_{top} \right| \quad (4.3.2a)$$

$$\mathcal{W}_I^{cav} = \mathcal{C}_p \cdot \mathcal{V}_I^2 = \mathcal{C}_p \cdot \left(\frac{3}{2} \cdot \left(r_w - \frac{r_w^3}{3} \right) \cdot \frac{t_p \cdot p_3^S}{\varepsilon_{33}^S} \cdot \Delta T + 4 \cdot \frac{\pi \cdot t_p \cdot e_{31}}{L^2 \cdot \varepsilon_{33}^S} \cdot r_w \cdot (z_p - z_o) \cdot w_S^C \right)^2 \quad (4.3.3b)$$

The fact of constraining the beam in the architecture reduces the performances of the second Stirling cycle. For that cycle, the performances are given by (4.3.3a) and (4.3.3b), and differ from the previous equations only by the sign of the tertiary pyroelectric effect. The difference of performances between these two cycles is mainly due to the value of the thermal asymmetry linked to the position of the pyroelectric layer with respect to the bimetallic beam.

$$\mathcal{V}_{II}^{cav} = |\mathcal{V}_S^S| = |\mathcal{V}_{SB}^S| = \left| \frac{t_p \cdot p_3^S}{\varepsilon_{33}^S} \cdot \Delta T_{cav} + 4 \cdot \frac{\pi \cdot t_p \cdot e_{31}}{L^2 \cdot \varepsilon_{33}^S} \cdot (z_p - z_o) \cdot w_{top} \right| \quad (4.3.4a)$$

$$\mathcal{W}_{II}^{cav} = \mathcal{C}_p \cdot \mathcal{V}_{II}^2 = \mathcal{C}_p \cdot \left(\frac{3}{2} \cdot \left(r_w - \frac{r_w^3}{3} \right) \cdot \frac{t_p \cdot p_3^S}{\varepsilon_{33}^S} \cdot \Delta T - 4 \cdot \frac{\pi \cdot t_p \cdot e_{31}}{L^2 \cdot \varepsilon_{33}^S} \cdot r_w \cdot (z_p - z_o) \cdot w_S^C \right)^2 \quad (4.3.4b)$$

Finally, the third Stirling cycle is characterized by the voltage drop due to the beam's heating and the voltage of the beam's snap. These two quantities are given by (4.3.5a) and (4.3.5b). As a consequence, the energy generated by the third type of Stirling cycle is given by (4.3.5c). This last equation shows that by decoupling the heating and cooling phases from the beam's snap and snap-back, the energy associated to the cross-term of the primary and tertiary pyroelectric effect is lost.

$$u_{III,heating}^{cav} = \frac{t_p \cdot p_3^S}{\varepsilon_{33}^S} \cdot \Delta T_{cav} \quad (4.3.5a)$$

$$u_{III,snap}^{cav} = 4 \cdot \frac{\pi \cdot t_p \cdot e_{31}}{L^2 \cdot \varepsilon_{33}^S} \cdot (z_p - z_o) \cdot w_{top} \quad (4.3.5b)$$

$$\mathcal{W}_{III}^{cav} = \mathcal{C}_p \cdot \left(\left(\frac{3}{2} \cdot \left(r_w - \frac{r_w^3}{3} \right) \cdot \frac{t_p \cdot p_3^S}{\varepsilon_{33}^S} \cdot \Delta T \right)^2 + \left(4 \cdot \frac{\pi \cdot t_p \cdot e_{31}}{L^2 \cdot \varepsilon_{33}^S} \cdot r_w \cdot (z_p - z_o) \cdot w_S^C \right)^2 \right) \quad (4.3.5c)$$

If we plot the evolution of these energies as a function of the thermal hysteresis (Fig.4.3.2a and Fig.4.3.2b), we can see that depositing PZT on the active layer produces slightly more energy with the first Stirling cycle than PZT on the passive layer with the second Stirling cycle. This is mainly due to the position of the neutral axis that is closer to the piezoelectric layer position for the beam with PZT on the passive layer, making this type of beam more sensitive to the temperature. Because this difference is weak, in the rest of this chapter we will keep focusing on the performances of the second Stirling cycle. To see how the cavity's thinning impacts the performances of the heat engine, we extract from the previous equations the Figure of Merit of the energy per cycle and the electro-thermal coupling factor of the pyroelectric layer. Hence, the FOM becomes (4.3.6a) whereas the electro-thermal coupling factor is given by (4.3.6b).

$$FOM_W^{PBSHE,cav} = FOM_W^{pyro} \cdot \left(\frac{3}{2} \cdot \left(r_w - \frac{r_w^3}{3} \right) + 4 \sqrt[3]{4} \cdot r_w \cdot \frac{z_p - z_o}{L} \cdot \frac{e_{31}}{p_3^S} \cdot \sqrt[3]{\frac{M_\alpha}{N_e \cdot L}} \cdot \frac{1}{\sqrt[3]{\Delta T^2}} \right)^2 \quad (4.3.6a)$$

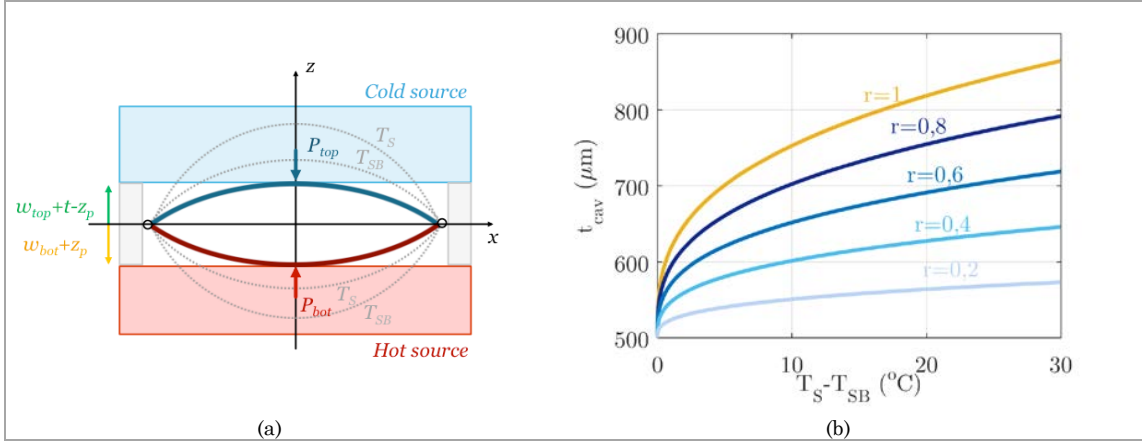


Figure 4.3.1. a. Schematic of the harvester. b. Cavity thickness as a function of the intrinsic thermal hysteresis of the beam (thermal hysteresis not modified by the mechanical action of the cavity on the beam).

$$k_{PBSHE,cav}^2 = k_{pyro}^2 \cdot \frac{L \cdot v \cdot \rho_{pyro} \cdot c_{pyro}}{C_v} \cdot \left(1 + \frac{8 \cdot \sqrt[3]{4}}{3 \cdot \left(1 - \frac{r_w^2}{3}\right)} \cdot \frac{z_p - z_o}{L} \cdot \frac{e_{31}}{p_3^S} \cdot \sqrt[3]{\frac{M_\alpha}{N \cdot L}} \cdot \frac{1}{\sqrt{\Delta T^2}} \right)^2 \quad (4.3.6b)$$

These two parameters are increasing functions of the factor r_w and are represented in Fig.4.3.2c and Fig.4.3.2d. Fig.4.3.2d shows that the advantage of using a bimetallic strip heat engine rapidly disappears: the Carnot efficiency of the device becomes lower than the efficiency of a simple pyroelectric generator when the beam's natural thermal hysteresis increases or when the cavity's thickness becomes smaller. For a beam with a hysteresis of 3°C, the efficiency of the system stays above the Carnot efficiency of the pyroelectric generator (around 0.2%). However, it should be noted that, contrary to the pyroelectric generator, the system now harvests heat from thermal gradients instead of harvesting heat from temperature temporal variations. Thus it is possible to define an equivalent ZT for the system in order to compare it with Seebeck generators. By inverting the expression of the Carnot efficiency of a Seebeck generator we can find the equivalent ZT of the generator (4.3.7a). Given that the electro-thermal coupling is weak, the heat engine's ZT can be linearly approximated by (4.3.7b).

$$ZT_{PBSHE,cav} = \left(\frac{1 + \frac{T_{SB}}{T_S} \cdot k_{PBSHE,cav}^2}{1 - k_{PBSHE,cav}^2} \right)^2 - 1 \quad (4.3.7a)$$

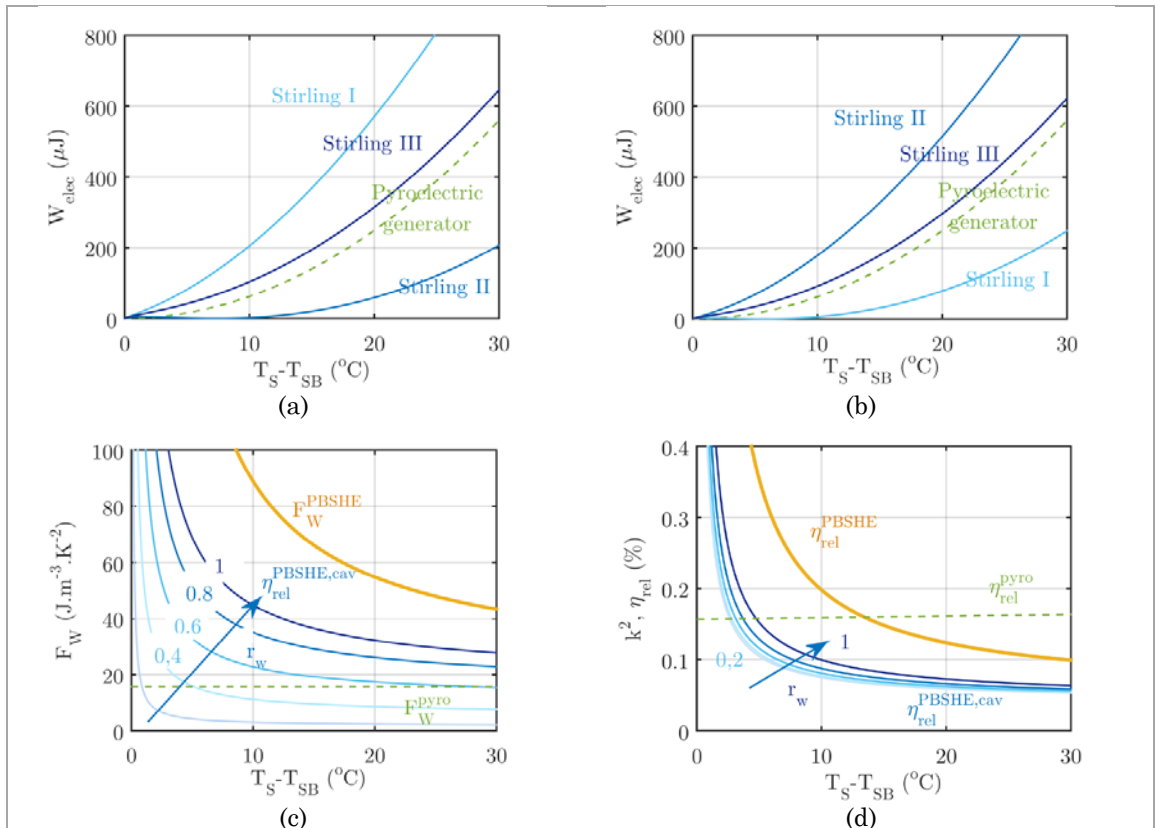
$$ZT_{PBSHE,cav} \approx 2 \cdot \left(1 + \frac{T_{SB}}{T_S} \right) \cdot k_{PBSHE,cav}^2 \quad (4.3.7b)$$

The Carnot efficiency and the equivalent ZT of various pyroelectric materials are represented in Fig.4.3.3a and Fig.4.3.3b. It shows that PMN-PT is still the best materials with an efficiency of 2% and an equivalent ZT of 0.081. The use of PZT ceramics enables to reach a Carnot efficiency of 0.22% with a ZT of 0.0089.

b. Dynamic performance of the harvester for fixed external temperature and no architectural leakage

Now that we determined the static performances of the harvester, we need to combine the previous equations with the lumped capacitance model developed in the previous chapter in order to extract the expression of the dynamic performances of the heat engine. Previously, we showed that the working frequency of the bimetallic strip between two heat sources depends on the two hot sources temperatures and the beam's thermal hysteresis in the cavity according to (4.3.8a), where R_{CC} and R_{CH} were the contact resistances between the heat sources and the beam. The comparison between the experimental measurements and the theoretical model showed that it is possible to get good results by taking them both equal to $10 \text{ K}\cdot\text{W}^{-1}$. Moreover, because the frequency is maximized if the median temperature of the hysteresis is equal to the average value of the hot and cold sources temperatures, the equation of the frequency can be simplified to (4.3.8b).

Figure 4.3.2. *a. Comparison of the output energy per cycle when the piezoelectric layer is deposited on the active layer with $r_w=1$. b. Comparison of the output energy per cycle when the piezoelectric layer is deposited on the passive layer. c. Evolution of the Figure of Merit as a function of the beam's thermal hysteresis and the cavity's thinning ratio and comparison with the intrinsic figure of Merit of the PBSHE and the pyroelectric generator. d. Evolution of the Carnot efficiency of the device.*



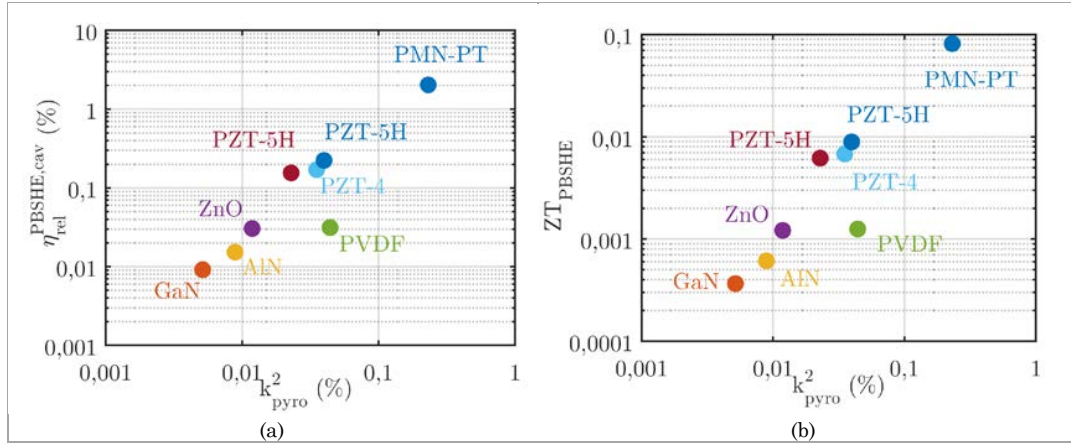


Figure 4.3.3. a. Carnot efficiency of the harvester with various pyroelectric materials, assuming a mean temperature of 100°C. b. Equivalent ZT of various pyroelectric materials.

$$f = \frac{1}{C_v \cdot \left(R_{CC} \cdot \ln \left(\frac{T_{S,cav} - T_C}{T_{SB,cav} - T_C} \right) + R_{CH} \cdot \ln \left(\frac{T_H - T_{SB,cav}}{T_H - T_{S,cav}} \right) \right)} \quad (4.3.8a)$$

$$f = \frac{1}{2 \cdot R_{CC} \cdot C_v \cdot \left(\ln \left(1 + \frac{\Delta T_{cav}}{T_H - T_C} \right) - \ln \left(1 - \frac{\Delta T_{cav}}{T_H - T_C} \right) \right)} \quad (4.3.8b)$$

With these equations, the average power produced by the harvester is simply the product of the working frequency by the electrical energy produced during a complete cycle, which means in terms of equation (4.3.9a). Developing this last equation as a function of the thermal hysteresis in the cavity leads to (4.3.9b).

$$P_E = \mathcal{W}_H^{cav} \cdot f \quad (4.3.9a)$$

$$P_E = \frac{L \cdot v \cdot t_p \cdot F_W^{pyro} \cdot \left(\Delta T_{cav} + 8 \cdot \frac{r_w}{\sqrt[3]{(3 \cdot r_w - r_w^3)}} \cdot \frac{z_p - z_o}{L} \cdot \frac{e_{31}}{p_3^S} \cdot \sqrt[3]{\frac{M_\alpha}{N_e \cdot L}} \cdot \sqrt[3]{\Delta T_{cav}} \right)^2}{2 \cdot R_{CC} \cdot C_v \cdot \left(\ln \left(1 + \frac{\Delta T_{cav}}{T_H - T_C} \right) - \ln \left(1 - \frac{\Delta T_{cav}}{T_H - T_C} \right) \right)} \quad (4.3.9b)$$

This equation is quite complex to understand. In order to simplify the study of this function, we introduce the quantity x corresponding to the ratio between the thermal hysteresis of the beam in the cavity and the temperature difference $T_H - T_C$ across the device (4.3.10a). In the same way, we define β_{pyro} the non-linear term coming from the tertiary pyroelectric effect (4.3.10b).

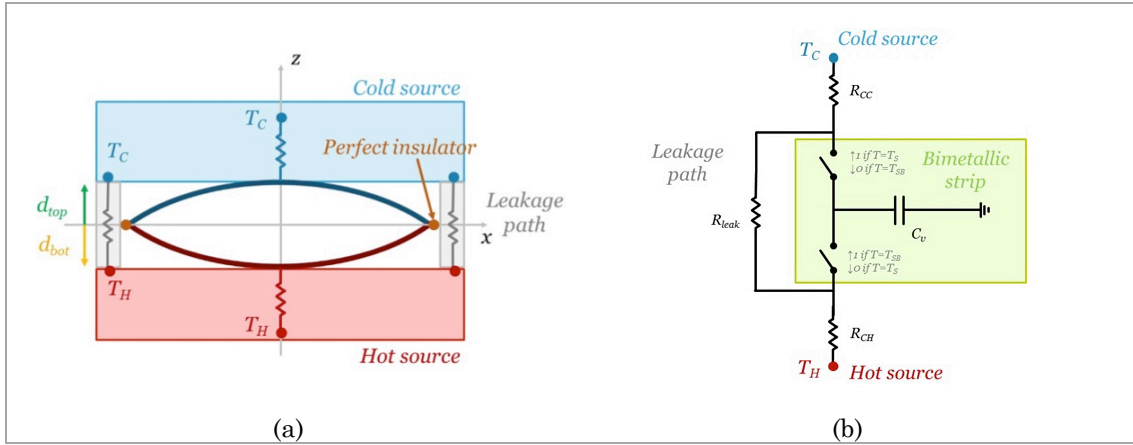


Figure 4.3.4. *a. Carnot efficiency of the harvester with various pyroelectric materials, assuming a mean temperature of 100°C. b. Equivalent ZT of various pyroelectric materials.*

$$x = \frac{\Delta T_{cav}}{T_H - T_C} \quad (4.3.10a)$$

$$\beta_{pyro} = 8 \cdot \frac{r_w}{\sqrt[3]{(3 \cdot r_w - r_w^3)}} \cdot \frac{z_p - z_o}{L} \cdot \frac{e_{31}}{p_3^S} \cdot \sqrt[3]{\frac{M_\alpha}{N_e \cdot L}} \cdot \frac{1}{\sqrt[3]{(T_H - T_C)^2}} \quad (4.3.10b)$$

This way, the power can be re-expressed as (4.3.11).

$$P_{mean} = \frac{L \cdot v \cdot t_p \cdot F_W^{pyro} \cdot (T_H - T_C)^2 \cdot (x + \beta_{pyro} \cdot \sqrt[3]{x})^2}{2 \cdot R_{CC} \cdot C_v \cdot (\ln(1+x) - \ln(1-x))} \quad (4.3.11)$$

Fig.4.3.5a then represents the evolution of the output power generated by a PZT-Al-Invar beam as a function of the ratio x and for various values of the thermal gradient across the harvester. In the same time, to complete the description of the dynamic performances of the system, Fig.4.3.5b draws the evolution of the working frequency of the prime mover as a function of the ratio x . The first figure shows that for very small values of x (hystereses smaller than 2°C for an external temperature of 30°C), the output power is a decreasing function of the ratio x . However, it rapidly increases for values of x between 0.1 and 0.8. This means that the increase of the electrical energy per cycle for highly unstable beams outweighs the reduction of the working frequency for large values of the beam's thermal hysteresis. After reaching an optimal value, the output power decreases when the beam's thermal hysteresis in the cavity becomes closer to the external temperature difference. The optimal value of the beam's thermal hysteresis is 21°C for a ratio r_w of 1 and a temperature difference of 30°C. For this hysteresis value, the output power is of 25.7 μ W for a working frequency of 0.045 Hz. For an external temperature of 15°C, the optimal hysteresis value is of 9.6 °C, producing 8.9 μ W.

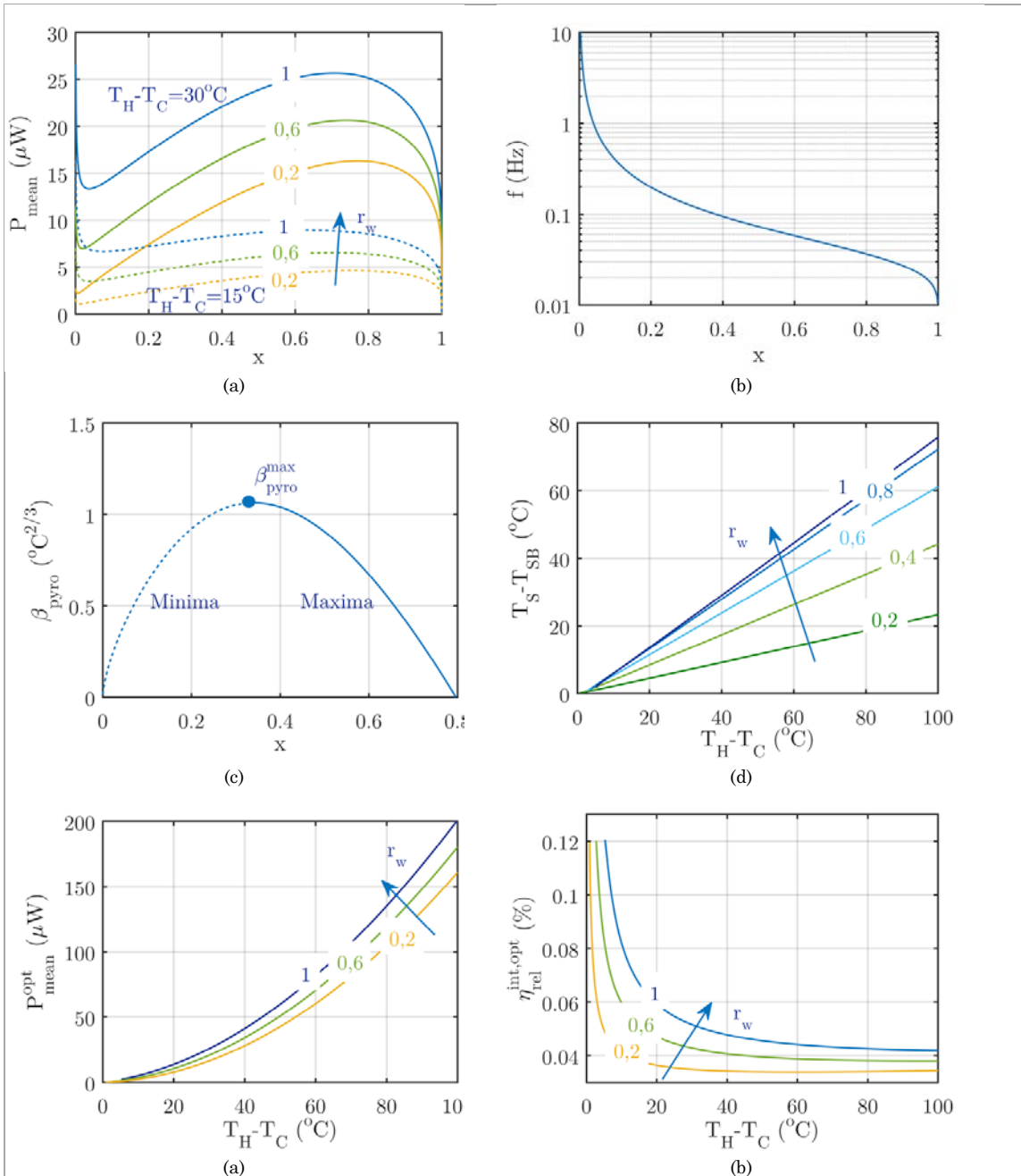


Figure 4.3.5. a. Output power generated by the PZT-Al-Invar beam as a function of the ratio x , for three values of the cavity's thickness ratio and two values of the external temperature difference. b. Working frequency of the device. c. Optimal values of x as a function of the parameter β_{pyro} . d. Choice of the hysteresis of the bistable beam as a function of external temperatures. e. Maximal power generated by the harvester when the thermal hysteresis is optimized. f. Carnot efficiency of the optimized system assuming that the mean temperature of the two heat sources is of 100°C .

When they exist, the extrema of power, either minimum or maximum, are solutions of (4.3.12a). The study of this function presented in Fig.4.3.5c shows that the optimum

values of x appear only for small values of β_{pyro} . These values must be lower than the limit value β_{pyro}^{max} given by (4.3.12b). The values of x maximizing the output power are then the extrema that are higher than 0.34 (4.3.12c). Indeed, for values of β_{pyro} higher than β_{pyro}^{max} , the power is a monotonic and decreasing function of x : the smallest the hysteresis, the higher the output power generated by the device.

$$\beta_{pyro} = -3 \cdot \sqrt[3]{x^2} \cdot \left(\frac{\ln\left(\frac{1+x}{1-x}\right) \cdot (x^2 - 1) + x}{\ln\left(\frac{1+x}{1-x}\right) \cdot (x^2 - 1) + 3 \cdot x} \right) \quad (4.3.12a)$$

$$\beta_{pyro} \leq \beta_{pyro}^{max} = 1,06 \quad (4.3.12b)$$

$$x_{opt} \geq 0,34 \quad (4.3.12c)$$

These equations thus enable to draw the dependence of the optimal natural thermal hysteresis of the beam on the external temperature difference (Fig.4.3.5d), the evolution of the maximal output power (Fig.4.3.5e), and the efficiency associated to the use of the beam having an optimal thermal hysteresis (Fig.4.3.5f). For a temperature difference of 40 °C, the maximal output power is 40 μ W (corresponding to a density of 10 μ W.cm⁻²) for a Carnot efficiency of 0.048%.

c. Dynamic performance of the harvester with Robin conditions

Now that we determined the performances of the harvester when the temperature across the harvester are fixed, we need to evaluate these same performances when the heat flowing through the system is evacuated by means of a heat sink, either planar or with fans, and when the harvester architecture is leaky. The equations describing this case were presented in the previous chapter. Assuming that the heat sink has a thermal resistance R_{sink} and exchanges heat with its surroundings at ambient temperature T_{amb} , and that the harvester architecture has a thermal resistance R_{leak} , the temperature difference across the bistable beam is given by (4.3.13a), whereas the thermal efficiency of the device is given by (4.3.13b), and the Curzon-Ahlborn efficiency of the device by (4.3.13c).

$$T_H - T_C = \frac{R_{leak}}{R_{leak} + R_{sink}} \cdot T_H - T_{amb} \quad (4.3.13a)$$

$$\eta_{TE}^{abs,ext} \approx \frac{R_{leak} \cdot P_E}{(T_H - T_C)} \quad (4.3.13b)$$

$$\eta_{TE}^{CA,ext} \approx \frac{R_{leak} \cdot P_E}{(T_H - T_C)} \cdot \frac{\sqrt{T_H + 273,15}}{\sqrt{T_H + 273,15} - \sqrt{T_C + 273,15}} \quad (4.3.13c)$$

In Fig4.3.7a, we plot the evolution of the evolution of the maximal power obtained with the optimal bimetallic beam as a function of the hot source temperature and when the system works with a plane heat sink ($h_{sink} = 10 \text{ W.m}^{-2}\text{.K}^{-1}$ or $R_{sink} = 250 \text{ K.W}^{-1}$ if it has the same surface area as the bimetallic beam) or with a bulk heat sink ($h_{sink} = 1000 \text{ W.m}^{-2}\text{.K}^{-1}$). In both cases, the thermal resistance of the architecture is taken equal to 625 K.W^{-1} . The first observation, already made in the previous chapter, is the necessity to use a heat sink with fans to boost the performance of the harvester.

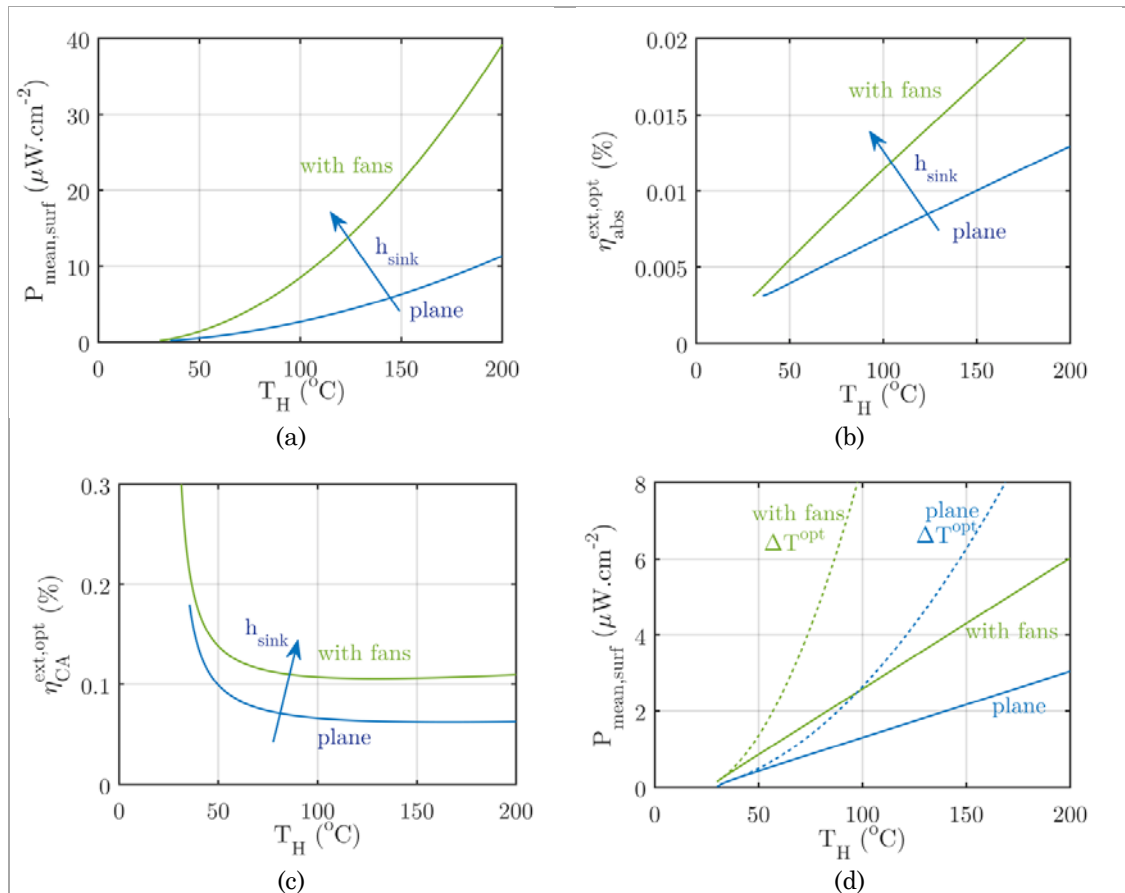


Figure 4.3.7. a. Maximal output power generated by the PZT-Al-Invar beam as a function of the hot source temperature and for an ambient temperature of 25°C. b. Thermo-electric efficiency of the system working with or without heat sink, when output power is maximal. c. Curzon-Ahlborn efficiency of the system as a function of the hot source temperature when output power is maximal. d. Comparison of the surface density of output power of a beam with hysteresis of 3°C working with our without heat sink, with the maximal surface density of output power produced with the optimal design of bimetallic beam.

As a consequence, with a hot source temperature fixed at 100°C, the surface density of power can be increased by a factor 3.3, from 2.6 $\mu\text{W}\cdot\text{cm}^{-2}$ to 8.5 $\mu\text{W}\cdot\text{cm}^{-2}$. Moreover, the using a heat sink improves the efficiency of the harvester by increasing the effective temperature difference across the energy harvester. The consequence of having a thermal conducting architecture can be mainly seen on the reduction of the thermo-electric efficiency of the system which is about $1.2 \cdot 10^{-5}$ % at 100°C (Fig.4.3.7b).

5 Coupling with an oscillating piezoelectric transducer

5.1 A short review of energy harvesting devices based on mechanical shock

The second type of thermal energy harvester using thermo-mechanically bistable beams is based on the use of a simple oscillating piezoelectric transducer that is impacted by the bistable beam each time the beam switches from the hot source to the cold source. Although it is the first time this technique is used in a thermal energy harvester, designing impact-based energy harvesters is not a new technique in the context of harvesting energy from mechanical vibrations. The first shock systems proposed were based on the impact of balls on piezoelectric transducers in order to harvest the energy of random vibrations, whereas classical piezoelectric harvesters used to harvest energy from vibrations close to their vibration frequency. Such devices were first proposed by [Umeda et al, 1996] and lately exposed in [Renaud et al, 2009] and [Alghisi et al, 2015]. These three teams also report the modeling of the shock between the harvester and the ball, however this model is not directly applicable to our system since the ball is not an oscillator. The use of impact has also been presented in [Gu and Livermore, 2011; Gu, 2011; Liu and Livermore 2015] in order to transfer the energy of a slowly-actuated, high-inertia oscillator to a higher-frequency piezoelectric oscillator. This kind of devices also enables to widen the bandwidth of the mechanical energy harvesters.

5.2 Modeling the shock between two oscillators

a. Mason model of the piezoelectric oscillator

In this part, we study three architectures represented in Fig.5.2.1a-b-c. In the first case (1a), the bimetallic strip is coupled with a clamped-clamped piezoelectric bimorph beam, which represents the current architecture of the piezoelectric system. The second architecture (1b) represents the coupling between the bimetallic strip and a simply supported beam. The last case (1c) corresponds to two cantilever beams having a length corresponding to half the length of the bimetallic beam. By using the constitutive equations of a piezoelectric layer of thickness t_p (properties d_{31} , ϵ_3 , E_p , located at a distance z_p of the neutral axis $z_{o,p}$) given in (2.2.9), and the local expression of the electric Gibbs energy (5.2.1a), it is possible to find the general expression of the piezoelectric oscillator's energy (5.2.1b) as a function of the mass m_p of the oscillator (or sum of the masses for the two cantilever beams), the equivalent bending stiffness of the beam $i_{e,p}$, the capacity of the piezoelectric layer C_p and the capacitor's voltage U_p . It must be noticed that the absolute value in the coupled term is used to define the use of one capacitor in the case of a simply supported beam or a cantilever beam, or three capacitors in the case of a clamped-clamped beam.

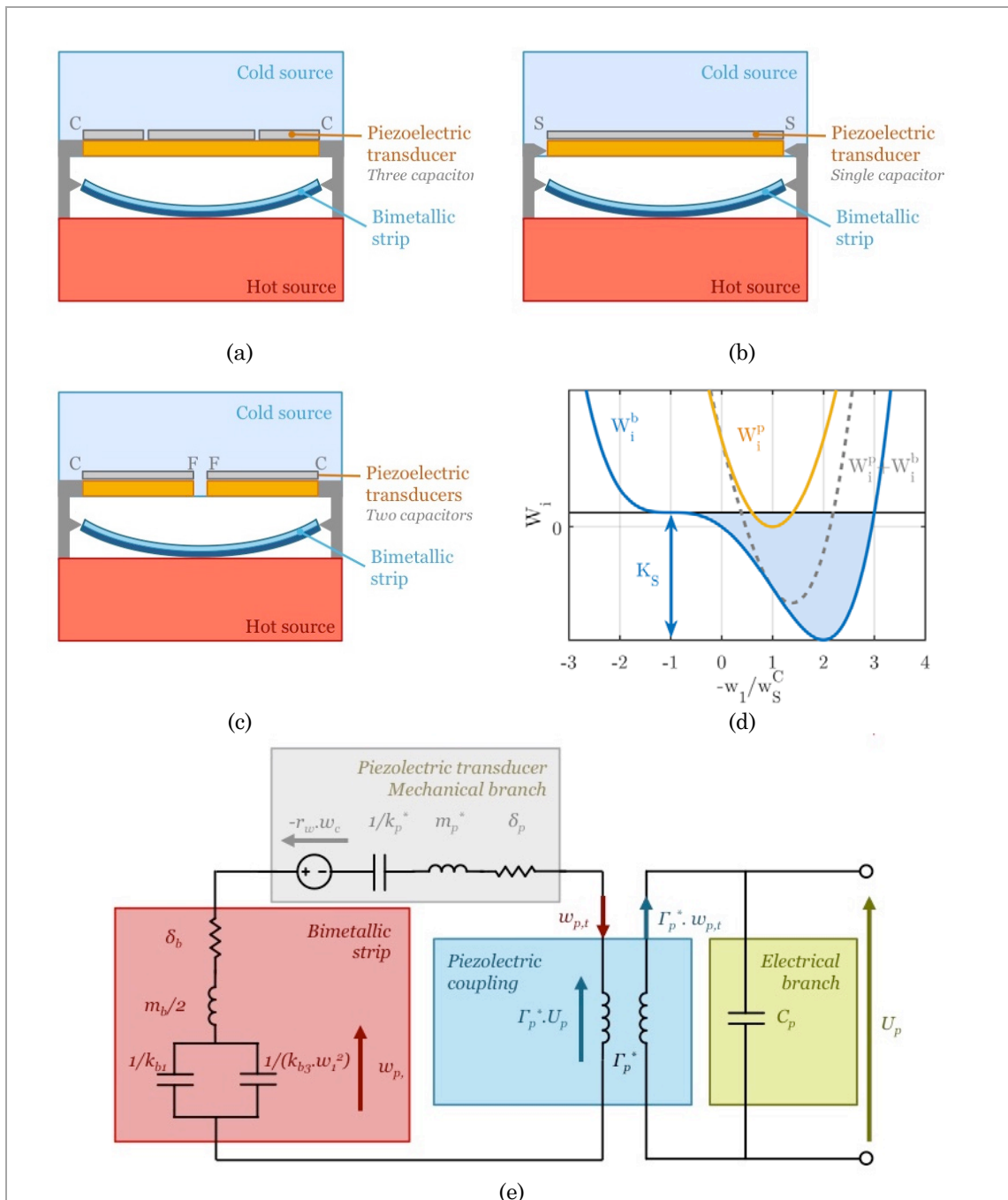


Figure 5.2.1. a. Architecture of the CC oscillator. b. Architecture of the SS oscillator. c. Architecture of the CF oscillator. d. Shape of the potential energy of both oscillators. e. Mason's model of the coupled oscillators.

$$d(\kappa + \mathcal{G}_{elec}) = \frac{1}{2} \cdot E \cdot d\mathcal{S}^2 - e_{31} \cdot d(\mathcal{E} \cdot \mathcal{S}) - \varepsilon_3^S \cdot d\mathcal{E}^2 + \frac{1}{2} \cdot \rho \cdot dw_{p,t}^2 \quad (5.2.1a)$$

$$\begin{aligned} \mathcal{K} + \mathcal{G}_{elec} = & \frac{m_p}{2 \cdot L} \cdot \int_{-L/2}^{L/2} w_{p,t}^2 \cdot dx + \frac{i_{e,p}}{2} \cdot \int_{-L/2}^{L/2} w_{p,xx}^2 \cdot dx \\ & - e_{31} \cdot (z_p - z_{o,p}) \cdot \mathcal{U}_p \cdot \int_{-L/2}^{L/2} |w_{p,xx}| \cdot dx - \mathcal{C}_p \cdot \mathcal{V}_p^2 \end{aligned} \quad (5.2.1b)$$

$$m_p = v \cdot L \int_0^t \rho \cdot dz \quad (5.2.1c)$$

$$EI = v \cdot \int_0^t E \cdot (z - z_{o,p}) \cdot dz \quad (5.2.1d)$$

$$\mathcal{C}_p = L \cdot v \cdot \frac{\varepsilon_3^S}{t_p} \quad (5.2.1e)$$

Using the boundary conditions corresponding to each type of oscillator, we can approximate the beam's shape by (5.2.2a-b-c) for the clamped-clamped beam (CC), the simply supported beam (SS) and the clamped-free beams (CF). It is possible to define generic parameters that enable to describe every type of piezoelectric oscillator (5.2.2d-e-f). These parameters are the equivalent mass m_p^* , the equivalent mechanical stiffness k_p^* , and the piezoelectric coupling coefficient Γ_p^* .

$$w_{p,CC}(x) = \frac{w_p}{2} \cdot \left(\cos\left(\frac{2 \cdot \pi \cdot x}{L}\right) + 1 \right) \quad (5.2.2a)$$

$$w_{p,SS}(x) = w_p \cdot \cos\left(\frac{\pi \cdot x}{L}\right) \quad (5.2.2b)$$

$$w_{p,CF}(x) = w_p \cdot \left(1 - \sin\left(\frac{\pi \cdot x}{L}\right) \right) \quad (5.2.2c)$$

$$m_{p,CC}^* = \frac{3}{8} \cdot m_p ; k_{p,CC}^* = \frac{2 \cdot \pi^4 \cdot EI}{L^3} ; \Gamma_{p,CC}^* = -\frac{4 \cdot \pi}{L} \cdot e_{31} \cdot (z_p - z_o) \quad (5.2.2d)$$

$$m_{p,SS}^* = \frac{1}{2} \cdot m_p ; k_{p,SS}^* = \frac{\pi^4 \cdot EI}{2 \cdot L^3} ; \Gamma_{p,SS}^* = -\frac{2 \cdot \pi}{L} \cdot e_{31} \cdot (z_p - z_o) \quad (5.2.2e)$$

$$m_{p,2CF}^* = m_p \cdot \frac{3 \cdot \pi - 8}{2 \cdot \pi} ; k_{p,2CF}^* = \frac{\pi^4 \cdot EI}{2 \cdot L^3} ; \Gamma_{p,2CF}^* = -\frac{2 \cdot \pi}{L} \cdot e_{31} \cdot (z_p - z_o) \quad (5.2.2f)$$

Hence, the oscillator's energy is given by (5.2.3a) and the mechanical equilibrium by (5.2.3b) where δ_p corresponds to the mechanical damping of the oscillator. The electrical equation of the oscillator is given by (5.2.3c). These equations enable to define the lumped parameter model of the oscillator, also called Mason model.

$$\mathcal{K} + \mathcal{U} = \frac{1}{2} \cdot m_p^* \cdot \dot{w}_p^2 + \frac{1}{2} \cdot k_p^* \cdot w_p^2 + \Gamma_p^* \cdot \mathcal{V}_p \cdot w_p - \frac{1}{2} \cdot \mathcal{C}_p \cdot \mathcal{V}_p^2 \quad (5.2.3a)$$

$$m_p^* \cdot \ddot{w}_p + k_p^* \cdot w_p + \Gamma_p^* \cdot \mathcal{V}_p + \delta_p \cdot \dot{w}_p = 0 \quad (5.2.3b)$$

$$\dot{\mathcal{Q}}_p = \Gamma_p^* \cdot \dot{w}_p - \mathcal{C}_p \cdot \dot{\mathcal{V}}_p \quad (5.2.3c)$$

b. Modeling of the shock

The bistable beam is modeled by a non-linear Duffing oscillator with negative linear stiffness, whose equivalent stiffness is deduced from the equation of equilibrium of the beam at the snap temperature (5.2.4a) (see Chapter 2, section 4). To model the losses due to the damping of the bimetallic strip, we define a damping coefficient δ_b .

$$\frac{1}{2} \cdot m_b \cdot \ddot{w}_1 - k_{b1} \cdot w_1 + k_{b3} \cdot w_1^3 + 2 \cdot k_{b3} \cdot w_S^C + 2 \cdot \delta_b \cdot \dot{w}_1 = 0 \quad (5.2.4a)$$

$$k_{b1} = \frac{3 \cdot N_e \cdot \pi^4}{8 \cdot L^3} \cdot w_S^{C2} = \frac{\pi^2}{2 \cdot L} \cdot (N_o - I_e \cdot \frac{\pi^2}{L^2}) \quad (5.2.4b)$$

$$k_{b3} = \frac{N_e \cdot \pi^4}{8 \cdot L^3} \quad (5.2.4c)$$

We assume that the neutral axis z_o^p of the piezoelectric oscillator is initially located at a distance $r_w \cdot w_S^C$ of the neutral axis of the bimetallic strip, so that when they are in contact, we have the equality (5.2.5). Naturally the ratio r_w still needs to be lower than 1 for the beam to be cycled between the two heat sources.

$$w_p = w_1 - r_w \cdot |w_S^C| \quad (5.2.5)$$

The shock between the two oscillators is quite complex to model mainly because of the non-linearity brought by the equilibrium equation of the bimetallic strip. Otherwise, if the bimetallic strip was a linear oscillator, (5.2.3.b) and (5.2.4a) could be easily solved independently when the two oscillators are not in contact and the coupling solved when they are in contact. If we assume that the initial speeds of the bimetallic strip and the piezoelectric oscillator are equal and that the capacitor is initially discharged, the oscillators stay stuck together because the piezoelectric transducer slows down due to the increase of its strain energy, and the bimetallic strip accelerates for the inverse reason. In this case, the equilibrium equation of the coupled oscillators is simply given by (5.2.6a), whereas the final position of equilibrium w_∞ is given by (5.2.6b). This equation can simply be solved with Cardan's formula.

$$\left(\frac{m_b}{2} + m_p^*\right) \cdot \ddot{w}_1 + (k_p^* - k_{b1}) \cdot w_1 + k_{b3} \cdot w_1^3 + (k_p^* \cdot r_w \cdot w_S^C + 2 \cdot k_{b3} \cdot w_S^{C3}) + (\delta_b + \delta_p) \cdot \dot{w}_1 + \Gamma_p^* \cdot \mathcal{V}_p = 0 \quad (5.2.6a)$$

$$r_\infty^3 + 3 \cdot (k_p^*/k_{b1} - 1) \cdot r_\infty + (3 \cdot k_p^*/k_{b1} \cdot r_w + 2) = 0 \quad (5.2.6b)$$

$$w_\infty = -r_\infty \cdot w_S^C \quad (5.2.6c)$$

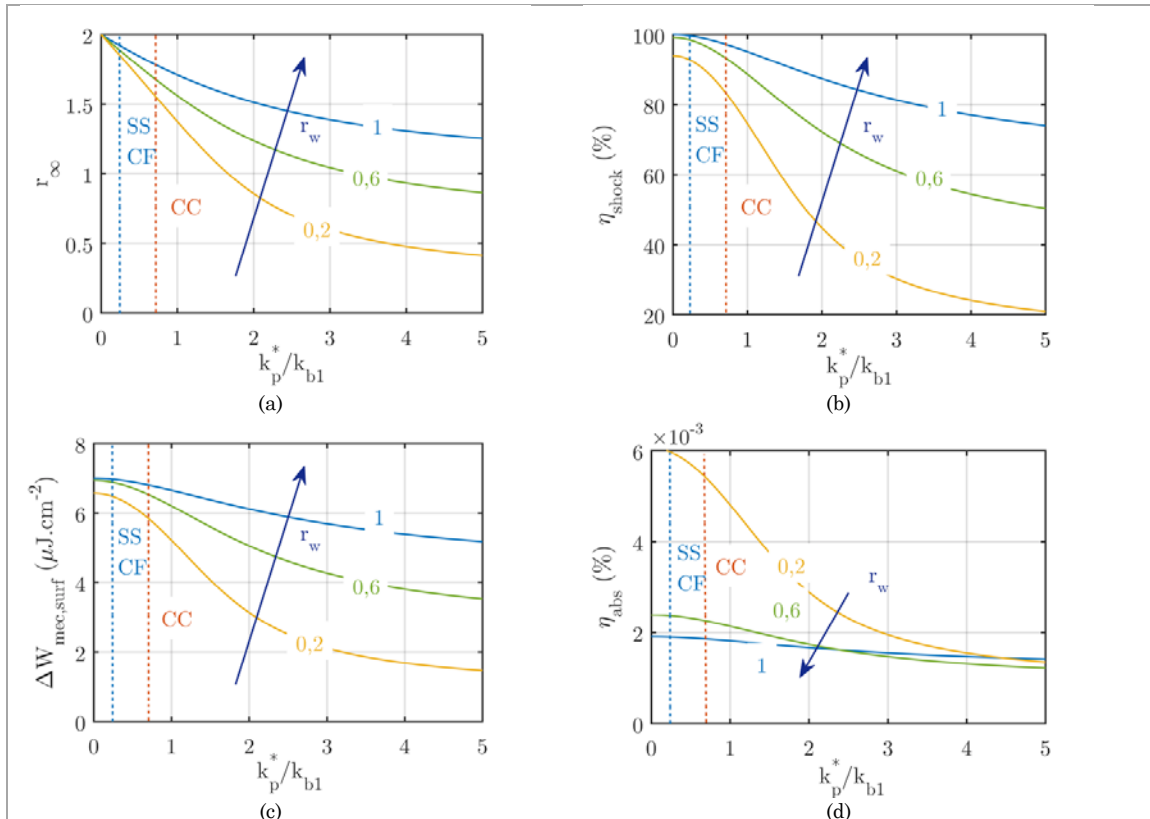
Assuming that the damping of the bimetallic strip is null before the impact, the conservation of energy enables to write that the initial kinetic energy of the coupled oscillators is given by (5.2.7a), whereas the maximal mechanical energy that can be harvested is given by (5.2.7b). Using the formula developed in the previous chapter, we can also express the efficiency of the thermo-mechanical transduction (5.2.7c), and the efficiency of the energy transfer during the shock (5.2.5e) by dividing the incident mechanical energy of the piezoelectric transducer by the kinetic energy of snap of the beam (5.2.7d).

Table 5.2.1. a. Properties of the two oscillators of Al-Invar and PZT-5H.

	L x v x t (mm)	t _{layers} (mm)	z _o (mm)	N _e (N)	I _e (N.m ²)	N _a (N.K ⁻¹)	M _a (N.m.K ⁻¹)	m _b (g)
Al-Invar	40x10x0,4	0,2 + 0,2	0,17	4,29.10 ⁵	5,22.10 ⁻³	3,54	4,17.10 ⁻⁴	0,86
Brass-PZT	40x10x0,1 8	0,08+0,1	0,08	1,41.10 ⁵	3,74.10 ⁻⁴	-	-	0,57

Table 5.2.1. b. Lumped parameters of the oscillators for a thermal hysteresis of 3°C. The last parameter is the fundamental frequency of the piezoelectric oscillator.

	Boundary conditions	k _{b1} (N.m ⁻¹)	k _{b3} (N.m ⁻³)	k _p [*] (N.m ⁻¹)	Γ _p [*] (N.V ⁻¹)	C _p (nF)	m _p [*] (g)	f _o (Hz)
Al-Invar	SS	1,75.10 ³	8,17.10 ¹⁰	-	-	52,1	0,86	-
Brass-PZT	CC	-	-	1,14.10 ³	3,41.10 ⁻³	52,1	0,21	367
Brass-PZT	SS	-	-	2,84.10 ²	1,71.10 ⁻³	52,1	0,28	159
Brass-PZT	2CF	-	-	2,84.10 ²	1,71.10 ⁻³	52,1	0,13	236

Figure 5.2.2. a. Evolution of the final equilibrium position as a function of the cavity's thickness ratio and the oscillators' stiffness ratio. **b.** Efficiency of the shock as a function of the oscillators' stiffnesses. **c.** Surface density of mechanical energy for the shock between a bistable Al-Invar beam and a piezoelectric oscillator. **d.** Thermo-mechanical efficiency of the mechanical transduction.

$$\frac{1}{2} \cdot \left(\frac{m_b}{2} + m_p^* \right) \cdot w_1^2 = \frac{4}{3} \cdot k_{b1} \cdot w_s^2 \quad (5.2.7a)$$

$$\Delta \mathcal{W}_M = \frac{k_{b1}}{12} \cdot w_s^2 \cdot ((r_w - 1)^3 \cdot (r_w + 3) + (r_\infty + 1)^3 \cdot (3 - r_\infty)) \quad (5.2.7b)$$

$$\eta_{TMM}^{abs} = \frac{2 \cdot \Delta \mathcal{W}_M}{C_v \cdot (3 \cdot r_w - r_w^3) \cdot \Delta T} \quad (5.2.7c)$$

$$\Delta \mathcal{K}_{snap} = \frac{27 \cdot N_e \cdot \pi^4}{32 \cdot L^3} \cdot w_s^4 = \frac{27}{12} \cdot k_{b1} \cdot w_s^2 \quad (5.2.7d)$$

$$\eta_{MM}^{abs} = \frac{\Delta \mathcal{W}_M}{\Delta \mathcal{K}_{snap}} = \frac{(r_w - 1)^3 \cdot (r_w + 3) + (r_\infty + 1)^3 \cdot (3 - r_\infty)}{27} \quad (5.2.7e)$$

In Fig.5.2.2a, we first plot the dependence of the final position on the ratio of the linear stiffness. Logically, we observe that the final position of the joined oscillators is a decreasing function of the piezoelectric transducer's stiffness and the ratio r_w : increasing the transducer's stiffness or bringing the transducer closer to the bimetallic strip opposes more resistance and the final position is reduced. The two extreme values of the transducers stiffness were already modeled in the previous chapter: if the transducer's rigidity is null, the bimetal can reach its natural equilibrium position corresponding to twice its critical amplitude before its snap. If the rigidity is infinite, we found that the value of r_∞ tends to r_w , as modeled in the previous chapter. These phenomena also explain the tendencies observed on the evolution of the shock's efficiency in Fig.5.2.2b. Reducing the transducer's thickness or increasing the gap between the two oscillators enables to let the bimetallic strip releases its kinetic energy more easily and so to transfer a maximal amount of this energy to the piezoelectric transducer.

In order to give the performances of a real device we consider the performances of an Al-Invar bimetallic beam having a thermal hysteresis of 3°C and impacting a brass-PZT5H beam whose properties are given in Table 5.2.1a. The PZT layer on the oscillator has the same thickness as the layer deposited on the bimetallic beam in section 3. The thickness of the brass is chosen so that the neutral axis is at the interface between the brass layer and the PZT layer in order to preserve electrical charges due to the inversion of the stress (tensile to compressive stress) in the PZT layer. In Table 5.2.1b, we give the lumped parameters of the Mason model of the piezoelectric transducers for the three types of boundary conditions. Logically, we observe that the effective mass and stiffness of the two clamped free beams are smaller than the clamped-clamped beam's effective mass and stiffness, however because of the reduction of the curvature of the beam, the piezoelectric coupling of the cantilever beams is weaker. The comparison between the simply supported beam and the cantilever beams shows that the effective mass of the cantilever beams is smaller, thus reducing its inertia.

In Fig.5.2.2a, we reported the values of the ratio between the effective stiffness of the piezoelectric transducer and the bimetallic strip's stiffness for the three types of boundary conditions. This clearly shows that, from a mechanical point of view, using two cantilever beams or a simply-supported transducer yields to better mechanical conversion efficiency than a clamped-clamped oscillator. Fig.5.2.2c represents the surface density of energy that can be generated with an Al-Invar beam and a PZT5H-brass transducer. The stiffness ratio is 16.3% for the SS and CF beams, and 65.3% for the CC beam. The maximal surface density of mechanical energy received by the piezoelectric transducer (if $r_w=1$) is 6.9 $\mu\text{J}\cdot\text{cm}^{-2}$ (99% efficiency) in the first case and 6.8 $\mu\text{J}\cdot\text{cm}^{-2}$ (97.5 % efficiency) in the second

case. The difference between the three systems is more visible if thicker transducers are used or if the device's cavity is thinner. Fig.5.2.2f gives the thermal efficiency of the conversion chain made of comprising the thermo-mechanical transduction by the bimetallic beam and the shock between the bimetallic beam and the piezoelectric transducer. Even if the shock is less efficient when the cavity is thin, when the transducer's stiffness is weak, the fact that the thermo-mechanical transduction is better for small thermal hysteresis has for consequence that the overall thermo-mechanical efficiency is better when the cavity's thickness is small. If the transducer stiffness becomes predominant, the device is more efficient when the cavity is thick.

c. Optimal mechanical energy

Even if it is not the final efficiency, we can define the maximal mechanical power that can be transferred to the piezoelectric transducer by following the same approach as in the previous chapter (Section 5.2). If the harvester works between two thermostatic heat sources, the mechanical power generated by the device is given by (5.2.8a). The study of a similar function was already presented in the previous chapter. The optimal thermal hysteresis that maximizes the output power is given by (5.2.8b). The equation of the maximal power is then given by (5.2.8c), whereas the mechanical efficiency associated to this optimum is given by (5.2.8d) (for a non-leaky architecture).

$$P_M^{int} = \frac{27}{4} \cdot \sqrt[3]{\frac{M_\alpha^4}{N_e \cdot L \cdot C_v^3 \cdot R_{CC}^3}} \cdot \frac{\eta_{MM}}{\sqrt[3]{(3 \cdot r_w - r_w^3)^4}} \cdot \frac{\sqrt[3]{\Delta T_{cav}^4}}{\ln\left(1 + \frac{\Delta T_{cav}}{T_H - T_C}\right) - \ln\left(1 - \frac{\Delta T_{cav}}{T_H - T_C}\right)} \quad (5.2.8a)$$

$$\Delta T_{cav}^{opt} = 0,589 \cdot (T_H - T_C) \quad (5.2.8b)$$

$$P_M^{int,opt} = 2,46 \cdot \frac{\eta_{MM}}{\sqrt[3]{(3 \cdot r_w - r_w^3)^4}} \cdot \sqrt[3]{\frac{M_\alpha^4}{N_e \cdot L \cdot C_v^3 \cdot R_{CC}^3}} \cdot \sqrt[3]{(T_H - T_C)^4} \quad (5.2.8c)$$

$$\eta_{TMM}^{abs,int,opt} = 11,3 \cdot \frac{\eta_{MM}}{\sqrt[3]{3 \cdot r_w - r_w^3}} \cdot \sqrt[3]{\frac{M_\alpha^4}{N_e \cdot L \cdot C_v^3}} \cdot \sqrt[3]{T_H - T_C} \quad (5.2.8e)$$

Similarly, if the heat is evacuated with a heat sink (resistance R_{sink}) and if the architecture conducts heat from the hot source to the heat sink (resistance R_{leak} lower than the equivalent resistance of the bimetallic strip), the maximal power is given by (5.2.9a) and the efficiency associated to this optimum by (5.2.9b).

$$P_M^{ext,opt} = 2,46 \cdot \frac{\eta_{MM}}{\sqrt[3]{(3 \cdot r_w - r_w^3)^4}} \cdot \sqrt[3]{\frac{M_\alpha^4}{N_e \cdot L \cdot C_v^3 \cdot R_{CC}^3}} \cdot \sqrt[3]{\frac{R_{leak}^4}{(R_{leak} + R_{sink})^4}} \cdot \sqrt[3]{(T_H - T_{amb})^4} \quad (5.2.9a)$$

$$\eta_{TMM}^{abs,ext,opt} = 2,46 \cdot \frac{\eta_{MM}}{\sqrt[3]{(3 \cdot r_w - r_w^3)^4}} \cdot \sqrt[3]{\frac{M_\alpha^4}{N_e \cdot L \cdot C_v^3 \cdot R_{CC}^3}} \cdot \sqrt[3]{\frac{R_{leak}^4}{R_{leak}^2 \cdot (R_{leak} + R_{sink})}} \cdot \sqrt[3]{T_H - T_{amb}} \quad (5.2.9b)$$

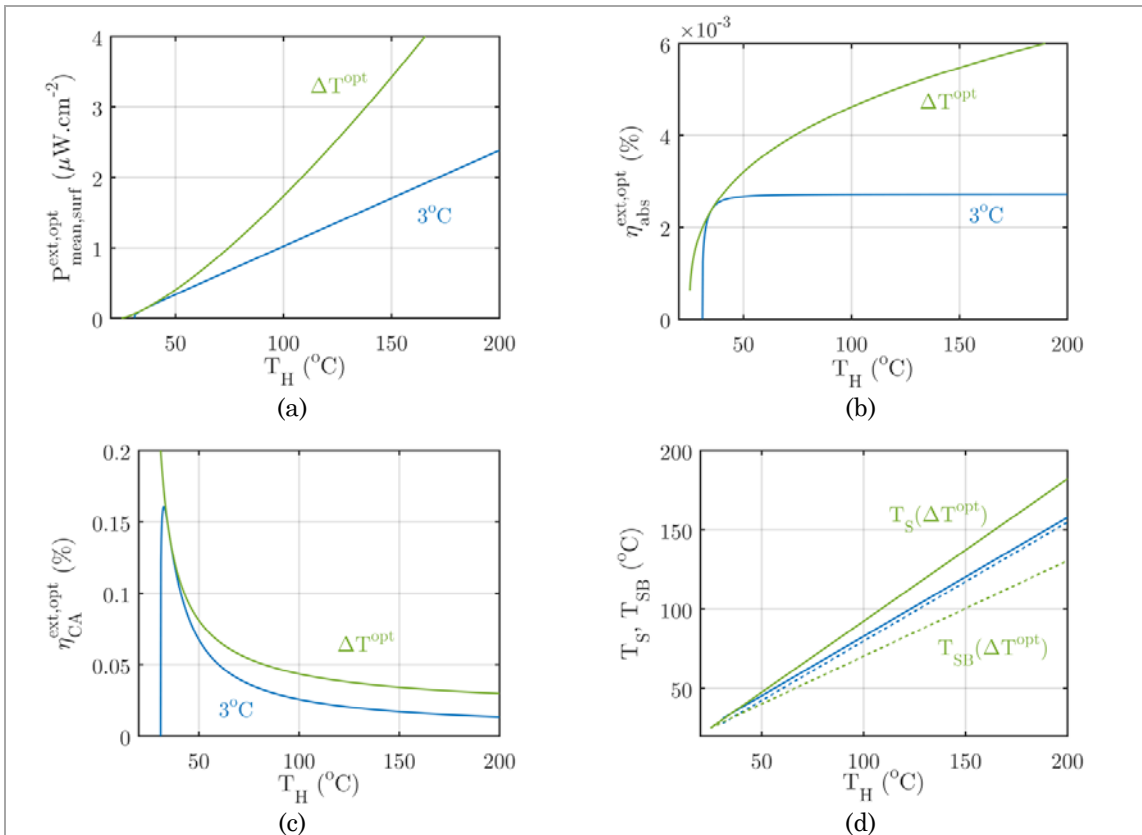


Figure 5.2.3. a. Mechanical energy released by the bimetallic strip to a clamped-clamped piezoelectric transducer as a function of the hot source temperature, for $r_w=1$ and $T_{amb}=25^\circ\text{C}$. b. Thermal efficiency of the transduction. c. Curzon-Ahborn efficiency of the transduction. d. Evolution of the snap and snap-back temperatures of the optimal bimetallic strip as a function of the hot source temperature.

Since in the current energy harvester the piezoelectric transducer is intended to be used as a planar heat sink, we focus our analysis on the performances of the harvester working without bulk heat sink. Fig.5.2.3a represents the maximal surface density mechanical power (corresponding to the maximal output electrical power if the efficiency of the electro-mechanical transduction is 100%) that is transferred to a clamped-clamped piezoelectric transducer with a bimetallic strip having an optimized thermal hysteresis or a thermal hysteresis of 3°C . At 100°C , for a bimetal thermostat 80°C - 83°C , the available output power is $1.0 \mu\text{W}\cdot\text{cm}^{-2}$, corresponding to 59% of the maximal power that can be obtained with the bimetal thermostat 70°C - 99°C ($1.7 \mu\text{W}\cdot\text{cm}^{-2}$). At that temperature, the thermal efficiency of the energy harvester using the optimal bimetallic strip is $4.10^{-3}\%$, corresponding to $4.3.10^{-2}\%$ of the Curzon-Ahborn efficiency.

5.3 Electrical performances of the system

a. Open circuit voltage

Now that we studied the mechanical performances of the harvester, we can look at the evolution of the output voltage generated by the harvester. In open circuit, the stiffness of the piezoelectric transducer is modified and the output voltage is given by (5.3.1a), the equilibrium equation becomes (5.3.1b), whereas the final position is given by (5.3.1c). The initial conditions are given by (5.3.1d) and (5.3.1e).

$$V_p^{oc} = \frac{\Gamma_p^*}{C_p} \cdot w_p \quad (5.3.1a)$$

$$\begin{aligned} \left(\frac{m_b}{2} + m_p^*\right) \cdot \ddot{w}_1 + \left(k_p^* - k_{b1} + \frac{\Gamma_p^{*2}}{C_p}\right) \cdot w_1 + k_{b3} \cdot w_1^3 \\ + \left(\left(k_p^* + \frac{\Gamma_p^{*2}}{C_p}\right) \cdot r_w \cdot w_S^c + 2 \cdot k_{b3} \cdot w_S^{c3}\right) + (\delta_b + \delta_p) \cdot \dot{w}_1 = 0 \end{aligned} \quad (5.3.1b)$$

$$k_{b1} \cdot r_\infty^3 + 3 \cdot \left(k_p^* + \frac{\Gamma_p^{*2}}{C_p} - k_{b1}\right) \cdot r_\infty + \left(3 \cdot \left(k_p^* + \frac{\Gamma_p^{*2}}{C_p}\right) \cdot r_w + 2 \cdot k_{b1}\right) = 0 \quad (5.3.1c)$$

$$w_1(0) = -r_w \cdot w_S^c \quad (5.3.1d)$$

$$\dot{w}_1(0) = v_o = -4 \cdot w_S^c \cdot \sqrt{\frac{k_{b1}}{m_b + 2 \cdot m_p^*}} \quad (5.3.1e)$$

We can solve the previous equation by using the Runge-Kutta method. In Fig.5.3.1, we plot the temporal evolution of the output voltage in open-circuit, the oscillator displacement amplitude, and the phase portrait obtained with the three possible configurations of piezoelectric transducers, assuming a mechanical quality factor of 14. These figures show that the output voltage is higher for the clamp-clamped transducer because of its piezoelectric coupling that is higher than those of the other configurations. As a consequence, this type of piezoelectric transducer will be the only one to be studied in the next part of this chapter. The value of 16.9 V of the first peak is close to the values experimentally measured (15 to 20 V), which validates the model.

An important fact that can be noticed is the asymmetry of the phase portrait, which is more pronounced in the case of clamped-free beams. When the stiffness of the piezoelectric oscillator is smaller than the linear stiffness of the bimetallic strip, (5.3.1b) describes the behavior a damped asymmetric bistable Duffing oscillator. Numerous examples of symmetric bistable Duffing oscillators (or twin-well oscillator) are reported in the literature [Tseng and Dugundji, 1971, Moon and Homes, 1979, Arrieta *et al*, 2010] and have extensively been studied, mainly because of the possible occurrence of chaotic behavior in forced regime [Holmes, 1979, Kovacic and Brennan, 2011]. Using bistable Duffing oscillators to widen the bandwidth of vibrations energy harvester was first suggested by [Ramlan *et al*, 2009] and is now an important field of research in energy harvesting given the large number of techniques to induce mechanical bistability (magnetic repulsion/attraction, buckling...). Extensive reviews of these applications are exposed in [Harne and Wang, 2013] and [Zhu *et al*, 2009]. In this chapter, we will only present two methods to approximate the solutions of this equation. Exhaustive overviews

of other mathematical methods are reported in [Kovacic and Brennan, 2011, Nayfeh and Mook, 1979, Jordan and Simith, 2007].

The first method uses Jacobi elliptic functions to approximate the behavior of the oscillator. When the piezoelectric oscillator's stiffness is greater than the bimetallic strip's stiffness, (5.3.1b) describes a hardening Duffing oscillator with a positive linear stiffness and a positive cubic stiffness in damped free regim. The beam's shape can be approximated by (5.3.2b) where w approximately verifies (5.3.2a) by defining the various coefficients by (5.3.2b) to (5.3.2e).

$$\ddot{w} + 2. \delta. \dot{w} + \alpha. w + \gamma. w^3 = 0 \quad (5.3.2a)$$

$$w_1(t) = w(t) + w_\infty \quad (5.3.2b)$$

$$\delta = \frac{\delta_b + \delta_p}{m_b + 2. m_p^*} \text{ assuming } \delta_b = \delta_p \quad (5.3.2c)$$

$$\alpha = 2. \frac{k_p^* - k_{b1} + \frac{\Gamma_p^{*2}}{C_p}}{m_b + 2. m_p^*} \quad (5.3.2d)$$

$$\gamma = 2. \frac{k_{b3}}{m_b + 2. m_p^*} \quad (5.3.2e)$$

The solution of (5.4.2a) is a damped elliptic Jacobi function (5.3.3a), where the amplitude and the initial phase shift must be solved with the initial conditions.

$$w_1(t) = w_\infty + w_o. e^{-\delta.t}. cn(\omega. t + \theta, k^2) \quad (5.3.3a)$$

$$w_o. cn(\theta, k^2) = (r_\infty - r_w). w_s^c = B \quad (5.3.3b)$$

$$w_o. sn(\theta, k^2). dn(\theta, k^2) = -\frac{1}{\omega}. (v_o + B. \delta) = -\frac{A}{\omega} \quad (5.3.3c)$$

Injecting this function in the differential equation leads to find the expression of the pulsation at the resonance, and the elliptic modulus k as a function of the initial amplitude and the physical parameters of the system. Finding the amplitude and phase shift is quite hard and this problem is generally solved with the assumption that the oscillator's initial speed is equal to zero [Kovacic and Brennan, 2011]. In our case, we found that the vibration amplitude is a solution of the polynomial (5.3.4c).

$$\omega^2 = \alpha + \gamma. w_o^2 - \delta^2 \quad (5.3.4a)$$

$$k^2 = \frac{\gamma. w_o^2}{2. \omega^2} \quad (5.3.4b)$$

$$w_o^4 + \frac{2. (\alpha - \delta^2)}{\gamma}. w_o^2 - B^2. \left(\frac{2. (\alpha - \delta^2)}{\gamma} + B^2 \right) - \frac{2. A^2}{\gamma} = 0 \quad (5.3.4c)$$

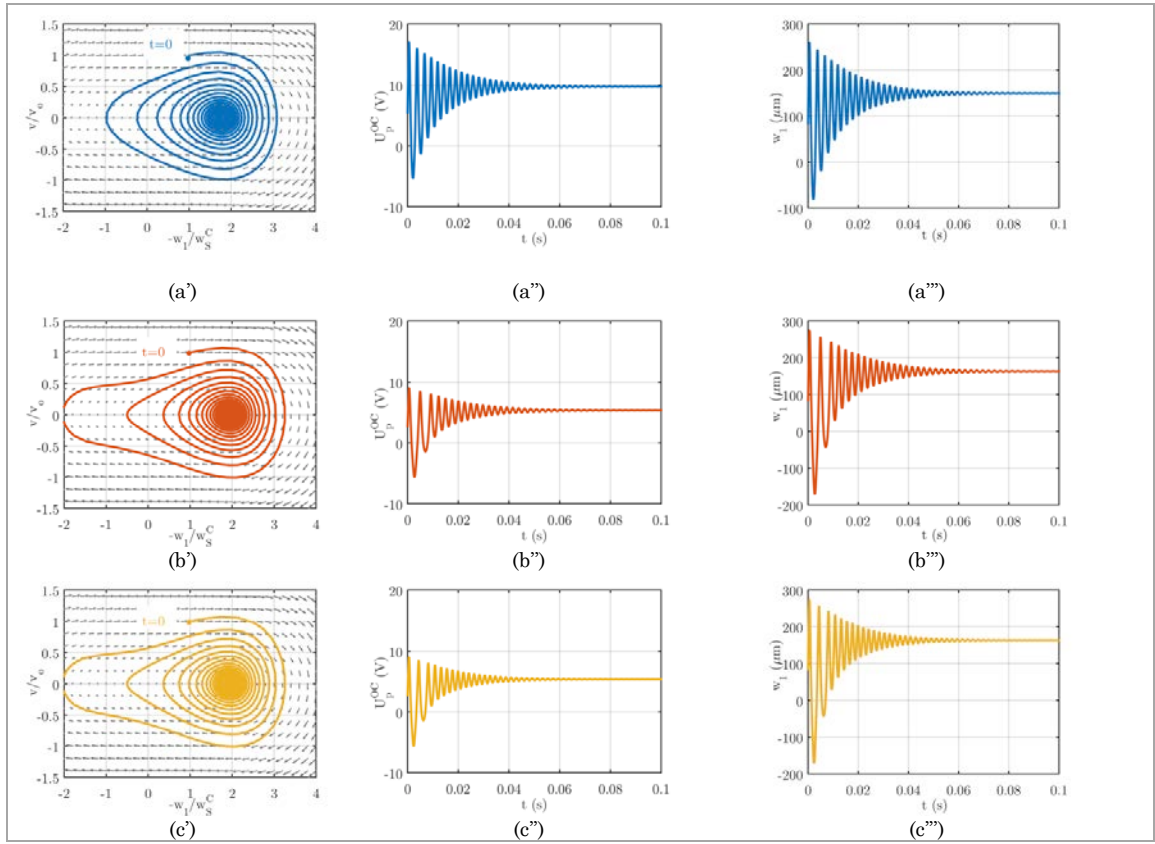


Figure 5.3.1. Phase portrait, Open-Circuit voltage and displacement of a clamped-clamped oscillator (a), simply supported oscillator (b) and two clamped free oscillators (c).

Elliptic functions being difficult to use and to compute, we can also approximate the solution of the equation with harmonic functions (5.3.5a) verifying the exact equation (5.3.5b), by defining the new parameters of the equation by (5.3.5c) and (5.3.5d).

$$w_1(t) = w_\infty + w(t) = w_\infty + w_0 \cdot e^{-\delta \cdot t} \cdot \cos(\omega \cdot t - \theta) \quad (5.3.5a)$$

$$\ddot{w} + 2 \cdot \delta \cdot \dot{w} + \alpha \cdot w + \beta \cdot w^2 + \gamma \cdot w^3 = 0 \quad (5.3.5b)$$

$$\alpha = 2 \cdot \frac{k_p^* + (r_\infty^2 - 1) \cdot k_{b1} + \frac{\Gamma_p^{*2}}{C_p}}{m_b + 2 \cdot m_p^*} \quad (5.3.5c)$$

$$\beta = -6 \cdot \frac{k_{b3} \cdot r_\infty \cdot w_S^c}{m_b + 2 \cdot m_p^*} \quad (5.3.5d)$$

Hence, by simply injecting (5.3.5a) in (5.3.5b), we can see that the quadratic term has no influence at the first order. By neglecting the second and third harmonics created by the non-linearity, we find an equation similar to (5.3.4a), showing the dependence of the frequency on the initial conditions. By writing the initial conditions, we demonstrate that the beam's shape amplitude also verifies a polynomial equation (5.3.6b), whereas the initial phase shift is given by (5.3.6c).

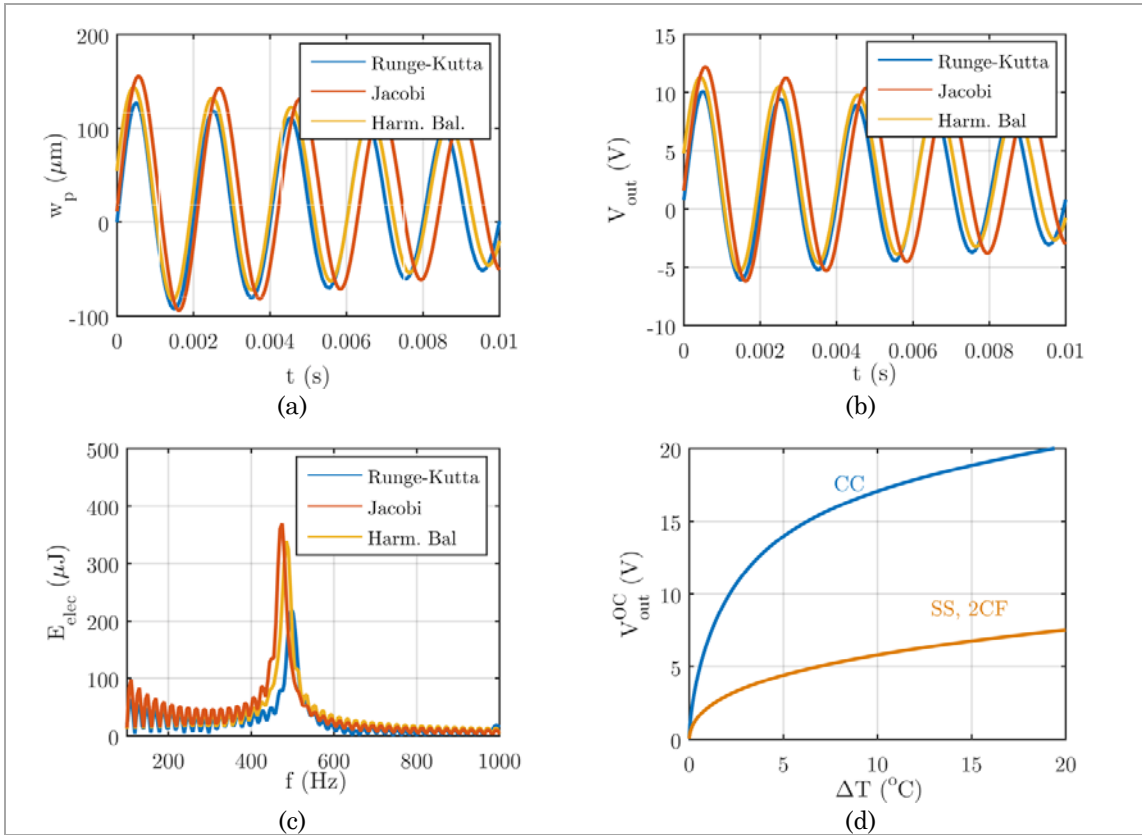


Figure 5.3.2. *a.* Detail of the transient evolution of the clamped-clamped PZT brass piezoelectric transducer when it is shocked by a bimetallic strip of 3°C. *b.* Detail of the transient evolution of the open-circuit output voltage of the piezoelectric transducer. *c.* FFT of the three signals and equivalent energy when using a load resistance of 10 MOhms. *d.* Evolution of the output voltage as a function of the bimetallic strip thermal hysteresis and the type of piezoelectric transducer (clamped-clamped, simply supported, clamped-free).

$$\omega^2 = \frac{1}{4} \cdot (4 \cdot \alpha + 3 \cdot \gamma \cdot w_o^2 - 2 \cdot \delta^2) \quad (5.3.6a)$$

$$w_o^4 + \left(\frac{4 \cdot \alpha - 2 \cdot \delta^2}{3 \cdot \gamma} - B^2 \right) \cdot w_o^2 - \frac{1}{3 \cdot \gamma} \cdot ((4 \cdot \alpha - 2 \cdot \delta^2) \cdot B^2 + 4 \cdot A^2) = 0 \quad (5.3.6b)$$

$$\theta = \arctan\left(\frac{\omega \cdot B}{A}\right) \quad (5.3.6c)$$

To evaluate the accuracy of these models, we represent in Fig.5.3.2a and Fig.5.3.2b the transient evolution of the transducer deflection and the output voltage generated by the piezoelectric oscillator, and in Fig.5.3.2c the Fast Fourier Transform of each signal. Here we assume an Al-Invar bimetallic strip (40 x 10 x (0.2+0.2) mm³) impacting a clamped-clamped PZT-brass oscillator (40x 10x (0.2+0.1) mm³), and a quality factor of 30 (see Table 5.3.1a). We can see in Fig.5.3.2a and Fig.5.3.2b the relatively good agreement between the three simulations. Fig.5.3.2c shows that the oscillation frequency is around 590 Hz, and that the energy stored in the capacity is 200 μJ assuming a load resistance of 10 MOhms

(obtained with the Runge Kutta method). Finally, we plot the evolution of the voltage of the first vibration peak as a function of the thermal hysteresis and the configuration of the piezoelectric transducer. Logically we observe that it is an increasing function of the thermal hysteresis, varying from 12 V for a hysteresis of 3°C to 18 V for a hysteresis of 15°C. We also see that clamped-clamped transducers produce greater output voltage peaks than simply-supported oscillators, mainly because of their better piezoelectric coupling.

Table 5.3.1. Lumped parameters of the oscillators of the thick piezoelectric transducer

	Boundary conditions	k_{b1} (N.m ⁻¹)	k_{b3} (N.m ⁻³)	k_p^* (N.m ⁻¹)	Γ_p^* (N.V ⁻¹)	C_p (nF)	m_p^8 (g)	f_0 (Hz)
Brass-PZT	CC	-	-	5,38.10 ⁵	-7,68.10 ⁻³	52,1	0,37	609
Brass-PZT	SS	-	-	1,35.10 ³	-3,84.10 ⁻³	52,1	0,49	263
Brass-PZT	2CF	-	-	1,35.10 ³	-3,84.10 ⁻³	52,1	0,22	391

b. Energy harvested with a SECE circuit.

In order to estimate the maximal energy that can be harvested with a SECE circuit, we assume that the oscillator has a quasi-linear behavior, meaning that harvesting charges does not modify its oscillation frequency contrary to what is predicted by (5.3.6a). The principle of SECE circuits consists in discharging the piezoelectric capacitor once the maximal output voltage is reached [Lefeuvre *et al*, 2007]. In order to find the law giving the energy we will make a mathematical induction. The n-th relaxed position of the beam (w_n) after the piezoelectric capacitor is discharged can be obtained from the expression of the deflection peak w_n before discharge by writing the conservation of the energy (5.3.7a). In order to obtain a linear expression, we only keep the quadratic term of the strain energy. Hence, we obtain a simple arithmetic progression (5.3.7b).

$$\frac{1}{2} \cdot (k_p^{*oc} + (r_\infty^2 - 1) \cdot k_{b1}) \cdot w_n'^2 + \Delta \mathcal{W}_{harvest} = \frac{1}{2} \cdot (k_p^{*oc} + (r_\infty^2 - 1) \cdot k_{b1}) \cdot w_n^2 \quad (5.3.7a)$$

$$w_n' = \sqrt{1 - \frac{\Gamma_p^{*2}}{C_p \cdot (k_p^* + (r_\infty^2 - 1) \cdot k_{b1}) + \Gamma_p^{*2}} \cdot w_n} \quad (5.3.7b)$$

$$k_p^{*oc} = k_p^* + \frac{\Gamma_p^{*2}}{C_p} \quad (5.3.7c)$$

At the n+1-th voltage peak, the energy extracted from the capacitor is a function of the n'-th beam's deflection peak (5.3.8a). As a consequence the deflection also follows an arithmetic (5.3.8b). We can deduce that the n-th maximal deflection is given by (5.3.8c) by defining a ratio depending on the piezoelectric coupling factor and the damping ratio (5.3.8d).

$$w_{n+1} = -w_n' \cdot e^{-\frac{\delta \cdot \pi}{\omega}} \quad (5.3.8a)$$

$$w_{n+1} = -\sqrt{1 - \frac{\Gamma_p^{*2}}{C_p \cdot (k_p^* + (r_\infty^2 - 1) \cdot k_{b1}) + \Gamma_p^{*2}}} \cdot e^{-\frac{\delta \cdot \pi}{\omega}} \cdot w_n \quad (5.3.8b)$$

$$w_n = -(-a_{r\delta})^n \cdot \frac{w_o}{a_{r\delta}} \cdot e^{-\frac{\delta \cdot \theta}{\omega}} \quad (5.3.8c)$$

$$a_{r\delta} = \sqrt{1 - \frac{\Gamma_p^{*2}}{C_p \cdot (k_p^* + (r_\infty^2 - 1) \cdot k_{b1}) + \Gamma_p^{*2}}} \cdot e^{-\frac{\delta \cdot \pi}{\omega}} \quad (5.3.8d)$$

The energy extracted from the piezoelectric transducer is then given by (5.3.9a). Using the same hypothesis on the quadratic dependence of the strain energy on the beam's deflection, we can approximate the mechanical losses by (5.3.9b), leading to the expression of the transduction efficiency give by (5.3.9c). By defining the equivalent electro-mechanical coupling factor of the coupled oscillator by (5.3.9d) and the equivalent mechanical quality factor by (5.3.9e), the efficiency is given by (5.3.9f).

$$\Delta \mathcal{W}_E = \frac{1}{2} \cdot \frac{\Gamma_p^{*2}}{C_p} \cdot w_o^2 \cdot e^{-\frac{2 \cdot \delta \cdot \theta}{\omega}} \cdot \sum_{n=0}^{+\infty} (a_{r\delta}^2)^n = \frac{1}{2 \cdot (1 - a_{r\delta}^2)} \cdot \frac{\Gamma_p^{*2}}{C_p} \cdot w_o^2 \cdot e^{-\frac{2 \cdot \delta \cdot \theta}{\omega}} \quad (5.3.9a)$$

$$\Delta \mathcal{W}_{loss} = \frac{\left(1 - e^{-\frac{2 \cdot \delta \cdot \pi}{\omega}}\right)}{2 \cdot (1 - a_{r\delta}^2)} \cdot (k_p^* + (r_\infty^2 - 1) \cdot k_{b1}) \cdot w_o^2 \cdot e^{-\frac{2 \cdot \delta \cdot \theta}{\omega}} \quad (5.3.9b)$$

$$\eta_{ME} = \frac{\Gamma_p^{*2}}{C_p \cdot (k_p^* + (r_\infty^2 - 1) \cdot k_{b1}) \cdot \left(1 - e^{-\frac{2 \cdot \delta \cdot \pi}{\omega}}\right) + \Gamma_p^{*2}} \quad (5.3.9c)$$

$$k_{eq}^2 = \frac{\Gamma_p^{*2}}{C_p \cdot (k_p^* + (r_\infty^2 - 1) \cdot k_{b1})} \quad (5.3.9d)$$

$$Q_{eq} = e^{-\frac{2 \cdot \delta \cdot \pi}{\omega}} \quad (5.3.9e)$$

$$\eta_{ME} = \frac{k_{eq}^2}{1 - Q_{eq} + k_{eq}^2} \quad (5.3.9f)$$

In Fig.5.3.3a, we show the electrical energy that can be harvested by using SECE techniques each time the bimetallic strip heats the piezoelectric transducer. We still observe that the clamped-clamped oscillator is the best configuration: with a bistable beam having a thermal hysteresis of 5°C, this configuration generates 40 μJ when the mechanical quality factor is 15. In the same conditions, the simply-supported transducer only generates 20 μJ per snap. Fig.5.3.3b also shows the advantage of using a clamped-clamped piezoelectric oscillator to boost the efficiency of the transduction. With a 5°C hysteresis, the conversion efficiency is around 45%. The fact that the efficiency is a decreasing function of the thermal hysteresis is linked to the increase of the bistable beam's stiffness. To improve the conversion efficiency, the stiffness of both beams must be matched.

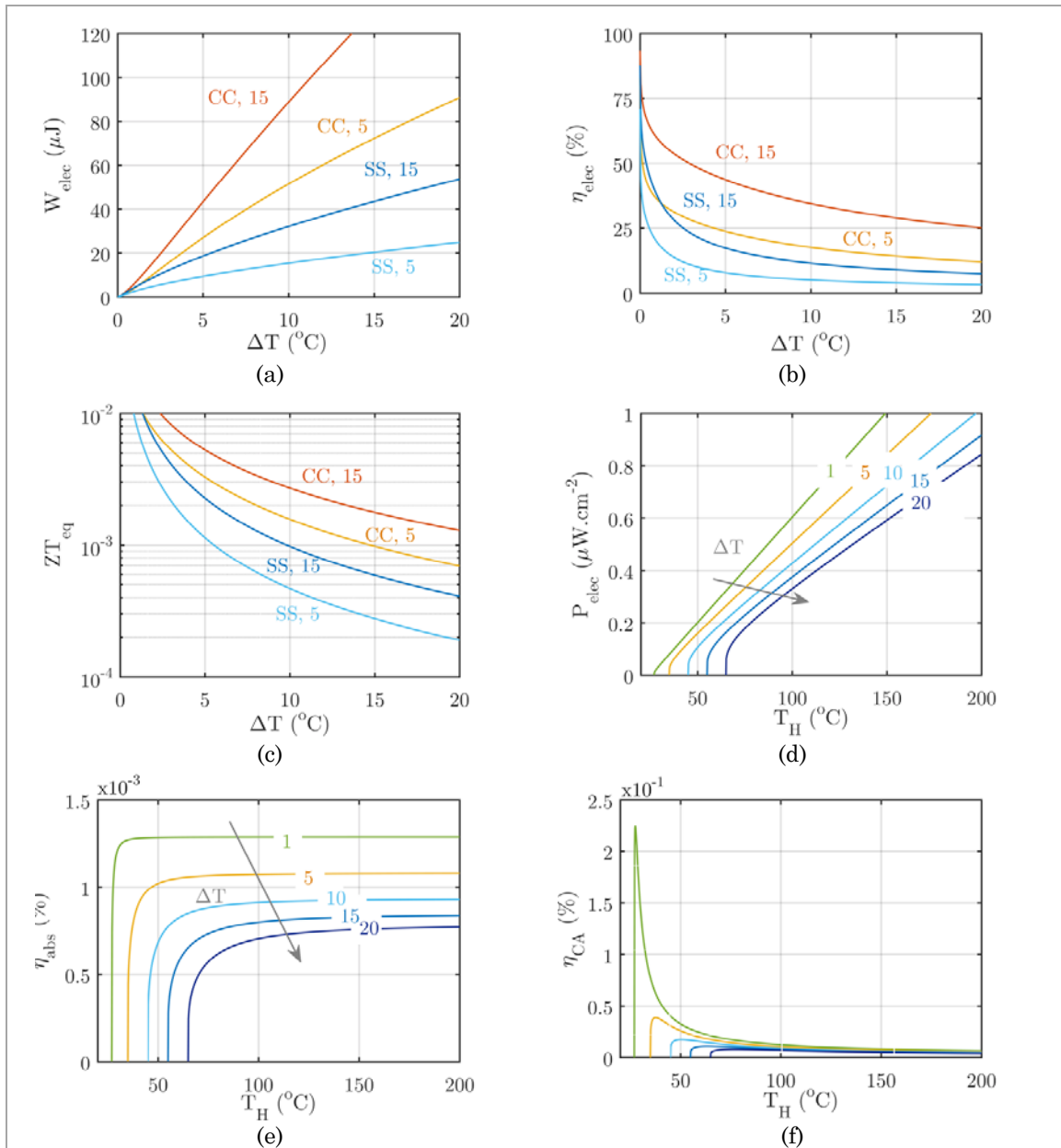


Figure 5.3.3. *a. Evolution of the available electrical energy per cycle as a function of the type of piezoelectric transducer, the mechanical quality factor of the system and the thermal hysteresis of the bistable beam. b. Transduction efficiency associated to the shock. c. Equivalent ZT of the harvester. d. Surface density of power of the bimetallic strip heat engine (clamped-clamped transducer) as a function of the hot source temperature and for various values of thermal hysteresis. e. Thermal efficiency of the energy harvester as a function of the hot source temperature. f. Curzon-Ahlborn efficiency of the system.*

c. Overall performances of the energy harvester

Now that we have modeled the full chain of conversion of the current energy harvester, we can evaluate its performances when it is cycled between a hot source and a cold source,

assuming that the piezoelectric transducer is used as a planar heat sink. First, we give the intrinsic Carnot efficiency of the coupled oscillators (5.3.10a), by normalizing the electrical energy by the thermal hysteresis of the bimetallic strip in the cavity. This enables to give the equivalent ZT of the energy harvester in order to compare it with Seebeck generators (5.3.10b), whose evolution is presented in Fig.5.3.3c.

$$\eta_{TE}^{rel} = \frac{\Delta\mathcal{W}_E}{C_v \cdot \Delta T_{cav}^2} \cdot \left(T_o + \theta_{ref} + \frac{\Delta T_{cav}}{2} \right) \quad (5.3.10a)$$

$$ZT_{eq} \approx 2 \cdot \left(1 + \frac{2 \cdot T_o - \Delta T_{cav}}{2 \cdot T_o + \Delta T_{cav}} \right) \cdot \eta_{rel} \quad (5.3.10b)$$

By multiplying the electrical energy generated per snap, we can obtain the mean power generated by the harvester. We can also deduce all the various expressions of the performances of the system.

$$P_E = \frac{\Delta\mathcal{W}_E}{2 \cdot C_v \cdot R_{CC}} \cdot \frac{1}{\ln \left(1 + \frac{\Delta T_{cav}}{T_H - T_C} \right) - \ln \left(1 - \frac{\Delta T_{cav}}{T_H - T_C} \right)} \quad (5.3.10a)$$

$$\eta_{TE}^{abs,tot} = \frac{P_E}{R_{leak} \cdot (T_H - T_C)} \quad (5.3.10b)$$

In Fig.5.3.3d we represent the evolution of the surface density of output power for various values of the bimetallic strip's thermal hysteresis. This shows that the output power is maximized by the use of the smallest possible thermal hysteresis. For a hot source temperature of 100°C, the mean output power is 0.5 $\mu\text{W} \cdot \text{cm}^{-2}$. The output power of the current energy harvester is generally between 3 and 4 μW for a bimetallic strip surface of 6.48 cm^2 , corresponding to a power density of 0.6 $\mu\text{W} \cdot \text{cm}^{-2}$. The fact that both values are of the same order of magnitude validates the complete model of the harvester. To finish, we plot in Fig.5.3.3e the evolution of the thermal efficiency of the harvester and in Fig.5.3.3f the evolution of the Curzon-Ahlborn efficiency. This also demonstrates that the system is more efficient by choosing bimetal thermostats having weak thermal hystereses.

d. Ways to improve the efficiency of the transduction

Equation (5.3.9) shows that the efficiency depends both on the equivalent mechanical quality factor and the equivalent electro-mechanical coupling factor. There are thus two ways to improve the performances of the energy harvester. The first way is to enhance the electro-mechanical coupling factor of the piezoelectric transducer by two means: either by thinning the thickness of the oscillator to reduce its stiffness and thus increasing the efficiency of the shock, or using piezoelectric materials with better piezoelectric properties. The first solution is limited: the thickness of the metallic membrane cannot be decreased less than the thickness imposed by the position of the neutral axis in order to preserve the quantity of strain energy in the piezoelectric layer. The second solution is also limited by the current properties of piezoelectric materials. A second way to enhance the efficiency of the conversion is to improve the mechanical quality factor of the piezoelectric transducer. This second solution is the one that brings more results. In [Boughaleb *et al*, 2015], changing the materials used for the device's architecture (Teflon replaced by PEEK) and changing the type of clamp for the piezoelectric transducer (four metal screws instead of two metal flanges) enabled to improve the quality factor from 6 to 20 and the energy stored on the piezoelectric capacitor from 9 μJ to 90 μJ .

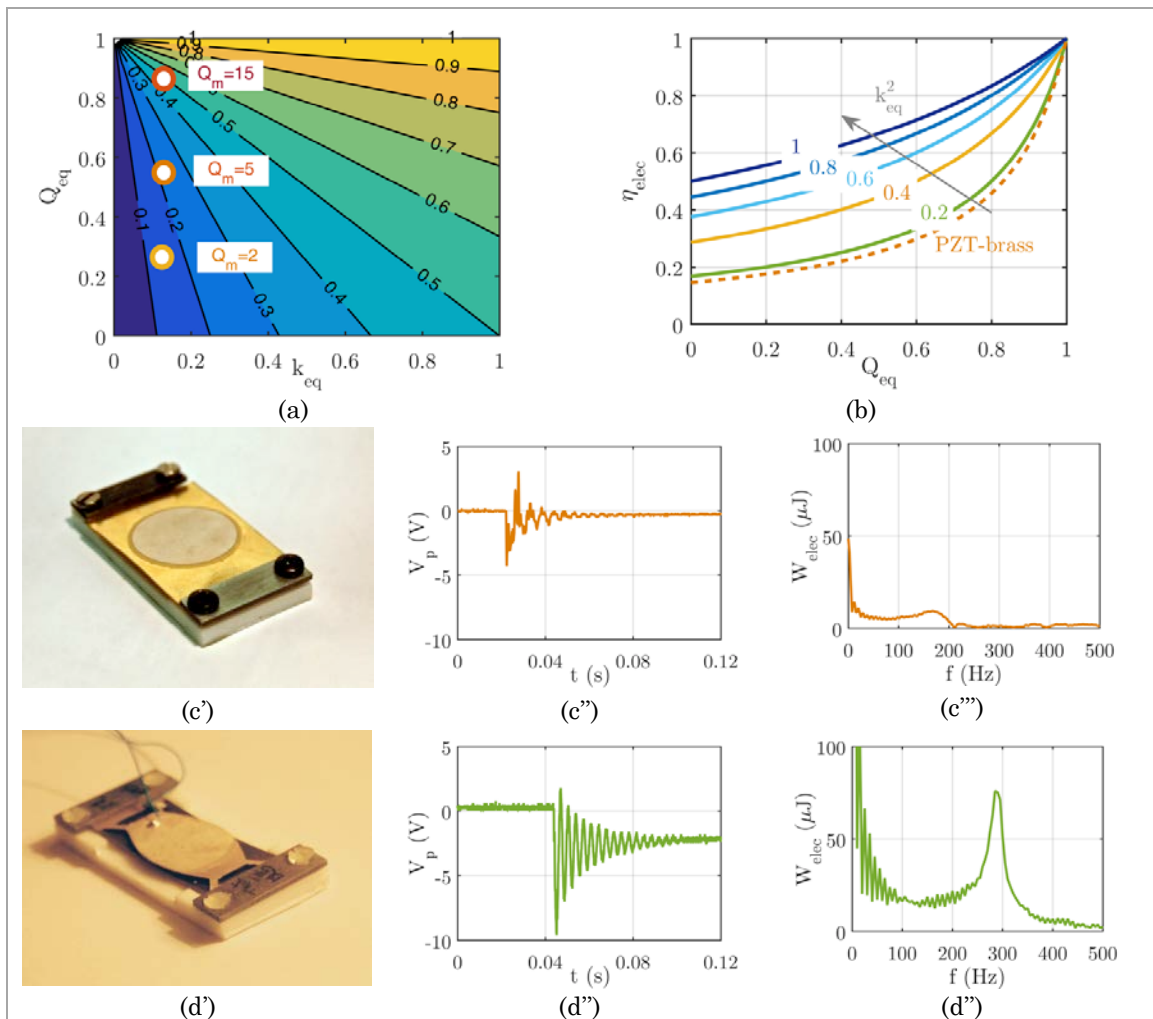


Figure 5.3.4. a. Map of the efficiency of the piezoelectric transduction and efficiency of the PZT-Brass oscillator for some values of mechanical quality factor. b. Dependence of the efficiency on the equivalent mechanical quality factor, and way of improvement of the efficiency of the PZT-Brass oscillator. c. Image of the non-optimized energy harvester and experimental measurement of the snap signal with a load resistance of 10 MOhms. d. Image of the optimized energy harvester and experimental measurement of the snap signal with a load resistance of 10 MOhms

Fig.5.3.4 presents another strategy we tried in order to improve the efficiency of the transduction without changing the material nor the shape of the cavity. To optimize the transducer design, numerical simulations of the oscillator are performed with Comsol software. The current transducer ($45 \times 2 \times (0.25+0.25) \text{ m}^3$) is first modeled with its clamp on an architecture made of PTFE, and the parameters representing the absorption of the vibration energy by the architecture are modified in order to fit the experimental data. The value of the PZT loss factor is fixed to 0.989 in order to represent a piezoelectric coupling coefficient of 0.3. The PTFE loss factor is taken equal to 3, so that the clamp diffuses 75% of its mechanical energy. With these values, we obtained an transduction efficiency of 28% and a mechanical quality factor of about 9.6.

The basic idea of this new harvester is to reduce the mechanical losses associated to the fact that the piezoelectric transducer is clamped on a leaky architecture, by reducing the mechanical efforts on the clamp. Fig.5.3.5b and Fig.5.3.5c compare the repartition of the mechanical stress inside the oscillator and the PTFE architecture, showing the stress reduction. In order to reduce this effort, four beams are cut in the brass membrane and their positions are lightly inclined and shifted from the clamp in order to reduce the mechanical efforts acting on the clamp. In the same time, reducing the width of the beams and increasing their length enables to reduce the transducer's stiffness in order to improve the efficiency of the mechanical energy transfer during the shock between the bimetallic strip and the piezoelectric oscillator. Fig.5.3.5d and Fig.5.3.5e show the evolution of the efficiency of the transduction linked to the optimization of the angle between the branches and the clamp and the length of the branches. As can be seen, the optimal shape of the harvester enables to increase the efficiency from 28% up to 70%.

The optimized piezoelectric transducer was processed with a milling machine at G2ELab. The results of the experimental measurements are presented in Fig.5.3.4. As can be seen, the reduction of the mechanical stiffness of the oscillator and the increase of its mechanical quality factor helped improving the performances of the thermal energy harvester. During a snap, the energy stored in the piezoelectric capacitor is now 75 μJ instead of 9 μJ and the quality factor increases from 6 to 14. These very positive results validate the possibility of improving the performances of the system without changing the type of piezoelectric materials used on the piezoelectric transducer.

6 Coupling with an electret transducer

The last physical coupling to be studied is the coupling between an electret and a bistable beam. Before explaining the modeling of this system, we give a short overview on electrets.

6.1 A short overview on electrets and electrostatic energy harvesting

a. A history of electrets

Even if properties of electrets were first reported in the mid-18th century, by Gray in 1732 studying the properties of waxes such as beeswax and creating the first thermoelectrets, by Franklin trapping charges in glass by means of Leyden jars, and first theorized by Faraday in 1839, the name of electret was first given by Heaviside in 1892 [Heaviside, 1970], hesitating between the term “electret” and “electric” even if this name was already an adjective. According to Heaviside, electrets are some dielectric materials for which electrization is not “perfectly elastic”, but for which there is “residual electrization when absorption occurs” when they are electrized. “Electret” thus is to electricity what “magnet” is to magnetism: “an intrinsically electrized body”.

A wider definition of “electret” could include piezoelectric materials [Sessler, 1987]. The first controlled fabrication of electrets is generally attributed to Eguchi in 1919, fabricating thermoelectrets by heating carnauba wax and applying an external electric field to orientate molecular dipoles in the wax. Among other significant advances, we can cite the fabrication of electrets by charge injection by means of electron beams by Selenyi in 1928, the fabrication of photoelectrets by Nadjakoff in 1938, or the discover of the piezoelectric effect of PVDF by [Kawai, 1969].

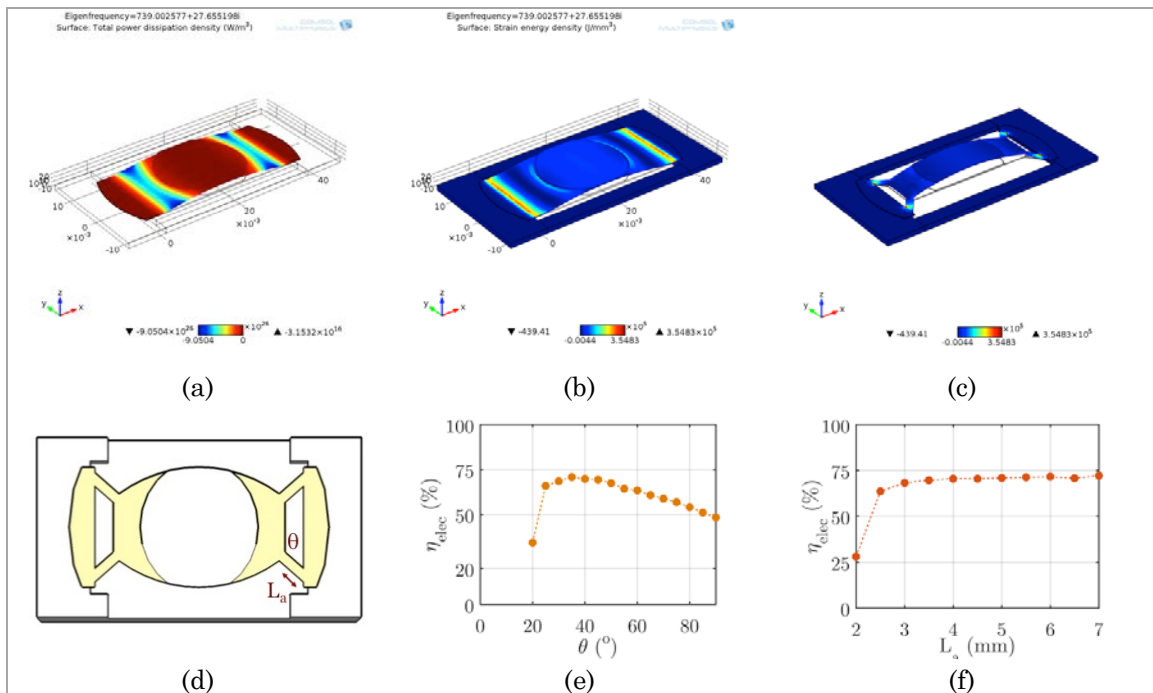


Figure 5.3.5. *a. Modeling of the mechanical energy losses in the current piezoelectric oscillator. b. Repartition of the stress in the current piezoelectric oscillator. c. Repartition of the stress in the optimized oscillator. d. Top view of the oscillator and optimized parameters. e. Evolution of the efficiency as a function of the angle of the beams. f. Evolution of the efficiency as a function of the length of the beams.*

Electrets are commonly used as sensors and transducers, finding applications in the design of microphones [Scheeper et al, 1994], light modulators, dosimeters [Sessler and West, 1973], etc. The applications of electrets in energy harvesting are more recent. A first electret motor was proposed by [Wieder and Kauffman, 1953], but the first theoretical modeling of their operation was proposed later [Jefimenko and Walker, 1978]. Later still, Tada improved the efficiency of the motor by using PTFE-based electrets [Tada, 1992].

b. Types of electret and production

Classification of electrets is generally based on their way of fabrication [Sessler, 1987, Kestelman *et al*, 2000], the origins of their electrization, or the type of dielectric materials used for the electrets. With the first classification, we can distinguish three main categories: “thermoelectrets”, fabricated by heating the dielectric sample and applying strong external electric fields to orientate dipoles and, similarly, “electroelectrets” which do not need any heat sources (but the electric field must be higher), “radioelectrets” based on the use of X -rays, β -rays, γ -rays or monoenergetic electron beams to charge the dielectric layers, “corona-electrets” based on the use of Corona discharge in order to implant ionized air molecules in the dielectric layers. The methods for obtaining the three types of electrets are represented in Fig.6.1.1 where the typical values of the applied electric fields are given.

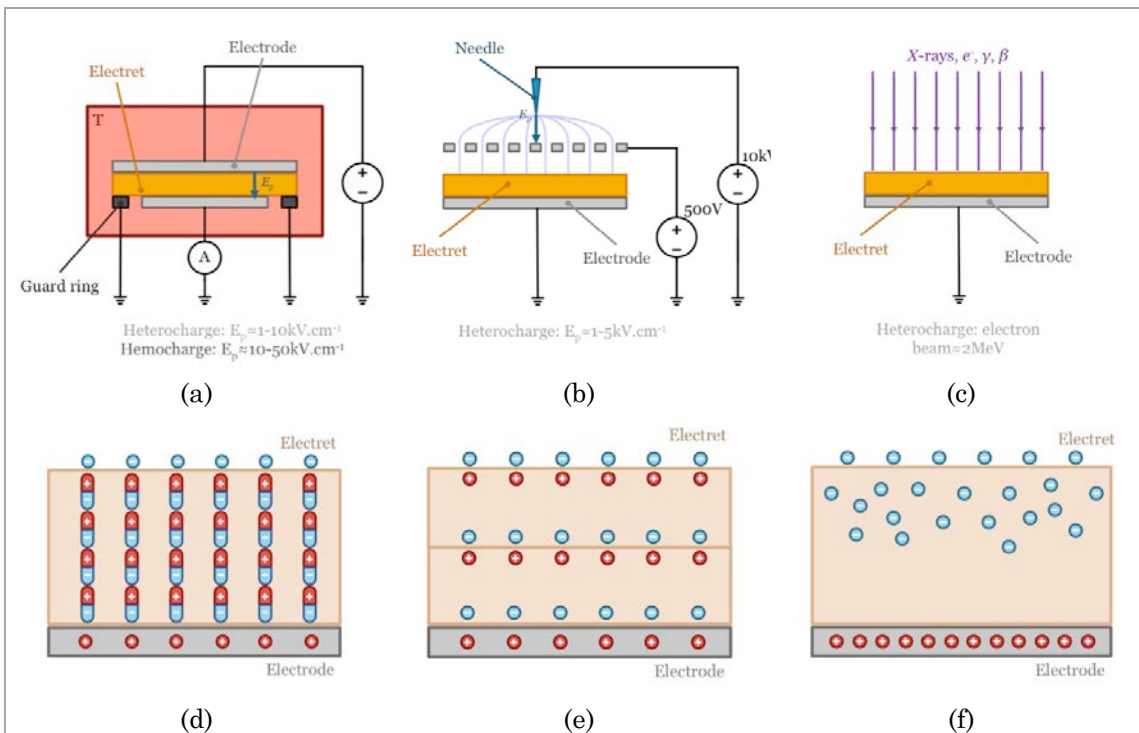


Figure 6.1.1. a. Fabrication of thermoelectrets. b. Fabrication of coronelectrets c. fabrication of radioelectrets. d. Dipolar electret with surface charge. e. Space-charge electret with two domains (also known as Maxwell-Wagner effect). f. Charge excess electret.

Other categories also exist: “magnetolectrets” obtained by heating polymers in an external magnetic field, “photolectrets” where light is used as a heat source but which also require an external electric field, “mechanolectrets” whose polarization appears by heating and compressing the dielectric materials, “metal-polymer electrets” quite similar to thermoelectrets obtained by triboelectricity or by liquid charging. Electrets can also be classified according to the source of their permanent polarization. We thus can distinguish a first category regrouping dipolar electrets whose polarization comes from the alignment of dipoles inside the dielectric layers. They are generally obtained by means of thermal charging method with strong electric fields (mainly thermoelectrets): as an example, piezoelectric films are obtained with electric fields of around $800 \text{ kV}\cdot\text{cm}^{-1}$ at high temperature or electric fields up to $4 \text{ MV}\cdot\text{cm}^{-1}$ at room temperature [Sessler, 1987]. Space-charge electrets are electrets that are globally neutral (like dipolar electrets) but whose polarization comes either from homocharges (charges generated by the electrodes) or heterocharges (charges directly generated in the dielectric layer). In the case of thermolectret, for low electric fields (around $1-2 \text{ kV}\cdot\text{cm}^{-1}$), the predominant type of charge is heterocharges. Increasing the electric field (around $10 \text{ kV}\cdot\text{cm}^{-1}$) leads to the creation of homocharges by Schottky effect or air gap breakdown.

The last type of electrets is designated by the term of charge excess electrets. This type of electret is generally obtained by Corona discharge (Coronelectrets), ion implantation or radiations (radioelectrets), for which the charge does not come from the dielectric layer nor the electrodes but are implanted into the dielectric layer.

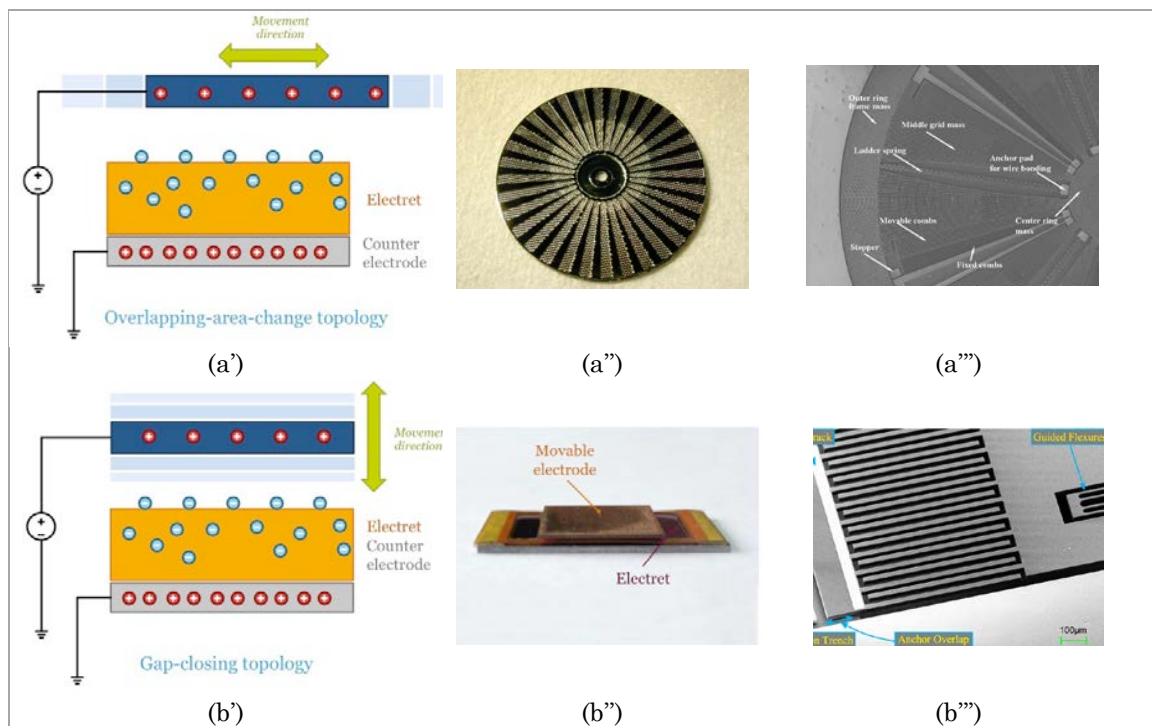


Figure 6.1.2. *a'. Principle of overlapping-area change topology. a''. Textured stator of a rotational energy harvester [Boland, 2003]. a'''. Rotary MEMS with interdigitated electrodes and overlapping-area change strategy [Yang, 2010]. b'. Principle of Gap-closing topology. b''. Out-of plane energy harvester [Chiu and Lee, 2012]. b'''. Device with interdigitated capacitors for in-plane vibration energy harvesting with gap-closing topology [Le et al, 2013].*

The advantage of Corona is its great simplicity and the speed of realization that makes it one of the most used fabrication techniques for electrets. Ion implantation has the advantage of being well mastered, the depth of implantation and the quantity of charges being easily controlled.

Classification of electrets based on dielectric materials distinguishes six categories [Kestelman et al, 2000]: natural waxes or resins (Carnauba, paraffin...), polymers (PTFE, PDVF, Parylene, Cytop...), biopolymers, low-melting organic dielectrics (benzoic acid), ceramic dielectrics (SiO_2 , Si_3N_4 , Al_2O_3 ...) and dielectric monocrystals if we take into account piezoelectric materials. Generally, ceramic dielectrics have better electrical properties since they trap more electrical charges than organic polymers, but they can encounter problems of long-term stability [Suzuki, 2011].

c. Energy harvesters exploiting electrets

As explained, the first electrets motors were proposed in the mid-20th century but realistic proofs of concept are due to [Jefimenko and Walker, 1978] and [Tada, 1992]. These first harvesters were based on the variation of capacity of the transduced due to the change of the overlapping area between the electret and the movable electrode (Fig.6.1.2a). This strategy can be exploited to harvest energy from rotational motions by using either textured electrets and textured electrodes [Jefimenko and Walker, 1978, Tada, 1992,

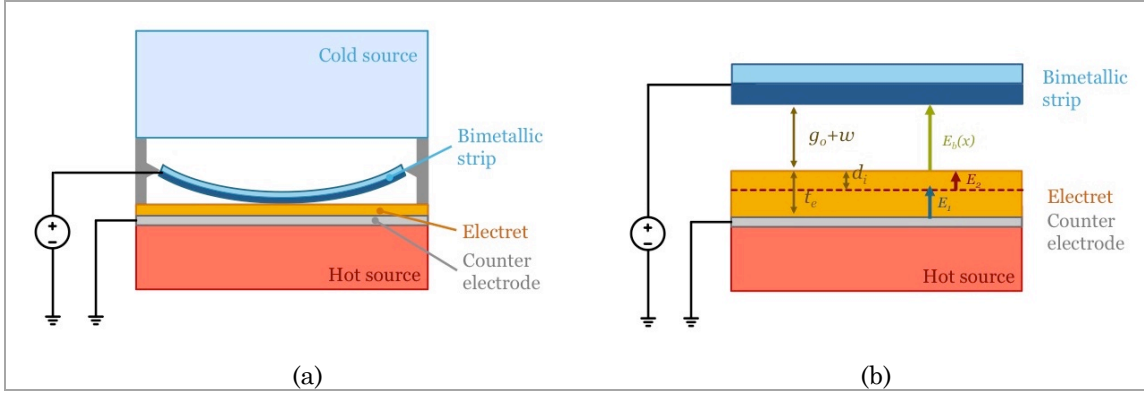


Figure 5.3.2. a. Simplified schematic thermal energy harvester. b. Detail of a portion dx .

Boland *et al.*, 2003, Nakano *et al.*, 2015], rotary-comb generator [Yang *et al.*, 2010], or unidirectional in-plane vibrations by using either plane textured electrets [Basset *et al.*, 2009, Tao *et al.*, 2015] or interdigitated capacitors [Le *et al.*, 2013] (Fig.6.2.1a”).

A second possibility to observe capacity variations of the electret transducers is to reduce the gap separating the electret from the counter-electrode, as in our case (Fig.6.1.2b). This strategy can be used with full-sheet electrets to harvest energy from out-of-plane motion [Mizuno and Chetwynd, 2003, Chiu and Lee, 2012, Perez *et al.*, 2015], or energy from in-plane motion using interdigitated capacitors [Oxaal *et al.*, 2015]. Other less frequent types of energy harvesters use the variation of capacity of an electret transducer due to the variation of the permittivity in the gap separating the electret from the counter-electrode [Suzuki, 2015].

6.2. Modeling the electret

a. Electric field and electrostatic pressure induced by an electret with a charge layer

In order to model the electrical field inside the harvester and calculate the charge induced by the electret on the electrode and the counter-electrode, we take the example of the simplified device’s architecture presented in Fig.6.2.1a, approximately corresponding to the energy harvester presented in [Boisseau *et al.*, 2013]. Given that the ratio of the beam’s deflection over the beam’s length is weak, we can consider that the electric field is perpendicular to the electret’s surface and the bimetallic strip is equivalent to a parallel infinitesimal small capacity. We thus consider the electric field acting on a surface $v \cdot dx$ and the equivalent diagram represented in Fig.6.2.1b, first assuming that the electric charge of the electret is implanted at a depth d_e . By simply writing the Gauss law, we can express the electric fields E_1 and E_2 inside the electret layer and the field in the cavity by (6.2.1a) and (6.2.1b).

$$\varepsilon_e \cdot (\mathcal{E}_2 - \mathcal{E}_1) = \sigma_e \quad (6.2.1a)$$

$$\varepsilon_o \cdot \mathcal{E}_b - \varepsilon_e \cdot \mathcal{E}_2 = 0 \quad (6.2.1b)$$

$$\varepsilon_1 \cdot (t_e - d_i) + \varepsilon_2 \cdot d_i + \varepsilon_b \cdot (g_o + w) = -\mathcal{V} \quad (6.2.1c)$$

From these three equations, we can deduce the expression of the electrical field seen by the electric charges carried by the bimetallic strip (6.2.2a). We can thus define the surface

potential of the electret by (6.2.2b), and the electret's capacitance by (6.2.2c). The electrical charge trapped in the dielectric layer is then simply related to other parameters by (6.2.2d)

$$\mathcal{E}_b \cdot \left(\frac{t_e}{\varepsilon_e} + \frac{g_o + w}{\varepsilon_o} \right) = -\frac{\mathcal{V}}{\varepsilon_o} + \frac{t_e - d_i}{\varepsilon_o \cdot \varepsilon_e} \cdot \sigma_e \quad (6.2.2a)$$

$$\mathcal{V}_e = \frac{t_e - d_i}{\varepsilon_e} \cdot \sigma_e \quad (6.2.2b)$$

$$C_e = \frac{L \cdot v \cdot \varepsilon_e}{t_e} \quad (6.2.2c)$$

$$Q_e = C_e \cdot \frac{t_e}{t_e - d_i} \cdot \mathcal{V}_e \quad (6.2.2b)$$

With all these parameters definition, we can simply express the electric field seen by the bimetallic strip by (6.2.3a). The density of electric charges induced by the electric field is then given by (6.2.3b). The electric pressure exerted by the electret on the beam is finally given by (6.2.3c).

$$\mathcal{E}_b(x) = -\frac{\mathcal{V} - \mathcal{V}_e}{\frac{\varepsilon_o}{\varepsilon_e} \cdot t_e + g_o + w} \quad (6.2.3a)$$

$$\sigma_b(x) = \varepsilon_o \cdot \mathcal{E}_b(x) \quad (6.2.3b)$$

$$p_e(x) = \frac{1}{2} \cdot \varepsilon_o \cdot \mathcal{E}_b(x)^2 \quad (6.2.3c)$$

By using these three equations, we will be able to describe the electrical behavior of the system as well as the influence of the electrets and the polarization of the bimetallic strip on its mechanical behavior

b. Electric equations of the thermally bistable electrode

By simply integrating the local expression of the surface charge density over the whole surface of the bimetallic strip, we obtain the electric charge carried by the bimetallic strip (6.2.4a). Once integrated this equation becomes (6.2.4b).

$$Q_b = v \cdot \int_{-\frac{L}{2}}^{\frac{L}{2}} \sigma_b(x) \cdot dx = -v \cdot \varepsilon_o \cdot (\mathcal{V} - \mathcal{V}_e) \cdot \int_{-\frac{L}{2}}^{\frac{L}{2}} \frac{1}{-\frac{L}{2} \frac{\varepsilon_o}{\varepsilon_e} \cdot t_e + g_o + w_1 \cdot \cos\left(\frac{\pi \cdot x}{L}\right)} \cdot dx \quad (6.2.4a)$$

$$Q_b = -C_o \cdot (\mathcal{V} - \mathcal{V}_e) \cdot \frac{4}{\pi \cdot \sqrt{1 - w_1^2/g_e^2}} \cdot \arctan\left(\frac{1 - w_1/g_e}{\sqrt{1 - w_1^2/g_e^2}}\right) \quad (6.2.4b)$$

$$g_e = g_o + \frac{\varepsilon_o}{\varepsilon_e} \cdot t_e \quad (6.2.4c)$$

$$C_o = \frac{L \cdot v \cdot \epsilon_o}{g_e} \quad (6.2.4d)$$

This equation being quite complicated to use, we exploit the fact that the deflection is necessarily smaller than the sum of the gap and the electret's thickness since it equals the gap between the beam and the hot source only when there is a contact between the two domains. Hence, we can obtain a simplified expression of the charge with (6.2.5a). By defining the capacitance of the movable electrode by (6.2.5b), this equation becomes (6.2.5c). We also define the charge Q^* by (6.2.5d), which will be important when we will study the performance of the energy harvester.

$$Q_b = -\frac{4 \cdot g_e}{\pi \cdot (g_e + w_1)} \cdot C_o \cdot (\mathcal{V} - \mathcal{V}_e) \quad (6.2.5a)$$

$$C_b = \frac{L \cdot v \cdot \epsilon_o}{g_o + w_1} \quad (6.2.5b)$$

$$Q_b = \frac{4 \cdot C_b \cdot C_e}{\pi \cdot (C_e + C_b)} \cdot (\mathcal{V}_e - \mathcal{V}) \quad (6.2.5c)$$

$$Q^* = \frac{4 \cdot (t_e - d_i)}{\pi \cdot t_e} \cdot Q_e = \frac{4}{\pi} \cdot C_e \cdot \mathcal{V}_e \quad (6.2.5d)$$

6.3. Mechanical equations of the bistable bimetallic electrode

a. Equilibrium of bistable beams under electrostatic pressure.

The main difficulty posed by the existence of the electrostatic pressure is that it adds an additional source of non-linearity to the problem of the thermal snap-through which is already non-linear. Given the expression of the electrostatic pressure, the equilibrium equation of the beam is given by (6.3.1).

$$\left(N_\alpha \cdot T - \frac{N_e}{2 \cdot L} \cdot \int_{-\frac{L}{2}}^{\frac{L}{2}} w_{,x}^2 \cdot dx - F_o \right) \cdot w_{,xx} + I_e \cdot w_{,xxxx} = \frac{1}{2} \cdot \frac{\epsilon_o \cdot v \cdot (\mathcal{V}_e - \mathcal{V}_b)^2}{(g_e - w)^2} \quad (6.3.1)$$

One of the consequences of the non-linearity brought by the electrostatic pressure is the occurrence of pull-in phenomenon. This can simply be understood by the fact that the equivalent stiffness of the electrostatic pressure tends to increase when the beam gets closer to the electret. As a consequence, the beam can lose its stability if the electrostatic force is always stronger than the restoring force of the beam. This phenomenon can be easily understood if we neglect the effect of the clamp's thrust on the mechanical equilibrium. As a consequence, the equilibrium equation becomes (6.3.2a). Using the *cosine* harmonic function to approximate the beam's shape, the equilibrium equation becomes (6.3.2b).

$$I_e \cdot w_{,xxxx} \cdot (g_e - w)^2 = \frac{1}{2} \cdot \epsilon_o \cdot v \cdot (\mathcal{V}_e - \mathcal{V}_b)^2 \quad (6.3.2a)$$

$$I_e \cdot \frac{3 \cdot \pi^4}{4 \cdot L^4} \cdot w_1 \cdot \left(\frac{4 \cdot g_e}{\pi} - w_1 \right)^2 = \frac{2}{\pi} \cdot \epsilon_o \cdot v \cdot (\mathcal{V}_e - \mathcal{V}_b)^2 \quad (6.3.2b)$$

By studying the stability of this equilibrium equation, we see that unstable positions can appear when (6.3.3a) is verified. The corresponding voltage is given by (6.3.3b) and (6.3.3c). This voltage is known as the pull-in voltage of the beam.

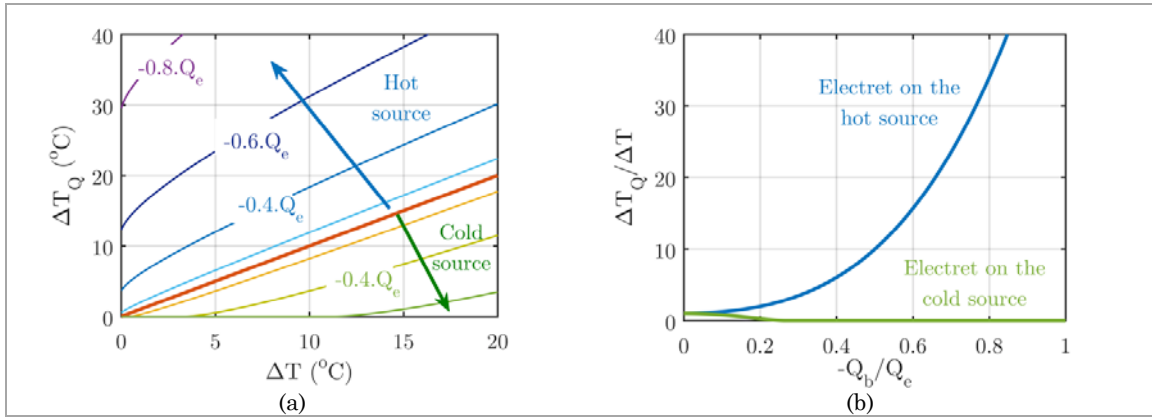


Figure 6.3.1. *a. Modification of the thermal hysteresis of a beam in open circuit as a function of the electrical charges carried by the bimetallic strip. b. Improvement factor of the beam's thermal hysteresis due to the movable electrode's charge.*

$$w_1 = \frac{4 \cdot g_e}{3 \cdot \pi} \quad (6.3.3a)$$

$$\frac{1}{2} \cdot C_o \cdot (\mathcal{V}_e - \mathcal{V}_b)^2 = \frac{64}{27} \cdot \frac{g_e^2}{L} \cdot I_e \cdot \frac{\pi^2}{L^2} \quad (6.3.3b)$$

$$\mathcal{V}_{PI} = \mathcal{V}_e + \frac{8\sqrt{2}}{3} \cdot \frac{g_e}{L} \cdot \sqrt{I_e \cdot \frac{\pi^2}{L^2} \cdot \frac{L}{C_o}} \quad (6.3.3c)$$

Another possible consequence of the electrostatic pressure is the snap of the thermally-bistable beam before it thermally snaps. The corresponding value of the electret voltage must be considered as the limit value of acceptable voltage. The complete study of equation (6.3.1a) has been the subject of several studies, mainly in the field of MEMS. As an example, [Krylov et al, 2008, Krylov and Dick, 2010, Das and Batra, 2009] proposed numerical solutions of this equation for initially-curved beams using the Galerkin method, showing the conditions of occurrence of electrostatic snap-through and pull-in.

b. Moderate electrostatic coupling

A solution to get around the non-linearity can be to approximate the electrostatic pressure, which is a function of x , by a constant value (6.3.4a). Hence integrating this equation twice yields equation (6.3.4b). Using the Galerkin method, this equation is equivalent to (6.3.4c).

$$p_t \approx \frac{1}{2} \cdot \frac{\epsilon_o \cdot v \cdot (\mathcal{V}_e - \mathcal{V}_b)^2}{g_e^2} \quad (6.3.4a)$$

$$k^2 \cdot w + w_{,xx} = \frac{1}{4} \cdot \frac{\epsilon_o \cdot v \cdot (\mathcal{V}_e - \mathcal{V}_b)^2}{I_e \cdot g_e^2} \cdot x^2 + \frac{M_\alpha}{I_e} \cdot T - \frac{M_o}{I_e} \quad (6.3.4b)$$

$$\begin{aligned} \frac{N_e \cdot \pi^2}{4 \cdot L^2} \cdot w_1^3 + \left(I_e \cdot \frac{\pi^2}{L^2} - N_\alpha \cdot T + F_o \right) \cdot w_1 + \frac{4}{\pi} \cdot (M_o - M_\alpha \cdot T) \\ = -\frac{L}{\pi^2 \cdot g_e} \cdot C_o \cdot (\mathcal{V}_e - \mathcal{V}_b)^2 \end{aligned} \quad (6.3.4c)$$

With this approximation, the simplest thermodynamic cycle to model is the Ericsson cycle (constant voltage during heating) since the electrostatic forces can be treated as a simple increase of the residual stress moment. As a consequence, the thermal hysteresis and the average temperature of the hysteresis are modified according to (6.3.5a) and (6.3.5b). The position of the electret with respect to the beam's initial shape is of great importance: if the electret is placed at the interface between the prime mover and the cold source, it will tend to lower the snap and snap-back temperatures, and to reduce the beam's thermal hysteresis by reducing the effective mechanical moment acting on the beam. Reversely, if the electret is placed between the hot source and the electret, the snap and snap-back temperatures will increase as well as the beam's thermal hysteresis.

$$T'_o = \frac{M_o + \frac{L \cdot C_o \cdot (\mathcal{V}_e - \mathcal{V}_b)^2}{4 \cdot \pi \cdot g_e}}{M} = \frac{M_o + M_V}{M_\alpha} \quad (6.3.5a)$$

$$\Delta T_V = \frac{2 \cdot L}{M_\alpha} \cdot \sqrt{\frac{1}{27 \cdot N_e} \cdot \left(N_o + \frac{n_\alpha}{m_\alpha} \cdot M_V - I_e \cdot \frac{\pi^2}{L^2} \right)^3} \quad (6.3.5b)$$

The case of the Stirling cycle is more complicated since the charge of the bistable electrode is kept constant during the displacement of the bistable beam. Hence, using (6.2.4) as an expression of the electric charge, the equilibrium equation is modified into (6.3.6a).

$$\frac{N_e \cdot \pi^2}{4 \cdot L^2} \cdot w_1^3 + \frac{4 \cdot M_Q}{\pi \cdot g_e^2} \cdot w_1^2 + \left(I_e \cdot \frac{\pi^2}{L^2} - N_\alpha \cdot T + F_o + \frac{8 \cdot M_Q}{\pi \cdot g_e} \right) \cdot w_1 + \frac{4}{\pi} \cdot (M_o + M_Q - M_\alpha \cdot T) = 0 \quad (6.3.6a)$$

$$M_Q = \frac{\pi \cdot L}{64 \cdot g_e} \cdot \frac{Q_b^2}{C_o} \quad (6.3.6b)$$

As a consequence, the criterion of bistability is modified (6.3.7a), and the hysteresis curve of the bistable beam becomes asymmetric. Hence, the beam's thermal hysteresis is given by (6.3.7c).

$$N_o + N_Q \geq I_e \cdot \frac{\pi^2}{L^2} - \frac{18}{\pi^4} \cdot \frac{L^2 \cdot M_Q^2}{g_e^4 \cdot N_e} \quad (6.3.7a)$$

$$P_Q = \frac{n_\alpha}{m_\alpha} \cdot M_Q - \frac{8 \cdot M_Q}{\pi \cdot g_e} \quad (6.3.7b)$$

$$\Delta T_Q = \frac{2 \cdot L}{m_\alpha} \cdot \sqrt{\frac{1}{27 \cdot n_e} \cdot \left(P_o + P_Q + \frac{18}{\pi^4} \cdot \frac{L^2 \cdot M_Q^2}{g_e^4 \cdot n_e} - I_e \cdot \frac{\pi^2}{L^2} \right)^3} \quad (6.3.7c)$$

In order to illustrate the influence of the electrical charges carried by the bimetallic strip, Fig.6.3.1a and Fig.6.3.1b plot the evolution of the beam's thermal hysteresis as a function of the electrical charge, taking the example of an Al-Invar beam (40 x 10 x 0.4 mm³) coupled with a 10 μm thick Cytop electret with -400 V surface potential. By setting the electret on the hot source, the thermal hysteresis of the bimetallic strip is widened by a factor 10 if the charges correspond to half the charge of the electret. On the opposite, for such values of electrical charges, the beam stability is lost if the electret is placed between the cold source and the bimetallic strip.

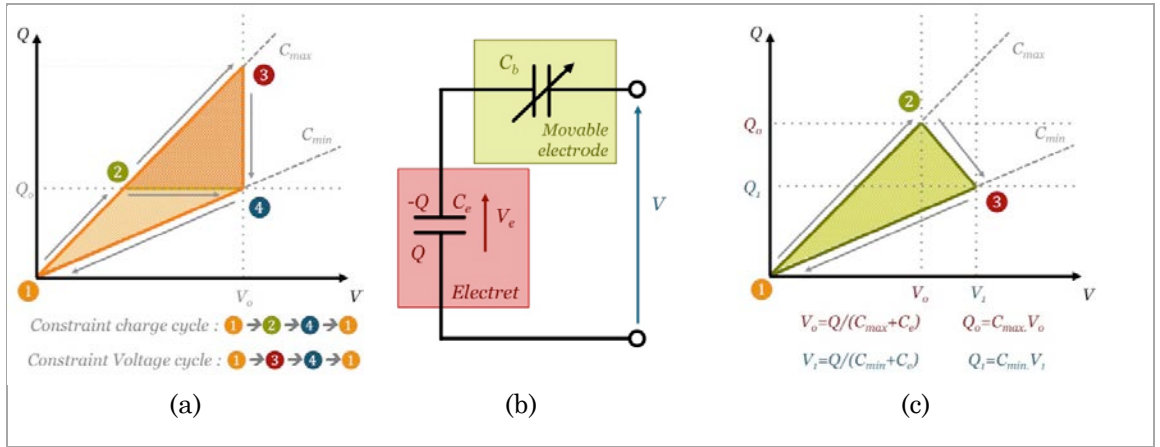


Figure 6.4.1 a. Thermodynamic cycles of an electrostatic energy harvester. b. Equivalent circuit of the electret energy harvester. c. Natural cycle of an electret energy harvester [Suzuki et al, 2015].

6.4. Harvesting heat with electret transduction

a. Possible thermodynamic cycles

In the case of common electrostatic heat engines (Fig.6.4.1a), two simple thermodynamic cycles can be implemented. The first is the charge-constrained cycle, which is quite similar to SECE and Stirling cycles, whereas the second is a voltage-constrained cycle [Meninger et al, 2001]. Given that the electrical charge is simply given by the product of the capacitance by the capacitor's voltage, the electric cycle is necessarily delimited by the curves of maximal and minimum capacitances (Fig.6.4.1b). In the case of the charge-constrained cycle, the electric charge is injected when the capacitance of the system is maximal. As a consequence, the displacement of the movable electrode causes an increase of the potential of the electrical charges that is maximal when the capacitance becomes smaller. The discharge of the circuit enables to harvest charges at a potential higher than their initial potential. Hence the energy generated by this first type of cycle is given by (6.4.1a). In the case of a voltage-constrained cycle, charges of high potential are injected during the initial step, when the capacitance is maximal. As a consequence, the deformation of the beam enables to harvest charges at high potentials. The comparison of both cycles shows that the energy harvested by the voltage-constrained cycle is greater than the energy harvested by SECE-like cycle. Similar observations can be made by comparing Ericsson and Stirling cycles.

$$\Delta W_E^Q = \frac{1}{2} \cdot \left(\frac{1}{C_{min}} - \frac{1}{C_{max}} \right) \cdot Q_0^2 \quad (6.4.1a)$$

$$\Delta W_E^V = \frac{1}{2} \cdot (C_{max} - C_{min}) \cdot V_0^2 \quad (6.4.1b)$$

Electrets-based energy harvesters have been introduced to bypass the problem of using an external voltage source to harvest energy, since the polarization of the movable electrode is ensured by the electret. Given that a counter-electrode is used, the equivalent circuit of the electret transducer is made of a variable capacitance representing the electrostatic effects of the out-of-plane movement of the electrode, and a fixed charge over the capacitance of the electret representing the permanent polarization of the device. Hence,

the natural cycle of the electrets energy harvester is composed of a first phase charging the moving electrode when its capacitance is maximal. During the displacement of the movable electrode, the charge and the voltage evolve in such manner that there is a global neutrality of the charge distributed between the movable electrode, the counter-electrode and the charge trapped in the dielectric layer. Finally, the movable electrode is discharged and returns to its initial state. The equivalent electric diagram of the harvester and its cycle are represented in Fig.6.4.1. It can thus be demonstrated that the energy harvested by this cycle is given by (6.4.12a) [Suzuki et al, 2015].

$$\Delta\mathcal{W}_E^E = \frac{1}{2} \cdot \left(\frac{C_{min}}{(C_{min} + C_e)^2} - \frac{C_{max}}{(C_{max} + C_e)^2} \right) \cdot Q^2 \quad (6.4.2a)$$

b. Intrinsic performances of the bimetallic strip heat engine.

We consider the implementation of the charge-constraint cycle with the bimetallic strip heat engine by assuming a weak electrostatic coupling. The bimetallic strip is free to move and its maximal excursion goes from $2.w_s^C$ to $-2.w_s^C$. We first recall the expression of the charge carried by the bimetallic beams as a function of its voltage V_e - V (6.4.3a). We can see that the maximal charge is obtained when the harvester is short-circuited ($V = 0$) and when the capacitance is maximal (6.4.3b), whereas the minimal charge is measured once the bimetal has snapped (6.4.3c) (it should be noticed that w_s^C is negative). As the bimetal is heated and snaps in open-circuit, the maximal voltage measured after it has snapped is given by (6.4.3.c). Similarly, when it snaps back, the minimal voltage measured is given by (6.4.3e).

$$Q_b = \frac{4 \cdot C_b \cdot C_e}{\pi \cdot (C_e + C_b)} \cdot (V_e - V_b) \quad (6.4.3a)$$

$$Q_b^{max} = \frac{C_b^{max}}{C_e + C_b^{max}} \cdot Q^* = \frac{\epsilon_o \cdot t_e \cdot Q^*}{\epsilon_o \cdot t_e + \epsilon_e \cdot (g_o + 2 \cdot w_s^C)} \quad (6.4.3b)$$

$$Q_b^{min} = \frac{C_b^{min}}{C_e + C_b^{min}} \cdot Q^* = \frac{\epsilon_o \cdot t_e \cdot Q^*}{\epsilon_o \cdot t_e + \epsilon_e \cdot (g_o - 2 \cdot w_s^C)} \quad (6.4.3c)$$

$$V_b^{max} = \frac{Q_b^{min} - Q_b^{max}}{Q_b^{max}} \cdot V_e \quad (6.4.3d)$$

$$V_b^{min} = \frac{Q_b^{max} - Q_b^{min}}{Q_b^{min}} \cdot V_e \quad (6.4.3e)$$

As a consequence, the energy that is generated during a cycle is given by (6.4.4a). The negative sign of this expression shows that the cycle is that of a generator. This expression can be rewritten as a function of the output voltages, in order to extract the theoretical value of the maximal available energy during the characterization of device.

$$\Delta\mathcal{W}_E^Q = \frac{1}{2} \cdot (Q_b^{max} - Q_b^{min}) \cdot (V_b^{max} - V_b^{min}) = \frac{1}{2} \cdot V_e \cdot \frac{(Q_b^{min} - Q_b^{max})^3}{Q_b^{min} \cdot Q_b^{max}} < 0 \quad (6.4.3c)$$

$$\Delta\mathcal{W}_E^Q = -\frac{2}{\pi} \cdot \frac{C_b^{min} \cdot C_e}{C_e + C_b^{min}} \cdot V_b^{max} \cdot (V_b^{max} - V_b^{min}) \quad (6.4.3c)$$

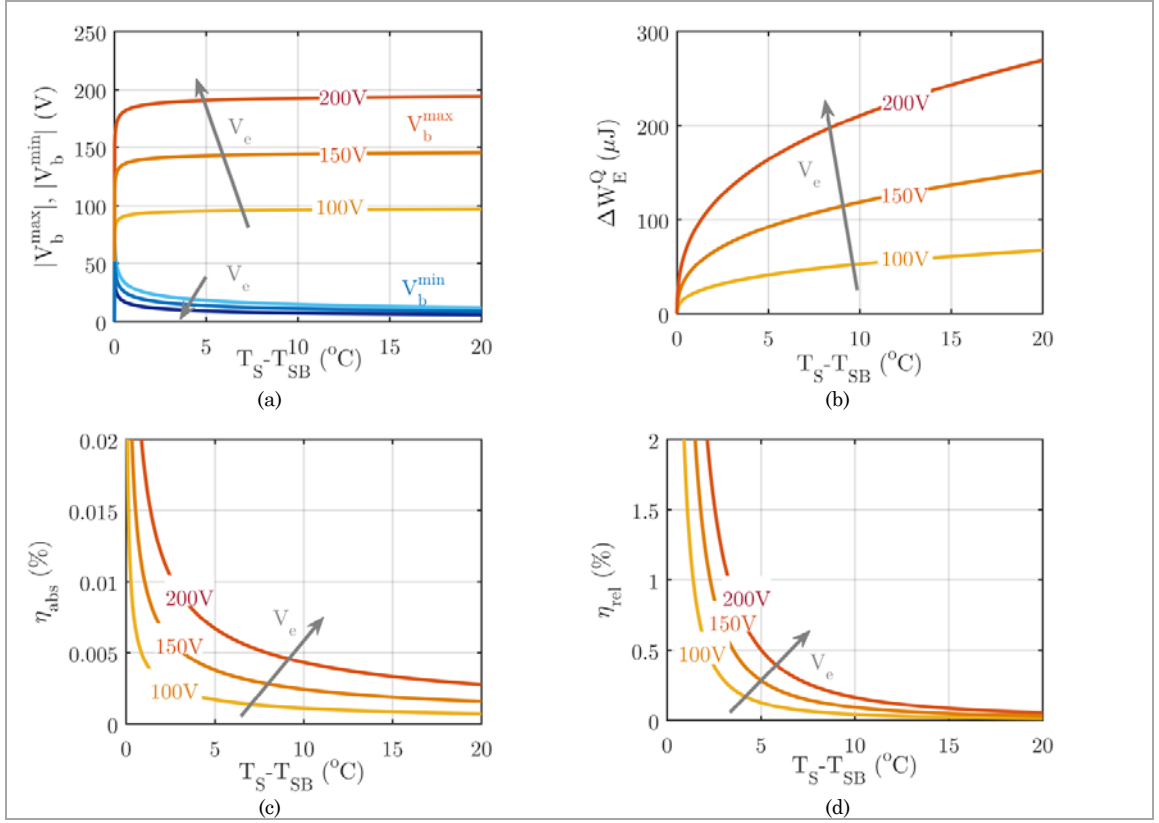


Figure 6.4.2. *a. Evolution of the snap snap-back voltages as a function of the beam's thermal hysteresis (assuming a ratio $rw = 1$) and for various values of the surface potential of a Cytop electret. b. Evolution of the electrical energy per cycle as a function of the thermal hysteresis. c. Thermal efficiency of the energy harvester. d. Evolution of the Carnot efficiency of the device as a function of the thermal hysteresis.*

Given that we need to see how the performance of the energy harvester depends on the properties of the bimetallic strip, we develop the expressions of the energy and output voltages as functions of the maximal deflection amplitude.

$$\Delta W_E^Q = -\frac{128}{\pi} \cdot \frac{\varepsilon_o \cdot \varepsilon_e^3 \cdot t_e \cdot w_S^3}{\left((\varepsilon_o \cdot t_e + \varepsilon_e \cdot g_o)^2 - 4 \cdot \varepsilon_e^2 \cdot w_S^2 \right)^2} \cdot C_e \cdot \mathcal{V}_e^2 \quad (6.4.4a)$$

$$\mathcal{V}_b^{max} = \frac{4 \cdot \varepsilon_o \cdot \varepsilon_e \cdot t_e |w_S^C|}{(\varepsilon_o \cdot t_e + \varepsilon_e \cdot g_o)^2 - 4 \cdot \varepsilon_e^2 \cdot w_S^2} \cdot \mathcal{V}_e \quad (6.4.4b)$$

$$\mathcal{V}_b^{min} = \frac{4 \cdot \varepsilon_o \cdot \varepsilon_e \cdot t_e |w_S^C|}{(\varepsilon_o \cdot t_e + \varepsilon_e \cdot g_o)^2 + 4 \cdot \varepsilon_e^2 \cdot w_S^2} \cdot \mathcal{V}_e \quad (6.4.4c)$$

To avoid making any hypothesis on the value of the gap g_o , we directly study the performances of a bimetallic strip constrained in a cavity. As a consequence, the gap g_o is given by (6.4.5a), enabling to simplify the expression of the device's performances.

$$g_o = r_w \cdot |w_S^C| \quad (6.4.5a)$$

$$\Delta W_E^Q = \frac{16}{\pi} \cdot \frac{\varepsilon_e^3 \cdot r_w^3 \cdot |w_S^C|^3}{\varepsilon_o \cdot t_e \cdot (\varepsilon_o \cdot t_e + 2 \cdot \varepsilon_e \cdot r_w \cdot |w_S^C|)^2} \cdot C_e \cdot \mathcal{V}_e^2 \quad (6.4.5b)$$

$$\mathcal{V}_b^{max} = \frac{2 \cdot \varepsilon_e \cdot r_w \cdot |w_S^C|}{\varepsilon_o \cdot t_e + 2 \cdot \varepsilon_e \cdot r_w \cdot |w_S^C|} \cdot \mathcal{V}_e \quad (6.4.5c)$$

$$\mathcal{V}_b^{min} = \frac{2 \cdot \varepsilon_o \cdot \varepsilon_e \cdot t_e \cdot r_w \cdot |w_S^C|}{(\varepsilon_o \cdot t_e + \varepsilon_e \cdot r_w \cdot |w_S^C|)^2 + \varepsilon_e^2 \cdot r_w^2 \cdot |w_S^C|^2} \cdot \mathcal{V}_e \quad (6.4.5d)$$

Assuming that the electret thickness is smaller than the beam deflexion, we can express the electrical energy as a function of the beam's thermal hysteresis, enabling to give the expression of the thermal efficiency of the harvester in the cavity (6.4.6a).

$$\Delta W_E^Q = \frac{4^3 \sqrt{4}}{\pi^2} \cdot \frac{\varepsilon_e \cdot r_w}{\varepsilon_o \cdot t_e} \cdot \sqrt[3]{\frac{M_\alpha \cdot L^2}{N_e}} \cdot \Delta T \cdot C_e \cdot \mathcal{V}_e^2 \quad (6.4.6a)$$

$$\eta_{TE}^{abs} = \frac{8^3 \sqrt{4}}{\pi^2 \cdot (3 - r_w^2)} \cdot \frac{\varepsilon_e}{\varepsilon_o \cdot t_e} \cdot \sqrt[3]{\frac{M_\alpha \cdot L^2}{N_e \cdot C_v^3}} \cdot \Delta T \cdot C_e \cdot \mathcal{V}_e^2 \quad (6.4.6b)$$

In order to present the performances of the heat engine predicted by the model, we study the performance of an Al-Invar beam (40 x 10 x 0.4 mm³) coupled with an electret made of a 20 μm thick Cytop electret with surface potential of -400 V. Fig.6.4.1a shows the evolution of the peak voltages generated by the beam when it snaps and when it snaps back. We can observe that the peaks are higher when the beam snaps, since the initial amount of charges carried by the bimetallic beam is more important as the capacitance is higher when the beam is in contact with the hot source. We observe that by increasing the beam's thermal hysteresis, the snap voltage converges toward the value of the electret's surface potential. The evolution of the electrical energy is plotted in Fig.6.4.2b. It is important to compare this figure with Fig.6.4.2.c. Given that the energy evolves as the cubic root of the thermal hysteresis (6.4.6a), we observe that the thermal efficiency of the system is a decreasing function of the thermal hysteresis, contrary to other energy harvesters presented in the previous parts. Using an electret with surface potential of 150 V, the available mechanical energy per cycle is of around 100 μJ for a thermal efficiency of 4.10⁻³% and a Carnot efficiency of 0,12%.

c. Dynamic performances of the heat engine

As for other energy harvesters, we can use the thermal lumped capacitance model to evaluate the maximal power that is generated by the electrostatic bimetallic strip heat engine. The main performances are given below: the mean output power (6.4.7a), the thermal efficiency of the harvester working between two heat sources (6.4.7b), and the Curzon-Ahborn efficiency of the device (6.4.7c). As a reminder, the temperature difference across the energy harvester can be expressed as a function of the external temperature and the thermal properties of the device (R_{leak}) and of the heat sink (R_{sink}).

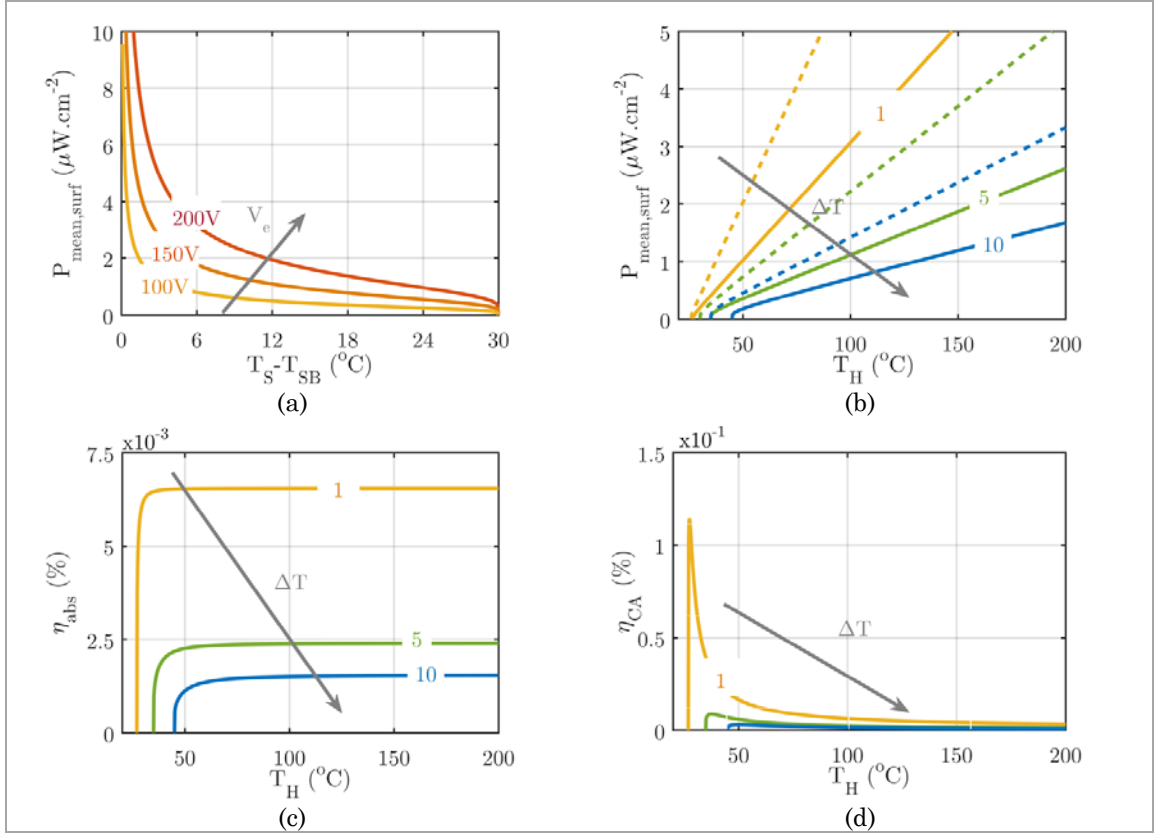


Figure 6.4.3. *a.* Mean power generated with a bimetallic strip placed in a cavity where a temperature difference of 30°C is maintained. *b.* Evolution of the mean power generated by three different bimetallic strips (hysteresis of 1°C, 5°C, 10°C) as a function of the hot source temperature (ambient temperature 25°C) and the type of heat sink (heat sink with fins represented by dashed lines, planar heat sink by continuous lines). The electret's surface potential is 100 V. *c.* Evolution of the thermal efficiency for various values of thermal hysteresis (device with a planar heat sink). *d.* Curzon-Ahlborn efficiency of the device as a function of the hot source temperature (device with planar heat sink).

$$P_E = \frac{4\sqrt[3]{4}}{\pi^2} \cdot \frac{r_w}{\sqrt[3]{(3 \cdot r_w - r_w^3)}} \cdot \frac{\varepsilon_e \cdot C_e \cdot V_e^2}{\varepsilon_o \cdot t_e} \cdot \sqrt[3]{\frac{M_\alpha \cdot L^2}{N_e \cdot R_{CC}^3 \cdot C_v^3}} \cdot \frac{\sqrt[3]{\Delta T_{cav}}}{\ln\left(1 + \frac{\Delta T_{cav}}{T_H - T_C}\right) - \ln\left(1 - \frac{\Delta T_{cav}}{T_H - T_C}\right)} \quad (6.4.7a)$$

$$\eta_{TE}^{abs,tot} = \frac{P_E}{R_{sink} \cdot (T_H - T_C)} \quad (6.4.7b)$$

$$\eta_{TE}^{CA,tot} = \frac{P_E}{R_{sink} \cdot (T_H - T_C)} \cdot \frac{\sqrt{T_H + 273}}{\sqrt{T_H + 273} - \sqrt{T_{amb} + 273}} \quad (6.4.7c)$$

$$T_H - T_C = \frac{R_{sink}}{R_{sink} + R_{leak}} \cdot (T_H - T_{amb}) \quad (6.4.7d)$$

The study of the performances is plotted in Fig.6.4.3. The first figure presents the dependence of the mean power on the beam's thermal hysteresis and on the electret's surface potential when a fixed temperature difference of 30°C is maintained in the device's

cavity. We already saw that the working frequency of the bimetallic strip is a decreasing function of the thermal hysteresis. As the amount of electric energy generated during a complete cycle increases as the cubic root of the thermal hysteresis, we observe that the bimetallic strips with the smallest thermal hysteresis generates more energy because of their high working frequency. Fig.6.4.3b represents the evolution of the output power when the hot source temperature evolves from 25°C to 200°C. We observe that at 100°C, the device generates up to 3 $\mu\text{W}\cdot\text{cm}^{-2}$ when the bimetallic strip has a thermal hysteresis of 1°C. Logically we can observe that the power can be boosted by the use of a heat sink with fins (up to 6 $\mu\text{W}\cdot\text{cm}^{-2}$ for a thermal hysteresis of 3°C). The other figures represent the evolution of the efficiency of the device for the same working conditions. Logically, the fact that the device's architecture is a path for thermal leakages explains why the efficiency of the energy harvester is degraded.

d. *Effect of the moderate electrostatic coupling on the performances of the heat engine*

In the previous part, we modelled the performances of the electrostatic bimetallic strip heat engine by assuming that we could neglect the effect of the electrostatic coupling on the mechanical behavior of the bimetallic strip. However, we can see that by using the previous equations, increasing the electret's polarization increases all the performances of the heat engine. In Section 6.3.c, we presented a simple approximation of the electrostatic pressure in order to determine its influence on the thermal hysteresis of the bimetallic strip. We now use this approximation to see the influence of the electric field on the output power. We assume that the electrostatic moment is equal to (6.4.8a), corresponding to a fixed charge on the bimetallic strip given by (6.4.8b). Hence, we need to modify the values of the beam's displacement by (6.4.8e) and the beam's thermal hysteresis by (6.4.8f), by introducing the corrective factor (6.4.8e).

$$M_Q = \frac{\pi}{4} \cdot \frac{\varepsilon_e \cdot L}{\varepsilon_o \cdot t} \cdot C_e \cdot \mathcal{V}_e^2 \quad (6.4.8a)$$

$$\frac{1}{Q} = \frac{1}{Q_b^{\min}} + \frac{1}{Q_b^{\max}} \quad (6.4.8b)$$

$$P_Q = \frac{N_\alpha}{M_\alpha} \cdot M_Q + \frac{8 \cdot \varepsilon_e \cdot M_Q}{\pi \cdot (\varepsilon_o \cdot t_e + \varepsilon_e \cdot r_w \cdot |w_S^c|)} \quad (6.4.8c)$$

$$\Delta T_Q = \Delta T \cdot \sqrt{F(\mathcal{V}_e)^3} \quad (6.4.8d)$$

$$w_{S^c}^c = w_S^c \cdot \sqrt{F(\mathcal{V}_e)} \quad (6.4.8e)$$

$$F(\mathcal{V}_e) = 1 + \frac{N_o + N_Q + \frac{18 \cdot M_Q^2}{\pi^4 \cdot N_e} \cdot \frac{\varepsilon_e^4 \cdot L^2}{(\varepsilon_o \cdot t_e + \varepsilon_e \cdot r_w \cdot |w_S^c|)^4}}{N_o - I_e \cdot \frac{\pi^2}{L^2}} \quad (6.4.8f)$$

Hence, the performances of the heat engine can be re-written in order to include the effect of the moderate coupling (6.4.9).

$$\Delta \mathcal{W}_E^Q = \frac{16}{\pi} \cdot \frac{\varepsilon_e^3 \cdot r_w^3 \cdot |w_S^c|^3 \cdot \sqrt{F(\mathcal{V}_e)^3}}{\varepsilon_o \cdot t_e \cdot (\varepsilon_o \cdot t_e + 2 \cdot \varepsilon_e \cdot r_w \cdot |w_S^c| \cdot \sqrt{F(\mathcal{V}_e)})^2} \cdot C_e \cdot \mathcal{V}_e^2 \quad (6.4.9a)$$

$$f = \frac{1}{2 \cdot R_{CC} \cdot C_v} \cdot \frac{1}{\ln\left(1 + \frac{\sqrt{F(V_e)^3} \cdot \Delta T_{cav}}{T_H - T_C}\right) - \ln\left(1 - \frac{\sqrt{F(V_e)^3} \cdot \Delta T_{cav}}{T_H - T_C}\right)} \quad (6.4.9b)$$

$$P_E = f \cdot \Delta \mathcal{W}_E^Q \quad (6.4.9c)$$

In order to see the influence of the electrostatic coupling on the performance of the electrostatic bimetallic strip heat engine, we plot in Fig.6.4.4 the evolution of the working frequency and the mean output power generated by the device. Fig.6.4.4a and Fig.6.4.4b represent their evolution when the electret is put on the cold source (electret made of 20 μm of CYTOP). As it reduces the beam's thermal hysteresis, the working frequency is first improved by the increase of the electric field, thus increasing the output power for small electric fields. After reaching a maximal value, the power decreases because of the reduction of the generated energy per cycle. The system stops when the beam becomes monostable. We can observe that the optimal value of the electret's polarization is a function of the thermal hysteresis. For a beam having a thermal hysteresis of 5°C, the maximal power is 0.4 $\mu\text{W} \cdot \text{cm}^{-2}$ for a working frequency of around 0.023 Hz. The shape of the curve indicates that we can find an optimal thermal hysteresis and an optimal electret potential surface that maximize the output power of the generator. In our case, the optimal hysteresis is 5°C and the optimal surface potential 110 V.

Fig.6.4.4c and Fig.6.4.4d represent the evolution of the performances when the electret is placed on the hot source. In this case we can observe that the frequency is a decreasing function of the electric field since the electric field increases the effective thermal hysteresis of the bimetallic strip. Even if the increase of the electric field improves the transduction of the thermal energy into electric energy during a complete cycle, decreasing the working frequency leads to an optimal value of the electret's surface potential that maximizes the output power generated by the device. This has already been observed during experimental measurements. Here again we can observe that the optimal value of the surface potential is a function of the thermal hysteresis and that the best performances are obtained for an optimal value of the thermal hysteresis. In our case, the optimal thermal hysteresis is 3°C and the optimal surface potential is about 80 V. In that case, the maximal output power is around 0.24 $\mu\text{W} \cdot \text{cm}^{-2}$ when a temperature difference of 30°C is maintained in the device's cavity. We also observe that the system stops working when the effective thermal hysteresis becomes equal to the temperature difference in the cavity.

To finish, we plot the performances predicted by the model for an Al-Invar bimetallic strip coupled with a Cytop electret (surface potential 100V) placed on the cold source, and assuming that the device works without heat sink. As we can see, the best thermal hysteresis is still 5°C. With this bimetallic strip, the energy harvester generates 0.5 $\mu\text{W} \cdot \text{cm}^{-2}$ at 100°C with a thermal efficiency of 1,4.10⁻³%.

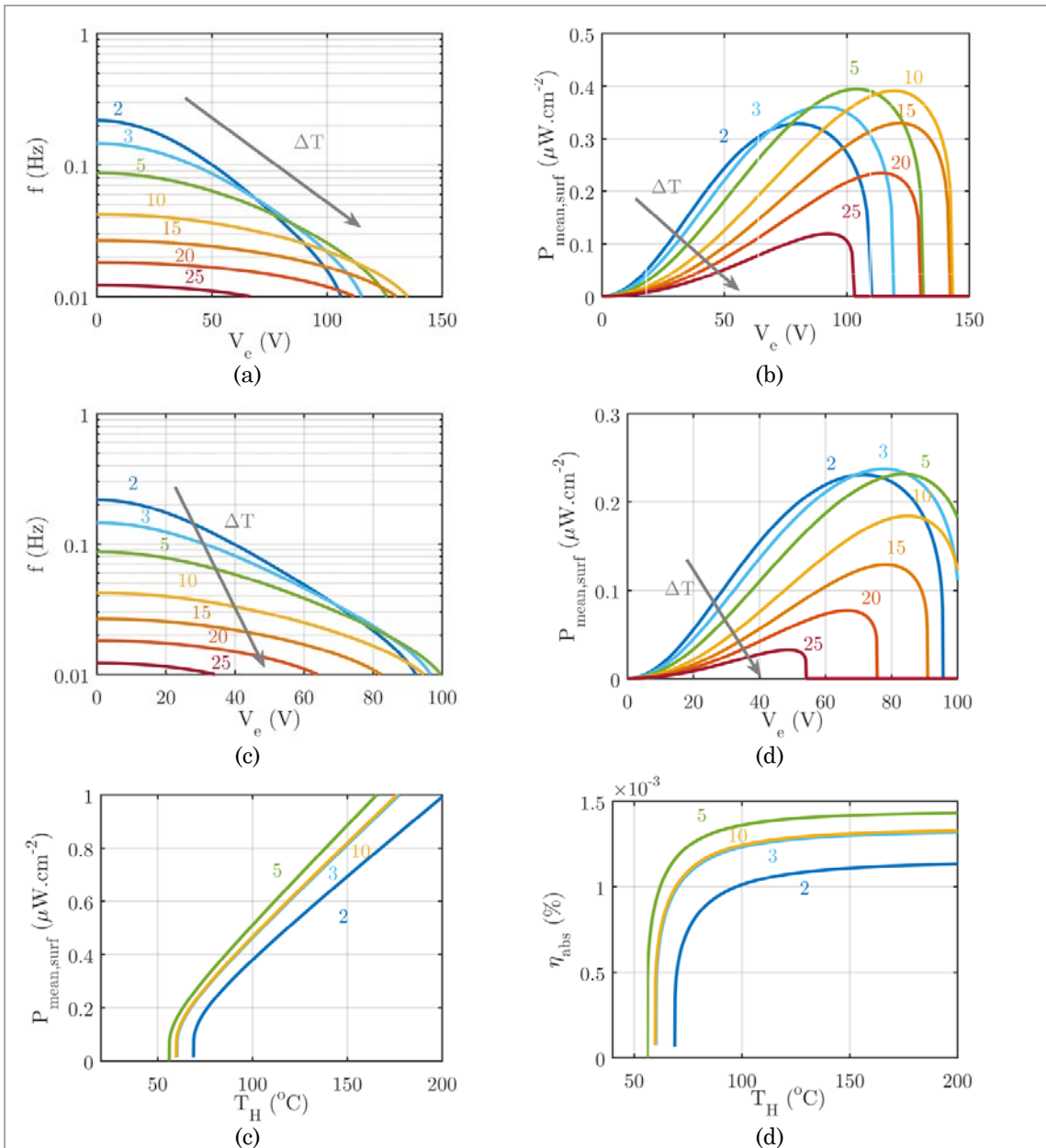


Figure 6.4.4. a. Evolution of the working frequency as a function of the electret’s surface potential when the electret is placed on the cold source (assuming a temperature difference in the cavity of 30°C). b. Output power of the energy harvester when the electret is placed on the cold source for various thermal hystereses. c. Working frequency as a function of the electret’s surface potential when the electret is placed on the hot source. d. Output power in the same conditions. e. Output power generated by an Al-Invar bimetallic strip coupled with a Cytop electret having a surface potential of 100 V and placed on the cold surface. f. Evolution of the thermal efficiency of the device as a function of the hot source temperature.

7 Synthesis

Now that we have established all the laws describing the operations of the pyroelectric, piezoelectric and electrostatic bimetallic strip heat engines, we are able to compare their performances in order to choose the best architecture of bimetallic strip heat engines, but also to sum up the various strategies to optimize their relative performances.

a. Design rules common to all harvesters

From chapter 2, we can say that to optimize the thermo-mechanical transduction, we should:

- Choose the bimetallic couple having the best Figure of Merit $F_W = 27 \cdot \sqrt[3]{\frac{m_a^4}{16 \cdot n_e \cdot L}}$: the influence of the heat capacitance is weak since it has quite the same value whatever the metal used. As a consequence, bimetallic strips made of Al-Invar or CuZn-Invar are the best materials since the difference between their coefficients of thermal expansion is the largest possible;
- Design a passive architecture that minizes the mechanical stress applied to the bimetallic strip ($r_w = 1$);
- Improve thermal transfers but reduce the thermal resistance of the contact between the heat sources and the bimetallic strip (decreasing RCC);
- Improve the evacuation of heat by using a heat sink with fins. This enables to maintain a large temperature difference inside the cavity and thus to boost the working frequency of the bimetallic strip and the output power (gain factor of around 3), to use bistable beams with larger thermal hysteresis and to widen the temperature operating range of the heat engine.

b. Design rules for pyroelectric bimetallic strip heat engines

In the case of the pyroelectric bimetallic strip heat engines, we should:

- Use pyroelectric bimetallic strips with the largest electro-thermal coupling factor $k_{pyro}^2 \cdot \frac{L \cdot v \cdot t_p \cdot \rho_{pyro} \cdot c_{pyro}}{C_v} \cdot \left(1 + \frac{8 \cdot \sqrt[3]{4}}{3 \cdot \left(1 - \frac{v_a^2}{3} \right)} \cdot \frac{z_p \cdot z_o}{L} \cdot \frac{e_{31}}{p_3^S} \cdot \sqrt[3]{\frac{m_a}{n_e \cdot L}} \cdot \frac{1}{\sqrt[3]{\Delta T^2}} \right)^2$. If the temperature difference inside the cavity is weak, the best pyroelectric material is the one that has both the best electro-thermal and electro-mechanical coupling factors. If the temperature difference is large, the tertiary pyroelectric effect becomes negligible and the best materials are those with the best electro-thermal coupling factors. As a consequence, we should use either PZT ceramics or MPM-PN ceramics;
- Implement the Stirling cycle by using a SECE power management circuit;

- Choose a bimetallic strip having a thermal hysteresis corresponding to 70% of the temperature difference in the cavity.

c. Design rules for piezoelectric bimetallic strip heat engines

In the case of the piezoelectric bimetallic strip heat engines, we should:

- Use bimetallic strips with a thermal hysteresis corresponding to 60% of the temperature difference in the cavity to maximize the mechanical power generated by the bimetallic strip (chapter 2);
- Use piezoelectric transducers with the smallest bending stiffness in order to maximize the energy transfer during the impact of the bistable bimetallic strip, and with a piezoelectric material having the largest electro-mechanical coupling factor. As a consequence, soft PZT ceramics are the best piezoelectric materials for this usage;
- Use a clamped-clamped piezoelectric transducer with three piezoelectric capacitors to maximize the piezoelectric coupling of the oscillator;
- Improve the mechanical quality factor of the piezoelectric transducer in order to reduce the mechanical losses. This can be done by improving the quality of the transducer's clamp or by changing the shape of the piezoelectric transducer;
- Use SECE or SSHI power management circuits.

d. Design rules for electrostatic bimetallic strip heat engines

In the case of the electrostatic bimetallic strip heat engines, we should:

- Choose the optimal thermal hysteresis that optimize the output power;
- Determine the value of the electret's surface potential that optimizes the power generated by the bimetallic strip heat engine.

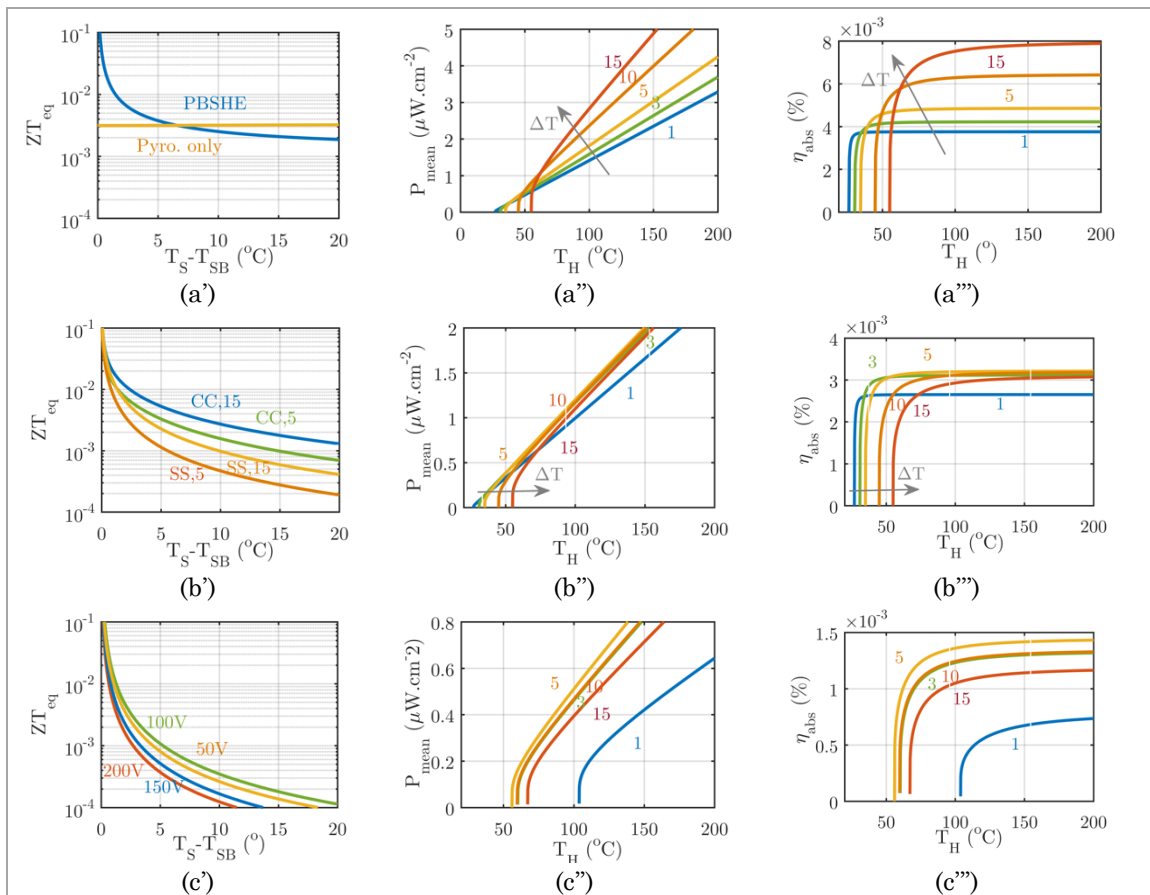


Figure 7.1.1. Performances of the a. pyroelectric, b. piezoelectric, and c. electrostatic bimetallic strip heat engines (equivalent ZT, mean power and thermal efficiency).

e. Comparison of the various heat engines

To finish we recall in Fig. 7.1.1 the performances of the three configurations of heat engines modelled in this chapter. The three bimetallic strip heat engines are made of Al-Invar beams ($40 \times 10 \times 0.4 \text{ mm}^3$) with either 0.1 mm of PZT deposited on the surface of the bistable beam, or a piezoelectric transducer made of 0.2 mm of brass and 0.1 mm of PZT, or coupled with a 20 μm thick CYTOP electret with surface potential 100 V.

As we can see by comparing the images in the first column, the piezoelectric engine is intrinsically the most efficient system for small thermal hystereses with an equivalent ZT around $5 \cdot 10^{-3}$ for a thermal hysteresis of 5°C (with a clamped-clamped piezoelectric transducer having a quality factor of 15), followed by the pyroelectric engine (ZT of $3 \cdot 10^{-3}$ for a thermal hysteresis of 5°C) and by the electrostatic engine (ZT of $1 \cdot 10^{-3}$ for a thermal hysteresis of 5°C). However the reduction of the ZT for greater values of thermal hysteresis is larger for the piezoelectric engine, and the pyroelectric engine finally becomes the most efficient device (ZT of $2 \cdot 10^{-3}$ for a thermal hysteresis of 15°C), ahead piezoelectric devices (ZT of $1,7 \cdot 10^{-3}$) and electrostatic devices (ZT of $1,8 \cdot 10^{-4}$).

The second and third columns present the dynamic performances of the three devices, working without heat sink between a cold source at 25°C and a hot source whose temperature varies. The output power is plotted for five different bimetallic strips. We can

see that the pyroelectric energy harvester is the one that generates the most power, because at a given hot source temperature, the bimetallic strip that maximizes the output power has a greater thermal hysteresis. At 100°C, using a bimetallic strip having a thermal hysteresis of 15°C, we can generate up to 2.8 $\mu\text{W}\cdot\text{cm}^{-2}$ with a thermal efficiency of 7.5 · 10⁻³%. With a piezoelectric device, the maximal power is obtained with a bimetallic strip of 10°C of hysteresis, which generates 1.28 $\mu\text{W}\cdot\text{cm}^{-2}$. Finally, with the electrostatic device, the maximal power is 0.51 $\mu\text{W}\cdot\text{cm}^{-2}$, obtained with a thermal hysteresis of 5°C. As a consequence, we can see that the system that must be preferably developed is the pyroelectric bimetallic strip heat engine since it is twice as efficient than the piezoelectric bimetallic strip heat engine, and over 5 times more efficient than the electrostatic bimetallic strip heat engine.

8 Conclusion

In this chapter, we presented and modelled three different energy harvesters: the pyroelectric, piezoelectric and electrostatic bimetallic strip heat engines. To model the pyroelectric generator, we came back to the local constitutive equations of pyroelectric materials and applied it to the case of a pyroelectric layer deposited either on the passive layer or the active layer of the bistable beams. We described three configurations of Stirling cycles and established the expressions of the generated power and the thermoelectric efficiency, enabling to compare the performances of these cycles, as a function of the geometry of the bimetallic strip, the pyroelectric materials, and the bimetallic strip's thermal hysteresis. We finally found that the power levels generated by the pyroelectric generators are of around 1 to 3 $\mu\text{W}\cdot\text{cm}^{-2}$ for an equivalent ZT of around 0,01.

In the case of the piezoelectric bimetallic strip heat engines, we determined the maximal theoretical performances by assuming a perfect mechanical coupling between the piezoelectric oscillator and the bimetallic strip. In that case of figure, we found that the perfect coupling is described by a non-linear Duffing equation we solved using either harmonic balance or Jacobi's elliptic functions. We thus found analytic expressions of the output voltages generated by piezoelectric oscillators for three types of oscillators: clamped-clamped oscillators, double supported oscillators, clamped-free oscillators. We found that the best performances are obtained with clamped-clamped oscillators whose bending stiffness is weaker than the bimetallic strip's stiffness in order to maximize stress and mechanical energy transfer. We then simulated the case of a SECE strategy to extract electrical energy from the piezoelectric oscillators. The analytical expressions we found showed us the interest of improving the quality factor of the piezoelectric transducer's mechanical oscillations in order to improve the electro-mechanical conversion's efficiency. From this observation, we designed new geometries of oscillators with better mechanical quality factors and smaller bending stiffness, enabling to increase the generators' performances by a factor 5. We find that the best performances are of around 1 $\mu\text{W}\cdot\text{cm}^{-2}$ for a generator working without any heat sink with fins. The fact that these levels of performances are simulated by assuming a perfect mechanical coupling between the piezoelectric transducer and the bimetallic strip explains why we cannot obtain them experimentally: most of the time, only one or two shocks between the bimetallic strip and the piezoelectric transducers occur, limiting the energy transfer between the two oscillators.

The last device we modeled consisted in coupling a bimetallic strip with an electret transducer. In that case of figure, we modeled both the weak coupling and strong coupling

between the electret and the bimetallic strip. We evaluated the performances of the generator in the case of a SECE energy harvesting strategy. This enabled us to show that there exists an optimal value of electret's surface potential that maximizes the power generated by the bimetallic strip heat engine. Typically, we found that this type of generators can generate up to $0,5 \text{ uW.cm}^{-2}$ without a heat sink with fins.

From this theoretical study, we can conclude that efforts must be made on developing pyroelectric bimetallic heat engine if we want to improve the performances of current energy harvester. As a final conclusion, we can say that in the best case, bimetallic strip heat engines are far from reaching the performances of thermoelectric generators. Typically, the maximal efficiency obtained with this generator is less than 1% of the thermoelectric generators' efficiency, and the slowness of thermal transfers inside the generator's architecture explained why the power levels generated by the bimetallic strip heat engines are far from being competitive with thermoelectric generators.

Now that we modeled the performances of the generator at the macroscale, we need to see how they evolve when the system is miniaturized using MEMS fabrication techniques. This is the topic of the next chapter.

9 Bibliography

- Arrieta, A., Hagedorn, P., Erturk, A. and Inman, D. (2010). A piezoelectric bistable plate for nonlinear broadband energy harvesting. *Appl. Phys. Lett.*, 97(10), p.104102.
- Arnaud, A., Boisseau, S., Monfray, S., Puscasu, O., Despesse, G., Boughaleb, J., Sanchez, Y., Battegay, F., Fourel, M., Audran, S., Boeuf, F., Delamare, J., Delepierre, G., Pitone, G. and Skotnicki, T. (2013). Piezoelectric and electrostatic bimetal-based thermal energy harvesters. *J. Phys.: Conf. Ser.*, 476, p.012062.
- Alghisi, D., Dalola, S., Ferrari, M. and Ferrari, V., (2015), Triaxial ball-impact piezoelectric converter for autonomous sensors exploiting energy harvesting from vibrations and human motion. *Sensors and Actuators A: Physical*. 2015. Vol. 233, p. 569-581.
- Bhalla, A. and Newnham, R. (1980). Primary and secondary pyroelectricity. *Physica Status Solidi (a)*, 58(1), pp.K19-K24.
- Boisseau, S. (2011). Récupération d'énergie vibratoire à électrets. PhD Thesis. Université de Grenoble.
- Boisseau, S., Despesse, G., Monfray, S., Puscasu, O. and Skotnicki, T. (2013). Semi-flexible bimetal-based thermal energy harvesters. *Smart Materials and Structures* 22(2), p.025021.
- Boughaleb, J., Arnaud, A., Cottinet, P., Monfray, S., Gelenne, P., Kermel, P., Quenard, S., Boeuf, F., Guyomar, D. and Skotnicki, T. (2015). Thermal modeling and optimization of a thermally matched energy harvester. *Smart Materials and Structures*, 24(8), p.085025.

- Boughaleb, J., Arnaud, A., Cottinet, P., Monfray, S., Quenard, S., Boeuf, F., Guyomar, D. and Skotnicki, T. (2015). Analysis of the thermal impact of a bimetal on the dynamic behavior of a thermal energy harvester. *Sensors and Actuators A: Physical*, 236, pp.104-115.
- Bowen, C., Taylor, J., Le Boulbar, E., Zabek, D. and Topolov, V. (2015). A modified figure of merit for pyroelectric energy harvesting. *Materials Letters*, 138, pp.243-246.
- Brissaud, M. and Balland, B. (2007). *Matériaux piézoélectriques*. Lausanne: Presses polytechniques et universitaires romandes.
- Callen, H. (1960). *Thermodynamics*. New York: Wiley.
- Capsal, J., David, C., Dantras, E. and Lacabanne, C. (2012). Piezoelectric sensing coating for real time impact detection and location on aircraft structures. *Smart Materials and Structures*, 21(5), p.055021.
- Chaplya, P., Mitrovic, M., Carman, G. and Straub, F. (2006). Durability properties of piezoelectric stack actuators under combined electromechanical loading. *Journal of Applied Physics*, 100(12), p.124111.
- Chiu, Y. and Lee, Y. (2012). Flat and robust out-of-plane vibrational electret energy harvester. *J. Micromech. Microeng.*, 23(1), p.015012.
- Clingman, W. and Moore, R. (1961). Application of Ferroelectricity to Energy Conversion Processes. *J. Appl. Phys.*, 32(4), p.675.
- Curie J., Curie P. (1880) Développement, par pression, de l'électricité polaire dans les cristaux hémihédres à faces inclinées. *Comptes rendus de l'Académie des Sciences* 91:294; 383; *Bulletin de la Société minéralogique* 3:90
- Curie J., Curie P. (1881) Contractions et dilatations produites par des tensions électriques dans les cristaux hémihédres à faces inclinées. *Comptes rendus de l'Académie des Sciences* 93:1137–1140
- Gu, L. and Livermore, C. (2011). Impact-driven, frequency up-converting coupled vibration energy harvesting device for low frequency operation. *Smart Mater. Struct.*, 20(4), p.045004.
- Gu, L. (2011). Low-frequency piezoelectric energy harvesting prototype suitable for the MEMS implementation. *Microelectronics Journal*, 42(2), pp.277-282. Häsler, E., Stein, L. and Harbauer, G. (1984). Implantable physiological power supply with PVDF film. *Ferroelectrics*, 60(1), pp.277-282.
- Harne, R. and Wang, K. (2013). A review of the recent research on vibration energy harvesting via bistable systems. *Smart Mater. Struct.*, 22(2), p.023001.
- Heaviside, O. (1970). *Electrical papers*. Bronx, N.Y.: Chelsea Pub. Co.
- Hehn, T., Hagedorn, F., Maurath, D., Marinkovic, D., Kuehne, I., Frey, A. and Manoli, Y. (2012). A Fully Autonomous Integrated Interface Circuit for Piezoelectric Harvesters. *IEEE J. Solid-State Circuits*, 47(9), pp.2185-2198.

- Holmes, P. (1979). A Nonlinear Oscillator with a Strange Attractor. *Philosophical Transactions of the Royal Society A: Mathematical, Physical and Engineering Sciences*, 292(1394), pp.419-448.
- IEEE Standard on Piezoelectricity (1988)," in ANSI/IEEE Std 176-1987
- Jefimenko, O. and Walker, D. (1978). Electrostatic Current Generator Having a Disk Electret as an Active Element. *IEEE Transactions on Industry Applications*, IA-14(6), pp.537-540.
- Jordan, D. and Smith, P. (2007). *Nonlinear ordinary differential equations*. Oxford: Oxford University Press.
- Kestelman, V., Pinchuk, L. and Gol'dade, V. (2000). *Electrets in engineering*. Boston: Kluwer Academic Publishers.
- Kosorotov, V., Kremenchugskij, L., Levash, L. and Shchedrina, L. (1994). Dynamic tertiary pyroelectric effect and its inertial properties. *GFER*, 160(1), pp.125-136.
- Kovacic, I. and Brennan, M. (2011). *The Duffing Equation*. Hoboken: John Wiley & Sons.
- Lang, S. (2005). Pyroelectricity: From ancient curiosity to modern imaging tool. *Phys. Today*, 58(8), pp.31-36.
- Le, C., Halvorsen, E., Søråsen, O. and Yeatman, E. (2013). Wideband excitation of an electrostatic vibration energy harvester with power-extracting end-stops. *Smart Mater. Struct.*, 22(7), p.075020.
- Lefeuvre, E., Audigier, D., Richard, C. and Guyomar, D. (2007). Buck-Boost Converter for Sensorless Power Optimization of Piezoelectric Energy Harvester. *IEEE Transactions on Power Electronics*, 22(5), pp.2018-2025.
- Lippmann M. G. (1881) Principle of the conservation of electricity. *Ann chimie et phys ser* 524:145–178
- Lipscomb, I., Weaver, P., Swingler, J. and McBride, J. (2009). The effect of relative humidity, temperature and electrical field on leakage currents in piezo-ceramic actuators under dc bias. *Sensors and Actuators A: Physical*, 151(2), pp.179-186.
- Liu, T. and Livermore, C. (2015). A compact architecture for passively-switched energy harvesters. *J. Phys.: Conf. Ser.*, 660, p.012090.
- Michael, A. and Kwok, C. (2006). Design criteria for bi-stable behavior in a buckled multi-layered MEMS bridge. *Journal of Micromechanics and Microengineering*, 16(10), pp.2034-2043.
- Mizuno, M. and Chetwynd, D. (2003). Investigation of a resonance microgenerator. *J. Micromech. Microeng.*, 13(2), pp.209-216.
- Moon, F. and Holmes, P. (1979). A magnetoelastic strange attractor. *Journal of Sound and Vibration*, 65(2), pp.275-296.
- Nakano, J., Komori, K., Hattori, Y. and Suzuki, Y. (2015). MEMS Rotational Electret Energy Harvester for Human Motion. *J. Phys.: Conf. Ser.*, 660, p.012052.

- Nayfeh, A. and Mook, D. (1979). *Nonlinear oscillations*. New York: Wiley.
- Olsen, R. and Evans, D. (1983). Pyroelectric energy conversion: Hysteresis loss and temperature sensitivity of a ferroelectric material. *J. Appl. Phys.*, 54(10), p.5941.
- Olsen, R., Bruno, D., Briscoe, J. and Dullea, J. (1984). Cascaded pyroelectric energy converter. *Ferroelectrics*, 59(1), pp.205-219.
- Olsen, R., Bruno, D. and Briscoe, J. (1985). Pyroelectric conversion cycles. *J. Appl. Phys.*, 58(12), p.4709.
- Oxaal, J., Foster, D., Hella, M. and Borca-Tasciuc, D. (2015). Investigation of gap-closing interdigitated capacitors for electrostatic vibration energy harvesting. *J. Micromech. Microeng.*, 25(10), p.105010.
- Perez, M., Boisseau, S., Gasnier, P., Willemin, J. and Reboud, J. (2015). An electret-based aeroelastic flutter energy harvester. *Smart Mater. Struct.*, 24(3), p.035004.
- Puscasu, O., Monfray, S., Savelli, G., Maitre, C., Pemeant, J., Coronel, P., Domanski, K., Grabiec, P., Ancey, P., Cottinet, P., Guyomar, D., Bottarel, V., Ricotti, G., Bimbaud, I., Boeuf, F., Gaillard, F. and Skotnicki, T. (2012). An innovative heat harvesting technology (HEATec) for above-Seebeck performance. 2012 International Electron Devices Meeting.
- Ramlan, R., Brennan, M., Mace, B. and Kovacic, I. (2009). Potential benefits of a non-linear stiffness in an energy harvesting device. *Nonlinear Dynamics*, 59(4), pp.545-558.
- Renaud, Michael, Fiorini, Paolo, van Schaijk, Rob and van Hoof, Chris, 2009, Harvesting energy from the motion of human limbs: the design and analysis of an impact-based piezoelectric generator. *Smart Mater. Struct.*. 2009. Vol. 18, no. 3, p. 035001. DOI 10.1088/0964-1726/18/3/035001. IOP Publishing
- Savelli, G., Coronel, P., Monfray, S. and Skotnicki, T. (2014). Systeme de conversion d'energie thermique en energie electrique. EP2732545 A1.
- Scheeper, P., van der Donk, A., Olthuis, W. and Bergveld, P. (1994). A review of silicon microphones. *Sensors and Actuators A: Physical*, 44(1), pp.1-11.
- Sebald, G., Lefeuvre, E. and Guyomar, D. (2008). Pyroelectric energy conversion: Optimization principles. *IEEE Transactions on Ultrasonics, Ferroelectrics and Frequency Control*, 55(3), pp.538-551.
- Sessler, G. (1998). *Electrets*. Morgan Hill, Calif.: Laplacian Press
- Sessler, G. and West, J. (1973). Electret transducers: a review. *The Journal of the Acoustical Society of America*, 53(6), p.1589.
- Suzuki, Y. (2011). Recent progress in MEMS electret generator for energy harvesting. *IEEEJ Transactions on Electrical and Electronic Engineering*, 6(2), pp.101-111.
- Tada, Y. (1992). Experimental Characteristics of Electret Generator, Using Polymer Film Electrets. *Jpn. J. Appl. Phys.*, 31(Part 1, No. 3), pp.846-851.

- Tao, K., Miao, J., Lye, S. and Hu, X. (2015). Sandwich-structured two-dimensional MEMS electret power generator for low-level ambient vibrational energy harvesting. *Sensors and Actuators A: Physical*, 228, pp.95-103.
- Thomson W. (1878) On the piezoelectric property of quartz. *Phil. Mag.* 5:4
- Tichy, J., Erhart J., Kittinger E., Privatska J. (2010). Fundamentals of piezoelectric sensorics. Berlin: Springer.
- Trioux, E., Monfray, S., Skotnicki, T., Muralt, P., Basrour, S. (2014). Fabrication of bilayer plate for a micro thermal energy harvester, in SENSORS, 2014 IEEE, pp.2171-2174, 2-5 Nov. 2014
- Tseng, W. and Dugundji, J. (1971). Nonlinear Vibrations of a Buckled Beam Under Harmonic Excitation. *Journal of Applied Mechanics*, 38(2), p.467.
- Tsujiura, Y., Suwa, E., Kurokawa, F., Hida, H. and Kanno, I. (2014). Reliability of vibration energy harvesters of metal-based PZT thin films. *J. Phys.: Conf. Ser.*, 557, p.012096.
- Tsutsumino, T., Suzuki, Y., Kasagi, N. and Sakane, Y. (n.d.). Seismic Power Generator Using High-Performance Polymer Electret. *19th IEEE International Conference on Micro Electro Mechanical Systems*.
- Umeda, Mikio, Nakamura, Kentaro and Ueha, Sadayuki, 1996, Analysis of the Transformation of Mechanical Impact Energy to Electric Energy Using Piezoelectric Vibrator. *Jpn. J. Appl. Phys.*. 1996. Vol. 35, no. Part 1, No. 5B, p. 3267-3273. DOI 10.1143/jjap.35.3267. Japan Society of Applied Physics
- Wieder, H. and Kaufman, S. (1953). Plastic electrets and their applications. *Electr. Eng.*, 72(6), pp.511-514.
- Xu-Sheng, W. (1993). Tertiary pyroelectric effect on thick ferroelectric crystal plates with partially uniform heating. *Ferroelectrics Letters Section*, 15(5-6), pp.159-165.
- Yang, B., Lee, C., Kotlanka, R., Xie, J. and Lim, S. (2010). A MEMS rotary comb mechanism for harvesting the kinetic energy of planar vibrations. *J. Micromech. Microeng.*, 20(6), p.065017.
- Zhu, D., Tudor, M. and Beeby, S. (2009). Strategies for increasing the operating frequency range of vibration energy harvesters: a review. *Measurement Science and Technology*, 21(2), p.022001.

Chapter 4

Theoretical performances of the energy harvester at the microscale

1 Introduction

The previous chapter proposed a demonstration of the operation of three types of thermal energy harvesters and the evaluation of their performances at the macroscopic scale. In this part we will focus on the evolution of these performances when the device is scaled down to the sub-millimetric scale and fabricated by conventional MEMS techniques. This chapter is divided in five parts. The first is devoted to the modeling of the bistable beams at the microscale, and the evaluation of the thermo-mechanical performances when reducing the size and when varying the type of beam clamp. The second and third parts explain the modeling of the pyroelectric generator and the electrostatic converter at the microscale. The fourth part synthesizes the various results obtained before and gives a description of the thermal transfers at the microscale.

2 Thermo-mechanical instability at the microscale

2.1. Equilibrium equation

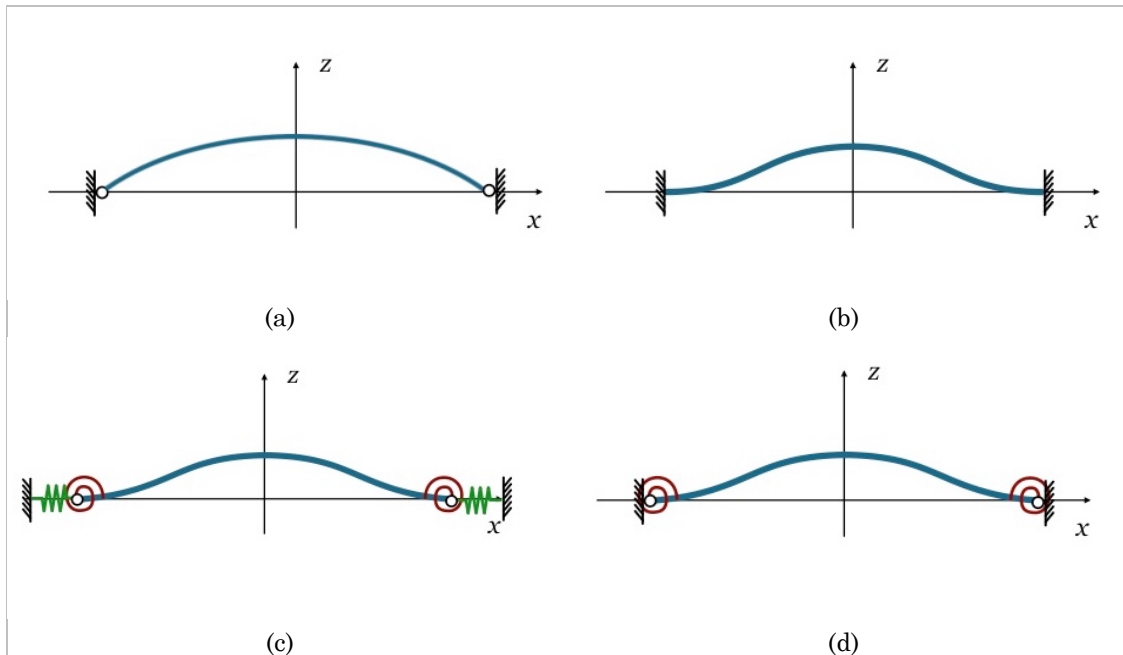
In Chapter 2 and Chapter 3, we assumed that, at the macroscale, the energy harvester was based on the use of pinned-pinned bimetallic beams instead of free bimetallic shells in order to obtain a simple description of the thermal snap-through. Since miniaturized beams are fabricated by the successive deposition of the material's layers, the beams' edges are generally assumed to be clamped to the wafer substrate. As a consequence, a

simple approach to model the behavior of beams would be to assume a perfect clamp of the beam's edges, meaning that no displacement or rotation of the edge are authorized. For instance, this type of boundary conditions suits the problem of the evaluation of the vibration frequencies of beams at the microscale. However, for problems involving the buckling of beams, the use of perfect clamp conditions leads to inadequacies between theoretical models and experimental data, for example in the case of Guckel structures used to locally determine the stress in thin films [Guckel *et al*, 1985, Fang and Wickert, 1996]. As a consequence, many works [Mullen *et al*, 1991, Meng *et al*, 1993, Kobrinski *et al*, 2000,] proposed to model micro-structures by using imperfect clamped conditions by means of finite torsional stiffness and compression stiffness at the beam's edges (see Fig.2.1.c). For example, [Alkharabsheh et Younis, 2013] compared the theoretical modeling of the dynamic snap-through of buckled beams with experimental data. In our model, we will only use finite torsional stiffness as in [Tung et al, 2013, Cabal and Ross, 2002]. As a recall, the strong formulation of the equilibrium projected on the axial displacement field u leads to the boundary equation (2.1.1a) and to the equilibrium equation (2.1.1b). Similarly, projected on the lateral displacement field w , it gives the equations (2.1.1c) and (2.1.1d).

$$[\mathcal{T}_{xx} \cdot du]_{\Omega} = 0 \tag{2.1.1a}$$

$$\int_0^t \mathcal{T}_{xx,x} \cdot dz = 0 \tag{2.1.1b}$$

Figure 2.1.1. Various types of boundary conditions: a. Pinned-pinned beam. b. Clamped-clamped beam. c. Imperfectly clamped beam with compression stiffness and torsional stiffness. d. Beam with torsional stiffness only.



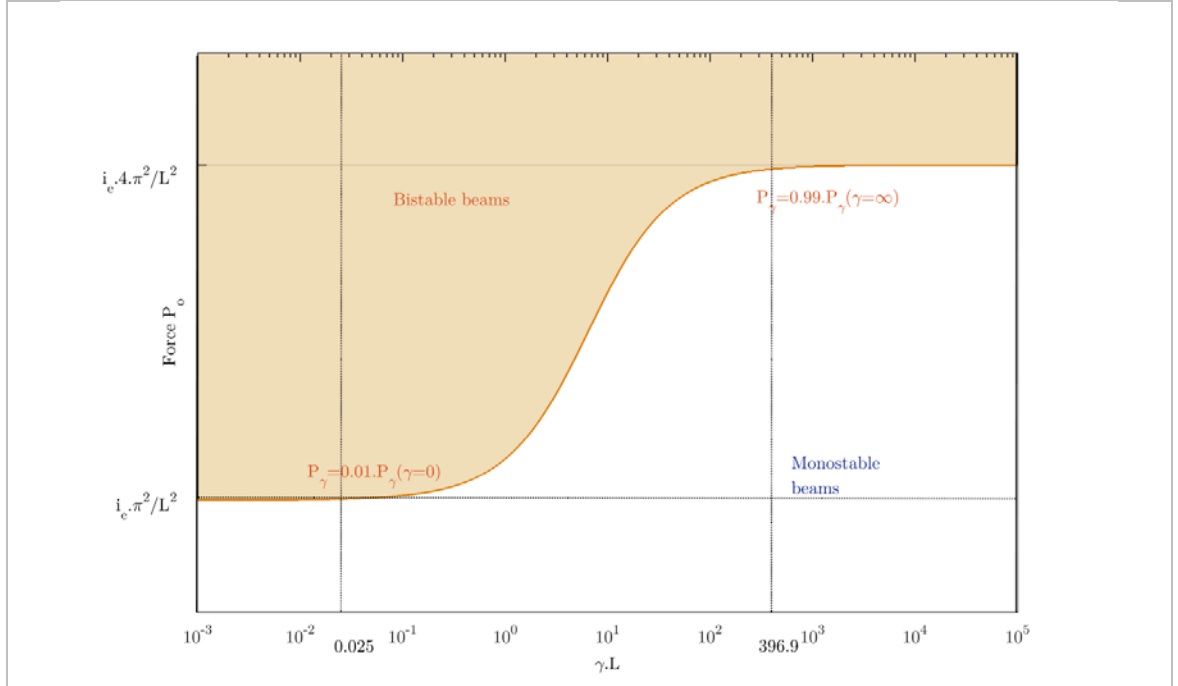


Figure 2.1.2. Evolution of the Euler load as a function of torsional stiffness.

$$\left[(\mathcal{T}_{xx} \cdot w_{,x} + z \cdot \mathcal{T}_{xx,x}) \cdot dw - z \cdot \mathcal{T}_{xx} \cdot dw_{,x} \right]_{\Omega} = 0 \quad (2.1.1c)$$

$$\int_0^t \left(\rho \cdot w_{,tt}^2 + (\mathcal{T}_{xx} \cdot w_{,x})_{,x} + z \cdot \mathcal{T}_{xx,xx} \right) \cdot dz = 0 \quad (2.1.1d)$$

These equations are verified if we define a torsional stiffness γ such that (2.1.2a) and (2.1.2b) are verified for w , and a compression stiffness κ_C such that (2.1.2c) is verified for u .

$$w_{,xx} \left(\frac{L}{2} \right) = -\gamma \cdot w_{,x} \left(\frac{L}{2} \right) - \frac{M_{\alpha} \cdot T - M_o}{I_e} \quad (2.1.2a)$$

$$w_{,xx} \left(-\frac{L}{2} \right) = \gamma \cdot w_{,x} \left(-\frac{L}{2} \right) - \frac{M_{\alpha} \cdot T - M_o}{I_e} \quad (2.1.2b)$$

$$i_e \cdot k^2 = \kappa_C \cdot u \left(\frac{L}{2} \right) = -\kappa_C \cdot u \left(-\frac{L}{2} \right) \quad (2.1.2c)$$

By following the same demarch as in the second chapter, we can demonstrate that the equilibrium is given by (2.1.3a). We can first see that the effect of the compression stiffness is equivalent to a reduction of the mean thermal asymmetry and the mean thermal stress, and the beam's axial stiffness. As a consequence, we can rewrite the equilibrium equation under the form (2.1.3b) by redefining the effective force P_o' by (2.1.3d).

$$N_e \cdot \frac{\lambda}{L} - N_\alpha \cdot \left(T - \frac{M_o}{M_\alpha} \right) + I_e \cdot k^2 \cdot \left(1 + \frac{2 \cdot N_e}{\kappa_C \cdot L} \right) = N_o = N_\alpha \cdot \frac{M_o}{M_\alpha} - F_o \quad (2.1.3a)$$

$$N_e' \cdot \frac{\lambda}{L} - N_\alpha' \cdot \left(T - \frac{M_o}{M_\alpha} \right) + I_e \cdot k^2 = N_o = N_\alpha' \cdot \frac{M_o}{M_\alpha} - F_o \quad (2.1.3b)$$

$$N_\alpha' = \frac{N_\alpha}{\left(1 + \frac{2 \cdot N_e}{\kappa_C \cdot L} \right)} ; N_e' = \frac{N_e}{\left(1 + \frac{2 \cdot N_e}{\kappa_C \cdot L} \right)} ; F_o' = \frac{F_o}{\left(1 + \frac{2 \cdot N_e}{\kappa_C \cdot L} \right)} \quad (2.1.3c)$$

$$N_o' = N_\alpha' \cdot \frac{M_o}{M_\alpha} - F_o' \quad (2.1.3d)$$

By using the boundary conditions, we can demonstrate that the beam shape can be written as the sum of symmetrical and asymmetrical functions (2.1.4a). The symmetrical function depends on the temperature and the residual stress asymmetry according to (2.1.4c) whereas the asymmetrical modes (2.1.4d) only appear when the wave vector k verifies (2.1.4e). For symmetrical buckling mode, the characteristic length λ verifies (2.1.4f)

$$w(x) = w_1(x) + w_2(x) \quad (2.1.4a)$$

$$w_1(x) = a \cdot \left(\cos(k \cdot x) - \cos\left(k \cdot \frac{L}{2}\right) \right) \quad (2.1.4b)$$

$$a = \frac{M_\alpha \cdot T - M_o}{I_e \cdot \left(k^2 \cdot \cos\left(\frac{k \cdot L}{2}\right) + \gamma \cdot k \cdot \sin\left(\frac{k \cdot L}{2}\right) \right)} \quad (2.1.4c)$$

$$w_2(x) = b \cdot \left(\sin(k \cdot x) - \frac{2}{L} \cdot \sin\left(\frac{k \cdot L}{2}\right) \right) \quad (2.1.4d)$$

$$\left(k^2 + 2 \cdot \frac{\gamma}{L} \right) \cdot \sin\left(\frac{k \cdot L}{2}\right) - \gamma \cdot k \cdot \cos\left(\frac{k \cdot L}{2}\right) = 0 \quad (2.1.4e)$$

$$\lambda = \frac{1}{4} \cdot (k^2 \cdot L - k \cdot \sin(k \cdot L)) \cdot a^2 \quad (2.1.4f)$$

Hence the criterion of bistability is given by (2.1.5a), showing that the force P_o must exceed the Euler load which depends on the torsional stiffness according to (2.1.5b). The equilibrium equation can finally be developed in (2.1.5c) as a function of k and a by using (2.1.4b) and (2.1.4c).

$$N_o' \geq I_e \cdot k_\gamma^2 \quad (2.1.5a)$$

$$k_\gamma \cdot \cos\left(\frac{k_\gamma \cdot L}{2}\right) + \gamma \cdot \sin\left(\frac{k_\gamma \cdot L}{2}\right) \quad (2.1.5b)$$

$$\frac{N_e'}{4 \cdot L} \cdot (k^2 \cdot L - k \cdot \sin(k \cdot L)) \cdot a^2 - \frac{N_\alpha' \cdot I_e}{M_\alpha} \cdot \left(k^2 \cdot \cos\left(\frac{k \cdot L}{2}\right) + \gamma \cdot k \cdot \sin\left(\frac{k \cdot L}{2}\right) \right) \cdot a + I_e \cdot k^2 = N_o' \quad (2.1.5c)$$

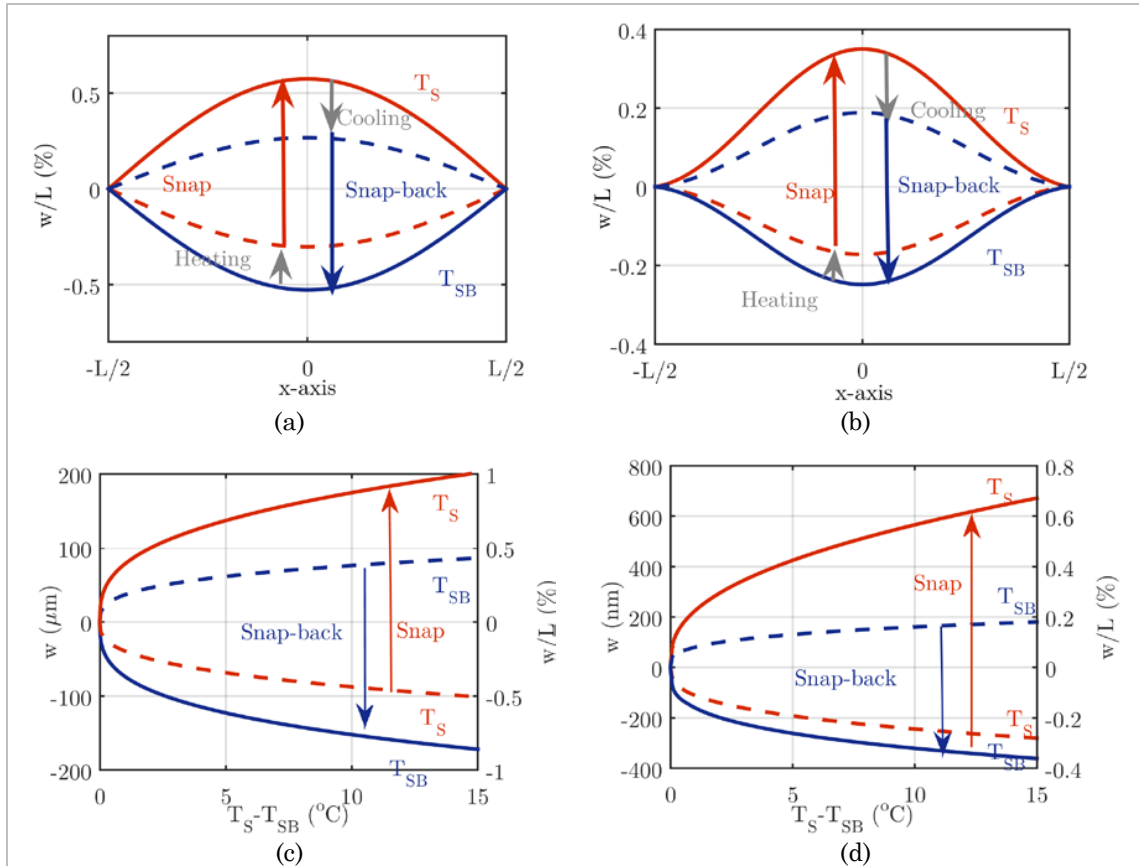


Figure 2.1.3. a. Shape of a pinned-pinned Al-Si beam with thermal hysteresis of 3°C. b. Shape of a clamped-clamped Al-Si beam with hysteresis of 3°C. c. Evolution of the beam amplitude of a macroscopic Al-Invar beam.

The evolution of the Euler load is plotted in Fig.2.2.1a as a function of the product $\gamma.L$, which is a non-dimensional number. When the torsional stiffness γ tends to infinity, the beam is double clamped and the Euler load is equal to 2π . When $\gamma = 0$, the beam is simply supported and $k_\gamma = \pi$. The observations made by [Fachin *et al*, 2011] are verified: γ does not need to be null or infinite for the beam to behave like a simply-supported beam or a double-clamped beam. If $\gamma.L = 36.7$, the beam's Euler load represents 90% of the Euler load of a perfectly clamped beam, and for $\gamma.L = 396.9$, the beam's Euler load reaches 99% of this limit value. This means that by choosing one of these values, we are able to describe the mechanical behavior of clamped beams but with the possibility to predict the effect of the residual stress asymmetry on the initial curvature of the beam. The torsional stiffness also determines the beam's shape, since the wavelength of is proportional to the square root of the Euler load. Fig.2.1.3a and Fig.2.1.3b represent two beams which snap and snap back at the same temperatures, one being simply supported and the other double clamped. The comparison of both figures reveals that the deflection of the clamped-clamped beam is about half the deflection of the simply-supported beam because the beam's edges cannot rotate because of the clamp's rigidity. In Fig.2.1.3c and Fig.2.1.3b we compare the evolution of the beam's deflection for a macroscopic Al-Invar beam (simply supported beam) and the deflection of a microscopic Al-Si beam. For 5 K hysteresis, the

beam's snap is associated with a displacement of 619 nm, representing 0.6% of the length of the beam. This value can be compared to the relative displacement of the Al-Invar beam (1%). This confirms the fact that the rigidity of the clamp limits the beam's displacement. These figures show that the reduction of the relative deflection of the beam at the microscale could be a problem for the electrostatic converter using the displacement of the beam to create a capacitance variation.

2.2. Thermo-mechanical performances of bimetallic strips

Now that we have established the equation giving the dependence of the beam's shape on the torsional stiffness, we can express the energy of the clamped beam. As the clamp is modeled by a torsional stiffness, it stores some energy due to the rotation of the beam's edges. As a consequence, the expression of the energy becomes (2.2.1a). Using the equation (2.1.4), it can be developed into (2.2.1b).

$$\mathcal{W}_M = \frac{N_e}{2.L} \cdot \lambda^2 + \frac{i_e}{2} \cdot \int_{-\frac{L}{2}}^{\frac{L}{2}} w_{,xx}^2 \cdot dx + (F_o - N_\alpha \cdot T) \cdot \lambda + (M_\alpha \cdot T - M_o) \cdot \int_{-\frac{L}{2}}^{\frac{L}{2}} w_{,xx} \cdot dx + \gamma \cdot k^2 \cdot \sin\left(\frac{k.L}{2}\right)^2 + \kappa_C \cdot (I_e \cdot k^2)^2 \quad (2.2.1a)$$

$$\mathcal{W}_M = \frac{N_e}{2.L} \cdot \lambda^2 + \left(I_e \cdot \left(k^2 - 2 \cdot \frac{k^3 \cdot \sin(k.L) + \gamma \cdot k^2 - \gamma \cdot k^2 \cdot \cos(k.L)}{k^2 \cdot L - k \cdot \sin(k.L)} \right) - N_\alpha \cdot T + F_o \right) \cdot \lambda + \kappa_C \cdot (I_e \cdot k^2)^2 \quad (2.2.1b)$$

From the expression of the beam's energy, we can deduce the expression of the beam's entropy by using the Maxwell relations. The beam's entropy is then given by (2.2.2).

$$S = C_v \cdot \ln(T + \theta_{ref}) + \left(4 \cdot I_e \cdot \frac{k^3 \cdot \sin(k.L) + \gamma \cdot k^2 - \gamma \cdot k^2 \cdot \cos(k.L)}{k^2 \cdot L - k \cdot \sin(k.L)} + N_\alpha \right) \cdot \lambda \quad (2.2.2)$$

As a consequence, we can plot the evolution of the total amount of energy released by the beam during its snap and snap-back (2.2.3b), as well as the efficiency of the transduction (2.2.3b) by calculating the amount of heat provided by the hot source to the beam (2.2.3c).

$$\Delta \mathcal{W}_M = \Delta \mathcal{K}(T_S) + \Delta \mathcal{K}(T_{SB}) \quad (2.2.2a)$$

$$\eta_M^{abs} = \frac{\Delta \mathcal{W}_M}{Q_H + \mathcal{L}_S} \quad (2.2.2b)$$

Table 2.2.1. a. Properties of the bimorph made of Al-Invar.

Dimensions (mm ³)	t _{Al} /t (1)	N _e (N)	I _e (N.m ²)	N _α (N.K ⁻¹)	M _α (N.m.K ⁻¹)	C _v (J.K ⁻¹)
20 x 2 x 1	0.2	2,59x10 ⁵	1.8x10 ⁻²	8,84 x10 ⁻¹	2.78x10 ⁻⁴	0.14

Table 2.2.1. b. Properties of the bimorph made of Al-Si.

Dimensions (μm ³)	t _{Al} /t (1)	N _e (N)	I _e (N.m ²)	N _α (N.K ⁻¹)	M _α (N.m.K ⁻¹)	C _v (J.K ⁻¹)
100 x 10 x 5	0.2	2,59x10 ⁵	1.8x10 ⁻²	8,84 x10 ⁻¹	2.78x10 ⁻⁴	0.14

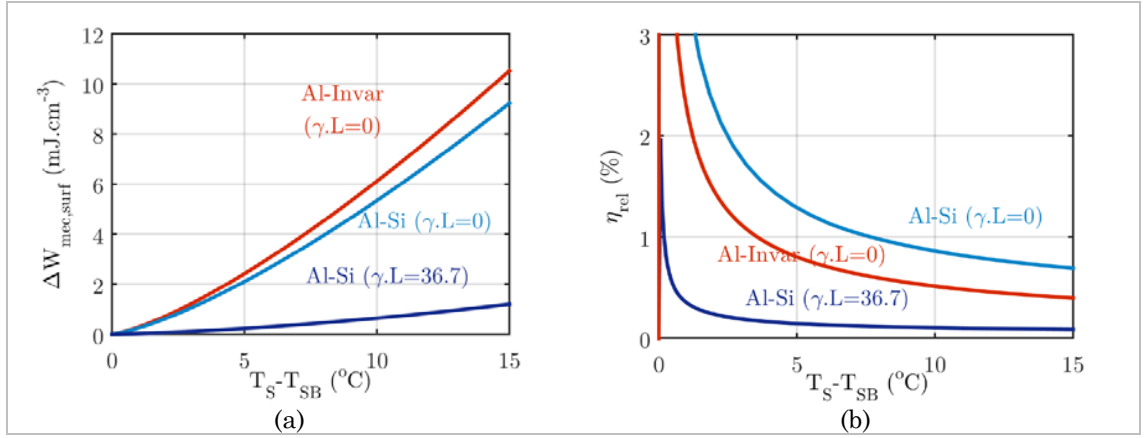


Figure 2.2.1. *a. Comparison of the density of energy produced by the three beams. c. Evolution of the Carnot efficiency of the thermo-mechanical transduction for each beam.*

$$Q_H + \mathcal{L}_S = \int_{T_{SB}, k_S^S}^{T_S, k_S^S} (T + \theta_{ref}) \cdot \mathcal{S}(k, T) \cdot dk \quad (2.2.2c)$$

The performances of the heat engine at the microscale and the macroscale are compared by taking the example of a macro-device using a 20 mm long Al-Invar simply-supported beam, and a micro-device using a 100 μm long Al-Si beam. The scaling factor of the length between these two devices is 200. Proportionally to the size of the beams, the properties are slightly different: the thermal asymmetries are similar but the bimorph Al-Si is lightly more rigid. The mean thermal expansion and heat capacity are higher for Al-Invar than for Al-Si. The experimental data reported in [Fachin *et al*, 2011] show that the boundary conditions are such that the Euler load of these beams often represents around 90% of the Euler load of a clamped-clamped beam. As a consequence, we assume a torsional stiffness verifying $\gamma.L = 36.7$ for our simulations.

The energy being an extensive parameter depending on the volume, in order to compare the energy produced by the macro- and microscopic bimetallic strips, we normalize the energy by the strip's volume to obtain adimensional data. Fig.2.2.1a shows that by clamping the beam to the substrate, the energy of the double-clamped Al-Si beam at the micro-scale is reduced by a factor of 8.6 compared to the simply-supported Al-Invar beam (1.2 mJ.cm⁻³ instead of 10.3 mJ.cm⁻³ for a thermal hysteresis of 15°C). Since the thermal efficiency and Carnot efficiency are dimensionless, we can directly compare energy harvesters at the macro-scale and at the micro-scale. As shown in Fig.2.2.1b, the heat engine's efficiency is strongly impacted by the boundary conditions. As the Al-Invar bimorph has a greater volume heat capacity than Al-Si (3.68 J.cm⁻³.K⁻¹ for Al-Invar and 1.64.J.cm⁻³.K⁻¹ for Al-Si), Al-Invar beams should be less efficient than Al-Si beams at converting heat into mechanical energy. Fig.2.2.1b shows that this is not the case: because of the rigidity of the clamp, for a hysteresis of 5°C, the efficiency of the double-clamped Al-Si beams is 6 times smaller than the efficiency of the simply-supported Al-Invar beams

(0.14% instead of 0.8%), and 9 times smaller than the simply-supported Al–Invar beams (1.3%).

2.3. Reduced-order model with the Galerkin method

a. Intrinsic performances

For both clamped-clamped and pinned-pinned beams, the use of the accurate model is quite complex if one wants to easily understand how physical parameters influence the performances and the mechanical behavior of bistable beams. A reduced-order model would enable to compute more quickly equilibrium equations, but also to couple more easily mechanical equations with piezoelectric or electrostatic equations in order to describe the performances of the complete heat engine. As the wave vector is close to the Euler load when the beam has a weak thermal hysteresis, we assume that the beam's shape at the equilibrium is given by (2.3.1a).

$$w_1(x) = w_1 \cdot \left(\cos(k_\gamma \cdot x) - \cos\left(k_\gamma \cdot \frac{L}{2}\right) \right) \quad (2.3.1a)$$

$$k_\gamma \cdot \cos\left(\frac{k_\gamma \cdot L}{2}\right) + \gamma \cdot \sin\left(\frac{k_\gamma \cdot L}{2}\right) = 0 \quad (2.3.1b)$$

As a consequence, the strain energy of the beam (2.2.1a) can be simplified into (2.3.2a), where the functions φ_1 and φ_2 are defined by (2.3.2b) and (2.3.2c). In the case of a simply supported beam ($\gamma \cdot L = 0$), the values of this coefficient are given by (2.3.2d), whereas for a clamped-clamped beam ($\gamma \cdot L = 36.7$), they are given by (2.3.2e).

$$\mathcal{W}_M = \frac{N_e}{32 \cdot L} \cdot \varphi_1^2 \cdot w_1^4 + (F_o - N_\alpha \cdot T + I_e \cdot k_\gamma^2) \cdot \frac{\varphi_1}{4} \cdot w_1^2 + 2 \cdot (M_o - M_\alpha \cdot T) \cdot \varphi_2 \cdot w_1 \quad (2.3.2a)$$

$$\varphi_1 = k_\gamma^2 \cdot L - k_\gamma \cdot \sin(k_\gamma \cdot L) \quad (2.3.2b)$$

$$\varphi_2 = k_\gamma \cdot \sin\left(\frac{k_\gamma \cdot L}{2}\right) \quad (2.3.2c)$$

$$\varphi_1(\gamma = 0) = \frac{\pi^2}{L} ; \varphi_2(\gamma = 0) = \frac{\pi}{L} ; \frac{\sqrt{\varphi_1 \cdot L}}{\varphi_2} = L ; \sqrt[3]{\frac{\varphi_2}{\varphi_1^2 \cdot L}} = \frac{1}{\pi} \quad (2.3.2d)$$

$$\varphi_1(\gamma = 0) = 3,79 \cdot \frac{\pi^2}{L} ; \varphi_2(\gamma = 0) = 0,3 \cdot \frac{\pi}{L} ; \frac{\sqrt{\varphi_1 \cdot L}}{\varphi_2} = 6,49 \cdot L ; \sqrt[3]{\frac{\varphi_2}{\varphi_1^2 \cdot L}} = \frac{0,28}{\pi} \quad (2.3.2e)$$

Again, we make the assumption that the thermal hysteresis is smaller than the difference between the average values of the snap and snap-back temperatures, so that the effect of the mean thermal expansion vanishes. The equilibrium equation is obtained by looking for the extrema of the energy, leading to (2.3.3a). The stability of the equilibrium is then given by (2.3.3b).

$$\frac{d\mathcal{W}_i}{dw_1} = \frac{N_e}{8 \cdot L} \cdot \varphi_1^2 \cdot w_1^3 + (I_e \cdot k_\gamma^2 - P_o) \cdot \frac{\varphi_1}{2} \cdot w_1 + 2 \cdot (M_o - M_\alpha \cdot T) \cdot \varphi_2 = 0 \quad (2.3.3a)$$

$$\frac{d^2 \mathcal{W}_i}{dw_1^2} = \frac{3 \cdot N_e}{8 \cdot L} \cdot \varphi_1^2 \cdot w_1^2 + (I_e \cdot k_\gamma^2 - N_o) \cdot \frac{\varphi_1}{2} \quad (2.3.3b)$$

Hence, as for simply-supported beams, we can express the critical amplitude of snap (2.3.4a) and the beam's thermal hysteresis (2.3.4b) as functions of the force P_o and the Euler load. Using the values given by (2.3.2d) and (2.3.2e), we can see that the thermal hysteresis of a doubly clamped beam is more sensitive to the residual stress than a simply supported beam but the displacement induced by the bistability is smaller. The initial deflection is given by (2.3.3d). The value of φ_3 is given by (2.3.3e) for the two boundary conditions.

$$w_S^C = - \sqrt{\frac{4 \cdot L \cdot (N_o - I_e \cdot k_\gamma^2)}{3 \cdot n_e \cdot \varphi_1}} \quad (2.3.3a)$$

$$\Delta T = 2 \cdot \frac{\sqrt{\varphi_1 \cdot L}}{\varphi_2} \cdot \frac{1}{M_\alpha} \cdot \sqrt{\frac{(N_o - I_e \cdot k_\gamma^2)^3}{27 \cdot N_e}} \quad (2.3.3b)$$

$$w_S^C = - \sqrt[3]{\frac{\varphi_2}{\varphi_1^2 \cdot L}} \cdot \sqrt[3]{4 \cdot \frac{M_\alpha \cdot L^2}{N_e} \cdot \Delta T} \quad (2.3.3c)$$

$$w_o = \left(1 - \cos\left(k_\gamma \cdot \frac{L}{2}\right)\right) \cdot w_1 = \varphi_3 \cdot w_1 \quad (2.3.3d)$$

$$SS : \varphi_3 = 1 ; CC : \varphi_3 = 1,99 \quad (2.3.3e)$$

The performances of the bimetallic strip can also be rewritten. The sum of the kinetic energy of snap and the kinetic energy of snap-back is given by (2.3.4a). Equation (2.3.4b) gives the value of the adimensionnal number depending on the boundary conditions. This shows that the energy produced by a clamped-clamped beam corresponds to 8.3% of the energy provided by a simply-supported beam, agreeing with the observation made in Section 2.2. The correcting factor also appears in the expression of the thermo-mechanical efficiency and the Carnot efficiency of the thermodynamic cycle (2.3.4c). Finally the maximal force generated by the beam when it switches is given by (2.3.4e).

$$\Delta \mathcal{W}_M = \sqrt[3]{\frac{\varphi_2^4 \cdot L^2}{\varphi_1^2}} \cdot 27 \cdot \sqrt[3]{\frac{(M_\alpha \cdot \Delta T)^4}{16 \cdot N_e \cdot L}} \quad (2.3.4a)$$

$$SS : \sqrt[3]{\frac{\varphi_2^4 \cdot L^2}{\varphi_1^2}} = 1 ; CC : \sqrt[3]{\frac{\varphi_2^4 \cdot L^2}{\varphi_1^2}} = 0.083 \quad (2.3.4b)$$

$$\eta_{TM}^{abs} = \sqrt[3]{\frac{\varphi_2^4 \cdot L^2}{\varphi_1^2}} \cdot 27 \cdot \sqrt[3]{\frac{M_\alpha^4 \cdot \Delta T}{16 \cdot N_e \cdot C_v^3 \cdot L}} \quad (2.3.4c)$$

$$\eta_{TM}^{rel} = \sqrt[3]{\frac{\varphi_2^4 \cdot L^2}{\varphi_1^2}} \cdot 27 \cdot \sqrt[3]{\frac{M_\alpha^4}{16 \cdot N_e \cdot C_v^3 \cdot L}} \cdot \frac{T_o + \theta_{ref}}{\sqrt[3]{\Delta T^2}} \quad (2.3.4d)$$

$$F_{max} = 2 \cdot \varphi_2 \cdot m_\alpha \cdot \Delta T \quad (2.3.4e)$$

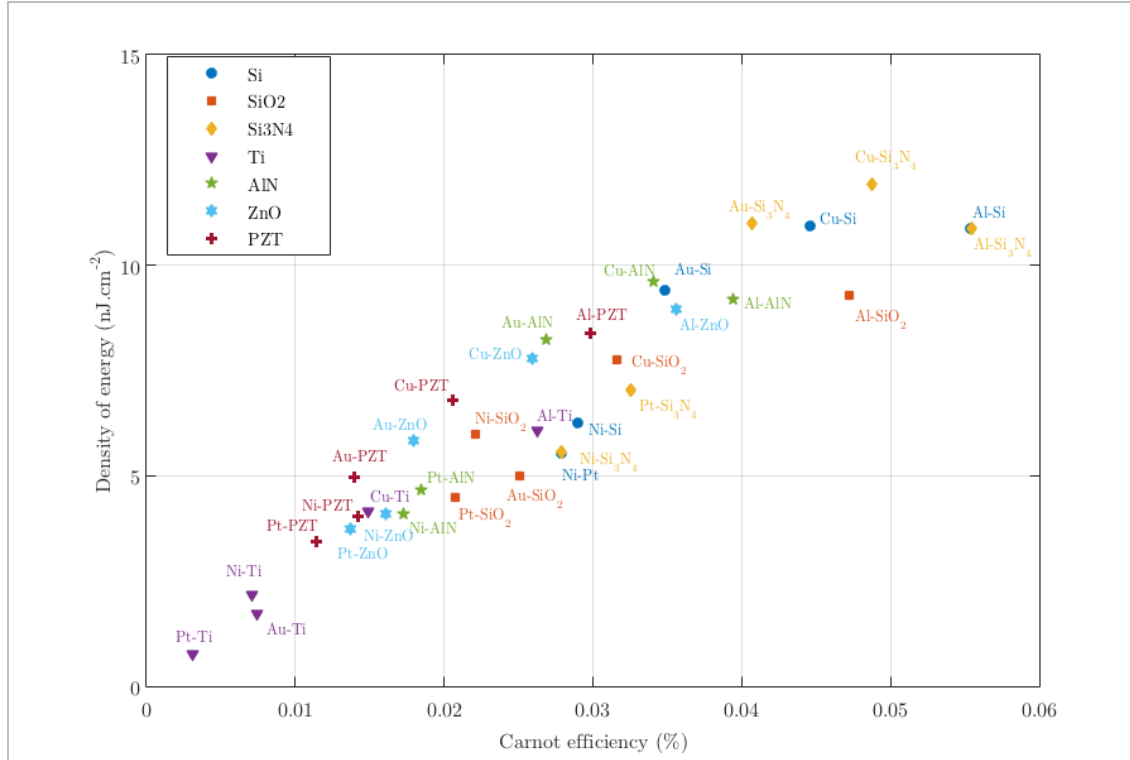


Figure 2.3.1. Evolution of the Euler load as a function of torsional stiffness.

Beside the complexity of the energy harvester using the shock between the bimetallic strip heat engine and a piezoelectric transducer, the decrease of the efficiency of the thermo-mechanical conversion, and the decrease of the force and the increase of the stiffness of clamped-clamped beams enables to discard this type of architecture for the MEMS integration of the heat engine.

b. Extrinsic performances

The results presented in Chapter 2 can be directly adapted to the use of the torsional stiffness, just by taking into account that the crucial parameter is the initial deflection of the beam and not its amplitude. The cavity's thickness ratio r_w must be defined by (2.3.5a) so that the equations are not changed. As a reminder, the thermal hysteresis in the cavity is given by (2.3.5a), the mechanical energy by (2.3.5c) and the efficiency by (2.3.5d).

$$w_{bot} = \varphi_3 \cdot w'_{bot} = \varphi_3 \cdot r_w \cdot w_S^c \quad (2.3.5a)$$

$$\Delta T_{cav} = \frac{3}{2} \cdot \left(r_w - \frac{r_w^3}{3} \right) \cdot \Delta T \quad (2.3.5b)$$

$$\Delta \mathcal{W}_{M,cav} = \frac{8}{9} \cdot \left(r_w^2 - \frac{r_w^4}{3} \right) \cdot \Delta \mathcal{W}_M \quad (2.3.5c)$$

$$\eta_{TM}^{abs,cav} = 4 \cdot r_w \cdot \sqrt[3]{\frac{\varphi_2^4 \cdot L^2}{\varphi_1^2}} \cdot \sqrt[3]{\frac{4 \cdot M_\alpha^4}{N_e \cdot L \cdot C_v^3}} \cdot \Delta T = \frac{16}{27} \cdot r_w \cdot \eta_{TM}^{abs} \quad (2.3.5d)$$

c. Performances of the materials used in microelectronics

To complete the thermo-mechanical description of the bimetallic strip, we use (2.3.4a) and (2.3.4d) to compare the performances of some couples of materials that are available in microelectronics (Si, SiO₂, Si₃N₄, Ti, AlN, ZnO, PZT, Al, Cu, Ni, Au and Pt). We choose a reference bimetal thermostat having a length of 400 μm, a total thickness of 4 μm (2 μm + 2 μm) and a 3 K thermal hysteresis (98,5°C-101,5°C). The evolution of the Carnot efficiency against the surface density of energy for these couples is represented in Fig.2.3.1. This figure shows that the most efficient couples are Al-Si and Al-Si₃N₄ with an efficiency of 0.056% of Carnot for an energy density of 11 nJ.cm⁻², followed by Cu-Si₃N₄ and Al-SiO₂. The couples using Ti as a passive layer are the least efficient since Ti has a large coefficient of thermal expansion. If we look at the performances of piezoelectric materials, we can see that the best couples are Al-PZT and Al-AlN.

d. Impact of the variability of the residual stress on the performances of the bistable beams

The reduced order model also enables to study how the variability of the residual stress can impact the behavior of the bistable beams. As demonstrated by [Orthwein, 1984], bistable systems are very sensitive to the variability of manufacturing process. Variability of residual stress in thin films could have many origins: variability between wafers, variability of stress along the wafer surface, variability of stress through the thickness of the deposited thin films etc.

For thermally bistable beams, the impact of the residual stress variability is especially visible on the evolution of the snap and snap-back temperatures. In the case of a bimorph beam, if we only consider local variations of the stress, by using (2.3.3b), we can simply write the dispersion of the thermal hysteresis (2.3.6a) and the dispersion of the mean temperature of the hysteresis (2.3.6b) as a function of the variabilities of the stress in both layers, (simplified expression when both layer have the same thickness and Young modulus).

$$\langle \sigma_{\Delta T} \rangle = \frac{3 \cdot v \cdot t \cdot \Delta T}{(p_o - i_e \cdot k_\gamma^2)} \cdot \frac{\alpha_2 + \alpha_1}{\alpha_2 - \alpha_1} \cdot \langle \sigma_o \rangle \quad (2.3.6a)$$

$$\langle \sigma_{T_o} \rangle = \frac{2 \cdot T_o}{\alpha_2 - \alpha_1} \cdot \langle \sigma_o \rangle \quad (2.3.6b)$$

The formulae show that the impact of the residual stress variability is all the more important when the difference in thermal expansion coefficients is small, the residual stress force is large, and when the beam is clamped-clamped (sensitivity enhanced by a factor 6). To illustrate this, we consider the impact of the variability of the residual stress in the Aluminum layer of a SiO₂-Al bimorph beam of dimensions 200 x 50 x (2+2) μm³, assuming a initial tensile stress of 100 MPa in Al. Around the value of -80 MPa, with a deviation of 2 MPa, we can observe that some beams are monostable whereas others have thermal hysteresis greater than 30 K. The variability is worse when the residual stress variability increases (see Fig.2.3.3b). Fig.2.3.3c represents the evolution of the standard deviation of the thermal hysteresis as a function of the mean thermal hysteresis as predicted by (2.3.6a).

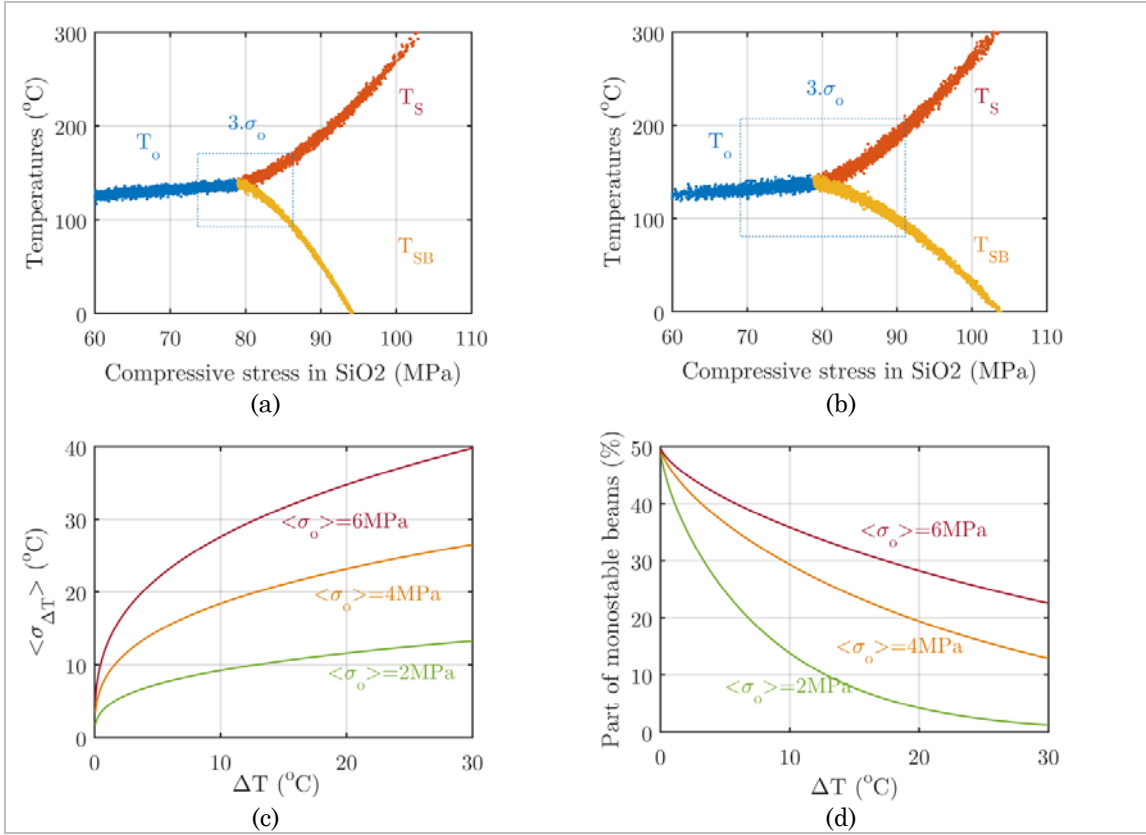


Figure 2.3.3. a. Dispersion of the snap and snap-back temperatures for an Al-SiO₂ clamped-clamped beam assuming a deviation of 2 MPa. b. Dispersions of the temperatures assuming a deviation of 4 MPa. c. Evolution of the standard deviation of the thermal hysteresis as a function of the mean value of the thermal hysteresis and for various deviations of the residual stress. d. Part of monostable beams linked to the variability of residual stress.

Assuming that the variability of the stress follows a Gaussian distribution, we can simply give an expression of the beams that are monostable due to the residual stress dispersion. Its evolution as a function of the thermal hysteresis is represented in Fig.3.3.2d. For example for a targeted hysteresis value of 3°C, 30% of the beams cannot harvest heat if the stress deviation is of 2 MPa and 40% for a deviation of 4 MPa. A similar study would have to be done to determine the part of bistable beams that would not work because their snap and snap-back temperatures are not framed by the heat sources' temperature.

$$\%_{monostable} = 50. \left(\operatorname{erf} \left(\frac{\Delta T}{\langle \sigma_{\Delta T} \rangle \cdot \sqrt{2}} \right) + 1 \right) \quad (2.3.6a)$$

3 Pyroelectric coupling

3.1. Equations of the piezoelectricity

In this part we assume that the bistable beam is either a bimorph beam whose passive layer is piezoelectric, or is made of a stack of materials that is already bistable and onto

which we deposit a piezoelectric layer. From the point of view of the modeling, there is no difference between the two cases. We only assume that the piezoelectric layer is directly deposited on a metallic layer so that the capacity is that of the piezoelectric layer only. The beam being clamped, we will consider two configurations represented on Fig.3.1.1a: in the first case, the piezoelectric layer is connected to a single electrode. In the second case, the piezoelectric layer is sandwiched between three electrodes, which positions are defined by the positions of the nodes delimitating areas of compressive and tensile stress. . In order to establish the equations describing the tertiary pyroelectric effect inside clamped-clamped beam, we come back to the expression of the electric displacement of the piezoelectric layer. In the case of a clamped-clamped beam, the strain tensor is given by (3.3.1b).

$$dD_3 = p_3^s \cdot d\theta + e_{31} \cdot dS_1 + \epsilon_{33}^s \cdot dE_3 \quad (3.1.1a)$$

$$dS_1 = \frac{d\lambda}{L} + (z - z_o) \cdot k_\gamma^2 \cdot \cos(k_\gamma \cdot x) \cdot dw_1 \quad (3.1.1b)$$

By integrating this equation, we obtain equation (3.1.2a) when a single piezoelectric capacitor is used, and (3.1.2b) when three piezoelectric capacitors are used and have a common electrode. The comparison of both equations shows that by using an architecture with three electrodes, the electrical charges created by the primary pyroelectric effect cannot be harvested. In the other case, by using a single electrode, the electrical charges stored in the piezoelectric capacitor are mainly those due to the primary pyroelectric effect and to clamp thrust, and weakly to the curvature of the beam because the term φ_2 is small for clamped-clamped beams.

$$dQ_e = C_p \left(-dV_p + \frac{t_p \cdot p_3^s}{\epsilon_{33}^s} \cdot d\theta + \frac{t_p \cdot e_{31}}{\epsilon_{33}^s \cdot L} \cdot \left(\frac{1}{2 \cdot L} \cdot \varphi_1 \cdot w_1 + 2 \cdot (z_p - z_o) \cdot \varphi_2 \right) \cdot dw_1 \right) \quad (3.1.2a)$$

$$dQ_e = C_p \left(-dV_p + 2 \cdot \frac{t_p \cdot e_{31}}{\epsilon_{33}^s \cdot L} \cdot (z_p - z_o) \cdot (2 \cdot k_\gamma - \varphi_2) \cdot dw_1 \right) \quad (3.1.2b)$$

3.2. Performances of the Stirling cycle

In this part as in the previous chapter, we neglect the effect of the piezoelectric coupling on the thermo-mechanical behavior of the bistable beam. Without detailing the operation of the Stirling cycle (already presented in the previous chapter), we give the expression of the maximal output voltage generated when the pyroelectric bistable beam is heated and snaps in open-circuit then is discharged once it has snapped (Fig.3.1.1b). If the pyroelectric bistable beam is polarized by a single plane electrode, the maximal output voltage is given by (3.2.1a). Hence we can give the expression of the electrical energy generated by the energy harvester (3.2.1b).

$$V_{le} = \left| \frac{t_p \cdot p_3^s}{\epsilon_{33}^s} \cdot \Delta T - 8 \cdot \frac{t_p \cdot e_{31}}{L \cdot \epsilon_{33}^s} \cdot \varphi_2 \cdot (z_p - z_o) \cdot w_S^c \right| \quad (3.2.1a)$$

$$W_{le} = C_p \cdot V_{le}^2 = C_p \cdot \left(\frac{t_p \cdot p_3^s}{\epsilon_{33}^s} \cdot \Delta T - 8 \cdot \frac{\pi \cdot t_p \cdot e_{31}}{L \cdot \epsilon_{33}^s} \cdot \varphi_2 \cdot (z_p - z_o) \cdot w_S^c \right)^2 \quad (3.2.1b)$$

In the case of the pyroelectric beam with three electrodes, the maximal output voltage is given by (3.2.2a), leading to the electrical energy (3.2.2b).

$$V_{IIIe} = \left| 8 \cdot \frac{t_p \cdot e_{31}}{L \cdot \varepsilon_{33}^s} \cdot (2 \cdot k_\gamma - \varphi_2) \cdot (z_p - z_o) \cdot w_s^c \right| \quad (3.2.2a)$$

$$\mathcal{W}_{IIIe} = C_p \cdot V_{IIIe}^2 = C_p \cdot \left(8 \cdot \frac{t_p \cdot e_{31}}{L \cdot \varepsilon_{33}^s} \cdot (2 \cdot k_\gamma - \varphi_2) \cdot (z_p - z_o) \cdot w_s^c \right)^2 \quad (3.2.2b)$$

Following the same approach as in the previous chapter, we define the figures of Merit for the electrical energy and the efficiency of the thermo-electrical transduction, as functions of the performances of a pyroelectric generator. For the device with three electrodes, they can be expressed as a function of the electromechanical coupling factor k_{31}^2 .

$$FOM_W^{Ie} = FOM_W^{pyro} \cdot \left(1 + 8^{\frac{3}{2}} \sqrt{4} \cdot \frac{z_p - z_o}{L} \cdot \frac{e_{31}}{p_3^s} \cdot \sqrt[3]{\frac{\varphi_2^4 \cdot L}{\varphi_1^2}} \cdot \sqrt[3]{\frac{M_\alpha}{N_e}} \cdot \frac{1}{\sqrt[3]{\Delta T^2}} \right)^2 \quad (3.2.3a)$$

$$k_{Ie}^2 = k_{pyro}^2 \cdot \frac{t_p \cdot \rho_{pyro} \cdot C_{pyro}}{t \cdot \rho_b \cdot C_b} \cdot \left(1 + 8^{\frac{3}{2}} \sqrt{4} \cdot \frac{z_p - z_o}{L} \cdot \frac{e_{31}}{p_3^s} \cdot \sqrt[3]{\frac{\varphi_2^4 \cdot L}{\varphi_1^2}} \cdot \sqrt[3]{\frac{M_\alpha}{N_e}} \cdot \frac{1}{\sqrt[3]{\Delta T^2}} \right)^2 \quad (3.2.3b)$$

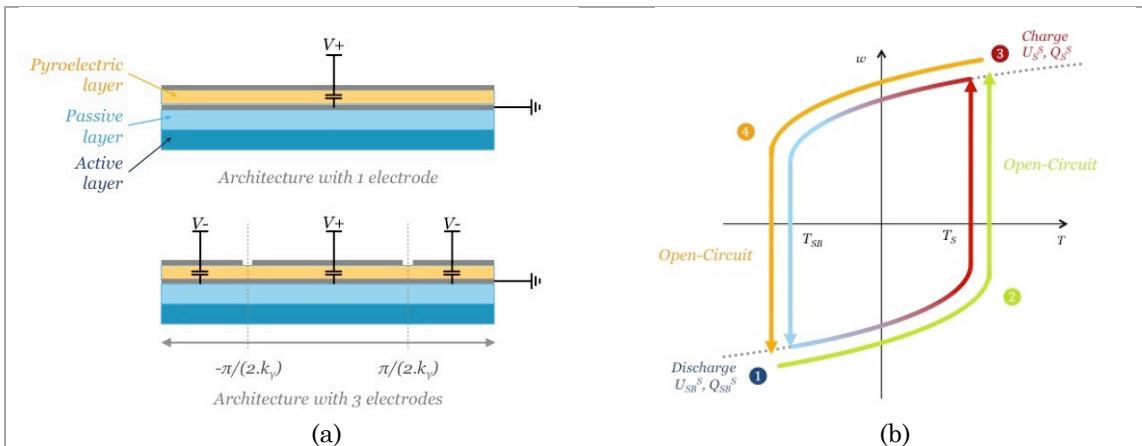
$$FOM_W^{IIIe} = k_{31}^2 \cdot \left(8^{\frac{3}{2}} \sqrt{4} \cdot \frac{z_p - z_o}{L} \cdot \sqrt[3]{\frac{\varphi_2 \cdot (2 \cdot k_\gamma - \varphi_2)^3 L}{\varphi_1^2}} \cdot \sqrt[3]{\frac{M_\alpha}{N_e}} \cdot \frac{1}{\sqrt[3]{\Delta T^2}} \right)^2 \quad (3.2.3c)$$

$$k_{IIIe}^2 = L \cdot v \cdot t_p \cdot \frac{k_{31}^2}{C_v} \cdot \left(8^{\frac{3}{2}} \sqrt{4} \cdot \frac{z_p - z_o}{L} \cdot \sqrt[3]{\frac{\varphi_2 \cdot (2 \cdot k_\gamma - \varphi_2)^3 L}{\varphi_1^2}} \cdot \sqrt[3]{\frac{M_\alpha}{N_e}} \cdot \frac{1}{\sqrt[3]{\Delta T^2}} \right)^2 \quad (3.2.3d)$$

Table 3.2.1. Properties of the bistable beam made of Al-Si and PZT-5H.

Dimensions (μm^3)	N_e (N)	I_e (N.m ²)	N_α (N.K ⁻¹)	M_α (N.m.K ⁻¹)	z_p (μm)
400 x 100 x (2+2+2)	64,3	1,26.10 ⁻¹⁰	4,60.10 ⁻³	5,49.10 ⁻¹⁰	1

Figure 3.1.1. a. Schematics of the pyroelectric bistable beam with a single electrode and three electrodes. b. Stirling cycle implemented with the beam at the microscale.



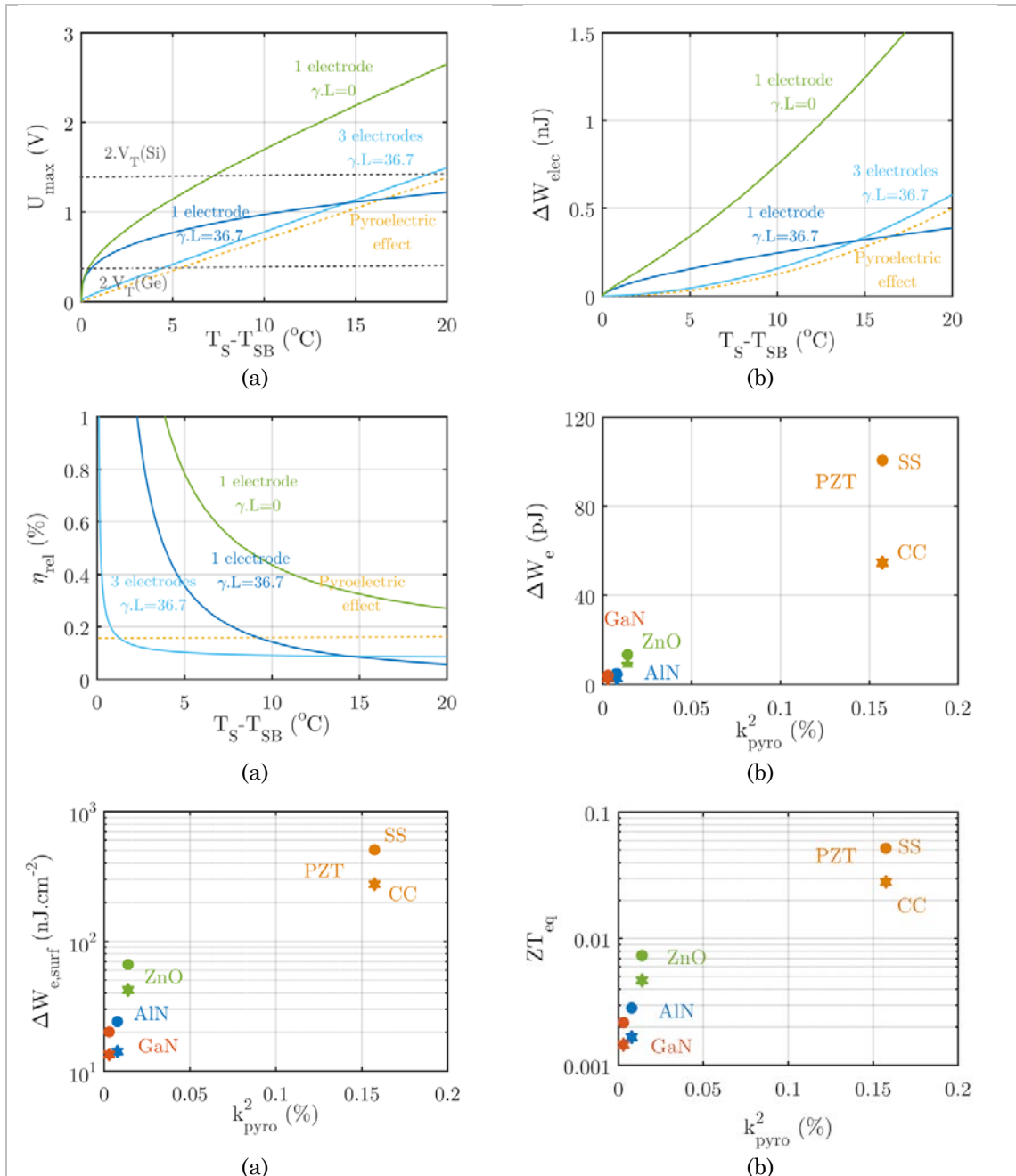


Figure 3.2.1. a. Evolution of the output voltage of an Al-Si-PZT beam. b. Evolution of the electrical energy produced by an Al-Si-PZT beam as a function of its thermal hysteresis. c. Carnot efficiency as a function of the thermal hysteresis. d. Available electrical energy as a function of the piezoelectric material deposited on the beam. e. Surface density of electrical energy. f. Equivalent ZT of the piezoelectric materials.

In order to quantify the performances of the pyroelectric bimetallic strip heat engine at the microscale, we take the example of a bistable Al-SiO₂-PZT beam (length 400 μ m,

width 100 μm) where each layer has a thickness of 2 μm . We assume that the PZT layer is sandwiched between two very thin metallic layers not taken into account in the model. The properties of the beam are given in Table 3.2.1. Fig. 3.2.1a plots the evolution of the output voltage of the device when the beam is clamped and when the two configurations of electrodes are used. They are then compared to the output voltage of a simple pyroelectric generator and to the output voltage of a simply-supported beam. With a thermal hysteresis of 5°C, the simply-supported beam is more effective than the clamped-clamped beam, generating voltages of around 1.1 V. For a clamped beam with 3 electrodes, the output voltage is of 0.77 V and of 0.41 V for the clamped beam with a single electrode, similar to the output voltage of the pyroelectric generator. These values can be compared with twice the value of the threshold voltage of silicon and germanium diodes: Below 5°C, it is difficult to reach the voltage imposed by the use of germanium diode bridges diodes. This limitation must be taken into account when designing the system since it imposes a minimum size for the bistable beams. Fig. 3.2.1b and Fig. 3.2.1c respectively represent the evolution of the electrical energy produced per cycle, and the Carnot efficiency associated to the thermal cycling of the pyroelectric bistable beam. As observed previously, clamped-clamped beams generate less energy than pinned-pinned beams, and for small thermal hysteresis, preference should be given to the architecture with three electrodes: for a thermal hysteresis of 5°C, the clamped-clamped beam with three electrodes produces 150 pJ of energy with a Carnot efficiency of 0.35%, whereas the beam with a single electrode produces 43 pJ with an efficiency of 0.1%.

To finish, we compare the performances of various pyroelectric bistable beams made of Al-Si when PZT is replaced by another piezoelectric material (hysteresis of 3°C). Fig. 3.2.1d shows that PZT is the most efficient material, with a density of energy of 273 $\text{nJ}\cdot\text{cm}^{-2}$ and an equivalent ZT of 0.03. To compare, AlN-based bistable beams produce 14 pJ of energy per cycle, corresponding to a surface density of 14 $\text{nJ}\cdot\text{cm}^{-2}$ for an equivalent ZT of 0.0017. These values of the surface density of electrical energy can be compared with the values reported in [Trioux, 2015], showing that during the snap, densities of 43 $\text{pJ}\cdot\text{cm}^{-2}$ can be obtained with 1.4 mm long AlN bistable beams. The difference can be partly attributed to the fact that there was no attempt to implement a Stirling cycle to maximize the energy harvested.

3.3. Dynamic behavior of the bimetallic strip at the microscale

a. Scaling law on the operation frequency

In Chapter 2, we modeled two types of thermal transfers. In the first case, the limiting mode of transfer is linked to the thermal contact between the heat sources and the prime mover. In that case, the device's operation frequency is given by (3.3.1a), where hc is the equivalent coefficient of thermal exchange associated to the thermal contact. The second mode of heat transfer assumes that the contact between the heat sources and the bistable beam is perfect and that the operation frequency of the device is associated to the propagation of heat in the beam, leading to (3.3.1b). Thus, at any time, we can consider

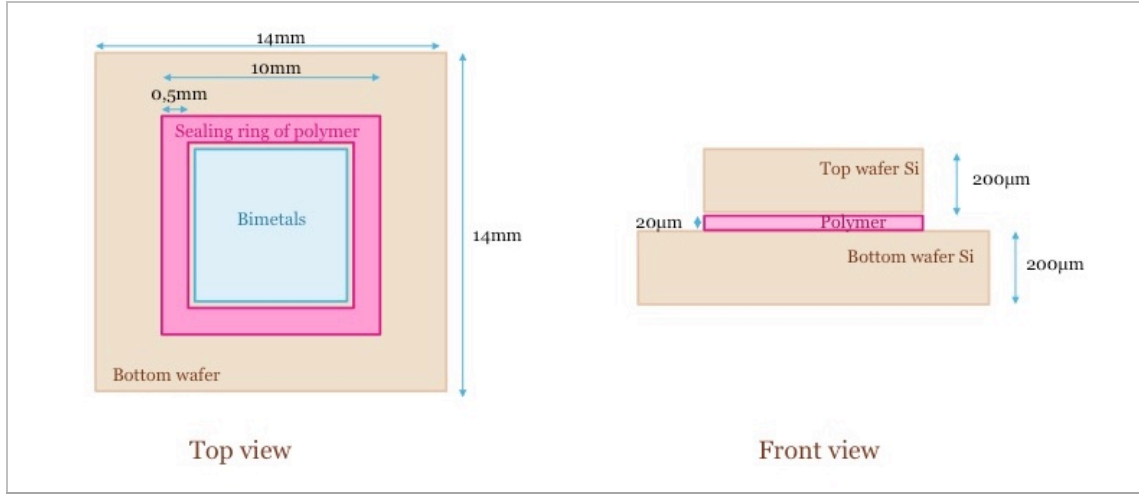


Figure 3.3.1. Simplified representation of the energy harvester at the microscale.

that the operation frequency of the device is given by (3.3.1c). The key hypothesis of the scaling law developed in [Puscasu et al, 2012; Puscasu et al, 2014], is that the operation frequency of the heat engine is associated to the thermal transfers in the beam. However, we showed in Chapter 2 that the characteristic time associated to the beam's thermal diffusivity is very small and the operation frequency of the device is limited by the thermal contact between the heat sources and the bistable beam (3.3.1c). The dimensional analysis of both frequencies shows that, if the temperature difference in the cavity is kept constant despite the reduction of the cavity's thickness at the microscale, the frequency associated to first type of thermal transfer is inversely proportional to the characteristic length of the system (3.3.1d), whereas the frequency of the second type of thermal transfer is inversely proportional to the square of the length (3.3.1e). As a consequence, even at the microscale, the limiting mode of thermal transfer remains associated to the thermal contact between the heat sources and the bistable beam.

$$f_1 = \frac{h_c \cdot L \cdot v}{C_v} \cdot \frac{1}{\ln\left(\frac{T_S - T_C}{T_{SB} - T_C}\right) + \ln\left(\frac{T_H - T_{SB}}{T_H - T_S}\right)} \quad (3.3.1a)$$

$$f_2 = \frac{\pi^2 \cdot \kappa_b}{2 \cdot L^2} \cdot \frac{1}{\ln\left(\frac{T_S - T_C}{T_{SB} - T_C}\right) + \ln\left(\frac{T_H - T_{SB}}{T_H - T_S}\right)} \quad (3.3.1b)$$

$$f = \frac{f_1 \cdot f_2}{f_1 + f_2} = f_1 = \frac{h_c \cdot L \cdot v}{C_v} \cdot \frac{1}{\ln\left(\frac{T_S - T_C}{T_{SB} - T_C}\right) + \ln\left(\frac{T_H - T_{SB}}{T_H - T_S}\right)} \quad (3.3.1c)$$

$$f_1 \propto \frac{1}{L} \quad (3.3.1d)$$

$$f_2 \propto \frac{1}{L^2} \quad (3.3.1e)$$

For the rest of this section, we choose $h_c = 2500 \text{ W}\cdot\text{m}^{-2}\cdot\text{K}^{-1}$ corresponding to a metallic contact resistance of $10 \text{ K}\cdot\text{W}^{-1}$ at the macroscale, as we found in Chapter 2.

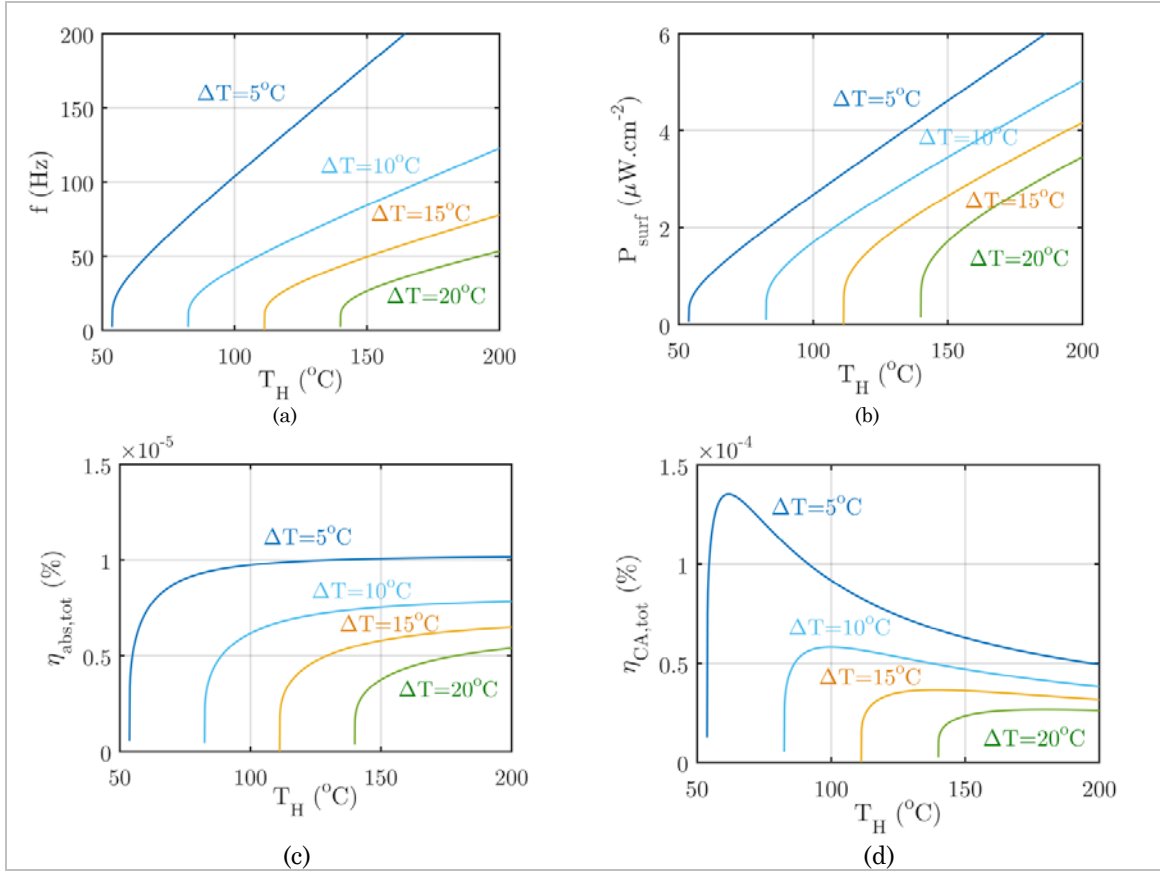


Figure 3.3.2. a. Evolution of the operation frequency of some Al-Si-PZT bistable beams as a function of external conditions. b. Output power of the energy harvester vs hot source temperature. c. Thermal efficiency of the device. d. Curzon-Ahlborn efficiency of the device.

b. Simplified model of the harvester at the microscale

In order to see the evolution of temperature in the cavity as a function of external conditions, we define a reference architecture presented in Fig.3.3.2. In this simple configuration, the harvester is made of two bonded wafers, separated by a polymer resist ring used to maintain the cavity under vacuum but also to limit the thermal transfers between the bottom wafer used as a hot source and the top wafer used as a plane heat sink, or on which it is possible to put a heat sink with fan. This system can be simply modeled as two series thermal resistances since the thermal resistance of the silicon wafers is negligible. The thermal gradient in the cavity is then given by (3.3.3a).

$$T_H - T_C = \frac{R_{\text{leak}}}{R_{\text{leak}} + R_{\text{sink}}} \cdot (T_H - T_{\text{amb}}) \quad (3.3.2a)$$

Without any bulk heat sink, the thermal resistance of the top wafer is taken equal to $1000 \text{ K}\cdot\text{W}^{-1}$ ($h_{\text{sink}} = 10 \text{ W}\cdot\text{m}^{-2}\cdot\text{K}^{-1}$), and the thermal resistance of the architecture to $2 \text{ K}\cdot\text{W}^{-1}$ ($k_{\text{polymer}} = 0.5 \text{ W}\cdot\text{m}^{-1}\cdot\text{K}^{-1}$). This limits the temperature difference in the cavity to 0.16°C when the hot source temperature is 100°C and the cold source 25°C .

Even if other values of conductivity can be taken, the main way to increase the temperature difference is to use a bulk heat sink. With a heat sink of resistance 10 K.W^{-1} ($h_{\text{sink}} = 1000 \text{ W.m}^{-2}.\text{K}^{-1}$), the temperature difference across the cavity can reach 13°C for a hot source at 100°C .

c. Performances of a bimetallic strip in a cavity

As with the thermo-mechanical performances of the bimetallic strip in the cavity of the energy harvester, we can easily demonstrate how the cavity influences the electrical behavior of the bimetallic strip. In brief, the performances of a clamped-clamped beam ($\gamma.L = 36.7$) with three electrodes are given by (3.3.3). Taking into account thermal leakages, the efficiency of the device is described by (3.3.3c), and the Curzon-Ahlborn efficiency of the harvester by (3.3.3d).

$$V_{elec} = 7,7.L \cdot \frac{r_w}{\sqrt[3]{3.r_w - r_w^3}} \cdot \frac{t_p \cdot (z_p - z_o)}{L^2} \cdot \frac{e_{31}}{\epsilon_{33}^S} \cdot \sqrt[3]{\frac{M_\alpha}{N_e \cdot L}} \cdot \sqrt[3]{\Delta T_{cav}} \quad (3.3.3a)$$

$$W_E = 59,3.L \cdot v \cdot t \cdot \frac{r_w^2}{\sqrt[3]{(3.r_w - r_w^3)^2}} \cdot \frac{t_p \cdot (z_p - z_o)^2}{t \cdot L^2} \cdot k_{31}^2 \cdot \sqrt[3]{\left(\frac{M_\alpha}{N_e \cdot L}\right)^2} \cdot \sqrt[3]{\Delta T_{cav}^2} \quad (3.3.3b)$$

$$P_E = \frac{29,7.L \cdot v \cdot r_w^2}{\sqrt[3]{(3.r_w \cdot r_w^3)^2}} \cdot \frac{t_p \cdot (z_p - z_o)^2}{t \cdot L^2} \cdot \frac{h_c \cdot k_{31}^2}{\rho_b \cdot c_b} \cdot \sqrt[3]{\left(\frac{M_\alpha}{N_e \cdot L}\right)^2} \cdot \frac{\sqrt[3]{\Delta T_{cav}^2}}{\ln\left(1 + \frac{\Delta T_{cav}}{T_H - T_C}\right) - \ln\left(1 - \frac{\Delta T_{cav}}{T_H - T_C}\right)} \quad (3.3.3c)$$

$$\eta_{TE}^{abs,tot} \approx \frac{R_{leak} \cdot P_E}{\Delta T_{cav}} \quad (3.3.3d)$$

$$\eta_{TE}^{CA,tot} = \frac{\eta_{TE}^{abs,tot} \cdot \sqrt[3]{T_H + 273}}{\sqrt[3]{T_H + 273} - \sqrt[3]{T_{amb} + 273}} \quad (3.3.3e)$$

A closer look at the expression of the power shows that it is a decreasing function of the beam's thermal hysteresis. As a consequence, the performances are maximized for small thermal hystereses. In Fig.3.3.2, we present some projections about the performances of the heat engine at the microscale. These projections assume that the energy harvester uses a massive heat sink to evacuate heat from the bistable beams. Without this heat sink, the size reduction of the cavity drastically increases the thermal leakage, impeding its ability to maintain a thermal gradient inside which a bistable beam can oscillate. We choose a thermal hysteresis of at least 5°C for which the output voltage is higher than $0,4\text{V}$. For this thermal hysteresis, the operating frequency of the device lies in the $50\text{-}200 \text{ Hz}$ range when the hot source's temperature varies from 75°C to 15°C . The maximal density of output power generated by the heat engine is then of about $4 \mu\text{W.cm}^{-2}$, for a maximal Curzon-Ahlborn efficiency of $1,3.10^{-4}\%$. Logically, bistable beams with higher thermal hysteresis can only work at higher temperatures for the temperature difference in the cavity to be large enough to create self-sustaining oscillations of the prime movers. We then observe a degradation of the performances, notably a decrease of the Curzon-Ahlborn efficiency.

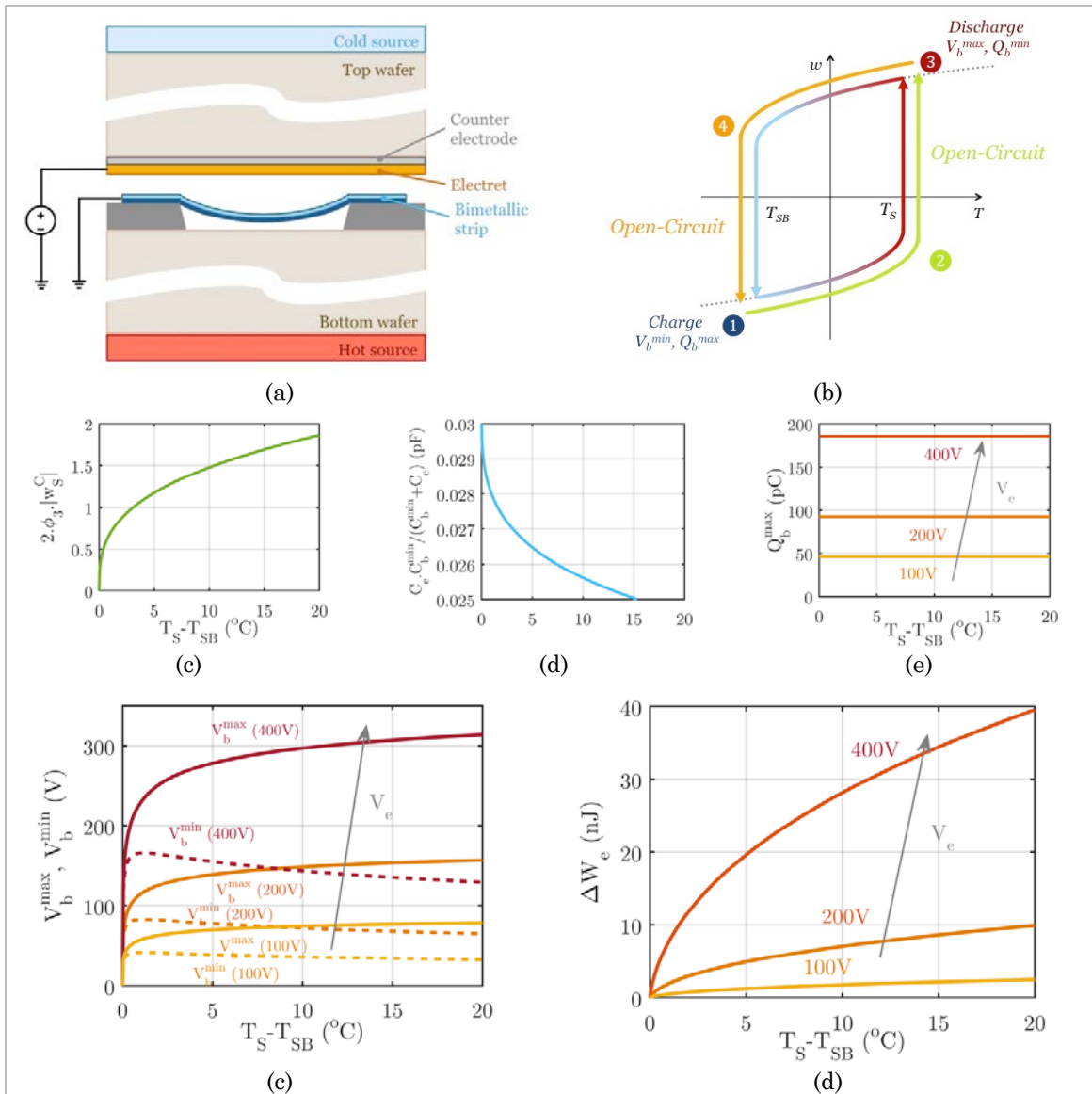


Figure 4.1.1. a. Simplified schematic of the electrostatic harvester at the microscale. b. Strategy for the polarization of the electrostatic energy harvester. c. Maximal displacement variation of an Al-Si beam as a function of its thermal hysteresis. d. Value of the minimal capacitance as a function of the thermal hysteresis. e. Maximal charge Q_b^{max} for various values of the electric field. f. Evolution of the output voltage as a function of the thermal hysteresis. g. Electric energy generated during a complete cycle for various values of the electret's potential.

4 Electrostatic coupling

4.1. Performances in weak coupling

By using the various results of Chapter 3, we can also study how the performances of the electrostatic bimetallic strip heat engine evolve when we scale the device down to the

microscale. Fig.4.1.1a shows a simplified diagram of the harvester at the microscale, where the electret is a SiO₂ layer deposited on the upper wafer of the device. In order to model the system, we first give the expression (4.1.1a) of the electric charge carried by the bimetallic strip when it is clamped-clamped, which can be approximated with (4.1.1b).

$$Q_b = -v \cdot \varepsilon_o \cdot (\mathcal{V} - \mathcal{V}_e) \cdot \int_{-\frac{L}{2}}^{\frac{L}{2}} \frac{1}{\frac{L}{2} \frac{\varepsilon_o}{\varepsilon_e} \cdot t_e + g_o - w_1 \cdot (\cos(k_\gamma \cdot x) - \cos(k_\gamma \cdot \frac{L}{2}))} \cdot dx \quad (4.1.1a)$$

$$Q_b = -v \cdot \varepsilon_o \cdot \frac{(\mathcal{V} - \mathcal{V}_e)}{\frac{\varepsilon_o}{\varepsilon_e} \cdot t_e + g_o - \varphi_3 \cdot w_1} \cdot \frac{4}{k_\gamma} \quad (4.1.1b)$$

By defining the capacitance of the bimetallic strip by (4.2.1a), the expression of the charge can be expressed by (4.2.1b). We can define the charge Q^* with (4.2.1c). From these first equations, we can deduce that the variation of the capacitance will be at best twice smaller with a clamped-clamped beam than with a simply-supported beam.

$$C_b = \frac{L \cdot v \cdot \varepsilon_o}{g_o - \varphi_3 \cdot w_1} \quad (4.1.2a)$$

$$Q_b = -\frac{4}{k_\gamma \cdot L} \cdot \frac{C_b}{C_e + C_b} \cdot (\mathcal{V} - \mathcal{V}_e) \quad (4.1.2b)$$

$$Q^* = \frac{4}{k_\gamma \cdot L} \cdot C_e \cdot \mathcal{V}_e \quad (4.1.2c)$$

Fig.4.1.1b recalls the way to polarize the bimetallic strip in order to realize a charge-constrained cycle: when the bimetallic strip is unsnapped and stable at the snap-back temperature, the capacitance of the bimetallic strip is maximal, the circuit is closed until the maximal charge Q_b^{max} is reached. Then the beam is heated and snaps in open-circuit, increasing the potential of the electric charges. The beam is then discharged, until Q_b^{min} , and it cools down and snaps back in open-circuit. Applying the equations demonstrated in Chapter 3, we find the following expressions when the bimetallic strip is not constrained in a cavity:

$$Q_b = \frac{4 \cdot C_b \cdot C_e}{k_\gamma \cdot L \cdot (C_e + C_b)} \cdot (\mathcal{V}_e - \mathcal{V}_b) \quad (4.1.3a)$$

$$Q_b^{max} = \frac{C_b^{max}}{C_e + C_b^{max}} \cdot Q^* = \frac{\varepsilon_o \cdot t_e \cdot Q^*}{\varepsilon_o \cdot t_e + \varepsilon_e \cdot (g_o + 2 \cdot \varphi_3 \cdot w_S^C)} \quad (4.1.3b)$$

$$Q_b^{min} = \frac{C_b^{min}}{C_e + C_b^{min}} \cdot Q^* = \frac{\varepsilon_o \cdot t_e \cdot Q^*}{\varepsilon_o \cdot t_e + \varepsilon_e \cdot (g_o - 2 \cdot \varphi_3 \cdot w_S^C)} \quad (4.1.3c)$$

$$\mathcal{V}_b^{max} = \frac{Q_b^{min} - Q_b^{max}}{Q_b^{max}} \cdot \mathcal{V}_e \quad (4.1.3d)$$

$$\mathcal{V}_b^{min} = \frac{Q_b^{max} - Q_b^{min}}{Q_b^{min}} \cdot \mathcal{V}_e \quad (4.1.3e)$$

The expression of the energy is unchanged and is recalled in (4.1.4a). It can be developed as a function of the maximal and minimal voltages. If we assume that the gap is at least

equal to the maximal beam's deflection to ensure a contact between the cold source and the bimetallic strip (4.1.4c), the final expression of the electrical energy is given by (4.1.4d).

$$\Delta \mathcal{W}_E^Q = \frac{1}{2} \cdot (Q_b^{max} - Q_b^{min}) \cdot (V_b^{max} - V_b^{min}) = \frac{1}{2} \cdot \mathcal{V}_e \cdot \frac{(Q_b^{min} - Q_b^{max})^3}{Q_b^{min} \cdot Q_b^{max}} < 0 \quad (4.1.4a)$$

$$\Delta \mathcal{W}_E^Q = -\frac{2}{\pi} \cdot \frac{C_b^{min} \cdot C_e}{C_e + C_b^{min}} \cdot \mathcal{V}_b^{max} \cdot (\mathcal{V}_b^{max} - \mathcal{V}_b^{min}) \quad (4.1.4b)$$

$$g_o = \varphi_3 \cdot r_w \cdot w_S^C \quad (4.1.4c)$$

$$\Delta \mathcal{W}_E^Q = \frac{16}{k_\gamma \cdot L} \cdot \frac{\varepsilon_e^3 \cdot r_w^3 \cdot \varphi_3^3 \cdot |w_S^C|^3}{\varepsilon_o \cdot t_e \cdot (\varepsilon_o \cdot t_e + 2 \cdot \varepsilon_e \cdot r_w \cdot \varphi_3 \cdot |w_S^C|)^2} \cdot C_e \cdot \mathcal{V}_e^2 \quad (4.1.4d)$$

Similarly, the expressions of the characteristic voltages are given by (4.1.5).

$$\mathcal{V}_b^{max} = \frac{2 \cdot \varepsilon_e \cdot r_w \cdot \varphi_3 \cdot |w_S^C|}{\varepsilon_o \cdot t_e + 2 \cdot \varepsilon_e \cdot r_w \cdot \varphi_3 \cdot |w_S^C|} \cdot \mathcal{V}_e \quad (4.1.5a)$$

$$\mathcal{V}_b^{min} = -\frac{2 \cdot \varepsilon_o \cdot \varepsilon_e \cdot t_e \cdot r_w \cdot |w_S^C|}{(\varepsilon_o \cdot t_e + \varepsilon_e \cdot r_w \cdot \varphi_3 \cdot |w_S^C|)^2 + \varepsilon_e^2 \cdot r_w^2 \cdot \varphi_3^2 \cdot |w_S^C|^2} \cdot \mathcal{V}_e \quad (4.1.5b)$$

In order to have a first idea of the performances of the energy harvester at the microscale, we plot in Fig.4.1.1c the evolution of the beam's displacement amplitude, in Fig.4.1.1d the maximal and minimal values of the bimetallic strip's capacitance and in Fig.4.1.1d the absolute values of the peak voltages V_b^{min} and V_b^{max} . The available electric energy is represented in Fig.4.1.1e as a function of the thermal hysteresis. The simulations are performed for an Al-Si beam (400 μm x 100 μm x (2+2 μm)) coupled with an electret made of a 2 μm thick SiO₂ layer. With an electret surface potential of 400 V, this can generate up to 20 nJ per cycle with output voltage of 280 and 180 V. However, the difficulty to harvest energy with the electrostatic harvester is due to the small values of the capacitances. For a thermal hysteresis of 5°C, the minimal capacitance is 26.5 fF, whereas the maximal capacitance is 460 fF. This highlights the problem of the influence of the parasitic capacitances on the efficiency of the electric conversion.

4.2. Performances in moderate coupling

Now that we have determined the performances in weak coupling, we can establish the equation describing the mechanical equilibrium of the beam. Taking into account the electrostatic pressure, we can describe the equilibrium with (4.2.1a). Neglecting the dependence on x of the electrostatic pressure, we can approximate this equation by (4.2.1b).

$$\left(N_\alpha \cdot T - \frac{N_e}{2 \cdot L} \cdot \int_{-L/2}^{L/2} w_x^2 \cdot dx - F_o \right) \cdot w_{xx} + I_e \cdot w_{xxxx} = \frac{1}{2} \cdot \frac{\varepsilon_o \cdot v \cdot (\mathcal{V}_e - \mathcal{V}_b)^2}{\varepsilon_o \cdot t_e + g_o - w} \quad (4.2.1a)$$

$$\begin{aligned} \frac{N_e}{2.L} \cdot \varphi_1 \cdot w_1^3 + (I_e \cdot k_\gamma^2 - N_o) \cdot w_1^2 + 4 \cdot \frac{\varphi_2}{\varphi_1} \cdot (M_o - M_\alpha \cdot T) \\ = \frac{-L^2}{8.\pi} \cdot \frac{\varepsilon_o \cdot v \cdot (\mathcal{V}_e - \mathcal{V}_b)^2}{\varepsilon_o \cdot t_e + g_o - \varphi_3 \cdot w_1} \end{aligned} \quad (4.2.1b)$$

By assuming a fixed charge Q^* (which is equal to $Q^{b_{max}}$) carried by the bistable electrode during the displacement, the equilibrium equation can be approximated by (4.2.2a) in the vicinity of the flat position by defining the equivalent moment M_Q given by (4.2.2b) and the equivalent gap g_e (4.2.2c).

$$\begin{aligned} \frac{n_e}{2.L} \cdot \varphi_1 \cdot w_1^3 + (I_e \cdot k_\gamma^2 - N_o) \cdot w_1 + 4 \cdot \frac{\varphi_2}{\varphi_1} \cdot (M_o M m_\alpha \cdot T) \\ = -4 \cdot \frac{\varphi_2}{\varphi_1} \cdot M_Q \cdot \left(1 - \frac{\varepsilon_e \cdot \varphi_3 \cdot w_1}{g_e}\right)^2 \end{aligned} \quad (4.2.2a)$$

$$M_Q = \frac{\varphi_1}{32 \cdot \varphi_2 \cdot \pi} \cdot \frac{\varepsilon_e \cdot L}{\varepsilon_o \cdot t_e} \cdot C_e \cdot \mathcal{V}_e^2 \quad (4.2.2b)$$

$$g_e = \frac{\varepsilon_o}{\varepsilon_e} \cdot t_e + r_w \cdot \varphi_3 \cdot |w_S^c| \quad (4.2.2c)$$

Hence we need can define the corrective factor $F(\mathcal{V}_e)$ by (4.2.3a) to see the influence of the electret's potential surface on the mechanical equilibrium of the beam. Hence the thermal hysteresis becomes (4.2.3b) and the critical amplitude (4.2.3c). Chosing a torsional stiffness $\gamma.L = 36.7$, we can approximate (4.2.3a) by (4.2.3d).

$$F(\mathcal{V}_e) = 1 + \frac{M_Q \cdot \left(\frac{N_\alpha}{M_\alpha} + \frac{8 \cdot r_w \cdot \varepsilon_e}{g_e} \cdot \frac{\varphi_2 \cdot \varphi_3}{\varphi_1} + M_Q \cdot \frac{32 \cdot r_w^2 \cdot \varepsilon_e^4}{3 \cdot n_e \cdot g_e^4} \cdot \frac{\varphi_2^2 \cdot \varphi_3^2 \cdot L}{\varphi_1^3} \right)}{N_o - I_e \cdot k_\gamma^2} \quad (4.2.3a)$$

$$\Delta T_Q = \Delta T \cdot \sqrt{F(\mathcal{V}_e)^3} \quad (4.2.3b)$$

$$\Delta T_Q = \Delta T \cdot \sqrt{F(\mathcal{V}_e)} \quad (4.2.3c)$$

$$F(\mathcal{V}_e) = 1 + \frac{M_Q \cdot \left(\frac{N_\alpha}{M_\alpha} + \frac{1,26 \cdot r_w \cdot \varepsilon_e}{g_e \cdot \pi} + M_Q \cdot \frac{0,07 \cdot r_w^2 \cdot \varepsilon_e^4 \cdot L^2}{\pi^4 \cdot n_e \cdot g_e^4} \right)}{N_o - 3,6 \cdot I_e \cdot \frac{\pi^2}{L^2}} \quad (4.2.3d)$$

The performances of the harvester in moderate coupling are described by (4.2.4): the available energy by (4.2.4a), the working frequency by (4.2.4b), the mean power by (4.2.4c), and the thermal efficiency by (4.2.4d).

$$\Delta \mathcal{W}_E^Q = \frac{16}{\pi} \cdot \frac{\varepsilon_e^3 \cdot r_w^3 \cdot \varphi_3^3 \cdot |w_S^c|^3 \cdot \sqrt{F(\mathcal{V}_e)^3}}{\varepsilon_o \cdot t_e \cdot (\varepsilon_o \cdot t_e + 2 \cdot \varepsilon_e \cdot r_w \cdot \varphi_3 \cdot |w_S^c| \cdot \sqrt{F(\mathcal{V}_e)})^2} \cdot C_e \cdot \mathcal{V}_e^2 \quad (4.2.4a)$$

$$f = \frac{1}{2 \cdot R_{CC} \cdot C_v} \cdot \frac{1}{\ln \left(1 + \frac{\sqrt{F(\mathcal{V}_e)^3} \cdot \Delta T_{cav}}{T_H - T_C} \right) - \ln \left(1 - \frac{\sqrt{F(\mathcal{V}_e)^3} \cdot \Delta T_{cav}}{T_H - T_C} \right)} \quad (4.2.4b)$$

$$P_E = \Delta \mathcal{W}_E^Q \cdot f \quad (4.2.4c)$$

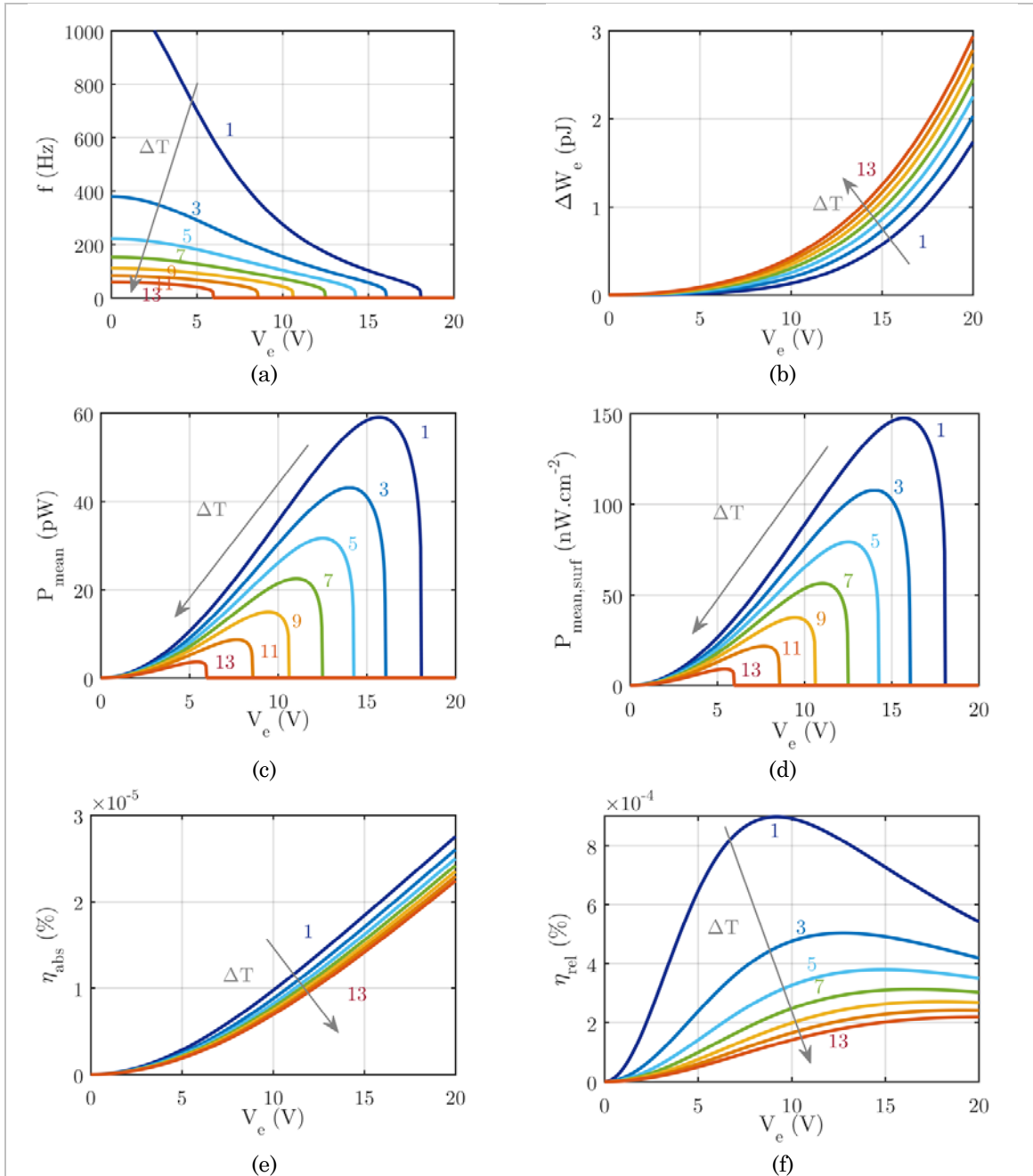


Figure 4.2.1. a. Evolution of the frequency of various bimetallic strips against the electret's potential surface. b. Available energy per cycle. c. Mean power per bimetallic strip. d. Mean surface power. e. Thermal efficiency of the energy harvester. f. Evolution of the Carnot efficiency as a function of the electret's potential surface.

$$\eta_{TE}^{abs} = \frac{\Delta W_E^Q}{C_v \cdot \Delta T_{cav} \cdot \sqrt{F(V_e)}} \quad (4.2.4d)$$

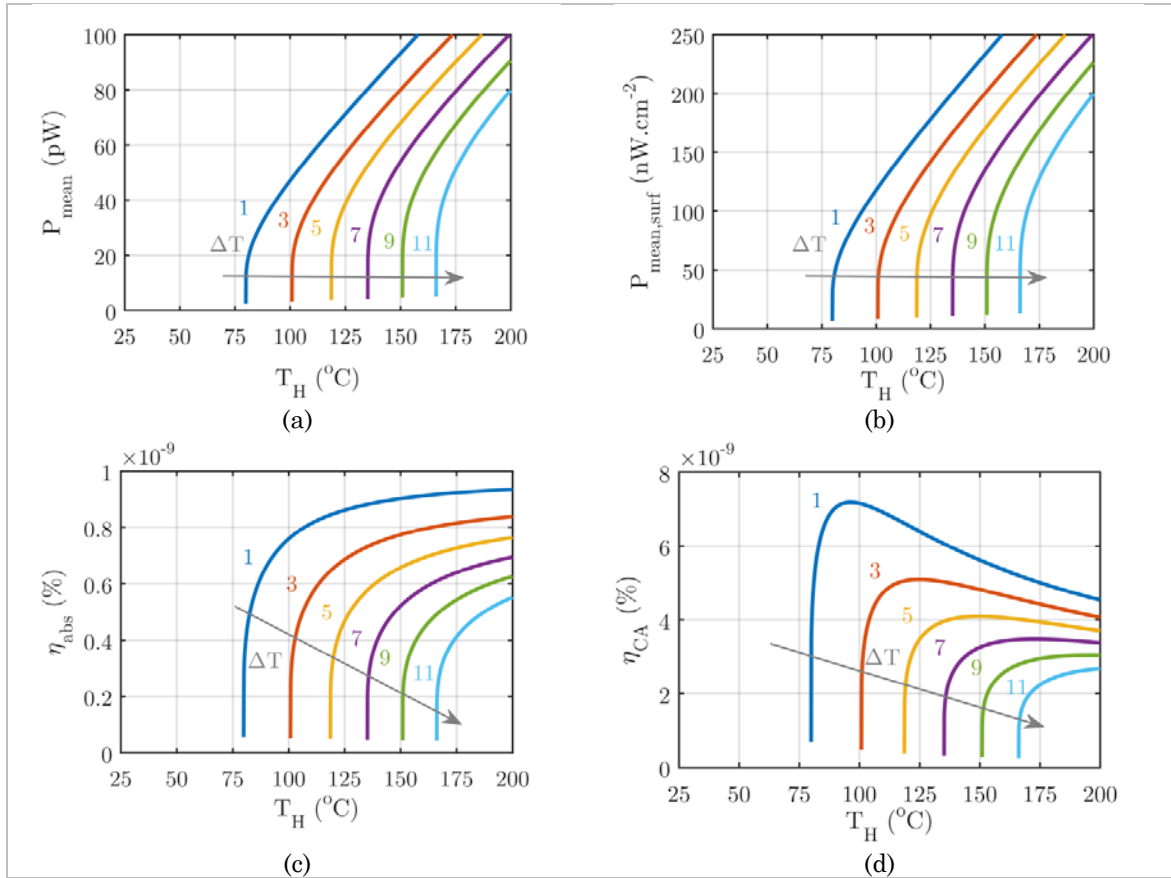


Figure 4.2.2. *a. Evolution of the power generated by a single bimetallic strip as a function of the hot source temperature and for an electret having a potential of 20 V. b. Available energy per cycle. c. Mean power per bimetallic strip. d. Mean surface power. e. Thermal efficiency of the energy harvester. f. Evolution of the Carnot efficiency as a function of the electret's potential surface.*

We simulate the performances of an Al-Si beam coupled with an electret made of a thick SiO₂ layer (20 μm) whose surface potential varies. Figs.4.2.1a-f present some of the performances: (a) working frequency, (b) energy per cycle, (c) mean power, (d) mean surface power, (e) thermal efficiency and finally (f) Carnot efficiency of the bistable beam. These simulations are performed assuming a temperature difference of 15°C in the cavity, corresponding to a device working between a hot source at 100°C and a cold source at 25°C and evacuating heat via a bulk heat sink. These figures first show that the optimal value of the surface potential is very low, around 15 V. Because of the size reduction of the device, the electric field increases like the scaling factor $1/L$ of the device, whereas the pull-in voltage decreases like the length L . For our model beam this voltage is 20 V for a beam measuring 400 μm , and 40 V for 200 μm [Hu and Chuang, 2007; Pamidighantam et al, 2002; Chowdhury et al, 2006]. Thus we cannot use an electret with high surface potential. Fig.4.2.1b shows that the energy generated for a surface potential does not exceed 1 pJ.cm⁻², which can be quite difficult to harvest. Moreover, for a bimetallic strip

having a thermal hysteresis of 1°C, the corresponding output power is about 60 pW, and the thermal efficiency and Carnot efficiency are 0.2 ppm and 9 ppm respectively for a surface potential of 15 V.

Finally, Fig.4.2.2 presents the evolutions of the dynamic performances of the electrostatic energy harvester when the external temperature changes. The thermal hysteresis of the bistable beam must be as small as possible to maximize the output power. The quantity of energy that can be harvested with a single bimetallic beam is very weak but is compensated by the increase of the switching frequency (around 1 kHz for a thermal hysteresis of 1°C). Normalized by the device's surface, the mean output power is 120 nW.cm⁻² for an energy harvester made of beams having a thermal hysteresis of 1°C working at 100°C. The thermal efficiency of the transduction is also weak, about 10⁻⁹%. These observations would tend to point to downscaling limits beyond which there might be little interest in scaling down the electrostatic energy harvester any further.

5 Synthesis

This last section is devoted to a synthesis on the performances of the miniaturized bimetallic strip heat engines where we recall all the previous results, but also where we refine the scaling rules that predict the evolution of these performances. In this part, we assume that the miniaturized energy harvesters are fabricated at the microscale when their length is lower than 1 mm.

a. Synthesis on the mechanical properties of the bimetallic strip heat engine

We first focus on the evolution of the mechanical performances of the bistable beams and we look at their evolution as a function of the scaling factor 1/L. Equation (5.1.1a) describes the evolution of the maximal deflection, (5.1.1b) the maximal force, and (5.1.1c) the energy produced during a complete cycle. They are valid for both clamp types by adjusting the constant $\varphi_1, \varphi_2, \varphi_3$.

$$w_o = \varphi_3 \cdot \sqrt[3]{\frac{\varphi_2}{\varphi_1^2 \cdot L}} \cdot \sqrt[3]{4 \cdot \frac{M_\alpha \cdot L^2}{N_e} \cdot \Delta T} \quad (5.1.1a)$$

$$F_{max} = 2 \cdot \varphi_2 \cdot M_\alpha \cdot \Delta T \quad (5.1.1b)$$

$$\Delta W_{mec} = \sqrt[3]{\frac{\varphi_2^4 \cdot L^2}{\varphi_1^2}} \cdot 27 \cdot \sqrt[3]{\frac{(M_\alpha \cdot \Delta T)^4}{16 \cdot N_e \cdot L}} \quad (5.1.1c)$$

As a consequence we can see that these parameters follow the following scaling rules. Logically, we observe that the energy is a volume parameter and the force a surface parameter. Their evolutions are represented in Fig.5.1.1a for a thermal hysteresis of about 3°C. The number given on each figure indicates the reduction of the parameter due to the change of configuration.

$$w_o \propto L \cdot \sqrt[3]{\Delta\alpha \cdot \Delta T} \quad (5.1.2a)$$

$$F_{max} \propto L^2 \cdot E \cdot \Delta\alpha \cdot \Delta T \quad (5.1.2b)$$

$$\Delta W_{mec} \propto L^3 \cdot E \cdot \sqrt[3]{\Delta\alpha^4 \cdot \Delta T^4} \quad (5.1.2c)$$

b. Synthesis on the dynamic behavior of the system

To see the evolutions of the dynamic performances with downscaling, we must study how the frequency of the device evolves with the scaling parameter. We choose to focus on two different strategies. The first strategy consists in maintaining a fixed thermal gradient in the cavity whatever the size of the prime mover. We recall first the expression of the frequency associated to the thermal transfer at the interface between a heat source and the prime mover (5.1.3a), and the frequency associated to the internal heat transfers (5.1.3b) and linked to the thermal diffusivity of the materials. We can approximate the real working period of the system as the sum of both periods. As a consequence, we can approximate the working frequency by (5.1.3c). For small values of the thermal hysteresis, we can linearize the expression of both frequencies, leading to (5.1.3d) and (5.1.3e).

$$f_{contact} = \frac{h_c \cdot L \cdot v}{2 \cdot C_v} \cdot \frac{1}{\ln\left(1 + \frac{\Delta T}{T_H - T_C}\right) - \ln\left(1 - \frac{\Delta T}{T_H - T_C}\right)} \quad (5.1.3a)$$

$$f_{internal} = \frac{\pi^2 \cdot \kappa_b}{4 \cdot L^2} \cdot \frac{1}{\ln\left(1 + \frac{\Delta T}{T_H - T_C}\right) - \ln\left(1 - \frac{\Delta T}{T_H - T_C}\right)} \quad (5.1.3b)$$

$$\frac{1}{f_{tot}} = \frac{1}{f_{internal}} + \frac{1}{f_{contact}} \quad (5.1.3c)$$

$$f_{contact} = \frac{h_c \cdot L \cdot v}{C_v} \cdot \frac{T_H - T_C}{\Delta T} \quad (5.1.3d)$$

$$f_{internal} = \frac{\pi^2 \cdot \kappa_b}{2 \cdot L^2} \cdot \frac{T_H - T_C}{\Delta T} \quad (5.1.3e)$$

The temperature difference in the cavity is given by the law (5.1.4a), which can be rewritten as (5.1.4b) by using an equivalent thermal resistivity to model the architecture's leakage paths and the heat sink by an equivalent thermal exchange coefficient.

$$T_H - T_C = \frac{R_{leak}}{R_{leak} + R_{sink}} \cdot (T_H - T_{amb}) \quad (5.1.4a)$$

$$T_H - T_C \approx \frac{2 \cdot w_o}{2 \cdot w_o + \frac{\rho_{leak}}{h_{sink}}} \cdot (T_H - T_{amb}) \quad (5.1.4b)$$

The only possible strategy to maximize the output energy is to maintain a fixed thermal gradient in the cavity in order to increase the frequency of the device (in the other case, the temperature difference in the cavity is so small that no bimetallic strip can switch from a hot source to the other). The scaling rules corresponding to this case are given in (5.1.5), and represented in Fig.5.1.2. As the equivalent resistance of the device decreases with the beam's maximal deflection, it is necessary to use a heat sink whose effective

coefficient of thermal transfer must be inversely proportional to the length of the prime mover in order to evacuate heat flowing through the energy harvester. As a consequence, we cannot maintain a constant temperature difference in the cavity by using a planar heat sink as was the case for the piezoelectric bimetallic strip heat engine.

$$h_{sink} \propto \frac{1}{L} \cdot \frac{\rho_{leak}}{\sqrt[3]{\Delta\alpha \cdot \Delta T}} \quad (5.1.5a)$$

$$f_{contact} \propto \frac{1}{L} \cdot \frac{h_c \cdot (T_H - T_{amb})}{\rho \cdot c \cdot \Delta T} \quad (5.1.5b)$$

$$f_{internal} \propto \frac{1}{L^2} \cdot \frac{\kappa_b \cdot (T_H - T_{amb})}{\Delta T} \quad (5.1.5c)$$

$$f_{tot} \approx f_{contact} \propto \frac{1}{L} \cdot \frac{h_c \cdot (T_H - T_{amb})}{\rho \cdot c \cdot \Delta T} \quad (5.1.5d)$$

$$P_{mean} = \Delta W_{mec} \cdot f_{tot} \propto L^2 \cdot \frac{h_c \cdot E \sqrt[3]{\Delta\alpha^4}}{\rho \cdot c} \cdot \sqrt[3]{\Delta T} \cdot (T_H - T_{amb}) \quad (5.1.5e)$$

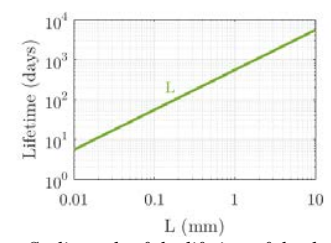
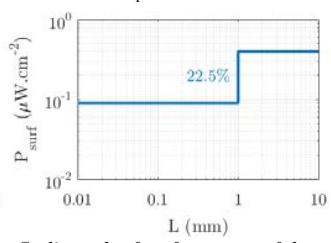
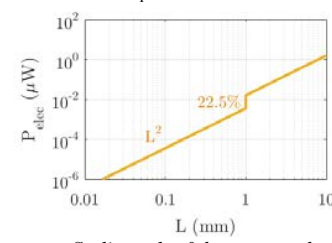
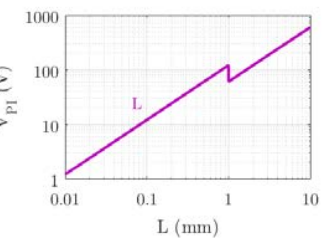
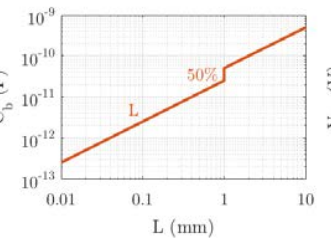
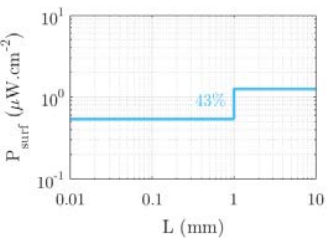
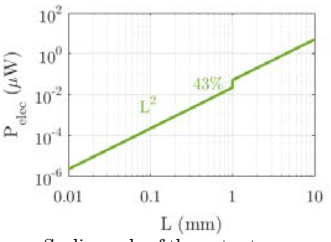
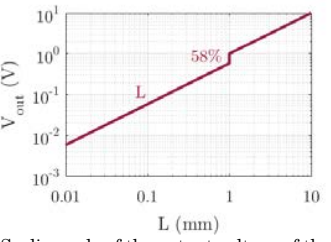
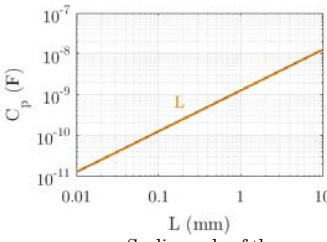
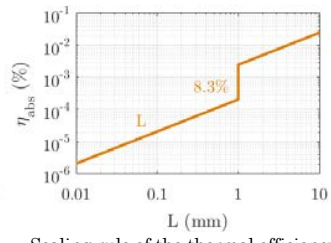
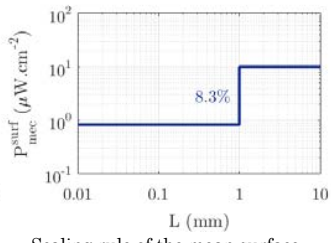
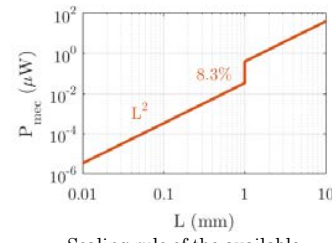
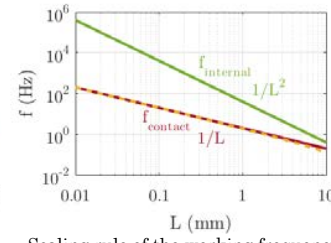
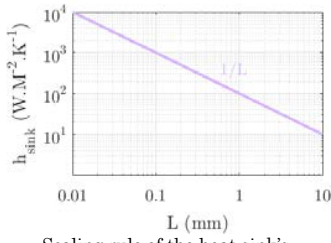
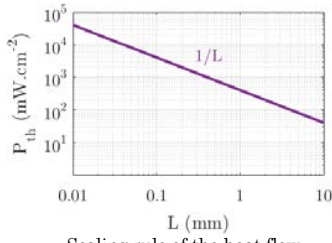
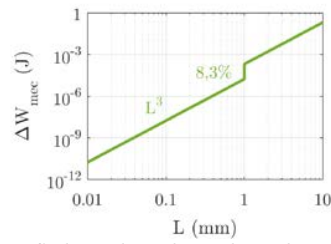
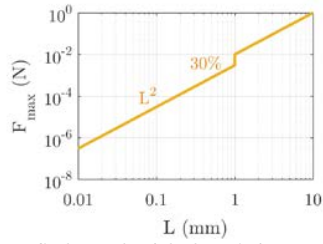
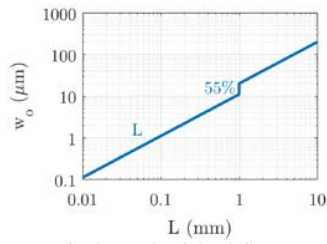
$$P_{mean}^{surf} = \frac{P_{mean}}{S} \propto \frac{h_c \cdot E \sqrt[3]{\Delta\alpha^4}}{\rho \cdot c} \cdot \sqrt[3]{\Delta T} \cdot (T_H - T_{amb}) \quad (5.1.5f)$$

$$P_{th}^{surf} = \frac{T_H - T_C}{2 \cdot w_o \cdot \rho_{leak}} \propto \frac{1}{L} \cdot \frac{T_H - T_C}{\rho_{leak} \cdot \sqrt[3]{\Delta\alpha \cdot \Delta T}} \quad (5.1.5g)$$

$$\eta_{abs} = \frac{P_{mean}^{surf}}{P_{th}^{surf}} \propto L \quad (5.1.5h)$$

If we look at the evolution of the switching frequency, we can see that the thermal transfers inside the prime mover are faster than the thermal transfers between the prime mover and the heat sources at the microscale. As a consequence, the prime mover's working frequency is determined by the thermal transfers between the heat sources and the bistable beam, which are proportional to the beam's length. Hence we found that the mechanical power generated by a single bimetallic strip is a function of the square of the length instead of being a linear function of the bimetallic strip's length. As a consequence, if the bimetallic strips were simply-supported at the micrometric scale, we would be able to generate as much power at this scale as at the macrometric scale if we used two devices having the same surfaces.

Finally the consequence of the linear increase of the frequency is visible on the thermal efficiency of the energy harvester since more heat flows through the leaky architecture than through the bimetallic strips at the microscale. The thermal efficiency thus decreases as the size factor of the device. Solutions to avoid these issues would be to use highly insulating materials like aerogels for separating the upper wafer from the bottom wafer. Aerogels are materials having very low values of thermal conductivity (around $0.24 \text{ W} \cdot \text{m}^{-1} \cdot \text{K}^{-1}$ [Bauer et al, 2011; He et al, 2015]), which can be fabricated using standard microelectronics process [Yokokawa et al, 2004].



c. *Synthesis on the pyroelectric bimetallic strip heat engines*

We start with the performances of the pyroelectric bimetallic strip heat engines and we recall the formula giving the expression of the available energy and the output voltage obtained with a Stirling cycle at the macroscale (5.1.6a-b) and at the microscale (5.1.6c-d). Logically we observe that the energy is always linked to the volume of matter, and that the voltage is a linear function of the length as the capacitance.

$$\mathcal{V}_{II}^{cav} = |\mathcal{V}_S^S| = |\mathcal{V}_{SB}^S| = \left| \frac{t_p \cdot p_3^S}{\varepsilon_{33}^S} \cdot \Delta T_{cav} + 4 \cdot \frac{\pi \cdot t_p \cdot e_{31}}{L^2 \cdot \varepsilon_{33}^S} \cdot (z_p - z_o) \cdot w_{top} \right| \quad (5.1.6a)$$

$$\mathcal{W}_{II}^{cav} = C_p \cdot \mathcal{V}_{II}^2 = C_p \cdot \left(\frac{3}{2} \cdot \left(r_w - \frac{r_w^3}{3} \right) \cdot \frac{t_p \cdot p_3^S}{\varepsilon_{33}^S} \cdot \Delta T - 4 \cdot \frac{\pi \cdot t_p \cdot e_{31}}{L^2 \cdot \varepsilon_{33}^S} \cdot r_w \cdot (z_p - z_o) \cdot w_S^C \right)^2 \quad (5.1.6b)$$

$$\mathcal{V}_{IIIe} = \left| 8 \cdot \frac{t_p \cdot e_{31}}{L \cdot \varepsilon_{33}^S} \cdot (2 \cdot k_\gamma - \varphi_2) \cdot (z_p - z_o) \cdot w_S^C \right| \quad (5.1.6c)$$

$$\mathcal{W}_{IIIe} = C_p \cdot \mathcal{V}_{IIIe}^2 = C_p \cdot \left(8 \cdot \frac{t_p \cdot e_{31}}{L \cdot \varepsilon_{33}^S} \cdot (2 \cdot k_\gamma - \varphi_2) \cdot (z_p - z_o) \cdot w_S^C \right)^2 \quad (5.1.6d)$$

$$C_p \propto L \cdot \varepsilon_r \quad (5.1.6e)$$

$$u_{II}^{cav} \propto L \cdot \frac{p_3^S}{\varepsilon_{33}^S} \cdot \Delta T_{cav} \quad (5.1.6f)$$

As we can see on Fig.5.1.1, the main challenges for piezoelectric energy harvester is the reduction of both the piezoelectric capacitance and output voltage. The break on the curves is due to the use of a configuration with three piezoelectric capacitors at the microscale.

d. *Synthesis on the electrostatic bimetallic strip heat engines*

In the electrostatic case, it is important to see how the bimetallic strip capacitance evolves and how the pull-in voltage depends on the dimensions of the bistable beam, since this gives an idea of the maximal value of the electret's potential surface at the microscale.

$$\mathcal{V}_{PI} = \frac{8\sqrt{2}}{3} \cdot \frac{g_e}{L} \sqrt{I_e \cdot \frac{\pi^2}{\varepsilon_o \cdot C_o \cdot L}} \propto L \quad (5.1.7)$$

The evolution of the mean value of the bimetallic strip capacitance, the pull-in voltage and the mean power are represented in Fig.5.1.1 as functions of the length scaling factor.

e. *Aging of the device*

A last consequence of the device's size reduction is the reduction of the lifetime of the device. Assuming a constant number of cycles before failure whatever the size of the device, the linear increase of the working frequency as a function of the length factor causes a linear reduction of the lifetime of the devices. As a consequence, it is expected that the miniaturized devices would work no more than a hundred days.

6 Conclusion

In this last theoretical chapter we developed new models to describe the mechanical behavior of bistable beams at the microscale. These models add a torsional stiffness and an axial stiffness to model the beam's clamp: we simulated bimetallic strip using either the non-linear Euler equation or an equivalent reduced-order model, and we showed that by clamping beams on the substrate, the thermo-mechanical performances of the harvester are reduced (down to 8.3% of the mechanical energy produced by a simply-supported beam). We also study the sensitivity of the properties of the bistable beams to the variability of the residual stress used to buckle the beams, showing that the change of the clamp conditions from supported beams to clamped beams sensibly increase this sensitivity. As a consequence, it appears quite impossible to consider an industrial fabrication of the miniaturized energy harvesters since variability issues may be a problem to create a reliable technology.

We then modelled the performances of the pyroelectric bimetallic strip heat engine at the microscale, proposing an expression of the power generated by a bistable beam made of three piezoelectric capacitor. We showed that such architecture does not allow harvesting the electrical charges created by the pyroelectric effect, thus reducing the performances of the device. Moreover, by reducing the size of the device, the output voltages, electrical capacitance and electrical charges are strongly reduced, creating difficulties to harvest them.

We also extended the model of the electrostatic bimetallic strip heat engine to describe the performances of a miniaturized energy harvester. We showed that an important parameter to be taken into account is the value of the pull-in voltage that can act as a limit value for the electret's surface potential. The reduction of the pull-in voltage for MEMS devices thus degrades the performances of the energy harvester at the microscale.

Finally we demonstrated that it is necessary to use a bulk heat sink to maintain a thermal gradient in the device's cavity. In these conditions, the reduction of the amount of heat converted into electrical energy by each bimetallic strip is counterbalanced by the increase of the switching frequency of the device, but the increase of the frequency is slower than predicted in Puscasu's work. As a consequence, the mean output power of miniaturized generators is not higher than the mean output power of macro energy harvester, but smaller. This last fact also justifies the fact of forgetting the idea of fabricating miniaturized energy harvesters. Contrariwise, it seems worth considering other opportunities for miniaturized thermo-mechanically bistable beams such as thermal sensing applications for example.

7 Bibliography

- Alkharabsheh, S. and Younis, M. (2013). Dynamics of MEMS Arches of Flexible Supports. *Journal of Microelectromechanical Systems*, 22(1), pp.216-224.
- Bauer, M., Bauer, C., Fish, M., Matthews, R., Garner, G., Litchenberger, A. and Norris, P. (2011). Thin-film aerogel thermal conductivity measurements via 3ω . *Journal of Non-Crystalline Solids*, 357(15), pp.2960-2965.
- Cabal, A. and Ross, S. D. (2002) Snap-through bilayer microbeam *Nanotech* 1 230–3
- Chowdhury, S., Ahmadi, M. and Miller, W. (2006). Pull-In Voltage Study of Electrostatically Actuated Fixed-Fixed Beams Using a VLSI On-Chip Interconnect Capacitance Model. *Journal of Microelectromechanical Systems*, 15(3), pp.639-651.
- Fachin, F., Nikles, S., Dugundji, J. and Wardle, B. (2011). Analytical extraction of residual stresses and gradients in MEMS structures with application to CMOS-layered materials. *J. Micromech. Microeng.*, 21(9), p.095017.
- Fang, W. and Wickert, J. (1996). Determining mean and gradient residual stresses in thin films using micromachined cantilevers. *J. Micromech. Microeng.*, 6(3), pp.301-309.
- Guckel, H., Randazzo, T. and Burns, D. (1985). A simple technique for the determination of mechanical strain in thin films with applications to polysilicon. *J. Appl. Phys.*, 57(5), p.1671.
- Hu, Y., Chang, P. and Chuang, W. (2007). An approximate analytical solution to the pull-in voltage of a micro bridge with an elastic boundary. *J. Micromech. Microeng.*, 17(9), pp.1870-1876.
- He, J., Li, X., Su, D., Ji, H. and Wang, X. (2015). Ultra-low thermal conductivity and high strength of aerogels/fibrous ceramic composites. *Journal of the European Ceramic Society*.
- Kobrinisky, M., Deutsch, E. and Senturia, S. (2000). Effect of support compliance and residual stress on the shape of doubly supported surface-micromachined beams. *Journal of Microelectromechanical Systems*, 9(3), pp.361-369.
- Meng, Q., Mehregany, M. and Mullen, R. (1993). Theoretical modeling of microfabricated beams with elastically restrained supports. *Journal of Microelectromechanical Systems*, 2(3), pp.128-137.
- Mullen, R., Mehregany, M., Omar, M. and Ko, W. (1991). Theoretical modeling of boundary conditions in microfabricated beams. *[1991] Proceedings. IEEE Micro Electro Mechanical Systems*.
- Pamidighantam, S., Puers, R., Baert, K. and Tilmans, H. (2002). Pull-in voltage analysis of electrostatically actuated beam structures with fixed-fixed and fixed-free end conditions. *J. Micromech. Microeng.*, 12(4), pp.458-464.
- Puscasu, O., Monfray, S., Savelli, G., Maitre, C., Pemeant, J., Coronel, P., Domanski, K., Grabiec, P., Ancey, P., Cottinet, P., Guyomar, D., Bottarel, V., Ricotti, G., Bimbaud, I., Boeuf, F., Gaillard, F. and Skotnicki, T. (2012). An innovative heat harvesting

- technology (HEATec) for above-Seebeck performance. *2012 International Electron Devices Meeting*.
- Puscasu, O., Monfray, S., Maître, C., Cottinet, P., Rapisarda, D., Savelli, G., Gaillard, F., Ricotti, G., Ancey, P., Boeuf, F., Guyomar, D. and Skotnicki, T. (2014). A disruptive technology for thermal to electrical energy conversion. *Microelectronics Journal*, 45(5), pp.554-558.
- Tung, R., Garg, A., Kovacs, A., Peroulis, D. and Raman, A. (2013). Estimating residual stress, curvature and boundary compliance of doubly clamped MEMS from their vibration response. *J. Micromech. Microeng.*, 23(4), p.045009.

Chapter 5

Silicon integration of thermo-mechanically bistable actuators

1 Introduction

In the second chapter, we explained that the beams' thermo-mechanical instability was induced by the antagonistic effects of the thermal expansion asymmetry and of the residual stress asymmetry or the initial curvature of the beam. As a consequence, two kinds of fabrication process have been considered and realized on 300mm facilities of STMicroelectronics, Crolles. This chapter separately presents these two manufacturing methods in the order they were created. As a result, the first part of this chapter is devoted to the fabrication of microstructures by means of the microlenses arrays, whereas the second part of this chapter presents the implementation of a second process based on the use of residual to create thermo-mechanically bistable beams.

2 A first fabrication process

2.1. A short overview on microlenses arrays

Microlens arrays are present in a lot of microelectronic technologies, being used to increase the light sensitivity of CCD and CMOS image sensors, to collimate the light from light-emitting diodes (LED), LCD displays, or lasers [Dal Zilio *et al*, 2010]. Several fabrication methods have been developed over the twenty last years like localized doping of glass, mechanical polishing, LIGA process, hydrophobic surfaces... [Daly, 2001]. The main technique, first developed by [Popovic *et al*, 1988] consists in melting photoresist

spots by heating resist above its glass transition temperature. During this reaction, surface tensions can be in competition with resist crosslinking reaction that can hinder the formation of the microlens by increasing the resist's glass transition temperature (Fig.2.1.1a). As a consequence, the formation process of microlenses can be stopped to an intermediary state where the microlens has a low curvature on its edges and a concave shape in the middle [Audran *et al*, 2010]. With the heating temperature, numerous parameters influence the final shape of the microlenses: the substrate type, more or less hydrophilic which modifies the contact angle between the microlenses and the substrate [Wei and Su, 2012], the resist layer's thickness, the resist spots' diameter. Extensive review on these techniques can be found in [Daly, 2001].

2.2. Fabrication process

The first fabrication consists in using microlenses as a sacrificial layer to give an initial curvature to the bimetallic strips. The process can be divided in three major steps: the fabrication of the microlenses, the deposition of the layers constituting the bimetallic strips and finally the etching of the bimetallic strips and of the microlenses to release the microstructures. Each step of this process is presented in Fig.2.2.1b. Details on these steps performed by the TSV team are presented below.

a. Microlenses process

- Spin-coating of a resist TOK TMR-TS01 on the substrate, using HMDS as an adhesion promoter at 900 rpm during 60s (3,8 μ m-thick layer).
- Post-Apply Bake of the resist at 90°C during 90 s to eliminate residual solvent and stabilize the film
- UV-exposition at 365 nm (I-line) (radiation dose between 175 mJ and 330 mJ)
- Development using TMAH 2,38%, two steps of 1 min
- UV-exposition (400mJ) to generate acid molecules used as a catalyzer of the resist crosslinking
- Melting of the resist at 140°C during 5 min
- Annealing at 200°C during 5 min to crosslink the resist polymer.

Fig.2.1.1c and Fig.2.1.1d shows some images of the microlenses obtained with this fabrication process.

b. Bimetallic layers deposition

The main parameters to be taken into account are the raise of the surface temperature during PVD deposition that must not exceed 210° C to avoid resist collapsing and the deposition time that must stay acceptable. As a consequence, deposition power must be adjusted to find a tradeoff between these two constraints. We give a first recipe that was initially used for Ti-Cu bimetallic strips. Similar prodedures are followed for PVD deposition of other materials.

- Three-step PVD deposition of Cu at 5000W (300 s + 300 s in idle mode) in order to create a 3 μ m-thick layer. The temperature stays between 160°C and 166°C.
- Ten-step PVD deposition of Ti at 5000W (210 s + 180 s in idle mode) in order to create a 3 μ m-thick layer. The temperature stays between 166°C and 170°C.

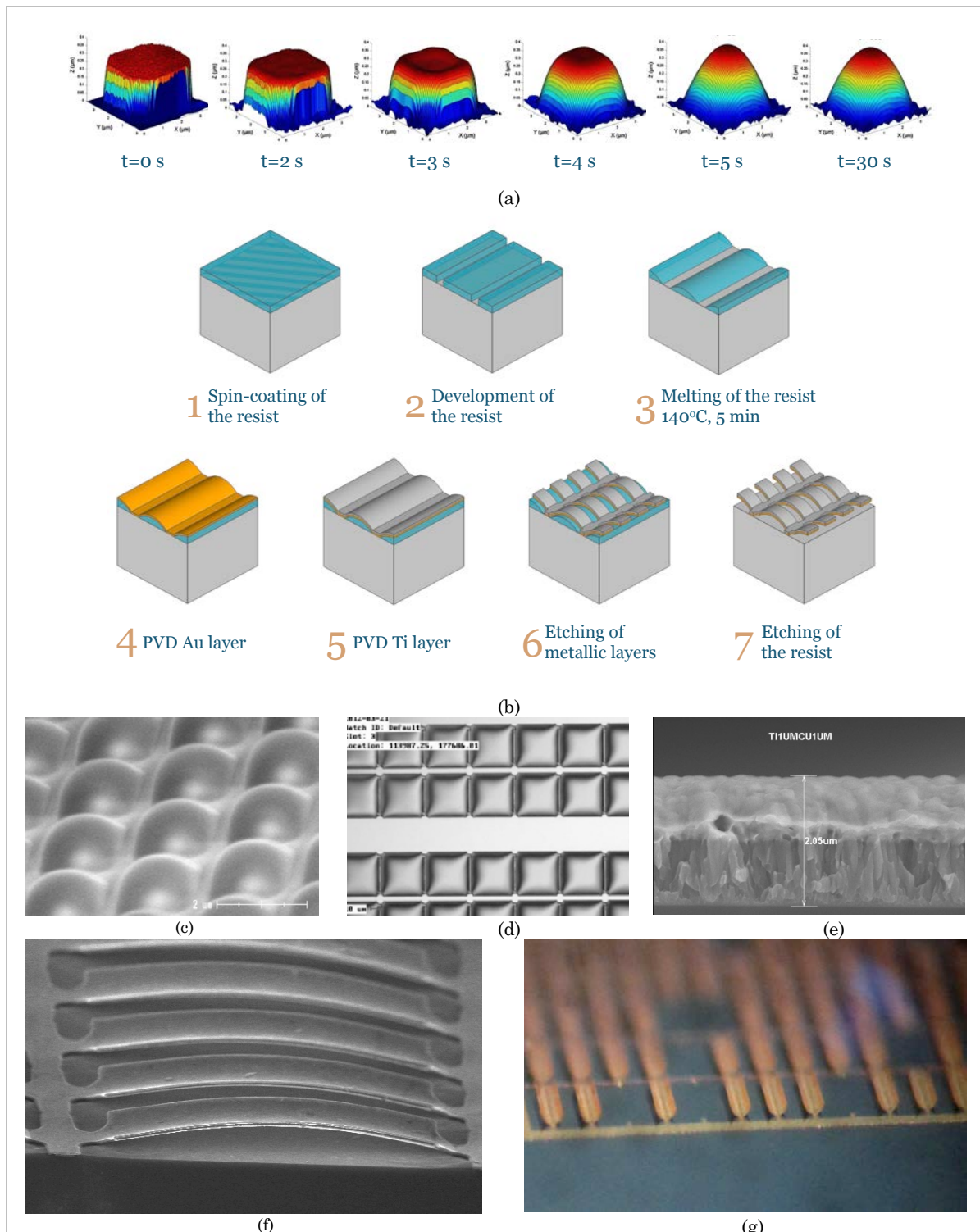


Figure 2.1.1. *a. AFM profiles of microlenses fabricated at STMicroelectronics with different times of heating [Audran et al., 2010]. b. Fabrication process of the bimetallic strips. c. Images microlenses developed at STMicroelectronics. d. Image of square microlenses developed for t_i bimetallic strips fabrication. e. SEM images of the Ti-Cu bimetallic strips (1 μm for each layer). f. Image of Ti-Cu bimetallic strips after releasing. g. Image of heated Ti-Cu bimetallic strips.*

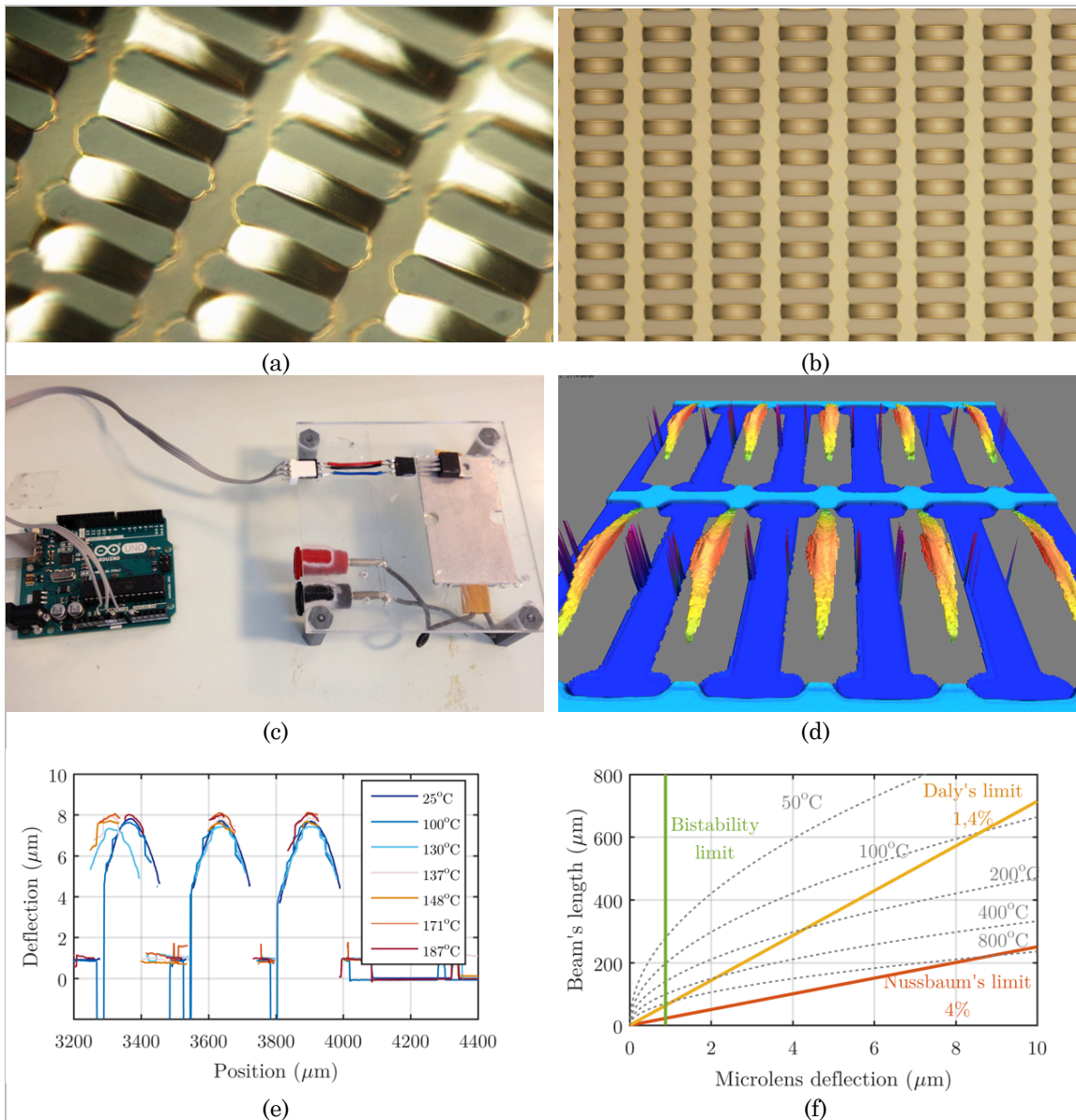


Figure 2.2.1. *a. Tilted image of 210 μm -long Au-Ti bimetallic strips ($0,25 \mu\text{m} - 0,25 \mu\text{m}$) fabricated with $8 \mu\text{m}$ -high microlenses b. Top view of the same bimetallic strips. c. Image of the heating bench. d. Interferometric measurement of the curvature of 210 μm -long Au-Ti bimetallic strips at ambient temperature. e. Profile of bimetallic strips at various temperatures. f. Limit of the use of microlenses.*

c. Etching of bimetallic strips and photoresist's removal

- Ti layer is etched using diluted HF 0,5%
- Copper layer and gold layer are etched with potassium iodide (KI, I_2)
- Wet etching of the microlenses using TMAH 2.38% and DMSO

2.3. Characterization of microstructures

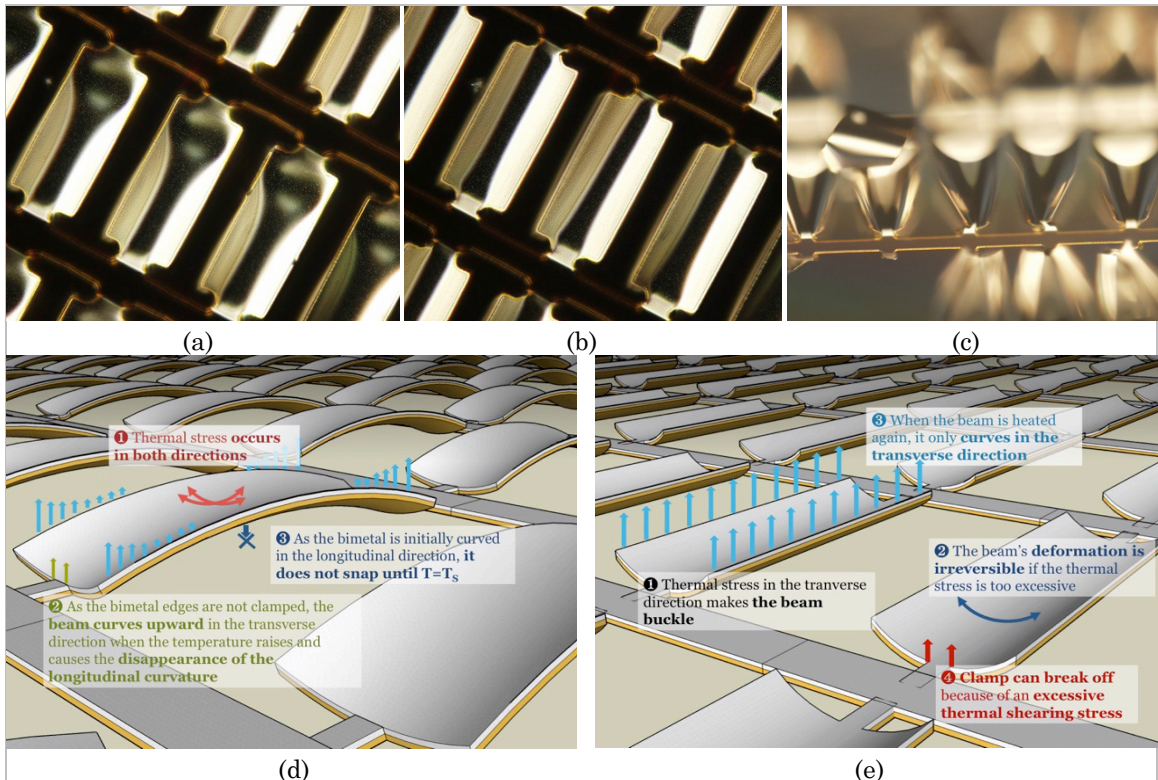
Bimetallic strips were successively made of Ti-Cu, Ti-Au and Ti-Au-Ti. First bimetallic strips made of Ti-Cu suffered from oxidation when they were heated (Fig.2.1.1g). As a consequence, copper layer is replaced by a gold layer that has a lower coefficient of thermal expansion but that does not oxidize. First tests were realized with a stack of Ti-Au in order to validate the possibility to deposit materials without observing collapse of the resist even though Ti-Au bimetallic strips cannot be functional given that Au layer must be on the inner side of the curved strips. Au-Ti bimetallic strips are then fabricated to create functional bimetallic strips. Given delamination issues due to the use of gold layer, a first thin layer of titanium is first deposited on the substrate. Several wafers are processed either with various values of resist thickness (2 – 4 – 8 μm) and various values of metallic layers thickness.

In order to characterize bimetallic strips, a heating bench is fabricated, made of a DBK HP03-09-240 heating resistance, whose temperature is either measured with a TI LM35 temperature sensors supplied by and communicating with an Arduino Uno board (Fig.2.3.1d), or calculated by measuring the input electrical power. Interferometric measurements are performed with a Polytec interferometer. Difficulties encountered with interferometric measurements are linked to the important curvature of bimetallic strips, which hinders the reflection of coherent light to the sensor of the interferometer. As a result, most of the bimetallic strip's surface is not visible on interferometric measurements. Fig.2.2.1f shows that for 210 μm bimetallic strips, no significant variation of the deflection is observed when the temperature raises until 187°C. This absence of deformation for the shortest bimetallic strips is due to their excessive curvature. To simply explain this, we take the example of simply supported beams modeled in Chapter 2. For bimetallic strips like Ti-Au, the minimum initial curvature must represent about 40% of the total thickness. In the case of the bimetallic strips presented in Fig.2.2.1, it is equal to 16 times the beam's thickness. As a result the expected thermal hysteresis is too much important so that bimetallic strips be functional.

To illustrate this, we plot in Fig.2.2.1f the evolution of the mean temperature of the hysteresis as a function of the beam's length and the initial curvature for Ti-Au beams having a total thickness of 4 μm . We also plot two limits found by Daly and Nussbaum defining the limit ratio between the microlens' diameter (which is also the beam's length) and the microlens' height: below these limit values, the diameter of the microlens is too much important and the microlens is not spherical but concave. As a result, bimetallic strip are not functional. As we can see on this figure, to obtain 200 μm -long bimetallic strips with small thermal hysteresis, the initial deflection must be of 0,88 μm . Yet for this value of deflection, the ratio between the beam's length and its initial deflection is far from the limit value experimentally found by Daly [Daly, 2001]. For bimetallic strips that are not clamped on their whole width, an irreversible mechanical deformation is observed. As the effect of residual stress and thermal stress has also an influence on the transverse curvature of bimetallic strips, transverse stress can cause the irreversible buckling of the membranes (Fig.2.2.2a). As a result, the initial curvature conferred by the microlens

finally disappears and the beam only transversally curves when it is heated again (Fig.2.2.2b). The effect of this transverse stress can also break the membranes' clamp (Fig.2.2.3b). As a consequence, microlenses-based fabrication process has many limitations. First, all materials currently used in microelectronics cannot be used to process bistable membranes because the deposition temperature cannot exceed the resist outgassing temperature. Second, the minimal curvature needed to produce beams with small thermal hystereses cannot be obtained with microlenses (Daly's limit or Nussbaum's limit). Third, the membrane's thermal hysteresis depends on the microlenses' curvature but also on the residual stress of the deposited materials layers. For all these reasons, the fabrication process based on the use of resist microlenses is finally abandoned in favor of a fabrication process using the residual stress to create initially buckled beams. In order to avoid the occurrence of transverse buckling, a new set of lithography masks is also designed.

Figure 2.2.2. *a. Image of heated 150 μm -long Au-Ti bimetallic membranes. b. Image of the same bimetallic strips after buckling. c. Tilted image of bimetallic strips suffering from excessive residual stress. d. Effect of thermal stress on partially clamped membranes. e. Post-buckling behavior of bimetallic membranes.*



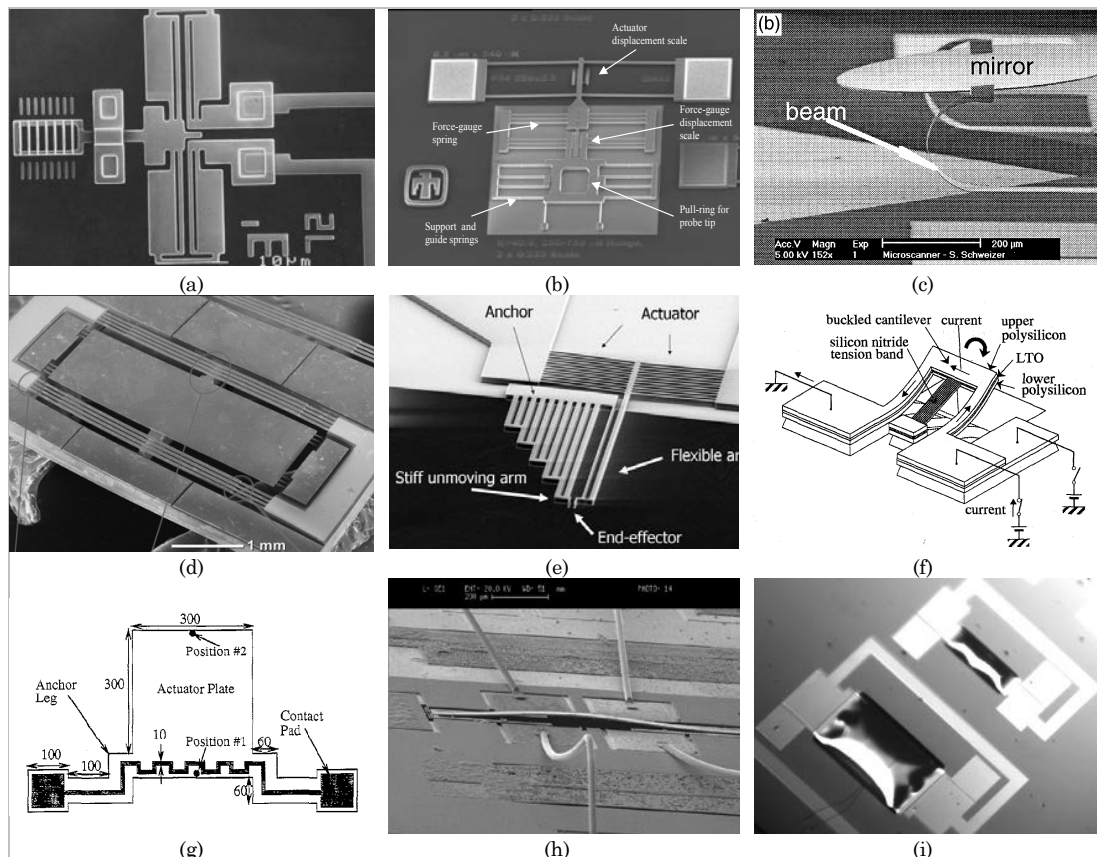


Figure 3.1.1. *a. Example of in-plane heaters presented in [Moulton and Ananthasuresh, 2001]. b. Image of V-Shape thermal actuators presented in [Baker et al, 2004]. c. Image of a thermally actuated micro-mirror presented in [Schweizer et al, 1999] based on bimorph/bimetal effect. d. Image of an out-of-plane micropositioners presented in [Kim et al, 2013] and based on bimorph effect. e. Example of microgrippers presented in [Andersen et al, 2008]. f. Architecture of bistable actuators developed by Matoba and Coworkers in [Matoba et al, 1994]. g. Schematic of bistable actuators proposed in [Lin and Lin 1998]. h. Bistable out-of-plane bimorph actuator developed by [Michael and Kwok, 2007]. i. Out-of-plane piezoelectric bimorph membrane presented in [Trioux, 2015].*

3 A second fabrication process

3.1. Short review on bistable thermal actuators

Even though the development of thermo-mechanically bistable microactuators is less frequent, numerous examples of electro-thermal microactuators, also called heaters [Comtois and Bright, 1997], are reported in the literature, heated by Joule effect and employing either difference of thermal expansion of two materials to produce lateral in-plane or out-of-plane displacements [Riethmuller and Benecke, 1988; Schweizer *et al*, 1999; Kim *et al*, 2013], thermal expansion difference of two legs made of a same materials

having different lengths [Andersen *et al*, 2008], different cross section [Guckel *et al*, 1992; Comptois and Bright, 1997], or an initial inclination of legs like V-shape thermal actuators [Baker *et al*, 2004].

Designing out-of-plane thermally buckled structures was first proposed by Seki and coworkers in [Seki *et al*, 1997]. Their goal was to increase thermal stress sensitivity of a Si beam near its snap temperature in order to create large displacements and important forces with small temperatures variations. They measured displacement of about 30 μm for a 2,5 mm-long, 20 μm -thick Si beam. Other examples of bistable thermal actuators are reported in [Hoffman *et al*, 1999] demonstrating an out-of-plane displacement of 50 μm of a 20mm long, 50 μm -thick silicon membrane supplied with 100mW of electrical power (temperature variation of 150°C), [Lin and Lin, 1998] describing the operation of in-plane actuators (620 μm -long poly-Si structure), displacing from around 4 μm between 200 and 400°C, or [Matoba *et al*, 1994] presented a buckled structure displacing of 6 μm when it supplied with 166 mW of electrical power. Closer to the properties of our own system, we can cite the works of Michael and Kwok [Michael and Kwok, 2006; Michael and Kwok 2007] on the thermal snap-through of multi-layered beams made of Silicon and Silicon oxide heated by Joule effect and snapping at 800°C, or bistable piezoelectric Al-AlN beams developed by Trioux in [Trioux, 2015]. Electro-thermal actuators, either continuous or bistable can be used as micropositionners [Kim *et al*, 2013;] micropumps or microvalves, micro-mirrors [Schweizer *et al*, 1999], optical fiber switches [Hoffman *et al*, 1999] or in the case of thermo-mechanically bistable MEMS as mechanical memory device by exploiting the Shape-Memory Effect of these structures. Applications as relays [Hoffman *et al*, 1999] are less frequent because of the their slow response time compared with electrostatic switches [Lopez-Walle *et al*, 2010].

3.2. Design of new lithography masks

In order to avoid transverse buckling of microstructures and to allow electrical characterization/ Joule heating of thermo-mechanical bistable beams, a new set of lithography masks was created, initially thought and designed for the integration of bimetallic strip heat engines fabricated with the microlenses-based fabrication process but finally used to design initially-buckled beams. Three masks are drawn for the whole fabrication process. A first mask is used to open trenches in the substrate that will be filled of sacrificial material. The second mask is used to design the bimetallic strip and the third mask is used for the creation of the polymer ring whose function is to allow the bonding of the upper wafer and the bottom wafer and to hold the cavity under vacuum. Fig.3.2.1a shows the structure of a single test chip for the characterization of the bimetallic strip heat engine, whereas Fig.3.2.1b is a top view of the three masks and Fig.3.2.1c is a top view of the pattern repeated on the whole surface of the 1X 300 mm-diameter lithography mask. This pattern is made of thirty chips having the same footprint even if each chip is dedicated to a single geometry of bimetallic strips (rectangular, trapezoidal or circular bimetallic strips).

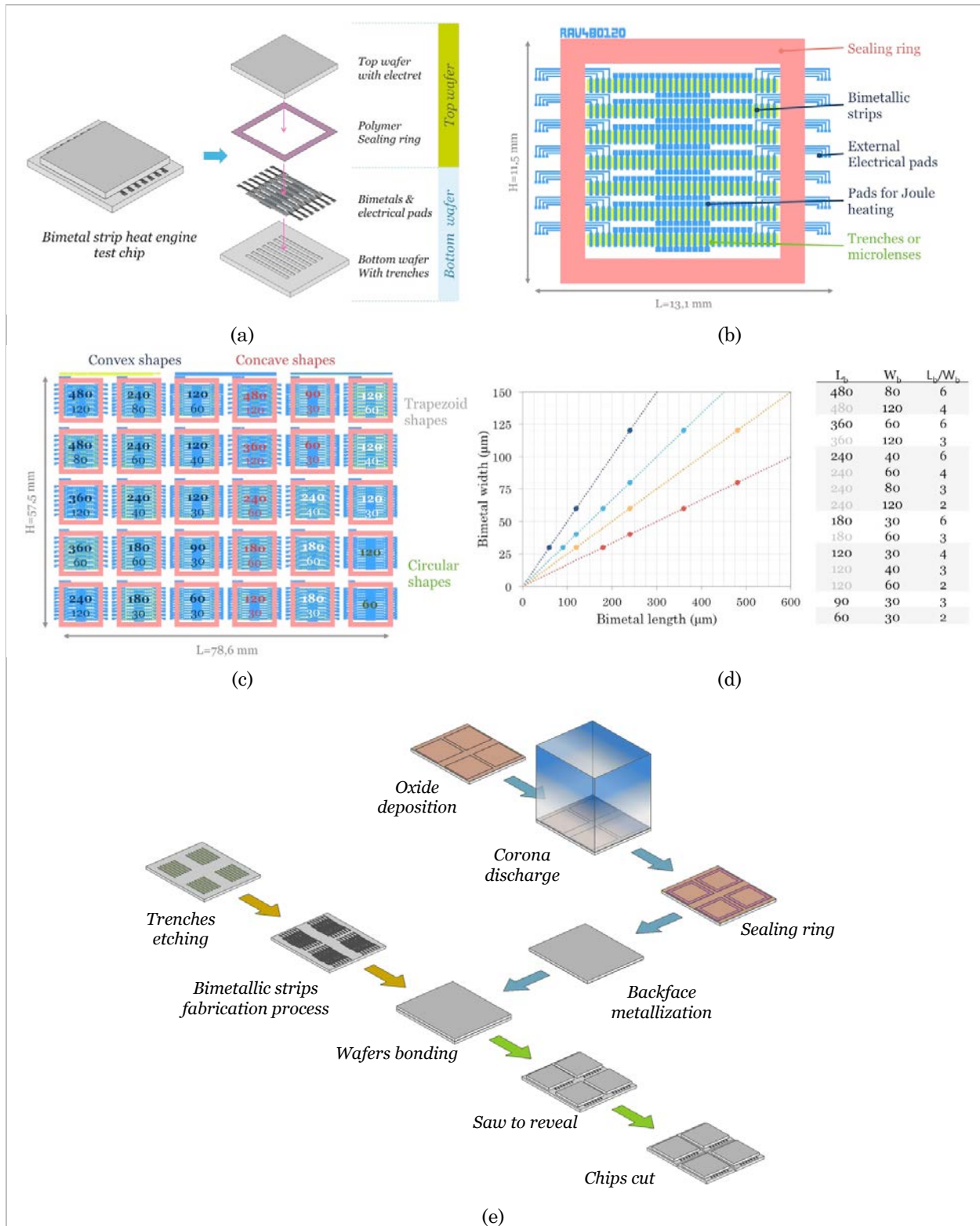


Figure 3.2.1. a. Architecture of the prototype of bimetallic strip heat engine. b. Basic structure of a test chip c. Basic pattern repeated on the set of lithography masks. d. Choice of the dimensions of the bimetallic strips. e. Silicon integration scheme of the bimetallic strip heat engines.

Fifteen different dimensions of bimetallic strips are defined, the beams' length varying from 60 μm to 480 μm and the beams' width from 30 μm to 120 μm , and the length-to-width ratio varying from 2 to 6 (Fig.3.2.1d).

Fig.3.2.1e presents the global fabrication process chosen for the electrostatic bimetallic strip heat engines. Two wafers are separately process: bimetallic strips are fabricated on the bottom wafer, and an oxide layer is created on the top wafer, either by thermal oxidation or by deposition. This oxide layer is then used to create a Corona electret. After having created the sealing ring on the top wafer, the two wafers are bonded together. The top wafer is then sawed in order to reveal the external electrical pads used for the characterization of the bimetallic strip heat engine. Chips are finally separated.

3.3. Design rules of the bimetallic strips

Before presenting the new fabrication process of bistable actuators, we first simulate the behavior of Al-SiO₂ microstructures. Given that the Young Moduli of Aluminum and Silicon oxide are quite equivalent, SiO₂ layer and Al layer will have the same thickness. In that case, we describe a simple procedure to directly process functional bimetallic strips having small thermal hysteresis. We first need to choose a value for the mean working temperature. Knowing the properties of the materials, we can simply find the relation between the mean working temperature and the residual stress (3.3.1a). We then use the criterion of bistability (3.3.1b) to find a relation between the beam's thickness, the beam's length and the residual stress (3.3.1c).

$$T_o = \frac{\sigma_2 - \sigma_1}{E.(\alpha_2 - \alpha_1)} + \theta_o \quad (3.3.1a)$$

$$P_o = i_e \cdot k_{\gamma}^2 \cdot \left(1 + \frac{2 \cdot n_e}{\kappa_C \cdot L}\right) \quad (3.3.1b)$$

$$\frac{\alpha_1 \cdot \sigma_2 - \alpha_2 \cdot \sigma_1}{\alpha_2 - \alpha_1} = v \cdot t^2 \cdot k_{\gamma}^2 \cdot \left(1 + \frac{2 \cdot E \cdot v \cdot t}{\kappa_C \cdot L}\right) \quad (3.3.1c)$$

In the case of Al-SiO₂ bimetallic strip, we can approximate these equations by the set of equations (3.3.2) where the stress is directly expressed in MPa. Given the high coefficient of thermal expansion of Aluminum, we can neglect the influence of the Aluminum film's residual stress in the expression of the bistability criterion.

$$T_o \approx 0,63 \cdot (\sigma_{Al} - \sigma_{SiO_2}) + 25^{\circ}C \quad (3.3.2a)$$

$$t \approx 2,1 \cdot 10^{-3} \cdot \sqrt{|\sigma_{SiO_2}|} \cdot L \quad (3.3.2b)$$

Fig.3.3.1a represents the evolution of the residual stress value in the SiO₂ layer associated to the bistability criterion. It shows that first-order mode buckling occurs for higher values of residual stress if the beam is thicker. For a 240 μm -long 4 μm -thick beam, bistability appears for -63 MPa, and for a 180 μm -long 4 μm -thick beam, bistability appears for a stress of -112 MPa. As we are limited by the thickness of deposited thin films, we will target a value of stress between 80 MPa and 100MPa in Aluminum layers (tensile stress) and between -60 and -100 MPa of compressive stress in SiO₂ layers.

Finally, Fig.3.3.1c and Fig.3.3.1d show the evolution of the thermal hysteresis of bistable beams as a function of the residual stress of each material layer.

3.4. Possible strategies for the development of the second process

A long and complicated step of the creation of the new fabrication process was the definition of the performances requirements for the bimetallic strip heat engines but also of the constraints on the availability of materials, manufacturing techniques and machines on Back-End-Of-Lines (BEOL) facilities of Crolles' 300 mm clean room. Yet a large range of manufacturing machines and process solutions are present in such industrial clean rooms, access to these facilities is generally limited in the case of the development of "exotic" technologies.

In the case of bimetallic strip heat engines, performances requirements are of two types. First, materials composing the thermo-mechanically bistable actuators must have excellent thermo-mechanical properties whose associated metrics are the thermal expansion coefficients difference, but also the Figure-of-Merit we defined in the previous chapter, giving the thermo-mechanical transduction efficiency and the mechanical energy produced during a complete cycle. From that figure, we can see that best bimorphs are mainly made of silicon compounds, like polysilicon, silicon oxide, silicon nitride and of aluminum, copper and gold. Even though polysilicon has very good mechanical properties, (explaining why it is often used as a materials for mechanical parts of MEMS) [Ghodssi and Lin, 2010; French, 2002], and though residual stress in polysilicon thin films can be easily controlled, this material is absent from TSV facilities and finally cannot be used. As a consequence, bistable actuators will be made of silicon oxide or silicon nitride used as passive materials. Because of its high coefficient of thermal expansion, aluminum is in the first instance preferred to copper that faced oxidation issues with the microlenses-based fabrication process and to gold which has a smaller thermal expansion coefficient.

The second requirement of the fabrication process is the capacity to control residual stress in thin films in order to obtain functional bistable actuators, meaning that their thermal hystereses must be small (few degrees) and their snap and snap-back temperature lower than 200°C so that the bistable membranes could harvest low grade heat flux flowing through the heat engine. It may be noted that, in the case where bistable membranes would be used as thermal sensors to disconnect circuits, the condition of weak thermal gradient would not be necessary. RF sputtering is a perfectly suitable deposition technique since it offers many parameters to adjust and control the residual stress in metallic thin films. The influence of RF sputtering process conditions on the residual stress of thin metallic films was highlighted by the successive works (among others) of Hoffman and Thornton [Hoffman and Thornton, 1977], Kim and his coworkers [Kim *et al*, 1998], Chinmulgund and his coworkers [Chinmulgund *et al*, 1995]. It is generally observed that for low temperatures, low substrate bias voltages and low Argon pressures, residual stress in metallic thin films is tensile whereas an increase of the RF power and Argon pressure creates a change from a tensile stress to a compressive stress.

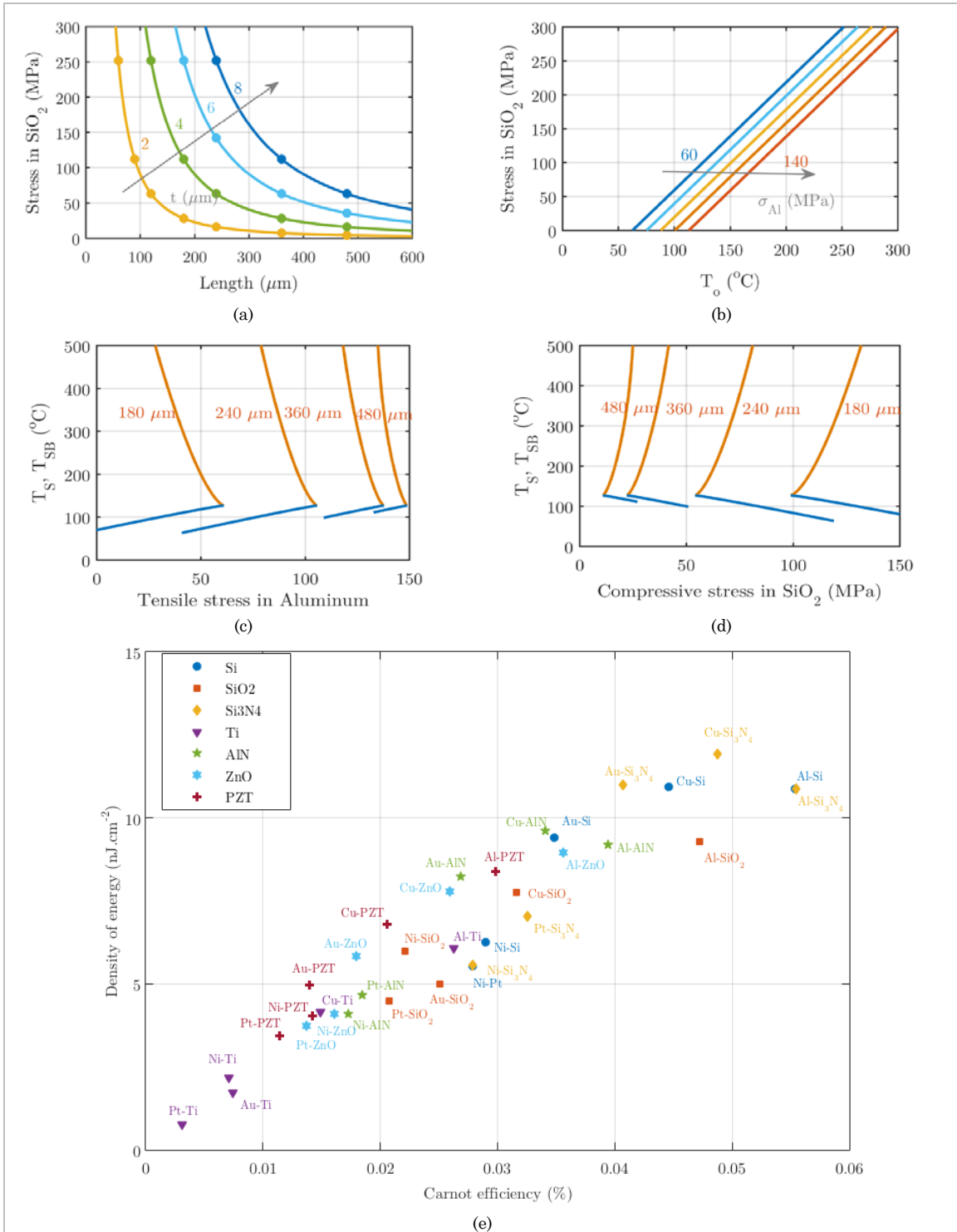


Figure 3.3.1. a. Dependence of the residual stress in SiO₂ on the beam's thickness and beam's length. b. Dependence of the average temperature of the thermal hysteresis on the residual stress in Al and SiO₂ layers. c. and d. Snap and Snap-back temperatures of Al-SiO₂ bistable beams as a function of the stress in materials. e. Figure of Merits of the performances of bimetallic strips.

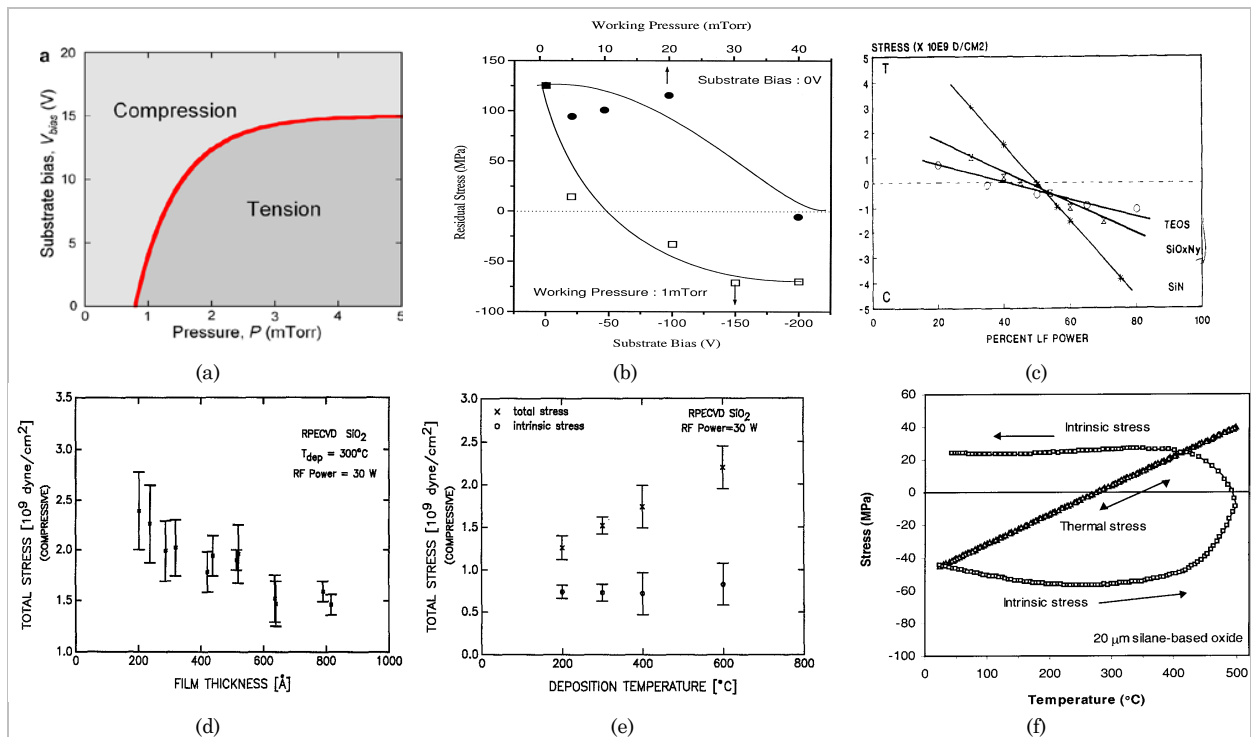


Figure 3.4.1. a. Image showing the dependence of residual stress of metallic thin films on RF sputtering conditions [Detor et al, 2009]. b. Dependence of metallic thin films' residual stress on substrate bias and working pressure according to [Kim et al, 1998]. c. Evolution of PECVD dielectric thin films' residual stress on RF duty cycle according to [Van de Ven et al, 1990]. d. Evolution of dielectric thin films' residual stress on layer thickness [Temple et al, 1993]. e. Dependence of thin films' residual stress on PECVD deposition temperature [Temple et al, 1993]. f. Reduction of thermal stress by thermal annealing [Zhang et al, 2001].

As explained by Windischmann [Windischmann, 1992], this evolution from a tensile stress to a compressive stress is mainly due to atomic peening: as the energy of Argon or metal particles increases with the raise of the substrate bias or temperature, they can cause a densification of thin films. [Hoffman and Thornton, 1977] explained the link between the film microstructure and the type of residual stress. For more informations, we can report to [Windischmann, 1992] and [Detor et al, 2009] presenting various modeling attempts to predict the evolution of the residual stress as a function of the RF sputtering conditions like substrate bias, temperature, film thickness, temperature etc.

Several techniques can be used to deposit SiO₂ or Si₃N₄ thin films, like LPCVD (low pressure chemical vapor deposition), PECVD (Plasma-enhanced chemical vapor deposition), sputtering etc. Details on these various deposition techniques can be found in [Ghodssi and Lin, 2010; Gad-el-hak, 2006]. As PECVD was the main available technique in our case, we only investigated techniques reported in the literature to control the residual stress in dielectric thin films. Residual stress in PECVD thin films is generally known to be a result of the incorporation of hydrogen atoms into the materials layer. Hydrogen atoms come from the reaction precursor SiH₄. Incorporation of hydrogen is more

important in the case of PECVD silicon nitride because of the use of NH_3 as a precursor instead of N_2O for PECVD silicon oxide [Hess, 1984]. As a result, hydrogen atoms cause the densification of the dielectric layer leading to excessive compressive stress. Yet, incorporation of hydrogen atom depends on power supply frequency. Low-frequency plasmas are known to ease diffusion of hydrogen in thin films whereas high frequency leads to porous tensile films. As a result, [Van de Ven *et al*, 1990; Guan *et al*, 2013; Tarraf *et al*, 2003] proposed to use a duty cycle between low-frequency plasma and high-frequency plasma to alternate deposition of compressive films and tensile porous films.

Van de Ven and his coworkers demonstrated a linear relation between the duty cycle and the residual stress [Van de Ven *et al*, 1990] (Fig.3.4.1c). Other parameters that can be adjusted are the Argon flow rate, the ratio between SiH_4 flow and O_2 flow, or the power supply. Raise of power supply, deposition temperature and Argon flow enhances compressive stress because of atomic peening [Temple *et al*, 1993], whereas the increase of the SiH_4/O_2 flow ratio reduces the compressive stress [Kim and Choi, 2000]. If residual stress is too much compressive, thermal annealing allows thin films outgassing hydrogen atoms in order to reduce compressive stress (Fig.3.4.1f). Such techniques are reported in [Zhang *et al*, 2001; Windischmann, 1991; Guan *et al*, 2013].

Now that we found materials and fabrication techniques adapted to the design of low-stress thermo-mechanically bistable actuators, we need to define the type of sacrificial materials adapted to the fabrication of bistable actuators. Sacrificial materials are chosen according their availability on TSV facilities, their etching recipes and etching techniques and the etching selectivity with respect to the materials composing the bistable actuators. We first examined various possible etching materials: Si_3N_4 , Si (bulk), polyimide, photoresist. Si_3N_4 is generally etched with the same liquid etchant than silicon oxide like Buffered Oxide Etch ($\text{NH}_4\text{F}+\text{HF}$ 60 nm/min), or with H_3PO_4 (20 nm/min at 180°C). Yet BOE etches faster silicon oxide (490 nm/min) and H_3PO_4 etches aluminum (530 nm/min). As a consequence Si_3N_4 is not the best sacrificial material. Another solution can be to directly use silicon substrate as a sacrificial layer. Isotropic etching of silicon can be realized by using either liquid etchants KOH (1100 nm/min at 80°C), $\text{NH}_4\text{F}+\text{HNO}_3$ (150 nm/min), SF_6 plasma [Larsen *et al*, 2006], plasmaless dry etching using XeF_2 , BrF_3 or ClF_3 , or by realizing a backside deep-RIE (SF_6 -based RIE with passivation steps using C_4F_8 , around 2000 nm/min). However, KOH rapidly etches aluminum (around 13000 nm/min) and etching selectivity of $\text{NH}_4\text{F}+\text{HNO}_3$ with silicon and SiO_2 is not important. Moreover, as the lithography mask was initially designed for microlenses, no holes were made in the membranes to ease silicon etching. In our case we did not want to release microstructure by using a backside RIE in order to keep the energy harvester's cavity under vacuum. As a result, we abandoned the idea of etching silicon. As we explained in the previous part, photoresists presents the drawback of outgassing at high temperature and to not be compatible with SiO_2 PECVD. Another solution, often applied to the fabrication of RF MEMS switches [Rebeiz, 2003], is to use polyimides as a sacrificial layer, which can be easily etched by using O_2 plasma with very good etching selectivity against SiO_2 and aluminum. Using O_2 plasma also present the advantage of preventing stiction issue that can happen during wet etching.

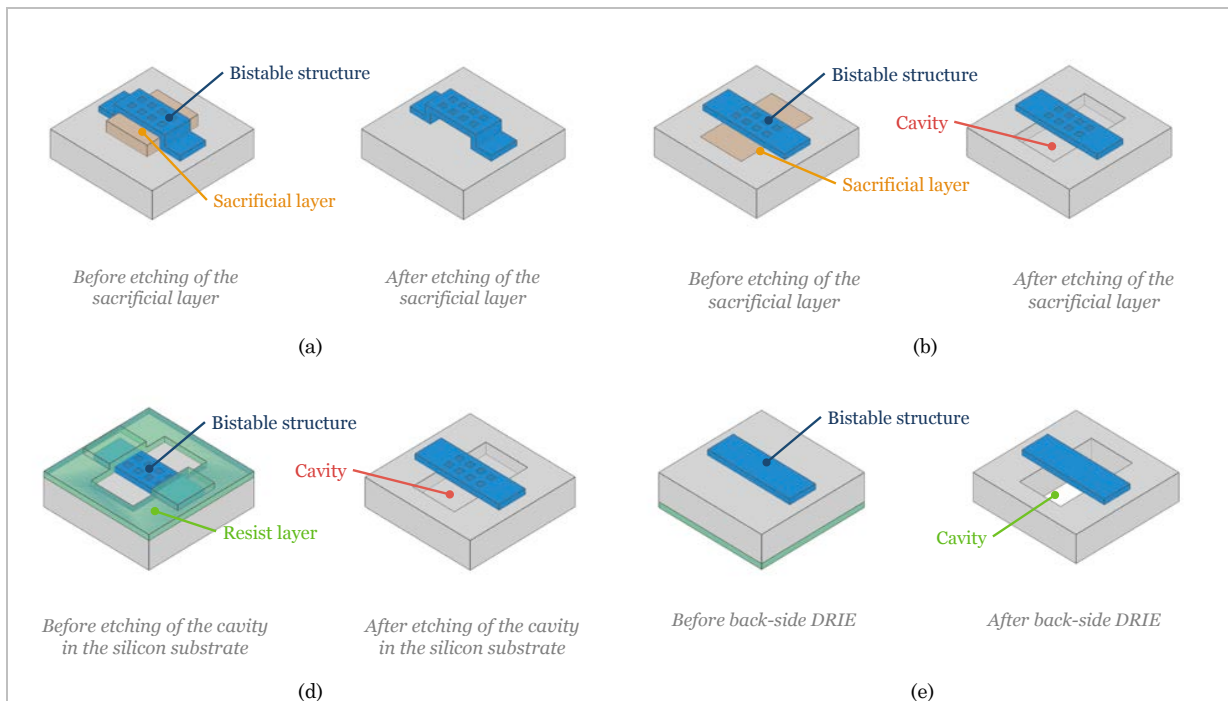


Figure 3.4.2. *a. Fabrication process based on etching of a sacrificial layer directly deposited on silicon substrate b. Fabrication process based on etching of a planarized sacrificial layer in a trench. c. Principle of a fabrication process based on isotropic etching of silicon substrate. d. Principle of a fabrication process based on a backside DRIE.*

3.5. Fabrication process developed at STMicroelectronics

Now that we have presented the various constraints and requirements that have led the design of the new architecture of thermo-mechanically bistable actuator, we detail each step of its fabrication process. The complete fabrication process is presented in Fig.3.5.1. A first lithography is realized using the microlenses' mask in order to define the position of the trenches (CT-3050 negative resist, coating at 800 rpm and softbake at 100°C during 120 s, development with TMAH 90s, and hardbake at 3230°C during 5 min). In order to validate the first fabrication step, etching tests are realized with (CF₄, O₂) RIE (Fig.3.5.1b), and DRIE. (Fig.3.5.1c).

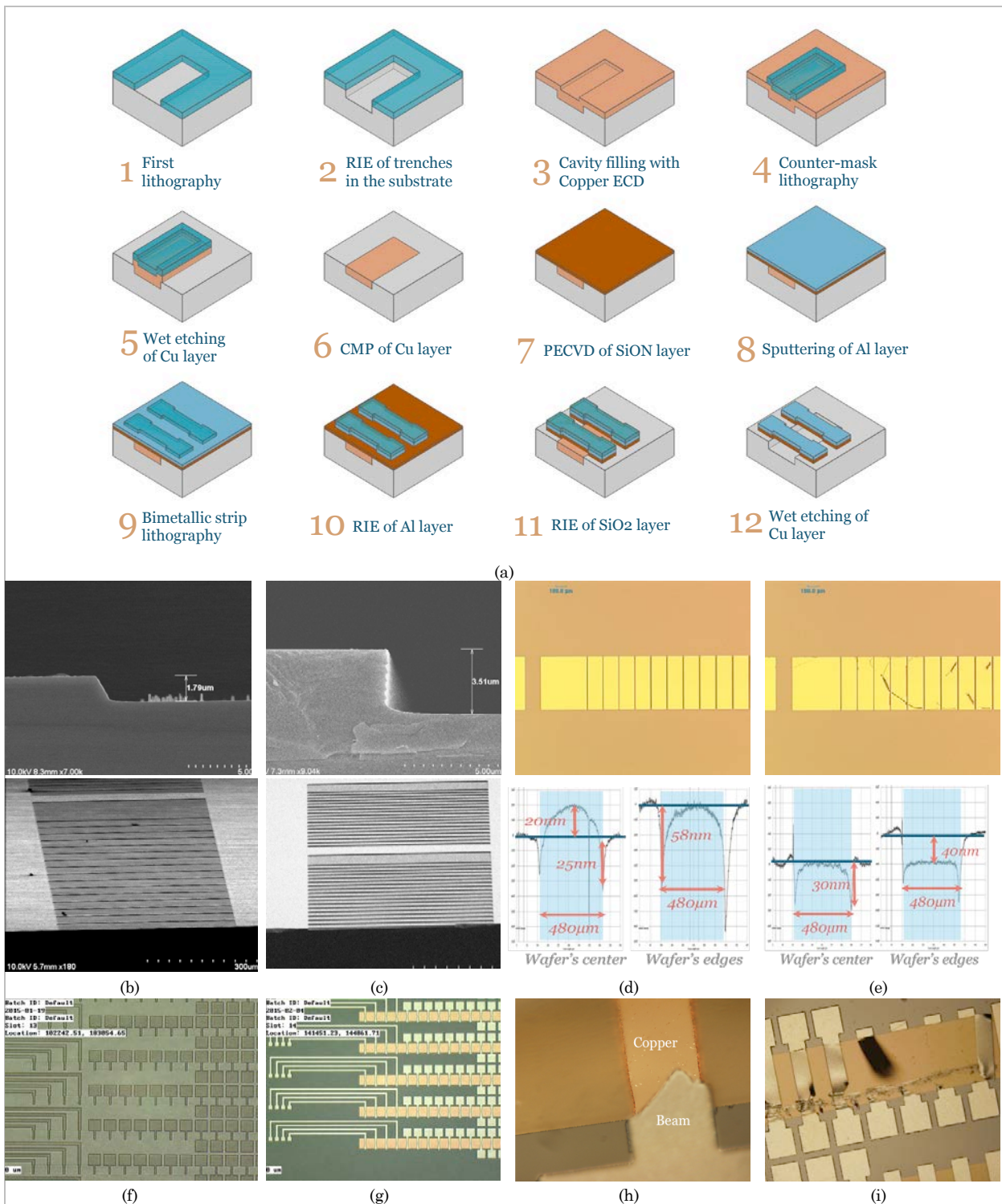


Figure 3.5.1. a. Flow of the second fabrication process. b. Images of trenches realized by RIE. c. Images of trenches realized by DRIE. d. Image and profiles of cavities after CMP. e. Image and profiles of cavities after CMP when a counter-mask is used. f. Image of the wafer after RIE of Al layer. g. Wafer after SiON etching. h. Destructive test on Wafer after NaI₂-based copper etching. i. Test after FeCl₃ etching.

Given the greater consumption of the resist and the over-etching observed with RIE than with DRIE and the better aspect ratio obtained with DRIE, DRIE technique is chosen for the next wafers. A Ti-W seed layer is then sputtered in the cavity to improve the adhesion of copper layer. In order to obtain a plane surface, a chemical-mechanical planarization is performed on the wafers. As the quality and the duration of a CMP step depends on the quantity of materials to be planarized, two solutions are tested: a counter-mask with the microlenses mask is first deposited on the copper layer and a wet etching of the copper layer is performed in order to reduce the surface of copper to be planarized (step 5 of Fig.3.5.1a). For other wafers, planarization is directly realized, without using a counter mask. Results of these two procedures are presented in Fig.3.5.1d and Fig.3.5.1e. The comparison of both methods reveals the presence of a copper protrusion of around 20 nm for the cavities located near the middle of the wafer and no protrusion for cavities near the edges of the wafer when no partial copper layer etching is realized before CMP. When a partial etching step is performed, we observe a better planarity near the center of the wafer and a light overetching at the periphery of the wafer. Moreover the curvature is reduced. In both case, near the edges of the cavities we observed an overetching of about 30 nm, which can be attributed to the scallops created by the DRIE and to the accumulation of slurries during the CMP. Yet it can be noted that the dimensions of protrusion and overetching are of tens nanometers whereas the cavity's length varies between 60 and 480 μm . Given the better results obtained when a partial etching is performed before CMP, this extra step is added to the fabrication process.

As we explained in the previous part, SiON is deposited by means of a PECVD step. The main parameters of these steps are: HF RF power: 245W LF RF load power: 120 W, SiH₄: 150 sccm, N₂O: 450 sccm N₂: 1000 mTorr. Measurements of the wafers' curvature indicated for the first series of wafers (thickness of 1.5 μm) a residual stress of -97 MPa. Aluminum is then deposited by PVD (thickness of 1.5 μm). Residual stress in Al layer is of 105 MPa. Al layer's etching is then realized using a RIE with a CL2 plasma and SiON layer's etching with a RIE with SF₆, C₄F₈ (Pressure between 10 and 48mTorr, source power of 2500 Watts, platen power at 675 Watts). First attempts to selectively etch copper layer with respect to Al layer were made using sodium iodide (NaI), an etching solution generally used to etch gold layers similar to potassium iodide (KI) [Green, 2014], but which can also etch copper with a good selectivity against aluminum. This etching step enabled to fully etch copper layer in the trenches. Yet we observed by destructive methods that NaI-based etching reaction only partially etched copper layer located below SiON-Al stack (Fig.3.5.1h). According to a CEA expert, this could be also linked to the electrochemical potential of Al layer during the etching that hinders the reaction between NaI and Cu. As a consequence, we tried other etching solutions at PTA clean room (CEA). The first solution was to use FeCl₃, which a common etching recipe for copper (at room temperature Cu: 3900 nm/min, Al: 35 nm/min, no significant etching of SiO₂ [Williams *et al*, 2003]). The second etching recipe is based on the use of (NH₄)₂S₂O₈ (at 30°C Cu: 2500 nm/min, Al: 0,3 nm/min, no significant etching of SiO₂ [Williams *et al*, 2003]). In both cases, we observe that structures were released (Fig.3.5.1i).

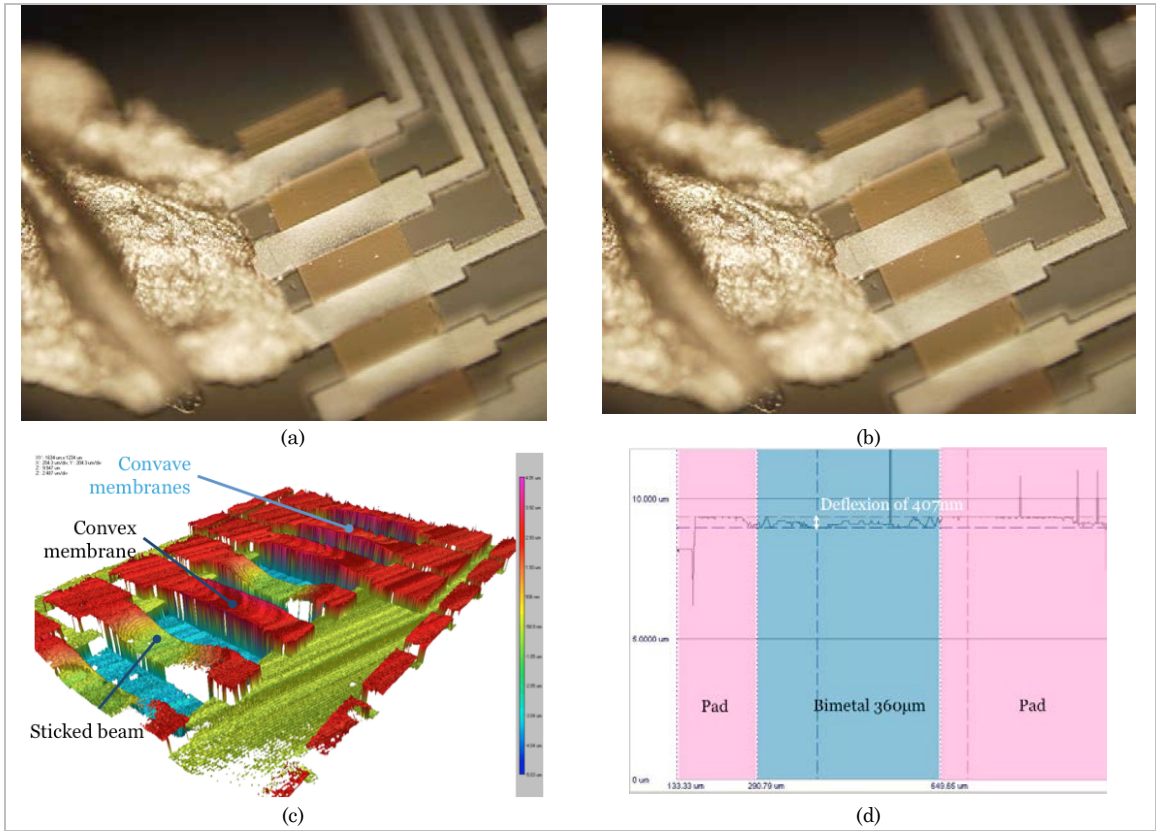


Figure 3.6.1. *a. Unsnapped shape of a 360 μm-long membrane. b. Snapped shape of a heated 360 μm-long membrane. c. Interferometric measurements of a 360 μm-long membranes. e. Longitudinal cut of a 360 μm-long membrane*

3.6. First characterizations of thermal actuators

Few characterizations have already been realized on the bimetallic strip. However these experimental measurements qualitatively demonstrated the thermo-mechanical bistability of some bimorph structures actuated by Joule effect. Yet, microscopy images did not allow precisely measuring the deflection and the curvature of snapping membrane. As a consequence, we will provide more informations on the measurements in the final manuscript.

3.7. Alternative fabrication process

In addition to the fabrication process we developed with TSV team, we developed an alternative fabrication process at CEA’s experimental clean room. Instead of sputtering copper to form a sacrificial layer, we proposed to release microstructures by selectively etching silicon under microstructures with XeF₂ (Fig.3.7.1a). As a result, the fabrication process begins by the PECVD of a SiON layer and the PVD of an Al layer, and is followed by the etching of the Al-layer using a mixture of H₃PO₄ and HNO₃. SiON layer is then etched using a CHF₃-based RIE. Finally, silicon is etched using XeF₂. Compared with the previous fabrication process, this one presents the advantage of being simpler, with fewer steps. The fact of using holes to ease releasing of the micro-structures plays also a role on

the reduction of the residual stress. Moreover, the masks designed for this fabrication process integrate more test structures for the measurement of residual stress in SiON and Al layers. As SiON layer's residual stress is expected to be compressive, we designed series of beams of various lengths so that their buckling allows locally determining the average value of the compressive residual stress. In order to determine stress gradient in SiON layer and in Al layer, we also designed cantilever beams whose curvature is directly proportional to this residual stress. By designing bimorph cantilever beams we can finally deduct the average tensile stress in Al layer. Another solution to determine this stress would have been to design Guckle rings on the lithography masks. As for the previous part, more details on these process and on structures' characterization will be provided later.

4 Conclusion

In this last chapter, we presented the work done on the fabrication of thermo-mechanically bistable actuators at the micro-scale. Three fabrication processes were presented. The first one adapted the microlenses' technology developed at STMicroelectronics for CMOS sensors to create initially curved membranes. Yet characterizations of bimetallic structures and bibliography work have shown the inability of this fabrication method to produce thermo-mechanically bistable structures operating with small thermal hysteresis and at low temperature ($<200^{\circ}\text{C}$). As a consequence, this fabrication process was finally abandoned and two new fabrication process were developed in order to exploit residual stress to fabricate initially buckled membranes. The first one, enabled to manufacture membranes exhibiting thermo-mechanical bistability even if few characterizations were made up to now. The second fabrication is in course of development in CEA's experimental clean room. Characterizations of microstructures are in progress to determine if there is an agreement between the experimental data and the predictive model.

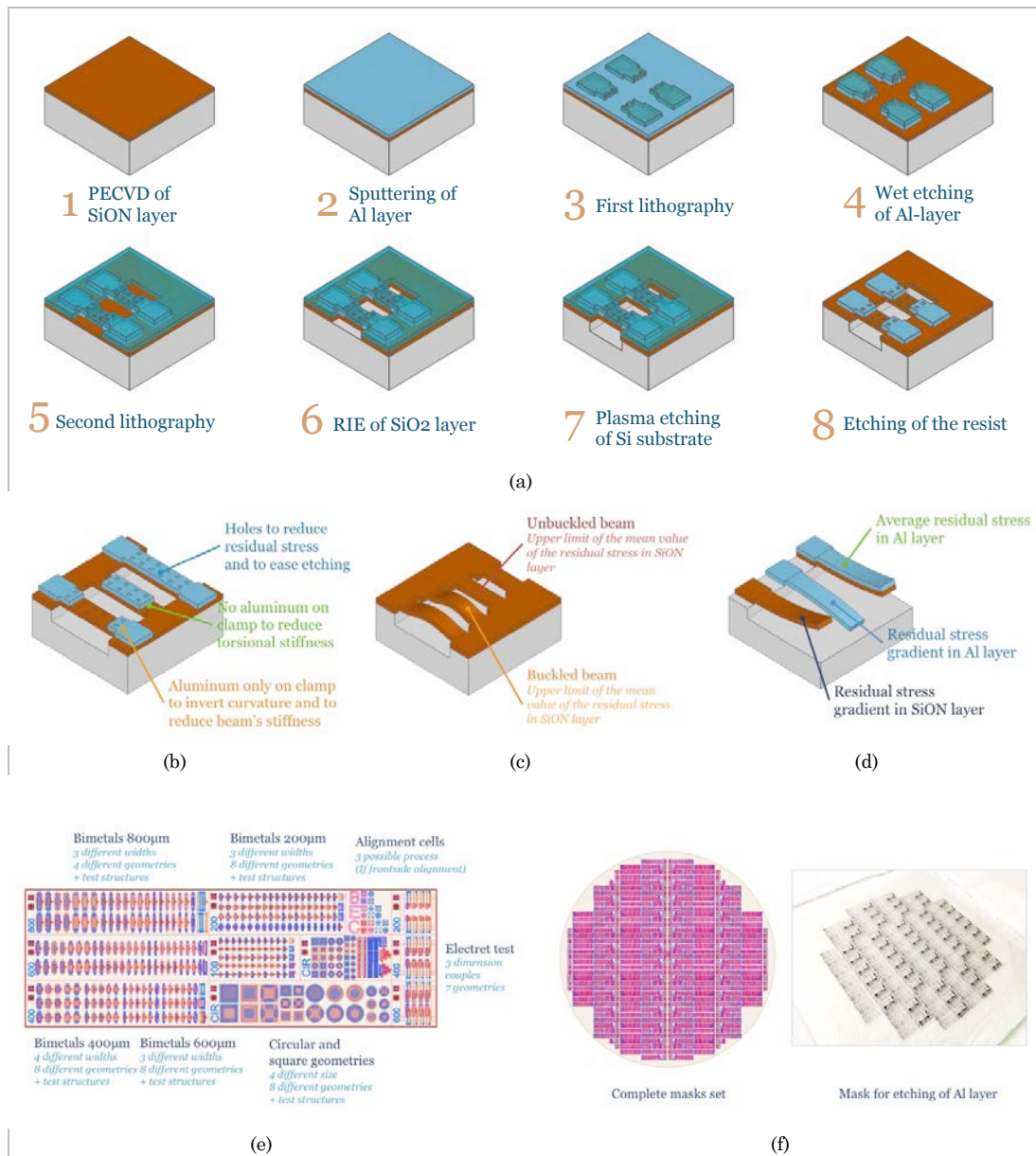


Figure 3.7.1. a. Third fabrication process. b. Example of alternative structures. c. Buckled beams to measure residual stress. d. Cantilevers to measure stress gradients. e. Detail of the lithography masks. f. Complete set of masks.

5 Bibliography

Andersen, K., Carlson, K., Petersen, D., Mølhave, K., Eichhorn, V., Fatikow, S. and Bøggild, P. (2008). Electrothermal microgrippers for pick-and-place operations. *Microelectronic Engineering*, 85(5-6), pp.1128-1130.

- Audran, S., Mortini, B., Faure, B. and Schlatter, G. (2010). Dynamical formation of microlenses by the reflow method: numerical simulation and experimental study of the process fabrication. *J. Micromech. Microeng.*, 20(9), p.095008.
- Baker, M. S., Plass, R. A., Headley, T. J. & Walraven, J. A. (2004) Final Report: Compliant Thermomechanical MEMS Actuators LDRD #52553, Sandia Report SAND2004-6635, Sandia National Laboratories, Albuquerque, NM
- Chinmulgund, M., Inturi, R. and Barnard, J. (1995). Effect of Ar gas pressure on growth, structure, and mechanical properties of sputtered Ti, Al, TiAl, and Ti3Al films. *Thin Solid Films*, 270(1-2), pp.260-263.
- Comtois, J. and Bright, V. (1997). Applications for surface-micromachined polysilicon thermal actuators and arrays. *Sensors and Actuators A: Physical*, 58(1), pp.19-25.
- Dal Zilio, S., Giustina, G., Brusatin, G. and Tormen, M. (2010). Microlens arrays on large area UV transparent hybrid sol-gel materials for optical tools. *Microelectronic Engineering*, 87(5-8), pp.1143-1146.
- Daly, D. (2001). *Microlens arrays*. London: Taylor & Francis.
- Detor, A., Hodge, A., Chason, E., Wang, Y., Xu, H., Conyers, M., Nikroo, A. and Hamza, A. (2009). Stress and microstructure evolution in thick sputtered films. *Acta Materialia*, 57(7), pp.2055-2065.
- French, P. (2002). Polysilicon: a versatile material for microsystems. *Sensors and Actuators A: Physical*, 99(1-2), pp.3-12.
- Gad-el-Hak, M. (2006). *MEMS*. Boca Raton, FL: CRC/Taylor & Francis.
- Ghodssi, R. and Lin, P. (2010). *MEMS materials and processes handbook*. New York: Springer.
- Green, T. (2014). Gold etching for microfabrication. *Gold Bulletin*, 47(3), pp.205-216.
- Guan, D., Bruccoleri, A., Heilmann, R. and Schattenburg, M. (2013). Stress control of plasma enhanced chemical vapor deposited silicon oxide film from tetraethoxysilane. *J. Micromech. Microeng.*, 24(2), p.027001.
- Guckel, H., Klein, J., Christenson, T., Skrobis, K., Laudon, M. and Lovell, E. (1992). Thermo-magnetic metal flexure actuators. *Technical Digest IEEE Solid-State Sensor and Actuator Workshop*.
- Hess, D. (1984). Plasma-enhanced CVD: Oxides, nitrides, transition metals, and transition metal silicides. *Journal of Vacuum Science & Technology A: Vacuum, Surfaces, and Films*, 2(2), p.244.
- Hoffman, D. and Thornton, J. (1977). The compressive stress transition in Al, V, Zr, Nb and W metal films sputtered at low working pressures. *Thin Solid Films*, 45(2), pp.387-396.
- Hoffmann, M., Kopka, P. and Voges, E. (1999). Bistable micromechanical fiber-optic switches on silicon with thermal actuators. *Sensors and Actuators A: Physical*, 78(1), pp.28-35.

- Kim, S., Choi, H. and Choi, S. (1998). A study on the crystallographic orientation with residual stress and electrical property of Al films deposited by sputtering. *Thin Solid Films*, 322(1-2), pp.298-302.
- Kim, S. and Choi, S. (2000). The origin of intrinsic stress and its relaxation for SiOF thin films deposited by electron cyclotron resonance plasma-enhanced chemical vapor deposition. *Thin Solid Films*, 379(1-2), pp.259-264.
- Kim, Y., Dagalakis, N. and Gupta, S. (2013). Creating large out-of-plane displacement electrothermal motion stage by incorporating beams with step features. *J. Micromech. Microeng.*, 23(5), p.055008.
- Larsen, K., Petersen, D. and Hansen, O. (2006). Study of the Roughness in a Photoresist Masked, Isotropic, SF6-Based ICP Silicon Etch. *Journal of The Electrochemical Society*, 153(12), p.G1051.
- Lin, L. and Lin, S. (1998). Vertically driven microactuators by electrothermal buckling effects. *Sensors and Actuators A: Physical*, 71(1-2), pp.35-39.
- López-Walle, B., Gauthier, M. and Chaillet, N. (2010). Dynamic modelling for thermal micro-actuators using thermal networks. *International Journal of Thermal Sciences*, 49(11), pp.2108-2116.
- Matoba, H., Ishikawa, T., Kim, C. and Muller, R. (1994). A bistable snapping microactuator. *Proceedings IEEE Micro Electro Mechanical Systems An Investigation of Micro Structures, Sensors, Actuators, Machines and Robotic Systems*.
- Michael, A. and Kwok, C. (2006). Design criteria for bi-stable behavior in a buckled multi-layered MEMS bridge. *J. Micromech. Microeng.*, 16(10), pp.2034-2043.
- Michael, A. and Kwok, C. (2007). Thermo-mechanical behavior of buckled multi-layered micro-bridges. *Sensors and Actuators A: Physical*, 137(1), pp.157-168.
- Moulton, T. and Ananthasuresh, G. (2001). Micromechanical devices with embedded electro-thermal-compliant actuation. *Sensors and Actuators A: Physical*, 90(1-2), pp.38-48.
- Popovic, Z., Sprague, R. and Neville Connell, G. (1988). Technique for monolithic fabrication of microlens arrays. *Appl. Opt.*, 27(7), p.1281.
- Rebeiz, G. (2003). *RF MEMS*. Hoboken, NJ: J. Wiley.
- Riethmuller, W. and Benecke, W. (1988). Thermally excited silicon microactuators. *IEEE Trans. Electron Devices*, 35(6), pp.758-763.
- Schweizer, S., Calmes, S., Laudon, M. and Renaud, P. (1999). Thermally actuated optical microscanner with large angle and low consumption. *Sensors and Actuators A: Physical*, 76(1-3), pp.470-477.
- Seki, T., Sakata, M., Nakajima, T. and Matsumoto, M. (1997). Thermal buckling actuator for micro relays. *Proceedings of International Solid State Sensors and Actuators Conference (Transducers '97)*.

- Tarraf, A., Daleiden, J., Irmer, S., Prasai, D. and Hillmer, H. (2003). Stress investigation of PECVD dielectric layers for advanced optical MEMS. *J. Micromech. Microeng.*, 14(3), pp.317-323.
- Temple, D., Reisman, A., Fountain, G.G., Walters, M., & Hattangady, S.V. (1993). Mechanical-Stress in SiO₂-Films Obtained by Remote Plasma-Enhanced Chemical Vapor-Deposition. *Journal of the Electrochemical Society*, 140 (2):564-567.
- Van de Ven, E., Connick, I. and Harrus, A. (1990). Advantages of dual frequency PECVD for deposition of ILD and passivation films. *Seventh International IEEE Conference on VLSI Multilevel Interconnection*.
- Vangbo, M. and Bäcklund, Y. (1998). A lateral symmetrically bistable buckled beam. *J. Micromech. Microeng.*, 8(1), pp.29-32.
- Wei, H. and Su, G. (2012). Fabrication of a transparent and self-assembled microlens array using hydrophilic effect and electric field pulling. *J. Micromech. Microeng.*, 22(2), p.025007.
- Williams, K., Gupta, K. and Wasilik, M. (2003). Etch rates for micromachining processing-part II. *Journal of Microelectromechanical Systems*, 12(6), pp.761-778.
- Windischmann, H. (1991). Intrinsic stress and mechanical properties of hydrogenated silicon carbide produced by plasma-enhanced chemical vapor deposition. *Journal of Vacuum Science & Technology A: Vacuum, Surfaces, and Films*, 9(4), p.2459.
- Zhang, X., Chen, K., Ghodssi, R., Ayón, A. and Spearing, S. (2001). Residual stress and fracture in thick tetraethylorthosilicate (TEOS) and silane-based PECVD oxide films. *Sensors and Actuators A: Physical*, 91(3), pp.373-380.

General conclusion

The work presented in this PhD manuscript thesis dealt with the modeling and the silicon integration of miniaturized electrostatic bimetallic strip heat engines whose function is to generate usable electrical power from heat flux created by thermal gradients.

In a first time, this thesis presented an overview of the various physical coupling phenomena that can be used to transform heat into electrical energy: among these, we presented heat engines using thermoelectric materials, pyroelectric/ferroelectric materials, ferromagnetic materials, but SMA and bimetallic strip. This first study allowed to highlight the interest of exploiting phase transitions to maximize thermal coupling. Finally, we compared the performances of these different technologies and we showed that thermoelectric materials are the most efficient materials to transform heat into electricity, followed by ferroelectric and ferromagnetic materials, Shape Memory Alloys and then fluids and solid materials, these three last categories needing a second conversion step to convert mechanical energy into electrical energy.

In order to provide design rules for the system and to theoretically evaluate the performances of the bimetallic strip heat engines, great efforts were made to understand the origins of the thermo-mechanical instability of bimetallic beams. We explained how initial curvature (or residual stress) and thermal expansion modify the mechanical behavior of composite beams. Thanks to this work, we were able to model the thermal snap-through of composite beams, to find the conditions on the bimetallic strips geometry and on the choice of the materials which must be filled to observe the occurrence of any hysteretic behavior. This enabled to theoretically demonstrate the possibility to convert heat into mechanical energy by placing a bistable bimetallic strip between two heat sources at different temperature, but also to evaluate the energetical performances of these heat engines. We then coupled this mechanical model with a thermal model of the device's architecture in order to predict the dynamic performances of the generator.

In a second time, we proposed several models to explain the performances of the current generators that are based either on pyroelectric coupling, piezoelectric coupling and electrostatic coupling. For each device, we gave laws describing the evolution of the energetical performances, thus allowing a comparison of between each generator. These models finally showed that the best solution to convert heat into electrical energy is to laminate a bimetallic strip with a pyroelectric material in order to create a tertiary pyroelectric effect that enhances the performances of the heat engine for small values of the bimetallic strip's thermal hysteresis.

Finally, we applied these various models to the prediction of the performances of the miniaturized bimetallic strip heat engines. This allowed us to establish scaling rules of the performances of the generators when they are miniaturized down to the sub-millimetric scale, and to give design rules for the silicon integration of the electrostatic generators. From these scaling laws, we deduced that there are limitations to the miniaturization of the bimetallic strip heat engines. Main issues are: important reduction of the energy generated during a complete cycle, reduction of the output voltages of pyroelectric bimetallic strip heat engines, reduction of the pull-in voltage limiting the maximal value of the electret potential surfaces, small capacitances, reduction of the conversion efficiency due to the increase of the thermal leakage. However, it is possible to find other applications to thermo-mechanically bistable beams: for instance, bistable beams could be used as electro-thermal switches integrated in CMOS circuits.

In the last part of this thesis, we presented three fabrication processes developed either in the 300-mm facilities of STMicroelectronics, Crolles, or in CEA's experimental clean room. The first fabrication process was an innovative solution based on the use of microlenses arrays. Yet we demonstrated that this type of fabrication process was unable to produce functional thermo-mechanically bistable beams. As a consequence, we developed two other fabrication processes exploiting residual stress in materials in order to buckle membrane and to control the thermo-mechanical behavior of these bistable membrane. Characterization of these structures is ongoing but we already qualitatively demonstrated the possibility to produce thermo-mechanically bistable membrane with these fabrication processes, opening the way to the development of bistable thermal actuators.

MODELING AND DESIGN OF THERMOMECHANICAL CONVERSION FOR THERMAL ENERGY HARVESTING APPLICATIONS

RESUME

Le développement de systèmes de récupération d'énergie (ou energy harvesting systems en anglais) va de pair avec l'émergence de l'Internet des Objets et notamment la prolifération de réseaux de capteurs devant répondre aux besoins croissants en informations, que ce soit dans le domaine de l'industrie, de la santé, de la domotique ou de l'environnement qu'il soit urbain ou naturel. Les progrès réalisés ces dernières années dans le domaine des Technologies de l'Information et de la Communication ont permis de lever certains verrous technologiques au développement de ces réseaux de capteurs intelligents et autonomes, notamment grâce à l'amélioration des performances intrinsèques des composants microélectroniques (vitesse, consommation), la conception de circuits plus économes en énergie, ou bien la mise en place de standards de communications radio adaptés à ces contraintes énergétiques. Étant donné l'ubiquité des sources d'énergie, la fabrication de générateurs permettant d'alimenter directement ces capteurs à partir de ces sources représente une alternative viable à l'utilisation de batteries pour prolonger la durée de vie de ces capteurs communicants. Diverses technologies de générateurs ont ainsi été proposées pour s'adapter aux différentes formes que peut prendre l'énergie, qu'elle soit d'origine thermique, mécanique, solaire ou électromagnétique.

Le présent travail est une contribution au développement de certains dispositifs de récupération thermiques basés sur l'exploitation des propriétés thermiques et mécaniques de bilames thermostatique. Ce type de générateurs, proposé et développé au sein de STMicroelectronics à Crolles, se veut être une alternative fiable et bas coût à l'utilisation de matériaux thermoélectriques exploitant l'effet Seebeck pour générer de l'énergie électrique. Divers dispositifs ont déjà été fabriqués, démontrant la capacité des moteurs thermiques à base de bilames thermostatiques à alimenter des capteurs autonomes en fonctionnement synchrone et asynchrone. L'objectif de cette thèse est alors de démontrer la possibilité de miniaturiser de tels moteurs thermiques grâce aux techniques de fabrications utilisées en microélectronique. Afin de garantir le fonctionnement de ces systèmes à micro-échelle, un important travail de fond a d'abord été effectué sur la compréhension et la modélisation des phénomènes de couplages thermomécaniques à l'origine du comportement bistable des membranes bimétalliques. Ce travail a débouché sur la démonstration théorique du fonctionnement des moteurs thermiques à base de bilames et sur l'évaluation de leur performances énergétiques (énergie disponible, efficacité thermique, efficacité de Carnot relative). Dans la continuité de ce premier modèle, d'autres travaux ont été menés pour évaluer les performances de moteurs thermiques exploitant différents phénomènes de couplage électromécanique en vue de convertir l'énergie mécanique générée par les bilames thermostatiques en énergie électrique exploitable par les capteurs autonomes. La simulation du comportement des micro-générateurs à l'aide de ces divers modèles a débouché sur des lois d'échelles sur les performances des moteurs thermiques. Finalement, divers procédés de fabrications ont été développés pour permettre la fabrication de microstructures thermiquement bistables ■

SUMMARY

The development of energy harvesting systems is linked to the emergence of the Internet of Things (IoT) and especially the proliferation of Wireless Sensors Networks that should respond to the growing needs for monitoring data in domains as diverse as the industry, the urban or natural environments, the home, or the human body etc. Recent progress in the field of information technologies have enabled to remove some of the technical obstacles to the deployment of these smart and autonom devices, in particular thanks to the improvement of the performances of microelectronic components, the design of ultra-low-power circuits, or the creation of wireless communications standards adapted to the energy needs of wireless sensors. Given the great availability of energy sources, energy harvesters are reliable alternatives to batteries in order to extend the autonomy of these sensors. Various technologies of generators have been developed to adapt to the type of local energy sources (heat, vibration, light, radio-frequencies).

The present work is a contribution to the development of thermal energy harvesters exploiting the thermal and mechanical properties of bimetal thermostats. This type of technology developed at STMicroelectronics are intended to be a reliable and low-cost alternative to the use of thermoelectric materials exploiting Seebeck effect to generate electricity from heat. Various devices were already fabricated at the macro-scale, demonstrating their ability to power wireless sensor nodes. In the continuity of these works, this PhD thesis aims to demonstrate the operation of these generators at the sub-millimetric scale. As a consequence, an important work on the modeling of the thermo-mechanical instability of bimetallic strips was made to understand the operation of bimetallic strip heat engines. This work enabled to theoretically demonstrate the capability of bimetallic to transform heat into mechanical energy and to evaluate the performances of such heat engines. Coupling between bimetallic strip heat engines and electro-mechanical transducers was also modeled to compare the performances of the current prototypes of generators. We then modeled the thermo-mechanical behavior of composite beams at the microscale and established scaling rules of the performances of the bimetallic strip heat engines, We finally developed microelectronic fabrication process to manufacture thermo-mechanically bistable beams at the microscale ■